INVESTIGATIONS OF THE MOVEMENT AND STRUCTURE OF D-REGION IONOSPHERIC IRREGULARITIES

By

W.K. HOCKING, B.Sc. (Hons)

A Thesis

presented for the degree of

DOCTOR OF PHILOSOPHY

at the

UNIVERSITY OF ADELAIDE

(Physics Department)

FEBRUARY 1981

VOLUME II

CONTENTS

Page

VOLUME II

CONTENTS Continued....

CONTENTS Continued....

CONTENTS Continued..... Page

CHAPTER XI Continued

APPENDICES

CHAPTER VI

THE EFFECTS OF NOISE ON THE SIGNAL

6.1 Introduction

It is of course desirable that the effects of noise be minimized in any experiment. Any noise which is recorded should at least be monitored, so an idea of its mean level can be gained. Averaging sets of successive points can help to reduce the effective noise level. This is a very useful technique if complex data is used, and the averaging length is less than about one quarter of the shortest period at which the signal varies (the procedure is generally called "coherent integration".) However, if amplitude-only data is recorded, great care must be taken when averaging sets of successive points. Such a procedure does reduce the noise - but also has the effect of distorting the signal. The purpose of this chapter is to show just when averaging is allowable, and what happens to the data if averaging is applied when it should not be.

It is shown that the presence of noise in a signal which is sampled with amplitude-only distorts the autocovariance of the signal, but sampling with powers (intensity) leaves the autocovariance looking similar to that for the signal alone, save for a noise spike at zero time lag. Formulae are derived from which the RMS noise can be calculated using the autocovariance of the intensity of the signal plus noise. The simplifications in obtaining such noise estimates when data is recorded as complex data are also pointed out.

6.2 Notation and Assumptions

6.2.1 Notation

In this chapter, the following notation will be adhered to as closely as possible.

Before detection, the total received signal will be considered to consist of 3 contributions.

$$\underline{y}(t) = \underline{S}(t) + \underline{r}(t) + \underline{e}(t) \quad (=y(t)e^{j\phi_y(t)}). \tag{6.2.1.1}$$

where

$$\underline{S}(t) = S(t)e^{j\phi_s(t)} \qquad S = |\underline{S}| \tag{6.2.1.2}$$

$$\underline{r}(t) = r(t)e^{j\phi_r(t)} \qquad r = |\underline{r}| \tag{6.2.1.3}$$

$$\underline{e}(t) = e(t)e^{j\phi_e(t)} \qquad e = |\underline{e}| \tag{6.2.1.4}$$

are three complex signals. (The notation $\underline{x}$ will represent a complex vector, and x will represent its magnitude).

$\underline{S}(t)$ shall be called a "specular component", though it may vary slowly in time.

$\underline{r}(t)$ shall be called a "random scatter" component. This is assumed to satisfy Rayleigh assumptions, with RMS value k_r. However, each successive point of $\underline{r}(t)$ is not assumed to be uncorrelated. It is assumed that the autocorrelation of $\underline{r}(t)$ has finite width. For example, $\underline{r}(t)$ might be the signal produced by scatter from turbulence.

Let

$$\underline{D}(t) = D(t)e^{j\phi_D(t)} = \underline{S} + \underline{r}: \; D(t) = |\underline{D}| = |\underline{S} + \underline{r}| \tag{6.2.1.5}$$

This will be called the "data component" of the total received signal (or the information or message). If $\underline{S}$ is a constant, $|D(t)|$ is Rice distributed.

The term $\underline{e}(t)$ shall be called the "external noise". It represents the unwanted component. This is also assumed to satisfy Rayleigh assumptions (as was $\underline{r}(t)$), with RMS value k_e. (The incoming noise on the antenna is wide-band, but becomes band-limited by the effect of the receiver. Impulsive noise such as atmospherics is excluded.)

Let

(6.2.1.6) $$\underline{n}(t)e^{j\phi_n(t)} = \underline{r} + \underline{e}. \quad \text{Here } n(t) = |\underline{r} + \underline{e}|$$

This represents the total random component of $\underline{y}$. It consists of a random component carrying useful data, $\underline{r}(t)$, and an external (unwanted) noise component $\underline{e}(t)$. $\underline{n}(t)$ has RMS value $k_n=(k_e^2+k_r^2)^{\frac{1}{2}}$ (see Chapter V).

Thus this situation represents the type of signal which may be received from the ionosphere, with a specular contribution, a random contribution (e.g. turbulent scatter) and an unwanted external noise contribution. The features are distinguished by their fading times (i.e. the time for the magnitude of their complex autocorrelation to fall to 0.5). The external noise has a fading time defined by the receiver bandwidth - if the frequency response is Gaussian and the bandwidth at halfpower is 25kHz (typical of the receivers used in this thesis), then the fading time is $.44/(25\times10^3)$ seconds $\simeq$ 18μs. At the PRFs used in this thesis ($\simeq$20Hz), the autocorrelations of this external noise will be uncorrelated after 1 shift. The random scatter component produces fading times in the region 1-3s. (e.g. beam broadening, turbulent fluctuations etc). The specular components have much longer fading times.

After detection an amplitude-only signal, which will be denoted as $y(t)(= |\underline{y}(t)|)$, will result.

If there had been no external noise, the amplitude detected would have been $D(t) = |\underline{S} + \underline{r}|$.

Notice in all these definitions, a line under the symbol (e.g. $\underline{y}(t)$) implies a complex vector, whereas the lack of such a line means the amplitude only (e.g. $y(t)$) is being considered.

The following parameters will also prove useful:

α = Rice Parameter of total received signal $y(t)$

It will be seen that the autocovariance of the amplitude-only signal looks like the following:

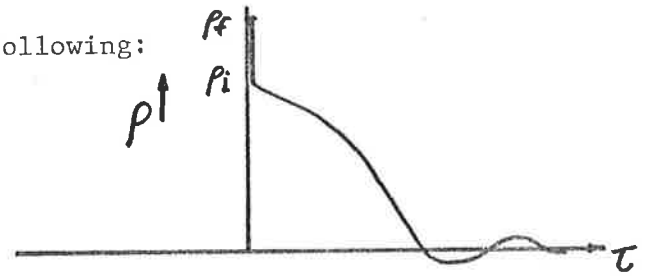

$\rho_y(\tau)$: The autocovariance of $y(t)$ will be denoted by $\rho_y(\tau)$.

ρ_f = Autocovariance of $y(t)$ at $\tau=0$ (the "full" autocovariance).

ρ_i = interpolated autocovariance at zero shift - i.e. the narrow spike due to the external noise is interpolated across.

Likewise, an autocovariance of the powers (intensity) can also be formed.

$\rho_{yp}(\tau)$ = autocovariance of the total power (intensity) $y^2(t)$

ρ_{fp} = autocovariance of the power $y^2(t)$ at $\tau=0$

ρ_{ip} = interpolated autocovariance of the intensity autocovariance at $\tau=0$.

A running mean of length δ on the data $y(t)$ will also be considered at times, to produce a function $m(t)$. Occasionally $y(t)$ will be written as $y(t)=m(t)+e_m(t)$, $e_m(t)$ being zero mean noise.

The following will also be used:

$E(y^n)$ = expectation value for y^n for the Rice distributed series $y(t)$.

δ_j = j^{th} interval used in splitting data into intervals (see later).

$[D]_j$ = constant value assumed for D(t) in δ_j.

$E_\delta(y^n)_j$ = expectation value in the j^{th} interval assuming a constant data signal $[D]_j$, plus noise.

$y_p(t) = (y(t))^2$

$m_p(t)$ = running mean of $y_p(t)$.

< > indicates overall average

$< >_i$ indicates average in interval i.

At one stage, it is assumed D(t) is Rice distributed, $(R_s(D))$ with specular component Ξ and RMS scatter component k_R. This has Rice parameter α_D.

$\rho_D(t)$ = autocovariance of information signal amplitude, had there been no noise.

$\rho_s = \rho_D(o)$

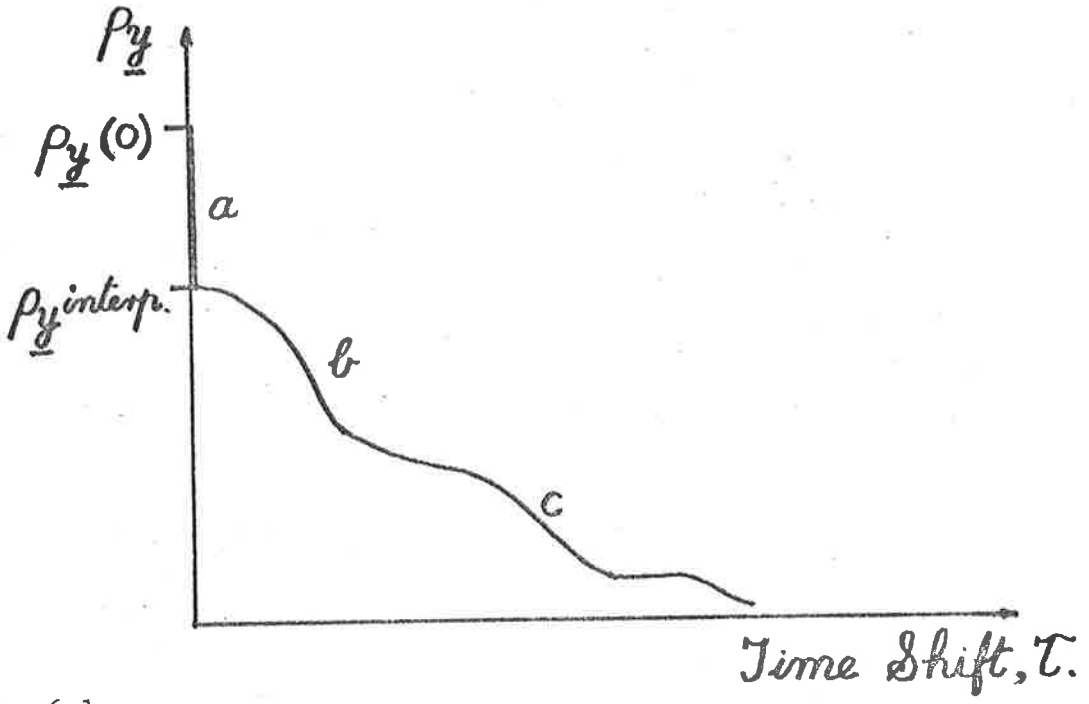

Fig. 6.1

Diagramatic illustration of the magnitude of the complex autocovariance of the signal $\underline{y}(t)$ described in Section 6.2. The Section (a) represents the autocovariance due to the noise, and becomes uncorrelated extremely quickly. Then there is a more slowly falling component (b) due to the random scatter contribution, and finally a very slowly falling component (c) due to the specular part of the signal.

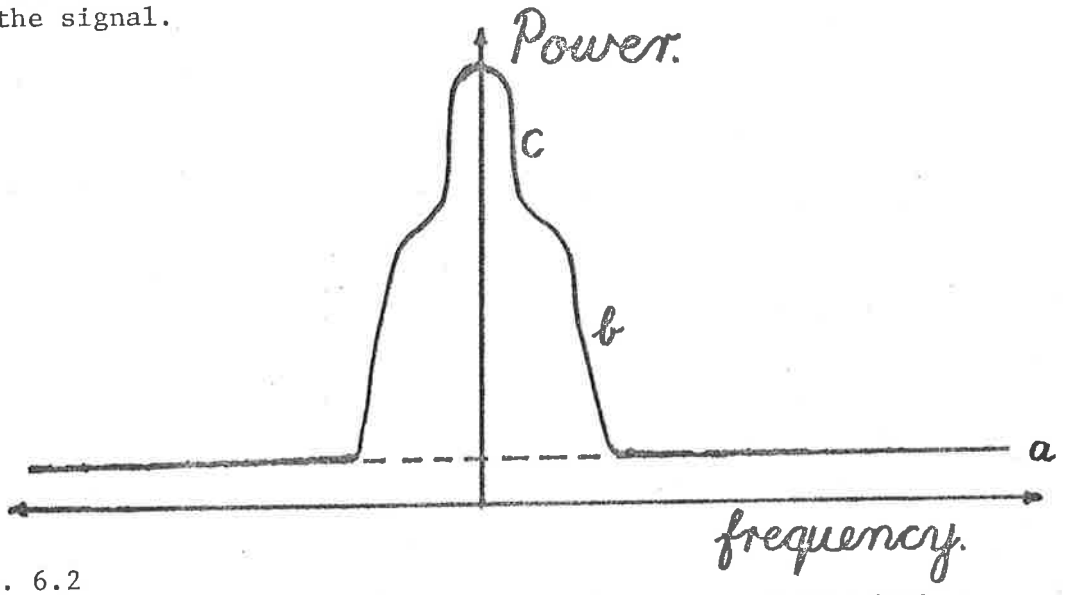

Fig. 6.2

Power spectrum of y(t). In actual fact, an individual power spectrum would show considerable fluctuation between successive points (e.g. see Chapter VII for examples), but this is the result after smoothing. The part (a) is the noise component, and would eventually fall to zero at large positive and negative frequencies (since the spike (a) in Fig. 61. has non-zero width). The part (b) is due to random scatter, and (c) is due to the specular component, just as in Fig. 6.1.

6.3 Complex Data

6.3.1 Determination of noise using complex data

Consider the complex autocovariance of the time series $\underline{y}(t)$ described in section 6.2. It will look like Fig. 6.1. Let the i^{th} point recorded be $\underline{y}_i = \underline{S}_i + \underline{r}_i + \underline{e}_i$. Then the autocovariance at zero lag is

$$(6.3.1.1) \qquad \rho_{\underline{y}}(0) = \frac{1}{N} \sum_{i=1}^{N} (\underline{y}_i - \overline{\underline{y}})\ (\underline{y}_i - \overline{\underline{y}})^*$$

$$= \frac{1}{N} \sum_{i=1}^{N} |\ \underline{D}_i + \underline{e}_i - \overline{\underline{D}}|^2,$$

since $\underline{y}_i = \underline{D}_i + \underline{e}_i$, and since $\overline{\underline{y}} = \overline{\underline{D}}$. The latter follows because the mean value of the external noise, $\overline{\underline{e}}$, is zero.

Thus

$$\rho_{\underline{y}}(o) = \frac{1}{N} \sum_{i=1}^{N} \{((D_{Ri} - \overline{D}_R) + e_{Ri})^2 + ((D_{Ii} - \overline{D}_I) + \underline{e}_{Ii})^2\},$$

where

$$\underline{D}_i = D_{Ri} + jD_{Ii},\ \underline{e}_i = e_{Ri} + j\ e_{Ii},\ j = \sqrt{-1}.$$

Expanding

$$\rho_{\underline{y}}(o) = \frac{1}{N} \sum_{i=1}^{N} \{(D_{Ri} - \overline{D}_R)^2 + (D_{Ii} - \overline{D}_I)^2\}$$

$$+ \frac{1}{N} \sum_{i=1}^{N} (e^2_{Ri} + e^2_{Ii}) + \frac{2}{N} \sum_{i=1}^{N} (D_{Ri} - \overline{D}_R)\ e_{Ri}$$

$$+ \frac{2}{N} \sum_{i=1}^{N} (D_{Ii} - \overline{D}_I)\ e_{Ii} \quad .$$

The first term is the autocovariance which would have been obtained had there been no noise. The second term is simply the mean squared noise, k_e^2. The last two terms are zero, (ignoring statistical fluctuations) since $(D_{Ri} - \overline{D}_R)$ and e_R are uncorrelated and each has zero mean. Likewise $(D_{Ii} - \overline{D}_I)$ and e_{Ii}.

Thus

(6.3.1.2) $\rho_{\underline{y}}(o)$ = Autocovariance due to the information (data) component of the signal $+ k_e^2$.

If the autocovariance at a small lag is considered, it is possible, in a similar way to the above, to show that the value obtained is simply the value which would have been obtained had there been no noise, and of course this is nearly the autocovariance due to the information component of the signal at 0 lag.

In fact, if the autocovariance is interpolated across the spike to produce $\rho_{\underline{y}_{interp}}$ in Fig. 6.1, then $\rho_{\underline{y}_{interp}}$ is equal to the autocovariance at 0 had there been no noise. This and 6.3.1.2 means that

(6.3.1.3) $$\rho_{\underline{y}}(o) = \rho_{\underline{y}_{interp}} + k_e^2.$$

Hence if the complex autocovariance function is obtained, $(\rho_{\underline{y}}(\tau))$, and $\rho_{\underline{y}}(o)$ and $\rho_{\underline{y}_{interp}}$ are obtained, the mean square external noise (noise power or intensity) can be easily obtained as

(6.3.1.4) $$k_e^2 = \rho_{\underline{y}}(o) - \rho_{\underline{y}_{interp}}$$

It is instructive to consider this derivation from another point of view. Since $\underline{S}(t)$, $\underline{r}(t)$ and $\underline{e}(t)$ are all uncorrelated, the power spectrum of $\underline{y}(t) = \underline{S} + \underline{r} + \underline{e}$ is simply the sum of the individual power spectra of $\underline{S}$, $\underline{r}$ and $\underline{e}$. The resultant is a function as shown in Fig. 6.2. Now the Fourier transform of the sum of several functions is the sum of the respective individual Fourier transforms, and the Fourier transform of the power spectrum is the autocovariance. Thus the autocovariance of $\underline{y}(t)$ is the sum of the individual autocovariances of $\underline{S}$, $\underline{r}$ and $\underline{e}$.

Hence we again see an autocovariance like Fig. 6.1 is produced. The spike (a) has a length equal to the area under part (c) of Fig. 6.2, which is of course the mean power, k_e^2. Thus it is again clear that 6.3.1.4 is valid (ignoring statistical fluctuations).

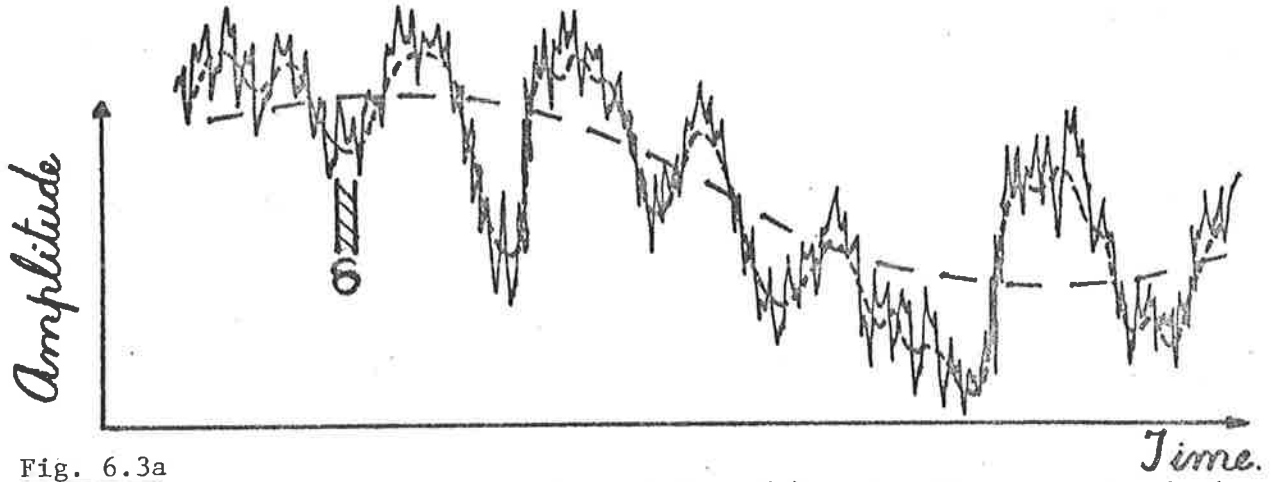

Fig. 6.3a

Typical amplitude-only data series y(t). The slowly varying broken line represents the amplitude of the specular component, and the faster varying broken line represents the amplitude which would have resulted if there had been no external noise, - that is, the information part of the signal, $D(t)=|\underline{S}+\underline{r}|$.

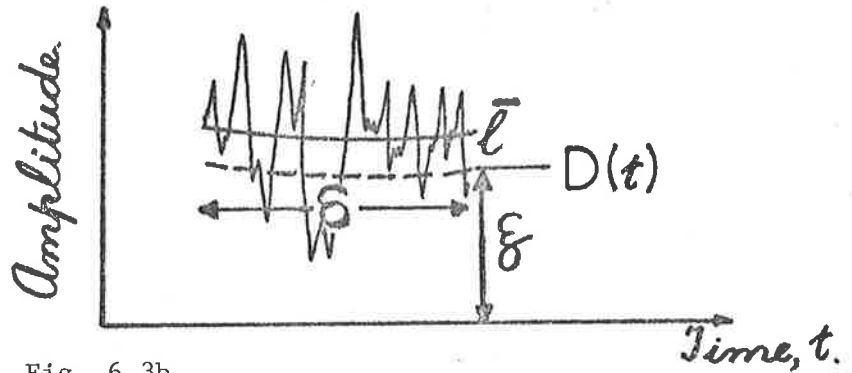

Fig. 6.3b

An expanded view of the section δ in Fig. 6.3a. The solid line $\bar{\ell}$ represents the average signal, and ξ is the effective "specular component" for this interval.

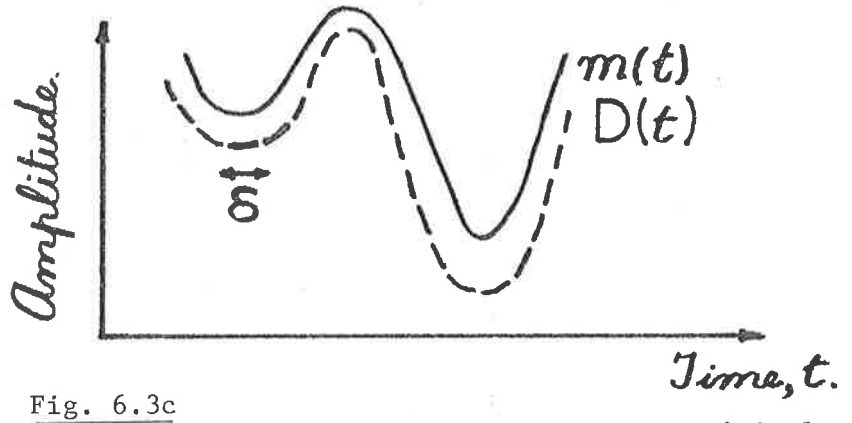

Fig. 6.3c

View of a section, several times δ in length, of the total signal, after a running mean of length δ has been applied. This is represented by m(t). The broken line shows the signal which would have resulted had there been no external noise, D(t).

6.4 Amplitude-Only Sampling

6.4.1 Effect of noise on the data series

Consider the time series of the amplitude-only series y(t), as shown in Fig. 6.3a. Now consider a length of data, δ, from this time series, sufficiently short that the information part of the signal ($\underline{D}(t)$) does not change significantly in this period. Then this section is Rice-distributed, with "steady component" ξ (ξ actually being due to the specular signal $\underline{S}$ and the random scatter signal $\underline{r}$), and RMS noise k_e. The distribution is given by equation 5.2.1.15 in Chapter V, with $k \to k_e$ and $S \to \xi$.

Suppose now an experimenter decides to reduce the effect of noise by averaging in blocks of length δ. Then the mean signal will be somewhat more than ξ, as shown in Fig. 6.3b. The mean is in fact given by equation 5.2.2.7, Chapter V; i.e.

$$\bar{y}_\delta = E_\delta(y) = k_e \, \Gamma(3/2) \, {}_1F_1 \, (-\tfrac{1}{2}; 1; -\alpha^2/2) \qquad (6.4.1.1)$$

Where $\alpha = \sqrt{2}\xi/k_e$, $\Gamma(3/2) = \sqrt{\pi}/2.$,

and $\bar{y}_\delta$, $E_\delta(y)$ refer to the mean in the interval δ.

The important thing is that $(E_\delta(y)-\xi)$ is a function of ξ (see Fig. 6.4). Thus if we were to imagine a running mean of length δ being applied to the data, the resultant would be as illustrated by the solid line in Fig. 6.3c. For large D(t), the mean is only slightly greater than the true D(t); for small D(t), the mean is significantly greater than D(t). When D(t) is zero, the mean is $\sqrt{\pi}/2 \; k_e$. A brief description as to why noise is least important for large D(t) is given in Fig. 6.4b. It is quite clear that this averaged signal is NOT the same in form as the amplitude which would have resulted had there been no external noise. The data series has been distorted.

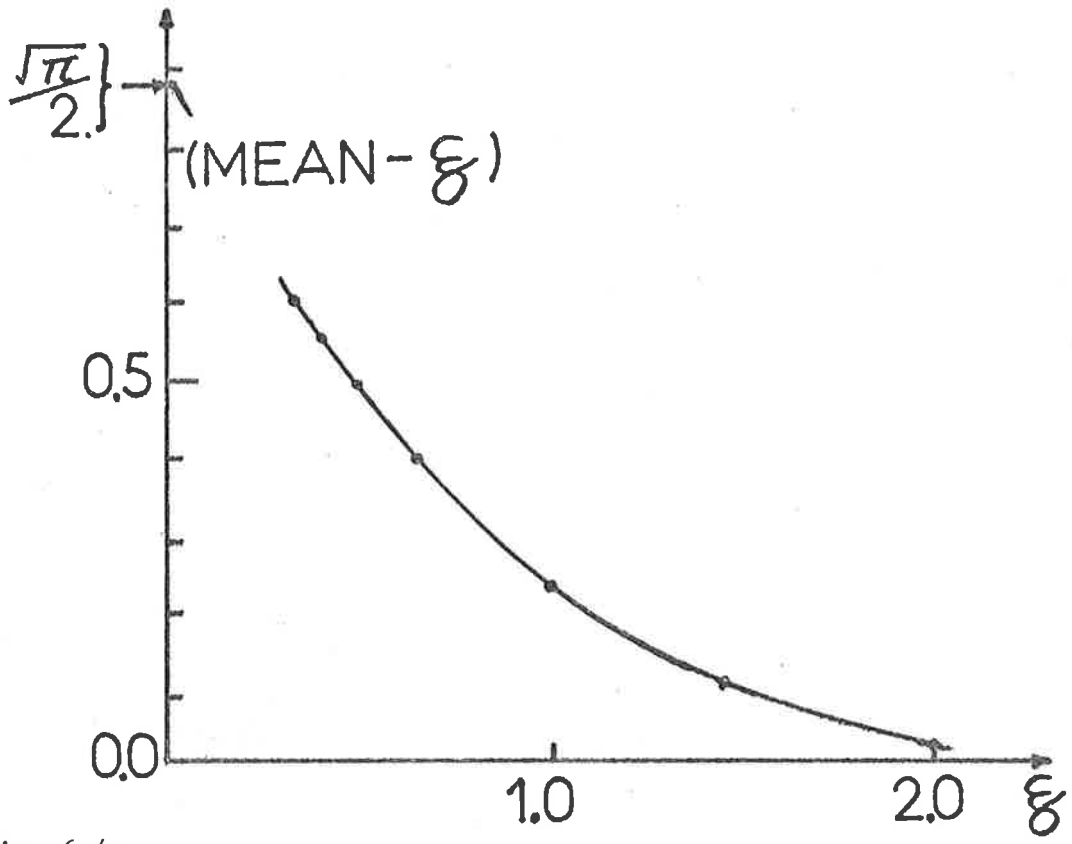

Fig. 6.4a

(Mean Value - specular component ξ) for a Rice distributed sample with RMS noise $k_e = 1.0$, as a function of the specular component ξ. Notice for zero specular component, the mean is that of the noise alone - i.e. $\frac{\sqrt{\pi}}{2} k_e$.

Fig. 6.4b

The mean value for a large specular component plus weak noise is approximately the specular component. This can be seen in this diagram. Here, $\underline{k}$ represents a typical noise vector, and it can have any orientation. The resultant $\underline{\ell} \simeq \underline{\xi}$ + the projection of $\underline{k}$ on ξ (the "in phase" component, say). The projection on ξ is taken as positive if it is in the same direction as $\underline{\xi}$, and negative in the case shown here. The projection of $\underline{k}$ on $\underline{\xi}$ has a mean which is close to zero for large ξ, so the mean of $|\underline{\ell}|$ tends to $|\underline{\xi}|$.

What if we had averaged powers (intensity) with our running mean? Then

(6.4.1.2) $$E_s(y^2) = \xi^2 + k_e^2 \quad \text{(chapter V, equation 5.2.2.10)}$$
$$= D(t)^2 + k_e^2$$

Clearly the average is once again greater than that which would have resulted had there been no external noise (i.e. $D^2(t)$) but at least the average is exactly the same in <u>form</u> as the series $D^2(t)$ - it has just been shifted up by a constant k_e^2.

Thus here lies the first warning - it is not valid to simply average blocks of amplitude-only data to reduce noise; it is, however, valid with intensity.

6.4.2 Effect of noise on the autocovariance

6.4.2a Introduction

In Section 6.3, noise was seen to add a narrow spike at zero lag to the complex autocovariance and it was possible to use this spike to estimate the RMS noise. In the case of amplitude-only data, a narrow spike is again produced on the autocovariance. Again the noise can be deduced from the height of this spike - but how? The problem is no longer simple. Further, is it not possible that the noise may affect more than just the zero lag value of the autocovariance? We have already seen that averaging the data distorts it. Perhaps noise could distort the autocovariance? Are there any advantages in using powers (intensity) rather than amplitudes? The next few sections will answer these questions. An understanding of these effects is essential when dealing with amplitude-only data. It is the author's belief that most of the following work is original. No references to similar material have been located.

The autocovariance of the real data series y(t), of length T, is

$$\rho_y(\tau) = \frac{1}{T}\int_0^T (y(t)-\bar{y})\ (y(t+\tau)-\bar{y})\ dt \qquad (6.4.2.1)$$

Then at zero lag ($\tau = 0$),

$$\rho_y(0) = \langle y^2\rangle - \langle y\rangle^2 = \rho_f \text{, say,} \qquad (6.4.2.2)$$

where $\langle x\rangle$ denotes the time average, $\frac{1}{T}\int_0^T x\,dt$. The autocovariance looks similar to Fig. 6.1, except that in this case $\rho_y(\tau)$ may become negative, whereas Fig. 6.1 is the magnitude of the complex autocovariance and hence is by definition always positive.

Now suppose, as discussed in Section 6.4.1, a running mean of length δ (δ being much less than the correlation time of the scatter component $\underline{r}(t)$) is applied, to produce the function m(t) in Fig. 6.3c. Recall D(t) in that diagram is the function which would have been recorded had there been no external noise (i.e. it is the information).

We can write

(6.4.2.3) $$y(t) = m(t) + e_m(t),$$

where $e_m(t)$ is a noise component with zero mean (by definition of m(t)). It should be clear that $e_m(t)$ is not equal to e(t).

The autocovariance of y(t) is then that of m(t) plus that of $e_m(t)$. This follows by similar arguments to section 6.3.1. The crucial reason why this can be stated is that $e_m(t)$ has zero mean. Thus the interpolated autocovariance at zero lag (i.e. ignoring the spike) is

(6.4.2.4) $$\rho_i = \langle m^2 \rangle - \langle m \rangle^2$$

If we can find a relation between ρ_f, ρ_i, and the RMS noise k_e^2, then it will be possible to use ρ_f and ρ_i to estimate k_e^2.

6.4.2b Power (Intensity) analysis

Because it is easier, let us firstly discuss the case where intensity is recorded, as distinct from amplitude. (The intensity can of course be obtained from the amplitude simply by squaring). Let

(6.4.2.5) $$y_p(t) = (y(t))^2$$

be the intensity. Let $m_p(t)$ be the running mean of $y_p(t)$, in a similar way to that in which m(t) was the running mean of y(t). Let $\rho_{yp}(\tau)$ be the autocovariance of $y_p(t)$, and let

(6.4.2.6) $$\rho_{fp} = \langle y_p^2 \rangle - \langle y_p \rangle^2$$

be the autocovariance at zero lag. Likewise, let

(6.4.2.7) $$\rho_{ip} = \langle m_p^2 \rangle - \langle m_p \rangle^2$$

be the interpolated autocovariance at zero lag.

For each interval δ, the information part of the signal is approximately constant (See Fig. 6.3b). Thus, if sufficient points are recorded in the interval δ, the amplitudes will have a Rice distribution, with an effective specular component $\xi = D(t)$. (In actual fact, the requirement that many points be recorded in an interval δ is not necessary. There will be many other sections in the full data sample with the same value $D(t)$, and when the summation is done to produce the autocovariance at zero lag, all these sections can be regarded together. Thus a more relaxed requirement is that there be sufficient points recorded to form a reasonable distribution when all the points with a common $D(t)$ are grouped together.)

Then the mean power in any interval δ_i is

(6.4.2.8) $$m_{pi} = E_{\delta i}(y^2),$$

the expectation of y^2 for a Rice distributed series, where $E_{\delta i}$ is given by equation 6.4.1.2.

Thus

(6.4.2.9) $m_{pi} = (D_i)^2 + k_e^2$, D_i being the amplitude of the information signal in this interval.

Then it follows that

(6.4.2.10a) $$\langle m_p \rangle = \frac{1}{N}\sum_{i=1}^{N}(D_i^2 + k_e^2) = \langle D^2 \rangle + k_e^2$$

and also

(6.4.2.10b) $$\langle m_p \rangle^2 = (\langle D^2 \rangle + k_e^2) = \langle D^2 \rangle^2 + 2 k_e^2 \langle D^2 \rangle + k_e^4 .$$

Also, by 6.4.2.9,

$$\langle m_p^2 \rangle = \langle (D^2(t) + k_e^2)^2 \rangle, \text{ so that}$$

(6.4.2.11) $$\langle m_p^2 \rangle = \langle D^4 \rangle + 2\langle D^2 \rangle k_e^2 + k_e^4 .$$

Hence

(6.4.2.12) $$\rho_{ip} = \langle m_p^2 \rangle - \langle m_p \rangle^2 = \langle D^4 \rangle - \langle D^2 \rangle^2 .$$

What of ρ_{fp}?

Consider grouping the data into blocks, again of length δ, to examine $\langle y_p \rangle$, $\langle y_p^2 \rangle$. Then let the mean of the points $y_p(t)$ in block "i" be $\langle y_p \rangle_i$. This is simply m_{pi}. Thus the overall mean of the y_p is the mean of the various $\langle y_p \rangle_i$, and hence equals $\langle m_p \rangle$.

(6.4.2.13) i.e. $$\langle y_p \rangle = \langle m_p \rangle = \langle D^2 \rangle + k_e^2$$

What of $\langle y_p^2 \rangle$? This is <u>not</u> equal to $\langle m_p^2 \rangle$. To form $\langle m_p^2 \rangle$, the powers were firstly averaged in the block δ_i, then squared, and then re-averaged. To form $\langle y_p^2 \rangle$, the individual points are squared, and then averaged in the blocks δ_i, and then these re-averaged. Thus in the block δ_i, let $\langle y_p^2 \rangle_i$ be the average. Then

(6.4.2.14) $$\langle y_p^2 \rangle_i = E_{\delta i}(y^4)$$

i.e. the expectation value of y^4 for a Rice distributed series $y(t)$, with specular component D_i and mean noise k_e^2.

Then $\langle y_p^2 \rangle_i = k_e^4 \, \Gamma(2+1) \; {}_1F_1 \left(-2;1; \frac{-\alpha^2}{2}\right)$, $\alpha = \sqrt{2}\, D_i/k_i$,

by equation 5.2.2.7, Chapter VII.

Hence

(6.4.2.15) $$\langle y_p^2 \rangle_i = D_i^4 + 4 k_e^2 D_i^2 + 2 k_e^4, \text{ and so}$$
$$\langle y_p^2 \rangle = \langle \langle y_p^2 \rangle_i \rangle = \langle D^4 \rangle + 4 k_e^2 \langle D^2 \rangle + 2 k_e^4 .$$

Thus by 6.4.2.6, 6.4.2.13, and 6.4.2.15

$$\rho_{fp} = \langle y_p^2 \rangle - \langle y_p \rangle^2 = \langle D^4 \rangle + 4 k_e^2 \langle D^2 \rangle + 2 k_e^4 - \langle D^2 \rangle^2 - 2\langle D^2 \rangle k_e^2 - k_e^4$$

(6.4.2.16) or $$\rho_{fp} = \langle D^4 \rangle + 2k_e^2 \langle D^2 \rangle + k_e^4 - \langle D^2 \rangle^2$$

We finally note, by 6.4.2.12, and 6.4.2.16, that

(6.4.2.17) $$\rho_{fp} - \rho_{ip} = 2k_e^2\langle D^2\rangle + k_e^4 .$$

But $$\langle D^2\rangle = \langle y_p\rangle - k_e^2 \text{ by 6.4.2.13,}$$

so 6.4.2.17 becomes

$$\rho_{fp} - \rho_{ip} = 2k_e^2(\langle y_p\rangle - k_e^2) + k_e^4.$$

This is simply a quadratic in k_e^2, with solution

(6.4.2.18) $$k_e^2 = \langle y_p\rangle \pm \sqrt{\langle y_p\rangle^2 - (\rho_{fp} - \rho_{fi})} .$$

All the terms $\langle y_p\rangle$, $\langle y_p\rangle^2$, ρ_{fp} and ρ_{fi} cqn be readily found, so an estimate of k_e^2 can be made. But should the $\sqrt{}$ be + or -?

Consider some examples.

(i) $y(t) = e(t)$ (all noise). Then $D(t) = 0$.

Thus $\rho_{ip} = 0$ by 6.4.2.12. (in principle - in practice, statistical fluctuations may mean this is not quite true). Further, by 6.4.2.17, $\rho_{fp} - \rho_{ip} = k_e^4$. So 6.4.2.18 implies $k_e^2 = k_e^2 \pm \sqrt{k_e^2 - (k_e^2)} = k_e^2 \pm 0$. i.e. the formula makes sense.

(ii) Consider the case of no noise, $y(t) = D(t)$, and $e(t) = 0$.

Then $\rho_{ip} = \rho_{fp}$. Then the mean square noise estimated by 6.4.2.18 is

$$\langle y_p\rangle \pm \sqrt{\langle y_p\rangle^2 - 0} = \langle y_p\rangle \pm \langle y_p\rangle .$$

It is clear the (-) sign should be chosen.

(iii) Suppose $D(t)$ = constant = D. Then $\rho_{ip} = 0$. The mean square noise estimated by 6.4.2.18 is

$$D^2+k_e^2 \pm \sqrt{(D^2+k_e^2)^2 - (D^4+2k_e^2D^2 + k_e^4-D^4)}$$

using $\langle y_p\rangle = D^2 + k_e^2$, and ρ_{fp} as given by 6.4.2.16. This is simply

$$D^2+k_e^2 \pm \sqrt{D^4} = D^2+k_e^2 \pm D^2 .$$

Again, the minus sign is necessary. Hence this suggests 6.4.2.18 should be

(6.4.2.19)
$$\boxed{\begin{aligned} k_e^2 &= \langle y_p\rangle - \sqrt{\langle y_p\rangle^2 - (\rho_{fp} - \rho_{fi})} \\ &= \langle y^2\rangle - \sqrt{\langle y^2\rangle^2 - (\rho_{fp} - \rho_{fi})} \end{aligned}}$$

Then the technique to obtain the mean square external noise from intensity data is:

(i) Find the autocovariance of the intensity

(ii) Find the autocovariance at $\tau=0$, i.e. ρ_{fp}

(iii) Find the interpolated autocovariance at $\tau=0$. To do this, use several points either side of $\tau=0$ and fit (say) a spline to these points, ignoring the value at $\tau=0$. This spline function is used to interpolate the value at zero, i.e. ρ_{fi}.

(iv) Find the mean square signal, $\langle y_p \rangle$ ($=\langle y^2 \rangle$). Note that this is done <u>without</u> removing the mean first (although the mean <u>is</u> removed to form the autocovariance).

(v) Use 6.4.2.19 to estimate k_e^2.

Some final comments are also worthwhile. Notice by 6.4.2.12 that $\rho_{ip} = \langle D^4 \rangle - \langle D^2 \rangle^2$. This is exactly the autocovariance which would have been obtained had there been no noise. In fact, from 6.4.2.9, we note that the function m_{pi}, which actually gives rise to the whole autocovariance except the value at 0 (i.e. after the noise $e_{mp}(t)$ becomes uncorrelated, $m_p(t)$ defines the autocovariance), is in fact the information signal power plus k_e^2. So the autocovariance of m_p is precisely that of the information signal alone. This was also pointed out in section 6.4.1, equation 6.4.1.2.

Then the autocovariance of the total signal is just that of the information signal, with a spike on top equal in length to

$$2k_e^2\langle D^2 \rangle - k_e^4.$$

The spike's length depends on the information signal mean $\langle D^2 \rangle$ because the noise e(t) adds a constant to $\langle D^2 \rangle$ to produce $\langle y_p \rangle$, and makes a new "effective zero mean noise" $e_{mp}(t)$ (c.f. equation 6.4.2.3).

6.4.2c Amplitude-only analysis

6.4.2c(i) Noise estimation

Now let us return to the problem of obtaining the autocorrelation using amplitudes. Again, consider a running mean m(t) of length δ, and write

(6.4.2.20) $$y(t) = m(t) + e_m(t) \quad ,$$

where $e_m(t)$ has zero mean. (see equation 6.4.2.3).

Then

(6.4.2.21) $$\rho_f = \langle y^2 \rangle - \langle y \rangle^2$$

(6.4.2.22) $$\rho_i = \langle m^2 \rangle - \langle m \rangle^2$$

In a similar way to the previous discussion,

(6.4.2.23) $$\langle y \rangle = \langle m \rangle \quad .$$

We also know

(6.4.2.24) $$\langle y^2 \rangle = \langle D^2 \rangle + k_e^2 \text{ by } 6.4.2.13 \ .$$

Thus we now seek $\langle m^2 \rangle$. Again consider successive blocks of length δ. Then

$$\langle m^2 \rangle = \langle (E_\delta(y))^2 \rangle$$

Where E (y) is mean of the Rice distributed series in interval δ_i.

By 6.4.1.1,

(6.4.2.25) $$E_{\delta i}(y) = k_e \Gamma(3/2)\, {}_1F_1(-\tfrac{1}{2}; 1; -\frac{\alpha^2}{2}), \text{ where } \alpha = \sqrt{2} D_i / k_e \ .$$

Thus

(6.4.2.26) $$E_{\delta i}(y) = \tfrac{1}{2}\sqrt{\pi} \sum_{n=0}^{\infty} \frac{(-\frac{1}{2})_n}{(n!)^2} \left(\frac{-\alpha^2}{2}\right)^n = \tfrac{1}{2}\sqrt{\pi} \sum_{n=0}^{\infty} \frac{(-\frac{1}{2})_n (-1)^n}{2^n (n!)^2} \alpha^{2n}$$

where $(a)_n = a.(a+1)(a+2)\ldots.(a+n-1)$ and $(a)_o = 1$. This is clearly a complicated function, and cannot readily be squared. Thus evaluation of $\langle m^2 \rangle$ is not as simple as the evaluation of $\langle m_p^2 \rangle$ was (equation 6.4.2.11). It is this problem which complicates the

issue of amplitude. Even if the expression could be expressed more analytically, the <D> and k_e terms would be mixed, which complicates the issue.

To make some progress with this problem, the following assumption will be made.

ASSUMPTION:

It will be assumed that the information signal $D(t) = |\underline{S}(t)+\underline{r}(t)|$ is Rice distributed itself, with a constant specular component Ξ, and a "random component" with rms value k_R. It must be pointed out that Ξ is not equal to S(t), unless S(t) is constant. The assumption really amounts to assuming $\underline{S}(t)$ is either constant or Rice distributed (since $\underline{r}(t)$ is Rayleigh distributed) although the phase variations are much slower than those for $\underline{r}(t)$ and $\underline{e}(t)$. This assumption may not always be valid (although it frequently is in the case of D region scatter, as we have seen), but it at least allows us to examine the problem in some detail in this specific case.

Let the probability that the information signal has an amplitude in the range D to D+dD be

(6.4.2.27) $\qquad R_S(D)\,dD$,

where

(6.4.2.28) $$R_S(D) = 2\,\Xi/k_R^2 \cdot e^{-\frac{(\Xi^2+D^2)}{k_R^2}} I_o\left(\frac{2\Xi D}{k_R^2}\right) dD,$$

with Rice parameter $\alpha_D = \sqrt{2}\,\Xi/k_R$. These statements follow from the Rice distribution formula (5.2.1.15).

Then the series y(t) is the sum of the Rice distributed series D(t) and the Rayleigh distributed noise e(t), so is Rice distributed with specular component Ξ and mean square noise = $k_R^2 + k_e^2$ (see the last paragraph of Section 5.2.1, Chapter V). Thus

(6.4.2.29) $\qquad \langle y^2\rangle = \Xi^2 + k_R^2 + k_e^2$, and

(6.4.2.30) $\langle y\rangle = \langle m\rangle$ (by 6.4.2.23) $= \frac{1}{2}\sqrt{\pi}k\{{}_1F_1(-\frac{1}{2};1;\frac{-\alpha_n^2}{2})\}$

where $\alpha_n = \sqrt{2}\,\Xi/\sqrt{k_e^2+k_R^2}$

and $k = \sqrt{k_e^2+k_R^2}$.

What of $\langle m^2\rangle$?

In the interval δ_j,

(6.4.2.31) $m_j = E_{\delta j}(y) = \frac{1}{2}\sqrt{\pi}\,k_e\,{}_1F_1\,(\frac{-1}{2};1;\frac{-\alpha_j^2}{2})$,

where $\alpha_j = \sqrt{2}D_j/k_e$, as stated in 6.4.2.25.

Let the probability of a mean value between m and m+dm be $P_m dm$.

Then

(6.4.2.32) $\langle m^2\rangle = \int m^2 P_m(m)\,dm$

But the probability of a mean value between m and m+dm is also the probability of a D value between the corresponding D and D+dD, since the RMS external noise is constant, so D and m have a 1 to 1 relationship. Thus

(6.4.2.33) $P_m(m)\,dm = R_S(D)\,dD$.

Hence by 6.4.2.32,

$$\langle m^2\rangle = \int m^2\,R_S(D)\,dD$$

where $m = \frac{1}{2}\sqrt{\pi}\,k_e\,{}_1F_1\,(\frac{-1}{2};\,1;\,-D^2/k_e^2)$.

Thus, finally,

——————*———*———*———*

(6.4.2.34) $\rho_f = \langle y^2\rangle - \langle y\rangle^2 = \Xi^2+k_R^2+k_e^2-\{\sqrt{\pi}k\,{}_1F_1(\frac{-1}{2};1;-\Xi^2/(k_e^2+k_R^2))\}^2$,

and

(6.4.2.35) $\rho_i = \langle m^2\rangle - \langle m\rangle^2 = (\int m^2 R_S(D)\,dD) - \{\frac{1}{2}\sqrt{\pi}k\,{}_1F_1(\frac{-1}{2};1;-\Xi^2/(k_e^2+k_R^2))\}^2$,

where $m = \frac{1}{2}\sqrt{\pi}\,k_e\,{}_1F_1\,(\frac{-1}{2};1;\,-D^2/k_e^2)$

and $k^2 = k_e^2 + k_R^2$

——————*———*———*———*

Fig. 6.5 shows a plot of m vs k_e for a value D=1.0. Fig. 6.6 shows a typical $R_S(D)$ plot (Ξ=1.0, $\alpha\rho$=0.5), and also a plot of

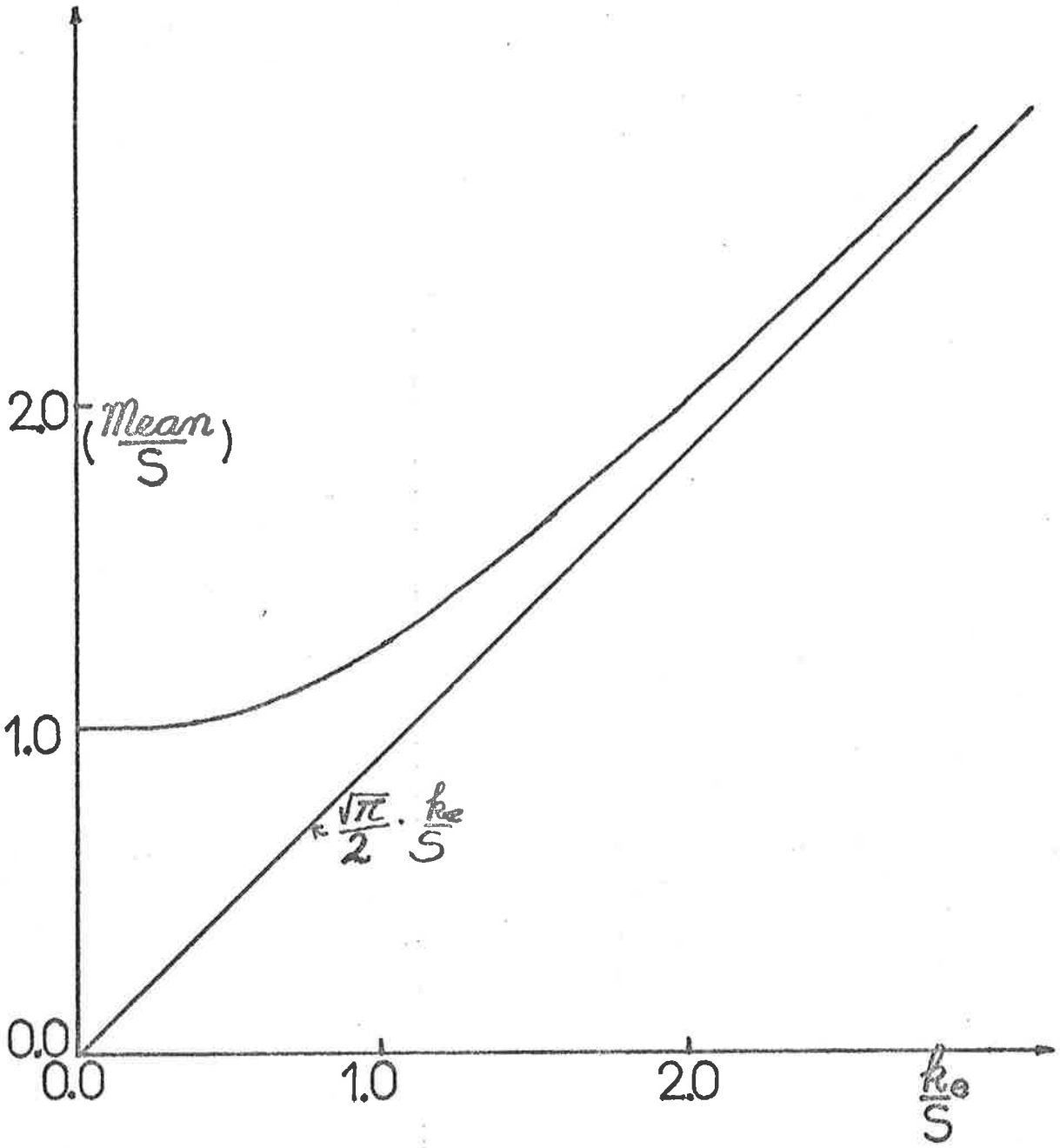

Fig. 6.5
Graph of $\frac{\sqrt{\pi}}{2} \cdot \frac{\sqrt{2}}{\alpha} \cdot {}_1F_1\left(\frac{-1}{2};1;\frac{-\alpha^2}{2}\right)$ as a function of $\frac{\sqrt{2}}{\alpha}$.
This is thus a graph of the mean value for a Rice distributed data set as a function of the RMS noise k_e, both the mean and k_e being normalized with respect to the specular component S.

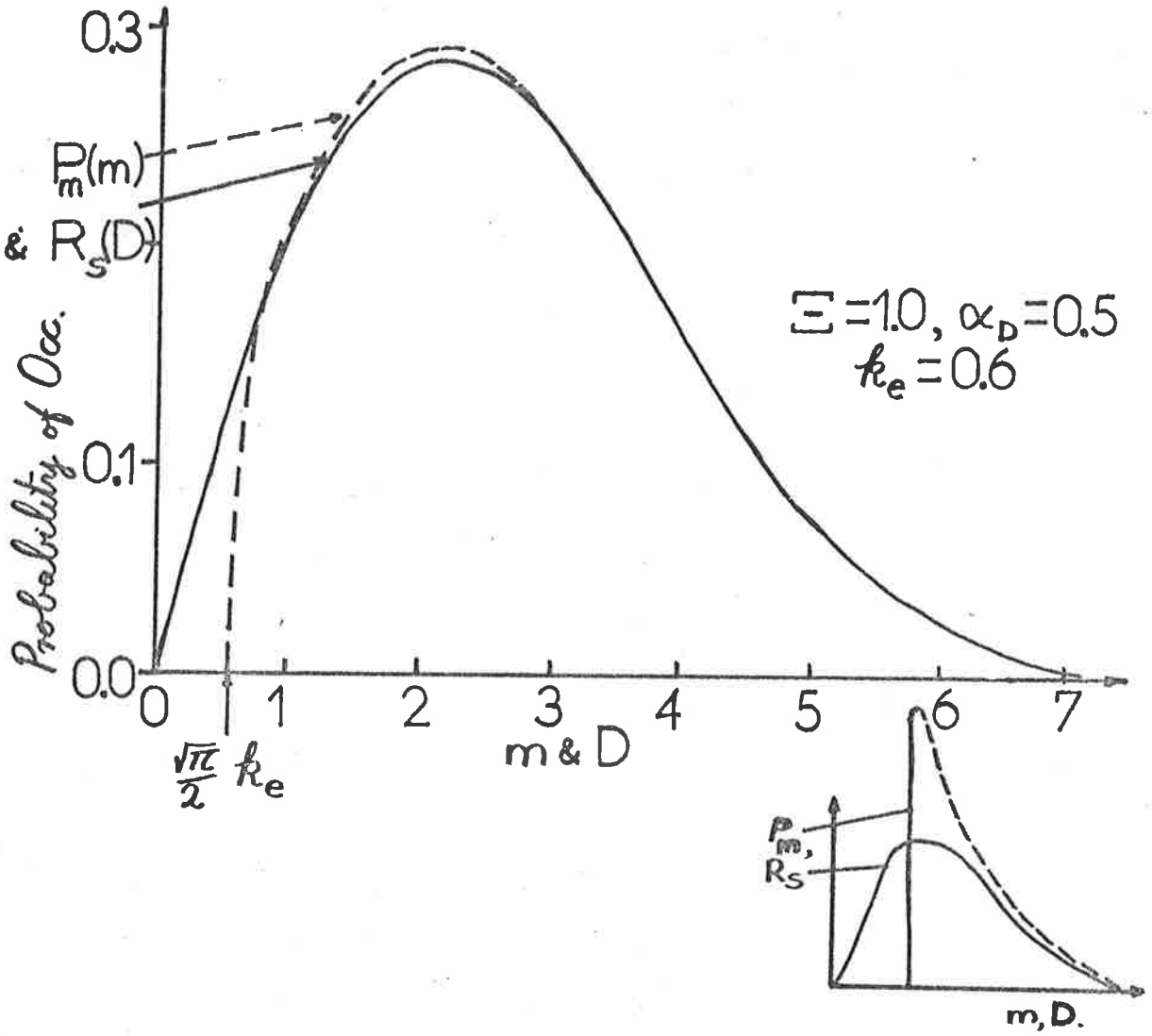

Fig. 6.6

Graphs of $P_m(m)$ vs m, and $R_s(D)$ vs D. Here D(t) is the information amplitude, and it is assumed to have a Rician distribution with "specular component" $\Xi=1.0$ and Rice parameter $\alpha_D=0.5$. The function m(t) is the running mean of the information signal D(t) plus an external noise component with RMS value $k_e=0.6$. $P_m(m)$ and $R_s(D)$ are the probability distribution functions of m(t) and D(t). (Note- do not confuse m(t) with the overall mean of the data sample. It is NOT this). It can be seen the mean never falls below $\sqrt{\frac{\pi}{2}}\, k_e$, the mean for noise alone (although there will be statistical fluctuations). The smaller graph shows a P_m distribution for a very large k_e value.

$P_m(m)$ vs m , ($P_m(m) = R_s(D)\ (\frac{dD}{dm})$), with external noise $k_e = 0.6$.

Note also that

$$\rho_f - \rho_i = \langle y^2\rangle - \langle m^2\rangle, \text{ so}$$

(6.4.2.36) $$\rho_f - \rho_i - \langle y^2\rangle = \left(\int m^2 R_s(D)\,dD\right)^2$$

where $m = \frac{1}{2}\sqrt{\pi}\ k_e\ {}_1F_1\ (\frac{-1}{2};1;\frac{-D^2}{k_e{}^2})$.

So by solving 6.4.2.36, it is possible to find k_e. That is

(i) Obtain the Rice parameter α_n for the total sample y(t) - this will equal $\sqrt{2}\Xi/\sqrt{k_e{}^2+k_R{}^2}$.

(ii) Then $\Xi^2 = \langle y^2\rangle\ (1 + 2/\alpha_n{}^2)^{-1}$ (by equation 5.2.4.1, Chapter V).

(iii) Solve 6.4.2.36 for this Ξ^2 value, subject to $k_R{}^2+k_e{}^2=\langle y^2\rangle-\Xi^2$ (by 6.4.2.29). This final step is possibly best done by graphical means. That is, plot $\left(\int m^2\ R_s(D)\,dD\right)^2$ as a function of k_e, using $k_R{}^2=\langle y^2\rangle-\Xi^2-k_e{}^2$. Then find that k_e value where this expression equals the appropriate $\rho_f-\rho_i-\langle y^2\rangle$.

It can hence be seen that it is also possible to estimate the true external noise using the spike on the amplitude-only autocorrelation. However, the problem is more difficult than that described by the intensity equation 6.4.2.19, and in this thesis, the power (intensity) autocorrelation was always used to estimate the noise. Equation 6.4.2.19 also has the advantage that it is applicable for any type of specular contribution S(t), whereas 6.4.2.36 assumed S(t) was either constant or Rice distributed.

Having estimated k_e, this can then be used to get ideas of the signal to noise ratio and the true Rice parameter (Chapter V, equations 5.2.3.2 and 5.2.3.3).

6.4.2c(ii) Autocovariance distortion

In section 6.4.2b, it was mentioned that apart from producing the spike at zero, Rayleigh distributed noise does not alter the

shape of the autocovariance of the intensity. This statement ignores statistical effects. Some computer experiments were done to check it. Data recorded at Townsville in complex form were used, and the autocovariance of the powers was found. Then a specular component was added to the complex data, and the autocovariance function again found. The two autocovariance functions should be identical, since adding a specular component should simply result in the addition to the powers of the square of this specular component (on average). The two autocovariance functions were quite similar in form, but not completely identical. This may indicate that the theory developed is not entirely accurate. However, by adding on this specular component, the distribution of the powers (after removal of the square of the specular component) will differ from the original distribution, due simply to statistical fluctuation, and the difference in the two autocovariance functions may simply reflect this statistical fluctuation. The disagreement was worst when the fading of the information signal was fastest. Presumably, rapid fading may mean there were insufficient points recorded in an interval of constant information-signal for equations like $\langle y^2 \rangle_i = \langle D^2 \rangle_i + k_e^2$ to hold exactly. Changes in k_e^2 during the records (1 minute blocks were used) may also distort the autocovariance. If the noise was not Rayleigh distributed, the formulae may also break down. Noise estimated by equation 6.4.2.19 were also performed. In principle, they should be the same in each case. This was not quite true, but agreement was reasonable (better than 50%). However, overall it is fair to say that noise does not distort the autocovariance of the power too greatly.

But what about the autocovariance of the amplitudes? If there had been no noise e(t), then y(t) = D(t), and the autocovariance of the information signal, $\rho_D(\tau)$, would have been formed. Suppose that the autocovariance at zero lag is

(6.4.2.37) $$\rho_D(0) = \rho_s .$$

How is ρ_s related to ρ_i? As previously, assume D(t) is Rice distributed. Then

$\rho_s = \langle D^2\rangle - \langle D\rangle^2$, so

(6.4.2.38) $$\rho_s = \Xi^2 + k_R^2 - \tfrac{1}{2}\sqrt{\pi}\, k_R \; {}_1F_1\left(\frac{-1}{2}; 1; -\Xi^2/k_R^2\right).$$

This is to be compared to ρ_i, as in 6.4.2.35.

It should be noted that $\frac{\rho_s}{\Xi^2}$ is a function only of $\alpha_D = \sqrt{2}\Xi/k_R$. Also $\frac{\rho_i}{\Xi^2}$ is a function only of α_D and $\alpha_e = \frac{\sqrt{2}k_e}{\Xi}$.

These statements follow because

$r = \tfrac{1}{2}\sqrt{\pi}\, k \; {}_1F_1\left(\frac{-1}{2}; 1; \frac{-\xi^2}{k^2}\right)$ is the mean for a Rice distributed series of specular component ξ and Rice parameter $\alpha = \frac{\sqrt{2}\xi}{k}$, and

$\frac{r}{\xi} = \tfrac{1}{2}\sqrt{\pi}\left(\frac{\sqrt{2}}{\alpha}\right) {}_1F_1\left(\frac{-1}{2}; 1; \frac{-\alpha^2}{2}\right)$ is a function only of α. Thus ρ_s/Ξ^2 is dependent only on α_D. In 6.4.2.35, the second term divided by Ξ^2 is clearly dependent only on

$$\alpha = \sqrt{2}\Xi/(k_e^2 + k_R^2)^{\frac{1}{2}} = \left(\frac{2\Xi^2}{k_e^2 + k_R^2}\right)^{\frac{1}{2}} = (\alpha_e^{-2} + \alpha_D^{-2})^{\frac{1}{2}},$$

and so dependent only on α_e and α_D. What about

$\frac{1}{\Xi 2}\int m^2 R_s(D)\,dD$ in 6.4.2.35? This equals $\int \left(\frac{m}{\Xi}\right)^2 R_s(D)\,dD$.

Now $\frac{m}{\Xi}$ is a function only of $\sqrt{2}D/k_e$. Also,

$$R_s(D)\,dD = 2\Xi/k_R^2 \exp\left\{-\left(\frac{\alpha_D^2}{2} + \frac{D^2}{k_R^2}\right)\right\} I_o\left(\alpha_D \cdot \frac{\sqrt{2}D}{k_R}\right) dD$$

so

(6.4.2.39) $$R_s(D)\,dD = \frac{1}{\alpha_*}\,\alpha_D^2 \exp\left\{-\left(\frac{\alpha_D^2}{2} + \frac{\alpha_*^2}{2}\right)\right\} I_o(\alpha_D\alpha_*)\; d\alpha_* .$$

where $\alpha_* = \sqrt{2}D/k_R$.

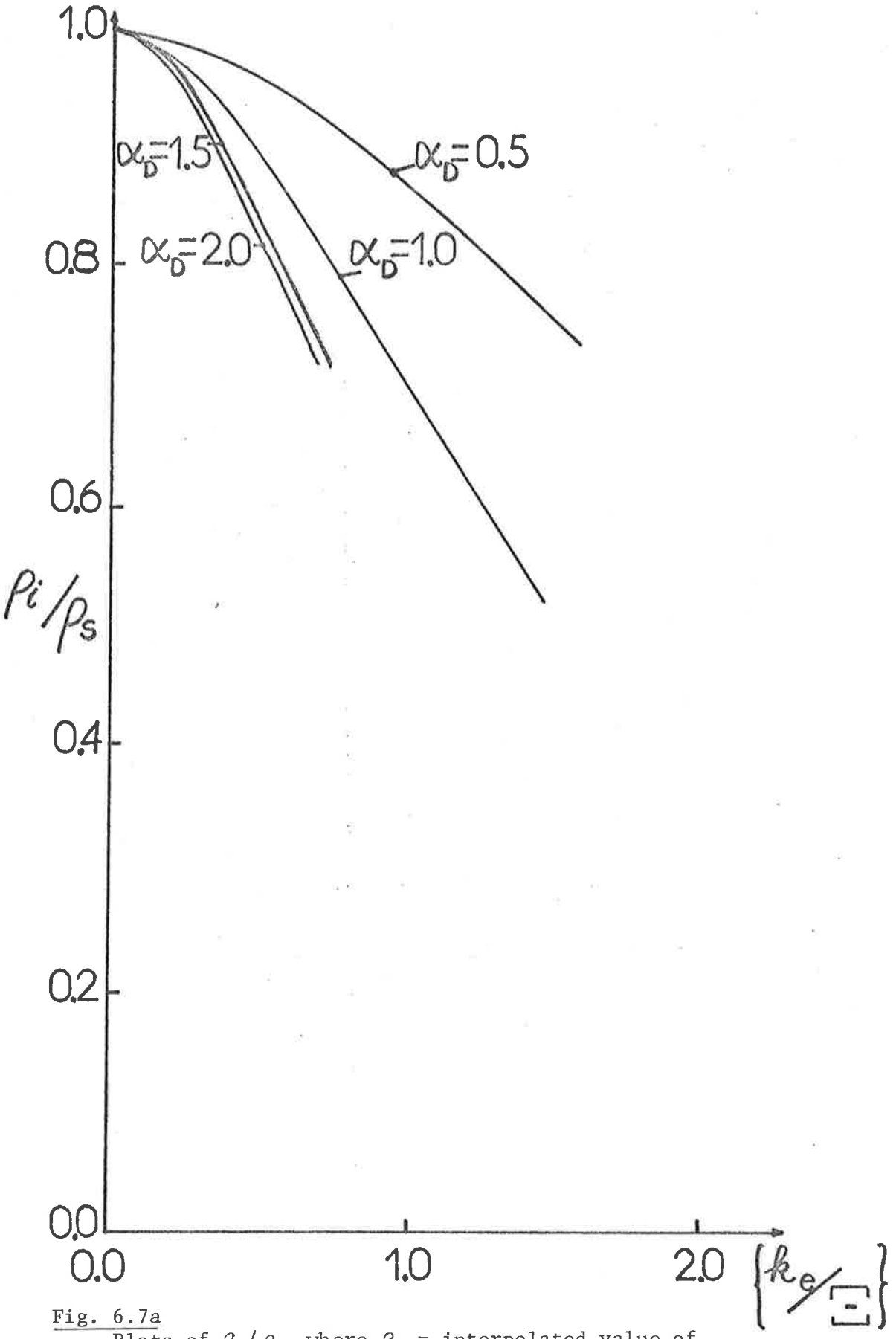

Fig. 6.7a

Plots of ρ_i/ρ_s, where ρ_i = interpolated value of the autocovariance at τ=0 for the total signal, and, ρ_s = the autocovariance at τ=0 which would have resulted had the information signal alone been recorded, plotted as a function of the{external RMS noise k_e divided by the "specular component" of the Rice distributed information signal}. Only values which are felt to be accurate (for the computer program used) are plotted. The parameter α_D is the Rice parameter for the information signal (this signal is assumed to be Rice distributed).

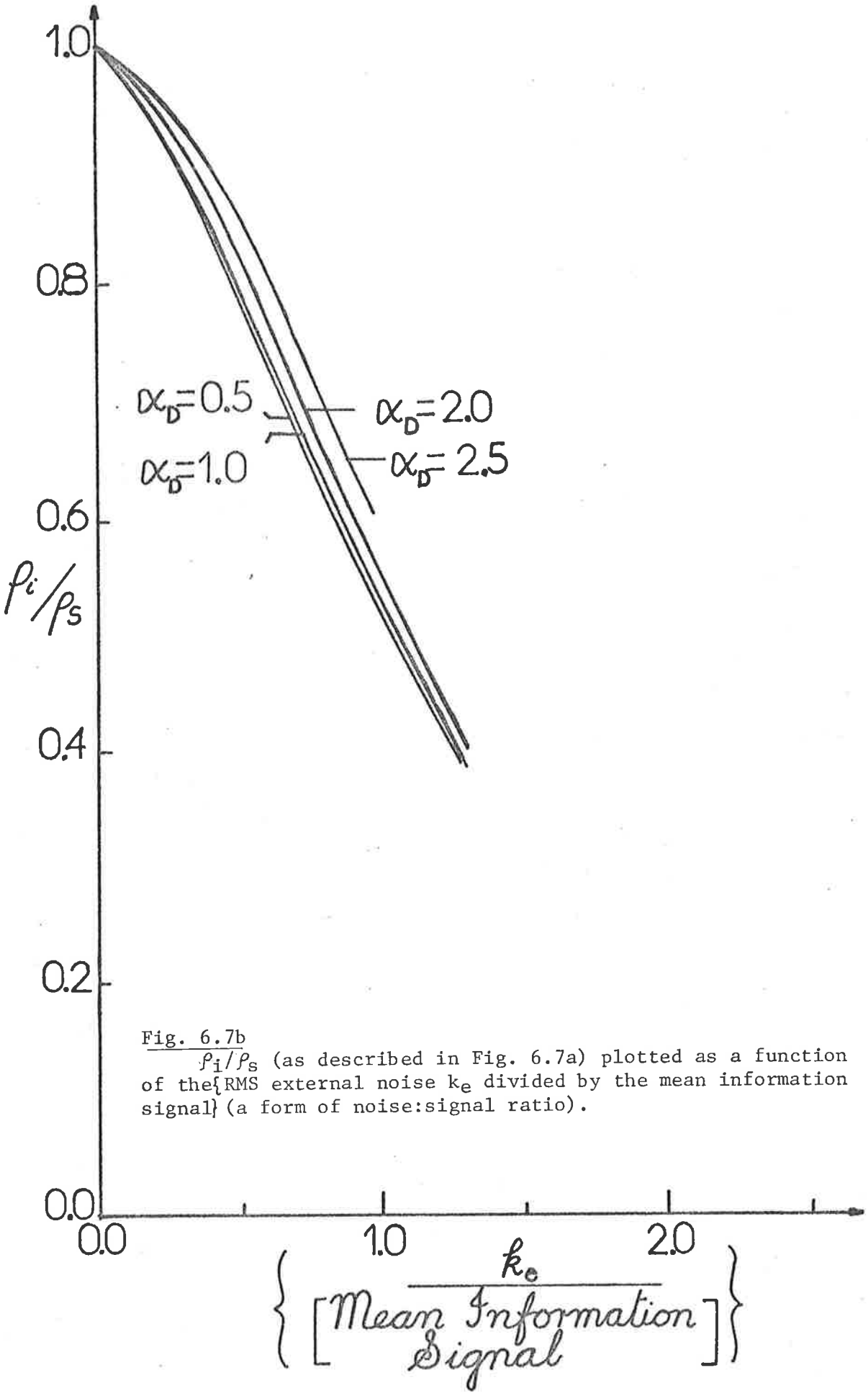

Fig. 6.7b
ρ_i/ρ_s (as described in Fig. 6.7a) plotted as a function of the{RMS external noise k_e divided by the mean information signal} (a form of noise:signal ratio).

Thus $(m/\Xi)^2$ is a function only of $\sqrt{2}D/k_e=(\sqrt{2}D/k_R)(k_R/k_e)=\alpha_*.\alpha_e/\alpha_D$ i.e. $(m/\Xi)^2$ is a function only of α_*, α_e, α_D. $R_s(D)dD$ is a function of only α_* and α_D. Thus this integration may be performed, and the only dependent variable left will be α_e, α_D. The integration may be done either by using the change of variables suggested by 6.4.2.39, or simply in the form $\frac{1}{\Xi^2}\int m^2 R_S(D)dD$, using any particular values for Ξ, k_e, k_R.

The term $\rho_s/\rho_i = (\rho_s/\Xi^2)/(\rho_i/\Xi^2)$ is clearly dependent only on α_e and α_D, since we have just shown that both the numerator and denominator are dependent only on these terms. Fig. 6.7a shows plots of ρ_s/ρ_i as a function of k_e/Ξ $(=\sqrt{2}/\alpha_e)$ for various α_D. Larger values of α_D imply shallower fading for the "specular component" S. Notice that $\rho_s<\rho_i$. (Simpson's rule was used to calculate $\int m^2 R_s(D)dD$ on a digital computer. Since we have shown ρ_s/ρ_i is dependent only on α_D and α_e, ρ_s/ρ_i could be calculated using any one set of numbers Ξ, k_R, k_e).

It will also be noted that $k_e/\langle D\rangle = \frac{\sqrt{2}}{\alpha_e}\cdot\frac{\Xi}{\langle D\rangle}$, and we have seen $\langle D\rangle/\Xi$ is dependent only on α_D, so ρ_s/ρ_i, being dependent only on α_e and α_D, can also be considered as dependent only on α_D and $k_e/\langle D\rangle$. Fig. 6.7b shows plots of ρ_s/ρ_i as a function of $k_e/\langle D\rangle$. These graphs are the most useful, since $k_e/\langle D\rangle$ is the amplitude noise to signal ratio. The graphs appear quite similar for all α_D plotted.

Thus Fig. 6.7b is a good guide to the value ρ_s/ρ_i for a given signal to noise ratio, for quite a wide range of Rice distributions. The important point is that $\rho_s \neq \rho_i$ and agreement gets worse for larger k_e values.

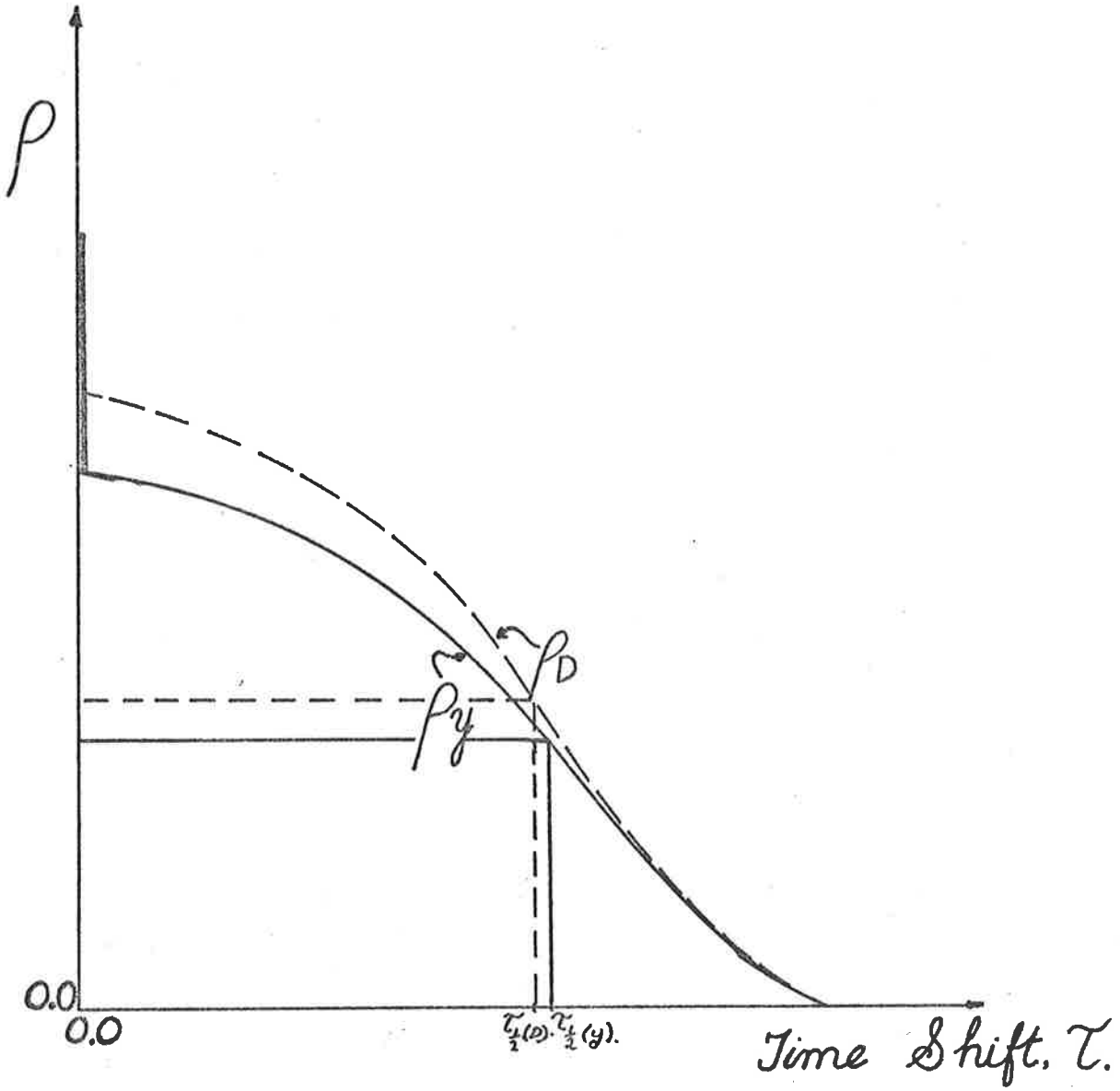

Fig. 6.8

Diagramatic comparison of autocovariances of the total signal y(t) (ρ_y) and of the information signal D(t) (ρ_D). Notice in particular the decrease of the interpolated value of ρ_y at τ=0.

Is it possible to explain why $\rho_i < \rho_s$? Indeed it is. Examine Fig. 6.3c again. Recall, too, that the autocovariance away from $\tau=0$ is defined by the running mean m(t). We see that m(t) is significantly larger than the information signal amplitudes D(t) when the latter are small, but m(t) becomes closer to the D(t) at large amplitudes. Thus m(t) is "bunched up" closer to its mean than D(t) was, as illustrated below.

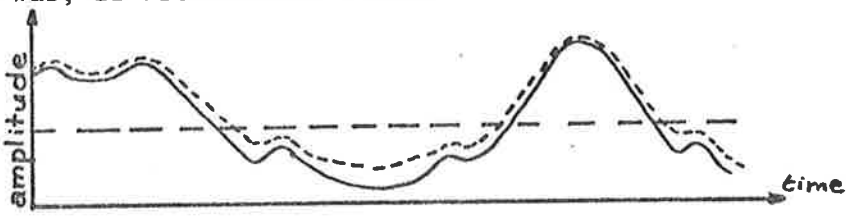

This reduces the covariance, since fluctuations from the mean are less.

However, it is reasonable to expect that the autocovariance of m(t) (and hence y(t)) falls to zero at a similar point to that at which D(t) fell to zero. Thus if we compare $\rho_y(\tau)$ and $\rho_D(\tau)$, the picture is as illustrated in Fig. 6.8. The re-normalized autocorrelation of ρ_D and ρ_y (spike removed) will thus be different .

The width of the autocorrelation may also be altered, although the form of this alteration is uncertain. Fig 6.8 suggests a widening (larger $\tau_{\frac{1}{2}}$), and this will be so if the autocorrelation near the minimum takes a similar form to the original, but this is not necessarily so. The author expects a widening (variations in signal strength are less rapid: sharp peaks and dips on amplitude vs. time plots become smoother) but this has not been proven.

What about the effect of noise on cross-correlations? If two receivers record ionospheric data, and the records are cross-correlated, it might be expected that

(i) the individual autocorrelations will be distorted, and

(ii) if the receivers record different noise levels, one running mean m(t) may be distorted more compared to its true information

signal than the other, decreasing the degree of correlation of the two signals.

From these comments, then, it is quite clear that data analysis should be done using intensity (powers) rather than amplitude, since intensity suffers less distortion. This is why, in this thesis, powers were used for forming autocorrelation functions, and in any averaging procedures.

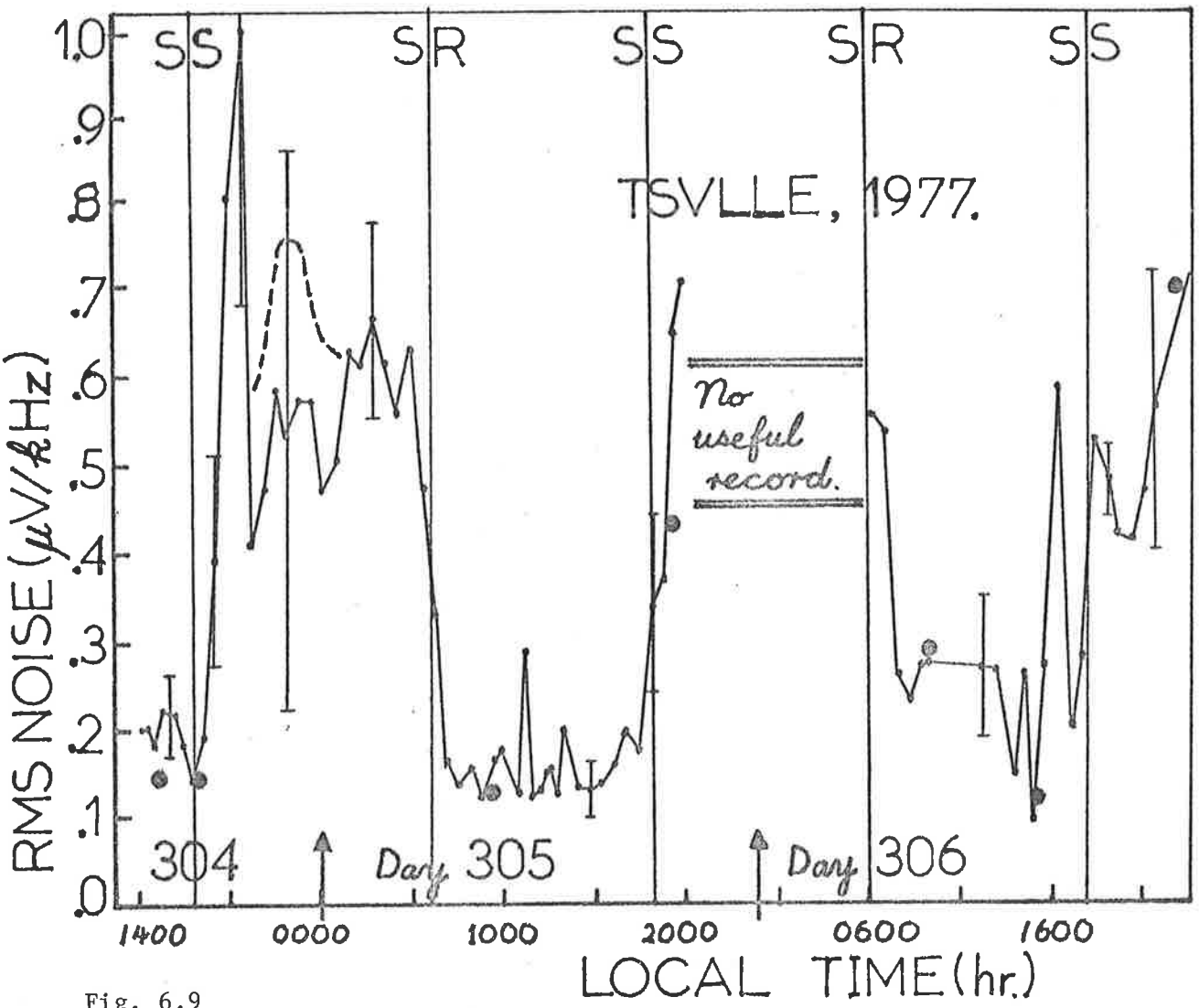

Fig. 6.9

The solid line represents noise estimates at Townsville for days 77/304-306, using equation 6.4.2.19. Autocovariances were formed with one min data blocks at all 10 heights recorded, and then these noise estimates were averaged in groups of about 30 mins to 1 hour. However, data was not always recorded during the whole period - generally only 3 mins of data was collected every 5-10 mins. The error bars are sample standard deviations, and thus give some idea of the variability of individual noise measurements. Only typical error bars in each period are given. These tend to be smallest in daylight hours. The variability in individual noise measurements is partly a reflection of real noise fluctuations, and partly an indication of the statistical fluctuations inherent in the method.

Noise estimates were converted to μV and then divided by the receiver bandwidth (≃25kHz) to give the RMS noise in μV/kHz. No coherent integration was used.

Also shown are some actual measurements of the noise, made with the transmitter turned off (black dots).

The broken line indicates behaviour which sometimes appears to exist, with noise being quite high until midnight and then falling. It can be seen that the error bars are much larger before midnight than after, indicating much more variability of noise before 0000hrs.

The vertical lines refer to the times 0600 (denoted SR, or sunrise) and 1800 (denoted SS, or sunset). The vertical arrows denote midnight.

6.5 Experimental results

We have now developed the theory for estimation of noise from the total signal. Equation 6.4.2.19 was used in this thesis when amplitude-only data was recorded. If complex data was available, equation 6.3.1.4 could be used. But how does the theory work out in practice?

Fig. 6.9 shows the first indication. The data was recorded at Townsville at a central frequency of 1.94MHz, and the receiver had a half-power bandwidth of about 25kHz. Results are presented in units of μV/kHz at the receiver input (50Ω impedance). Agreement between experimental observations and calculations using equation 6.4.2.19 seems to be excellent in places where a comparison can be made. The diagram also illustrates well the diurnal variation in noise. A rapid rise can be seen at sunset, as D region absorption decreases, allowing noise to propagate over much longer distances. The increase in noise may also perhaps be partly due to people switching on appliances (In such cases, the Rayleigh assumptions may not be valid, which may explain any errors in estimates of the RMS noise.) The noise is quite clearly high all night, and then around sunrise decreases dramatically, as the D region grows in electron density, absorbing out much of the noise arriving from large distances. There was also at times indications that the noise level followed the broken line in Fig. 6.9, with noise quite high until midnight, and then falling to a lower value, (possibly due to people going to bed?). Even in Fig. 6.9 it can be seen that the maximum noise levels were largest in the period of sunset to 0000 hrs, since the error bars extend to quite high values, suggesting large variability in noise at this time. The

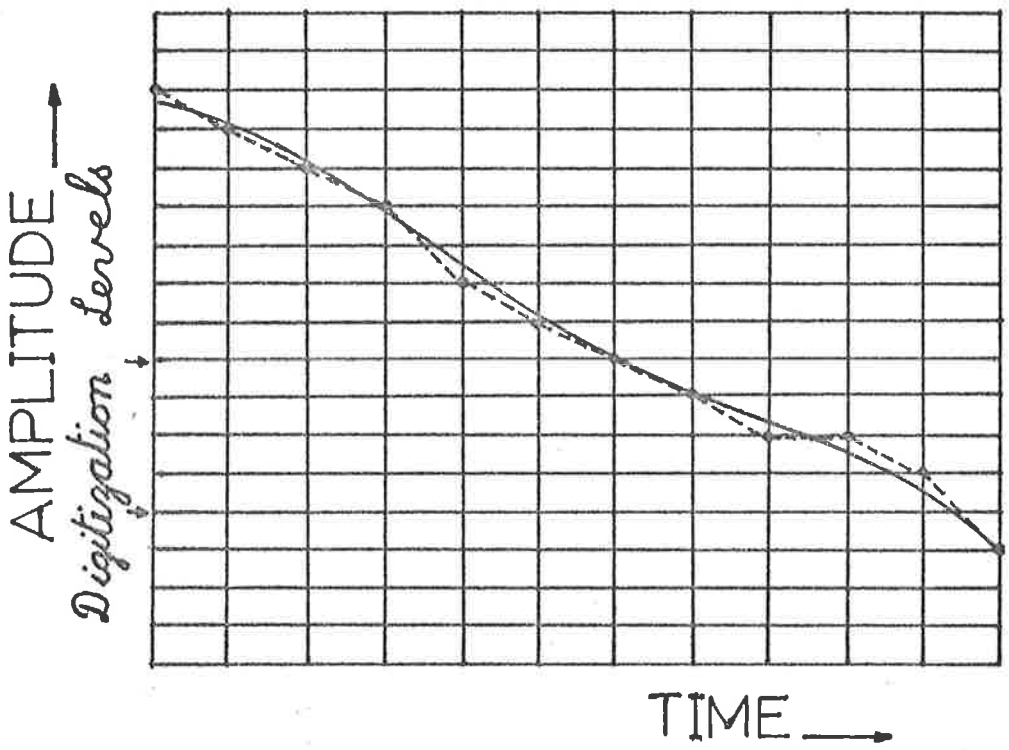

Fig. 6.10

Illustration of digitization noise. The smooth solid curve represents the true temporal variation A(t), and the dots represent the digitized values. These dots have been joined by a broken line to make their fluctuations more obvious. Such "noise" is not really governed by Rice statistics, but has perhaps a Poisson distribution about the signal. However, when the signal to noise is large, both Poisson and Rice distributions tend to Gaussian distributions, so the theory in this chapter is relevant for this type of noise also.

minimum in noise at 2000 hrs on both days 304 and 305 is an interesting feature, although it is unclear whether this is a regular characteristic.

Often, in dealing with noise, the signal to noise ratio is a more important parameter than the actual noise level itself. In such cases, estimation of noise by the procedures outlined in this chapter is actually better than by direct measurement of the noise level with the transmitter turned off. The first reason concerns receiver-generated noise. In Chapter III it was mentioned that often an attenuator was used before the signal entered the receiver, and this attenuation factor was taken into account after the data was recorded. If there is receiver noise mixed in with the signal, then this noise is also multiplied up by the attenuation factor, even though it occurred after the attenuator. However, generally when actual noise measurements were made, the attenuation was set to zero dB, so the noise measured by this method, whilst being a true measure of the noise, is not the best measure to use insofar as estimating signal to noise ratios is concerned, since it has not been multiplied up by the attenuation factor. However, generally this is only a minor consideration whenever non-receiver noise dominates. This is usually the case, particularly at night. In the day time, however, receiver noise can be important.

The second reason concerns digitization. Digitization can be regarded as a form of noise, as illustrated in Fig. 6.10. The recorded signal clearly has fluctuations which were not evident in the real data. Estimation of noise by the methods described in this chapter takes such effects into account. In fact, some real data recorded at Townsville, with the receiver gain alternating from high to low on successive minutes, illustrated this effect

quite well. Noise estimates made with low gain always exceeded those made on high-gain. This would be expected if digitization "noise" was important. Again, this is an effect which should be considered for proper signal to noise ratio estimates. However, actual measurement of noise is more accurate if it is the actual noise which is sought. Such measurement also considers the effects of special interference, which may not be uncorrelated after 1 shift.

One point which did come out of these experimental investigations was that noise estimates were only really useful whenever the fading times (noise spike removed) of the powers were greater than about 1.5-2s. This was because for shorter fading times, interpolation of the autocovariance at zero often produced an over-estimate of ρ_i. Thus it was usual to reject all noise measurements made with fading times of less than 1.5-2s. Data which saturated, or for which the gain was not high enough, was also rejected.

The installation of equipment cpapble of recording the complex signal at Townsville (see Chapter III) considerably improved the signal to noise levels. Data was recorded at 20Hz, and then an 8 point coherent integration was done. In principle, this reduces the noise powers by 8 times. This follows as a direct result of the central limit theorem, which states in part that by averaging n estimates of a parameter, the variance for the mean is reduced by n times compared to the variance of a single measurement. (e.g. see Huntsberger and Billingsley, 1973, §6.5). However, the variance of the in phase and quadrature components is simply $k_e^2/2$, as seen in Chapter V (equation 5.2.2.3), k_e^2

being the mean noise power. Hence this is reduced by n times when coherent integration over n points is done. Indeed, this coherent integration did produce a significant reduction in noise. As seen in Fig. 6.9, the RMS day time noise before coherent integration was $\simeq$.1 - .2 μV/kHz. After coherent integration, measurements taken on day 79/082 gave RMS noise values of about .04 to .08 μV/kHz. Thus k_e is reduced by about 2.5 times, or k_e^2 by about 6 times.

The installation of this equipment allowed another test of the theory presented in this chapter. Noise estimates could be made by both equations 6.3.1.4 and 6.4.2.19 for the same data. This was done using 1 minute data blocks for all heights used at any time, and these results were then averaged in 10 minute blocks. Then noise estimates made by the two techniques were plotted on a correlation graph. The results are presented in Fig. 6.11a and b. Generally, the two sets of measurements (i.e. by 6.3.1.4 and 6.4.2.19) appear to agree well. The small offset in 6.11a has not been explained. Notice the powers are greater in 6.11b, in showing the effect of digitization noise discussed earlier.

Fig. 6.11a

Estimates of k_e^2 (the mean square noise power) using the complex autocovariance (equation 6.3.1.4) and the power autocovariance (equation 6.4.2.19) for Townsville in March, 1979, plotted on a correlation graph.

Each point is the mean of a set of 10 mins of 1 min estimates, each 1 min estimate using estimations at 4 separate heights (60, 68, 78 and 80km). The receiver alternated in gain from high to low and back every 2 mins, to record echoes of different strengths. This set of data corresponds to that recorded at high gain.

In principle, all points should lie on the solid line (slope=1). For some unknown reason there appears to be an offset of about $.4(\mu V)^2$ vertically. However, apart from this, agreement is good.

Fig. 6.11b

Estimates of k_e^2 by complex and power autocovariances, as for Fig. 6.11a, for basically the same time period as for that figure, but for low gain. (The period 1600-1629 hrs is not included here).

In this case, data was not rejected when fading times were less than 2 seconds, and this accounts for some of the points far from the expected line (the expected line is the solid line of slope 1).

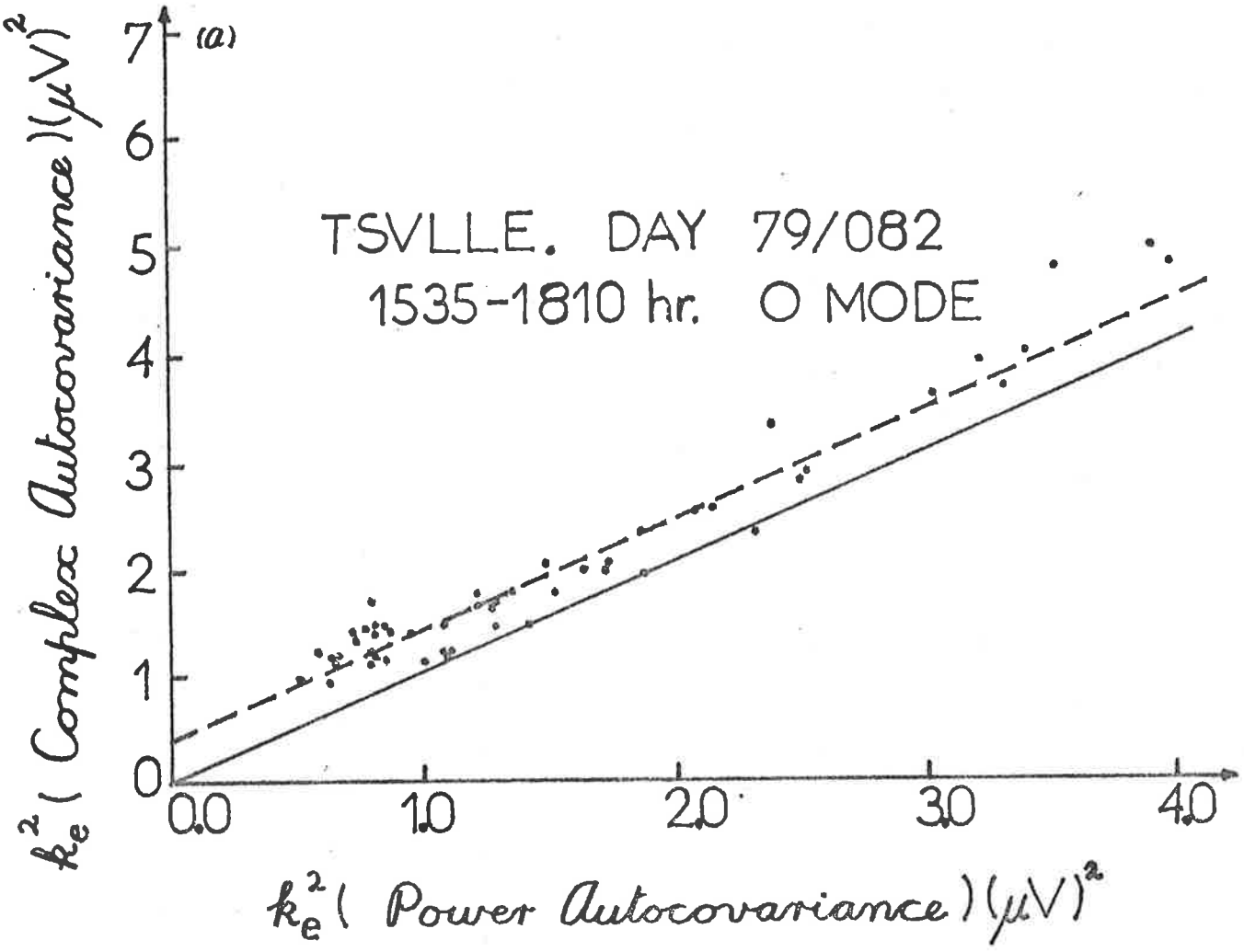
(a)
TSVLLE. DAY 79/082
1535-1810 hr. O MODE
k_e^2(Complex Autocovariance)$(\mu V)^2$
k_e^2(Power Autocovariance)$(\mu V)^2$
0
1
2
3
4
5
6
7
0.0
1.0
2.0
3.0
4.0

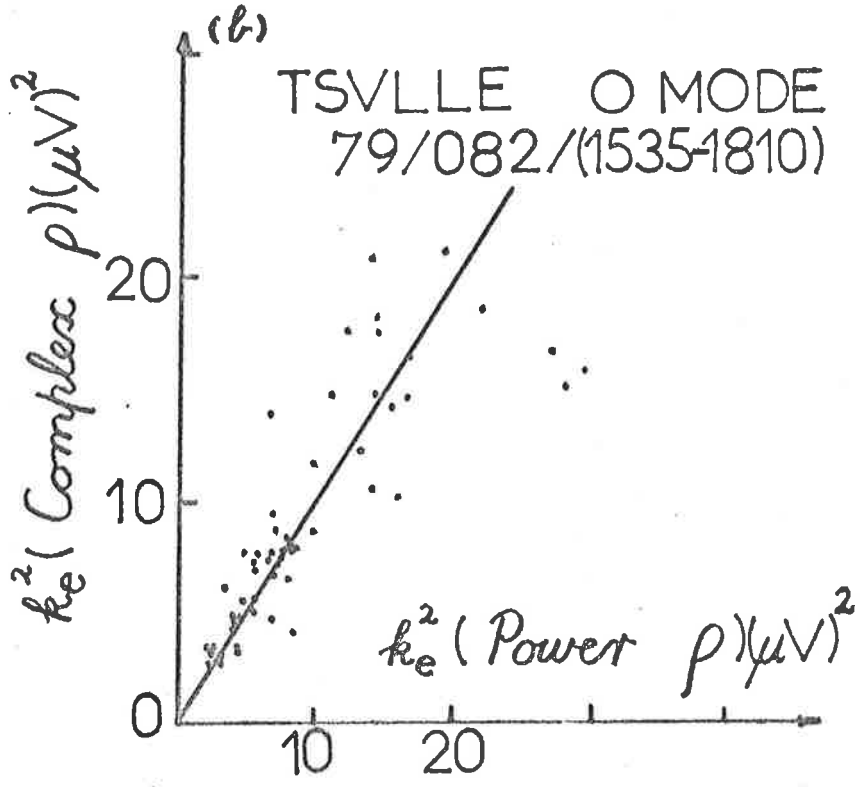
(b)
TSVLLE O MODE
79/082/(1535-1810)
k_e^2(Complex ρ)$(\mu V)^2$
k_e^2(Power ρ)$(\mu V)^2$
0
10
20
10
20

6.6 Conclusions

The results of this chapter suggest the following.

(i) The effect of uncorrelated noise on a signal recorded as complex data ($\underline{y}(t)$) is to add a spike to the autocovariance at $\tau=0$ of height k_e^2 = mean power of the uncorrelated noise.

(ii) If the signal is sampled with powers only ($(y(t))^2$ say) the effect is to add a spike to the autocovariance of the powers at $\tau=0$ of height

$$2k_e^2\langle y^2\rangle - k_e^4 \ .$$

The mean square noise can be estimated as

$$k_e^2 = \langle y^2\rangle - \sqrt{\langle y^2\rangle^2 - (\rho_f - \rho_i)} \qquad (6.4.2.19)$$

where ρ_f = autocovariance at $\tau=0$,

and ρ_i is the interpolated autocovariance at $\tau=0$ (i.e. spike removed).

The form of the autocovariance, apart from the noise spike, is unchanged (in principle) by the noise.

(iii) If the signal is sampled with amplitude y(t), not only is a spike produced at $\tau=0$ lag by the uncorrelated noise, but the interpolated value of the autocovariance at $\tau=0$ is less than it would have been had there been no uncorrelated noise. Thus the autocovariance with spike removed is different to that which would have been obtained had there been no uncorrelated noise.

(iv) Experimental investigations suggest that the methods developed in this chapter give reasonable estimates of the uncorrelated noise powers (correlated noise such as interference from another transmitter is another problem), provided adequate rejection criteria are used (rejection of saturating data, or data recorded with the gains too low, and rejection of data with fading times less than about 1.5-2s), and provided a reasonable degree of averaging is used.

CHAPTER VII

OBSERVATIONS USING COMPLEX DATA

CHAPTER VII

Observations using Complex Data

7.1 Introduction

In Chapter IV, it was pointed out that although amplitude-only data was quite adequate for observing atmospheric motions on scales of minutes and more, complex data was desirable for examination of shorter term processes. The ease of dealing with complex data has also been discussed. This chapter will concentrate on the results of observations made using such complex data. By recording in such a way, all the information contained in the received signal is utilized.

The chapter begins with some typical observations. Some features of this data may appear to be a little strange, and so some computer simulations will be made to help clarify interpretation of this information. The discussion of these simulations is rather lengthy, but it is felt that its inclusion is essential.

Following this, some observations are discussed. The discussion will centre almost exclusively on observations made on day 80/072, since that day shows most of the main features to be discussed. Interpretation of this data will be shown to lead to estimates of parameters such as the turbulent energy deposition rate and eddy diffusion coefficient. It will also be shown that Doppler measurements of wind velocities and estimates by Partial Reflection Drifts, are in excellent agreement.

Some space will also be devoted to a discussion of the relative roles of turbulence and gravity waves.

Finally, a brief discussion on the possibilities and merits of deconvolution will be undertaken.

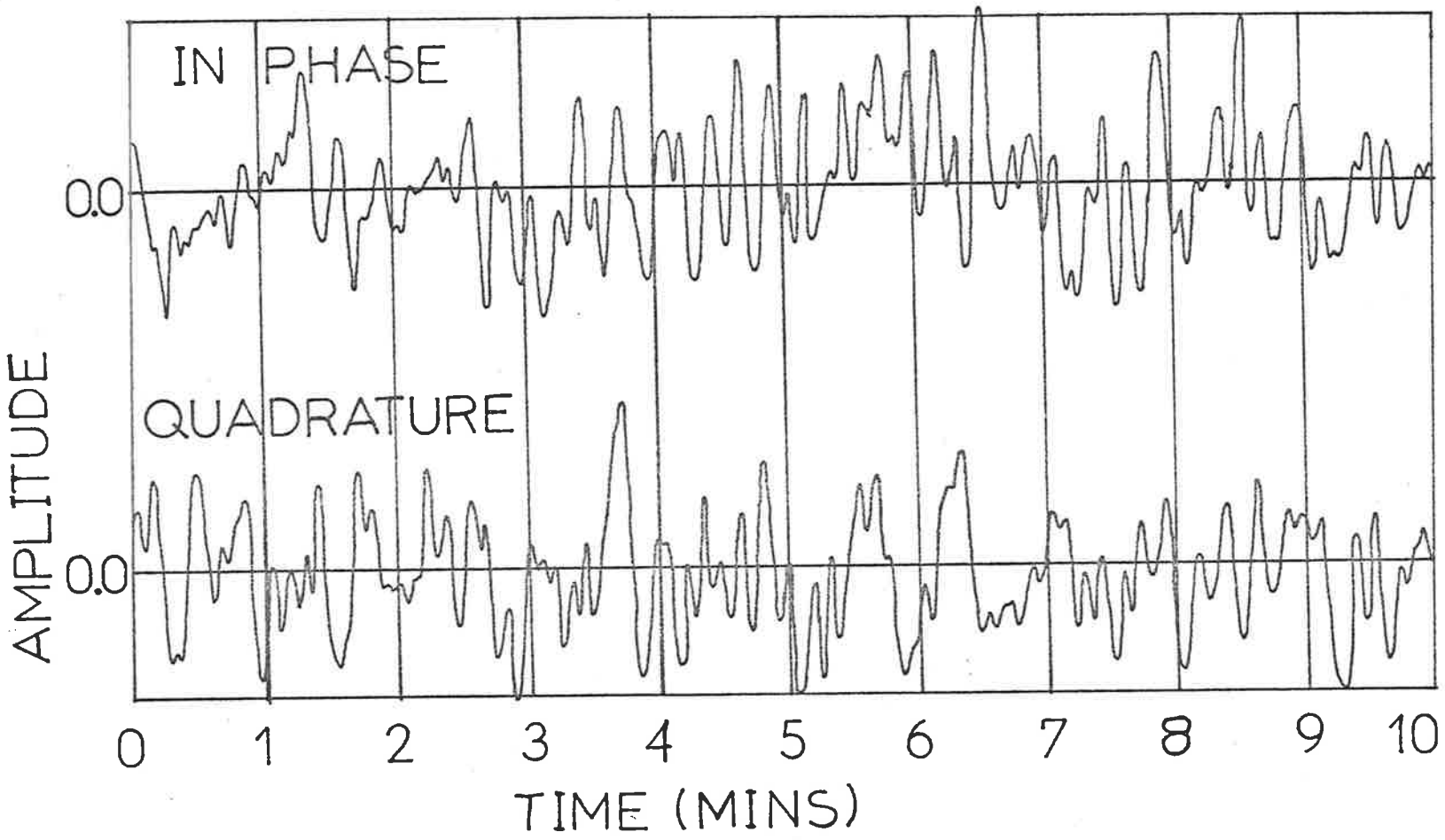

Fig 7.1 Example of typical in-phase and quadrature components received in an ionospheric D-region HF scatter experiment from heights above 80 km. The time series are actually formed by a computer, and represent the data series corresponding to a Gaussian power spectrum of half-power-half-width of .07 Hz, with random phase (see text). However, the essential features are the same as those for real scatter data, and so these are adequate for illustrative purposes. The half-width of the corresponding auto-correlation function is 3.1 seconds.

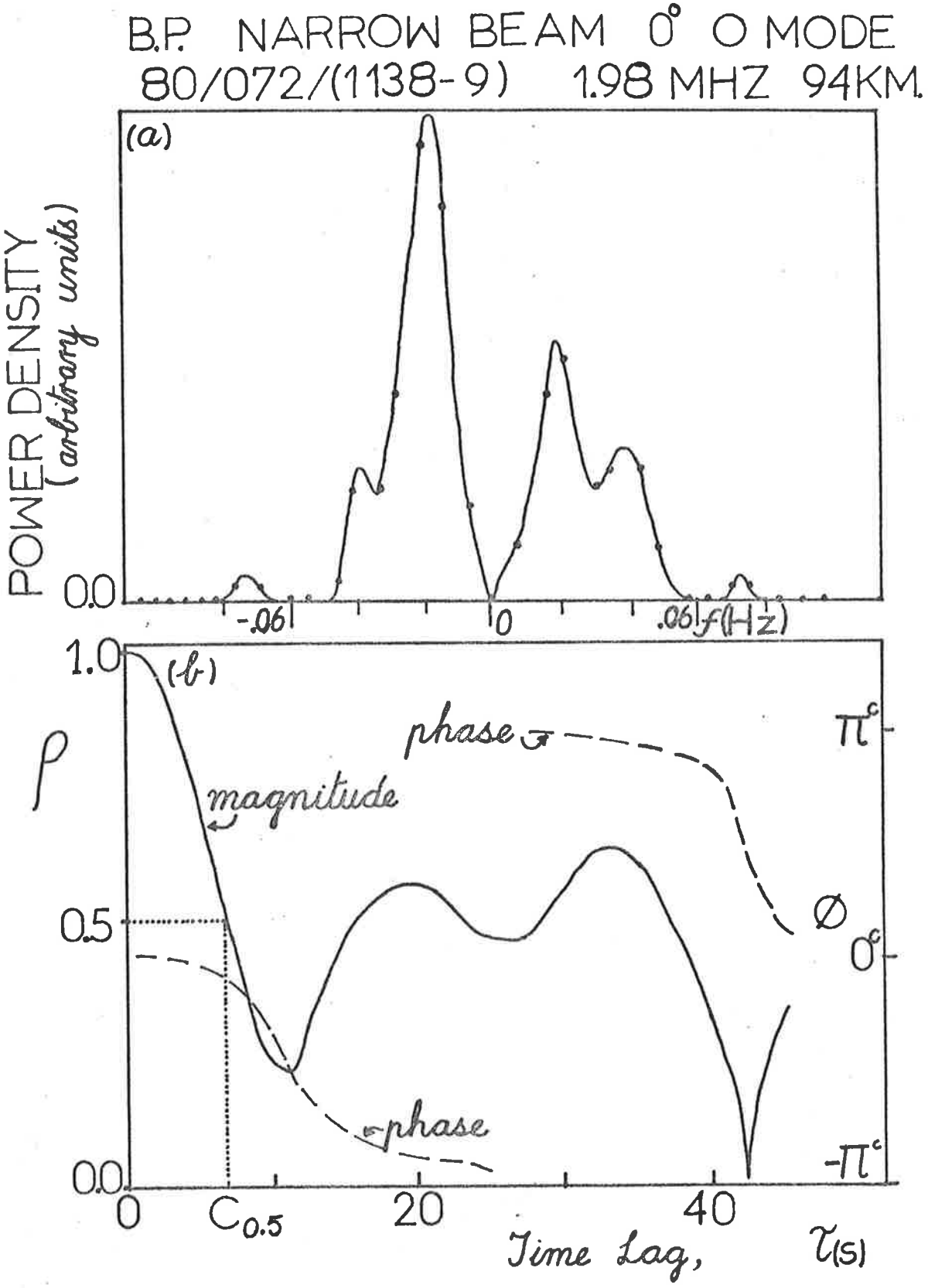

Fig 7.2 (a) Power Spectrum, and (b) Complex auto-correlation function, for a typical 1 minute series of data obtained at Buckland Park for heights above 80 km, using a vertical narrow beam. Notice the existence of a few quite narrow spectral peaks (much less than the expected beam broadening - see text), and the corresponding oscillations in the auto-correlation. The spectral peaks are not reliable and neither is $C_{0.5}$ (see text).

7.2 Some simple observations

7.2.1 Short duration data (1-2 minutes)

Fig 7.1 shows a typical 10 minute series of data which could be produced by ionospheric scatter. The data was actually produced by a computer simulation (see Section 7.3), but is quite similar to real data in form. This has been verified by visual inspection. This data has a complex fading time of about 3 seconds. Experimental data fades more slowly at heights below 80 km, and of course the overall mean amplitude varies more. For example, the existence of larger bursts of scatter lasting 2-3 minutes from below 80 km has already been discussed. However, the diagram is adequate for illustrative purposes.

Figs 7.2a and 7.2b show a quite typical power spectrum and the corresponding auto-correlation function for a recording of 1 minute of actual data. Note the existence of quite narrow spectral peaks in the power spectrum. These might be interpreted as being due to a few specular scatterers, but are in fact misleading, and will be considered shortly.

In Chapter IV, fading times ($\tau_{1/2}$) using amplitude-only data were presented. With the installation of equipment to record complex data, it is only natural that fading times be taken from the magnitude of the complex autocorrelation. These will be denoted $C_{1/2}$ (or $C_{0.5}$). How do $C_{1/2}$ and $\tau_{1/2}$ measurements compare ? Fig 7.3 provides part of the answer to this question. It shows calculations of $C_{1/2}$ and $\tau_{1/2}$ using the same data, plotted on a scatter plot. It can be seen that in general larger $\tau_{1/2}$ values imply larger $C_{1/2}$ values, and vice versa. However, there is quite a scatter of points. It can also be seen that $C_{1/2}$ is generally larger than $\tau_{1/2}$, which is not surprising in view of the discussion in Chapter IV, section 4.3.1b. For

Fig 7.3

Correlation graphs (also called scatter slots, regression diagrams) of $C_{\frac{1}{2}}$, the fading time estimated from the magnitude of the autocorrelation of complex data, and $\tau_{\frac{1}{2}}$, the fading time estimated from the amplitude-only auto-correlation. Each point represents a mean of 1 minute fading times estimated from 4 successive 1-minute blocks, the same data being used for both $C_{\frac{1}{2}}$ and $\tau_{\frac{1}{2}}$.

The broken lines represent slopes of 2, $\sqrt{2}$ and 1.

The graphs are discussed in the text. Notice also that fading times below 84 km are significantly greater than those above, as has also been seen previously.

$C_{1/2}$ vs $\tau_{1/2}$. TSVLLE. O MODE. WIDE BEAM
79/082/(1535-1820)

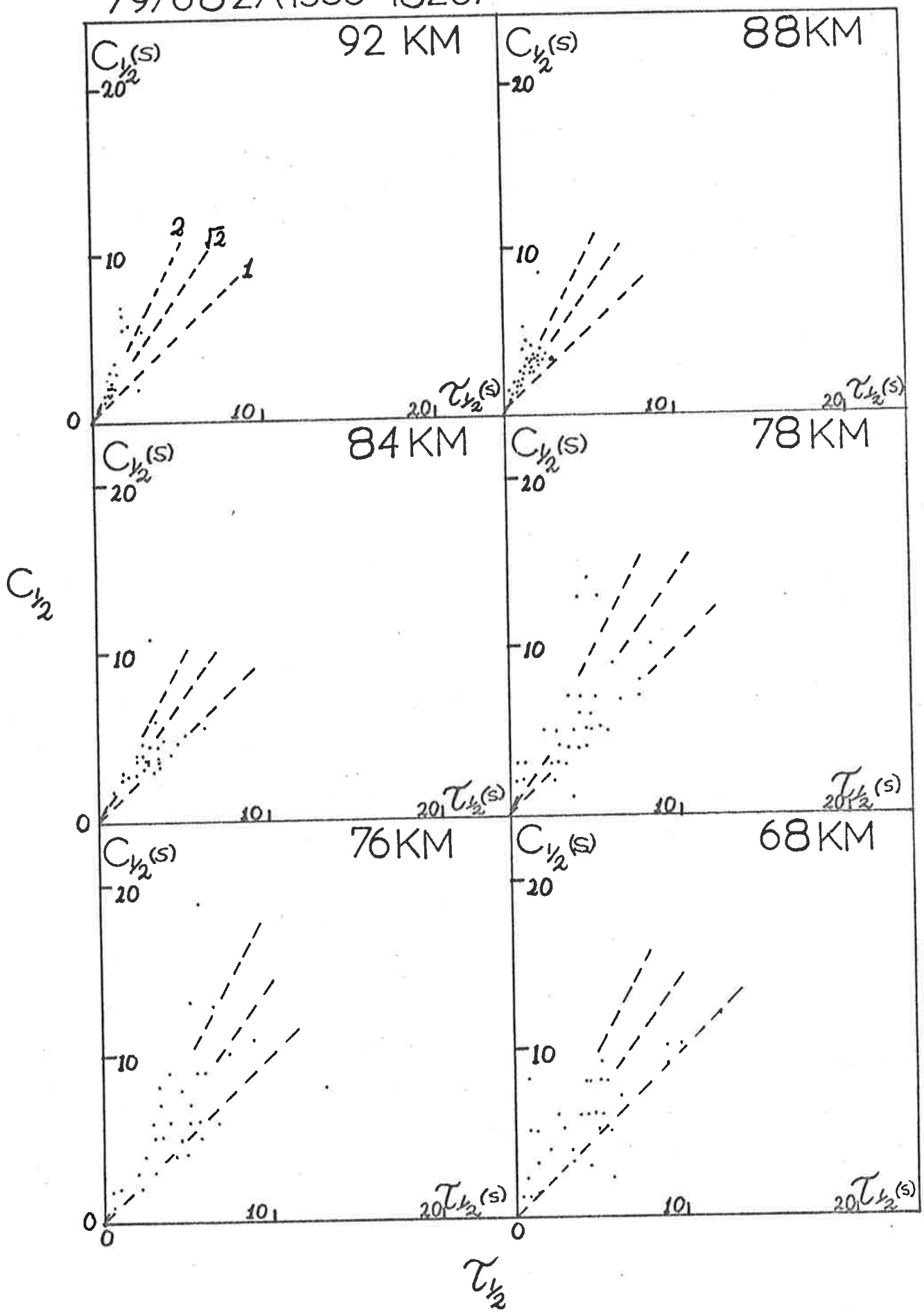

turbulent scatter, it is to be expected that $C_{\frac{1}{2}} \approx \sqrt{2}\ \tau_{\frac{1}{2}}$ (by equations 2.2.3.11 and 2.2.3.12, Chapter II ; this ignores beam broadening, but in fact $C_{\frac{1}{2}} \sim \sqrt{2}\ \tau_{\frac{1}{2}}$ is also expected if beam broadening acts, too). This would appear to be the case at 88 km, and perhaps 84 km. At 92 km, the echo is largely due to a low sporadic E-type structure. In this case it appears $C_{\frac{1}{2}} \sim 2\ \tau_{\frac{1}{2}}$. The reflection was quite specular. Processes such as those discussed for specular scatterers in Chapter IV, Section 4.3.1 may be important. At heights below 80 km the relation is possibly more 1:1. However, it is difficult to be sure, as there is considerable scatter. This is partly due to the "burstiness" of these echoes. On this day the amplitude of echoes could burst up and die within 20 seconds or less at times, and this process largely defined the fading times. Fig 7.4 shows typical height profiles of $C_{\frac{1}{2}}$ and $\tau_{\frac{1}{2}}$ for day 80/072. Again, it is clear that $C_{\frac{1}{2}}$ is larger than $\tau_{\frac{1}{2}}$. The 1:1 relation at heights below 80 km is not always apparent. It occurs only for rapidly bursting short-lived echoes. For steadier echoes, it is often true that $C_{\frac{1}{2}}$ is considerably larger than $\tau_{\frac{1}{2}}$ (often $C_{\frac{1}{2}} \sim 2\ \tau_{\frac{1}{2}}$). This is shown quite well in Fig 7.4 where it can be seen that at heights below 80 km, $C_{\frac{1}{2}}$ is considerably larger than $\tau_{\frac{1}{2}}$. This situation is more typical at Buckland Park, and for those more stable Townsville echoes.

However, the relation between $C_{\frac{1}{2}}$ and $\tau_{\frac{1}{2}}$ is generally approximately monotonic, which is useful. In the region 85-92 km, $C_{\frac{1}{2}} \sim \sqrt{2}\ \tau_{\frac{1}{2}}$, so some type of turbulent scatter may be important. This supports previous evidence pointing to an important turbulence contribution from above 80 km. (e.g. see Chapters IV and V).

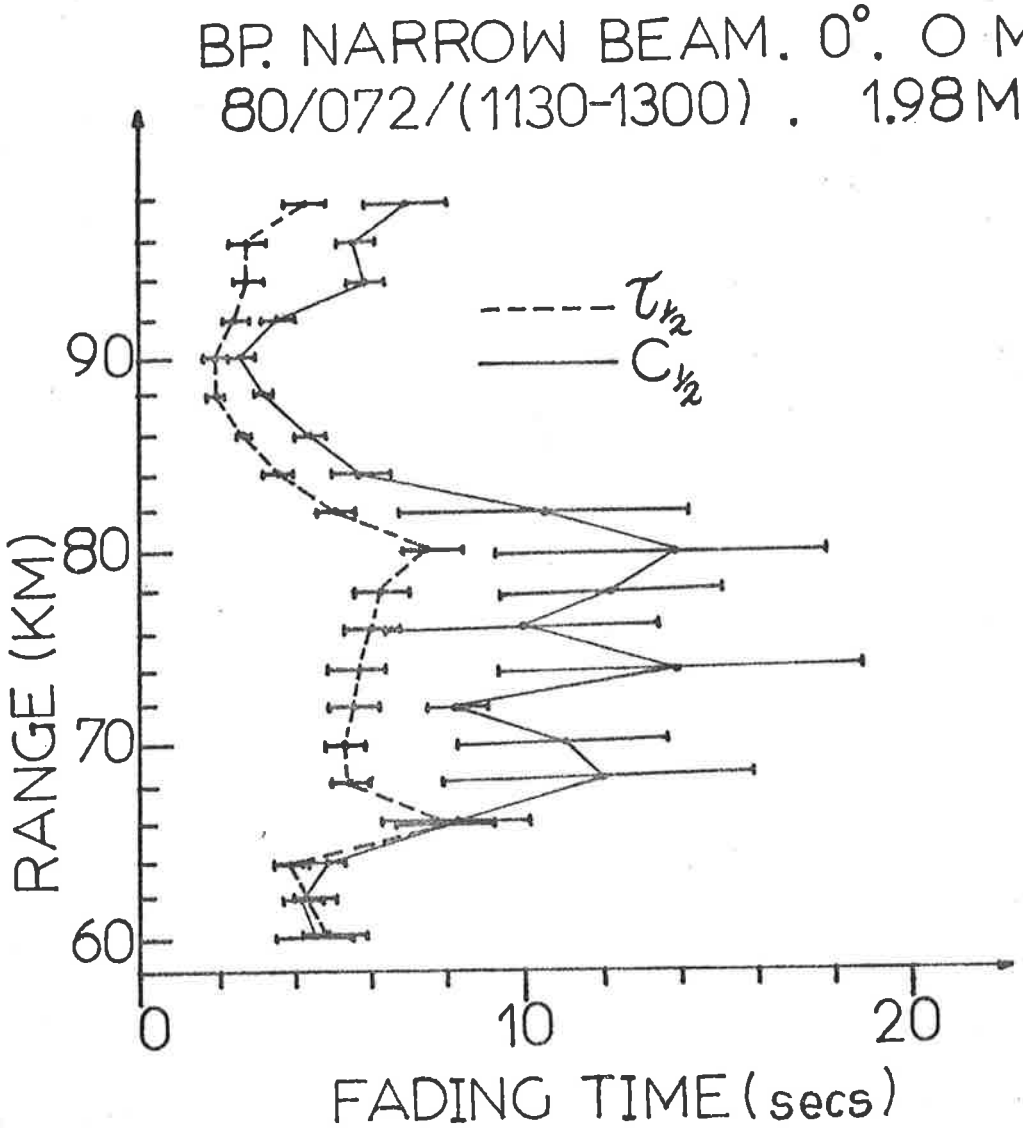

Fig 7.4 Typical profiles of $C_{1/2}$ and $\tau_{1/2}$ for the vertical narrow beam at Buckland Park using 1-minute data blocks and averaging. ($C_{1/2}$ and $\tau_{1/2}$ are less for an 11.6° tilt of the beam). The data is for 80/072 (March, 1980).

The fading times above 92 km are probably due to the tail of the E-region, and at 60-62 km may be in part due to the ground echo. At ~ 90 km, $C_{1/2} \sim \sqrt{2}\ \tau_{1/2}$, but at ranges below 80 km, $C_{1/2}$ is up to twice $\tau_{1/2}$.

The error bars are standard deviations for the mean. The data for ranges 80-98 km were taken in the period 1132-1143, and for ranges of 60-78 km in the period 1245-1254. They are fairly typical for this day. There is a large variability of $C_{1/2}$ values below 80 km, as evidenced by the large error bars. This is a reflection of the "burstiness" and temporal variability of the echoes, as discussed in Chapter IV.

7.2.2 Interpretation of short-term data

The magnitude of the autocorrelation function for the full 10 mins of data in Figure 7.1 has a Gaussian form, with a $C_{0.5}$ value of 3.1 seconds. This means that the power spectrum is also Gaussian, with a half-power-half-width of

$$(7.2.2.1) \qquad f_{\frac{1}{2}} = (\ell n 2/\pi)\ C_{\frac{1}{2}}^{-1} \approx 0.22/C_{\frac{1}{2}}$$

Thus in this case $f_{\frac{1}{2}}$ should equal 0.07 Hz. Yet the individual power spectral peaks in Fig 7.2a are much narrower than this. In fact, several peaks occur within a frequency band of .14 Hz. The question arises then, as to how these narrow peaks are to be interpreted? Further, how are they related to the form of the autocorrelation ?

7.3 Interpretation of ionospheric scatter data

7.3.1 Simulation of beam broadening

Imagine a horizontal wind, of speed V, blowing horizontally over an aerial array at D-region heights. Then a range of Doppler shifted frequencies will be received from scatterers moving with this wind, since scatter comes from a range of angles. (beam broadening). The range of frequencies will be defined by the combined polar diagram effects of the array and the scatterers. If the scatterers are isotropic, this polar diagram will be essentially that of the array. The resultant power spectrum will peak at 0 Hz, and fall away on either side. Let us assume it is Gaussian in form. The half-power-half-width of the power spectrum will be approximately

(7.3.1.1) $$f_{\frac{1}{2}} = \frac{2}{\lambda} v_{r_{\frac{1}{2}}}$$ (see Chapter III, section 3.2e)

where $v_{r_{\frac{1}{2}}}$ is the radial velocity observed at an angle $\theta_{\frac{1}{2}}$ from the zenith, $\theta_{\frac{1}{2}}$ being the angle at which the effective polar diagram falls to half power. For isotropic scatter monitored with the narrow beam at Buckland Park, $\theta_{\frac{1}{2}} \sim 4.5^\circ$ (Chapter III). Thus

(7.3.1.2) $$f_{\frac{1}{2}} \approx \frac{2}{\lambda} . V \sin \theta_{\frac{1}{2}}$$

A more accurate value for $f_{\frac{1}{2}}$ will be given shortly, but for now this equation is adequate. As an example, if $\lambda = 151.5$m, $V = 75$ ms^{-1}, and $\theta_{\frac{1}{2}} = 4.5^\circ$, then $f_{\frac{1}{2}} \approx .08$ Hz.

Thus a beam broadened spectrum produced at Buckland Park should have such a width. But as discussed in the last section, 1 minute power spectra do not produce such forms. Do the narrow peaks perhaps refer to discrete scatterers ?

To investigate this, the following computer simulation was performed. A Gaussian power spectrum was formed, with a half-power-half-width of .07 Hz. Phases were assigned randomly to each point of the power spectrum. These powers and phases were used to form the complex spectrum, and this was then Fourier transformed to produce a time series of complex data. The range of frequencies, and frequency spacing of successive points of the power spectrum were chosen so that this final time series was a simulation of a 10 minute record of data recorded at Buckland Park, with a data acquisition rate of 1 point every 0.8 seconds. Fig 7.1 shows this final time series.

Having obtained this time series, power spectra were then formed, using various lengths of this data. One minute power spectra did indeed look like Fig 7.2a. Looking at Fig 7.1, it is easy to see why. One minute of data only contains a few cycles of oscillation. Often, "regular oscillations" can be seen (with periods $\sim 8C_{\frac{1}{2}}$, i.e. $\sim$ 20-30 seconds) maintaining themselves over 2 or 3 cycles. A Fourier spectrum of such short lengths of data will inevitably only pick a few frequencies. Bearing in mind that this data was produced from a randomly phased power spectrum, two points are obvious;

(1) the existence of a "regular oscillation" maintaining itself over 2 or even 3 cycles is not immediate evidence of a genuine oscillation. We have seen here that such oscillations can occur from random data.

(2) Power spectra of one minute samples are inadequate for describing the statistics of this situation.

Fig 7.5

Running 1 minute power spectra formed on the data in Fig 7.1. See text for details. For clarity each power spectrum has been shifted vertically from the previous one. The times indicated are the start times of each 1 minute block. Each successive spectrum corresponds to a 12s shift in the data block used. A 3 point smooth ($\frac{1}{4}$, $\frac{1}{2}$, $\frac{1}{4}$) has been applied to the spectra as well.

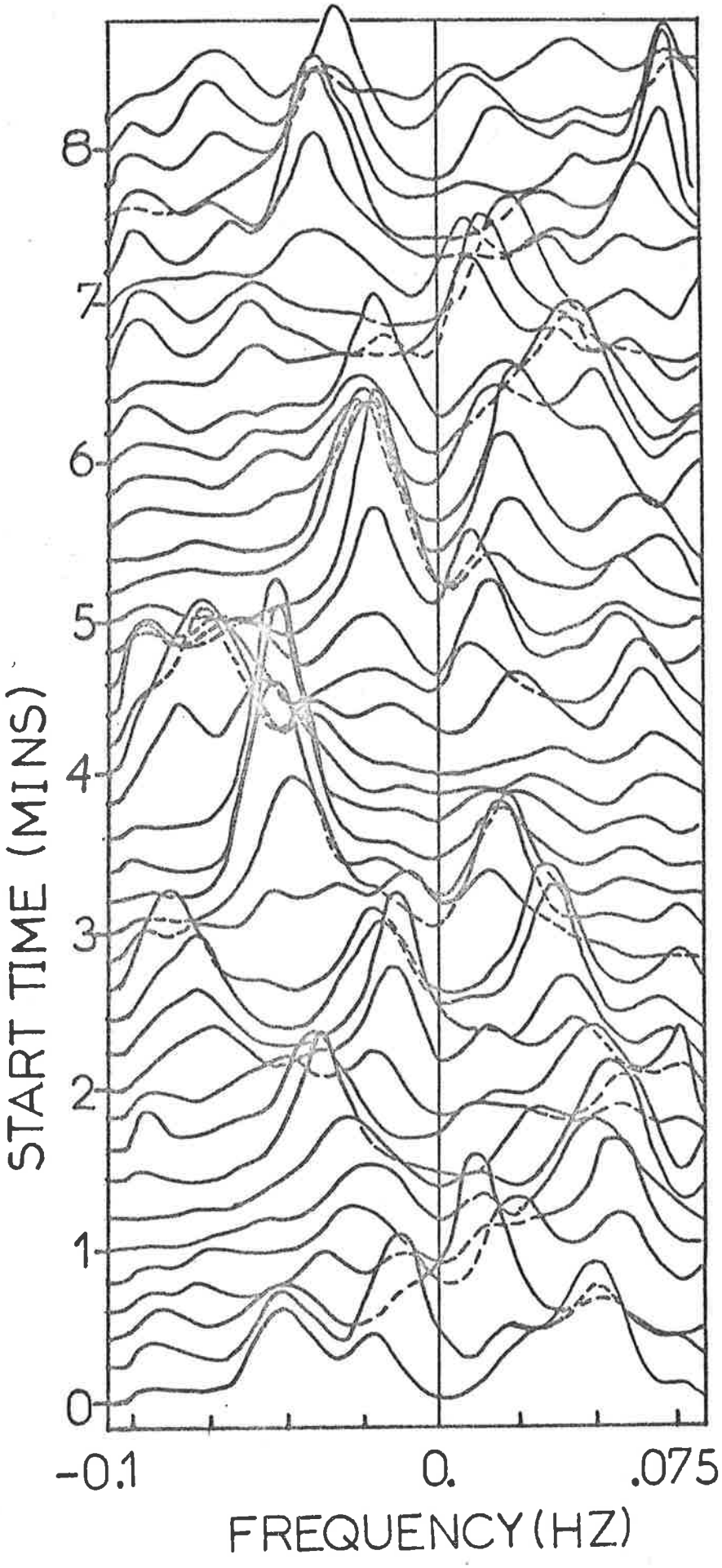
8
7
6
5
4
3
2
1
0
START TIME (MINS)
-0.1
0.
.075
FREQUENCY (HZ)

Fig 7.6a

Power spectrum produced from the first 8 minutes of the data shown in Fig 7.1. The points are for the actual direct power spectrum, with no smoothing.

Notice also the presence of a large spike (indicated by "arrow").

Fig 7.6b

Magnitude and phase of the autocorrelation of the first 8 minutes of data in Fig 7.1.

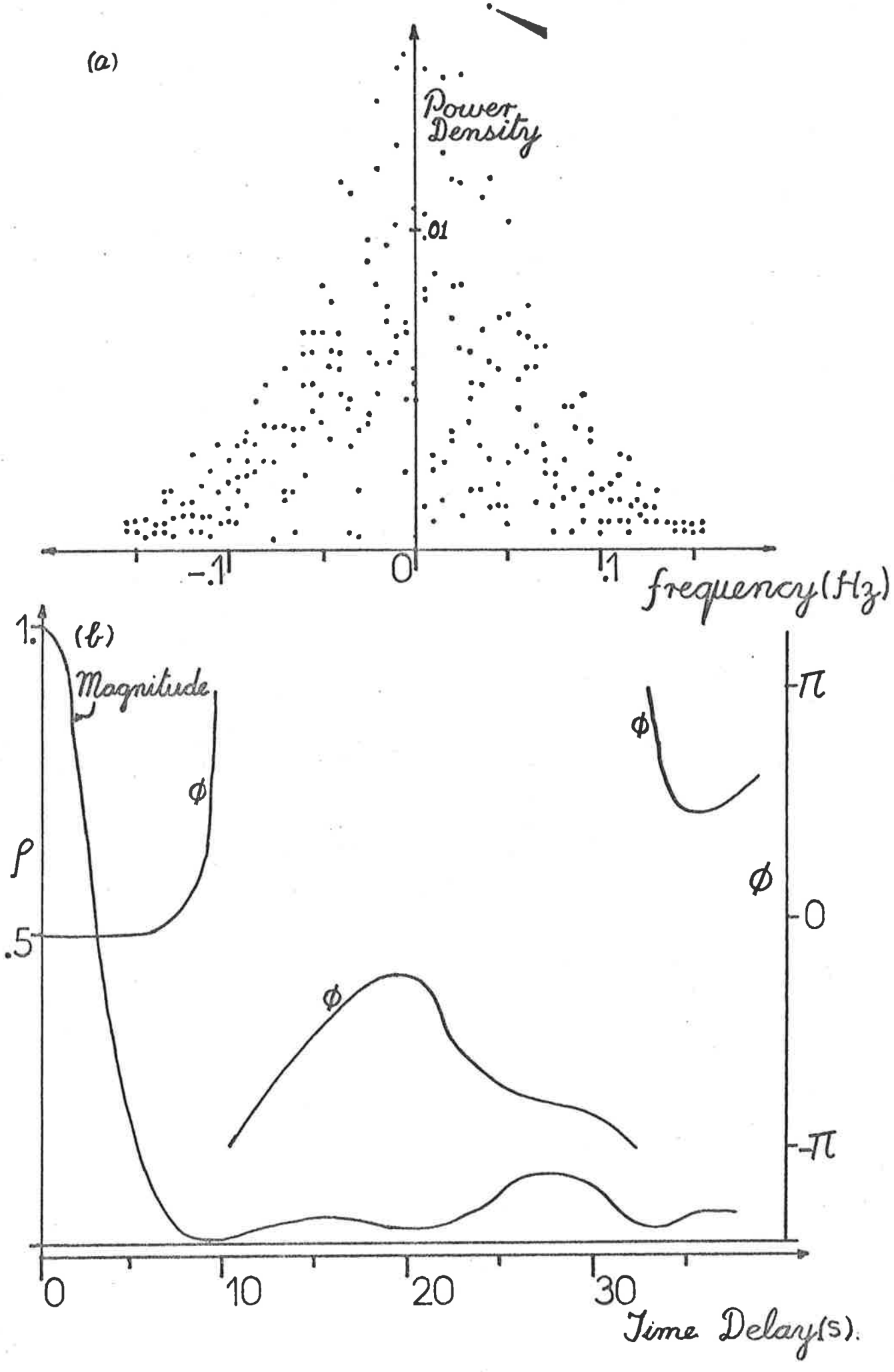
(a)
Power Density
.01
-.1
0
.1
frequency (Hz)
1.
(b)
Magnitude
ρ
.5
φ
φ
π
φ
0
-π
φ
0
10
20
30
Time Delay (s).

Fig 7.6c

This power spectrum is simply Fig 7.6a, but with frequencies averaged in blocks. The averages have been presented in a histogram form. A running mean may perhaps have been better, but this is adequate. A smooth Gaussian-shaped curve has been fitted through the spectrum by eye, and the half-power-half-width is measured as .065 Hz.

Fig 7.6d

This is also an average of Fig 7.6a, but points with values greater than .014 have not been used. This procedure is used to reject very large spectral peaks in the raw spectrum which may bias the averages (see text).

Notice in all these diagrams (7.6 a-d), the mean was first removed before performing the power spectra. This is why the averaged power spectra have dips near 0 Hz.

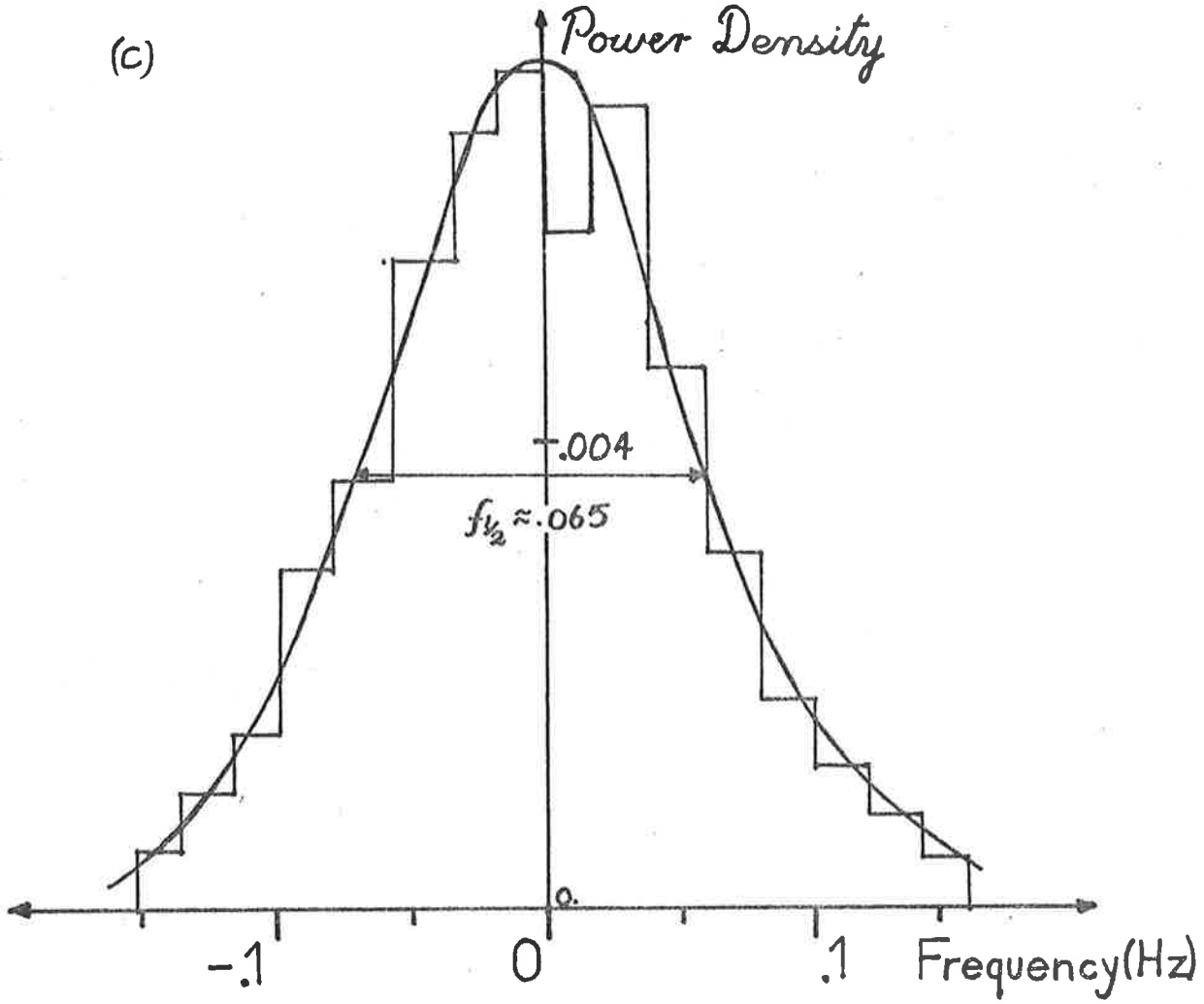
(c)
Power Density
.004
$f_{1/2} \approx .065$
0.
-.1
0
.1
Frequency(Hz)

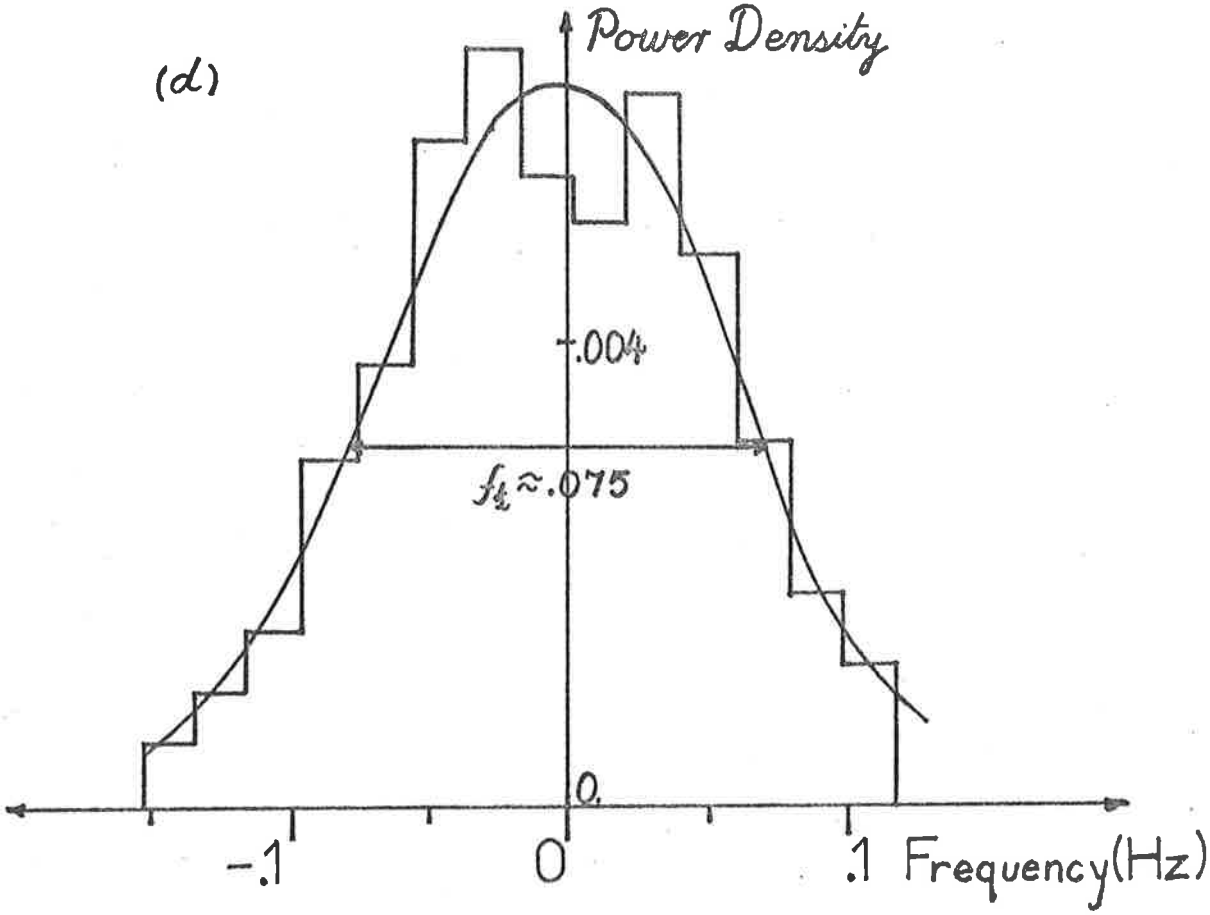
(d)
Power Density
.004
$f_{\frac{1}{2}} \approx .075$
0.
-.1
0
.1
Frequency(Hz)

Fig 7.5 shows the inadequacy of 1 minute power spectra quite well. It is a running 1 minute power spectrum. That is, the power spectrum of the first minute was formed. Then, the power spectrum of the data block from 12s to 72s was formed. Then, the power spectrum of the data block from 24s to 84s was formed, and so on, shifting the data block by 12s on each occasion. Each of these power spectra was smoothed by a simple 3 point running mean, and then plotted on Fig 7.5, one "behind" the other, with a successive upward offset. All the spectra look like Fig 7.2a, and it is quite clear the narrow peaks in Fig 7.2a cannot be interpreted as discrete scatterers within the beam. They have no physical meaning, apart from the fact that they are the power spectra of the short data series. Notice in Fig 7.5 that successive spectra do bear some resemblance,but this is not surprising considering consecutive spectra have 48s of data in common. A similarity between spectra 5 shifts apart would be surprising however, and does not appear to occur. If it did occur in some real data, it could indicate a discrete scatterer producing a narrow spectral peak.

What if longer lengths of data are used to form the power spectra ? Fig 7.6a shows the power spectrum for the first 8 minutes of Fig 7.1. A smooth Gaussian-type envelope is evident, even though each point shows large scatter. The half-width of this envelope is roughly .14 Hz. Fig 7.6b shows the corresponding autocorrelation function. To remove the scatter of points in Fig 7.6a, the power spectrum was averaged in blocks of 20 points, and Fig 7.6c shows the result. This is beginning to look like the original power spectrum from which the data was derived. It is a little narrower than the original. The reason for this can be seen in Fig 7.6a, where it will be noted there are some values in this "raw power spectrum", close to zero Hz, significantly larger than the rest. These are due to statistical fluctuations. If they are not used in the averaging process, Fig 7.6d result, which has a half-width close to .075 Hz. It may seem to unfairly bias the data by

Fig 7.7a

Direct power spectrum of the first 5 minutes of the data shown in Fig 7.1.

Fig 7.7b

Fig 7.7a, with spectral points averaged in blocks of 20. The smooth curve shows an approximately Gaussian curve fitted by eye to the data. In a real experiment, a least squares fitting procedure would be desirable, but in this case the diagrams are principally illustrative.

Notice also the large "spike" in this spectrum. This arises from purely random effects.

Notice also that the columns of this histogram are wider than those in Fig 7.6. This is simply because there was only 5 minutes of data, so the frequency spacing between successive frequencies is larger in this case.

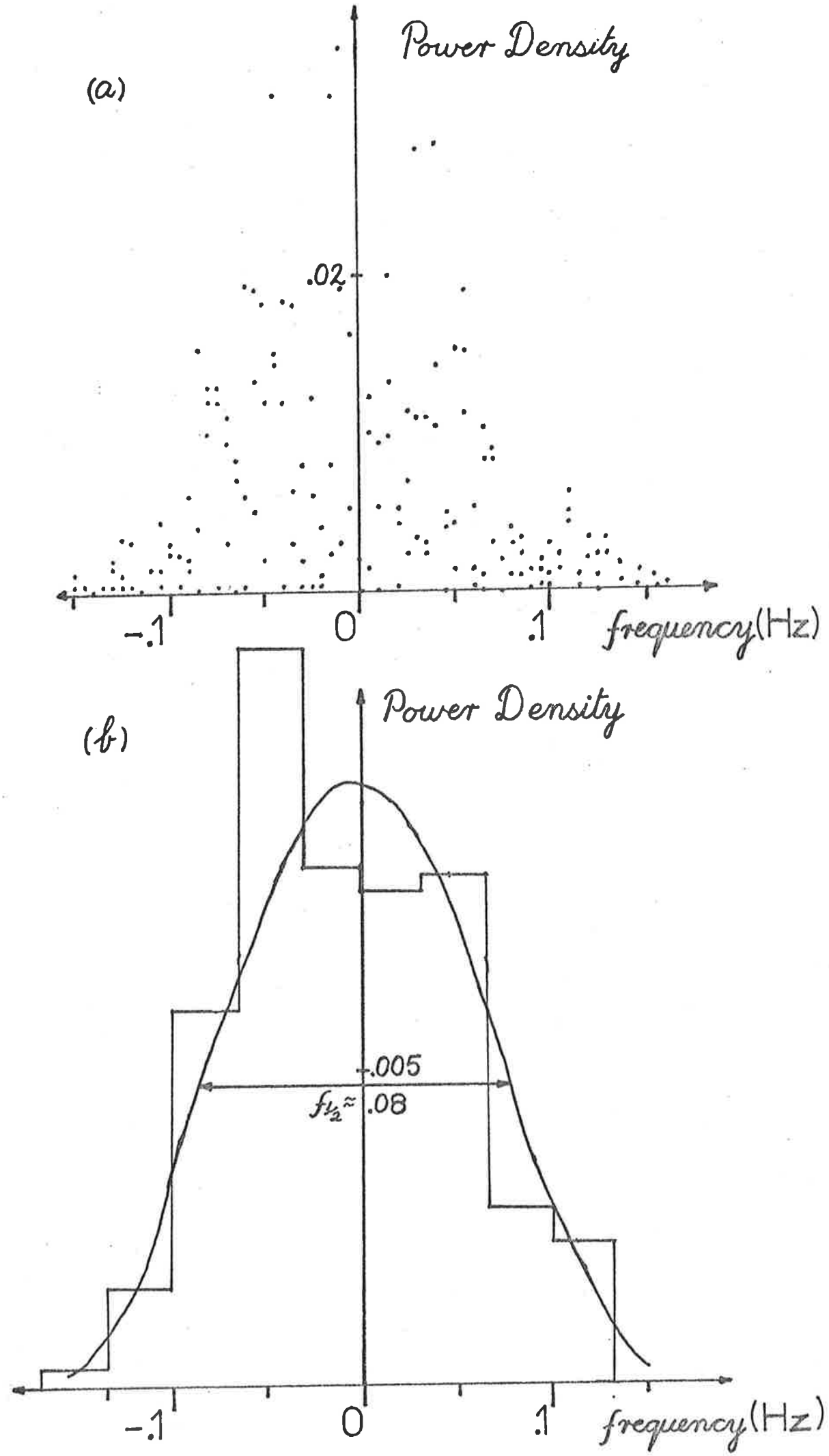
(a)
Power Density
.02
-.1
0
.1
frequency (Hz)
(b)
Power Density
.005
$f_{1/2} \approx$ .08
-.1
0
.1
frequency (Hz)

ignoring these large "spikes" near 0 Hz, but this is not really so. The "average" is not really a good statistic; the presence of one abnormally large value can unfairly bias the average. Thus in averaging these blocks of 20 frequencies, it is in fact fairer to leave abnormally large values out. The difficulty lies in deciding what constitutes "abnormally large".

However, the important point is that with adequate data lengths and sufficient care, the original power spectrum can be reproduced. (The power spectrum of the full 10 minutes reproduces the original power spectrum exactly of course.)

The process outlined above was repeated using 5 minutes of data. It was again possible to approximately reproduce the original power spectrum, and this is shown in Figs 7.7a and b. Notice in this case that the large spikes near 0 Hz are quite severe, and even show in the "smoothed" power spectrum.

It was found that for data lengths greater than about 3 or 4 minutes, it was possible to reproduce the original power spectrum. Thus, it appears that a data length of

$$T \gtrsim (90 \rightarrow 120)\ C_{\frac{1}{2}} \qquad (7.3.1.3)$$

is necessary to form a useful power spectrum. This is an important result (It also has repercussions in other fields, too - for example, the analysis of winds. The width of the power spectrum of gravity-wave-produced winds is less than about $0.2\ \text{min}^{-1}$ (- the minimum period of oscillation is about 5 min above 80 km), so the "fading time" would be greater than $.22/.2 \sim 1$ min (assuming a roughly Gaussian power spectrum). Thus, at least 100 mins of data is necessary to form anything like a reliable wind spectrum. Further, only those frequencies which can fit at least about 100/8 (i.e. ~ 12) cycles into the data length have reliable power densities.)

It will be noticed that only one autocorrelation function is shown in Figs 7.6. Yet autocorrelations could be formed as the Fourier transforms of both Figs 7.6c and 7.6d. However, these do not differ much from Fig 7.6b - the main difference is an attenuation in the oscillations at large lags. This is not surprising. Averaging the power spectra in blocks is equivalent to doing a running mean on them, with a box function of length 20 frequency spacings. This is also a convolution, as the box function is symmetric. Thus in the Fourier transform space, the original Fourier transform is simply multiplied by the Fourier transform of this box function. Since the box function is quite narrow, it's Fourier transform is wide, and so the original autocorrelation is not greatly modified by it. Another way to look at it is that averaging removes the rapid fluctuations in the power spectrum, and these rapid fluctuations correspond to the larger lags of the autocorrelation.

It may seem better to use the fading times as estimated from the autocorrelations to estimate the spectral width. However, investigations of this showed similar difficulties to those using the power spectra. One minute autocorrelations frequently showed oscillatory character, reflecting the dominance of only a few spectral peaks in the associated power spectrum. (Also see Awe, 1964).

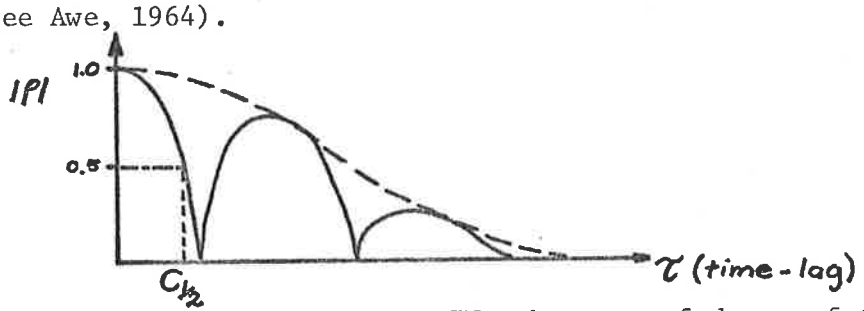

As discussed in Chapter IV, the rate of decay of the envelope is related to the width of the individual spectral peaks. However, in this case the width of the individual spectral peaks is defined purely by the data length, and has no meaning. The individual $C_{\frac{1}{2}}$ values are not really

meaningful, since they simply reflect the frequency differences between the ~2 to 4 peaks of the power spectrum. However, the 1 minute spectral peaks do generally lie within the expected spectrum, and averages of many 1 minute power spectra generally reproduce the original spectrum. In a similar way, a group of $C_{1/2}$ estimates should carry information about the original spectrum and autocorrelation function. Various procedures were tried, based on simplistic assumptions. For example, one resulting procedure was to find $C_{1/2\ \text{av.}} = (\Sigma(C_{1/2\ i})^{-1})^{-1}$. Surprisingly, the simple average of all the $C_{1/2}$ values seemed to more nearly reproduce the expected $C_{1/2}$ value (3.1s) for the whole sample. However, this was not tested in a great deal of detail. Five minute power spectra showed slow oscillations upon the general expected form, as illustrated below.

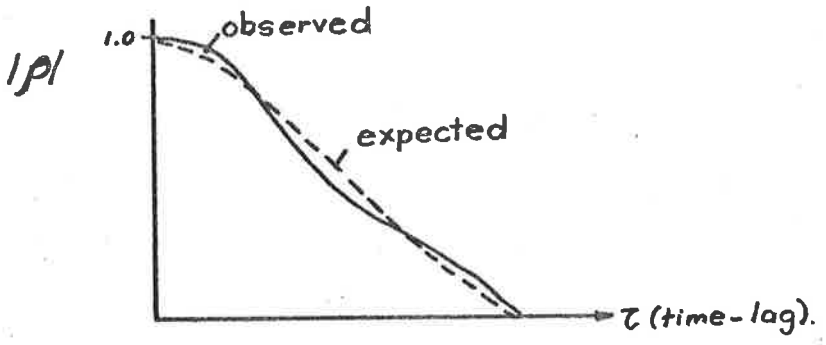

This tended to make estimation of $C_{1/2}$ difficult. These oscillations are due to the presence of "spikes" in the power spectrum, as shown in, say, Fig 7.7a. It is easier to remove these effects from the power spectrum than from the autocorrelation function.

The general results of this section would, then, appear to be that it is possible to simulate the "true" power spectrum of an ionospherically scattered radiowave data sample, provided data lengths of at least 100 $C_{1/2}$ are used (if smaller lengths are used (e.g. 1 minute), individual spectra must be averaged together), and provided sufficient smoothing is applied to the power spectrum. The error in estimation of spectral widths appears to be

of the order of 10%, or better if sufficient care is taken.

These results are not just valid for data produced by beam broadening either. They are valid for any type of Gaussian power spectrum, and probably (in perhaps slightly modified form) for any power spectrum which decays smoothly with increasing frequency.

The possibility of spurious "spikes" in the power spectrum also exists. These should be removed before obtaining the true power spectrum.

It is not claimed that this work has revealed any properties of power spectra which are not well known to professional statisticians. However, at times it does appear that some of these points are not fully appreciated by practical workers.

7.3.2 More accurate estimates of expected spectral widths

In equation 7.3.1.2, it was assumed that the half-power-half-width of the spectrum produced by beam broadening was simply related to the half-power-half-width of the polar diagram. However, the approximation used is not completely valid, although it does provide a useful first order estimate.

A power spectrum of ionospheric scatter data is produced by several effects -

(i) beam broadening

(ii) vertical motions

(iii) turbulent fluctuations

(iv) shear broadening (for off-vertical tilted beams only).

One objective of this chapter is to make estimates of the energy dissipation rates for turbulence. To do this, the spectrum must be measured, and then the other effects removed. Term (iv) will be discussed later, and term (ii) will be essentially ignored; vertical motions generally oscillate with periods greater than about 5 minutes, and simply produce a shift in the peak of the spectrum from 0 Hz (provided the length of data used is less than about ½ to ¼ of the shortest oscillation period).

To effectively remove term (i), the expected half-power-half-width of the spectrum produced exclusively be beam broadening must be known. This section will produce this, and some interesting effects will also be seen for the case of a wide beamed receiver.

The problem can be expressed as follows:-

"Find the power spectrum received (as a function of virtual range) with a coherent radar, for the case of some scatterers, with backscatter cross-section of $\sigma(\underline{r})$, $\underline{r}$ being the vector to the scatterer, moving in a wind of speed v in a direction defined by ϕ_0, given the radar polar diagram".

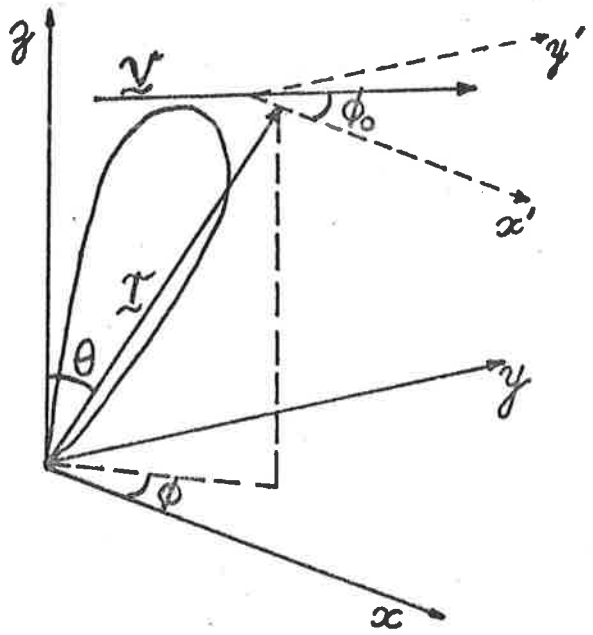

Fig 7.8a Diagrammatic representation of first problem discussed in Section 7.3.2.

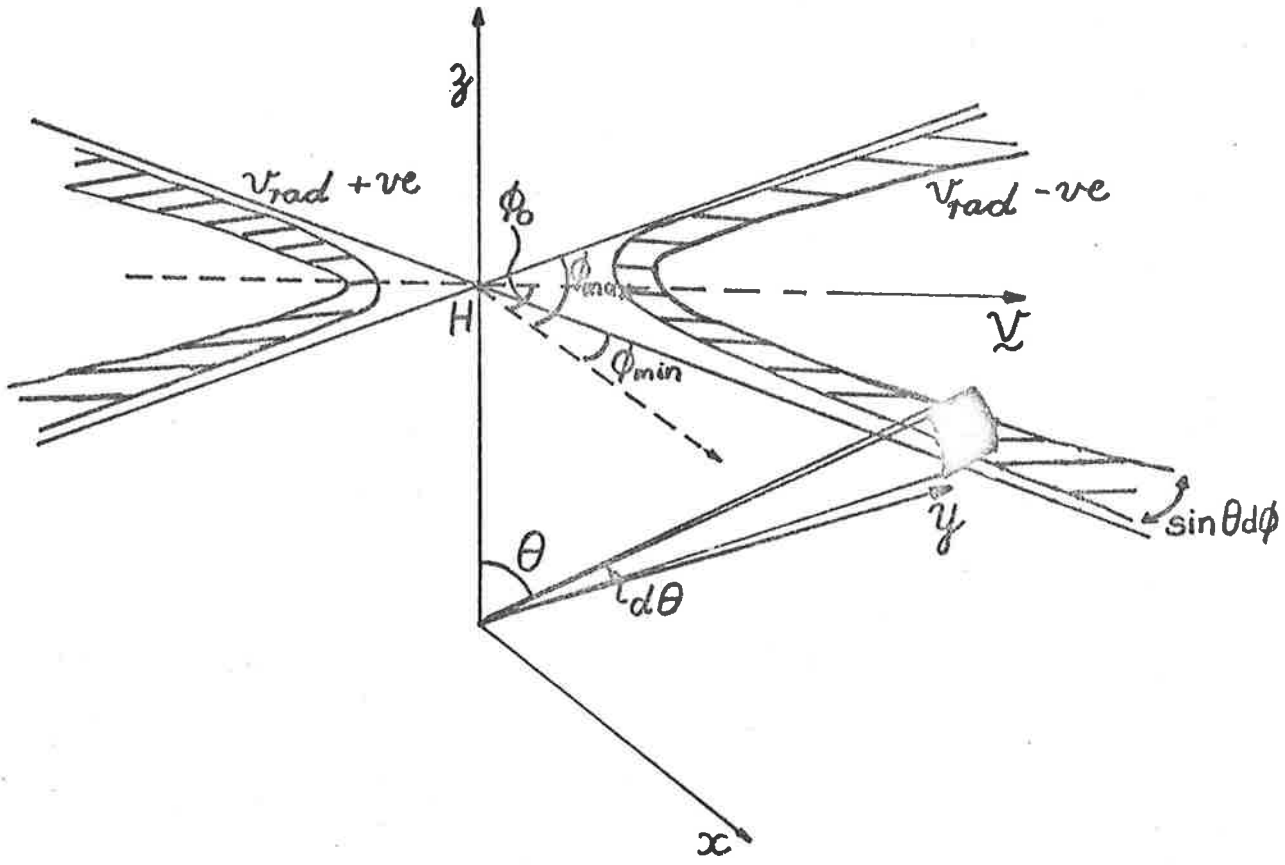

Fig 7.8b Contours of constant radial velocity at height H.

Fig 7.8a illustrates the problem. If $\underline{i}$, $\underline{j}$ and $\underline{k}$ are unit vectors in the x, y and z directions, $\underline{v} = v\cos\phi_0\,\underline{i} + v\sin\phi_0\,\underline{j} + 0\underline{k}$, and the component of velocity observed for scatter from a scatterer at $\underline{r}$ is

(7.3.2.1) $v_r = \underline{v} \cdot \hat{\underline{r}}$, where $\hat{\underline{r}}$ is a unit vector and equals

$(\sin\theta\cos\phi)\underline{i} + (\sin\theta\sin\phi)\underline{j} + (\cos\theta)\underline{k}$.

Define a normalized radial velocity by

(7.3.2.2) $V = v_r/v$.

Then by (7.3.2.1),

(7.3.2.3) $V = \cos\phi_0 \sin\theta \cos\phi + \sin\phi_0 \sin\theta \sin\phi$.

After squaring this, and applying appropriate manipulation, it becomes clear that

(7.3.2.4) $V = \sin\theta . \{\frac{1}{2}(1 + \cos 2(\phi_0 - \phi))\}^{\frac{1}{2}}$

The square root is taken as positive if ϕ lies between $\phi_0 + \pi/2$ and $\phi_0 + 3\pi/2$, and negative otherwise. This is to say a velocity is considered positive if v_r is towards the receiver.

Thus equation (7.3.2.4) defines the surface of constant V values in the θ, ϕ space. In Fig 7.8b, the surface producing V values between V and V + dV is shown, for a given $d\phi$.

It will be noticed that there are limiting values of ϕ, ϕ_{min} and ϕ_{max}. These are defined as the points where (7.3.2.4) becomes imaginary, i.e.

(7.3.2.5) $$\phi_{\substack{min \\ max}} = \phi_0 \pm \tfrac{1}{2} \cdot \cos^{-1} (2V^2 - 1)$$

If V is positive, use $(\phi_{\substack{min \\ max}} + \pi)$.

The surface shown in Fig 7.8b, given dV and $d\phi$, can be found as follows. Using equation (7.3.2.4), squaring and differentiating, one obtains

(7.3.2.6) $$2 \sin\theta \cos\theta \, d\theta = (2V/X)dV - 2(V^2/X^2)\sin 2(\phi_0-\phi)d\phi$$

where

$$X = \tfrac{1}{2}(1 + \cos 2(\phi_0-\phi))$$

Thus this defines $d\theta$, given $d\phi$ and dV.

The solid angle defined by $d\phi$ and dV is

(7.3.2.7) $$d\Omega = \sin\theta d\theta d\phi \qquad \text{(fig 7.8b)}$$

$$= (2V/X)dV.\,(d\phi/(2\cos\theta)) - 2(V^2/X^2)\sin 2(\phi_0-\phi)/(2\cos\theta).(d\phi)^2 \quad \text{by (7.3.2.6)}$$

We now seek the power scattered from solid angle $d\Omega$. Let the backscattering cross-section at (r, θ, ϕ) per unit volume into unit steradian be $\sigma(r, \theta, \phi)$. Let the polar diagram for the radar be $P(\theta, \phi)$. Then the power received from solid angle $d\Omega$ and at a virtual range R, is proportional to

(7.3.2.8) $$T(R, \theta, \phi)d\Omega$$

$$= P(\theta, \phi).\left[\frac{\sigma(r, \theta, \phi)}{r^4} \cdot (r^2 d\Omega) \otimes g(r)\right]$$

Here, $g(r)$ defines the pulse transmitted into the atmosphere. It was seen in Appendix B (equation B.26b) that the scattered signal was a convolution between the pulse and the scattering function. The r^{-4} term arises because of an r^2 fall off with distance from the transmitter, and a further r^2 fall off after scatter. (These effects were not considered in Appendix B). The $r^2 d\Omega$ term arises due to the scattering area. In this formula, absorption has been ignored. A better formula will be derived later in Chapter VIII, but for present purposes absorption can be ignored.

Equations (7.3.2.7) and (7.3.2.8) can now be used to estimate the scattered power received in the velocity range V to $V + dV$ by integrating (7.3.2.8) over all acceptable θ, ϕ. Thus, for any virtual range R, a power spectrum can be produced.

For computer application, a layer of isotropic scatterers, with base height H, and thickness $d << H$, was considered. (The program used is shown in Appendix E ("Specpol").)

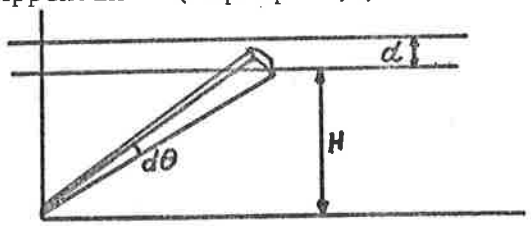

Let

$$(7.3.2.9) \qquad F(V, R) = \int_{\phi=\phi_{min}}^{\phi_{max}} P(\theta, \phi) \, [\, \sigma/r^2 \otimes g(r) \,] d\Omega \,,$$

where ϕ_{min}^{max} are defined by equation (7.3.2.5), θ is given by (7.3.2.4), and $d\Omega = \dfrac{V(dV)\,d\phi}{X \cos\theta}$, where $X = \frac{1}{2}(1 + \cos 2(\phi_0 - \phi))$

(ignoring the second term in (7.3.2.7), which is a second order effect, as it involves $(d\phi)^2$). Here,

Fig 7.9a

Expected beam broadened power spectra for the vertical narrow Buckland Park beam at 1.98 MHz (transmitter polar diagram included) for a layer of isotropic scatterers extending from 80 to 82 km and of infinite horizontal extent. The numbers on the graphs refer to the ranges (in km) of the data used to form the spectrum. The "normalized velocity" is equal to the radial velocity divided by the horizontal wind velocity. The power pulse used was of the form

$\cos^4 (h/8.5 \times \pi)$ between $h = \pm 4.25$ km, and zero elsewhere.

The broken curves simply refer to ranges greater than the range of maximum power. The power units are rather arbitrary, but can be compared to Fig 7.9b. The graph in the inset shows the half-power-half-width of the various graphs. Notice this is a function of the range. The reason for this can be seen in the diagram (i) below (not to scale), where it can be seen that significant scatter comes from a wider range of angles at ranges R_2 and R_3 than at range R_1 so larger beam broadening is to be expected.

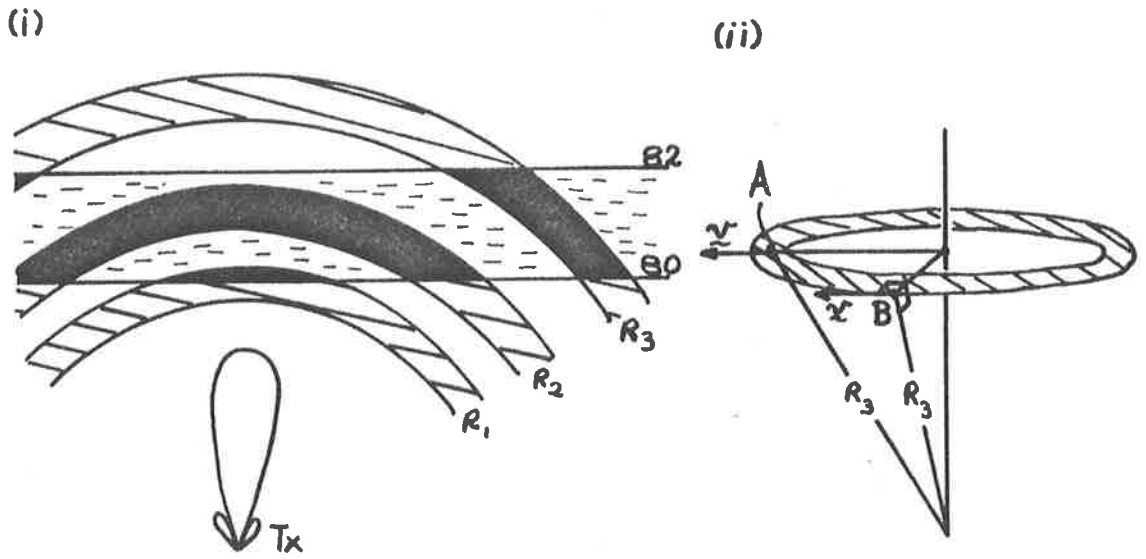

Notice in the "R_3" case, there is no scatter from directly overhead, so it might seem that no scatter with zero Doppler shift should occur. However, it should be borne in mind that fig (i) is a 2-dimensional slice through a 3-dimensional system, and fig (ii) illustrates this. Scatter from the point B would in fact produce zero doppler shift so there would still be a significant zero frequency contribution to the spectrum. However, fig (i) does illustrate why the spectra are broader and the side lobes are larger at 83 and 84 km range in Fig 7.9a. This 3-dimensional nature should also be borne in mind when considering Figs 7.9b and c.

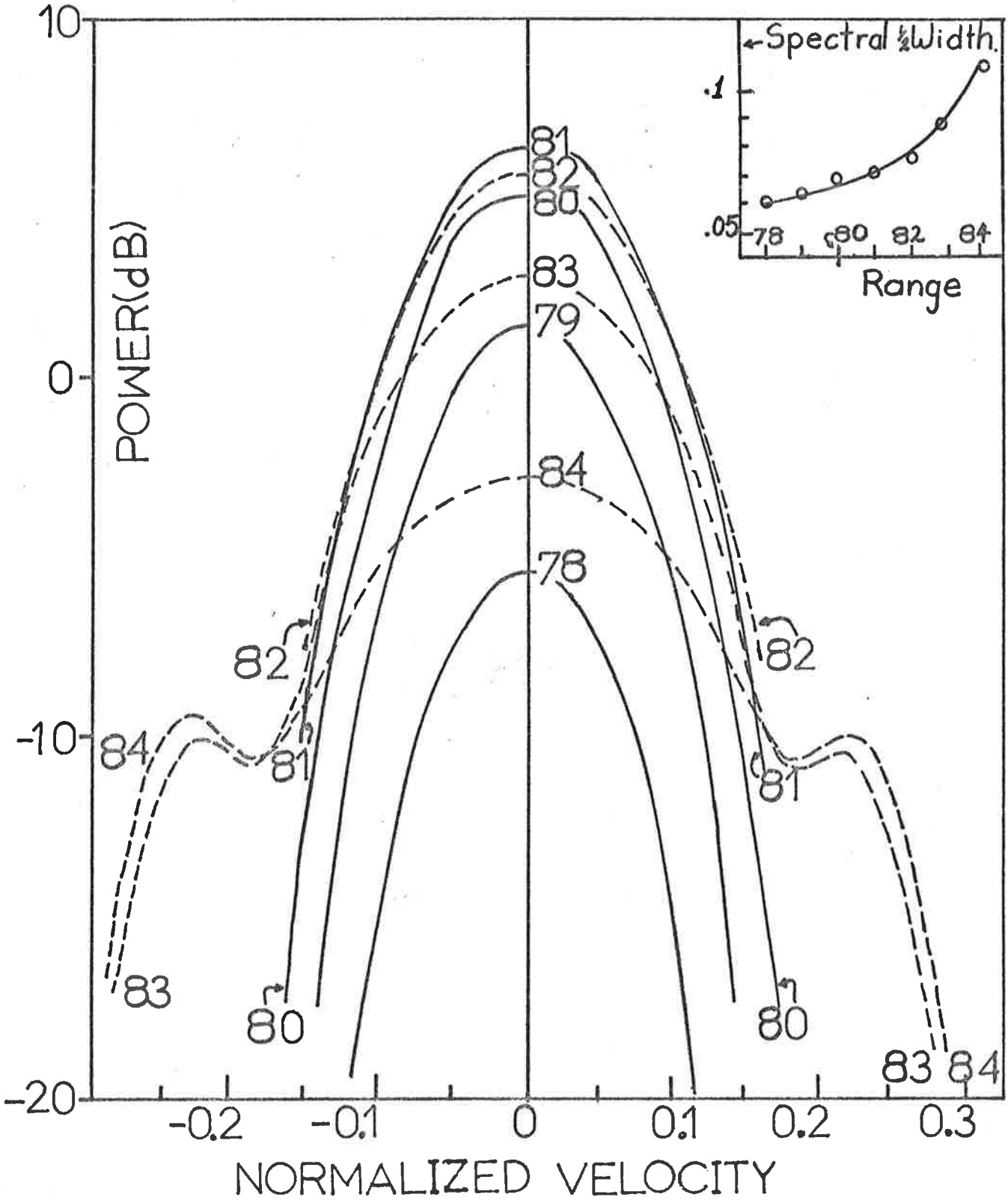
10
0
-10
-20
POWER(dB)
-0.2
-0.1
0
0.1
0.2
0.3
NORMALIZED VELOCITY
81
82
80
83
79
84
78
82
84
81
83
80
82
81
80
83
84
Spectral ½Width
.1
.05
78
80
82
84
Range

Fig 7.9b

Expected beam-broadened power spectra for the narrow Buckland Park beam at 1.98 MHz, tilted at 11.6° in the direction of the wind, for a layer of isotropic scatterers extending from 80 to 82 km and of infinite horizontal extent. The numbers on the graphs refer to the ranges (in km) of the data used to form the power spectrum. The pulse used was the same as that for Fig 7.9a. The power units are rather arbitrary, but can be compared directly to Fig 7.9a.

The graph in the inset shows the half-power-half-width of the spectra, and the offsets of the peak, as a function of range. Notice after maximum scattered power is reached, the half-width falls. The reason

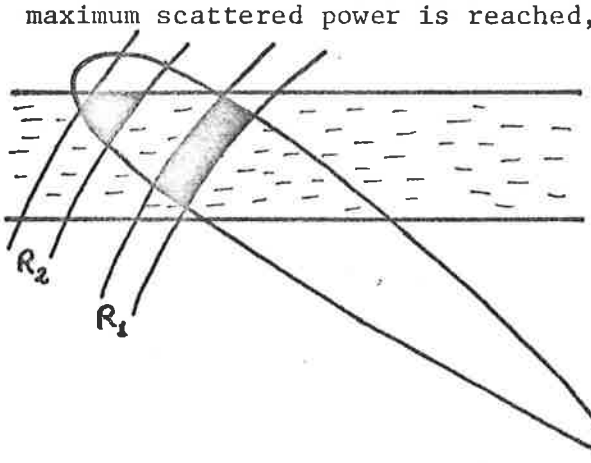

for this can be seen in the diagram - it can be seen the layer thickness itself limits the effective width of the polar diagram.

Notice also that only at the peak of power is the offset equal to the expected normalized velocity of - 0.2. This is thus a warning for Doppler measurements of the wind - the spectrum used must correspond to the range of maximum scattered power, or else erroneous numbers will result.

(The "normalized velocity" is equal to the radial velocity divided by the horizontal wind. Radial velocities away from the receiver are taken as negative).

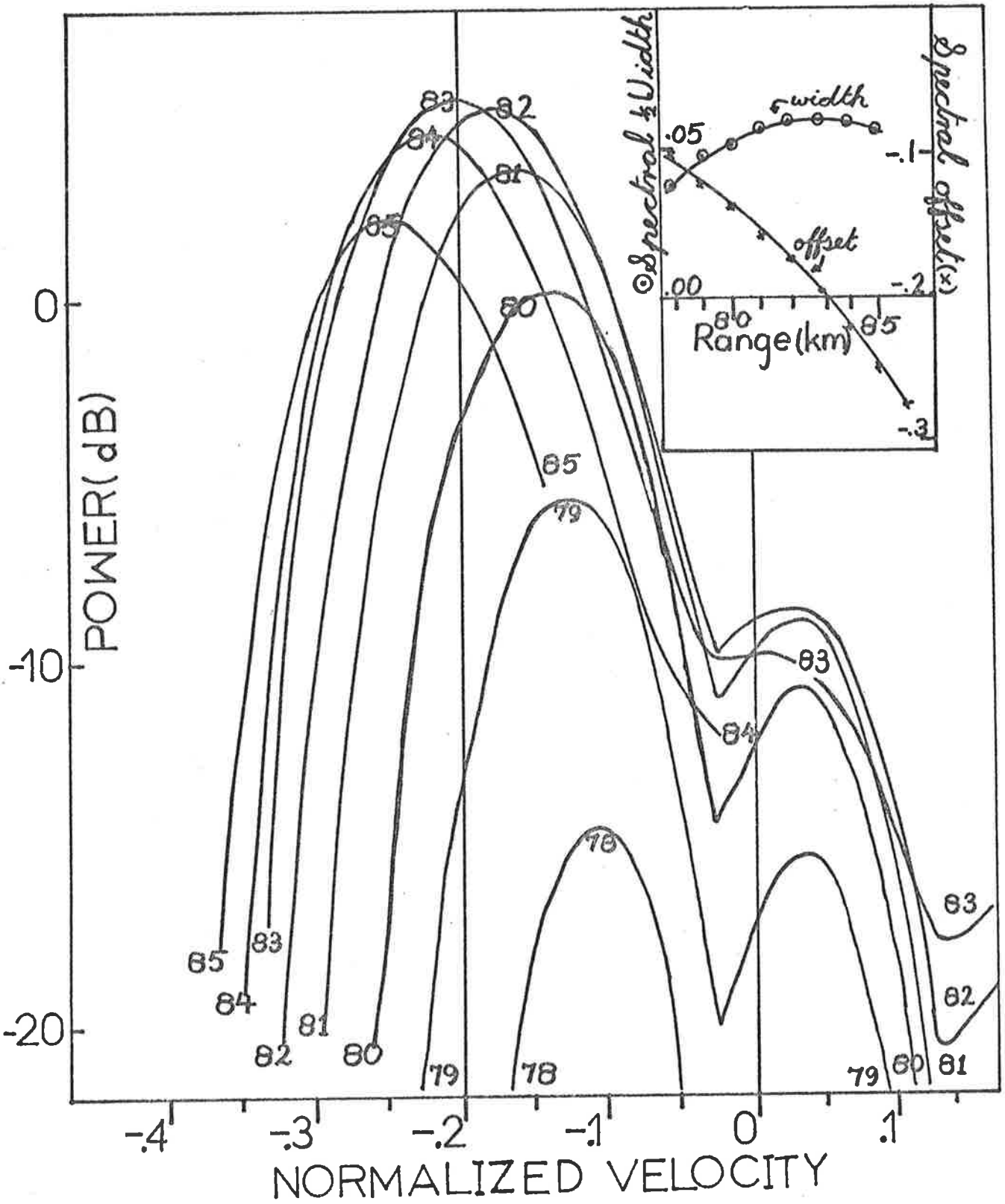
0
-10
-20
POWER(dB)
-.4
-.3
-.2
-.1
0
.1
NORMALIZED VELOCITY
Spectral ½ Width
Spectral offset(x)
width
offset
.05
.00
-.1
-.2
-.3
80
85
Range(km)
83
82
84
81
85
80
79
78
65
83
84
81
82
80
79
78
83
84
83
82
79
80
81

Fig 7.9c

Expected beam broadened power spectra for an isotropic transmitter - receiver system for a layer of isotropic scatterers extending from 80 to 82 km and of infinite horizontal extent. The numbers on the graphs correspond to the ranges (in km) of the data used to form the spectra. The pulse used was the same as that in Figs 7.9a, b. The power units are arbitrary, and cannot be compared to Figs 7.9a, b.

Notice that at large ranges the spectrum splits. The reason for this can be seen in the following diagram.

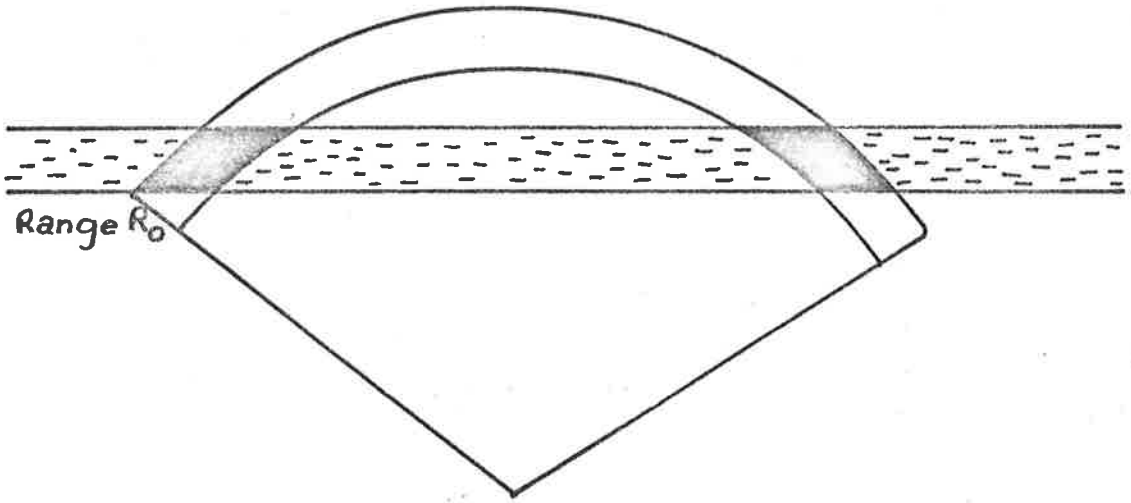

A similar effect acted in Fig 7.9a, but in that case the polar diagram was quite narrow and double peaked spectra were thus not produced. Notice, however, that significant powers still occur at zero frequency, and this is due to the 3-dimensional nature of the problem, as discussed in Fig 7.9a.

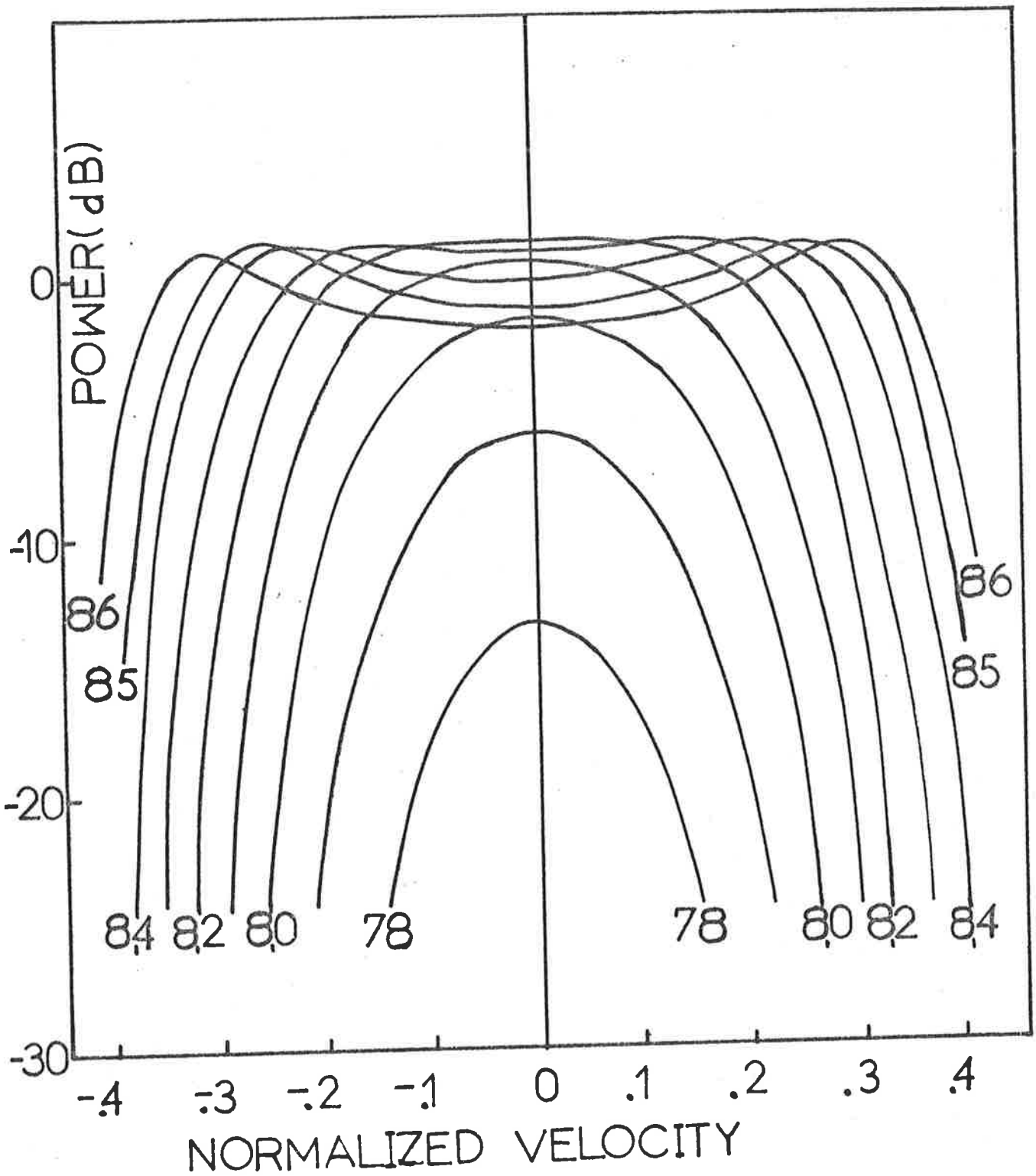
POWER(dB)
0
-10
-20
-30
86
85
84
82
80
78
78
80
82
84
85
86
-.4
-.3
-.2
-.1
0
.1
.2
.3
.4
NORMALIZED VELOCITY

	$\phi_0 = 0^c$			$\phi_0 = \pi/2^c$		
	R_M(km)	$V_{\frac{1}{2}}$	$\theta_{\frac{1}{2}}$(deg)	R_M(km)	$V_{\frac{1}{2}}$	$\theta_{\frac{1}{2}}$(deg)
2 MHz beam pointing vertically	81	.072	4.13°	81	.072	4.13°
6 MHz beam pointing vertically	81	.025	1.43°	81	.025	1.43°
2 MHz beam pointing 11.6° off vertical	82.7	.062	3.55°	82.7	.075	4.30°

[$V_{\frac{1}{2}}$ errors typically ± .003] ($V_{\frac{1}{2}}$ dimensionless)

TABLE 7.1

$V_{\frac{1}{2}}$ and effective $\theta_{\frac{1}{2}}$ values (to be used in equation 7.3.1.2) for a 2 km deep layer with base height at 80 km, for a range R_M corresponding to maximum scattered power (this is approximately the distance required to reach the midpoint of the layer in the direction of tilt of the polar diagram). The transmitted pulse is as defined in Figures 7.9. Various polar diagrams and wind directions ϕ_0 are given. Here, ϕ_0 can be taken as the angle of the wind vector from the plane of tilt of the diagram. (The vertical polar diagram is not quite symmetric in aximuth but is close enough for most purposes.)

Particularly, notice the different $V_{\frac{1}{2}}$ values at 11.6°. This is not really unexpected, considering the different configuration.

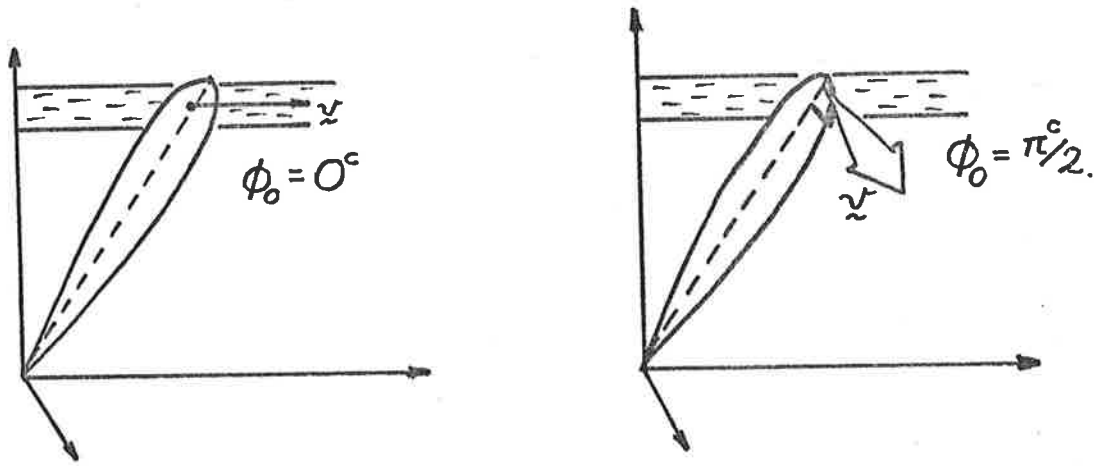

Notice for $\phi_0 = 0$ the peak of the power spectrum has an offset of $V = -0.2$ whilst for $\phi_0 = \pi/2$, there is no offset of the peak. The above diagrams illustrate why this is so.

$$\sigma/r^2 \otimes g(r) = \int_{-\infty}^{\infty} \sigma/r^2 \, g(R-r)\,dr,$$

and $\sigma = 1$ within the layer and zero outside.

Then $F(V, R)$ was calculated for various R values, and plotted as a function of V. This was done for various polar diagrams -

(i) the narrow beam at Buckland Park looking vertically (2 and 6 MHz)

(ii) the narrow beam at Buckland Park tilted to 11.6° off zenith (2 and 6 MHz), and

(iii) an isotropic radar.

Various layer thicknesses d, and various wind directions ϕ_0, were used. Figs. 7.9 show typical spectra. The full polar diagram, as described in Chapter III, were used for these calculations. A large amount of information is contained in these spectra. It is not possible to present all of this here, and the spectra have still not been fully exploited. As an example, it can be seen in Fig 7.9b that the peak of the power spectra change as the range changes. Only at the range of peak power (which lies near the midpoint of the layer) is the measured peak at the correct V shift. (This is a warning - clearly Doppler wind measurements will be erroneous if this range is not carefully selected). If these spectral peaks are plotted as a function of range, a near-straight line is produced. This slope is a function of the layer depth, and provides a possible way to measure the depths of scattering layers at 80-95 km. However, the matter is more complicated if a wind shear exists within the layer. Similarly, the half-power-half-width of these spectra are a function of range. The situation is certainly far more complicated than equation (7.3.1.2) suggests.

Table 7.1 shows $V_{\frac{1}{2}}$ values (half-power-half-width) and effective $\theta_{\frac{1}{2}}$ values which could be used to make the approximation (7.3.1.2) valid, for various polar diagrams and wind directions.

The spectral power spectrum half-width for any wind vector can be found from tables like 7.1 as

(7.3.2.10) $$f_{\frac{1}{2}} = 2/\lambda \{ (V_{\frac{1}{2}(1)} v_1)^2 + (V_{\frac{1}{2}(2)} v_2)^2 \}^{\frac{1}{2}}$$

where the wind vector has been resolved into a component parallel to the direction of tilt of the beam, v_1 (with the corresponding $V_{\frac{1}{2}(1)}$ being found in Table 7.1), and a component v_2 perpendicular to this tilt.

This statement is not totally obvious, but can be proved as follows. Let the power spectrum due to each component be

$\exp \{-(f/f_a)^2\}$ and $\exp \{-(f/f_b) \}^2$. The resultant power spectrum is the convolution at these two, which is $\exp \{ f^2/(f_a^2 + f_b^2) \}$. Thus, if the two original spectra had half-widths of $f_1 = f_a\sqrt{\ell n 2}$ and $f_2 = f_b\sqrt{\ell n 2}$, the resultant half-width is $(f_1^2 + f_2^2)^{\frac{1}{2}}$. Hence follows (7.3.2.10) (by using the equation $f = (2/\lambda) \cdot v_{rad}$ from Chapter III, Section 3.2e).

Notice for a vertical beam, $V_{\frac{1}{2}(1)} = V_{\frac{1}{2}(2)}$, so

$$f_{\frac{1}{2}} = 2/\lambda \, V_{\frac{1}{2}} \, v_{tot}, \quad v_{tot} \text{ being the total wind vector.}$$

However, it must be borne in mind that Table 7.1 is only applicable for the range of maximum scattered power.

The assumption that the resultant power spectrum is a convolution between the power spectra produced by the 2 orthogonal wind components is also an approximation. It relies on the assumption that all parallel cross-sections through the polar diagram are constant in form. That is, if the polar diagram, looking from above,

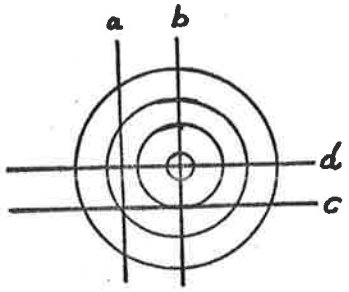

has contours as illustrated here, then cross-sections a and b must be the same in form, and c and d must also be the same. This is not really true, particularly if the side lobes are considered. However, the side lobes make a negligible contribution, and the assumptions outlined above are close enough for most work.

7.3.3 Two unequal spectral peaks, and their effect on the autocorrelation

(OR "the phase of the sum of two sine waves beating together")

In the preceding discussion, the relevance of narrow spectral peaks in the power spectrum has been considered. It was found that if sufficient data was not taken, these peaks may not be meaningful. But suppose sufficient data is used, and two spectral peaks still result ? Fig 7.9c shows examples of such cases. Then what affect does this have on the autocorrelation ? In particular, what effect do these peaks have on the phase of the auto-correlation function ? It is important to understand this problem, because often the rate of change of phase of the autocorrelation function at zero lag is used to deduce Doppler velocities (e.g. Woodman and Guillen, 1974). If perhaps two specular scatterers contribute to the power spectrum, then how is this rate of change of phase related to the respective Doppler velocities of the scatterers ? Rastogi and Bowhill (1976b) have also considered this problem, and have proposed a very complex formula. This tends to hide the physics of the problem, so the problem will be discussed here from a pictorial viewpoint.

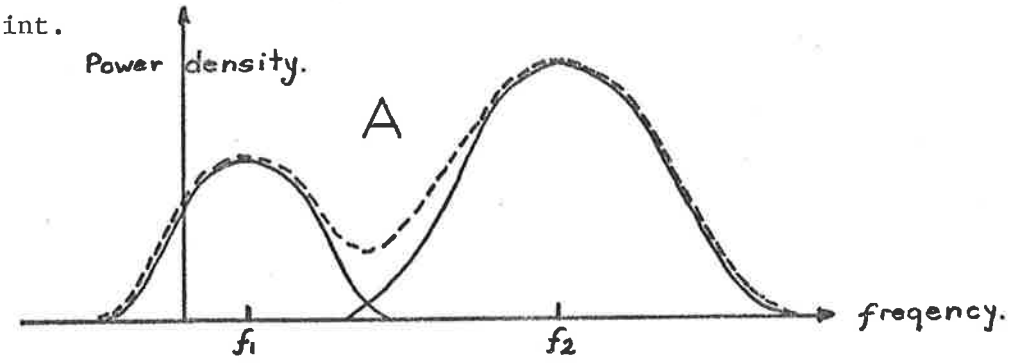

Consider a power spectrum function like that shown by the broken line above. This spectrum is taken as the sum of the two Gaussian-like solid curves. The Gaussian-like curves are assumed to have the same form.

This spectrum may be considered as the convolution of two narrow peaks at f_1 and f_2 convolved with the Gaussian-like curve, i.e.

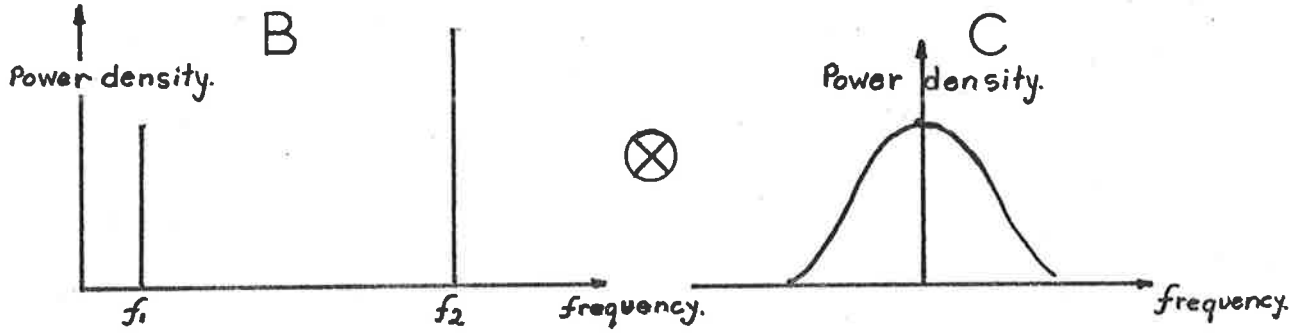

The three power spectra drawn above will be denoted A, B and C, as labelled.

Then the autocorrelation function corresponding to figure A (i.e. the Fourier transform of A) is the Fourier transform of spectrum B multiplied by the Fourier transform of spectrum C. This follows from the convolution theorem of Fourier analysis (e.g. see Champeney, 1973, p. 73). The effect of the Fourier transform of spectrum C is simply to make the envelope of the Fourier transform of spectrum B fall away more rapidly with increasing lag; it does not affect the phase. Thus the phase variation of the required autocorrelation is the same as the phase variation of the Fourier transform of spectrum B. This considerably simplifies the problem. Further, the functions defined by spectrum B are just two sinusoidal waves of frequencies f_1 and f_2. Thus the problem becomes just that of examining the amplitude and phase variations of two sinusoidal waves, with angular frequencies ω_1 and ω_2, beating together.

The easiest way to consider this problem is to consider two waves of equal frequency, but with one gradually changing in phase. i.e.

$$\cos \omega_2 t = \cos (\omega_1 t - \phi), \quad \text{where} \quad \phi = (\omega_1 - \omega_2)t.$$

Let these waves be $A_1 \cos \omega_1 t$ and $A_2 \cos(\omega_1 t - \phi)$. The resultant is

$$A_1 \cos \omega_1 t + A_1 \cos(\omega_1 t - \phi)$$

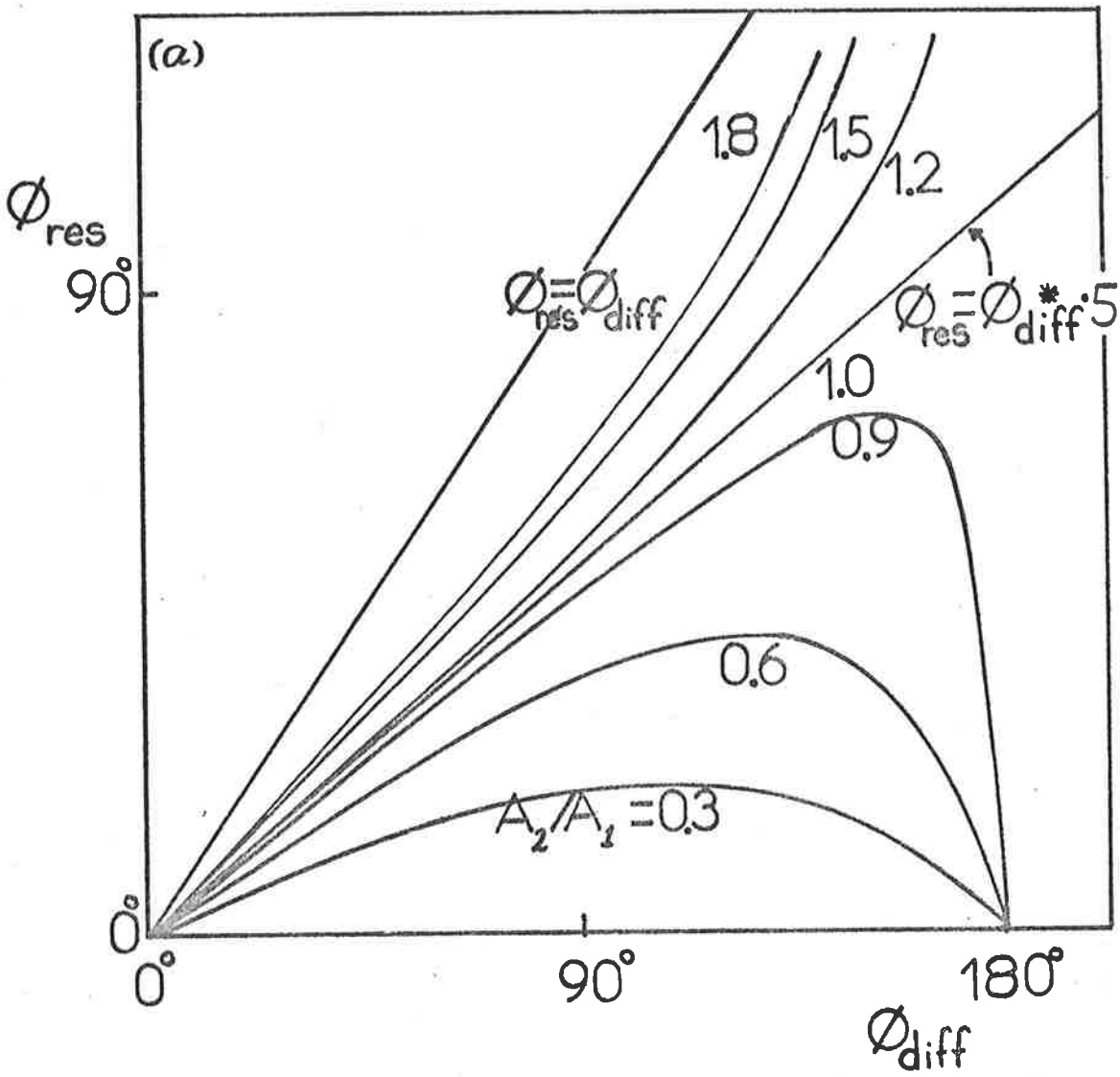

Fig 7.10a

Graphs of the resultant phase ϕ_{res} of the sum of two sine waves (frequencies ω_1, ω_2 and amplitudes A_1, A_2) of different frequencies plotted as a function of the phase difference ϕ_{diff} between the two sine waves; ϕ_{diff} (= $(\omega_1-\omega_2)t$). The results are intuitively reasonable. The numbers on the graphs are A_2/A_1 values. For small A_2/A_1 values, $\phi_{res} \approx 0$, and the ω_1 wave dominates; for large A_2/A_1 values, $\phi_{res} \to \phi_{diff}$ and the ω_2 wave dominates. For $A_2 = A_1$, $\phi_{res} = \phi_{diff}/2$. The amplitude of the resultant maximizes at $\phi_{diff} = 0$, and falls to a minimum at $\phi_{diff} = 180°$.

Fig 7.10 b, c, d. (schematic only)

Graphs of the phase and amplitude of the sum of two sine waves of different frequencies plotted as a function of time. Case (b) gives the phase with respect to that of one of the sine waves (angular frequency ω_1) and Case (c) gives the phase with respect to some third sine wave, angular frequency ω_*. Case (d) shows the situation when $A_1 = A_2$.

Notice in all these cases, $\omega_2 > \omega_1$ and both are greater than ω_*.

This is not always necessary, of course, and in cases with ω_1, $\omega_2 < \omega_*$, $\dot{\phi}_{res}$ decreases with time. The important thing is that the phase fluctuates around the phase variation which the frequency of largest amplitude would have. (The broken lines show that phase variations of the pure sine curves). Phase changes occur most rapidly at the minima in amplitude. In the case (d), $(A_1 = A_2)$, a $2\pi^c$ ambiguity means the phase can be regarded as fluctuating around either the phase of ω_1 or that of ω_2.

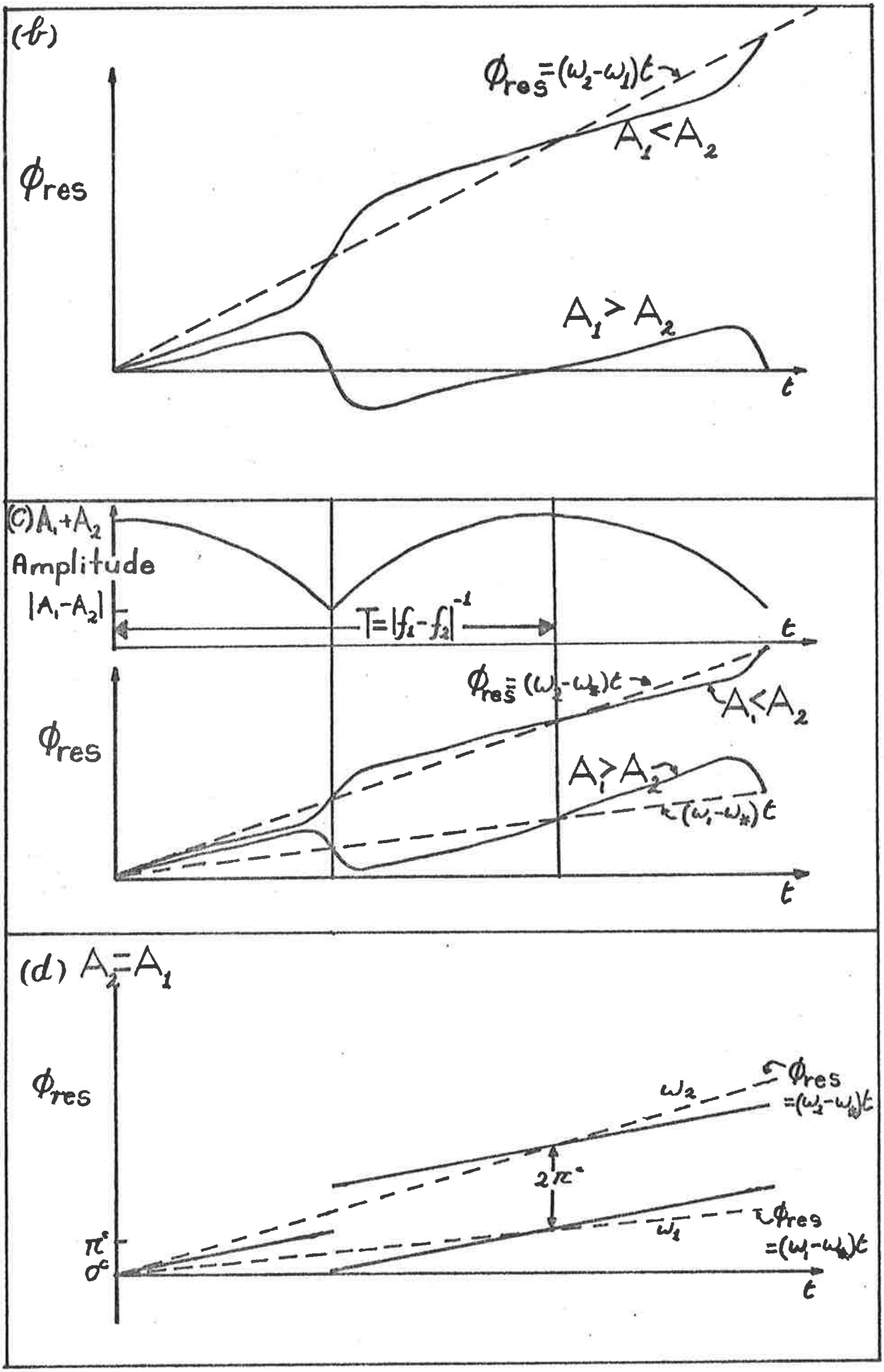
(b)
$\phi_{res} = (\omega_2 - \omega_1)t$
$A_1 < A_2$
ϕ_{res}
$A_1 > A_2$
t
(c) $A_1 + A_2$
Amplitude
$|A_1 - A_2|$
$T = |f_1 - f_2|^{-1}$
t
$\phi_{res} = (\omega_2 - \omega_1)t$
$A_1 < A_2$
ϕ_{res}
$A_1 > A_2$
$= (\omega_1 - \omega_2)t$
t
(d) $A_2 = A_1$
ϕ_{res}
ω_2
ϕ_{res}
$= (\omega_2 - \omega_1)t$
2π
π
0
ω_1
ϕ_{res}
$= (\omega_1 - \omega_2)t$
t

(7.3.3.1) $= A_* \cos(\omega_1 t - \phi_{res})$

(7.3.3.2) where $\tan \phi_{res} = (A_2 \sin \phi)/(A_1 + A_2 \cos \phi)$

(7.3.3.3) and $A_*^2 = A_1^2 + 2 A_1 A_2 \cos \phi + A_2^2$.

If ϕ_{res} is plotted as a function of ϕ for various A_2/A_1 values, curves result like those in Fig 7.10a. Here, ϕ_{res} is the phase of the resultant with respect to $\cos \omega_1 t$. If now we use $\phi = (\omega_1 - \omega_2)t$ and plot ϕ_{res} as a function of t, and also A_* as a function of t, curves result like those in Fig 7.10b. Two curves are plotted. Curve 1 results if $A_1 > A_2$, and Curve 2 if $A_2 > A_1$. The line $\phi_{res} = (\omega_2 - \omega_1)t$ is the phase of $\cos \omega_2 t$ with respect to $\cos \omega_1 t$. Thus the phase oscillates about the line of phase of the frequency with dominant amplitude. Note also that the magnitude of the phase fluctuation depends on the ratio $A_1 : A_2$.

Now, in a real experiment in which two Doppler frequencies f_1 and f_2 are received by a receiver, they are usually converted down to a low frequency by beating with a third frequency f_*. In the cases dealt with in this thesis, f_* is just the transmitted frequency. Then, let us finally suppose that we consider the phase with respect to a third frequency ω_*. Then the amplitude and phase are as shown in Fig 7.10c. The lines $(\omega_1 - \omega_*)t$ and $(\omega_2 - \omega_*)t$ represent the phase of the individual frequencies with respect to ω_*. The phase of the resultant oscillates around the phase line of the frequency of largest amplitude.

I have drawn the phase as 0 at t=0. For an autocorrelation function the phase is always zero at zero lag. Consider Fig 7.10c as an auto-correlation. Then the important point to note is that the slope of the phase at zero lag is NOT simply related to ω_1 or ω_2. It depends on the relative amplitude of the two. This is important, because, as discussed, in much

Doppler work, the slope of the phase of the autocorrelation at zero is used to obtain the frequency shift, and hence the velocity (e.g. Woodman and Guillen, 1974). Clearly, in the case presented here, erroneous results would be obtained. To get the correct frequencies, fit a straight line through the phase fluctuations. This line will give the frequency of the dominant amplitude, f_a say. The other frequency f_b can then be found by using the fact that the beat frequency is $(f_a - f_b)$. Whether f_b is greater or less than f_a can easily be found by seeing whether the resultant phase curve has a steeper or lesser slope than the phase of the dominant frequency at zero lag. (This description also explains the main features of the autocorrelation function in Fig 7.2b).

The case of equal amplitudes A_1 and A_2 is interesting. The phase varies as shown in Fig 7.10d. The phase can be made to appear to oscillate about either the $(\omega_2 - \omega_*)t$ line or the $(\omega_1 - \omega_*)t$ line by utilizing the $2\pi^c$ shift which occurs at the point of rapid phase change.

Another interesting case related to this theory concerns observations of atmospheric tides. Often a minimum in amplitude of the 24 hour tide can be observed at 90 km with a corresponding large phase jump (e.g. see Elford and Roper, 1961; Stubbs and Vincent, 1973; Elford and Craig, 1980). This could easily be explained as being due to the fact that the tide is the sum of 2 modes, with different vertical wavelengths. The amplitude and phase would vary with height in a similar manner to the variation in time shown in Fig 7.10c. A rapid phase change would occur at minima in strength.

However, the major purpose of this section has been to show the possible errors in Doppler measurements which could result when 2 scatterers exist with different Doppler shifts, if the slope of the phase at 0 lag is used "blindly" to estimate the Doppler velocity. Notice also, with regard to

Fig 7.2b, that not only is there insufficient data, resulting in false peaks, but also evaluation of $d\phi/d\tau$ at $\tau=0$ gives a slope depending on all the frequency peaks in Fig 7.2a. Thus even if the peaks were real, evaluation of $d\phi/d\tau$ would not help get the correct Doppler velocities.

Fig 7.11

Plots of power and horizontal winds as a function of height for day 80/072.

The mean power profile (0 mode, vertical narrow beam) was obtained between 1133 and 1142 hours above 80 km, and between 1220 and 1229 hours below. The mean noise has been removed. Layers were present at heights of about 66-68 km, 72-75 km, 78-80 km and 86-88 km on this day. (The layer at ~ 74 km does not show very clearly, so has been indicated by exaggerating the minimum at 76 km (broken line). The layer could easily be seen when watching the temporal variation of the echo profile). The rise in echo power above 94 km is due to the E-region, and that below 62 km is due to a ground echo.

With regards to the winds, the unlabelled error bars denote Partial Reflection Drift (PRD) measurements. Single points denote that only one acceptable measurement was obtained. E denotes eastward, N denotes northward.

When the narrow beam at Buckland Park is tilted towards the "west", it actually points 4° south of west. In this chapter, the statement "the beam was tilted 11.6° to the west" means the beam was tilted at a zenith angle of 11.6° in the vertical plane 4° south of west. The triangles in this diagram represent the wind vector component (deduced from the partial reflection drifts) parallel to this tilt direction of the narrow beam. The error bars with a square are Doppler measurements made with the beam tilted at 11.6° to the "west". They should be compared to the triangles.

The PRD measurements are the averages over the period 1310 to 1340 hours. The Doppler measurements were taken in the periods 1146-1153, 1233-1241 and 1413-1421 hours.

All error bars denote standard deviations for the mean. The broken lines show the best fit wind profiles (eye-fit only) using all data. Note that Doppler measurements may be under-estimates below 80 km, as described in the text, and indicated by the inset diagram.

The wind profile is probably dominated by tidal winds above 80 km.

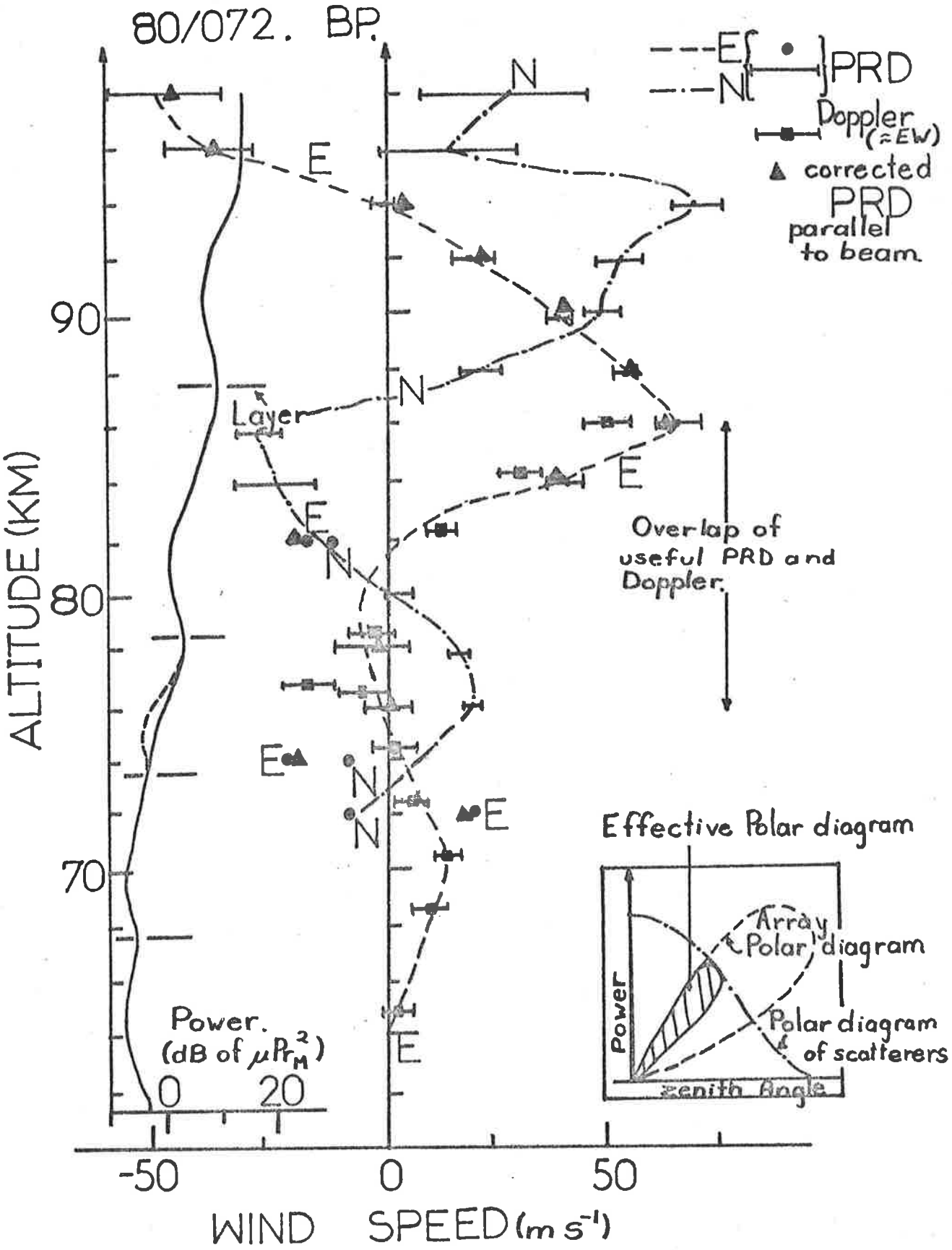
80/072. BP.
E
N
PRD
Doppler (≈EW)
corrected PRD parallel to beam
90
80
70
ALTITUDE (KM)
Layer
Overlap of useful PRD and Doppler.
Power. (dB of μPr_M^2)
0
20
Effective Polar diagram
Array Polar diagram
Power
Polar diagram of scatterers
zenith Angle
-50
0
50
WIND SPEED ($m\ s^{-1}$)

7.4 Experimental Data

7.4.1 Doppler Winds

As discussed in Chapter I, there has been some debate over recent years as to the validity of Partial Reflection Drift measurements. Briggs (1980/81) has shown that Doppler measurements and PRD measurements effectively measure the same thing, and comparisons with other techniques (rockets, meteors - see Chapter I) suggest PRD measurements do measure the neutral wind. Fig 7.11 shows further support for these statements. It shows PRD and Doppler wind measurements made on day 80/072 at Buckland Park. Doppler wind values are the means of 10 min sets of data, and were calculated from the phase of the autocorrelation function, after consideration of the effects discussed in Section 7.3.3. Agreement would appear to be good at heights where both techniques produced measurements. In fact, the measurements complement each other. Below 76 km, few PRD measurements were obtained (this is rather unusual, however) and Doppler measurements give an indication of winds here. Above 92 km, Doppler measurements gave velocities of the order of 150-200 ms^{-1}. It turned out this was due to leakage from the strong 86-88 km layer through a side lobe of the polar diagram at about 30° from the zenith. When this was considered, these Doppler measurements thus gave further estimates of the winds at 86-88 km, and agreed well with those presented on Fig 7.11. (These latter wind measurements have not been plotted). Thus Doppler measurements could not give winds above 92 km, whereas PRD measurements did.

It is also worth commenting on the accuracy of Doppler measurements below 76 km. These are very likely under-estimates. This is because the scatter from these heights is highly aspect sensitive (e.g. see Chapter IV; also see later in this chapter). Thus, as shown in the inset of Fig 7.11

the effective polar diagram is not tilted at the same angle as the beam. In all Doppler calculations, it is normal to assume that scatter is strongest from the direction in which the beam is tilted. If this is not true, Doppler estimates will be in error. PRD measurements do not suffer from this problem. This point has also been discussed by Röttger (1980) and Vincent and Röttger (1980).

Fig 7.12

Running power spectra, with a 3 point running mean (¼, ½, ¼), at 12s steps, for day 80/072 at 86 km range using the narrow beam pointing vertically. Positive frequencies mean a Doppler component towards the receiver. Compare this to Fig 7.5. There appears little evidence of any one spectral peak maintaining itself for several minutes. Spectral peaks do often appear to persist for up to a minute; but this is not surprising, since spectra with less than a 1 minute separation have common data. This point was also discussed in Section 7.3.1.

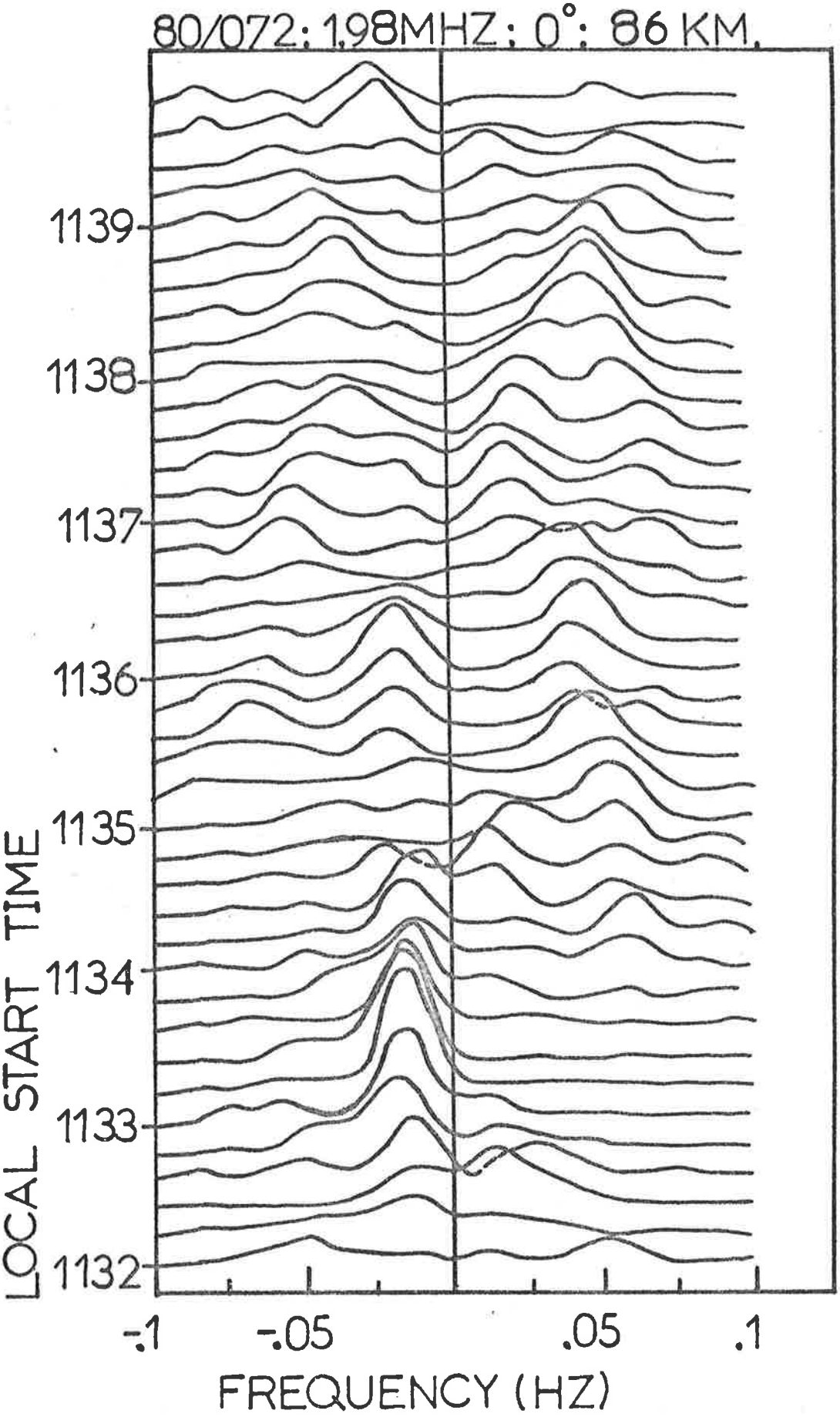
80/072: 1.98MHZ; 0°; 86 KM.
1139
1138
1137
1136
1135
1134
1133
1132
LOCAL START TIME
-.1
-.05
.05
.1
FREQUENCY (HZ)

7.4.2 Spectral widths using the vertical beam

On day 80/072 there were principal scattering layers at heights near 65 km, 74 km, 78 km and 86-88 km. Thus most investigations of data using the vertical beam will be done at these ranges, since it has already been seen that incorrect choice of the range can bias the results.

Fig 7.12 shows a running power spectrum (1 minute blocks) for day 80/072. Each spectrum has been smoothed with a 3-point running mean. There does not appear to be any evidence of one peak being sustained over more than about 5 spectra, suggesting little specular scatter (as discussed in the caption, some persistency over time shifts of up to 1 minute can be expected).

Hence the only important contributions to the long term power spectrum's width are beam broadening and turbulence. The beam broadened power spectrum can be assumed to be

$$B(f) \alpha \exp \{ - \ln 2 (f)^2 / ((2/\lambda).v.V_{\frac{1}{2}})^2 \} \qquad (7.4.2.1)$$

Where v is the horizontal wind velocity. This follows because the half-width in terms of radial velocities is $v_{r_{\frac{1}{2}}} = v V_{\frac{1}{2}}$ and $f = (2/\lambda).v_r$. The turbulence spectrum can be written as

$$T(f) \alpha e^{- \frac{f^2}{2((2/\lambda).v_{RMS})^2}} , \qquad (7.4.2.2)$$

since it can be assumed the component of velocities of eddies due to turbulence along the line of sight is distributed as

$$e^{- \frac{v^2}{2 v_{RMS}^2}} .$$

Here v_{RMS} is the RMS velocity along the line of sight associated with

Fig 7.13

(a) Nine minute power spectrum (after averaging in frequency blocks) for the vertical narrow beam at Buckland Park, at 1.98 MHz, for a range of 88 km, on day 80/072 (12th March, 1980), taken between 1133 hours and 1142 hours.
Positive frequencies imply movement towards the receiver.

Also shown is an approximate Gaussian fit to the spectrum (fitted by eye only).

(b) The corresponding autocorrelation function for Fig 7.13(a).

NARROW BEAM: 0°: O MODE: 88 KM.

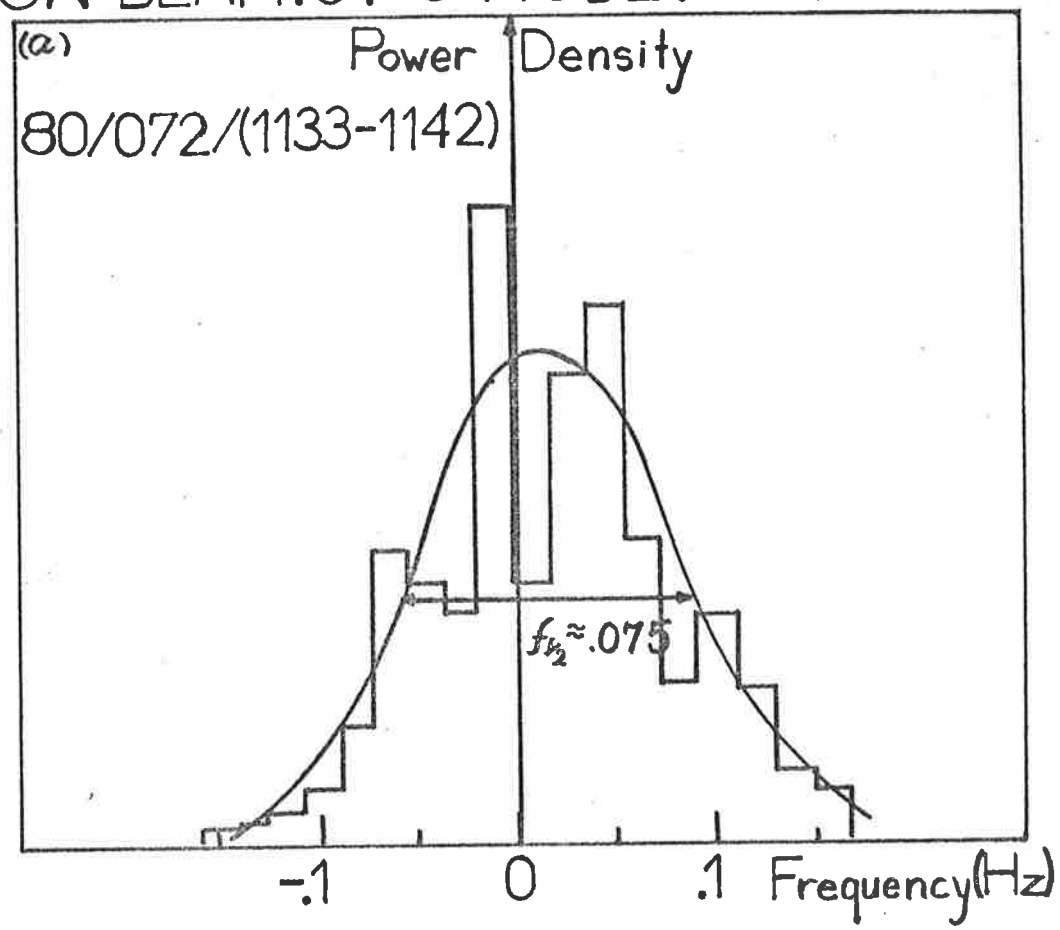

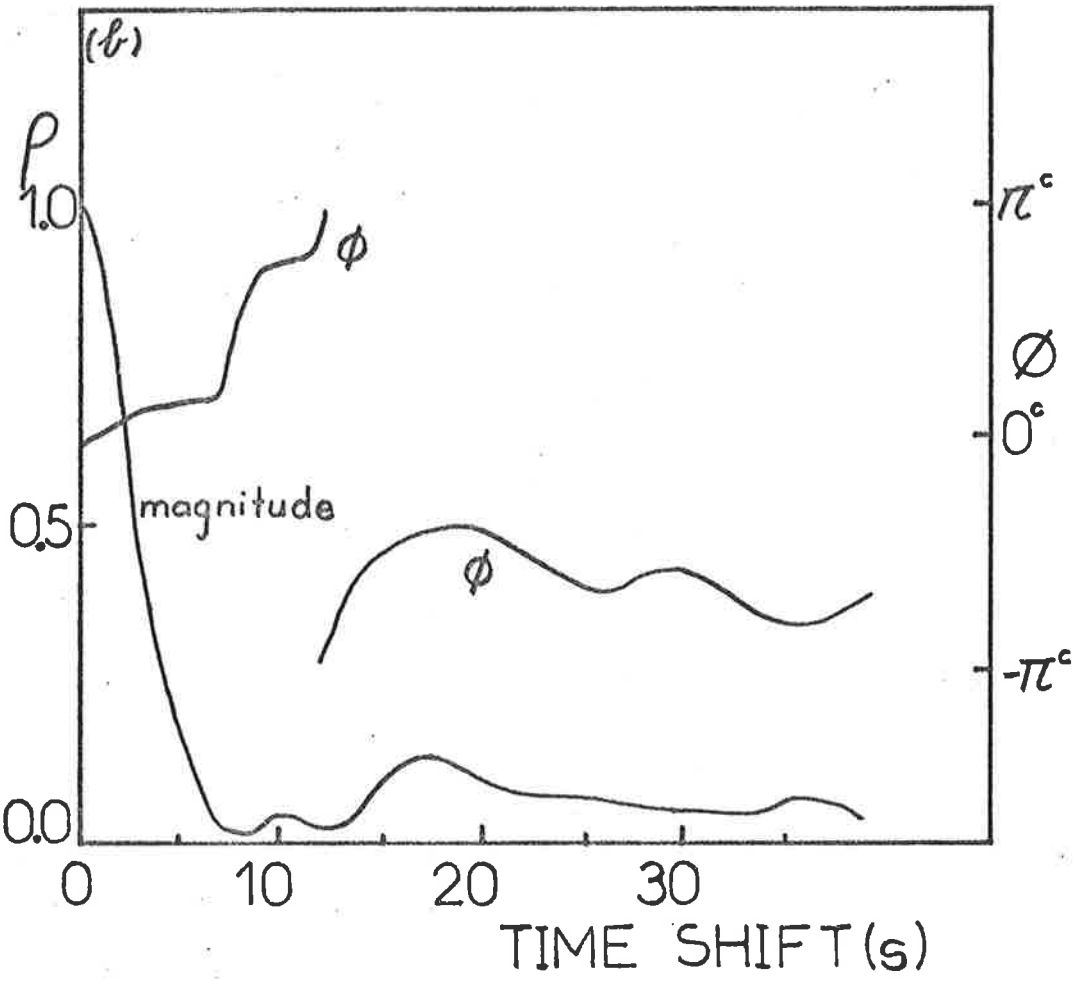

scales $\lambda/2$ metres, and it has been assumed that the turbulence is isotropic, so the situation looks the same in all directions. If this were not so, the turbulence spectrum would vary depending on the angle at which the turbulence was viewed.

If both turbulence and beam-broadening are active, the resultant power spectrum is a convolution of B and T (this is not proved here; however it seems intuitively reasonable and will be proved to be true later (see equation (7.4.4.14)) and can be written as

$$(7.4.2.3) \qquad P(f) = \exp\{ - \frac{f^2}{(2/\lambda)^2} \cdot (v\, V_{\frac{1}{2}})^2 / \ell n\ 2 + 2v_{RMS}^2)^{-1} \},$$

so the half-power-half-width is

$$(7.4.2.4) \qquad f_{\frac{1}{2}} = 2/\lambda\ [\ v\, V_{\frac{1}{2}})^2 + 2v_{RMS}^2 \ell n\ 2\ ]^{\frac{1}{2}}$$

Consequently if $f_{\frac{1}{2}}$ can be measured, v_{RMS} can be found as

$$(7.4.2.5) \qquad v_{RMS} = \{\ [\ (\lambda/2\, f_{\frac{1}{2}})^2 - (v\, V_{\frac{1}{2}})^2\ ]/(2\ \ell n\ 2)\}^{\frac{1}{2}}$$

Fig 7.13 shows the smoothed power spectrum of 9 minutes of data for day 80/072 using the narrow beam at Buckland Park at 1.98 MHz. (The raw power spectrum looked similar to Fig 7.6a). The half-power-half-width is about .075 Hz. Now, $V_{\frac{1}{2}} = .072$, so if the mean wind is taken as that at 86 km, (≈ 75 ms^{-1}), then $v\, V_{\frac{1}{2}} = 5.4$ ms^{-1}. If the mean wind is that at 87 km, $v\, V_{\frac{1}{2}} = 4.3$ ms^{-1}. These provide upper and lower limits to $v\, V_{\frac{1}{2}}$.

Thus the expected half-power-half-width due to beam broadening alone is $2/\lambda$ (5.4 → 4.3 ms^{-1}) = .071 → .057 Hz. This is comparable to the observed $f_{\frac{1}{2}}$ and suggests there is very little turbulent contribution. There must clearly be some error in the estimate of $f_{\frac{1}{2}}$ - perhaps ± 10%. In fact, the 86 km power spectrum had a half-width close to .055 → .06 Hz. However, an upper limit could be placed on the width, and hence on v_{RMS},

Fig 7.14

Running power spectra with a 3-point running mean (¼, ½, ¼) at 12s steps, for day 80/072 at 74 km range using the narrow beam pointing vertically. Positive frequencies mean a Doppler component towards the receiver.

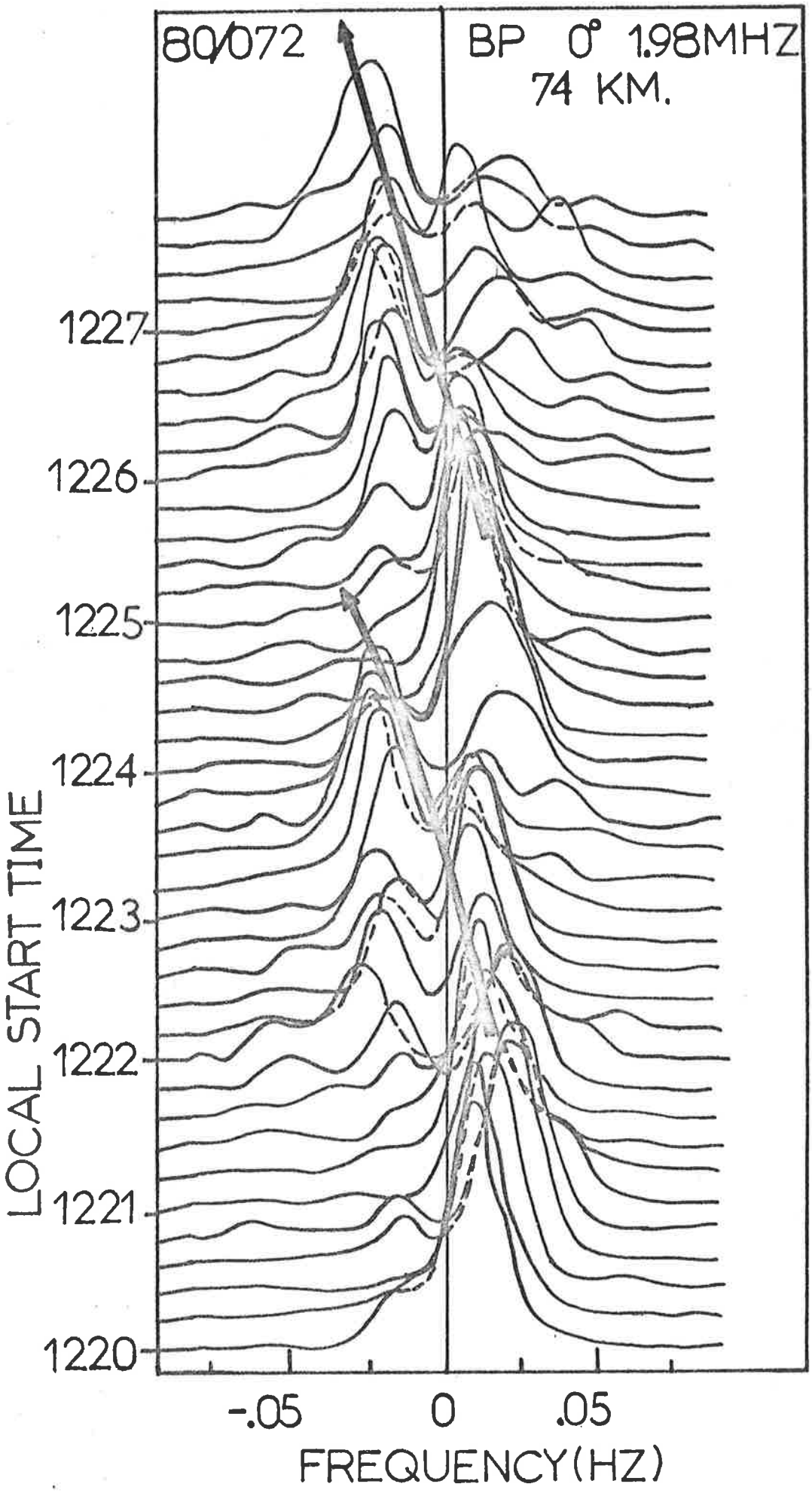
80/072
BP 0° 1.98MHZ
74 KM.
1227
1226
1225
1224
1223
1222
1221
1220
LOCAL START TIME
-.05
0
.05
FREQUENCY(HZ)

and it was found that

$$v_{RMS} \lesssim 2\text{-}3 \text{ ms}^{-1} \text{ (for scales of 75 metres).}$$

(It should perhaps also be pointed out in connection with these power spectra that a noise level also exists (e.g. see Chapter VI). This should be removed before any fitting procedures are applied, although in most cases it was a very small effect at 2 MHz. At 6 MHz, noise became more important).

Notice also the narrow spikes which occur in the power spectrum in Fig 7.13. To some extent these are to be expected, due to statistical fluctuation, as pointed out in Section 7.3.1. However, Röttger (1980) has also observed such spikes in some of his power spectra from trospospheric and stratospheric data, and interprets some of the very large ones as being due to specular scatter. Such specular scatterers would produce a very narrow effective polar diagram, and thus a narrow width to the spectral lines they produce. The spikes in Fig 7.13a are probably not due to specular scatter, particularly in view of the running power spectra, which did not show any sustained frequency. However, some other large spikes did occur at times which could indicate specular scatter. However, these will not be discussed in detail, since their interpretation is not certain. (The possibility also exists that slowly varying specular scatter could enhance the powers at low frequencies, artificially narrowing the spectrum. This should be borne in mind. Determination of Rice parameters can help determine if this is happening).

Fig 7.14 shows a running power spectrum for day 80/072 at 74 km range, 2 MHz, 0° with the narrow beam at Buckland Park. In this case, there may well be frequency trends which persist for a long time. The two arrows in Fig 7.14 show the movement of the spectral peaks and could be interpreted as

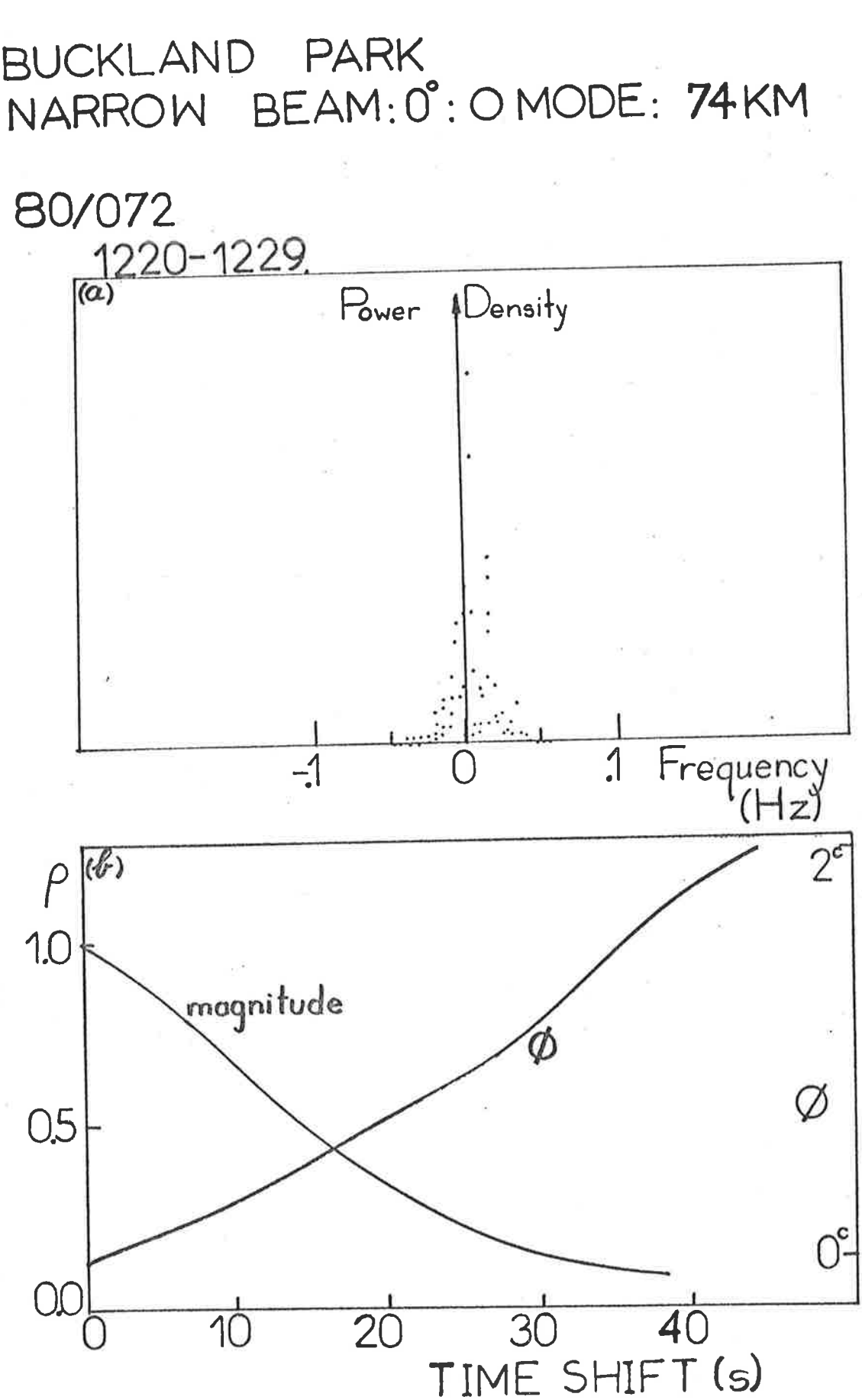

Fig 7.15 (a) Nine minute power spectrum for the vertical narrow beam at Buckland Park, at 1.98 MHz, for a range of 74 km, on day 80/072, taken between 1220-1229 hours. No averaging of the spectrum in frequency bands has been applied. Positive frequencies imply movement towards the receiver. (b) The corresponding autocorrelation function for Fig 7.15a.

indicative of scatterers moving into the beam, moving overhead, and then away. Note that the original power spectra had the zero frequency power set to zero. The non-zero values result due to the smoothing applied, but are not representative of the true zero frequency powers. This is part of the reason for the apparent "doubly peaked" spectra at about 1223-1224.

Measurements of the half-power-half-width of 5-10 min power spectra from ranges below 80 km were also obtained. The widths were quite similar to those expected due to beam broadening - perhaps even a little less, as might be expected due to the aspect sensitive nature of the scatterers. (this would narrow the effective polar diagram). For example, taking a wind speed of 23 ms^{-1} at 74 km gave an expected spectrum half-width of .022 Hz. The measured half-width was of the order of .015 Hz. This narrow scattering spectrum is also evident in Fig 7.14 where it can be seen that few echoes occur with frequencies less than -.02 Hz or greater than + .02 Hz .

Fig 7.15 shows a typical 9 minute spectrum and corresponding auto-correlation function for ranges less than about 80 km. The spectrum is quite narrow, and the autocorrelation correspondingly wide. As discussed, this is partly due to the anisotropy of the scatterers, and partly due to the low wind speeds on this day at these heights. Consequently the beam-broadened spectrum is quite narrow.

In connection with specular scatter, an interesting problem arises. We have already seen (Section 7.4) that anisotropic scatter can distort Doppler measurements of horizontal wind. Could the form of the specular scatterer introduce extra complications ? Imagine the case of a specular scatterer in the form of the cap of a sphere; or a cylinder, moving in a direction perpendicular to the cylinder axis.(Such a form could result from, say, the perturbation of an electron density gradient by a gravity wave. One half

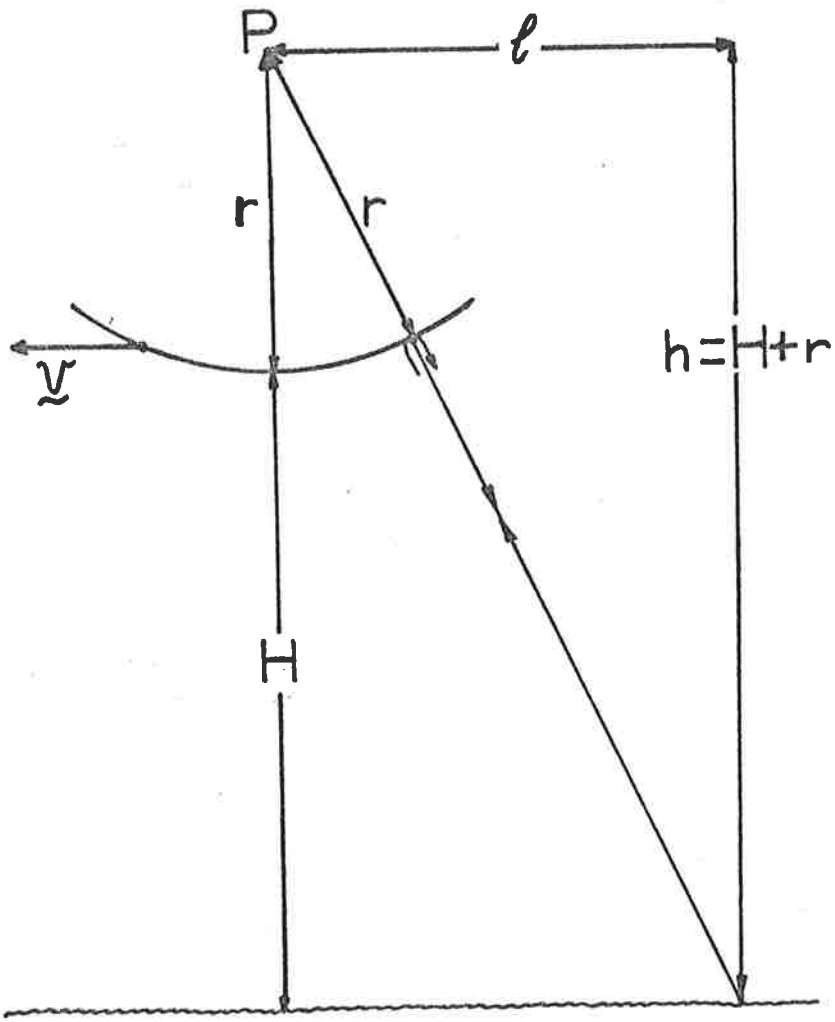

Fig 7.16

Diagrammatic illustration of a particular type of "specular reflector" (see text).

cycle of the gravity wave perturbation could have such a form. In this case, the horizontal speed of the wave would be measured.)

Such a situation is illustrated in Fig. 7.16.

Suppose the reflector is moving horizontally at velocity $\underline{v}$. Then what would the measured horizontal velocity be ?

The phase at time t, as illustrated in Fig 7.16, would be

$$\phi = 2\pi/\lambda[(\sqrt{(H + r)^2 + \ell^2}) - r]$$

So the rate of change of phase is

$$\frac{d\phi}{dt} = 2\pi/\lambda \frac{d}{dt}(\sqrt{(H+r)^2 + \ell^2}$$

as r is a constant.

This is precisely the rate of change of phase for a point scatterer at point P, with velocity $\underline{v}$. Thus in this case the Doppler velocity measurements would give the correct horizontal velocity. The point of reflection on the cap changes in just a way so as to look like a point scatterer at a higher height. I find this an interesting result. However, there are certainly many cases where things are not so simple. A flat reflector could not have its horizontal velocity measured by Doppler measurements, for example. (Probably in most cases the reflectors are quite flat, but it is still interesting to consider other cases). Indeed Doppler measurements are not particularly good for measurements of winds then the scatterers are strongly aspect-sensitive reflectors.

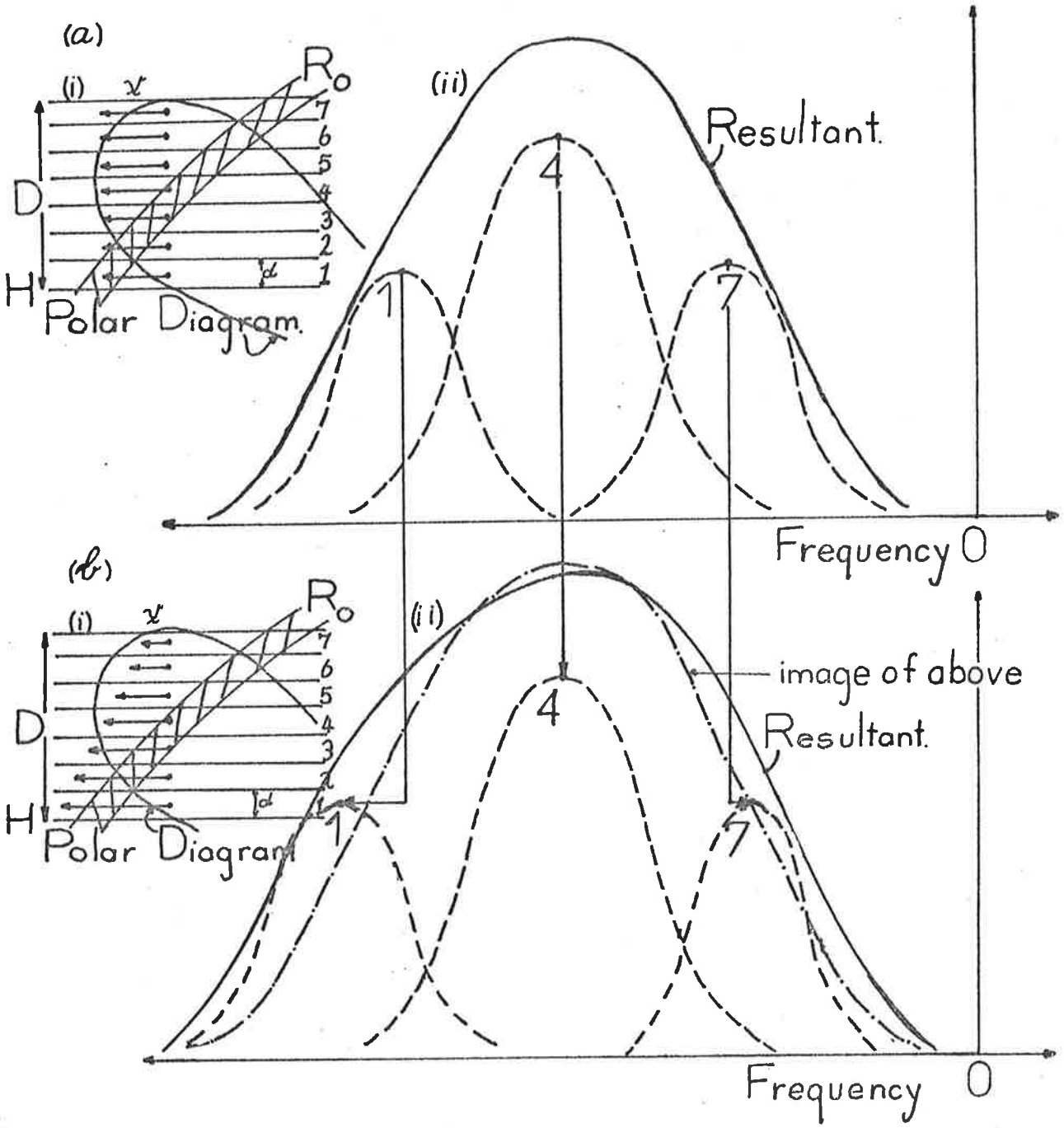

Fig 7.17

Illustration of the effect of wind shear broadening (see text for details). Positive frequencies imply movement towards the receiver. Arrows in the layers indicate wind vectors.

7.4.3 Spectral width using the tilted beam

The most obvious reason to tilt the beam is to make Doppler velocity measurements. As seen in relation to Fig 7.9b, the measured Doppler velocity is a function of the range, even if the wind speed is constant with height, due to the finite thickness of the scattering layer. Plots of this Doppler shift as a function of range were made for the data of day 80/072, and agreed closely with that expected for a 1-4 km thick layer. However, the effect of the wind shear was not fully considered, so this result may be coincidence.

Let us now consider the processes contributing to the width of the power spectrum for a tilted beam. Beam broadening acts, of course. But if the wind vector is not constant with height across a scattering layer, wind-shear broadening can also be important.

To consider the effect of wind-shear-broadening examine Fig 7.17. Consider a layer based at height H, depth D (Fig 7.17a(i)). Suppose initially that the wind speed is constant with height. Consider the power spectrum observed for a range R_o. This is also the sum of the power spectra produced by the separate layers 1-7. Now the power spectrum due to layer 4 is that for a layer of depth d, based at height H+3d. The power spectrum for layer 3 is that for a layer of depth d, based at height H + 2d - or it can be approximately regarded as that for a layer based at H + 3d, like layer 4, and a range $\approx R_o.\left\{\frac{H+3d}{H+2d}\right\}$. Thus the final spectrum is approximately the sum of the spectra for different R_o values for a single layer of depth d at height H + 3d, with "R_o" values varying from $(H + 3d)/H \times R_o(\text{true})$ to $(H + 3d)/(H + 6d) \times R_o(\text{true})$. Fig 7.9b shows such power spectra, so the sum is the sum of spectra like those shown in Fig 7.17a(ii), plotted as a function of Doppler frequency, f, not as a function of V. The resultant is the envelope.

Now imagine the wind profile is as shown in Fig 7.17b(i). Then the individual power spectra are as shown in Fig 7.17b(ii). Notice (1) has shifted to the negative considerably, and widened, whilst spectrum (7) has shifted

towards zero, and narrowed. The result is a wider spectrum with some asymmetry. Notice in Fig 7.17b that curve 1 suffers a larger absolute shift in frequency. Why ? If the wind increases by x times in layer 1, it becomes x^{-1} of its former value in layer 7 (compared to Fig 7.17a(i)). Thus the peak of 7 occurs at a frequency $x^{-1}f_7$, and that of 1 occurs at xf_1 , f_1 and f_7 being the original frequencies of the peaks of 1 and 7. Thus the shift in frequency of curve 1 is $f_1 \cdot (x-1)$, and for curve 7 is $f_7 \cdot (1-1/x) = (f_7/x) \cdot (x-1)$. The latter term is less than the former for all $x > 1$ (and indeed for $x > f_7/f_1$). If x is much less than 1, it means the wind velocity increases with height, in which case reverse asymmetry may be expected. This illustrates wind-shear-broadening. However, notice that if the wind shear had been such that wind speed increased with height, then in Fig 7.17b(ii), graphs (7) and (1) would move toward spectrum (4) and the resultant power spectrum would narrow. (The fading rate would decrease and thus the fading time would be larger than for the narrow beam) Thus wind-shear-"broadening" is a misleading term.

Notice that the major contributor to the change in spectral shape is the shift of the contributing spectral peaks. This does not occur for a vertical beam, so wind-shear "broadening" is generally only important for tilted beams.

Wind-shear broadening is not easily dealt with by approximate methods. Thus the program "Specpol" (Section 7.3.2; Appendix E) was modified to treat a layer as the sum of several narrow layers, and sum of all the power spectra, to produce a good estimate of the beam-broadened and shear-broadened spectra. Quite general wind profiles through the layer were possible.

A 2 km thick layer was assumed between 86 and 88 km, and a wind profile appropriate to that shown in Fig 7.11 (day 80/072) assumed. The resultant power spectra for ranges corresponding to a peak of the scattered power were then formed. For a vertical beam, it was found that $f_{\frac{1}{2}} = .06$ Hz. (Compare this to the approximation of $f_{\frac{1}{2}} \sim .058$ to .071 Hz made previously and see the discussion of Fig 7.13, following equation (7.4.2.5)). However, this improved

Fig 7.18

Expected power spectra for the narrow beam at Buckland Park pointed at 11.6° to the West (using modified version of program SPECPOL, as discussed in the text), for the following cases:

(a) a layer of isotropic scatterers between 86 and 90 km, with a wind profile approximately given by that in Fig 7.11;

$(v_{EW} = 66.5 + (h - 86) \times (53-66.5)/)88-86))$

$(v_{NS} = -28 + (h - 86) \times (22.5 + 28)/(88-86))$ and

(b) a layer of isotropic scatterers between 86 and 88 km, with a wind profile approximately given by that in Fig 7.11, as above.

Each spectrum corresponds to a range which is approximately the range of peak power. (90 km for (a), 89 km for (b)).

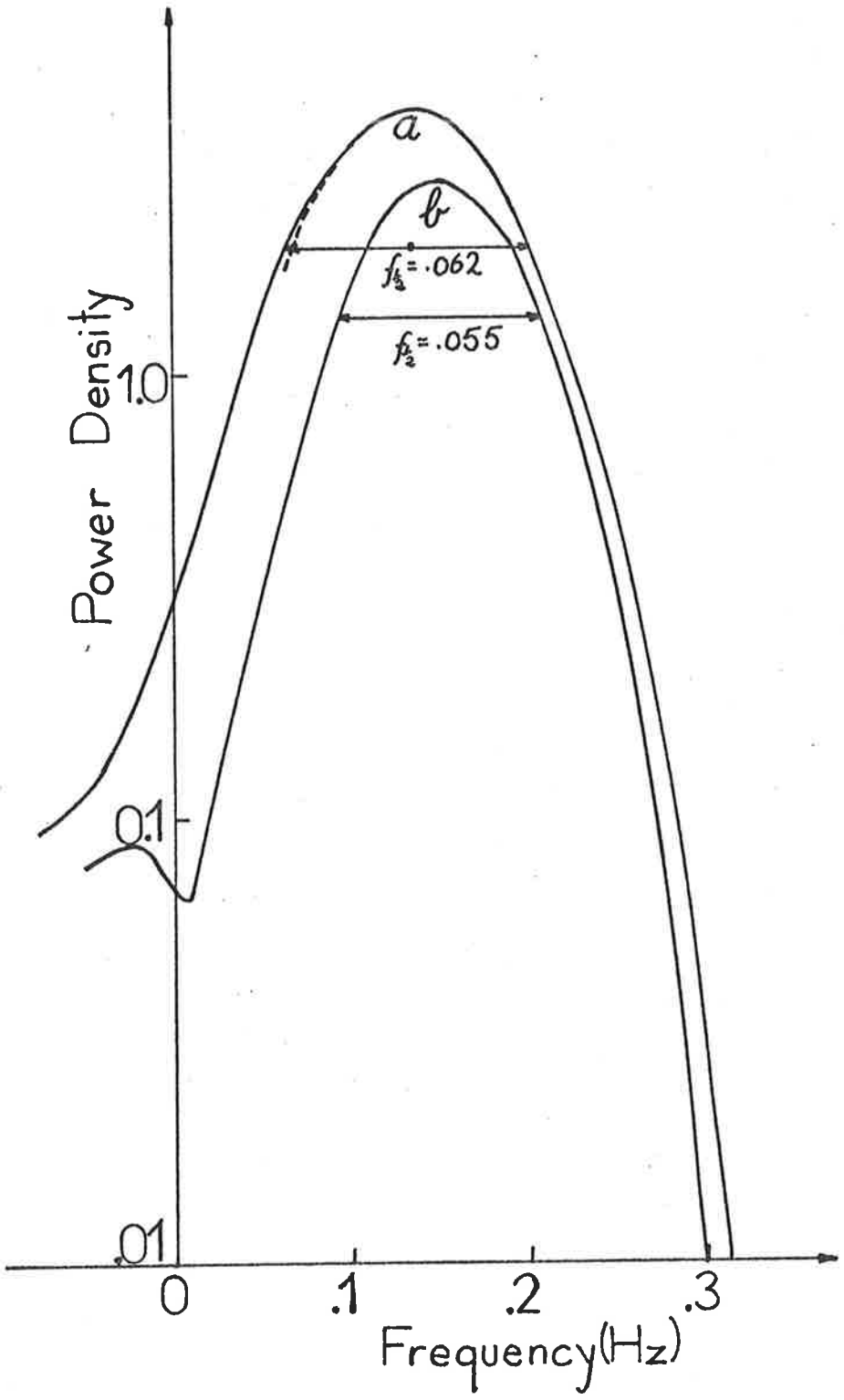
a
b
$f_{\frac{1}{2}}$ = .062
$f_{\frac{1}{2}}$ = .055
Power Density
1.0
0.1
.01
0
.1
.2
.3
Frequency(Hz)

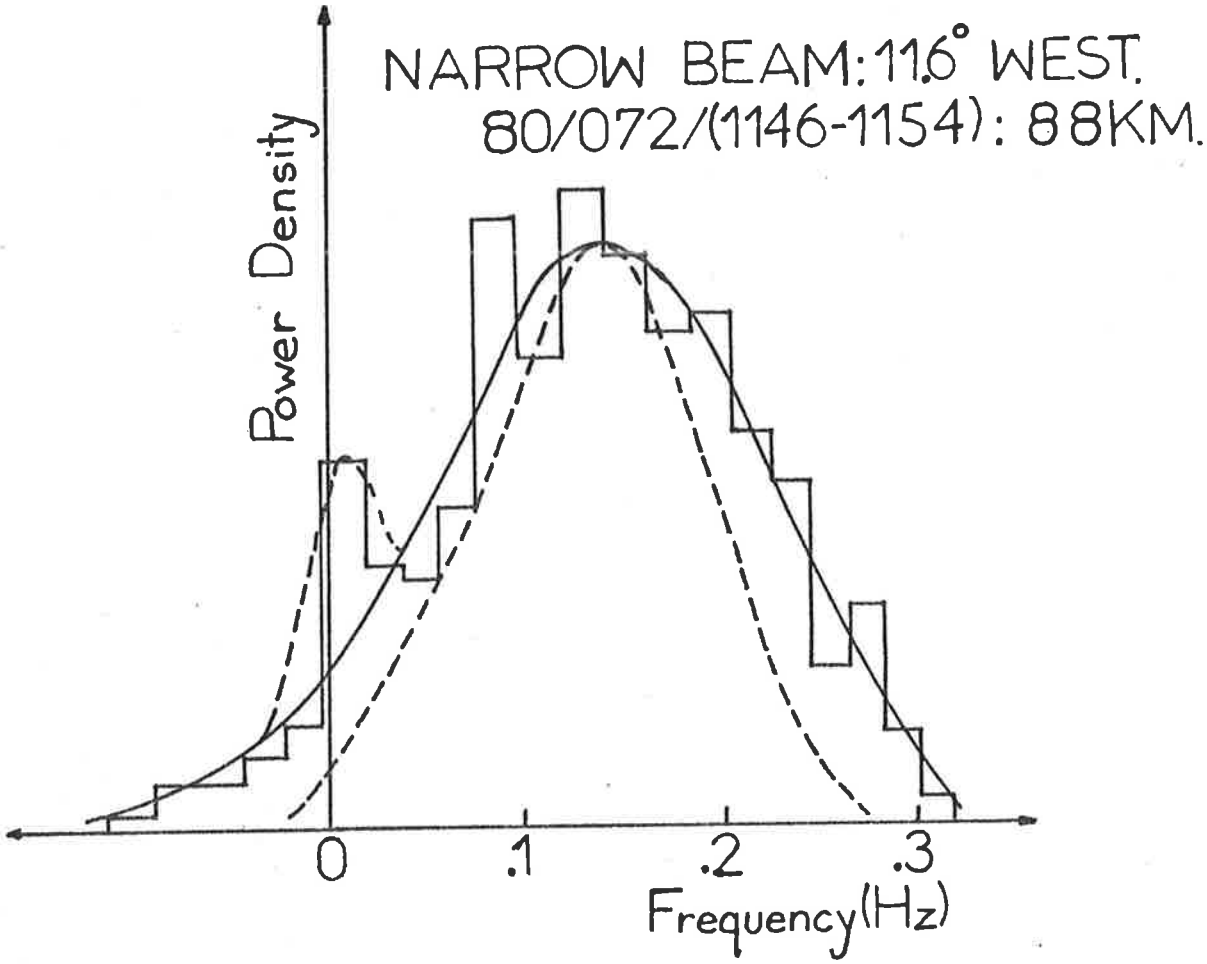

Fig 7.19

Observed power spectrum using 8 mins of data for the narrow beam tilted at 11.6° to the west on day 80/072. The broken curve centred at 0.14 Hz shows the expected spectrum for a 4 km thick layer at 86-90 km (see Fig 7.18), with no turbulence.

Positive frequencies imply motion towards the receiver. It will be noticed that the observed spectrum is considerably wider than the expected non-turbulent one.

The asymmetry of the curve suggests the layer is greater than 2 km thick, since a 2 km thick layer would produce a fairly symmetric spectrum (see Fig 7.18b). If the layer were greater than ~ 4 km thick, this could be seen by a widening of the mean power profile for this layer. Thus it appears the layer was between 2 and 4 km thick.

The small peak at 0 Hz is interesting. Fig 7.18b suggests such a peak should occur due to side lobes of the polar diagram, but not as large as this. For a 4 km thick layer, the peak should be smeared out (Fig 7.18a). However, the presence of this peak suggests that the side lobes of the polar diagram of the array are larger than those estimated by function BPRES in program "SPECPOL", and/or that there is some component of specular scatter from these heights, enhancing the vertical scatter component. Probably both factors contribute. Certainly it is known that scatter from ~ 80-90 km is <u>not</u> entirely isotropic - as seen in Chapter IV. A specular component may not be surprising. It was also seen in Chapter V that there is often a specular component of scatter at ~ 86 km.

estimation of $f_{\frac{1}{2}}$ did not change the conclusions reached. For a beam tilted at 11.6° towards the west and a 2 km thick layer, it was found $f_{\frac{1}{2}}$ was expected to be .055 Hz (i.e. wind shear "broadening" actually narrows the spectrum). Fig 7.18b shows the expected power spectrum for a 2 km thick layer. Fig 7.18a shows the expected spectrum for a 4 km thick layer, and in this case $f_{\frac{1}{2}} \approx$ .062 Hz. As suggested in the caption to Fig 7.18, the layer was probably between 2 and 4 km thick - possibly nearer 4 km. Thus $f_{\frac{1}{2}}$ is between .055 and .062 Hz.

Fig 7.18 shows an 8 minute power spectrum for day 80/072 at 88 km. The half-power-half-width is about .095 Hz (± 10% ?) - definitely much larger than the predicted .055 - .06 Hz. Since all factors except turbulence have been considered, this suggests the extra width is due to turbulence. Yet the vertical beam showed no such indication of turbulence, so this means the turbulence must be highly anisotropic, with eddies oscillating primarily in the horizontal. This is surprising, because scales of $\lambda/2 = 75$ m are close to the Kolmogoroff microscale at 80-90 km (Fig 1.9a) and so might be expected to be associated with isotropic turbulence. This enigma will resolve itself shortly. For the present, however, we must devise a means to estimate the horizontal v_{RMS} values. This is done in the following section.

The explanation of this widened spectra at off-vertical tilts proves to be quite simple, but it is believed that this is the first time that this explanation has been recognized.

7.4.4 Theoretical Spectra for anisotropic turbulence

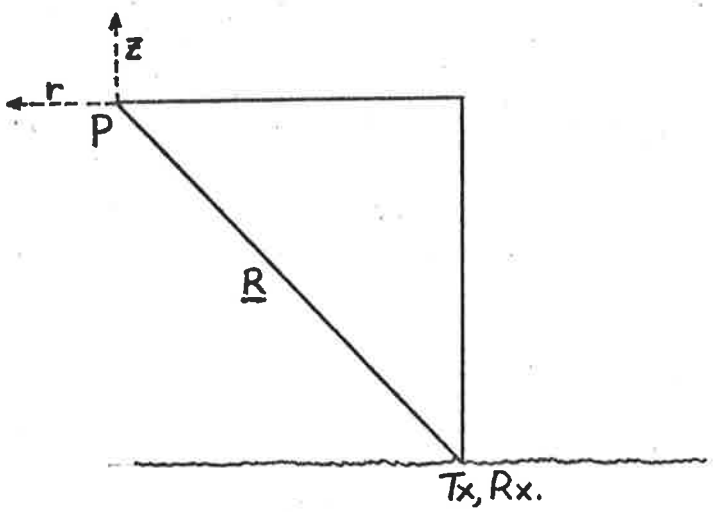

Consider the spectrum produced by a point P in space, at which turbulence is active. What is the received power spectrum ? Let a scatterer have vertical velocity v_z, and horizontal velocity v_r. (assume isotropy in the horizontal plane). The component of velocity observed at the receiver is

(7.4.4.1) $$v_{rad} = v_r \sin\theta + v_z \cos\theta$$

Let v_r have a probability distribution function

(7.4.4.2) $$P_r(v_r)dv_r = K_r \exp\{ - v_r^2/(2v_H^2) \} dv_r$$

and v_z have a probability distribution function

(7.4.4.3) $$P_z(v_z)dv_z = K_z \exp\{- v_z^2/(2v_v^2) \}dv_z.$$

Then v_H is the RMS velocity along any direction in the horizontal, and v_v is the RMS velocity in the vertical direction.

Then the probability of observing a radial velocity v_{rad}, from the point P, is equal to the probability of a horizontal velocity v_r, times the probability of a vertical velocity

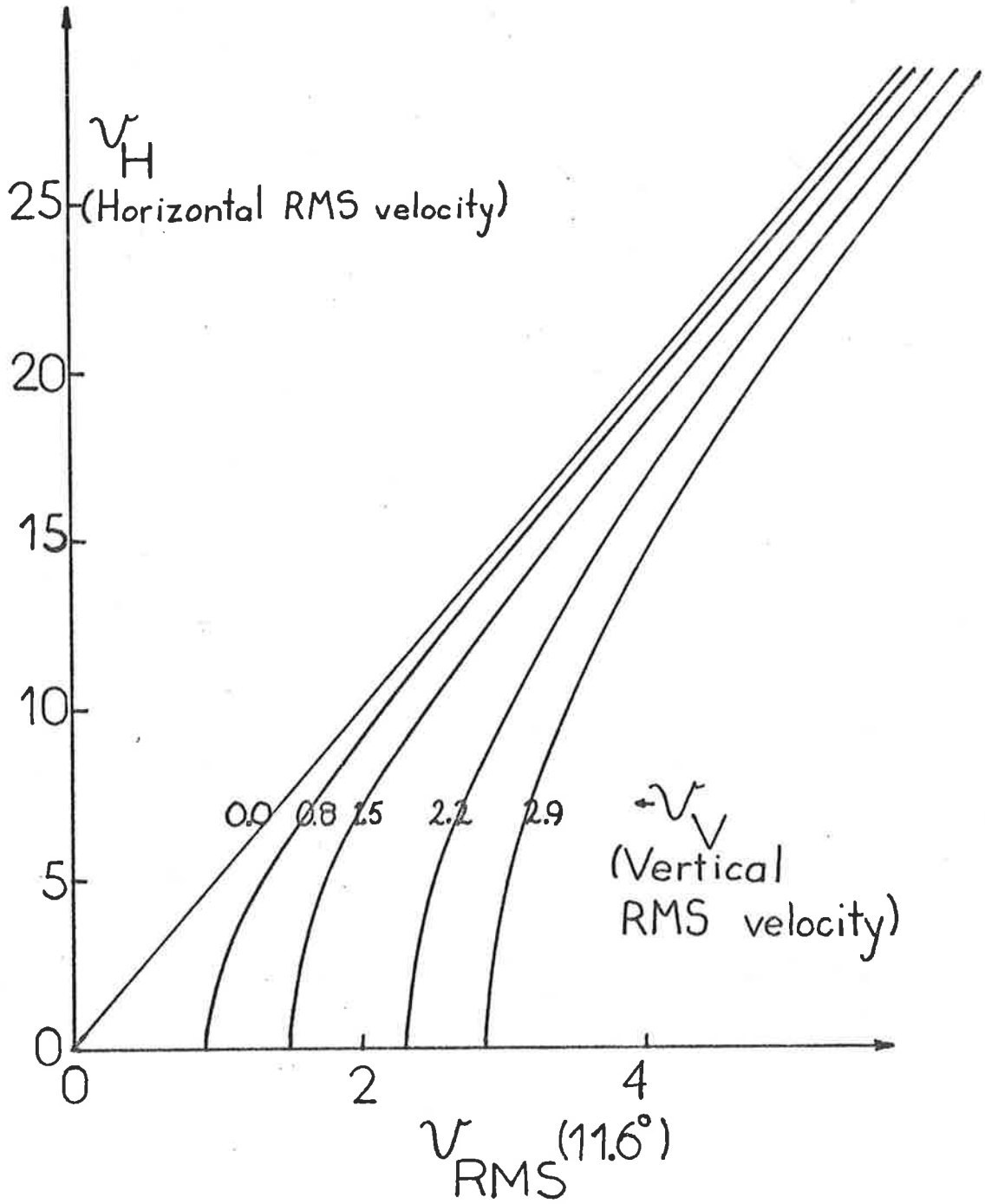

Fig 7.20

Plots of the expected observed RMS velocity for a beam tilted at 11.6°, when the scattering eddies have horizontal RMS velocity v_H, and vertical RMS velocity v_v.

(7.4.4.4) $v_z = (v_{rad} - v_r \sin\theta)/\cos\theta$ (by (7.4.4.1))

and integrated over all acceptable v_r.

Thus

(7.4.4.5) $P_{v_{rad}}(v_{rad}, R, \theta, \phi)(dv_{rad})(dV)$

$$= K_1 K_2 dV \int_{\text{all } v_r} e^{-v_r^2/2v_H^2} dv_r \; e^{-((v_{rad} - v_r \sin\theta)/\cos\theta)^2/2v_v^2} \times d((v_{rad} - v_r \sin\theta)/\cos\theta)$$

where dV represents a volume of space $= R^2 \sin\theta d\theta d\phi dR$.

Ignoring terms involving $(dv_r)^2$, this becomes, upon evaluation,

(7.4.4.6) $P_{v_{rad}}(v_{rad}, R, \theta, \phi) dv_{rad} dV$

$$= C.\, dv_{rad} dV.\, \exp\{-v_{rad}^2/(2v_{RMS}^2)\}$$

where C is a constant, and

(7.4.4.7) $$v_{RMS}^2 = v_v^2 \cos^2\theta \left[1 - \frac{v_H^2 \sin^2\theta}{v_v^2 \cos^2\theta + v_H^2 \sin^2\theta}\right]^{-1}$$

Notice v_{RMS} is the root mean square velocity observed for turbulent scatter from the point P.

Notice if $v_v = v_H$, then $v_{RMS} = v_H = v_v$. Thus the observed RMS velocity is the true RMS velocity along any direction for isotropic turbulence. It can also be shown that $v_{RMS} = v_v \cos\theta$ when $v_H = 0$ and $v_{RMS} = v_H \sin\theta$ when $v_v = 0$. Fig 7.20 shows plots of v_{RMS} vs. v_H for various v_v values.

Now the above formulae are purely for turbulence at P. What happens when we integrate the effects over a full region ? What is the final power spectrum when turbulence and beam broadening are considered ?

This is best done by building on equation (7.3.2.8), which is repeated below as (7.4.4.8);

$$T(R, \theta, \phi)d\Omega = P(\theta, \phi) \left[\frac{\sigma(r, \theta, \phi)}{r^4} \cdot (r^2 d\Omega) \otimes g(r) \right] . \tag{7.4.4.8}$$

The scattered power for a radial velocity $v_{rad\ t}$ (due to turbulence effects alone) observed at range R, from angles θ, ϕ is

$$P_t(R, \theta, \phi, v_{rad\ t})d\Omega = P(\theta, \phi) \left[\frac{\sigma(r, \theta, \phi)}{r^2} \cdot P_{vrad}(v_{rad\ t}, r, \theta, \phi) \otimes g(r) \right] d\Omega \tag{7.4.4.9}$$

Then the power observed with total velocity v_T is

$$\int_{\text{all } \theta, \phi} P_t (R, \theta, \phi, v_{rad\ t})d\Omega \tag{7.4.4.10}$$

where the integration is performed over the region where

$$\theta = \sin^{-1} V/\{\tfrac{1}{2} (1 + \cos \theta(\phi_0-\phi))\}^{\frac{1}{2}} \quad \text{(by (7.3.2.4))} \tag{7.4.4.11}$$

and where $V = (v_T - v_{rad\ t})/v_{horiz}$,

v_{horiz} being the horizontal wind speed blowing in the direction ϕ_0. Thus the final result is a complicated type of convolution.

Now consider the case for a scattering layer in which the turbulent conditions are independent of position within the layer. Then σ covers the radial dependence of $P_{v_{rad}}$ in the convolution in (7.4.4.9), so $P_{v_{rad}}$ can be regarded as a function of $v_{rad\ t}$, θ and ϕ only, and can be taken outside of the convolution. This simplifies the problem, because now (7.4.4.10) becomes

$$\int_{\substack{\text{all} \\ v_{rad\ t}}} \int_{\substack{\text{all} \\ \text{accetable} \\ \theta, \phi}} P_{v_{rad}} (v_{rad\ t}, \theta, \phi) P_{NT}(R, \theta, \phi, v_{rad}, v_{rad\ t})d\Omega\, dv_{rad\ t}, \tag{7.4.4.12}$$

where P_{NT} is just the integrand in (7.3.2.9), and where θ is defined by (7.4.4.11).

Notice that if $P_{v_{rad}}$ is also independent of θ and ϕ, then (7.4.4.12) becomes

$$(7.4.4.13) \qquad \int_{\text{all } v_{rad\ t}} P_{v\ rad}(v_{rad\ t}) \int_{\substack{\text{all} \\ \text{acceptable} \\ \theta,\ \phi}} P_{NT}(R,\theta,\phi,\ v_*)d\Omega\ dv_*$$

where $v_{rad\ t} = v_T - v_*$, and (7.4.4.11) holds.

This is simply

$$(7.4.4.14) \qquad P_{v\ rad}(v_{rad}) \otimes F_v(v_{rad},\ R)$$

where $F_v(v_{rad},\ R) = F(V,\ R)$ in equation (7.3.2.9), and

$v_{rad} = V.\ v_{horiz}$, v_{horiz} being the horizontal wind speed.

Hence if $P_{v\ rad}$ is independent of θ, ϕ (i.e., the direction of viewing) and is independent of its position within the scattering region, then the resultant spectrum is a convolution of the turbulence spectrum and the non-turbulence-produced spectrum. This was assumed in deriving equation (7.4.2.5), which is valid for isotropic turbulence.

Thus (7.4.4.14) is valid for isotropic turbulence, and any polar diagram. It is also approximately valid for anisotropic turbulence observed with a narrow beam tilted significantly from the vertical, since, as a first order approximation, $P_{v\ rad}$ is roughly independent of θ and ϕ within the main lobe of the beam, and contributions from outside this lobe are small.

For a vertical beam observing anisotropic turbulence (7.4.4.14) is strictly not valid. However, if v_v is much larger than $v_H \sin \theta_{\frac{1}{2}}$, $\theta_{\frac{1}{2}}$ being

the half-power-half-width of the polar diagram, then only vertical components are important, and (7.4.4.14) is again valid.

In the work presented in the following section, (7.4.4.14) will be assumed valid for the narrow beam at Buckland Park tilted to 11.6° from the zenith.

Thus, the v_{RMS} value due to turbulence alone can be calculated by equation (7.4.2.5), viz,

$$(7.4.4.15) \qquad v_{RMS} = \{[((\lambda/2)f_{\frac{1}{2}})^2 - (v_{r\frac{1}{2}})^2]/(2\ \ell n\ 2)\}^{\frac{1}{2}}$$

and then (7.4.4.7) can be used to estimate v_H, provided v_V is known.

Here, $v_{r\frac{1}{2}}$ is the half-power-half-width of the spectrum (plotted as a function of radial velocity) expected due to non-turbulent processes (beam broadening, shear "broadening"), and $f_{\frac{1}{2}}$ is the measured half-width of the spectrum.

7.4.5 Interpretation of spectral width using tilted beam

Let us now reconsider Fig 7.19. As seen, $f_{\frac{1}{2}} = .095$ Hz. Yet the expected $f_{\frac{1}{2}}$ for non-turbulent scatter was shown to be .055-.06 Hz in section 7.4.3 for day 80/072, using a beam tilted at 11.6° to the West. This section is primarily for illustrative purposes, so take $f_{\frac{1}{2}} = .055$. If $f_{\frac{1}{2}} = .06$ is used, some of the numbers produced will vary slightly, but none of the general conclusions will be changed. Thus by equation (7.4.4.15)

$$v_{RMS}^2 = [(\frac{151.5}{2}(.095))^2 - (\frac{151.5}{2}(.055))^2]/2 \ln 2$$

so, $v_{RMS} = 5.0\ ms^{-1}$. (If $f_{\frac{1}{2}} = .06$ Hz, $v_{RMS} = 4.5\ ms^{-1}$)

Now we have seen, using the vertical beam, that $v_v \lesssim 3\ ms^{-1}$. (This derivation, in Section 7.4.2, effectively assumed the resultant spectrum was a convolution of the turbulent and non-turbulent spectra. As seen in the in the last section, this is not strictly valid for a vertical beam observing anisotropic turbulence, but is close enough if $v_v \gtrsim v_H \sin(4.5^\circ)$, and will be assumed here).

Then, from Fig 7.20, with $v_{RMS} = 5\ ms^{-1}$ and v_v between 0 and $3\ ms^{-1}$, we see $v_H \sim 21\text{-}26\ ms^{-1}$. This is a large value, and it seems unreasonable that scatterers with scales of the order of 75 m could be associated with such an RMS velocity ($\varepsilon = kv^3/\ell$; if $\ell \sim 75$ m, $v \sim 25\ ms^{-1}$, $\varepsilon \sim 200 Wkg^{-1}$, and even if $k \sim 10^{-2}$, $\varepsilon \sim 2 Wkg^{-1}$. But in Chapter II, equation (2.2.3.3b) it was shown $k \sim 10^{-1}$).

However, consider the possibility that the horizontal wind speed is not constant over the observing period. Then the spectrum will move about, smear out, and hence be significantly broadened. What then could cause such wind fluctuations on scales of the order of 8 mins ? At least two possibilities exist, these being gravity waves, and turbulence. But in this case, the RMS velocities associated with the turbulence are not those associated with the scattering eddies, but with scales of the order of $\overline{uT}$,

$\bar{u}$ being the mean wind speed, and T the observing time. This statement follows Taylor's frozen turbulence hypothesis (e.g. Gage, 1979), which assumes that turbulence can be regarded as being "frozen" in the background wind. This would also explain the anisotropy, since at scales of this size ($\bar{u} \sim 70$ ms^{-1}, $T \sim 8$ min $\Rightarrow \ell \sim 33$ km), turbulence is decidedly two dimensional. (In actual fact, the observed v_H is the integrated effect of all scales from the smallest up to about $\bar{u}T$, but this will be considered later).

If the spectral width is due to turbulent fluctuations of winds on scales of about $\bar{u}T$, as suggested, then it can be expected that if the duration of observation T is changed, so should v_H change. A 5 minute power spectrum, using the first 5 minutes of data used in preparing Fig 7.19, was generated, and this had a half-power-half-width of .085 Hz, somewhat less than the .095 Hz produced by 8 minutes of data. A 3-minute power spectrum gave $f_{\frac{1}{2}}$ = .075 Hz. These results, then, would appear to support the above explanation of the spectral widths observed.

This explanation does not appear to have been presented before in any literature. Fukao et al (1980b) have also noted a dependence of the spectral width upon the length of observation at VHF, but only recorded for data lengths up to 100 seconds. Further, they only tilted their beam by about 3° off-vertical, so the effect they observed may not be the same as the above - they may not have used sufficient observation times and beam tilt to see the above effect. The author feels this process offers an important facility for estimation of turbulent energy dissipation rates (ε_d), and this will be illustrated below.

Let us assume that the fluctuating velocities are due to turbulence alone. (The role of gravity waves will be discussed later). Then we may expect that

(7.4.5.1a) $\varepsilon_d \approx T_*^{-1} \; v_H^3/\ell, \quad \ell \sim \bar{u}T$,

in a similar way to equation (2.2.3.3c") in Chapter II. However, equation (2.2.3.3b) may be more appropriate, as that was derived for eddy sizes ℓ . Then

(7.4.5.1b) $\varepsilon_d \approx 1/10 \; v_H^3/\ell, \quad \ell = \bar{u}T.$

The derivation of this equation was not given in Chapter II, but it may be fruitful to consider it here.

The structure function

(7.4.5.2) $\sigma_\tau^2 = \{ < [u_i(t) - u_i(t+\tau)]^2 > \}^{\frac{1}{2}}$ (i = component)

is related to the overall RMS velocity v_R by the relation

(7.4.5.3) $\sigma_\tau^2 = 2 v_R^2 (1 - R(\tau))$ (e.g. Gage, 1979)

where $R(\tau)$ is the autocorrelation function for the wind fluctuations.

The parameter v_H measured is not v_R, however, but is quite similar to σ_τ. But

(7.4.5.4) $\sigma_\tau^2 = A_i \varepsilon_d^{\frac{2}{3}} \ell^{\frac{2}{3}}$

where $\ell = \bar{u}T$, by Taylor's transformation. Here, A_i is a constant; A_ℓ refers to the longitudinal wind component, and A_t to the transverse components. As seen in Chapter II, Section 2.1, (A_i here is equivalent to A_{vi}^2 there), $A_\ell \sim 1.75$ to 2, and $A_t \sim 2.35$, for isotropic turbulence. Gage (1979) points out $A_t = 4/3 \; A_\ell$ for a isotropic turbulence, and $A_t = 5/3 \; A_\ell$ for 2-dimensional turbulence. Thus for 2-dimensional turbulence, $A_t =$ 2.9 to 3.3.

Then assuming $v_H = \sigma_\tau$, (7.4.5.4) gives

(7.4.5.5) $\varepsilon_d \approx A_i^{-\frac{3}{2}} v_H^3/\ell$, where $\ell = \bar{u}T$.

This derivation is similar to that of Lloyd et al (1972), except that those authors did not look at the component form of σ_τ, but rather the full vector structure function, (hence v_H is not quite relevant to their formula). Thus they derived equation (7.4.5.1b). Thus (7.4.5.5) suggests that

(7.4.5.6a) $$\varepsilon_d \approx T_{2D}^{-1} \frac{v_H^3}{\ell}$$

where $T_{2D} \sim 2.3$ to 2.8 for the longitudinal component,

$T_{2D} \sim 4.9$ to 6 for the transverse component.

So both (7.4.5.1b) and (7.4.5.6a) suggest that

T_{2D} lies between about 2.3 and 10.0.

It was pointed out above that the measured value v_H is in fact an integrated effect of all scales less than about $\bar{u}T$. Do the above formulae for ε_d consider this effect ? In fact they do, and this is best seen by examining the turbulence spectra.

Let us assume the value v_H observed is due to the effect of all scales less than $\ell_1 = \bar{u}T$. In actual fact, larger scales will have some effect, but the larger the scale the less the effect will be. These effects will be ignored. Assume v_H is a longitudinal or transverse component. Then

$$\overline{v_H^2} \approx \int_{k_1}^{\infty} E_i(k_i)dk_i = \int_{k_1}^{\infty} \alpha_i \varepsilon_d^{\frac{2}{3}} k^{-5/3} dk.$$

where $k_1 = 2\pi/\ell_1$

[Recall that two normalizations can be used;

(i) $\int_{k_1}^{\infty} E_i(k_i)dk_i = \overline{u'^2}$ and

(ii) $\int_{k_1}^{\infty} E_i(k_i)dk_i = \overline{u'^2}/2.$

where u' is the fluctuating component. I shall use case (i), as the formulae derived will involve longitudinal and transverse spectra, and the α_ℓ, α_t values given in Table 2.1, Chapter II, assumed this normalization.]

Thus;

$$\overline{v_H^2} \approx \alpha_i \varepsilon_d^{\frac{2}{3}} (2\pi/\ell_1)^{\frac{2}{3}}, \quad \text{or}$$

(7.4.5.6b) $$\varepsilon_d \approx T_{2D}^{-1} \frac{v_H^3}{\ell_1}, \quad \text{assuming } (\overline{v_H^2})^{3/2} \approx v_H^3.$$

Thus we see a form like (7.4.5.6a) again results, and it can be seen that formula does consider all scales. In this case,

$$T_{2D} \approx 11.5\, \alpha_i^{3/2}.$$

Notice by Tatarski (1961 ,equation 2.22), that

(7.4.5.6c) $\alpha_i \approx .2488\, A_i$ (after appropriate change of notation, and compensation for the fact that the normalization

$\int E_i(k_i)dk_i = \overline{u'^2}/2$ is used in Tatarski

Hence, $T_{2D} = 1.427 A_i^{3/2}$.

It is interesting to compare this with (7.4.5.6a), where it can be seen that $T_{2D} = A_i^{3/2}$. The two different approaches give a difference in T_{2D} of a factor of ~ 1.4.

Thus for the longitudinal component, with $A_\ell = 2.0$, $T_{2D} \approx 4.0$ and for the transverse component in 2-D turbulence, using $A_t \approx 3.3$, $T_{2D} \approx 8.55$. Thus these values also lie between 2.3 and 10.0, as proposed in (7.4.5.6a).

[Notice that if the non-component form of the spectrum is used, and the "normalization" $\int E(k)dk = \overline{u'^2}/2$ is used, then $\alpha \sim 1.4$ to 1.6 (Chapter II), and T_{2D} becomes $23.0\ \alpha^{3/2} \approx 42$. This can be compared with a value of 10 produced in the structure-function derivation (see 7.4.5.1b)). However, it should perhaps be realized that the constant in equation (7.4.5.1b) (taken as 10 here) actually assumed $\alpha = 1$ (see Chapter II, equation 2.2.3.3b). If in fact α is taken as ~ 1.4 to 1.6 the constant would be ~ 20, and it is this which should really be compared to the value $T_{2D} \approx 42$].

So it seems that equation (7.4.5.6a) is quite valid. Let us try and put it into practice.

For the 5 minute spectrum,

$$v_{RMS} \approx \{ [(.085)^2 - (.055)^2] / (2 \ln 2) \}^{\frac{1}{2}} . (75.75) \approx 4.2\ ms^{-1}$$

For $v_v = 0$-$3\ ms^{-1}$, Fig 7.20 implies $v_H \sim 16$-$21\ ms^{-1}$. Also, $\ell \sim 5 \times 60 \times 60$ metres, assuming a mean wind speed of $60\ ms^{-1}$.

Thus, $\varepsilon_d = T_{2D}^{-1} (16^3 \Rightarrow 21^3)/(18 \times 10^3) = \underline{T_{2D}^{-1} (.23 \rightarrow .51) Wkg^{-1}}$.

for the 3 minute spectrum,

$v_{RMS} \approx 3.3\ ms^{-1}$, giving $v_H \sim 9$-$16\ ms^{-1}$, and so

$$\varepsilon_d \sim \underline{T_{2D}^{-1} (.07 \rightarrow .38) Wkg^{-1}}.$$

For the 8 min spectrum, $v_{RMS} \approx 5\ ms^{-1}$ so Fig 7.20 implies $v_H \sim 21$-$26\ ms^{-1}$; Hence $\varepsilon_d = \underline{T_{2D}^{-1} (.32 \rightarrow .61)\ W\ kg^{-1}}$, so all estimations are reasonably consistent.

Notice the region of common overlap for these v_H^3/ℓ estimates is $.32 \Rightarrow .38\ m^3 s^{-1}$, so if we take .35 as the true value, then for the 8 min spectrum, $v_H = 22\ ms^{-1}$, for the 5 min spectrum, $v_H = 18.5\ ms^{-1}$, and for the 3 min spectrum, $v_H = 15.6\ ms^{-1}$. Thus using these v_H values, and v_{RMS} values as measured, Fig 7.20 can be used to make estimates of v_v. For the 8 min spectrum, $v_v \approx 2\ ms^{-1}$. For the 5 min spectrum, $v_v \sim 1.5$ - 2.2 ms^{-1}. For the 3 min spectrum, $v_v \sim 0.8$ - $1.5\ ms^{-1}$. Notice for

$T_{2D} \sim 10$, $\varepsilon_d \sim .035\ \text{Wkg}^{-1}$. Thus it appears $v_v \sim 1\text{-}2\ \text{ms}^{-1}$. This vertical RMS component is also the RMS velocity associated with the scattering eddies, so we expect, by equation (2.2.3.3c), that $\varepsilon_d \sim T_*^{-1}\ (1^3 \Rightarrow 2^3)/\ (\frac{151.5}{4\pi}) \sim T_*^{-1}\ (0.083 \rightarrow .66)$. As shown in Chapter II, T_* is a different value to T_{2D}, since it refers to radio wave scatter. Using $T_* \approx 15\pi$ (see 2.2.3.3c''), $\varepsilon_d \sim .002 - .015\ \text{Wkg}^{-1}$. This is somewhat less than the estimate using v_H (i.e. $.035\ \text{Wkg}^{-1}$), but is not inconsistent with that value, particularly if $v_v \sim 2\ \text{ms}^{-1}$ is assumed, given the uncertainty of the T_* and T_{2D} values).

The possibility also exists for estimation of eddy diffusion coefficients. If it can be assumed that the wind profile given in Fig 7.11 is the true one, and there exist no smaller scale fluctuation, then the wind shear around 86-88 km is about $25\ \text{ms}^{-1}\text{km}^{-1}$. The validity of this assumption that we have sufficient resolution to observe the true wind profile is questionable , however. Certainly in the troposphere and stratosphere, a resolution of 2-4 km would not resolve the true wind profile; there are finer scale fluctuations. This has been pointed out by van Zandt et al (1978) and Crane (1980), and has been discussed in Chapter II, Section 2.3.2. However, let us assume sufficient resolution has been achieved. (The outer scale at these heights is around $300 \rightarrow 600$ m (Fig 1.9a) so fluctuations of the mean wind on a scale finer than this are unlikely, since turbulence would smear them out). If it can be assumed the turbulence is wind shear generated, then $R_i = \omega_B^2/(\frac{\partial U}{\partial z})^2 = 0.25$, giving $\omega_B^2 = 1.5625 \times 10^{-4}$ rad s^{-1}, or $T_B = 8.4$ minutes. T_B is the Brunt-Vaisala period.

But $\omega_B^2 = \frac{g}{T}\left[\frac{dT}{dz} + \Gamma_a\right]$,

giving $\frac{dT}{dz} = -6.45\text{K km}^{-1}$ as the temperature gradient. The mean temperature gradient at 30°S in March at 80-85 km is $\sim -1\text{K km}^{-1}$ according to

CIRA 72, part 2 Table 18b (assuming 30°S in March to be the same as 30° N in September), and according to CIRA 72, part 1, Fig 10. However, temperature gradients of $\sim -5K\ km^{-1}$ are not uncommon (e.g. CIRA 72, part 1, Fig 10, "median" curve), so this result is not unreasonable.

Then $K = C_1\ \varepsilon_d\ \omega_B^{-2}$ is the eddy diffusion coefficient with $C_1 \sim 1$-3 (see Chapter II, Section 2.2.4). I shall use $C_1 = 2.0$. Then $K = 64 - 128\ m^2 s^{-1}$ for $\varepsilon_d = .02 - .04\ W\ kg^{-1}$. Then, given ε_d and K, the outer scale is

$$L = (K^3/\varepsilon_d)^{\frac{1}{4}}\ m\ r^{-1}, \quad \text{or} \quad L_o = 380\text{-}530 \text{ metres.}$$

The energy supply rate, ε, and bouyancy dissipation rate, are roughly $1.4\ \varepsilon_d$ and $0.4\ \varepsilon_d$ respectively, using $C_2 = C_3 = 1$, $C_1 = 2$ in equation (2.2.4.12).

Thus a picture emerges of a shear-generated turbulent layer at 86-88 km with RMS velocities associated with scales of 75 m of $\sim 2\ ms^{-1}$, and with larger scale horizontal fluctuations in the wind. It appears that $\varepsilon_d \sim .02$ to $.04\ W\ kg^{-1}$. Use of $T_{2D} = 10$, and $T_* = 15\pi$, produce reasonably consistent results. This picture can adequately explain the observed power spectra. Furthermore, analysis of power spectra in this way provides an excellent way of evaluating turbulence parameters in the middle atmosphere above 80 km - provided gravity waves do not contribute greatly to the wind fluctuations.

Before discussing the role of gravity waves, however, one more point deserves comment. It was mentioned in Chapter II, Section 2.2.3, that if the fading time for ionospheric scatter could be found with the fading due to the movement of the irregularities with the mean wind removed, then this fading time could be used to estimate v_{RMS}, as indicated by equation (2.2.3.11) and (2.2.3.12). It was shown that such a v_{RMS} could be found using full correlation analysis. However, the question now arises as to how this v_{RMS}

estimate should be interpreted. S.M. Ball (1981) has made estimates of v_{RMS} for Buckland Park winds data and finds $v_{RMS} \sim 4\text{-}5\ ms^{-1}$. In light of the previous discussion, it would seem reasonable that this v_{RMS} is related to v_H, the horizontal RMS turbulent velocity. However, several authors have calculated v_{RMS} using this FCA technique and assumed that this v_{RMS} is the velocity associated with scales of the order of $\lambda/2$ metres. If this observed v_{RMS} is related to v_H, as the author feels, then estimates of ε_d produced by the FCA technique are wrong. For example, Manson and Meek (1980) have done this. Thus it would seem fair to dismiss their results, calculated using their equation (2). Even when it is realized that v_{RMS} is related to v_H, a conversion needs to be found to obtain v_H. This is considerably more difficult than for the case of a tilted beam discussed earlier. The scales associated with v_H are of the order of $(\bar{u}\,T)$, where $\bar{u}$ is the mean wind and T is the length of time used to obtain each drift estimate (generally 1-2 minutes). If $\bar{u}$ and T are approximately constant, then $\varepsilon = v_H^3/L$ is proportional to v_H^3 and if v_{RMS} is linearly related to v_H (see Fig 7.20; this is true for an 11.6° tilt for large v_H), then the formula $\varepsilon \sim k\, v_{RMS}^3/\lambda$ may work, because k will be constant. But the whole thing is an extremely crude analysis, and cannot be relied on. The value k would have to be adjusted seasonally as $\bar{u}$ varied.

Interestingly, Wright and Pittaway (1978) have investigated the case of scatterers oscillating in the horizontal in a mean wind, and found that the parameter "V_c" which is produced in Full Correlation Analysis is approximately equal to the RMS fluctuating velocity of these scatterers. Thus it may seem that V_c is equivalent to v_H described above, where in this case v_H is the RMS wind velocity associated with scales corresponding to about one minute of data (1 minute generally being the data lengths used for FCA). If this were so, turbulence estimates would be possible. However, Stubbs (1977) has shown that V_c is typically $\sim$ 40 to 80 ms^{-1}, which is much

larger than the v_H values expected to be associated with scales corresponding to about one minute of data. (It may be expected that $v_H \sim (T_{2D}\ \varepsilon_d\ \bar{u}.\ 60\ \text{secs})^{\frac{1}{3}} \sim 12\ \text{ms}^{-1}$ for $\varepsilon \sim .04\ \text{W kg}^{-1}$, $\bar{u} \approx 70\ \text{ms}^{-1}$). It thus appears that the scheme proposed by Wright and Pitteway is not quite the same as that for scattering eddies being moved around by large scale turbulence, or that some other process not considered by Wright and Pitteway also contributes to the experimental V_c.

While discussing the paper by Manson and Meek (1980), a comment on their equation (3) may be worthwhile. They use an equation

$$\varepsilon_d = \tfrac{1}{3}\ \overline{v_{RMS}^2}\ f_b.$$

f_b being the Brunt-Vaisala frequency in Hz. This seems a strange relation, since v_{RMS} is a function of the scattering scale, and f_b is a constant, suggesting that ε_d is a function of the scattering scale! It would appear there is an error here. Possibly v_{RMS} in this case should be the velocity associated with the Kolmogoroff microscale. But again, the v_{RMS} measured by the system is not so much related to turbulent velocities associated with scattering scale, but rather to v_H. Thus this formula appears to be inapplicable to the data of Manson and Meek, and again their results may be in error.

Schlegel et al (1978) have produced ε estimates which are even less reliable than those of Manson and Meek. These authors simply used the fading times measured directly from their data, without even an attempt to remove the effect of movement of the irregularities with the mean wind. Consequently, a large contribution to $\tau_{\frac{1}{2}}$ probably comes from beam broadening, and their data is possibly unreliable. The "seasonal dependence" of ε_d that they see is most likely due to seasonal variations of the mean wind, thus varying the "beam broadening" effect, and so varying $\tau_{\frac{1}{2}}$ and thus

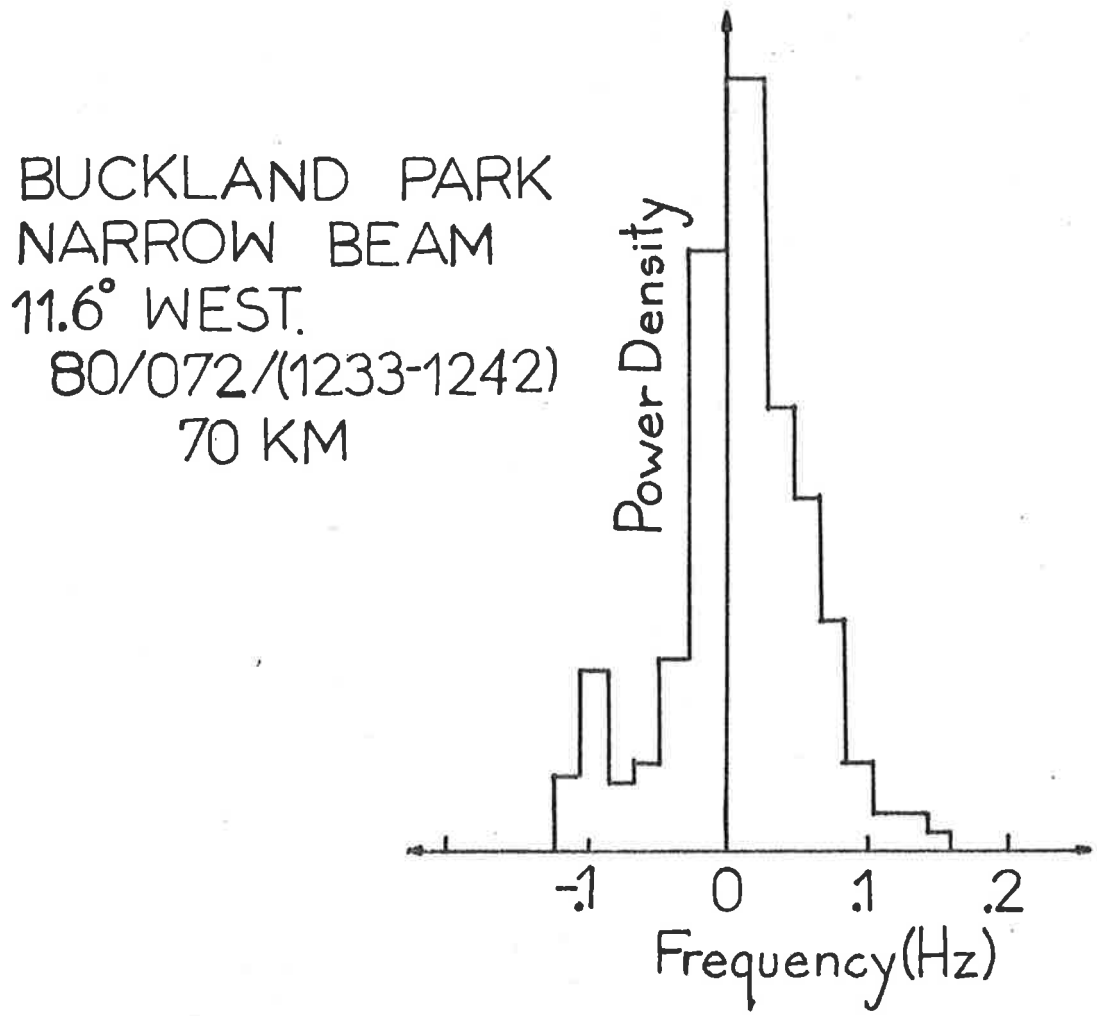

Fig 7.21

Typical power spectrum obtained with the tilted narrow beam at Buckland Park for ranges below about 76-80 km.

" v_{RMS} " . Unfortunately, due to the uncertainty with k in the relation $\varepsilon_d = k\, v^3/\ell$, authors are able to adjust their results to give "reasonable" ε_d values and so give their results an artificial tag of "acceptable".

Little has been said regarding 11.6° power spectra below 80 km. The reason for this was given in connection with Fig 7.11. That is, the anisotropy of scatter means that the spectra are unreliable for estimating winds. The velocities obtained in Fig 7.11 are averages of the velocities indicated by ~ 1-3 min spectra. However, Fig 7.21 shows a full 9 min spectrum at 70 km and 11.6°. It is clearly narrow, and somewhat similar to that for 0° suggesting that much of the scatter is leakage from the vertical. It is in fact possible that the small, apparently secondary peak at - 0.1 Hz may in fact be the contribution from the off vertical (and even then, the bulk of it may be from angles less than 11.6°). If it were assumed the scatter was from 11.6° for this "sidebbe", it would suggest a wind speed of ~ 40 ms^{-1}. However, the wind direction is opposite to that indicated in Fig 7.11. Thus this peak may be due to some other effect (e.g. a strong, short burst leaking into the beam from the opposite side to that of the beam), or the values in Fig 7.11 may be wrong. More investigation of such effects is necessary.

7.4.6 The relative roles of gravity waves and turbulence in the mesosphere

Before Hines (1960) showed the importance of gravity waves in the mesosphere, most non-tidal fluctuations were assumed to be due to turbulence (e.g. the ε_d estimates of Booker and Cohen (1956) of ~ 25 W kg^{-1} were wrong for this reason). After Hines' paper, the pendulum appears to have swung the other way, and the effects of turbulence with time scales of minutes and tens of minutes appear to have been largely ignored. The majority of oscillations at these periods have been assumed to be due to gravity waves. (At smaller scales, the role of turbulence has been appreciated, and most measurements of turbulence parameters have been done at short scales (e.g. rocket measurements (e.g. Rees et al 1972), meteor measurements (e.g. Elford and Roper, 1967)). It is worthwhile to briefly reconsider the relative roles of gravity waves and turbulence, particularly in view of the ε_d estimates made in the previous section.

In the troposphere, wind fluctuations with scales less than about 2-4 km (and hence time scales up to $\sim$ 4-8 minutes for wind speeds ~ 10 ms^{-1}) appear to be primarily due to turbulence (e.g. Kaimal et al 1972; Doviak and Berger, 1980). Even at scales of 8-16 km, (time scales $\sim$ 13-25 mins) turbulence makes a major contribution to the wind spectra, although some spectral peaks due to coherent waves can occur (e.g. see Doviak and Berger, 1980, Fig 10). Even at temporal scales of 10 to 200 minutes, turbulence makes the major contribution to wind fluctuations (Gage, 1979).

To properly investigate the effects of turbulence in the mesosphere, structure functions should be formed for the longitudinal and transverse components and a fit to the "two thirds" law attempted (e.g. see Gage, 1979). The constants A_ℓ and A_t described in equation (7.4.5.4) should be found, and if they are in the ratio 3:5, this would also support a turbulence

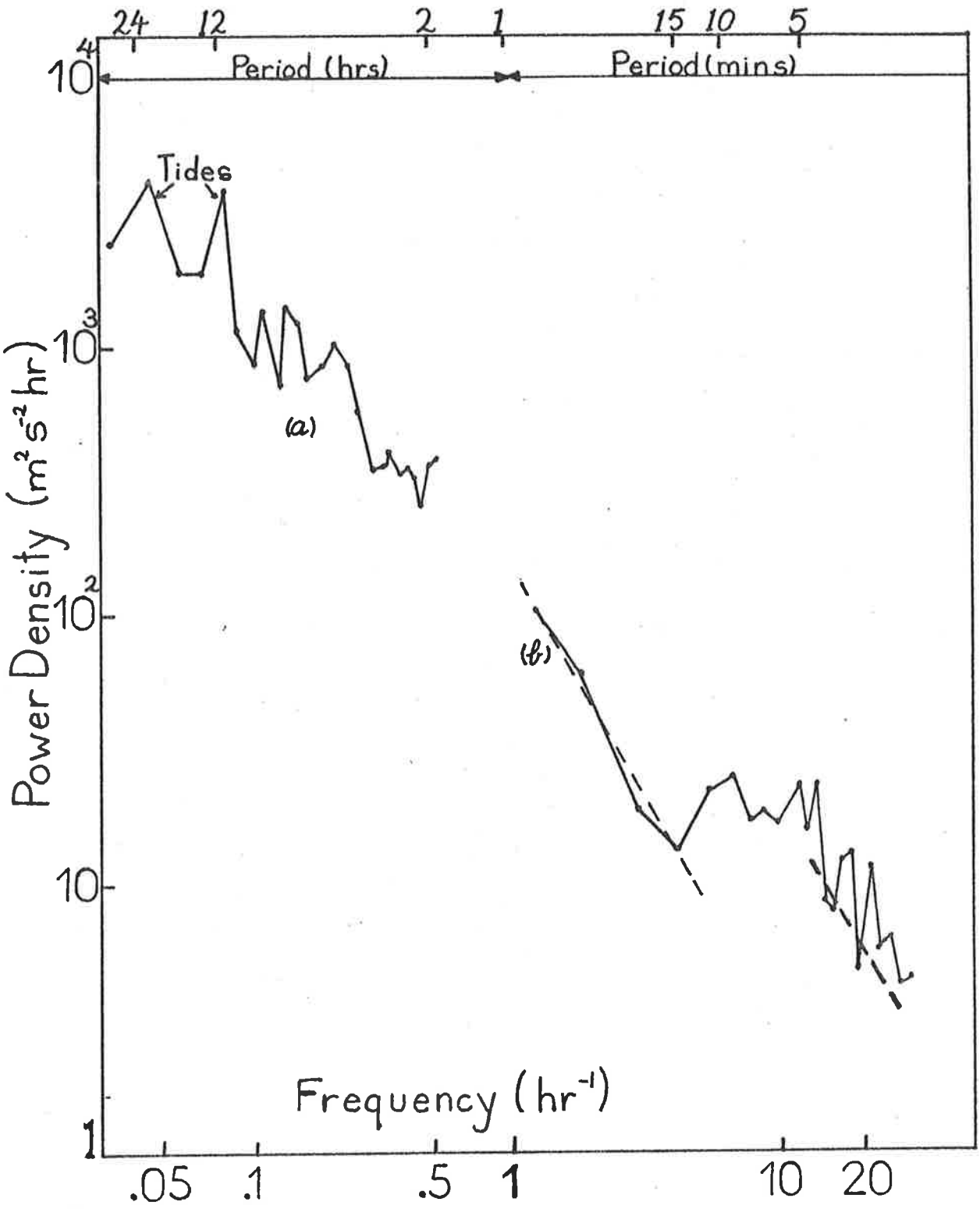

Fig 7.22

"Typical" (see text) power spectrum of winds measured by the PRD technique for Buckland Park for June, 1978 and for a height of 88 km. Section (a) was formed using about 10 days of data, and section (b) is the average of a few 3 hour blocks. Separate spectra for the North-South and East-West wind components have been averaged together. (Also shown (broken lines) are slopes of - 5/3). The spectrum is from Ball (1981). Note "power density" means power per unit frequency band.

contribution. A slightly inferior, but still useful technique (see Tatarski, 1961, for a discussion of the advantages of structure function) is to plot power spectra. These should ideally be plotted as a function of $k = 2\pi u^{-1} f$, f being the frequency and u the total mean wind. The spectra should then follow a form $E(k) = \alpha_i \varepsilon_d^{\frac{2}{3}} k^{-5/3}$, assuming Taylor's "frozen turbulence" hypothesis (e.g. see Gage, 1979). If the $k^{-5/3}$ law does appear to hold, then this suggests that the winds may be due to turbulence. However, it is not conclusive. For example, suppose gravity waves were generated in the troposphere by turbulence effects, and propagated to the mesosphere. If no filtering of these waves occurred (e.g. see Pitteway and Hines 1965; Hines and Reddy, 1967), then it might not be entirely unreasonable to suppose that the gravity wave spectrum would be similar to that of the source region - and so a "$k^{-5/3}$ law" could occur. Thus other tests should also be conducted - for example, are α_ℓ and α_t (see equation (7.4.5.6a to 7.4.5.6b) in the expected ratio ? The mean wind in the source region and in the region of observation are unlikely to be the same in direction, so if α_t and α_ℓ were in the ratio (5:3), this would be suggestive of turbulence. Cospectra (e.g. see Kaimal et al 1972) could also be obtained and compared to turbulence theories. Energy dissipation rates ε_d could also be calculated - if these were consistent with accepted turbulence values, this would also support a turbulence hypothesis.

No spectra plotted as a function of k for the mesosphere could be found in the literature, and shortage of time has prevented the author from doing this. However, Ball (1981) has plotted spectra as a function of frequency for Adelaide and Townsville mesospheric winds. If u is constant for the duration of the data interval used, then it can be expected that the energy $E(f) \propto f^{-5/3}$ for turbulence. Fig 7.22 shows a log-log

spectral plot due to Ball (1981), using winds measured by partial reflection drifts, and several facts can be noticed. A slope of $-5/3$ occurs for periods of $\sim$ 15 min to 1 hour. This may indicate much of the wind fluctuation could be due to turbulence in this period range, but the reservations discussed above should be borne in mind. For periods between 15 mins and $\sim$ 5 mins, the $-5/3$ slope is not followed, indicating that gravity wave effects are almost certainly important. At periods less than about 5 minutes no gravity wave activity is expected, this being less than the Brunt-Vaisala period. The graph in Fig 7.22 does show that at periods less than 5 minutes a $-5/3$ slope may again be evident. The "peaks" present may be due to acoustic waves, but recall that the vertical scale is a log plot, and these "peaks" at low powers could well be statistical fluctuations. Personal experience suggests that the fluctuations are statistical, and acoustic waves do not make a significant contribution to wind fluctuations at these scales.

Notice that the line of slope $-5/3$ for periods less than 5 minutes is displaced from that for periods of 15-20 mins to 1 hour. This is perhaps not surprising since gravity waves would supply an extra source of turbulence for these smaller scales, and so increase the energy dissipation rate for these scales.

Many other spectra have been produced for Adelaide and Townsville (Ball, 1981), and the above description appears to be generally applicable, although the role of gravity waves varies. The case presented here is one in which gravity waves were particularly active. The fit of the $-5/3$ slope for periods of 15 - 60 minutes is particularly good in this case, too; not all cases fit quite so well. (To be fair, I have been a little selective in choosing this graph, to emphasize the point. However, it is not atypical).

It is instructive to estimate the energy dissipation rates ε_d

associated with the $-5/3$ slopes mentioned above. If a "normalization" of the spectra

$$\int E_i(k_i)\,d\,k_i = \overline{u_i^2} \quad \text{is used (as was used by Ball),}$$

then $$E_i(k_i) = \alpha_i\, \varepsilon_d^{\frac{2}{3}}\, k_i^{-5/3} ,$$

where $\alpha_\ell = 0.5$ for the longitudinal component. For the transverse component in isotropic turbulence, $\alpha_t = (4/3)\alpha_\ell$ (e.g. Tatarski, 1961, Chapter 2; Kaimal et al, 1972; Gage, 1979). For two-dimensional turbulence however, (which is undoubtedly applicable here), $\alpha_t = 5/3\ \alpha_\ell$ (e.g. see equation (7.4.5.6c) ($\alpha_i \propto A_i$), and Gage, 1979 ($A_t = 5/3\ A_\ell$)).

Then if a frequency spectrum $S_{if}(f_i)$ ($i = \ell$ (longitudinal) or t(transverse)) is generated such that

$$\int S_{if}(f_i)df_i = \overline{u_i^2} ,$$

it follows that

$$S_{if}(f_i) = \alpha_i\, \varepsilon_d^{2/3}\, (u/2\pi)^{2/3}\, f_i^{-5/3} .$$

Since the spectrum presented is an average of the NS and EW components, there is some doubt as to the appropriate α_i. I shall use both $\alpha_t = 0.5$ and $\alpha_t = 5/3 \times 0.5 = .83$. Taking $u \approx 20$ to 50 ms^{-1} (typical for 88 km at Adelaide during this observation period (June, 1978)) gives, for the spectrum in Fig 7.22;

$\varepsilon_d = .085 \rightarrow .5$ W kg^{-1} in the periods 15 mins to 1 hour,

and $\varepsilon_d = 1.2 \rightarrow 6.3$ W kg^{-1} for periods less than 5 minutes.

The estimates of ε_d presented in the caption to Fig 1.9a for model 2 ($\varepsilon_d \sim .01 - .5$ W kg^{-1}) were generally made at fairly small scales ($\lesssim$ kms), so should correspond to the latter set of ε_d estimates (recall that it is to

be expected that ε_d be less in the 15 min - 1 hour period range, as explained above). It thus appears that these ε_d estimates are slightly too large, which might imply some non-turbulent contribution. However, also bear in mind that this region of investigation is NOT in the inertial range of turbulence, so the above α_i may not be relevant. (Also the effect of noise may have pushed the spectrum to higher values than the true energies at these scales. This could be quite important at low powers). Recall from Chapter II, Fig 2.2, that Weinstock's "first bouyancy range" had a $k^{-5/3}$ dependence, but the constant α differed from that for the inertial range. In a similar way, $\alpha_i = 0.5$ may not be relevant for the scales being observed in Fig 7.22 - a larger α_i may be needed. For example, an increase of α_i by x times reduces ε by $x^{3/2}$ times. It thus appears some more experimental estimates of this constant are necessary at such large scales. Likewise, the α_i used by Gage (1979) may not be relevant at his scales. Of course, if α_i must be changed, then the T_{2D} values estimated earlier may also need to be changed. A value $\alpha_i = 0.5$ was associated with $T_{2D} \approx 4$. (see equation (7.4.5.6b). If in fact $T_{2D} \approx 10$ is more relevant, as suggested in Section 7.4.5, then $\alpha_i \approx 0.9$ (using $T_{2D} = 11.5\ \alpha_i^{3/2}$ - see equation (7.4.5.6b), and this reduces the ε_d estimates by about 2.5 times. It appears that more work is necessary in deriving these α values at large scales.

The author feels, given the uncertainties involved in the α_i, and given that noise may have played an important role at the low powers, that the ε_d value associated with periods $\lesssim$ 5 mins is consistent with the speculation that all fluctuations at these scales are due to turbulence.

Manson and Meek (1980) have also presented such power spectra, and similar conclusions appear valid for some of their data, although those authors do not discuss the role of turbulence. For example, Fig 2 of that

reference, for the NS components at 82-85 km, shows a reasonable $k^{-5/3}$ fit for periods of 15 to 90 minutes, and the other graphs in that figure show similar trends.

What repercussions, then, does this have for the estimates of ε_d made previously (Section 7.4.5) ? For the 8-minute power spectrum, periods up to 8 minutes contribute to v_H^2, and periods up to ~ 16 minutes will make a lesser contribution (these complete more than a half-cycle in 8 minutes). We may write

$$\overline{v_H^2} = \overline{v_{H(turb)}^2} + \overline{v_H^2}_{(GW)}$$

where GW refers to gravity waves and acoustic waves. It has already been stated that it is felt that acoustic waves make little contribution to the spectra. Gravity waves may make some contribution in the period range 5 to 10 minutes, however. Suppose gravity waves and turbulence make equal contributions. Then

$$\overline{v_H^2} \approx 2\,\overline{v_H^2}_{(turb)},$$

so the ε_d estimate in Section 7.4.5 may be perhaps $2^{3/2} \approx 2.8$ times too large. However, it is felt that the ε_d estimates made in Section 7.4.5, are unlikely to be out by more than a factor of about 4. The assumed T_{2D} was taken as 10 - it could be as low as 2.5, which would increase the ε_d estimates by ~ 4 times; and consideration of the gravity wave effect above is unlikely to decrease ε_d by more than ~ 4 times. The above gravity wave effect may also explain why ε_d estimates made using an 8 minute power spectrum in Section 7.4.5. were larger than those using 5 minute or 3 minute spectra - gravity waves were making a larger contribution to $\overline{v_H^2}$ for the 8 minute spectrum. This illustrates that to properly utilize the technique developed in Section 7.4.5, spectra of less than about 5-8 minutes of data should be used - otherwise gravity waves will make too much contribution.

This discussion brings into question another technique for estimating energy dissipation rates. Vincent and Stubbs (1977) and Manson and Meek (1980 , equation 4) used a formula

$$\varepsilon_w = \frac{\overline{V^2}\, V_g}{h_o}$$

to estimate the energy loss rate of gravity waves. Here, $\overline{V^2}$ is the mean square horizontal perturbation velocity of internal gravity waves within some specified frequency band, h_o is the scale height of the energy density $\rho_o \overline{V^2}$, and V_g is a typical gravity wave vertical group velocity. This formula cannot be applied without some care. It must be established that in the frequency band being considered, gravity waves dominate the spectrum, (e.g. 5 - 15 minute periods in Fig 7.22). Otherwise, both $\overline{V^2}$ and h_o will be affected by turbulence contributions to $\overline{V^2}$. Vincent and Stubbs used periods in the range 1-4 hours, and obtained ε_w values in reasonable agreement with turbulent energy dissipation rates estimated by rocket and meteor measurements (e.g. Rees et al (1972); Elford and Roper, 1967). This could perhaps be taken as evidence that gravity waves do dominate the spectrum in the range 1 hour to 4 hours. However, the author feels that further investigation of the spectrum in the period range 15 minutes to 1 hour may be necessary to establish the contributions from turbulence in that region. Gravity waves dominate at periods of $\sim$ 5 - 20 minutes, and turbulence appears to dominate at periods $<$ 5 minutes.

7.5 Deconvolution

The recording of complex data allows deconvolution of the scattered signal to be achieved. This offers the possibility of improving the height resolution of the system. However, in practice this is a procedure which must be treated carefully. Röttger and Schmidt (1979) discussed the pitfalls and requirements involved in deconvolution procedures.

One important point is that if a resolution of x metres is required, then data must be recorded at least at intervals of $x/2$ metres. There is no point in recording data at 2 km steps, and expecting to get a resolution better than 4 km.

A second major point concerned with deconvolution concerns the effects of noise. For reliable deconvolution, the high wavenumber components of the power spectra of the complex amplitude vs. height profile must be recorded accurately. These are usually the weakest signals. Suppose that the critical wavenumber k_c is reached where the signals are so weak that they are comparable to noise levels and that at larger k_c the signal is even weaker. Then no information can be obtained at resolutions less than about $(2\pi/k_c)$. Digitization, as discussed in Chapter VI, represents one type of limiting noise, and estimations show that for the pulse used at Buckland Park, and the receivers used and the digitization employed, resolutions of better than about 1 km are not really possible. The major limitation to deconvolution in dealing with ionospheric data is the fact that the signal is continually varying, so an instantaneous profile must be used to do the deconvolution (or, at best, a profile produced from coherent integration of about 1s of data). Little averaging is possible to reduce the noise. This contrasts with cases where the signal structure does not change with time. In such cases averaging can be used to reduce the noise, and deconvolution becomes a useful technique.

For these reasons outlined above, then, no deconvolution has been attempted in the work for this thesis. Rather, procedures such as watching the variation of the height of echoes, as discussed in Chapter IV, proved

more useful for investigations of "layer" widths and structures.

However, crude deconvolutions of the mean power can be attempted. For example, on day 80/072, the transmitted pulse had a half-power-half-width of 3 km. The measured half-power-half-width of the 10 minute mean profile was about 3.5-4 km (Fig 7.11). If it is assumed that the height variation of the layer is Gaussian in form, with half-power-half-width equal to d km, then

$$d^2 + 3^2 = 3.5^2 \rightarrow 4^2$$

so this implies $d \sim 1.8 \rightarrow 2.6$ km.

Of course, this is crude, but is not inconsistent with previous estimates of a layer of width $\sim$ 2-4 km (although in those cases a sharp edged layer was assumed).

7.6 Conclusions

One of the more important early discussions in this chapter concerned the significance of spectra formed with complex data and it was found that these were unreliable unless they were formed with time intervals at least $\sim 100\ \tau_{\frac{1}{2}}$ in length, $\tau_{\frac{1}{2}}$ being the fading time derived from the complex correlation function. The use of running power spectra was also discussed.

Some space had been devoted earlier to comparisons of fading times using amplitude-only data and complex data, for data lengths of the order of 1 minute. It was found that the parameters were approximately proportional, but considerable scatter exists in the relation between individual points. The reasons for this became clear when it was realized that power spectra formed with 1 minute of data were somewhat unreliable.

Another important experiment was to look for the effects of turbulence using a vertical beam. To do this, beam broadening effects had to be removed, and considerable care was taken to estimate such effects. It was found that turbulence estimates using the vertical beam could not be made, since beam broadening was the dominant contributor to the spectra.

Some comparisons of partial reflection drifts (PRD) measurements and Doppler measurements of wind speeds were made. Agreement was excellent in the region where both techniques could be used.

The spectra taken using a tilted beam proved to be extremely interesting, being considerably wider than the expected beam-broadening and wind-shear-"broadening" effects would predict. It was possible to interpret this as due to turbulence effects associated with scales of the order of $\bar{u}\,T$, T being the observing period and $\bar{u}$ the mean wind speed. A procedure was developed by means of which horizontal RMS velocities associated with

scales of the order of $\bar{u}\,T$ could be calculated, and it was then shown that energy dissipation rates could be calculated. This was one of the major original contributions of this chapter.

However, it was pointed out that there was some uncertainty in such ε_d estimates, due to the uncertain contribution from gravity waves. If there are no gravity wave effects, then

$$\varepsilon_d = T_{2D}^{-1} v_H^3/(\bar{u}\,T),$$

v_H being the horizontal RMS velocity measured from the spectrum produced by the tilted beam. It was decided that T_{2D} lay between 2.3 and 10, and a value of about 10 seemed to provide the greatest consistency for the data presented.

The possibility of using root mean square velocities deduced from Full Correlation Analysis of partial reflection drifts was discussed. It was shown that often formulae which the author feels are erroneous have been used to estimate ε_d values.

CHAPTER VIII

COMPARISON OF PARTIAL REFLECTION PROFILES AND ROCKET MEASUREMENTS OF ELECTRON DENSITY

Chapter VIII Comparison of partial reflection profiles and rocket measurements of electron density

8.1 Introduction

Although considerable information concerning the scatter characteristics of D-region scatterers has been presented in this thesis, it has not been possible to positively define the actual forms of the scatterers. One technique which can be used to obtain a better description is to actually measure the electron density as a function of height using sensitive probes positioned on rockets. However, no simultaneous observations of partial reflection scatter profiles and rocket measurements seem to have appeared in the literature. This chapter discusses perhaps the first such near-simultaneous observations ever made.

Before presenting this data, however, some theory is necessary. If the electron density profile is known, it is desirable that an accurate expected HF scatter profile can be computed from it. For this reason, the next section is devoted to a discussion of the propagation of an HF radio pulse through the D-region. Some simple results are also presented.

Having produced accurate formulae for these processes, the rocket data is then analysed in the following section, and important insights into the nature of these D-region scatterers are thus obtained.

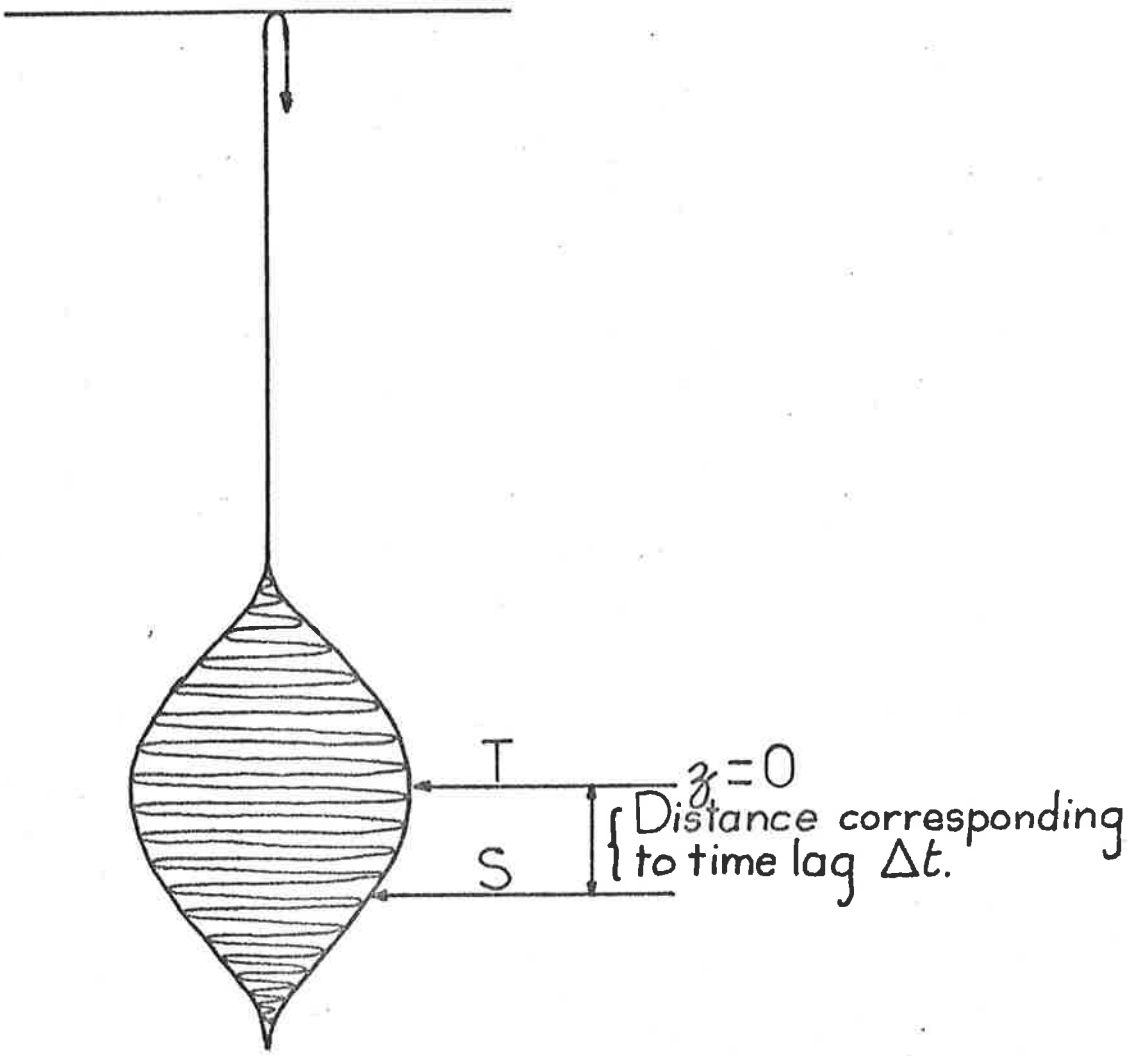

Fig 8.1

Illustration of a pulse at 0 time, with symbols appropriate to the discussion in the text. The peak of the pulse is at $z = 0$ at zero time. The point S will be at $z = 0$ at $t = \Delta t$.

8.2 Reflection of a radio pulse in a horizontally stratified ionosphere

8.2.1 Theory

Already in this thesis it has been mentioned that the height-profile (of complex amplitude) produced by HF scatter from the D-region is approximately a convolution between the pulse shape and the reflection coefficient profile (e.g. Appendix B equation B26b; Chapter 4 equation 4.5.2.4; and also in a 3-dimensional form in Chapter 7, e.g. equation 7.4.4.8). However, let us develop a more sophisticated formula.

8.2.1a Pulse Convolution

Consider a wave-packet composed of spherical wavefronts. If we consider only the vertically propagating part of the wavefronts, then the time and space description at time t and height z, is given approximately by (e.g. see Appendix B, equation B.17)

$$(8.2.1.1) \qquad E_o \; \frac{1}{z} \; g_t\left(t - \int_o^z \frac{(\Re e(\mu'_g)}{c}\, ds\right). \; e^{-j\frac{n}{c}\int_o^z \underline{\mu}.ds} \; e^{j\omega t}$$

(Henceforth, let $E_o=1$)

Here $\underline{\mu}$ is the mean (complex) refractive index of the frequencies contributing to the wavepacket, and μ_g' is related to the group refractive index (see Appendix B). For most purposes in this chapter μ_g' can be taken as approximately equal to the group refractive index μ_g. $\Re e$ means "real part of", and c denotes the speed of light in a vacuum.

Note that this formula is not actually precise, for example, the z^{-1} dependence should also have been associated with an $\mu^{-\frac{1}{2}}$ effect, to properly preserve flux. Also, at a frequency of 2MHz this ray theory is only valid in the D-region; as $\underline{\mu}$ approaches zero (e.g. E-region), a full wave theory is necessary (see Appendix B).

Let us now imagine that the pulse is reflected from a weak reflector at height z_1 (Fig 8.1). The following assumptions will be made.

(i) The reflector will be assumed to be at least 1 Fresnel Zone in horizontal extent, so that a reflection coefficient can be evaluated. In fact, only the vertical space co-ordinate is considered, so in effect the ionosphere is assumed to be horizontally stratified.

(ii) The Born approximation will be used. That is, after the pulse is weakly reflected at some height, it will be assumed that the remaining forward propagating radiation has strength equal to that which it would have had if there had been no reflection. This is generally valid as the reflection coefficients are usually less than 10^{-2}.

(iii) It will be assumed that the ray travels in a straight line, i.e. suffers no significant bending of its path.

The reflected pulse returns to the ground, and the echo strength at time t, assuming the reflection coefficient was $R(z_1)$, is

$$(8.2.1.2)\quad (R(z_1)/2z_1).g_t(t - 2\int_o^{z_1} \frac{\Re e(\mu_g)}{c}\, ds).\, e^{j\omega(t - 2\int_o^{z_1} \frac{\bar{\mu}}{c}\, ds)}$$

The amplitude recorded due to reflection of part S of the pulse in fig 8.1 from height z_1 at time

$$(8.2.1.3)\quad \tau = 2\int_o^{z_1} \frac{\Re e(\mu_g)}{c} ds + \Delta t$$

is thus, substituting in (8.2.1.2),

$$(8.2.1.4)\quad g_t(\Delta t)\; e^{j\omega(\tau - \int_o^{z_1} \frac{\bar{\mu}}{c}\, ds)}\; (2z_1)^{-1}.R(z_1).$$

Now assume there are reflectors at all heights. We seek the total signal received at time τ. Then we simply sum (8.2.1.4) over all z_1 values, for fixed τ. Thus for a given τ, each different point of the pulse was reflected from a slightly different reflection height, so all arrive at the

ground at this time τ.

Let us also use the virtual height, so

(8.2.1.5) $\tau = 2z_o/c$ (e.g. see Appendix B)

Let $R(z) = r(z)dz$. Then integrating (8.2.1.4) gives the returned amplitude at virtual height z_o as

$$(8.2.1.5)\quad \underline{A}(z_o) = e^{\frac{j\omega 2z_o}{c}} \int_{z_1=o}^{\infty} g_t\{ \frac{2}{c}(z_o - \int_o^{z_1} \Re e(\mu_g)d\xi) \} \cdot x\{ r(z_1)\frac{1}{2z_1} e^{-2j\omega \int_o^{z_1} \frac{\bar{\mu}}{c} \cdot d\xi} \} dz_1$$

$\underline{A}(z_o)$ is complex. This can be written as

$$(8.2.1.6)\quad \underline{A}(z_o) = e^{\frac{2j\omega z_o}{c}} \cdot \{ g_z(z_*) \otimes S_{ef*}(z_*) \} (z_o)$$

where $g_z(z_*) = g_t(\frac{2}{c} z_*)$ and $z_* = \int_o^{z_1} \Re e(\mu_g)d\xi$ is the optical group path length

and where $S_{ef*}(z_*) = S_{ef}(z_1) = r(z_1)(1/2z_1)\, e^{-2j\omega \int_o^{z_1} (\frac{\bar{\mu}}{c})\, d\xi}$ is an "effective scatter function."

Thus, $A(z_o)$ is a convolution, but not as simple as suggested by equation B.26b in Appendix B. That form is only valid if $\bar{\mu} = \mu_g = 1.0$ (in particular, it assumes zero absorption), and there is no $(2z_1)^{-1}$ dependence. In that case, (8.2.1.6) equals B26b.

This formula, then, gives some insight into a formula for the reflected pulse. However, for computer operations, it is still a little inaccurate. A more precise procedure is described in the following section.

8.2.1b Fourier Procedure

The greatest weakness of the above formulae is that they all assume that the shape of the pulse envelope does not change as it propagates. If the phase refractive index changes too rapidly, and too non-linearly, as a

function of frequency, then this assumption is not valid, and the group refractive index becomes a meaningless term. (In fact, often if μ_g is calculated under such circumstances (see Appendix B, equation B.21)) μ_g can be less than 1.0, suggesting information can propagate at speeds greater than c. What this really means though, is that the envelope changes form as it propagates.

To properly consider these effects, the following procedure was adopted.

(i) the transmitted pulse was first Fourier analyzed on a digital computer into its various spectral components,

(ii) thus each spectral component corresponds to a continuous wave, and (8.2.1.6) can be used with $g_z(z_*) = \text{constant}$.

Thus, the echo strength at angular frequency ω and virtual height z_o is, by (8.2.1.6),

$$(8.2.1.7) \quad \underline{A}_\omega(z_o) = R_x(\omega)\, e^{\frac{j\omega 2z_o}{c}} \int_o^\infty S_{ef}(z_1)\, dz.$$

$$\text{where } S_{ef}(z_1) = r(z_1)\, \frac{1}{2z_1} \cdot e^{-2j\omega \int_o^{z_1} \frac{\mu_\omega}{c}\, d\xi}$$

and where $R_x(\omega)$ is the frequency response of the receiver, (this term was not included in equation 8.2.1.6).

Here, μ_ω is the actual refractive index at frequency ω, and is quite exact. This is another advantage over equation 8.2.1.6; the $\bar{\mu}$ used was something of an approximation, but here, because we are only dealing with one frequency, it is precisely μ for that frequency.

Thus, this term (8.2.1.7) is calculated for each frequency ω obtained in the Fourier transform in step (i),

(iii) Finally, the terms (8.2.1.7) are multiplied by the Fourier component deduced in step (i) and re-added. The resultant is a complex number which gives the amplitude and phase of the received signal. (It is usually necessary to "mix the signal down" to 0 Hz before the received form produced in a real experiment is properly simulated).

This procedure thus, in some ways, simulates Nature's own approach to the problem. It has the following advantages

(a) $r(z_1)$ can be calculated at each frequency, rather than using an average value for all the frequencies concerned (see Appendix B, equation B.25);

$$r(z)dz = \frac{\mu(z + dz) - \mu(z)}{\mu(z + dz) + \mu(z)}$$

(b) absorption effects are calculated independently at each frequency;

(c) problems involved with the pulse envelope changing are not important - in fact, if the envelope <u>does</u> change, this procedure will show it ;

(d) the approach also considers the receiver frequency response.

The program used is given in Appendix F; program "SCATPRF". It will be noticed that the Sen-Wyller equations are used to obtain refractive indices.

8.2.2 Some Simple Applications

Having produced program "SCATPRF", it was a simple procedure to put in model electron density profiles and examine the reflected power. It will be recalled from Chapter III, that the parameter used to measure the scattering effect of scattering during the observations made in this thesis was an effective reflection coefficient, which was exactly the amplitude received divided by the amplitude which would have been received had there been total reflection and no absorption. If the amplitude produced by "SCATPRF" is multiplied by twice the height of scatter, exactly the same parameter is produced by this numerical simulation. This made it possible to examine more clearly the types of scattering structures necessary to produce the observed received powers.

As an example, it was found that with a typical D-region profile, but with a sharp 5% change in electron density at 86 km, an effective 0 mode reflection coefficient of 2×10^{-4} was produced. Likewise, a sharp 10% change in electron density at 73 km produced an effective 0 mode reflection coefficient of about 4×10^{-5}. (The "typical electron density profiles" used were those shown in figs. 8.4 and 8.5 and small artificial steps in electron density were then put in those profiles for these investigations). These are reasonable values - typical reflection coefficients are about $1 - 4 \times 10^{-4}$ at 70 km and $2 - 6 \times 10^{-4}$ at 86 km. The collision frequencies, magnetic fields etc., used in these calculations can be found in Appendix B, fig B.1, or in Section 8.3.3. of this chapter).

One point does deserve some comment. In all the above calculations, and indeed in those to follow, abrupt changes in electron densities were used. The collision frequency was assumed to vary slowly. The possibility that abrupt changes in collision frequency can cause RF reflections exists, but it is generally assumed that such sharp changes do not occur. Piggott and Thrane (1966) and Lindner (1972) have pointed out that changes to the Differential Absorption theory (see Chapter I) would be necessary if collision

frequency changes are important. The collision frequency is proportional to the pressure, and sharp steps in pressures are generally assumed not to occur. However, it should be noted that sharp steps in pressure do occur in the troposphere (e.g. see Merrill, 1977). In the work presented in this chapter, it will be assumed that a sharp change in electron density has no associated collision frequency change. This approximation is usually assumed for Differential Absorption measurements (e.g. see Thrane et al, 1968) and some experimental data supporting this assumption has been produced by Belrose et al (1972).

8.3 Analysis of simultaneous rocket and particle reflection measurements

8.3.1 Introduction

A review of stratification of HF partial reflection profiles and the relation to structures in high resolution electron density profiles has been presented in Chapter I, section 1.4.1d. There is little point in re-producing that here, except to remind the reader that the few analyses so far carried out have been of a statistical nature (e.g. Manson, Merry and Vincent, 1969).

It is also useful to recall the work presented in Chapter IV, section 4.5.2, where it was shown that to achieve significant scatter, the reflecting structure should consist of a change in refractive index which takes place within a thickness of less than about one quarter of the probing wavelength. However, if an extremely large refractive index change occurs, it is still possible that significant scatter can occur even if the changes occur over several wavelengths thickness. But generally, for changes in electron density of less than about 10% (which most changes seem to be (e.g. see Manson, Merry and Vincent 1969)), the change should be completed within about a quarter wavelength to be important.

The following section presents some measurements of electron density and partial reflection profiles made at Woomera, Australia (31^{o}S, 136^{o}E). The measurements were very nearly simultaneous in space and time, and it is believed that they were the first of their type.

8.3.2 Experimental details

8.3.2a Technique

Two rockets were flown at Woomera, Australia (31^{o}S, 136^{o}E), and partial reflections at 1.98 MHz were monitored close to and during these flights. Aboard the rockets were Langmuir probes, which were capable of quite high resolution measurement of electron density along the rocket path. The voltage outputs of the Langmuir probe were recorded on photographic film, and later digitized for computer calculations. The partial reflection experiment was located about 30 km from the rocket launch site (see Vincent et al (1977) for details of equipment and location with respect to the launch area and the rocket range).

The first flight was denoted AP6/6 , and was fired at 1230 hrs Australian Central Standard Time (ACST) on 27th May, 1976. The appropriate solar and geomagnetic parameters at the time were

(i) solar zenith angle $\chi = 54^{o}$

(ii) sunspot number $R_z = 0$, and monthly mean $\overline{R} = 13$

(iii) three-hourly K_p index ≈ 1, and mean $\overline{K}_p \approx 0$

(for (ii) and (iii) see Lincoln, 1976)

This was the main flight analyzed.

The second flight was denoted AV5/1 and was fired at 1106 hours ACST on 30th June 1976. Unfortunately, the data from this flight was digitized at only a quite coarse resolution, and then the film was lost before the author obtain it. Hence a detailed analysis of this data could not be carried out. This was extremely unfortunate, because it appears that it would have been better data to analyze.

The partial reflection data were recorded in a similar way to the procedures described in Chapter III. Amplitudes were recorded at 2 km steps

from 82 to 100 km, each range being recorded 5 times per second. The primary purpose of these rocket flights was for comparisons of partial reflection drift measurements and neutral winds measured by rocket released chemicals, and the main height regime of interest was between 80 and 100 km. Consequently, few measurements of partial reflection echoes below 80 km were obtained, and this limited the region where detailed comparisons of partial reflection profiles and Langmuir probe measurements could be made. Some 62 to 80 km data were recorded about an hour after the flight on the 30th June, but in this chapter we will concentrate on the 82-100 km region. It should also be pointed out that none of the partial reflection amplitudes were calibrated so no absolute measurements of reflection coefficients were possible. Typical reflection coefficients for the echoes at Woomera are known, however.

The experiment suffered one other problem. Although Langmuir probes show fine scale fluctuations in electron density very well, the current produced by them does not bear a constant relationship to the electron density. The ratio between the mean electron density and the Langmuir probe current usually changes slowly with height (e.g. see Bennett et al, 1972, fig. 9), and it is generally necessary to adjust the fine scale Langmuir probe measurements to fit an electron density profile made by some other procedure which, while not producing the high resolution of the Langmuir probe, does at least produce a reliable electron density profile. In the experiments performed for this chapter, no such coarse-resolution measurementss were made. They had been planned, but never eventuated due to practical difficulties. The procedure adopted was to fit the Langmuir probe measurements to a typical quiet-day electron density profile - namely, one due to Mechtly et al, (1972, table 5,"Quiet Sun"). This procedure is quite adequate for the purpose of this chapter, since the fine scale fluctuations are the important structures

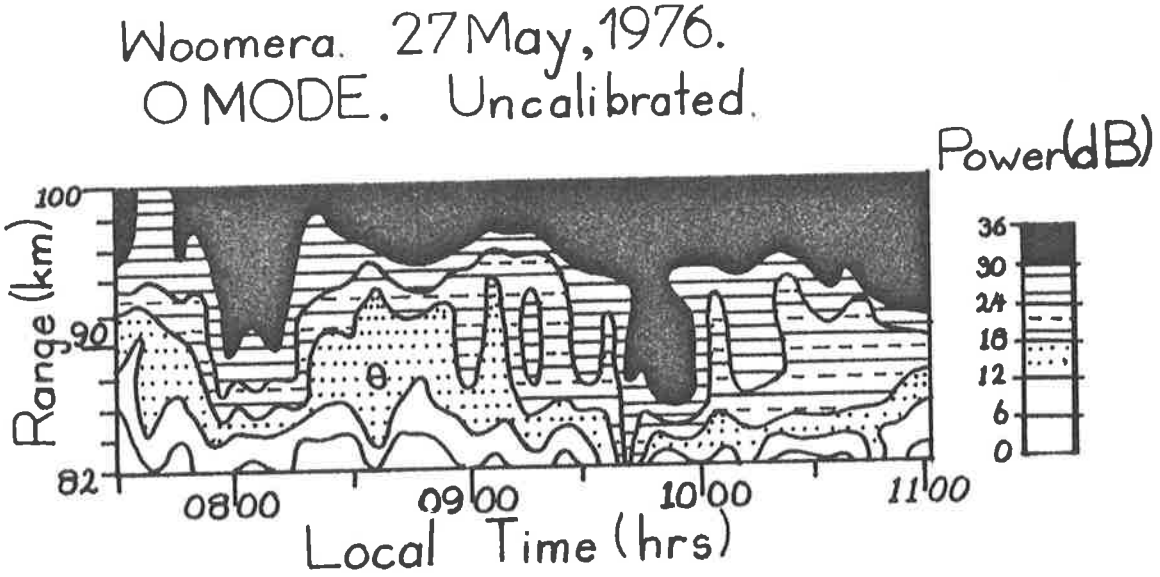

Fig 8.2

Smoothed contour plot of 5 min means of power plotted against range and time, for the period leading up to the rocket flight (1230 hours) on 27th May, 1976. Notice the presence of a 90 km echo, and a strong blanketing sporadic-E above 100 km. The data is uncalibrated and power units arbitrary.

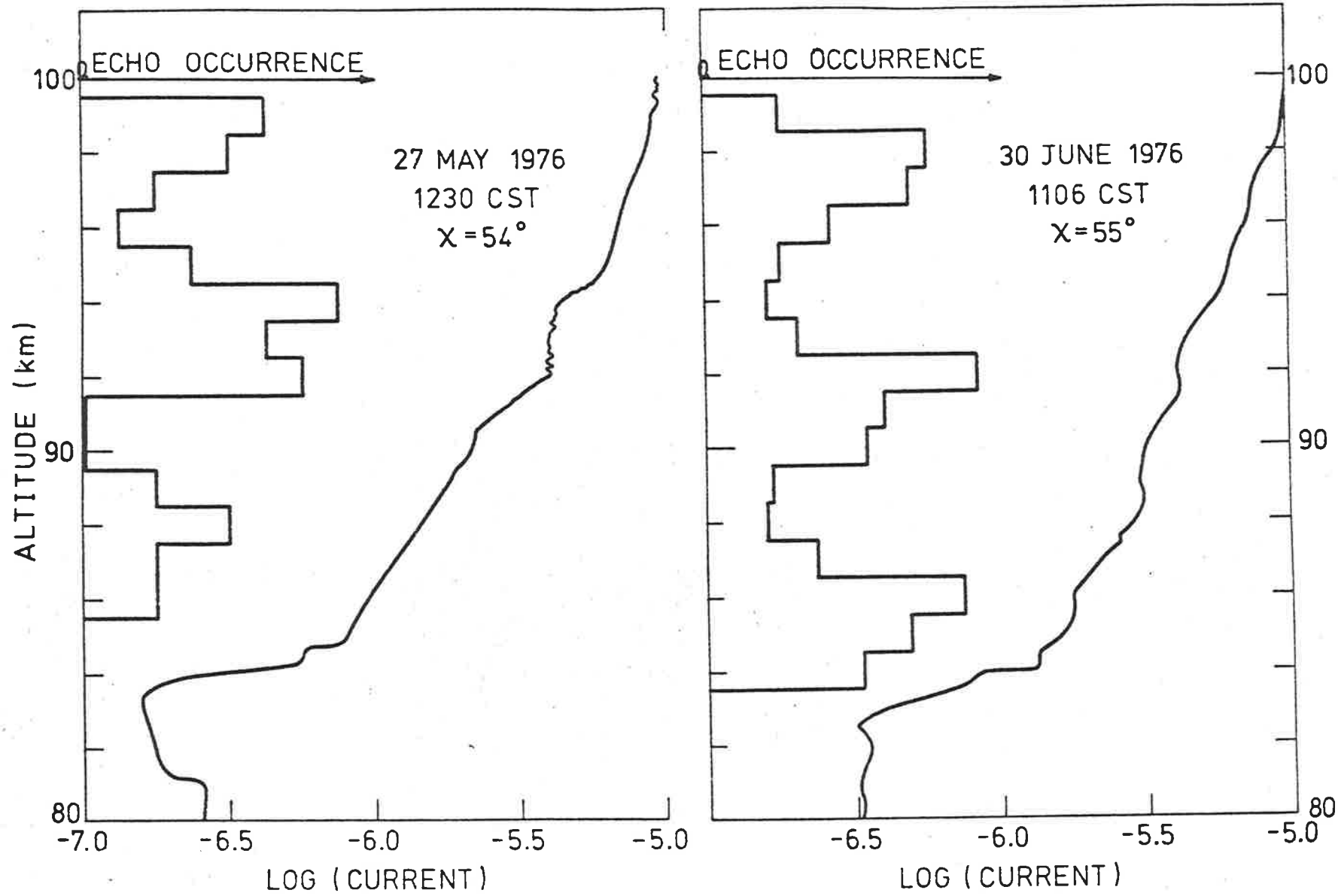

Fig 8.3 Histograms of frequency of occurrence of echoes vs. height (it can be assumed that height and range are approximately equivalent - see text). Plotted alongside Langmuir probe currents (solid lines).

to be examined, and the true electron density profile is unlikely to have differed too much from that of Mechtly et al, since the solar and geomagnetic parameters matched theirs quite well.

8.3.2b Results

Figure 8.2 shows a contour plot of 5 minute means of the received power plotted as a function of range and time for 27th May, 1976. Data were recorded up to 1200 hrs, half an hour before the rocket flight. Notice the presence of a layer at about 90 km. It will be noted that the mean power varies as a function of time, as is to be expected (see Chapter IV). The strong powers above 94 to 96 km was due to a strong sporadic E layer (E_s) at 105-110 km. This resulted in total reflection of the incident radio pulses, with subsequent large powers at heights several kilometres either side of the peak (due to the pulse width) hiding the much weaker partial reflections from above 94-96 km.

By using 5 minute means the E_s echo dominates. However, if the profile is observed on scales of the order of seconds, the fading of the echoes can at times weaken the E_s effect at these heights above 92-94 km, and D-region partial reflections can at times show. For this reason, the instantaneous profiles of amplitude as a function of range were analyzed, and the peaks of the amplitude profiles found. These were then tabulated as a function of range, and the results are shown in Fig 8.3. (The histogram shows the vertical scale as altitude. In actual fact it should be range, but on average the two are equivalent. Part of the width of each peak may be due to oblique scatter, but the peaks of the histogram can be taken to indicate scattering layers close to the height indicated). Also shown in fig 8.3 are the upleg Langmuir probe currents, plotted at a relatively coarse resolution. The histograms for 27th May were taken from randomly selected instant amplitude profiles during the period 1018 hours to 1204 hours ACST. The histogram for

30th June is for the period 1105-1108 hours, which surrounded the firing time (1106) of the rocket.

A visual inspection of this data alone shows ;

(i) a very steep ledge in current occurs at around 84 km, and this was undoubtedly associated with a large increase in electron density;

(ii) echoes occurred preferentially at heights of about 84-88 km, just at the top of the strong ledge just mentioned. (Note that on 27th May, the rocket was fired half an hour after the last partial reflection echo was recorded, so the slight disagreement between the 84 km layer and the echoes at 86-88 km must be a result of this. The partial reflection results and rocket electron density profiles were simultaneous on June 30th, and the 84-86 km ledge and partial reflections agreed well then); and,

(iii) echoes also occurred preferentially at heights of 90-94 km, and may be related to irregular electron density fluctuations at that height, particularly on 27th May.

Echoes also appear to occur preferentially at about 98 km, but it is not possible to ascertain how much of this is due to interference effects associated with the E and E_s echoes. Therefore these will not be discussed in detail.

A peak in scattered power was also seen to occur at about 80-81 km, which does not show on the diagram, since partial reflection data was only recorded above 82 km. This may be associated with the small ledge at 81 km on 27th May.

Having noted these correlations, the film from flight AP6/6 (27th May 1976) was digitized at a higher resolution. A resolution of better than 30-40 metres was produced by this digitization. These Langmuir probe currents were then compared to the Mechtly et al (1972) "Quiet Sun" profile discussed

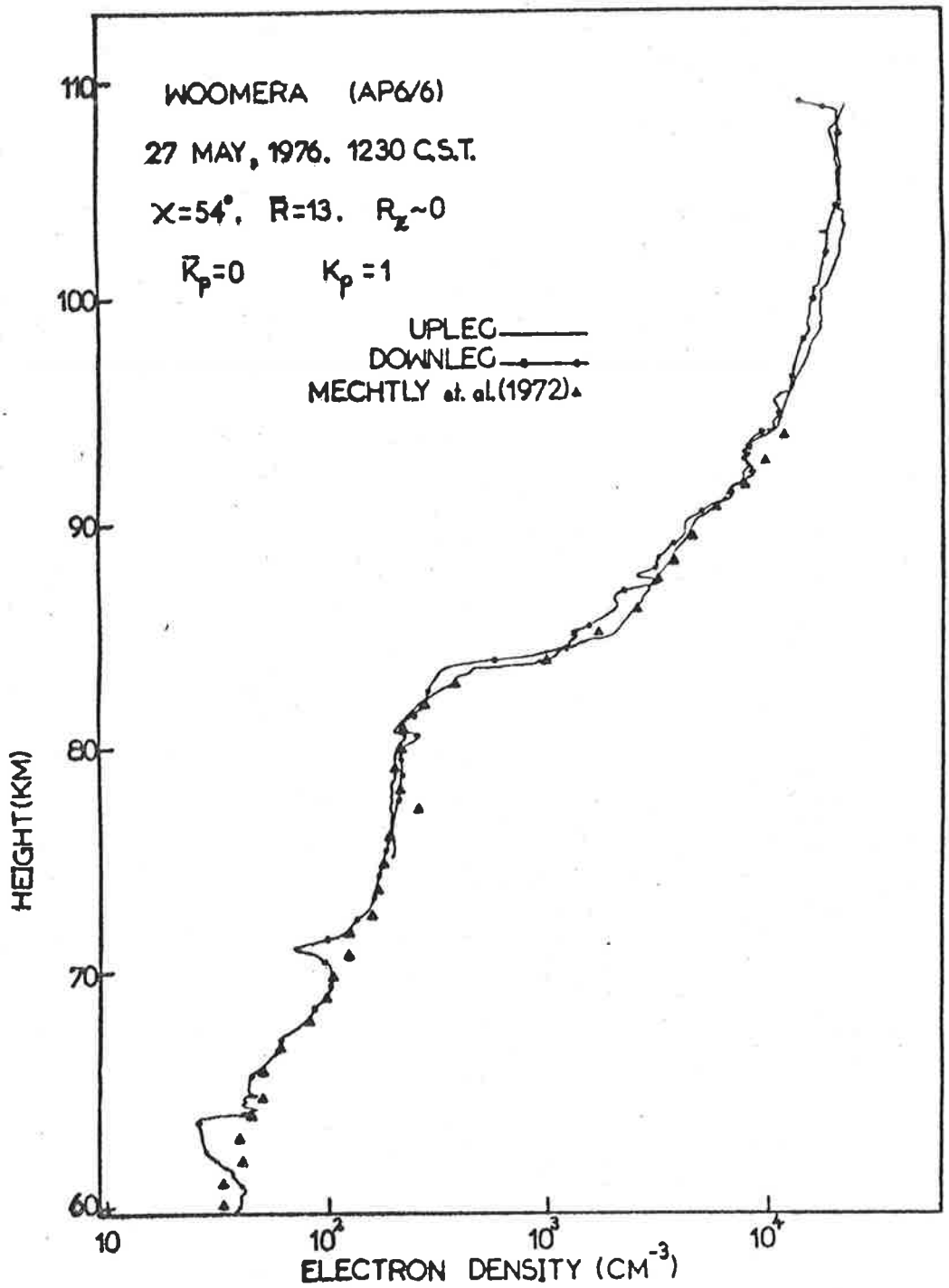

Fig 8.4

Electron density vs. height profiles for 27th May 1976. Both the upleg and downleg are shown, as well as the values from Mechtly et al (1972). The dip above 70 km on the downleg is a result of the rocket tipping over, and so is not a real effect. The Mechtly profile has been shifted down about 1.2 km from that presented in table 5 of Mechtly et al (1972).

earlier. Henceforth this will be called the "Mechtly profile". This Mechtly profile was shifted down in height by 1.2 km in order that the large ledge at 84 km matched the Langmuir probe ledge. It is not surprising that such a shift was necessary; Trost (1979) has shown that this ledge, which is a common feature of many electron density profiles, varies considerably in height over even a few hours. It was found that above about 83 km, the mean Langmuir probe current and the Mechtly profile bore a constant ratio, R, say. Below 80 km, the Langmuir profile current to Mechtly electron density ratio was about 1.6R on the upleg, and 2.8R on the downleg. The fact that this ratio differed on the up and down legs may indicate that the electron densities differed on the two legs; or it may be simply an instrumental effect or perhaps a wake effect of the rocket. Whatever the reason, both sets of data have been adjusted to the Mechtly values. Between 80 and 83 km, the probe current to Mechtly density ratio was assumed to change linearly from R at 83 km to 1.6R or 2.8R (depending on the leg being considered) at 80 km. This had the effect of changing the shape of the 80 to 83 km section in fig 8.3, but the main features are still present.

Figure 8.4 shows the electron densities calculated in this way for both the up and down legs on 27th May, 1976. The Mechtly profile is also shown. Notice that the main features are essentially unchanged when compared to fig 8.3 and are the same on both legs. However, notice that the downleg has some irregular structure at about 85 km not present on the upleg. This may imply the ledge is at times turbulent, or at least unstable in some way.

The ledge at 84 km was discussed in Chapter I, section 1.2.1. It was mentioned that Chakrabarty et al (1978c) have claimed to be able to explain the ledge and associated dip at 81 km on chemical grounds. They claimed that it is associated with chemical effects due to the variations of the production

rates of O_2^+ and NO^+ with height. It is also useful to note that at this height, the concentration of hydronium ions falls off rapidly, and NO^+ becomes the dominant ion (see Chapter I fig 1.2b). This is partly due to the rise in temperature above the mesopause, which slows down the rate of transfer of molecular ions to hydronium ions, and partly due to the decreasing trend of total neutral density. It could be perhaps speculated that the change of the Langmuir current to Mechtly density ratio at 80-83 km may be related to the transition from hydronium ion dominance below 80 km to NO^+ dominance above. However, it could also indicate a real difference between the Mechtly electron densities and those for Woomera on 27th May 1976, so this point has not been pursued.

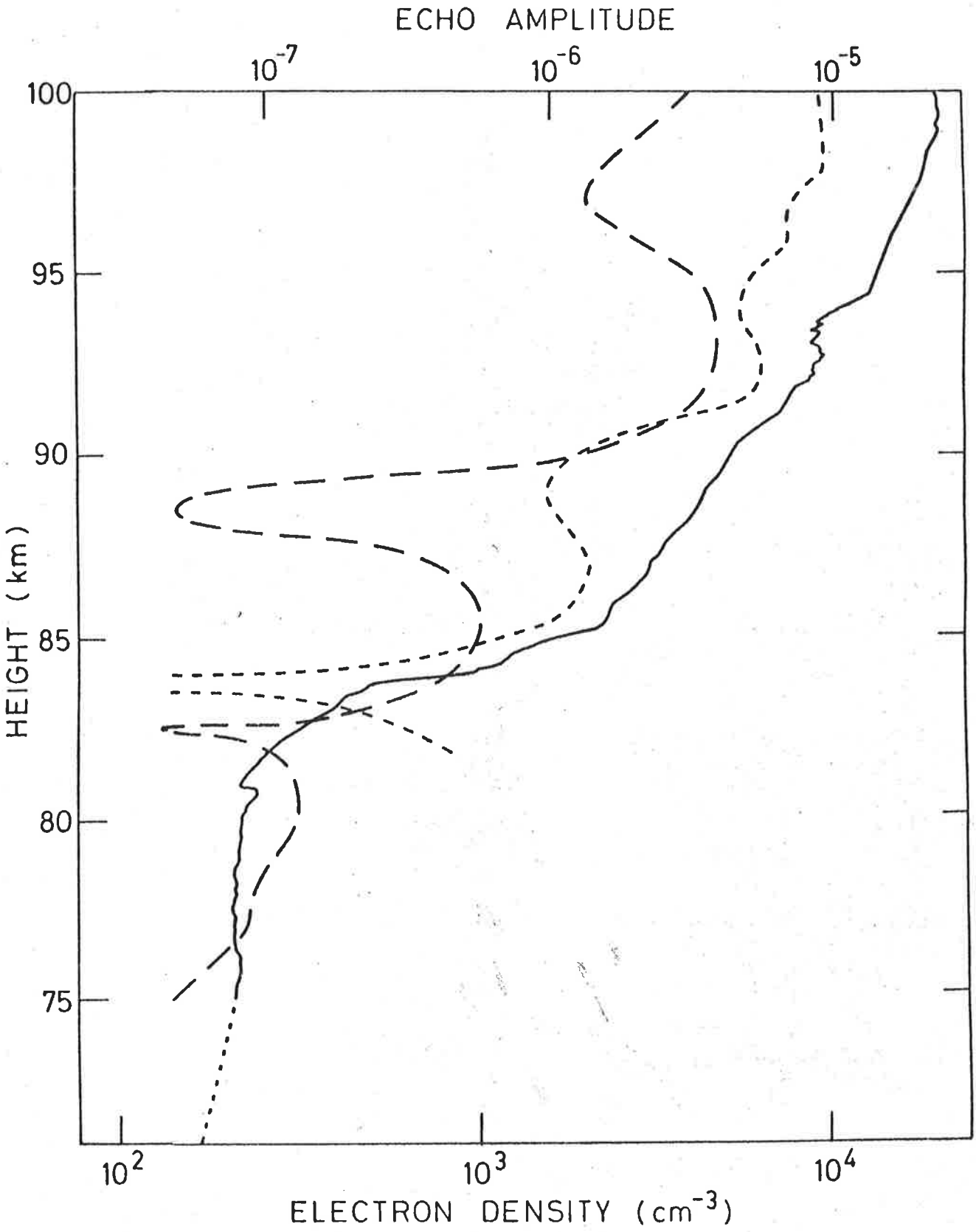

Fig 8.5 Electron density vs. height (——) for upleg on 27th May 1976. Also plotted are a sample true echo amplitude profile vs. height at 1156 hrs, oo secs (-----), with an effective reflection coefficient of 10^{-3} at 92 km, and the calculated echo profile (by program SCATPRF - Appendix F) for this electron density profile (— —).

8.3.3 Computer simulation of partial reflection height profile

Having obtained the relatively high resolution electron density profile the next step was to use it with program "SCATPRF" discussed in Section 8.2, to observe the expected amplitude-height profile. However, bear in mind the assumption made, and in particular realize that this treatment does not fully reproduce the echo produced by reflection from the E-region. Hence the observed and calculated profiles cannot be compared above about 95 to 100 km, since in the real case the tail of the strong E reflection affected the profile at these heights. (To properly produce the E-region echo (which was in fact due to a sporadic E layer), a full wave treatment is necessary (see Appendix B)). The program also assumed horizontal stratification, which may not be valid. For example, some of the fine structure at 85 km on the downleg may have horizontal dimensions only of the order of their depth, if they are due to turbulence. This is much less than one Fresnel zone (a Fresnel zone has a radius of $(\lambda z)^{\frac{1}{2}} = 3.6$ km for a wavelength λ of 151.5 m and a height z of 85 km).

The following parameters were used for the calculations.

(i) the magnetic field was taken to be

$B = 6 \times 10^{-5} \times (1.0 + z/6370)^{-3}$ Webers m^{-2},

z = height above ground in km,

(ii) the ray direction was taken to be at 22.5^{o} to the magnetic field.

(iii) the electron collision frequency with neutral particles was taken as

$$\nu_m = \begin{cases} 3.579 \times 10^{10} \exp\{ - z/7.47 \} & z \leqslant 71 \text{ km} \\ 1.434 \times 10^{11} \exp\{ - z/6.39 \} & z \geqslant 71 \text{ km.} \end{cases}$$

(iv) the control frequency of the pulse was taken at 1.98 MHz, with a half-amplitude full width of 28 μs.

The results of the analyses are shown in fig 8.5 for the upleg flight of 27th May, 1976. Also shown is a typical amplitude-height profile for around 1200 hrs. This latter curve has been somewhat arbitrarily calibrated by assuming a reflection coefficient of 10^{-3} for the 90 km echo, which is quite typical (actual measurements were not made on this day , as discussed previously). Thus the theoretical and observed profiles can be compared in amplitude to some degree. However, echo strengths vary considerably with time (see fig 8.2), so a detailed amplitude comparison is not warranged. Suffice to say that the amplitudes are of similar orders of magnitude in the two cases, which is very promising. More importantly, the observed and calculated profiles do have similar shapes, and peak at similar altitudes. This would thus appear to verify the previous speculation that the causes of the echoes are

(i) the small ledge at 81 km

(ii) the top part of the very large ledge at ~ 85 km, and

(iii) the irregular structure at around 92 km.

Notice that the 85 km echo occurs due to a ledge much greater than a quarter wavelength in vertical extent, but this is because of the large electron density change involved. To verify that the echo was indeed produced by this ledge, and not some small unseen step less than a quarter wavelength deep near 85 km, an analytical profile similar to the real ledge was used as well, and the echo was again reproduced.

The assumed electron density profile had a constant electron density of $10^{2}cm^{-3}$ below 83 km, an exponential increase from 83 km to 85.4 km, and then a constant electron density of $10^{3.36}cm^{-3}$ above this height, as illustrated below(*i*).

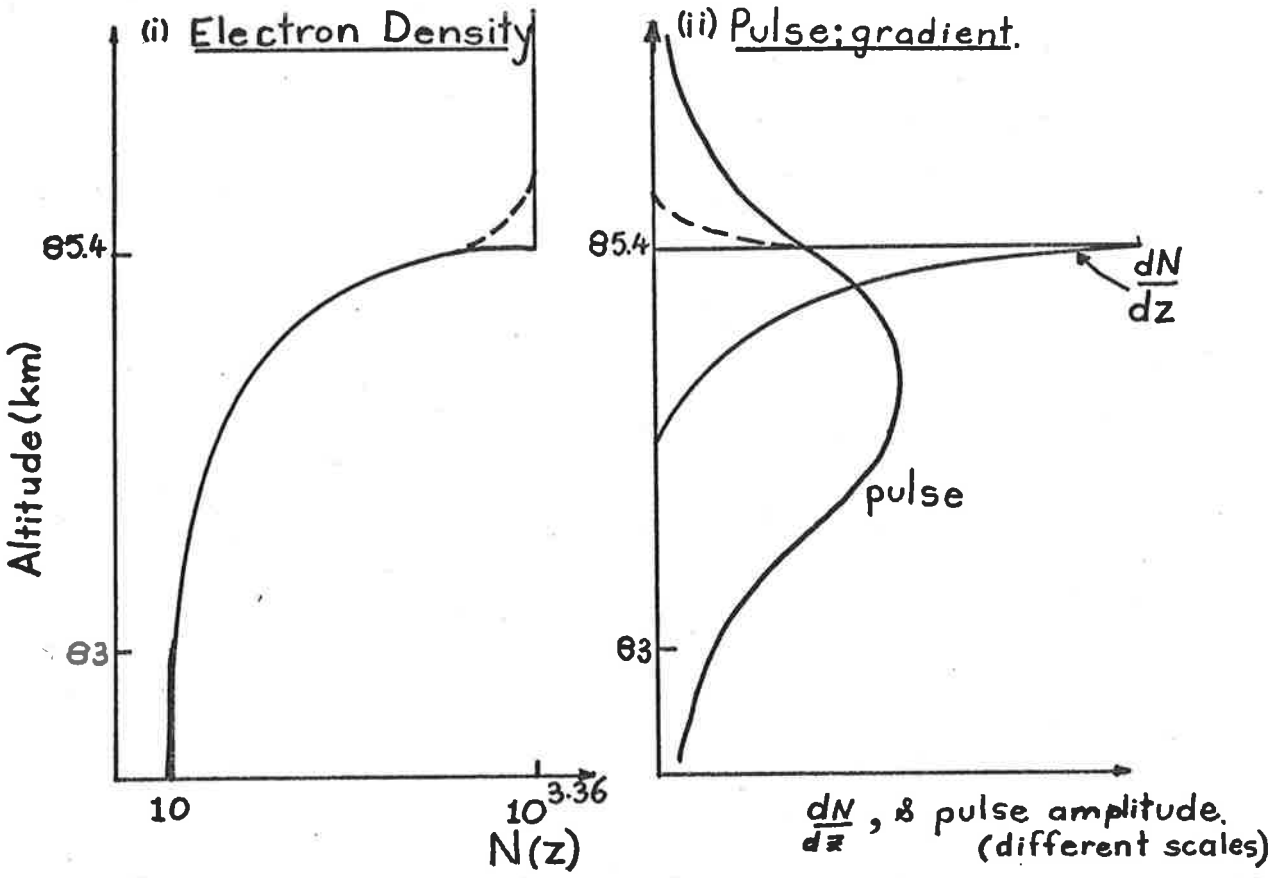

The effect of the assumed sharp change in slopes at 85.4 km could be questioned, but this is not expected to be important. The resultant scattered pulse is approximately a convolution between the pulse and $\frac{dN}{dz}$ profile shown above (see previously). Rounding off the corner of the electron density profile, as indicated by the broken line in the first diagram above, modifies $\frac{dN}{dz}$ as shown by the broken line in the second diagram, and this will not affect the convolution significantly.

The above diagrams also illustrate why the scattered pulse matches the top of the electron density ledge; - the electron density gradient is maximum there.

It thus appears that specular reflection from this ledge at least caused some part of the echo observed at 85 km. Of course it has been seen in

Chapter IV that scatter from above 80 km is generally somewhat isotropic, so there is almost certainly another mechanism also contributing. This is consistent with observations of Rice parameters for the ~ 85 km echo discussed in Chapter V, in which it was determined that there is a specular reflection component, but also a significant random scatter component. The assumption of horizontal stratification for the ledge at 84 km and small dip at 81 km would appear to be valid, since both features appear on both legs. The extra source of more isotropic scatter could quite likely be turbulent scatter. The expected turbulent scatter from such a ledge will be discussed in Chapter IX and it will be seen that it is significant. The irregular structure at the top of the 85 km ledge on the downleg could possibly be suggestive of such turbulence.

The assumption of horizontal stratification may give some cause for worry at 92 km. The fine structure at 92 km does show some similarities on both legs, but is not exactly the same (see fig 8.4), so may not be entirely horizontally stratified.

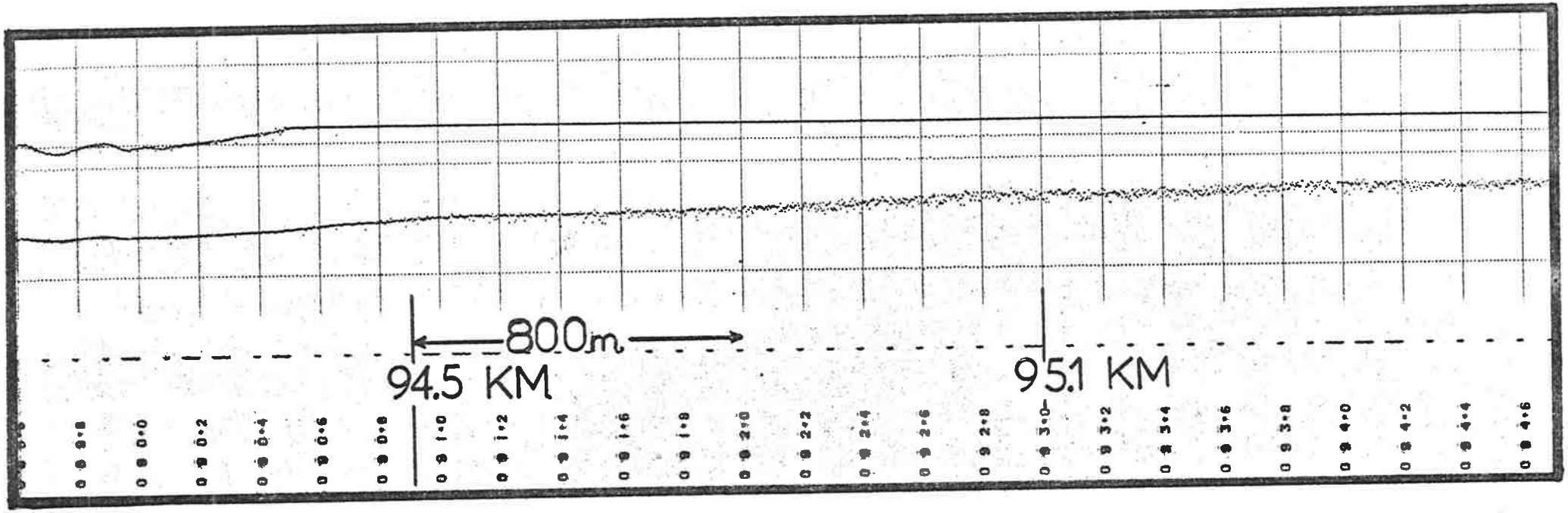

Fig 8.6 An example of a period when the normally narrow Langmuir probe voltage trace becomes diffuse in character. The upper trace is the same as the bottom but with approximately 3 times the magnification of the lower line. However, the upper line is at saturation for much of this record. The numbers at the bottom indicate the time in seconds after the launch of the rocket minus 10 s.

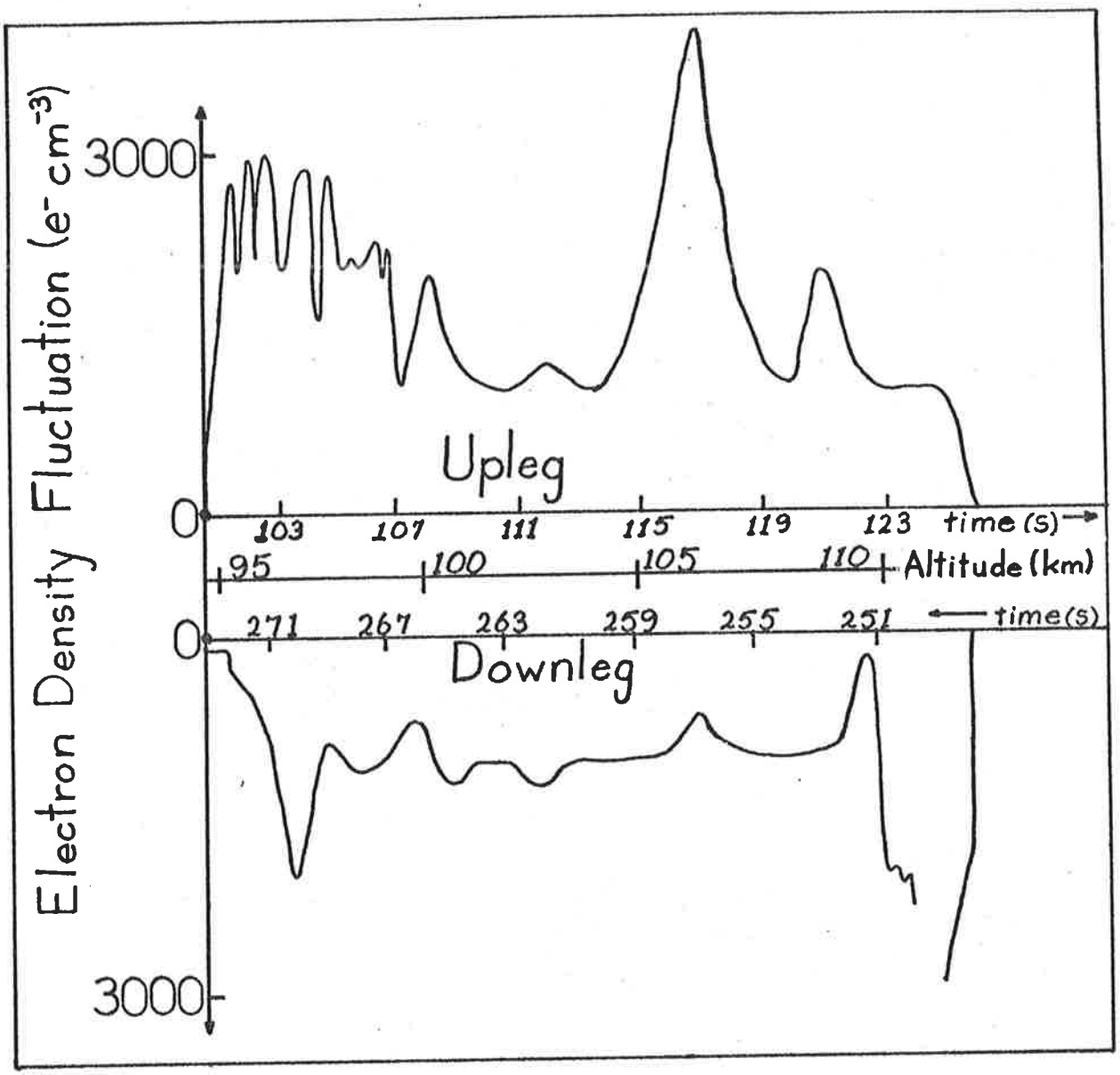

Fig 8.7 Plots of the full-width of the diffuseness of the Langmuir probe voltage lines as a function of height for both the up and down legs. The width of the fluctuations (diffuseness) has been approximately converted to electron density units. (Note that fluctuation intensity increases downwards on the bottom graph). There is no diffuseness at all below 94.5 km, and only a small patch at ~ 116-120 km above 112 km. This similarity in heights of the diffuseness is the most important point of this diagram. Both plots also show peaks around 95-96 km. (Much of the finer scale fluctuation is different on the two legs). The times shown are time from rocket launch, and so are 10 s different to those shown on the film (e.g. fig 8.6).

8.3.4 Some extra observations of interest

8.3.4a Diffuse fluctuations in electron density measurements

One point of possible interest related to the Langmuir probe results concerns the form of the voltage output on the film. Over all heights below 94.5 km, the record of voltage output was simply a line. But above about 94.5 km, the line sometimes became a diffuse smear. Fig 8.6 shows an example. For digitization purposes, the middle of this broad line was used. But it was felt worthwhile to investigate the cause of the diffuseness. The width of the line was plotted as a function of height for both the up and down legs. The result can be seen in Fig 8.7. The voltage line goes from a thin line to a fully developed diffuse line within about 800 metres at 94.5 km. The diffuseness appears to be no accident, since it agrees well in height on both legs (see fig 8.7). There was also a cutoff at about 112 km (apart from a small patch at 116-120 km, not shown on fig 7), and elsewhere the voltage output was a straight line (the rocket reached a maximum altitude of 128 km).

It is conceivable that this diffuseness was caused by very fine scale fluctuations of electron density, and turbulence could perhaps be a cause. The cutoff at around 112 km may support this conjecture, the daytime turbopause being somewhere around this height (see Chapter I, Section 1.3.3). The small amount of diffuseness at 116-120 km may contradict this hypothesis, although Rees *et al* (1972) have found evidence for some degree of turbulence up to 130 km.

There is one argument which possibly is against this speculation. Recall that the irregular fluctuations at 85 km on the downleg were proposed as possibly indicating turbulence. Should this region not also show such diffuseness ? However, it should be borne in mind that the electron densities there are around one tenth of those at 94 km, so the fluctuations would be less. Further, the energy dissipation rate is considerably less at

85 km than at 94 km (see fig 1.9c (ω_B^2 is approximately constant between 85 and 95 km)) by a factor of perhaps 3 times, which may also reduce the fluctuations. So perhaps the fluctuations are simply not visible at 85 km. At greater height, the region was perhaps laminar, until about 94.5 km, where the region became turbulent.

However, as a further argument against the concept, the 92 km echo appears related to irregular fluctuations around 92 km, as discussed. Scatter from such heights is usually quasi-isotropic, so these fluctuations would probably also be associated with turbulence. Yet no diffuseness shows at 92 km; but that region has similar electron densities (and presumably similar energy dissipation rates to that at 94 km) so should show the effect.

Whatever the reason for the diffuseness, however, it does seem to be a real effect. As an experiment, appropriate random fluctuations of electron density were superimposed on the mean profile used earlier, and program "SCATPRF" re-run. A considerable increase in scattered power was produced. Of course such fluctuations would hardly be horizontally stratified, and the fluctuations would not be totally random (turbulence has a spatial auto-correlation function which has non-zero width), but this does illustrate that these random fluctuations would enhance the scattered power.

8.3.4b Structure below 80 km

In Section 8.2.2, typical electron density changes necessary to produce typical reflection coefficients were presented, and it was found that ~ 5-10% fluctuations completed within less than a quarter wavelength produced reflection coefficients of similar magnitudes (perhaps down by a factor of 3 or 4) to those observed. As pointed out by Manson, Merry and Vincent (1969), several such scatterers could easily explain the observed reflection coefficients.

The Langmuir probe film was searched by eye for such changes. Some such rapid changes were found (e.g. fig 8.8) which would not have shown in the digitized data. Recall also that VHF echoes occur from these heights, so the changes in electron density should really be completed within less than a few metres to cause VHF scatter. However, it was difficult to distinguish between instrumental and real effect. Without any partial reflections to compare with, there is little point in any more discussion, save to say that it is possible that some echo-causing electron density changes have been seen below 80 km.

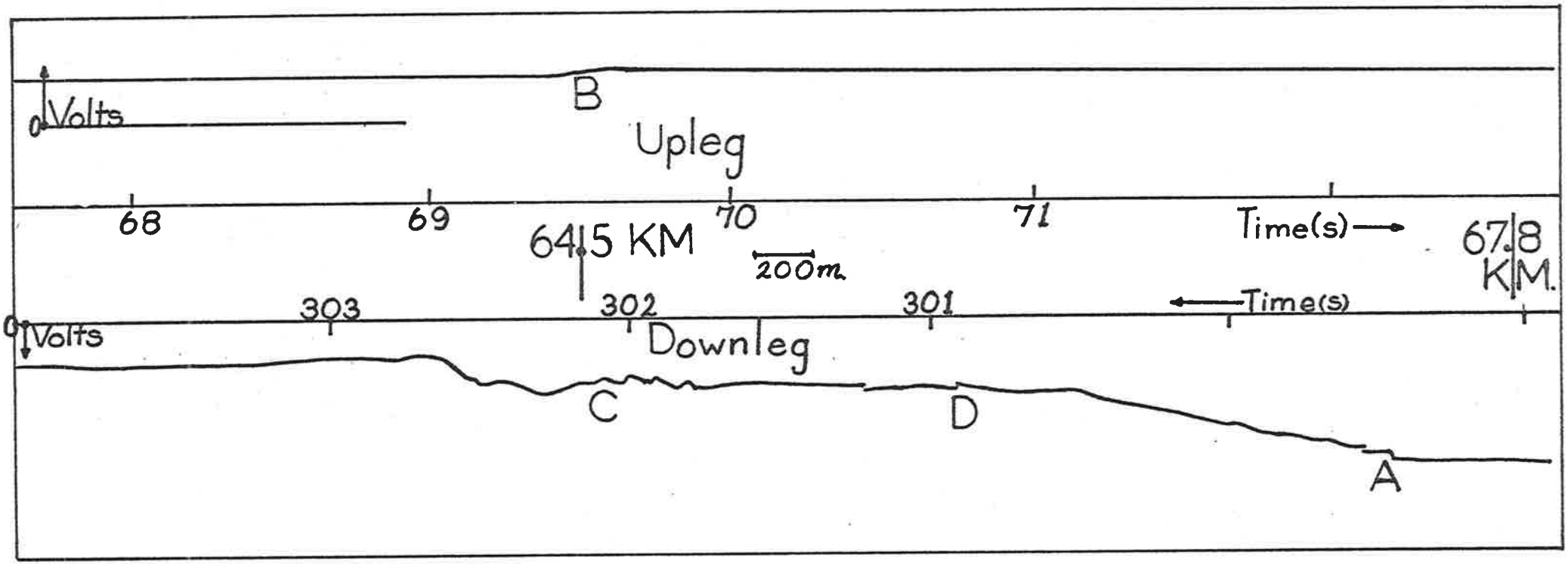

Fig 8.8 A height regime at the lower heights which shows some evidence of irregular structure. (27th May 1976). The top graph is for the upleg, the lower graph for the downleg. These are reproductions of the actual traces of the Langmuir probe voltage. The times are taken from launch time. The top graph has weaker magnification (mode 2) than the lower one (mode 1). (The voltage output on the film was magnified with respect to the current to keep the value from saturating or becoming too close to zero). Note that voltage increases downward on the lower graph. The similarity of curves B and C suggests this kink is real. The abrupt changes in voltage which occur (e.g. C and D) are also interesting. Those at D may well be due to switching processes in the instrumentation, but the one at A may be real. However, without better equipment it is not possible to be definite about this. (Since the scatterers below 80 km reflect VHF radiation, kinks in electron density of less than 3 m must exist, however - this is why the jumps at A and D would be interesting if they could be shown to be real).

8.4 Conclusions

Studies of Langmuir-probe-produced electron density profiles and partial reflections suggest that the echoes observed can be related to features on the electron density profile.

(i) the 80-81 km echoes appears to be related to a small ledge of decreasing electron density at 81 km,

(ii) The 84-86 km echoes appear to be related to a large ledge of increasing electron density at 84-85 km, and it is possible there may also be some related turbulence causing scatter of a more isotropic nature

(iii) the 92-94 km echoes appear related to an irregular region of electron density fluctuations at around 92 km.

One dimensional computer simulations support these conclusion, particularly with regard to the 81 and 84-86 km echoes.

It is also interesting to recall from Chapter IV, section 4.23, that an 86 km echo discussed there was also felt to be associated with a rapid increase in absorption (i.e. large electron density ledge).

CHAPTER IX

INVESTIGATION INTO THE GENERATION OF THE HF SCATTERERS

Chapter IX Investigation into the generation of the HF scatterers

9.1 Introduction

In the preceding chapters, considerable space has been given to investigations of the nature of the scattering properties at H.F. of the scatterers in the D-region. Some speculation as to the actual cause of the scatterers has been presented, but little in the way of concrete data has been given. The purpose of this chapter is to investigate the possible causes of the scatterers.

The chapter begins by looking for correlation between mean wind shears, (vertical resolution ~ 4 km) and the presence of scattering layers. Having found that strong mean wind shears do not appear to account for the majority of the layers, investigations into other processes are presented. It is found that gravity waves do appear to play some role, and several examples will be presented.

Having presented these results, some investigations into the scattered powers associated with turbulence will be presented, and it will be shown that isotropic turbulence is unlikely to contribute to the scatter below about 80 km. This is consistent with speculation presented so far. Then a simple model is presented, and it is shown that it is possible to simulate the observed facts regarding the isotropy of scatter (see chapter IV) quite well using this model.

Some brief speculation regarding the reasons for preferred heights is presented, but the majority of such discussions will be left until the summarizing chapter (chapter XI).

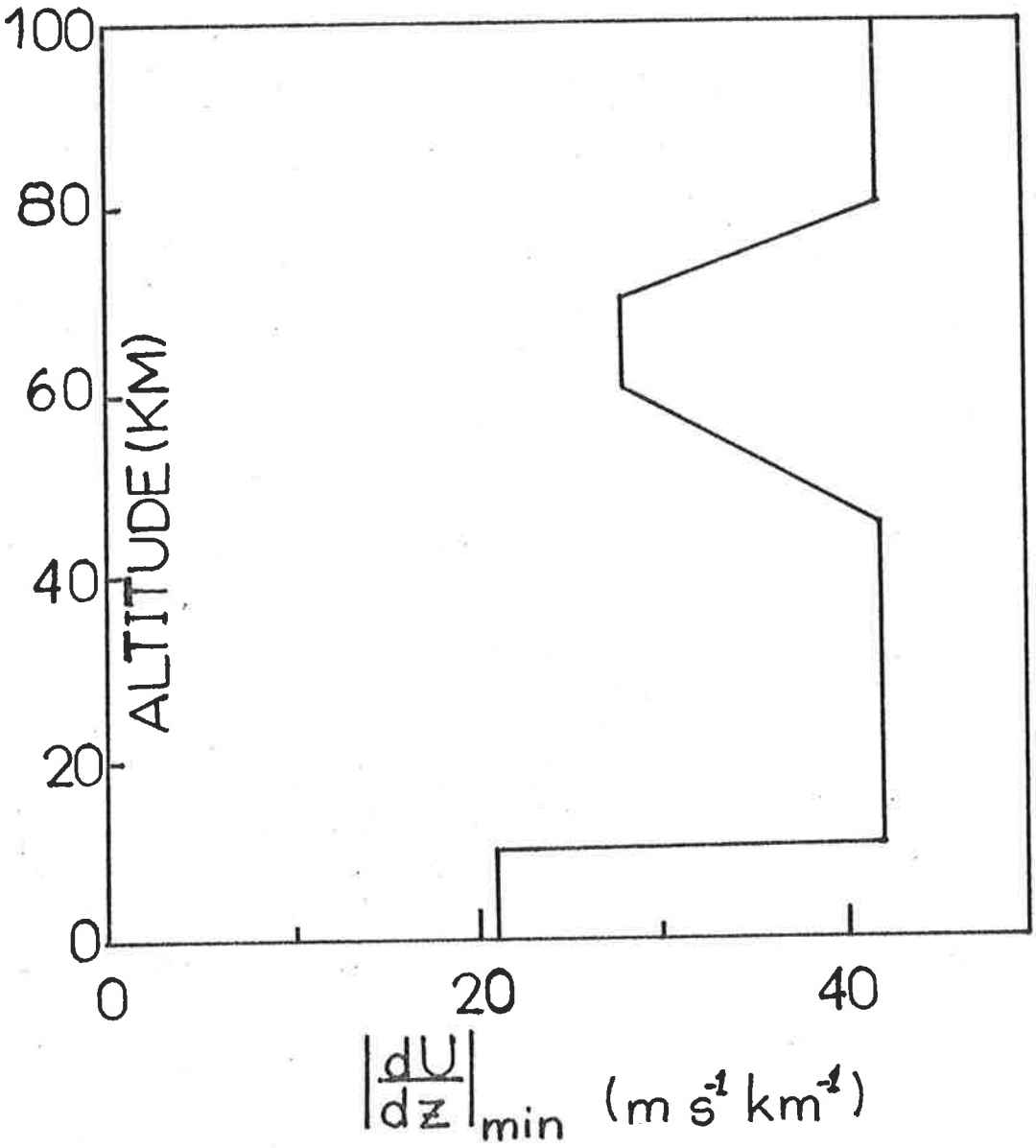

Fig 9.1

Minimum wind shears necessary to produce turbulence for the Brunt-Vaisala period profile given in Fig 1.9a, Chapter I. However, this profile should not be regarded as final and absolute - considerable local fluctuations in ω_B and hence $\left|\frac{dU}{dz}\right|_{min}$ can occur (see text).

9.2 Scatterer correlations with winds

9.2.1 Correlations between mean wind profiles and scattering layers.

9.2.1a Experimental observations

If turbulence is important in causing the HF radio scatter observed from the D-region, then this requires either a hydrostatically unstable temperature gradient, or high wind shears. More precisely, it requires that

(9.2.1.1) $$R_i = \omega_B^2 / \left(\frac{dU}{dz} \right)^2 \leqslant 0.25$$

(see Chapter II, equation 2.2.2.3)

where $\omega_B^2 = \left[\frac{g}{T} \left(\frac{dT}{dz} + \Gamma_g \right) \right]^{\frac{1}{2}}$ is the Brunt-Vaisala frequency,

T being the temperature, Γ_g the adiabatic lapse rate, z the height, g the acceleration due to gravity and $\underline{U}$ the wind vector.

With the equipment available, it was not possible to accurately deduce the temperature profile, but information was available about the wind velocities as a function of height. Thus it seemed reasonable to attempt to find correlations between wind shears and scattering layers.

Fig 9.1 shows a plot of the minimum wind shear necessary to produce turbulence ($R_i = 0.25$) for the Brunt-Vaisala frequency profile shown in fig 1.9a in Chapter I. (i.e. $\left| \frac{dU}{dz} \right|_{min} = 2\omega_B$). It is clear that shears of the order of 20 to 40 $ms^{-1}km^{-1}$ are necessary to produce turbulence. However, it should be borne in mind that this ω_B profile is an average - smaller vertical scale fluctuations of temperature could occur with much less stable temperature gradients, and the temperature gradient can change in time. Fig 9.1 is thus a guide, but should not be taken as final.

Vertical resolution is not only important with regards to temperature profiles. The wind measurements used in the work for this thesis had a vertical resolution of about 4 km. Thus even if the measured wind gradient is less than the values indicated by fig 9.1, there may be finer scale ,

unseen wind shears present which are capable of causing turbulence. It is unlikely that these finer scale fluctuations would occur on vertical scales of less than the outer scale of turbulence, but this is certainly less than the 4 km resolution. ($L_o \sim$ 300-600 m at about 85-90 km; see chapter 1, fig 1.9a). This point has already been emphasized in Chapter II, (section 2.3.2) and van Zandt et al (1978) have developed a theory (for the troposphere and stratosphere) which considers the probability of getting potentially turbulent wind shear fluctuations hidden in a mean wind shear. One important feature of the theory is that larger mean wind shears have a larger degree of fluctuation of wind shears on finer scales than the equipment resolution, so for a given temperature profile, a larger mean wind shear implies more turbulence.

Although the resolution used in these experiments was inadequate to properly consider the generation of turbulence, it was decided that it was still fruitful to look for a possible correlation between mean wind shears and scattering layers.

Perhaps the most striking example of such a correlation is that shown in chapter 7,fig 7.11. The North-South velocity wind-shear maxima and the heights of the scattering layers appear to be at similar heights. It is not clear however, why the East-West winds played no role. In this case, an attempt was made to estimate ω_B^2 for this day at 86 km, assuming that scatter from that height was due to a mean wind shear defined by fig 7.11. (chapter 7, section 7.4.5).

It turns out, however, that this correlation of wind shears and scattering layers is the exception rather than the rule. Many measurements of wind velocity as a function of height were produced during the work for this thesis, and these were plotted and compared to the height profiles of scatter. The wind velocities used varied from 10 minute means to hourly means. Examples are shown in figs 9.2, 9.3 and 9.4. The cases shown are believed to be quite typical. For example, hourly profiles for Buckland

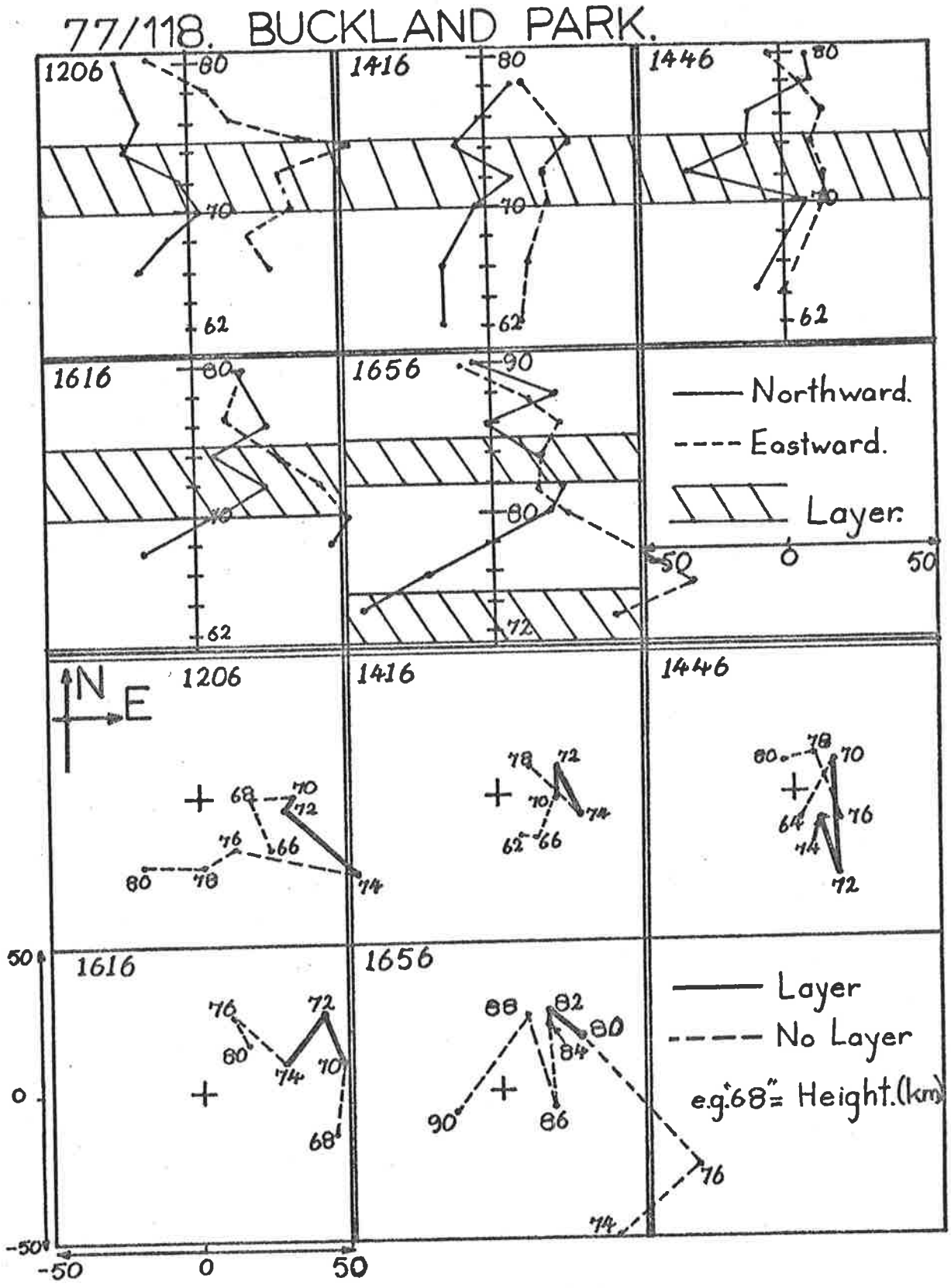

Fig 9.2 Height profiles (top 5) and matching hodographs (bottom 5) for 5 x 10 minute periods on day 77/118 at Buckland Park (28th April 1977). The numbers given in the top left hand corners are the start times of each 10 minute block (local time). Notice that not all heights always have wind values. Missing points indicate that no acceptable partial reflection wind measurements were obtained in the period (for a detailed discussion of the rejection criteria used in partial reflection wind measurements see Stubbs, 1976). The scale of the graphs is such that each square is 100 ms^{-1} wide. The vertical scale on the upper graphs is height in kilometres. Northward and Eastward winds are taken as positive. The numbers on the hodographs are heights in kilometres. The heights of HF scattering layers are also indicated on all graphs.

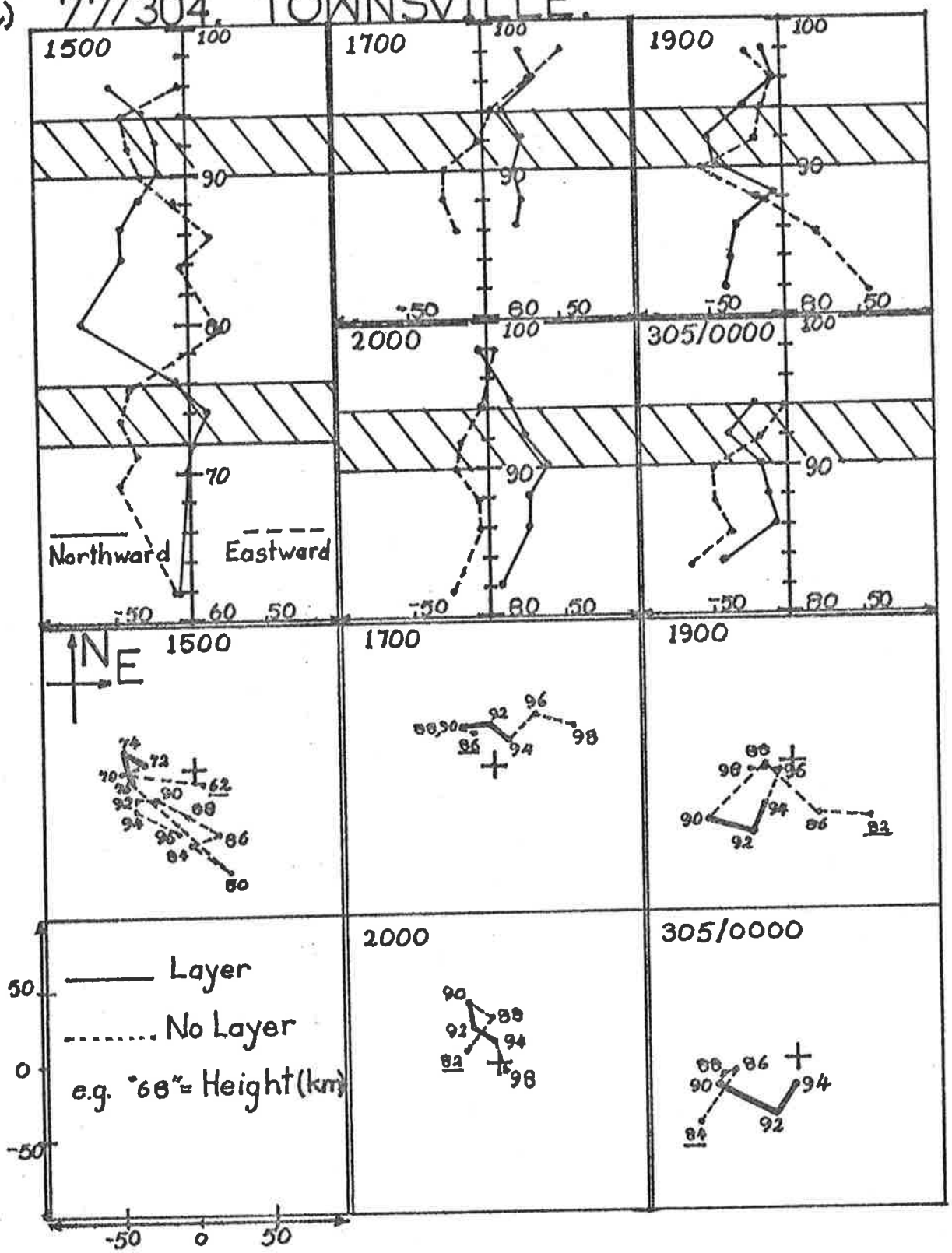

Fig 9.3 Height profiles and hodographs prepared from hourly means for days (a) 77/304, (b) 77/305, and (c) 77/306 for Townsville (November 1977). The numbers in the top left hand corners are the start times (local time) for each hour. All heights are in km, and all velocities in ms^{-1}. Notice the scale on these graphs is different to that for fig 9.2. Scattering layers are also indicated. The daytime ~90 km echo appeared to be strongest during the period 305/1500 - 305/2000 (fig b), when tidal effects were quite weak, and total wind speeds were somewhat less than those on days 304 and 306. However, the winds on day 305 were quite variable. On day 306, a quite clear tide became important and hodographs for this period were often quite smooth (e.g. fig c). The echo strengths on day 306 seemed to be quite weak, if present at all (the E echo hid whatever 90 km echo was present - hence the question marks on the 90 km "layer" in fig c).

93(b) 77/305 TOWNSVILLE

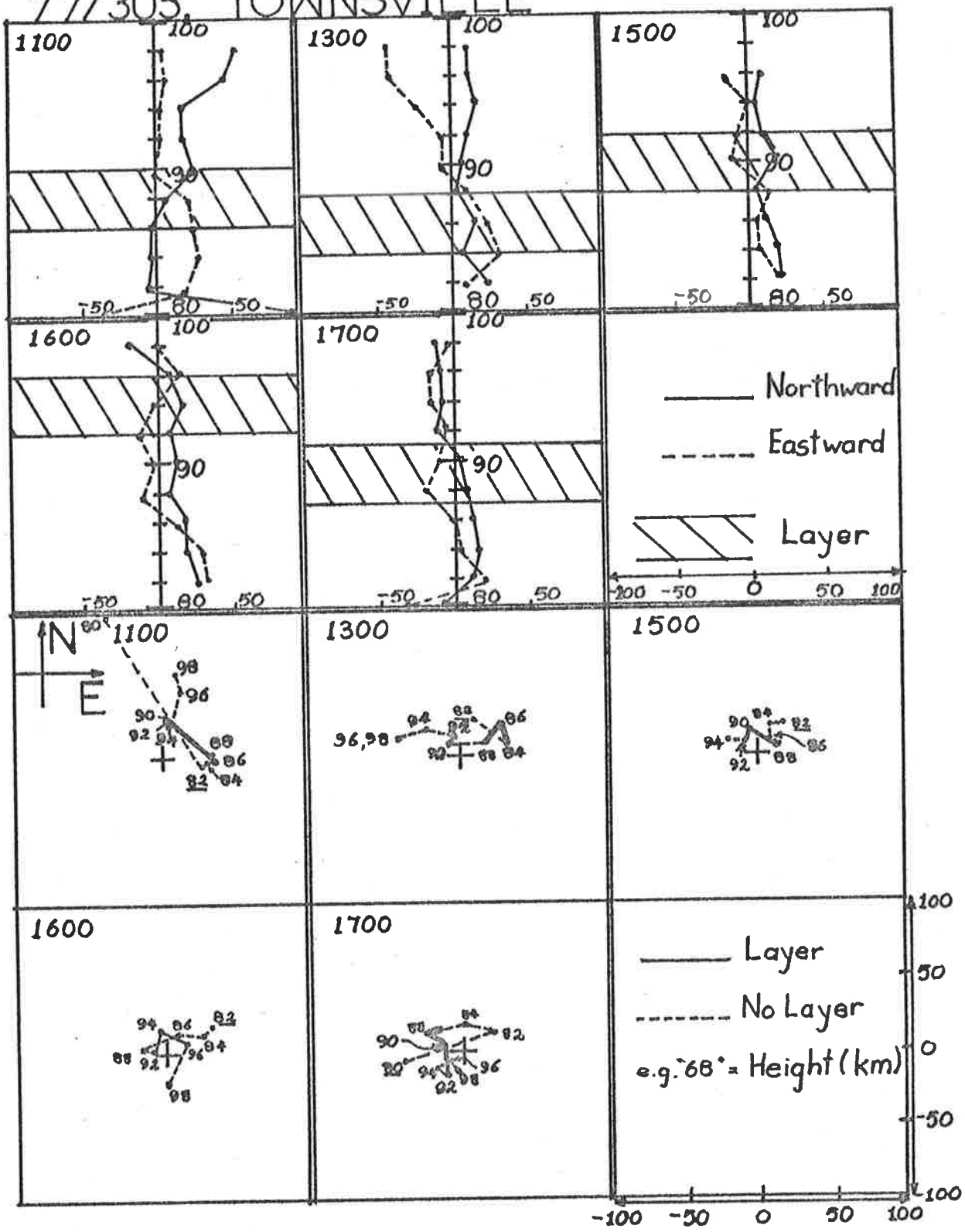

93(c)

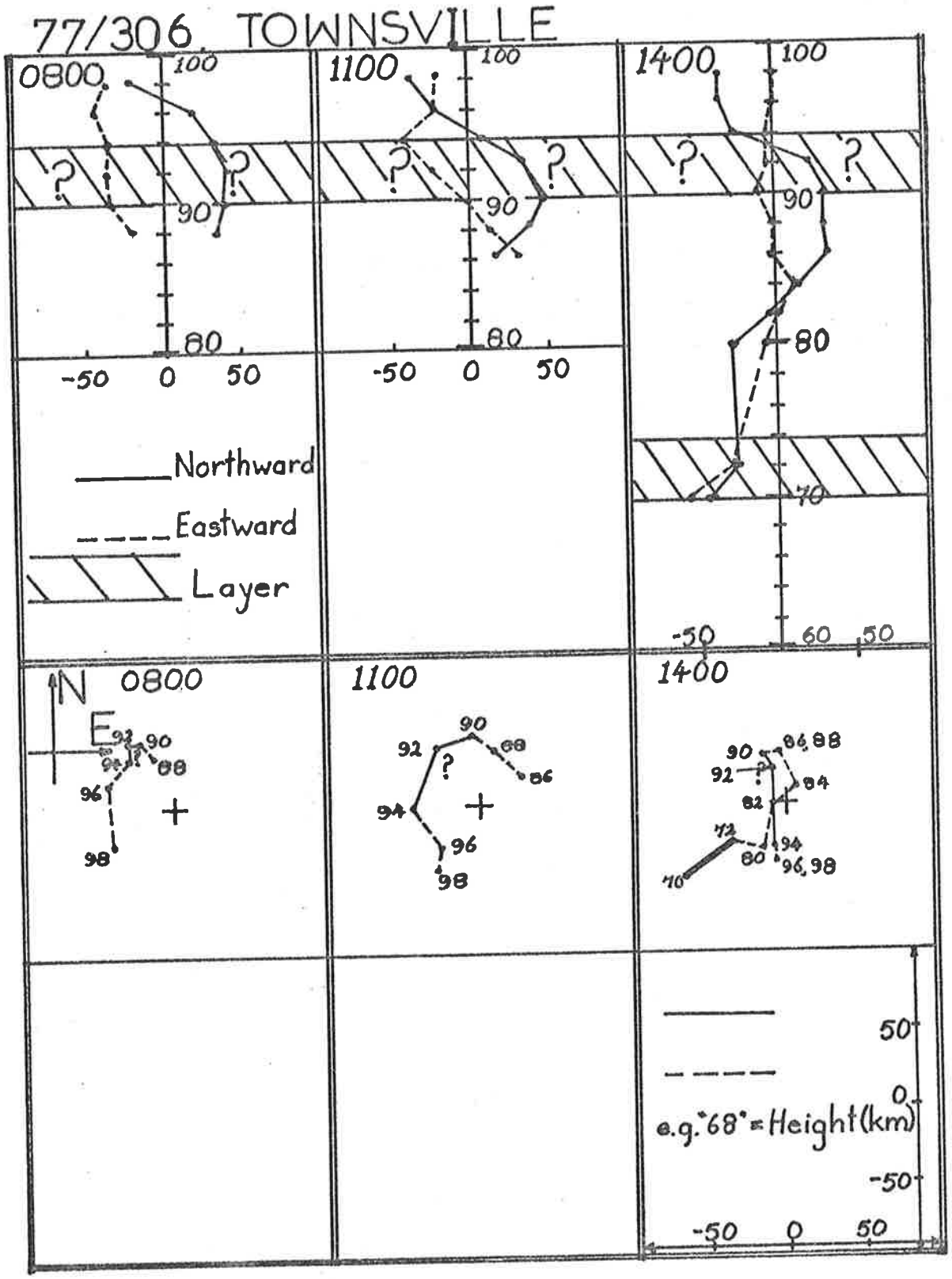
77/306 TOWNSVILLE
0800
1100
1400
100
90
80
70
60
?
-50
0
50
Northward
Eastward
Layer
N
E
0800
1100
1400
92
90
88
86
94
96
98
84
82
72
80
70
e.g. "68" = Height (km)

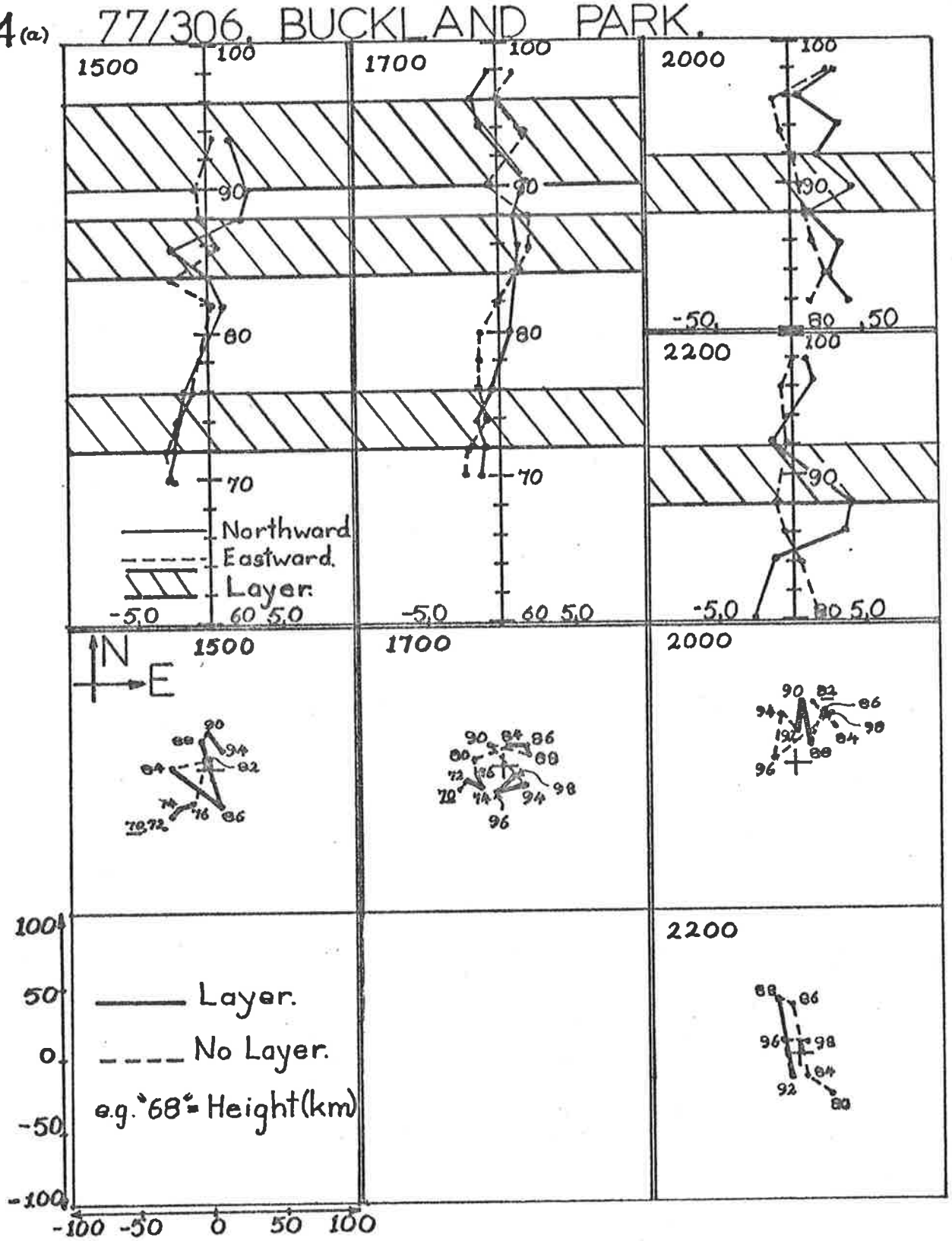

Fig 9.4 (a) Height profiles and hodographs prepared from hourly means for days (a) 77/306 and (b) 77/307 for Buckland Park (November 1977). The numbers in the top left-hand corners are the start times (local times) for each hour. Scattering layers are also indicated. As a point of interest, fig 9.4(a) at 1700 shows quite a good example of a tide (except for the 90 km and 98 km points): λ_z is around 24 km, so this could be a S_1^1 mode.

9.4(b) 77/307 BUCKLAND-PARK.

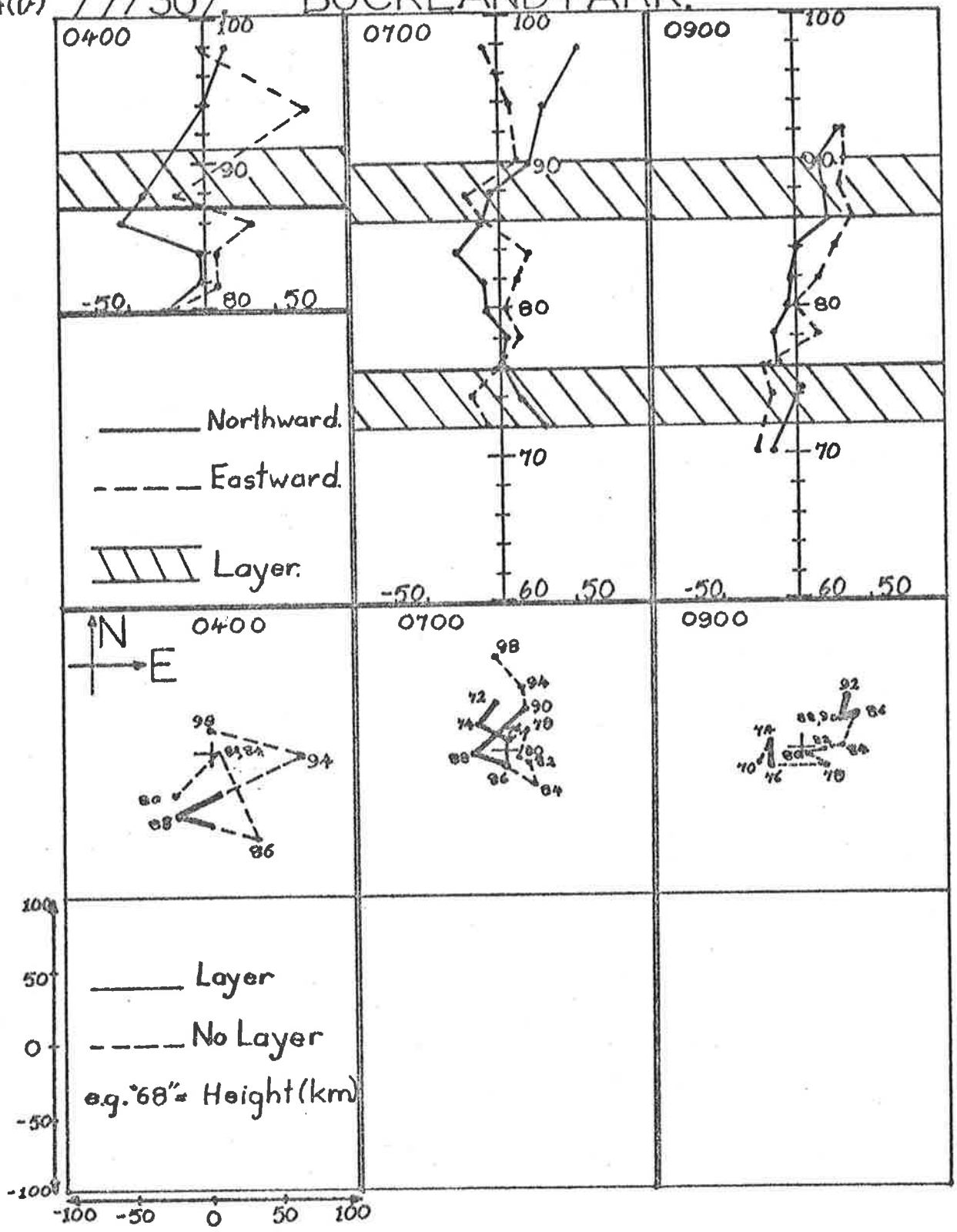

Park were produced for 5 days in November, 1977, and those diagrams shown in fig 9.4 are typical of that period. The graphs are presented both in the form of height profiles, and hodographs. Examination suggests, as it did for most of the data examined, that the scattering layers do not always appear to be associated with the largest wind shears. For some data, even higher temporal-resolution (1-2 minutes) was used. With this resolution, it again did not appear that the scattering layers were associated with wind shears. Certainly cases were found in which power bursts occurred during a wind shear enhancement, but this was by no means the rule; in fact, it almost appeared to be the exception.

The possibility exists that turbulence could form but produce no backscatter. After all, radio wave backscatter requires a large potential refractive index gradient as well as turbulence (chapter II, equations 2.3.2.11). This is a factor which could in part account for the lack of a correlation. Perhaps, too, the insufficient resolution may be the reason for a lack of correlation. The lack of temperature information also restricts the interpretation of the above result. On the other hand, perhaps the information suggests that wind-shear generated turbulence is not an important cause of the scatterers.

It can be stated, however, that measurements with a vertical resolution of the order of 4 km and temporal resolution of minutes to hours do not show any indication of a strong correlation between HF scatterers and wind shears. Wind shears can often be found associated with scattering layers, but stronger wind shears on the same height profile often occur with no associated scatterers. However, one point which may be important is that a strong wind jet usually exists at 70 - 74 km (eastward in winter, westward in summer; also see fig 1.7, chapter 1), and HF scatterers often occur preferentially near this jet. It has not been possible to determine unambiguously whether the two features are related however.

9.2.1b Results from other references

Having discussed the above observations, it is useful to look at similar work done by other authors. Few correlations between HF scatterers and wind shears have been attempted, but some work has been done with rockets in comparing wind profiles and layers of turbulence, particularly in the region of 80 to 110 km. It has already been proposed that turbulence may be important in producing HF scatter at these heights, so it is useful to consider these observations. However, even rocket wind measurements have vertical resolutions of at least 1-2 km, so again resolution could be a problem.

As pointed out in Chapter 1, section 1.3.3., turbulence is spatially and temporally intermittent at heights of 80 to 110 km. Often turbulence appears in horizontal bands. Blamont and Barat (1967) suggested that turbulence appeared to be strongest at maxima in the winds, not at the maxima in wind shears. They also felt that gravity waves played an important role in the generation of turbulence. Roper (1971) also has suggested that gravity waves are more important in the generation of turbulence than wind shears in the mean wind. Roper's explanation involved the generation of unstable temperature regimes due to gravity waves. Rees et al (1972) found little correlation between turbulence and wind shears and suggested that the turbulence may be associated with unstable temperature gradients. Anandarao et al (1978) have also noted that turbulence is temporally and spatially intermittent, but claimed to find a strong correlation between wind shears and turbulence, in contrast to the previous authors. Teitelbaum and Sidi (1976) and Sidi and Teitelbaum (1978) have also proposed that strong wind shears may be important in the generation of turbulence, but the wind shears they proposed were induced by non-linear interaction between tides and gravity waves. Lloyd, Low and Vincent (1973) have also found correlations between turbulence and high wind shears and suggested that shear waves (waves induced by strong wind shears) play

an important role in the generation of turbulence.

Thus it appears some authors see wind-shears associated with strong turbulence, but that this is not always the case. Other processes are also important for the generation of turbulent laminae, and one of the principal suggestions is that of gravity waves. The next section of this chapter will examine gravity waves and their relation to HF scatterers.

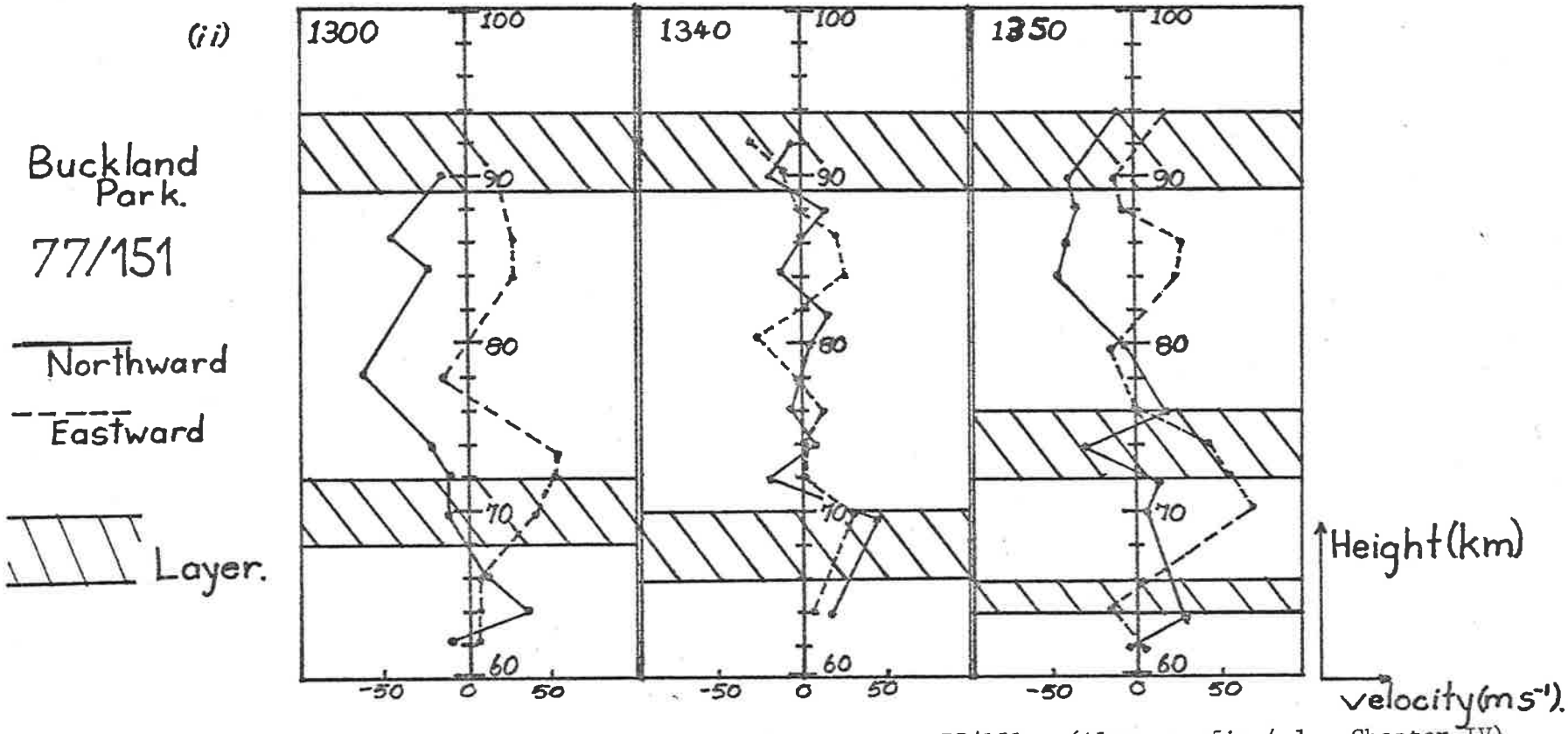

Fig 9.5(a) (i) Contour diagrams of powers at Buckland Park on day 77/151. (Also see fig 4.1c, Chapter IV), with associated North-South wind variations at 74 km. (the points are averages of the winds at 72, 74 and 76 km; all these heights showed the oscillation, with no phase shift between heights). A correlation between maximum Northward winds and power bursts appears to exist. (ii) Typical height profile of 10 m mean winds, with scattering layers shown, for times just before the time period shown in (i). The numbers in the top left hand corners are the start times of the 10 min block used to obtain the profile. The profiles are quite typical for this day. In particular, the strong eastward jet was prominent during the time interval shown in (i) and the structure above 76 km was quite irregular during this period. Since the profiles are typical, none are shown for the period 1445-1530. For these profiles, the layer of scatterers near 74 km appear to be above or below the peak jet velocity, and could be taken to be associated with maximum wind shears of the jet. However, the author feels that this is not always so, and is coincidental in these cases.

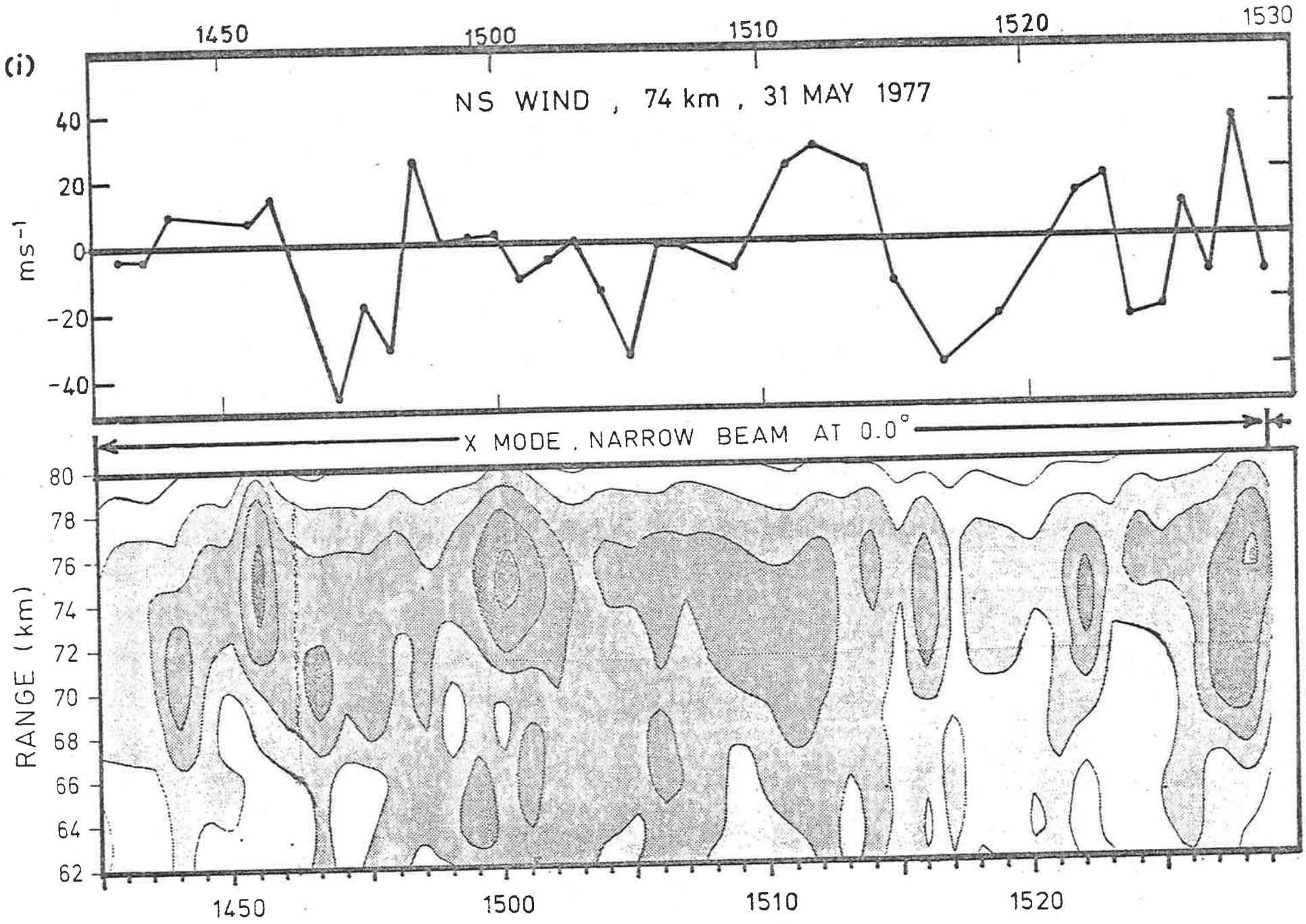
(i)
1450
1500
1510
1520
1530
NS WIND , 74 km , 31 MAY 1977
40
20
0
-20
-40
ms⁻¹
X MODE . NARROW BEAM AT 0.0°
80
78
76
74
72
70
68
66
64
62
RANGE (km)
1450
1500
1510
1520

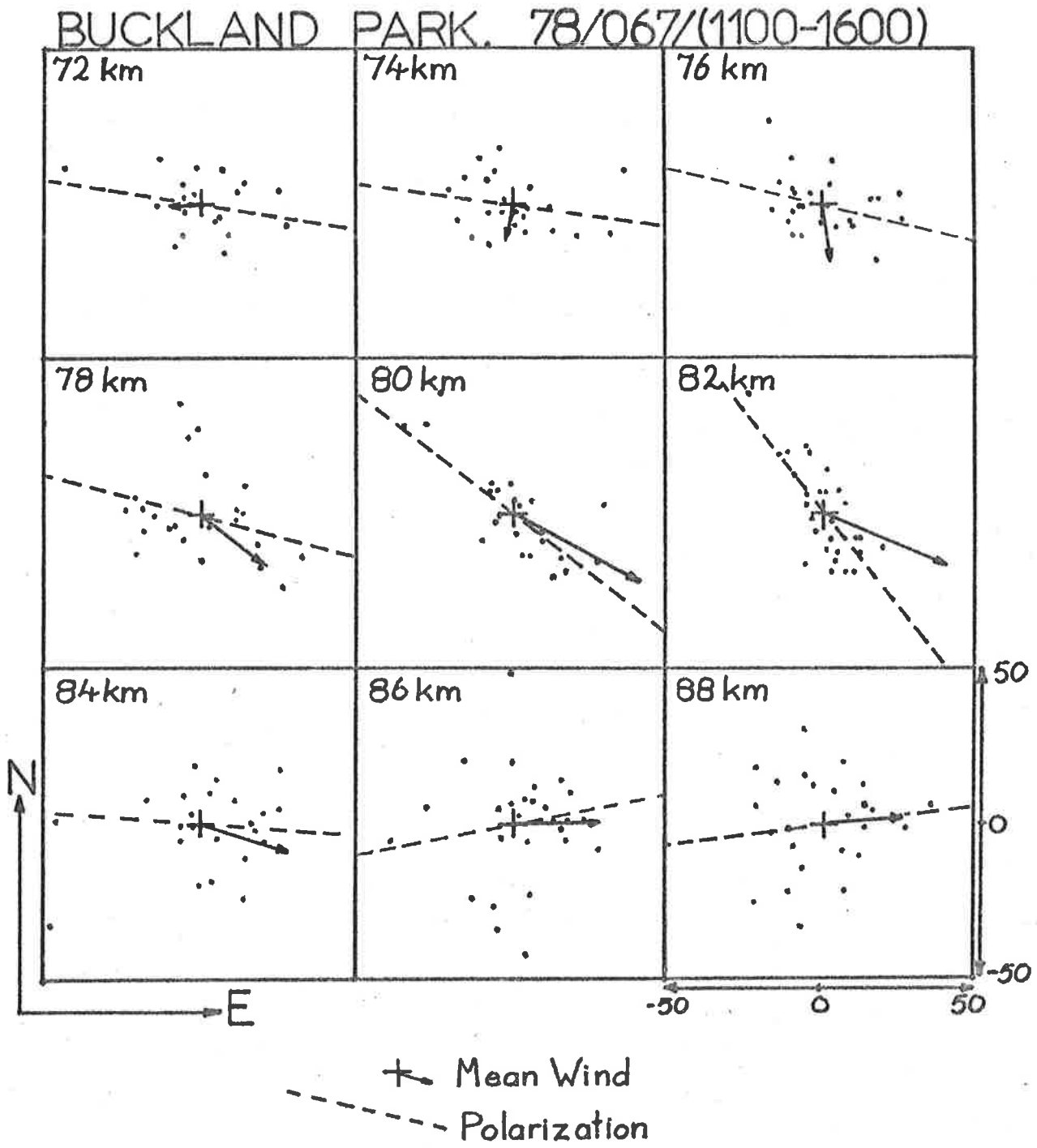

Fig 9.5(b) Fluctuating components of the winds on day 78/067 at Buckland Park. The arrows show the mean wind during the period 1100-1600, and the dots represent 5 min mean winds, with the mean for the full period 1100-1600 subtracted. The broken lines indicate best fit lines. Of particular interest is the polarized form of these fluctuating components at 80 and 82 km. Layers of strong HF radio wave scatter occurred at ~ 70-74 km and ~ 84-86 km. The graphs are due to S. Ball, (1981).

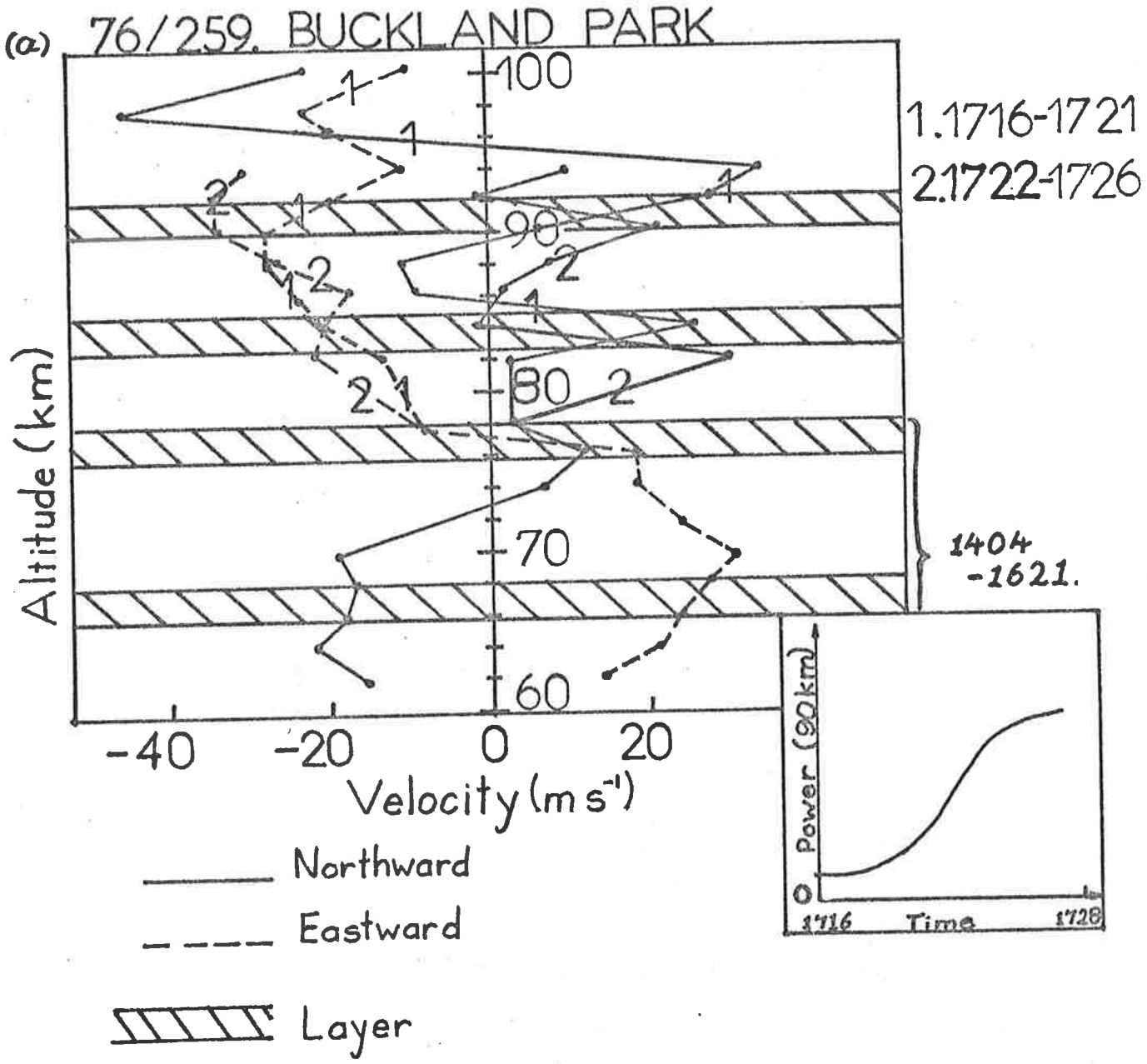

Fig 9.6(a) Typical height profiles of winds on day 76/259 (15th September, 1976). Two profiles produced from 5 min blocks of data are shown for heights above 80 km, and the profile below 80 km is the mean profile for the period 1404-1621 hrs. Heights of scattering layers are also indicated. The inset shows the scattered-power variation (approximately to scale) for the 90 km echo. Notice the strong wind shear at 76 to 78 km, which may be related to the scattering layer at that height. Also notice that the scattering layer at 66-78 km is again associated with a strong wind jet. There seems to be considerable gravity wave activity present on this day, judging by the regular wind oscillations with height in this figure. Fig 9.6(b) shows further evidence for gravity wave activity on this day.

Fig 9.6(b) Temporal variations of the power and winds for day 76/259 at 66-68 km. (a scattering layer occured at this height). The powers are uncalibrated and are 3 minute means for 68 km. The points are plotted at the middle of each 3 min block. The 1 minute wind means for heights of 66 to 70 km are joined by the broken lines, and an approximate 5 min running mean is represented by the solid line. The squares on these solid lines are 5 min means for the period ~ 2½ mins to either side (Although at ~ 1455, the large northward velocity "spikes" have been ignored).

The vertical lines at the base of graph (i) show times when large power bursts begin, and these correlate reasonably well with maxima in the Northward wind velocity. These fluctuations have a period of about 7 to 10 minutes.

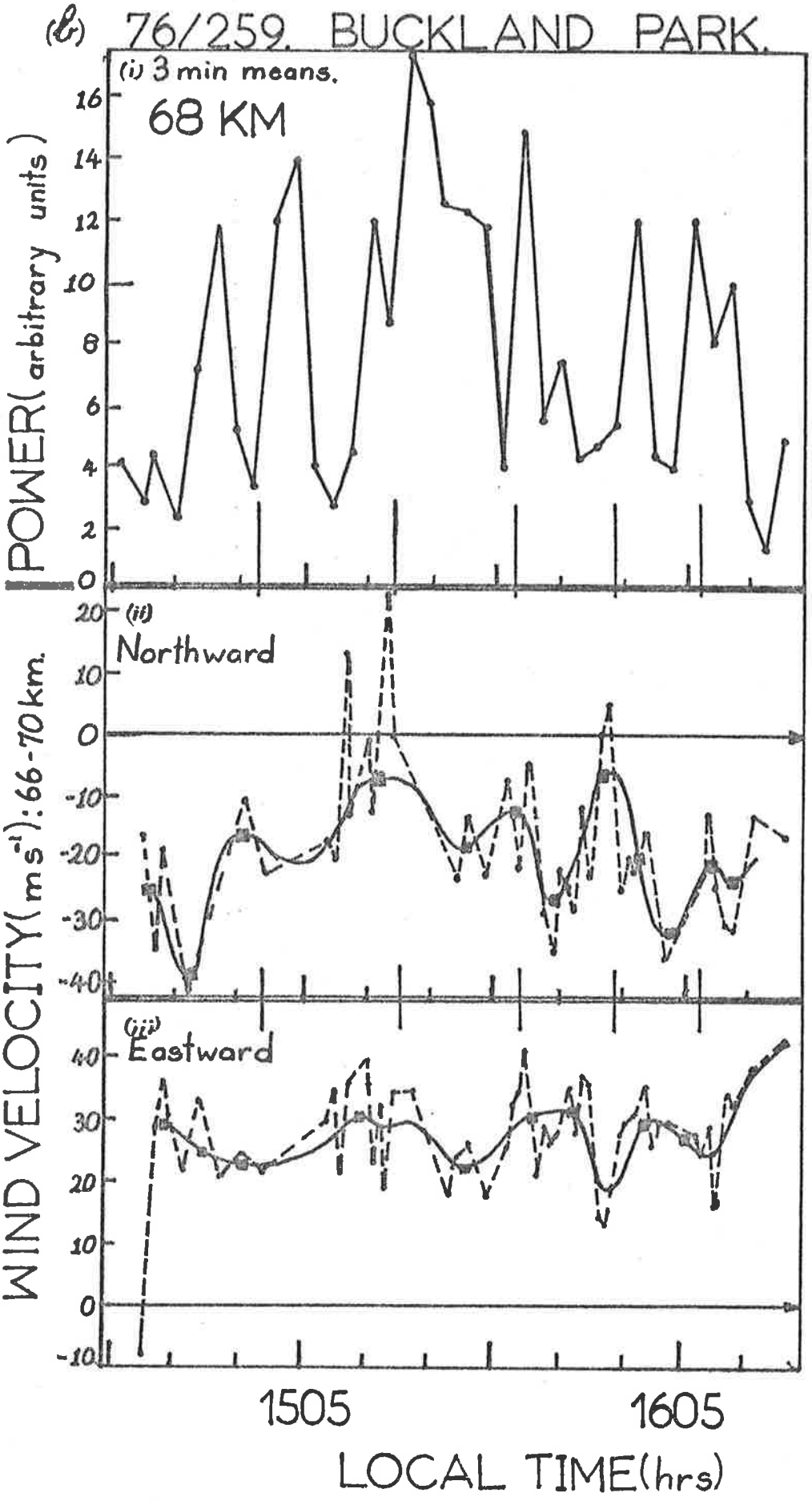
(b) 76/259. BUCKLAND PARK.
(i) 3 min means.
68 KM
POWER (arbitrary units)
16
14
12
10
8
6
4
2
0
(ii)
Northward
20
10
0
-10
-20
-30
-40
(iii)
Eastward
40
30
20
10
0
-10
WIND VELOCITY (m s⁻¹): 66-70 km.
1505
1605
LOCAL TIME (hrs)

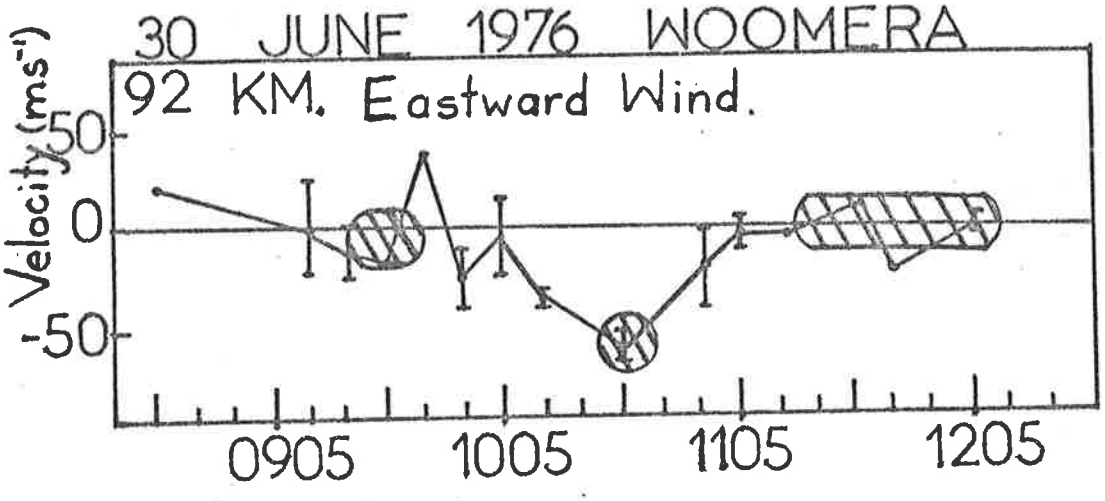

Fig 9.7 Eastward winds at 92 km for Woomera on 30th June, 1976, plotted as a function of time. The points are 10 min means, and the error bars are sample standard deviation. Single points indicate that only 1 point was recorded during the 10-minute interval. The shaded areas represent strong bursts of power which occurred in a layer at 90-94 km.

9.2.2 Gravity wave effects in producing scattering layers

Some indications of gravity wave effects associated with radio frequency scatterers in the D-region have already been presented in Chapter IV. For example, fig 4.8 showed a possible gravity wave induced variation of power and fading times. The power and fading times were possibly anti-correlated. Fig 4.9 showed evidence of downward moving patches of scatter, reproduced at quasi-regular intervals, and this was also tentatively interpreted as a gravity wave effect.

Fig 9.5(a) shows a further example of possible gravity wave effects. A strong correlation between power bursts and maximum northward winds appears to exist, with the northward winds showing a quasi-regular oscillation which could be indicative of a gravity wave. Also shown are typical 10 min mean wind height profiles near this time, and the similarity of the heights of the scattering layer and the 74 km wind jet can again be seen.

Fig 9.5(b) shows evidence of a gravity wave at 80-82 km. The graphs are due to Ball (1981). At heights below 78 km, little evidence of polarization shows, but at 80-82 km polarization is evident. This may indicate either some filtering of upward propagating waves below 80 km (e.g. see Hines and Reddy, 1967), amplification of the wave (perhaps, say, via an over-reflection process (e.g. Lindzen and Tung (1978)), or generation of a gravity wave in-situ. Wave ducting is another possibility. The wave does not appear to exist above 84 km. This could suggest a critical level absorption or over-reflection, or could suggest that the wave breaks. Layers of HF scatterers occurred at 70-74 km and 84-88 km on this day, and it is not impossible that the 84-88 km layer was associated with the gravity wave mentioned. We have seen in Chapter VIII that the 84-88 km layer may be associated with a large electron density ledge, and it will be seen shortly

that production of significant scatter by turbulence also required such a gradient. However, if a gravity wave were also to generate turbulence, for example, then this would enhance the scatter, and may help explain the temporal variability.

Figs 9.6 and 9.7 also illustrate possible gravity wave effects. In fig 9.6, as in fig 9.5(a), a correlation with North-South oscillations appears to exist. Evidence of a wind-shear effect at 76-78 km can also be seen in fig 9.6. The scatterers at 76-78 km were quite isotropic on this day, as discussed in Chapter IV, section 4.2, and fig 4.5. To be fair, the date presented in fig 9.7 is far from conclusive, there being only one cycle. However, it is included because it contrasts with fig 9.5(a) and fig 4.8, since power bursts occur twice per cycle, whereas the figs 9.5(a) and 9.6(b) and 4.8 show bursts of power only once per cycle.

The examples given above are rather special cases in which a gravity wave is clearly visible. It is not always possible to observe separate gravity waves, particularly if many are present. However, if gravity waves were important, it might at least be expected that scattering layers would be more evident on days when the wind motions appeared to be more variable. Some evidence for this at Townsville (November, 1977) seemed to exist, but no firm conclusions have been reached. (e.g. see fig 9.3).

Other examples of gravity wave-induced effects on scattering powers can be found in the literature. For example, Harper and Woodman (1977) have observed VHF scatter from $\sim$ 70 km with a powerful VHF radar, and found that power bursts occurred at approximately twice the frequency of gravity waves which appeared to be associated with the layer (most such gravity waves had periods of around 10 minutes). They also found that these gravity wave oscillations did not appear to extend more than a few kilometres above

or below the scattering layer. This is also consistent with many of the observations made for this thesis (e.g. the gravity wave seen in fig 9.5(a) could not be seen clearly above 78 km or below about 70 km). Harper and Woodman felt that this indicated that either the waves were generated at these levels and were evanescent, or that the waves had been trapped and ducted. Miller et al (1978) have found evidence of a correlation between breaking gravity waves and strong bursts of VHF scatter at 60-80 km.

In the troposphere, too, correlations between gravity waves and power bursts have been found. van Zandt et al (1979) have found bursts of power at VHF with frequencies approximately equal to associated gravity wave frequencies. Merrill and Grant (1979), using a radio-wavelength of about 10 cm, have presented quite a detailed account of a gravity-wave-critical-level encounter in the atmospheric boundary layer. In their model, a gravity wave is critically absorbed at a wind shear, and this process steepens the wind-shear. This generates turbulence, which smoothes out the wind shear. Thus the turbulence ceases, upon which the gravity wave absorption then begins to steepen the wind shear again, and the process repeats. However, the wavelength of the gravity waves was less than a few hundred metres, and such waves would not be observed in the D-region by present radars. The D-region gravity waves mentioned thus far may not have produced this effect directly, but could perhaps generate these smaller scale gravity waves in the higher atmosphere (e.g. by non-linear effects, or by breaking).

The reasons why gravity waves can generate radio wave scatterers is another problem. Several papers have been presented which show that critical absorption of gravity waves at a wind shear can quite significantly steepen the wind shear (e.g. Jones and Houghton, 1971; Fritts 1978, 1979). This can lead to Kelvin-Helmholtz instabilities (in the oceans and atmosphere below

130 km), and these may then induce layers of turbulence (e.g. Fritts, 1978 1979). Hodges (1967) has also pointed out that gravity waves can produce unstable temperature gradients, particularly if the background atmosphere is close to unstable. It is interesting to note that in this model, turbulence is expected to occur only once per gravity wave cycle.

There thus appears to be quite a few models which can explain the generation of turbulence by gravity waves. But it should be recalled that scatter from below about 80 km is usually quite specular. The usual concepts of turbulence do not appear capable of explaining this feature. This suggests that either the scatterers are not related to isotropic turbulence, or else turbulence can somehow produce stratification. Some evidence that the latter statement may be true has appeared in recent literature. For example, Bolgiano (1968) has proposed that intense turbulence could mix up a potential refractive index gradient, producing a constant mean value across the turbulent layer, with steps either side, as illustrated in the following diagram. This will be referred to frequently during this chapter, and will be called the Bolgiano model. It will be used primarily for illustrative purposes. This does not mean the author has accepted it.

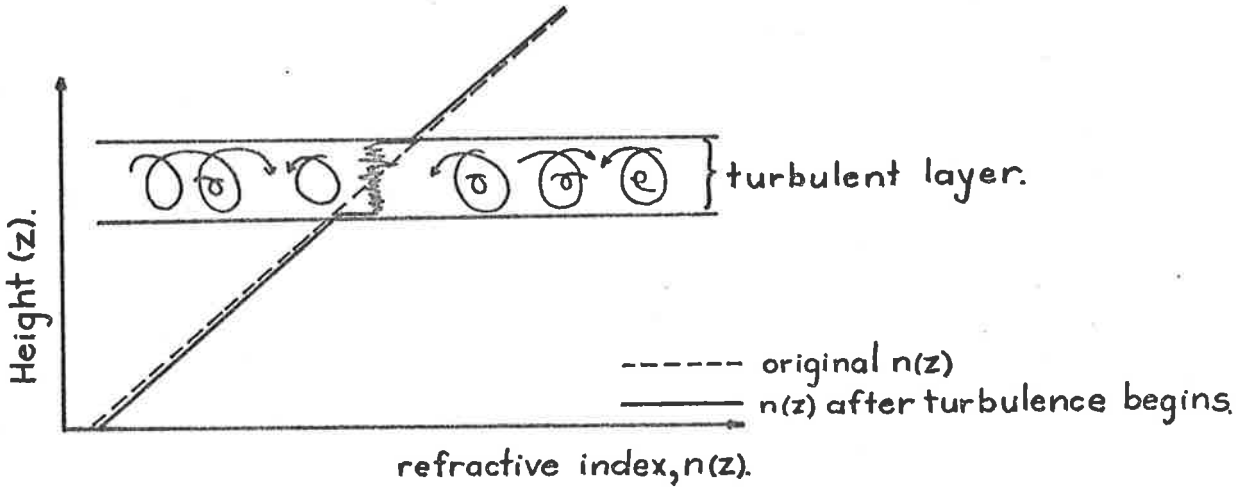

Bolgiano (1968) has also mentioned that turbulence in strong wind shears can be quite anisotropic. Other experiments have appeared which suggest that

once the generating source has been removed, turbulent regions settle out into horixontal layers. However, discussion of these effects will be left until Chapter XI.

At present, it is sufficient to say that gravity waves do appear to play a significant role in the generation of radio wave scatterers in the D-region.

Fig 9.8

As shown in Chapter II, equations 2.3.2.10a and 2.3.2.11, the refractive index structure constant C_n^2 is given by

$$C_n^2 = a^2 L_o^{4/3} |M|^2 \qquad \text{where}$$

$$M_e = \frac{\partial n}{\partial N} \cdot N \left\{ \frac{1}{T} \left(\frac{dT}{dz} + \Gamma_a \right) - \frac{d \ell n N}{dz} - (1.4 \times 10^{-4}) \right\} + \frac{\partial n}{\partial \nu_m} \frac{\partial \nu_m}{\partial z} .$$

and L_o is the outer scale, T is the absolute temperature, Γ_a is the adiabatic lapse rate, z is the height, n is the refractive index, N is the electron density, and ν_m is the electron collision frequency.

The electron density profile of Mechtly et al (1972, fig 5, quiet sun) (also see Chapter VIII) was adopted, and M_e calculated for this profile, using the full Sen-Wyller equations for calculations of the refractive index. The profiles are for 1.98 MHz.

Fig 9.8a shows the relative contributions of the terms

$$A = \frac{1}{T} \left(\frac{dT}{dz} + \Gamma_a \right), \quad B = \frac{d \ell n N}{dz}, \quad \text{and} \quad C = 1.4 \times 10^{-4}.$$

Notice the large effect of $\frac{d \ell n N}{dz}$ at 85 km, due to the large electron density ledge at that height (see Chapter VIII). The term $\frac{1}{T} \left(\frac{dT}{dz} + \Gamma_a \right)$ is only approximate, but is adequate for the purpose for which it is used.

In Fig 9.8b, $|M_e|^2$ and $\left| \frac{\partial n}{\partial \nu_m} \frac{\partial \nu_m}{\partial z} \right|^2$ are shown. It can be seen that the latter term does not make a large contribution to the potential refractive index gradient, except at the minima (and in these cases, it will be seen that turbulent scatter could not be detected anyway).

9.8 (a)

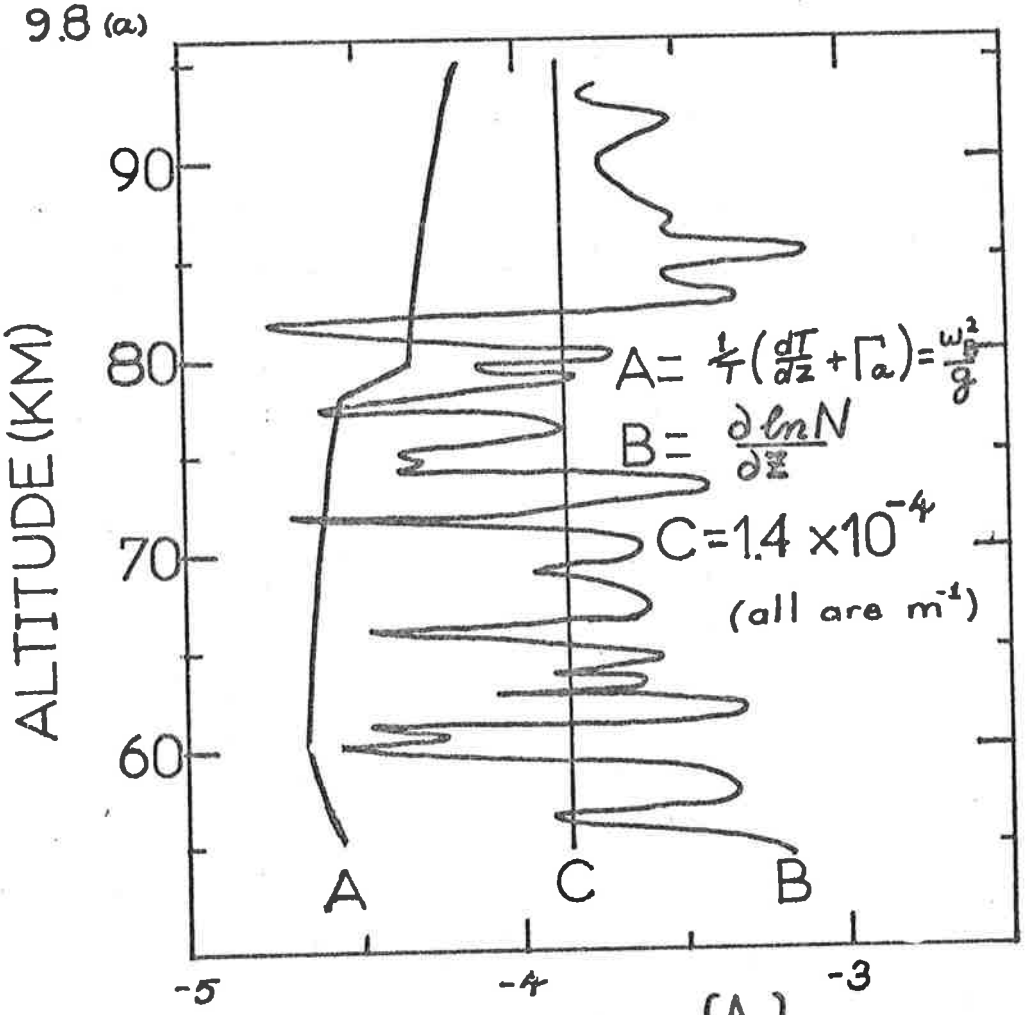
ALTITUDE (KM)
90
80
70
60
A= $\frac{1}{\gamma}\left(\frac{dT}{dz}+\Gamma_a\right)=\frac{\omega^2}{g}$
B= $\frac{\partial \ln N}{\partial z}$
C=1.4 ×10^{-4}
(all are m^{-1})
A
C
B
-5
-4
-3
$\log_{10}\{A, B, C\}$

9.8 (b)

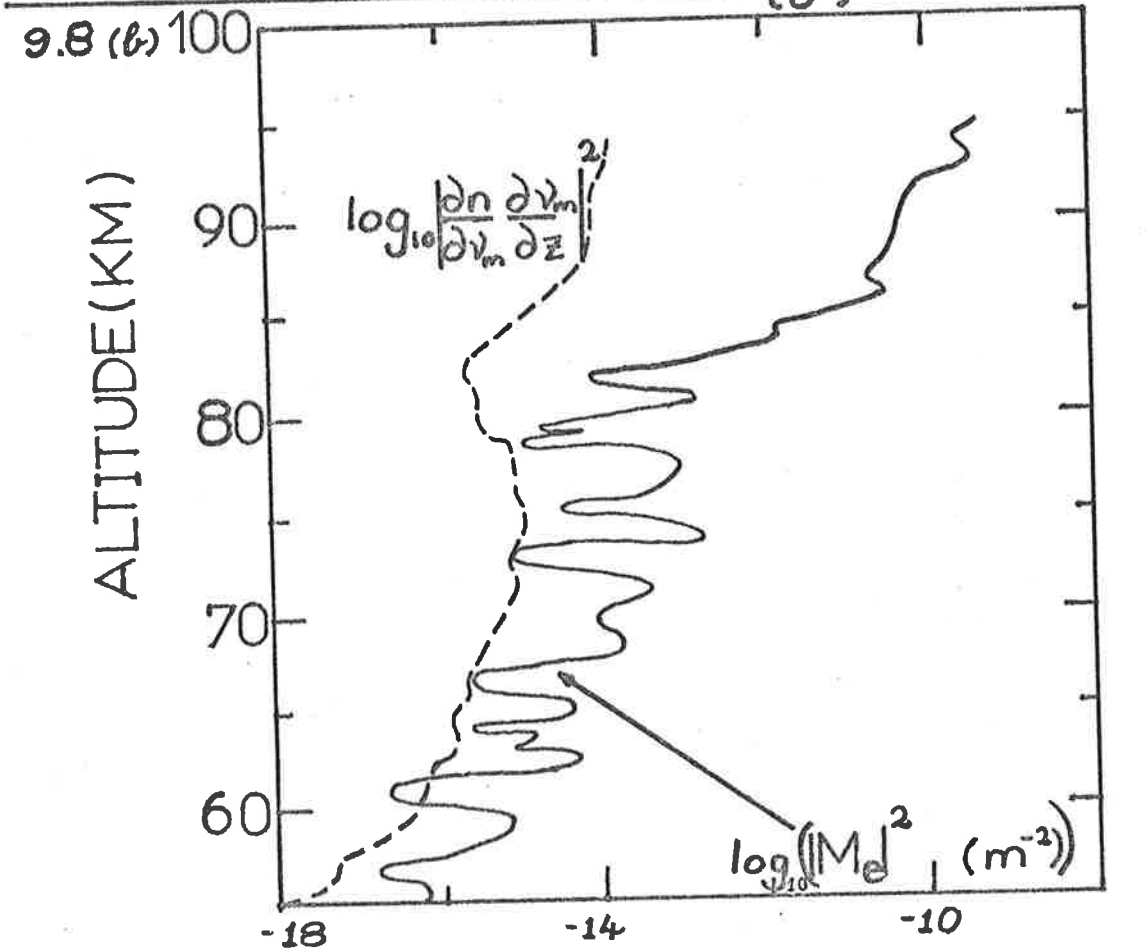
ALTITUDE (KM)
100
90
80
70
60
$\log_{10}\left|\frac{\partial n}{\partial \nu_m}\frac{\partial \nu_m}{\partial z}\right|^2$
$\log_{10}(|M_e|^2\ (m^{-2}))$
-18
-14
-10

Fig 9.8(c)

Plots of the assumed electron density profile, the potential refractive index profile, and the refractive index structure constant C_n^2 profile (using outer scales as given in Fig 1.9a, Chapter I, and assuming

$$C_n^2 = L_o^{4/3} \cdot |M_e|^2)$$

as a function of height, at 1.98 MHz. Also shown are the C_n^2 values required to produce effective reflection coefficients of $R = 10^{-5}$, 10^{-4}, and 10^{-3} (see equation 9.3.1.2), assuming turbulence fills the radar volume (solid vertical lines). Effective reflection coefficients of about 10^{-5} are just detectable with the Buckland Park array.

The broken line (---) shows the C_n^2 profile which would be produced if the electron density gradient term

$$N \frac{d \ln N}{dz} = \frac{dN}{dz}$$

was not important. Notice that at 85 km, an electron density ledge similar to that which occurs in this profile is necessary to produce significant turbulent scatter.

The C_n^2 values may be increased by increasing the energy dissipation rate ε_d ($L_o \sim \varepsilon^{\frac{1}{2}} \omega_B^{-3/2}$), which may occur in localized patches, thus producing the temporal variations of echo strength received. If turbulence does not fill the radar volume, this will reduce the observed effective reflection coefficient.

The important points to notice are

(i) turbulence <u>will</u> cause observable HF scatter above 80 km under normal conditions.

(ii) turbulence will <u>not</u> cause observable HF scatter below 80 km under normal conditions - and certainly cannot account for reflection coefficients of greater than 10^{-4}. An increase in ε_d of greater than 100 times is necessary to produce this, and if the layers are only a few hundred metres thick (e.g. Chapter IV; section 4.5.3), even larger ε_d values are necessary to explain the observed effective reflection coefficients.

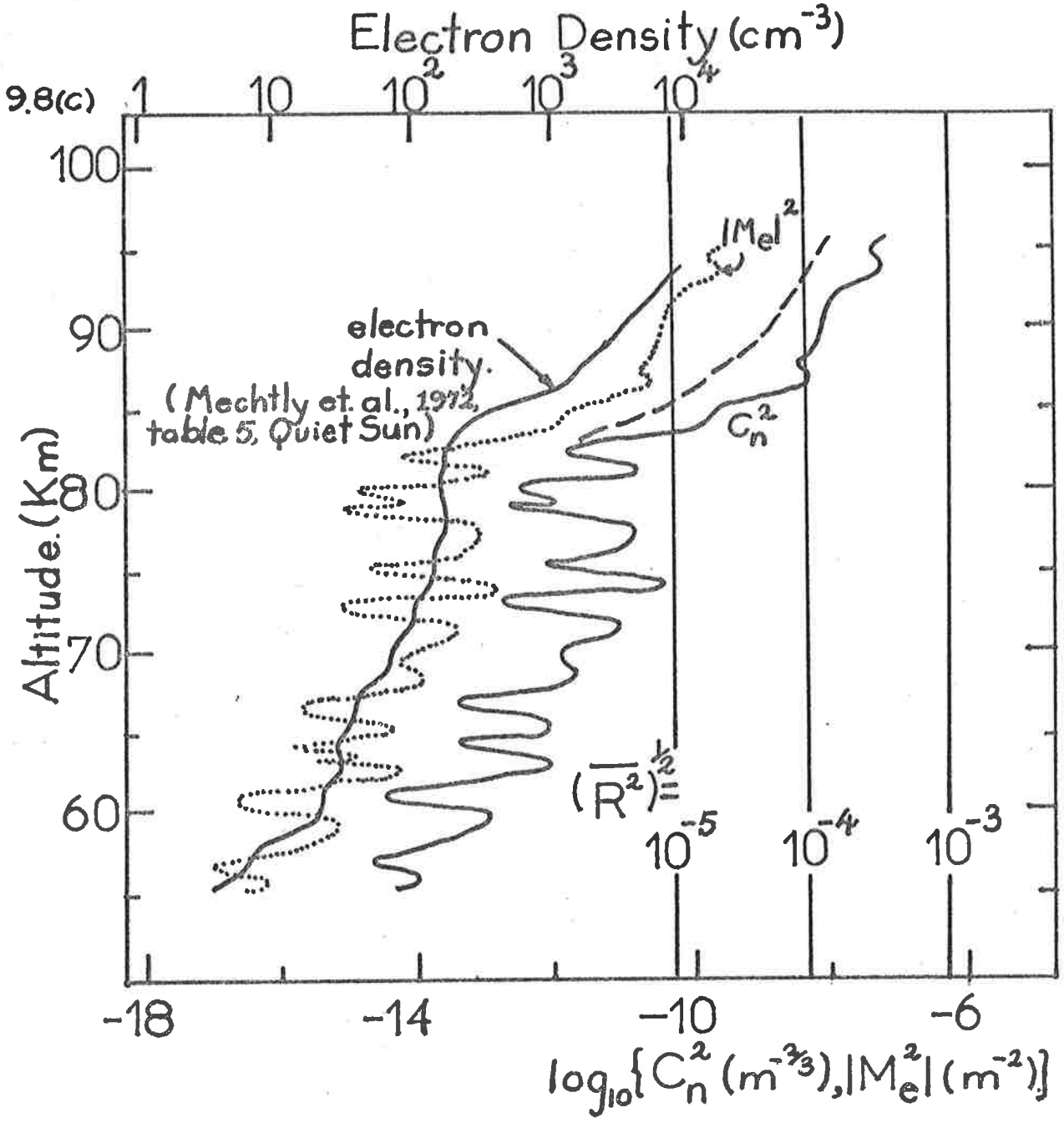
9.8(c)
Electron Density (cm^{-3})
1
10
10^2
10^3
10^4
100
90
80
70
60
Altitude (Km)
$|M_e|^2$
electron density.
(Mechtly et. al., 1972, table 5, Quiet Sun)
C_n^2
$(\overline{R^2})^{\frac{1}{2}}$ =
10^{-5}
10^{-4}
10^{-3}
-18
-14
-10
-6
$\log_{10}\{C_n^2\,(m^{-2/3}), |M_e^2|\,(m^{-2})\}$

9.3 The relative roles of turbulence and specular scatter

9.3.1 Turbulence

Turbulence has been regularly discussed in this thesis as a mechanism for producing the radio wave scatter observed. However, it is interesting to calculate the expected effective reflection coefficients for such scatter as a function of height, for typical atmospheric conditions. This can readily be done, by utilizing equations 2.3.2.10a", 2.3.2.11 and 2.4.1.5 from Chapter II, and equation 3.3.2.19, Chapter III.

Thus, assuming the turbulence fills the radar volume,

(9.3.1.1) $$\overline{R}^2 = \theta_{\frac{1}{2}}^2 \, L \, (.38) \, \lambda^{-1/3} \, C_n^{\,2} ,$$

and for the narrow beam at Buckland Park, the half power half width of the polar diagram in $\theta_{\frac{1}{2}} = +4.5^{o}$, the pulse length L is typically 4 to 6 km and the wavelength λ is 151.5 m at 2 MHz. So,

(9.3.1.2) $$\overline{R}^2 \approx 2.4 \, C_n^{\,2}$$ (where $C_n^{\,2} \approx L_o^{\,4/3} |M_e|^2$, by equation (2.3.2.11) ($a \approx 1$) for the Buckland Park array (narrow beam) and a pulse length of 6 km.

This equation was also presented in Chapter IV, section 4.2.1. It has been assumed that the effective radar volume is $(R_o \, \theta_{\frac{1}{2}})^2 \, \pi L$, R_o being the distance to the scattering region. In Chapter X, this approximation will be improved upon, but for these purposes it is quite adequate.

In Chapter IV, section 4.2.1, typical $\overline{R}^2$ values for turbulence were found, but a detailed height profile had not yet been prepared. In the work presented in this section, profiles of $C_n^{\,2}$, and hence $\overline{R}^2$, have been calculated for typical electron density profiles and typical outer scales.

The outer scales were taken from Fig 1.9a, Chapter I, and the electron density profile used was that due to Mechtly et al (1972, table 5, "quiet sun").

Recall this profile was also used in Chapter VIII. It was produced from several individual profiles, so any small scale irregular fluctuations have been smoothed out. The results of this analysis are shown in Fig 9.8. Perhaps the most important conclusion is that above 80 km, turbulent scatter is capable of causing reflection coefficients comparable to those observed. Recall that $L_o \sim \varepsilon_d^{\frac{1}{2}} \omega_B^{-3/2}$ (equation 2.2.4.2a'), so an increase of ε_d by 4 times can increase C_n^2 by 2.5 times. Thus a fairly small increase in the energy dissipation rate can vary the amount of HF scatter at 1.98 MHz.

It should be noted that in these calculations it has been assumed that turbulence fills the radar volume. If this were not so, and the turbulent layer were say one outer scale (L_o) in vertical extent, then in equation 9.3.1.1, L would be replaced by L_o. This would mean that $\overline{R}^2$ would have an $L_o^{2/3}$ dependence on L_o, not an $L_o^{4/3}$ dependence as suggested by equation 2.3.2.11. If, however, the layer thickness were L_o, equation 9.3.1.2, would have to be modified, and the constant 2.4 would be reduced. Bear in mind, though, that L_o need not necessarily be the thickness of turbulence. Rather, L_o is the scale over which turbulent fluctuations become comparable to changes in the mean values.

The expected scatter due to turbulence at the 85 km ledge is comparable to the specular scatter due to the ledge itself (as calculated in Chapter VIII). This is consistent with results from Chapter V - both specular and isotropic scatter play roles for the 86 km echo. If the ledge does not exist, turbulent scatter is quite weak, as is the specular reflection.

A second important conclusion is that direct turbulent scatter does not appear to be likely to be the reason for scatter from heights below 80 km.

The powers produced by this mechanism are much weaker than those observed. This also supports conclusions reached previously. This finding does not preclude turbulence as a cause of the scatter - if turbulence could produce stratified steps, perhaps as proposed by Bolgiano (see earlier discussion) the scatter could indeed be associated with turbulence - but not in the usual sense of turbulent scatter. If in fact an extremely large electron density gradient could be produced at these lower heights, then turbulent scatter could make a contribution, but if stratified scatter dominates when normal electron density gradients are present, then it could still be expected to dominate with high gradients. Haug et al (1977) have proposed just such a Bolgiano-type description to explain very strong reflection from 60 km (in the auroral region) with an effective reflection coefficient of between 10^{-3} and 10^{-2}. They found this very strong scatter occurred during a period of high electron precipitation, and proposed that the associated large electron density increase in the D-region produced the large electron density gradient necessary to produce this large effective reflection coefficient. A similar strong echo from 70 km ($\overline{R} \sim 10^{-3}$) at Townsville on 22nd January, 1980, has already been mentioned in Chapter IV, section 4.2.1, and presumably a similar large electron density gradient was associated with it. Whether the Bolgiano model, or some other mechanism, produces the electron density step producing this scatter is debatable.

However, the discussion in this section does show that

(i) turbulent scatter makes a significant contribution above 80 km

(ii) turbulent scatter does not make a contribution from below 75 to 80 km, unless very unusual conditions prevail.

Even if such conditions do prevail, it is possible that the specular processes causing scatter may still dominate. This will be discussed in the following section.

9.3.2 Expected specular to isotropic scatter ratios

We have seen that horizontal strata, and turbulence, both occur in the D-region. The expected turbulent scatter is (assuming turbulence fills the scattering volume)

$$(9.3.2.1) \qquad \bar{R}^2_{turb} \approx V_{eff} \ (.38) \ \lambda^{-1/3} \cdot L_o^{4/3} \ |M_e|^2 \ .$$

V_{eff} is the effective volume of scatter, $L_o \sim \varepsilon^{\frac{1}{2}} \omega_B^{-3/2}$ is the outer scale, and M_e is the potential refractive index gradient.

Now consider the following very simple model. Let us assume that in the atmosphere there exists patches of turbulence, and also horizontally stratified steps in electron density, of the order of a Kolmogoroff microscale (η) in vertical extent (e.g. the edges of the layer produced by the Bolgiano model). These steps, and patches of turbulence, may or may not be related. All they need do is exist.

Assume that the size of these steps is proportional to the electron density gradient. In the Bolgiano case, it would also be proportional to the layer width. Then the effective reflection coefficient is

$$(9.3.2.2) \qquad \bar{R}_{spec} = K_1 \frac{dn}{dz} \cdot E(z), \qquad (n = \text{refractive index})$$

where $E(z)$ describes the efficiency of scatter of the step, and z is the height, and K_1 is an unknown constant.

Then

$$(9.3.2.3) \qquad \bar{R}^2_{spec}/\bar{R}^2_{turb} \approx K_\lambda (V_{eff})^{-1} \ E(z)^2 \ L_o^{-4/3}$$

Here, it has been assumed that

$$\frac{dn}{dz} \approx \frac{\partial n}{\partial N} \frac{dN}{dz} \propto |M_e| \ , \quad \text{where} \quad N = \text{electron density.}$$

This approximation will be discussed shortly. ($\frac{\partial n}{\partial N}$ can be taken as approximately constant; e.g. see Chapter II, equation 2.4.1.8). L_o has

very weak variation with height (e.g. fig 1.9a, Chapter I), and can be assumed to be constant for the purposes of this calculation. This will be seen to be justified after the calculations, as it will be shown that E(z) is a much more rapidly varying term.

What is E(z) ? Let us assume that the steps mentioned have a Gaussian form, as illustrated below. Here, n(z) = refractive index, r(z)dz = effective reflection coefficient, and d is the e^{-1} full width of $\frac{dn}{dz}$.

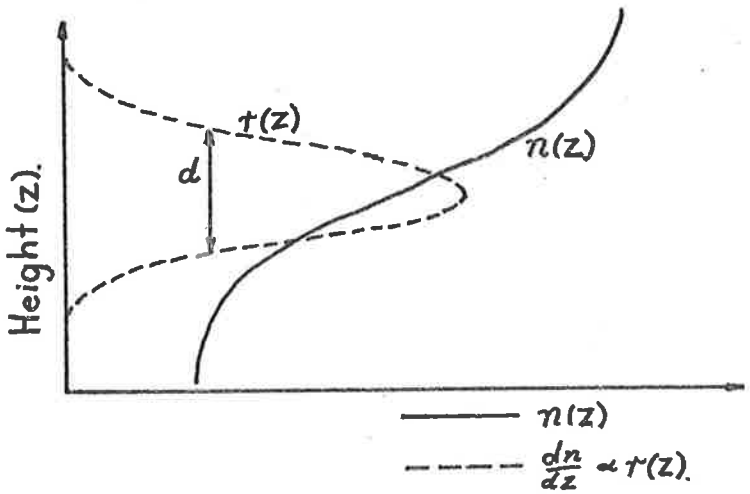

(Notice that this form is different to the form assumed in Chapter II, section 2.2.3, but the two forms both illustrate the same important points).

Then by equation 4.5.2.6, Chapter IV, (and noting the slightly different definition of d).

(9.3.2.4a) $\quad E(z) = \exp \{ - \pi^2 \, d(z)^2 \, \lambda^{-2} \}$

Let us assume $d(z) = \gamma \, \eta(z)$. Then

(9.3.2.4b) $\quad E(z) = \exp \{ - \pi^2 \, \gamma^2 \, \eta^2(z) \, \lambda^{-2} \}$

The profile of η shown in fig 1.9a, Chapter I was chosen for those calculations. Then

(9.3.2.5) $\quad \eta = 10^{\beta} \, 10^{\alpha z}$

where $\begin{cases} \alpha = .0444, \quad \beta = -2.532 \text{ for } 60 \text{ km} \leqslant z \leqslant 80 \text{ km} \\ \alpha = .0477, \quad \beta = -2.796 \text{ for } 80 \text{ km} \leqslant z \lesssim 100 \text{ km} \end{cases}$

Here, z is in kilometres, and η in metres.

$E(z)$ was calculated as a function of z, and then $\overline{R}^2_{spec}/\overline{R}^2_{turb}$ was plotted as a function of height in fig 9.9, using equation (9.3.2.3). The term $(K_\lambda V_{eff}^{-1} . L_o^{-4/3})$ was taken to be constant, and was obtained by comparing expected turbulent power at 70 km from fig 9.8 $(\overline{R}^2_{turb} \sim 2.4 \times 10^{-13})$ to powers observed for 70 km scatter $(\overline{R}^2 \sim 10^{-8})$. This assumes that all the scatter from 70 km is indeed specular, but this has been verified in the preceding chapters. Thus

(9.3.2.6) $$\overline{R}^2_{turb}/\overline{R}^2_{spec} \approx (4 \times 10^4) E^2(z) \quad \text{(Buckland Park)}.$$

It should be understood that the "constant" 4×10^4 could be wrong by as much as an order of magnitude.

The curves "BP, $\gamma=1$" "BP, $\gamma=\pi$", "BP, $\gamma=2\pi$" in fig 9.9 show plots of this ratio at 1.98 MHz, for the Buckland Park array. Notice that for $\gamma=2\pi$, the specular scatter becomes quite small at 80-85 km. The transition from "mainly specular" to "mainly turbulent" is quite sharp, and even a variation of the constant 4×10^4 of 10 times does not change this transition height greatly. Thus this model simulates the observed rapid transition from highly specular scatter to more isotropic scatter above 85 km quite well - provided $\gamma = 2\pi$ is valid.

If turbulence did not fill the radar volume, this would increase the ratio $\overline{R^2}_{spec}/\overline{R^2}_{turb}$. This would only be important above 85 km, and the adjustment would not be too great, as turbulence should at least have a vertical depth of the order of the outer scale L_o ($\sim$ 300 - 600 m above 80 km). Hence V_{eff} may be perhaps 10 times less than the value used, but we have seen that such a change does not have a great effect on the transition height. It is also interesting to note that $d = 2\pi\eta$ is approximately equal to k_ν^{-1} (metres) in Fig 1.9a - i.e. the lower limit of the Tchen range. A major weakness of this model is the assumption that the refractive index change across the step is proportional to $\frac{dn}{dz}$, as assumed in equation (9.3.2.2). Further, the assumption that $\frac{dn}{dz} \propto \frac{dN}{dz}$ is quite legitimate,

but $\frac{dN}{dz}$ and $|M_e|$ are only proportional if the temperature gradient and total electron density terms in equation (2.3.2.10a) are small. (The term $\frac{\partial n}{\partial \nu_m} \cdot \frac{\partial \nu_m}{\partial z}$ has been shown to be negligible, as discussed in Fig 9.8). As shown in Fig 9.8, this is only approximately valid above 85 km, but for the accuracies involved in these computations it is adequate.

Having done all this at 1.98 MHz, it seemed useful to repeat the calculations for the Jicamarca array at 50 MHz, in the light of the data presented in Fig 4.24, which showed the specularity of VHF scatter below 70 km . This required the calculation of a new constant for the equation (9.3.2.6), as well as a re-evaluation of E(z). Both $|M_e|$ and $\bar{R}_{spec}$ involve a term $\frac{\partial n(\lambda)}{\partial N}$ which describes the change in their values as the probing wavelength changes, so this term cancels in estimation of $\bar{R}^2_{spec}/\bar{R}^2_{turb}$. Hence the constant in (9.3.2.6) is simply $(4 \times 10^4)[V_{eff}(J)/V_{eff}(BP) \cdot (\lambda(J)/\lambda(BP)^{-1/3}]^{-1}$, where J refer to Jicamarca, and BP refers to Buckland Park. $\lambda(J) = 6$ m, $\lambda(BP) = 151.5$ m. For the Jicamarca array, the half-power-half-width is $\theta_{\frac{1}{2}} \sim 1^\circ$ and the pulse length is about 4 km. Hence the constant is about 4×10^5. Thus

$$\bar{R}^2_{turb}/\bar{R}^2_{spec} \approx 4 \times 10^5 \, E_J^2(z) \qquad \text{(Jicamarca)}$$

This was calculated and plotted on fig 9.9 also. (For fig 9.9, the constant used was 8×10^5, but this does not change the results significantly). In this case, for $\gamma = 2\pi$, turbulent scatter always dominate above 60 km. For $\gamma = \pi$, the transition height is about 62 km, and for $\gamma = 1$ is about 73 km. This suggests $\gamma \sim 1$ is best, by comparison with fig 4.24, Chapter IV. Thus, the two γ-estimates differ at Buckland Park and Jicamarca. This illustrates inadequacies in the model. The true turbulent scattering volume may only have a depth of 100 m or so (e.g. see Röttger et al , 1979). This would increase the constant above by perhaps (2 km/100 m) ~ 20 times, but this will not alter the transition heights greatly.

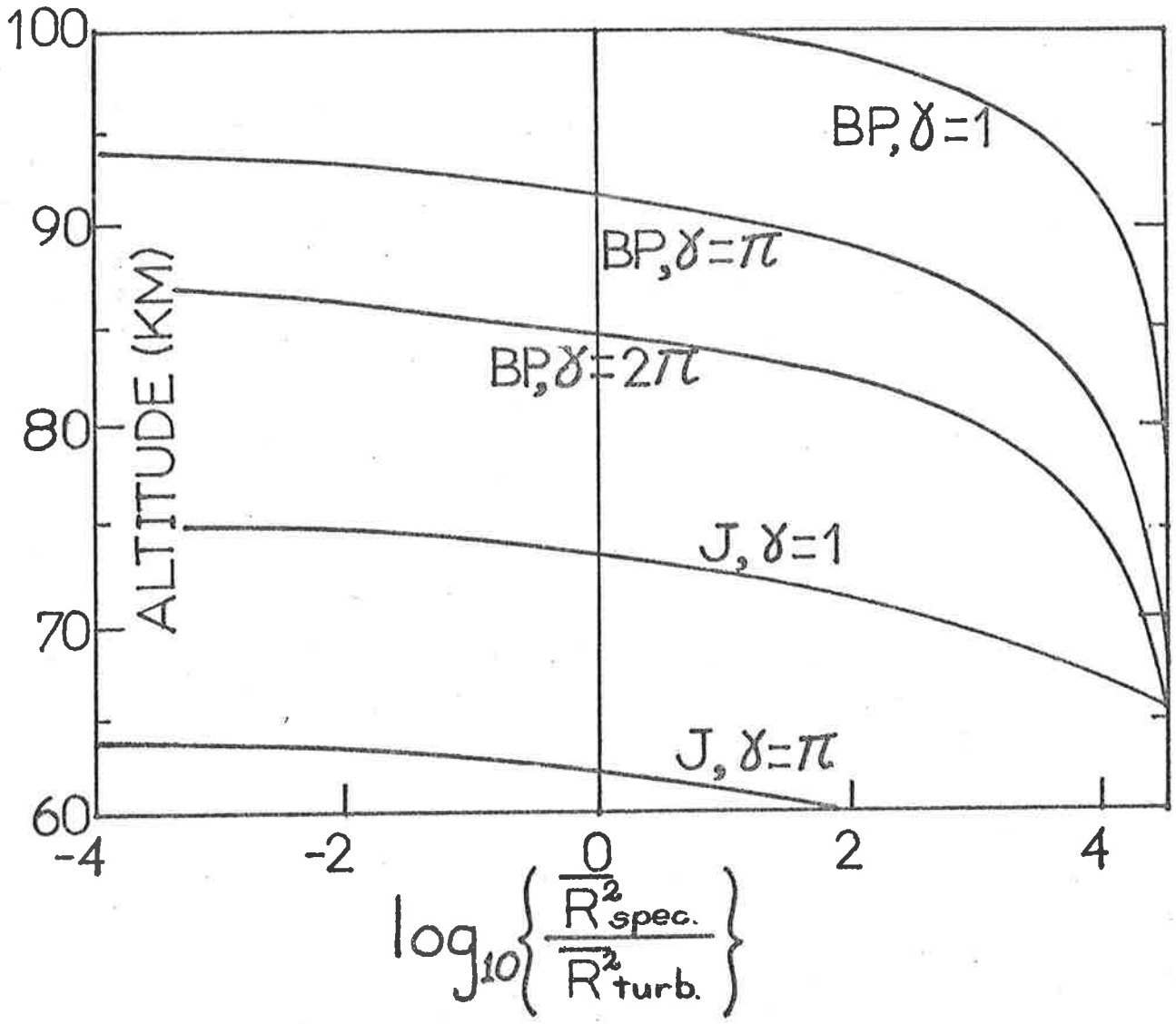

Fig 9.9 Expected specular scatter to turbulent scatter power ratio as a function of height, where it has been assumed that the atmosphere is filled with both turbulence and horizontally stratified steps of width $d = \gamma\eta$, η being the Kolmogoroff microscale. It has been assumed that all wavelengths receive scatter from scales in the inertial range, and that the turbulence fills the radar volume. The B.P. case corresponds to the narrow beam at Buckland Park at 1.98 MHz ($\theta_{\frac{1}{2}} = 4.5^{\circ}$, pulse length = 4 to 6 km), and the Jicamarca Case refers to the Jicamarca array at 50 MHz ($\theta_{\frac{1}{2}} = 1^{\circ}$, pulse length = 4 km).

Many factors could change the shape of these curves, as discussed in the text, but the important point is that specular reflection becomes extremely inefficient with increasing height.

One important point which will affect the Jicamarca curves is that scatter from heights above 65 km will be from scales in the viscous range of turbulence (see fig 1.9a, Chapter I). This will significantly alter the curves in fig 9.9 for heights above about 60 to 65 km, and the true specular to turbulent scatter ratio will increase. Thus $\gamma=\pi$ may perhaps be more valid at 50 MHz. The widths calculated at 50 MHz and 2 MHz can perhaps be adjusted to agree better by using a different profile for the step than that used. Assumption (9.3.2.2) may also need revision.

However, although there are clearly inadequacies in the model, it does show that specular scatter becomes inefficient at greater heights, and the transition from dominantly specular to dominantly turbulent scatter is quite sharp, just as is observed in the real atmosphere. It thus appears that both stratified steps and turbulent layers may occur at all heights in the atmosphere, and these scatter radiation with different efficiencies, thus resulting in the angular spectra observed for scatter from these irregularities.

As a final point, it should be mentioned that this discussion has not considered specular scatter from large electron density ledges, as discussed in Chapter VIII. That such specular scatter is important has already been illustrated.

9.4 Conclusions

The data presented in this chapter suggests that the following conclusions are valid.

(i) There does not appear to be a strong permanent correlation between HF scattering layers and wind shear measurements made with a vertical resolution of $\sim$ 4 km , and temporal resolution of between 1 minute and 1 hour. However, on occasions bursts of power and scattering layer, can be associated with wind shears. The wind jet at $\sim$ 70-74 km may be related to scatterers at this height.

(ii) There do appear to be strong gravity wave effects on these scatterers.

(ii) Some, if not most, of the scatter from above 80 km is due to irregularities produced by turbulence.

(iv) Very little, if any, of the scatter from below 75-80 km is due to isotropic turbulent scatter.

(v) It is quite possible that turbulence and horizontally stratified steps of the order of the Kolmogoroff microscale in vertical extent exist at all heights in the atmosphere. Whether these are caused by related mechanisms, or independent mechanisms, is unknown. However, such a picture is quite capable of causing the observed scatter characteristics.

The reasons for the thin steps in electron density are not known, and the problem still remains as to how they remain stable (they could perhaps be expected to diffuse out in a time of $t \sim H^2/K$ (K = eddy diffusion coefficient , H = depth), or $t \sim$ 1-10 s at $\sim$ 70 km (see Chapter I, section 1.4.1e). That they do exist, however, seems

fairly well established. Some clues as to the reasons for their existence will be given in Chapter XI.

(vi) The importance of an electron density ledge at ~ 85 km in causing the 85 km echo was again noted, and it was shown that with the ledge, quite standard atmospheric turbulence can cause the observed isotropic component of the scatter, on top of the specular scatter discussed in Chapter VIII. Without the ledge, neither significant specular or turbulent scatter generally occurs. At this height, steps in the refractive index of the order of 1 Kolmogoroff microscale thick could possibly produce scatter just comparable to the turbulent scatter, according to fig 9.9, $\gamma=2\pi$. However, the transition height of dominant specular to dominant turbulent scatter is generally found to be 76-80 km (see Chapter IV), so this is an unlikely reflection mechanism at 85 km. This suggests γ may be slightly larger than 2π in fig 9.9.

CHAPTER X

INVESTIGATIONS AT 6MHz

Chapter X Investigations at 6MHz

10.1 Introduction

Some space in this thesis has been devoted to general comparisons of D-region scatter experiments using different frequencies. However, simultaneous comparisons of scatter at two separate frequencies are desirable, since this could greatly improve understanding of the scatterers. Dieminger (1952) observed the scatterers with a sensitive ionosonde, and detected them over a frequency range of 1.6 to 4MHz (also see Chapter I, Section 1.4.1a). However, the sensitivity of this system was quite poor relative to the systems used in this thesis. Few other simultaneous observations of these scatterers at several frequencies have appeared in the literature, and those which have been published have not compared the scattered powers quantitatively. Belrose and Burke (1964) used frequencies of 2.66 and 6.27MHz, and found that scattered powers for the second case were about 20dB down compared to 2.66MHz, but no great accuracy was achieved. Little detailed comparison of powers for individual layers was presented. Titheridge (1962a) also compared powers at .72MHz and 1.42MHz, but again only general features were investigated, and the angular spectra of the scatterers were not considered properly.

The receiving array at Buckland Park is resonant at 1.98MHz, but can also receive radiation efficiently at the third harmonic, which is close to 6MHz. A transmitter operating at 5.995MHz was built at Buckland Park, and began operation in late 1979 (see Chapter III for details). It thus became possible to do simultaneous 2 and 6MHz experiments at Buckland Park, and detailed comparisons of power could be made once the systems had been correctly calibrated (see Chapter III).

This chapter presents results of such nearly simultaneous comparisons. It is also believed that this is the first time such comparisons have been made on 2 frequencies using equipment which could record both amplitude and phase. This allowed coherent integration, and also Doppler measurements of vertical motions. However, the facility to swing the narrow beam of the array has not yet been utilized at 6MHz.

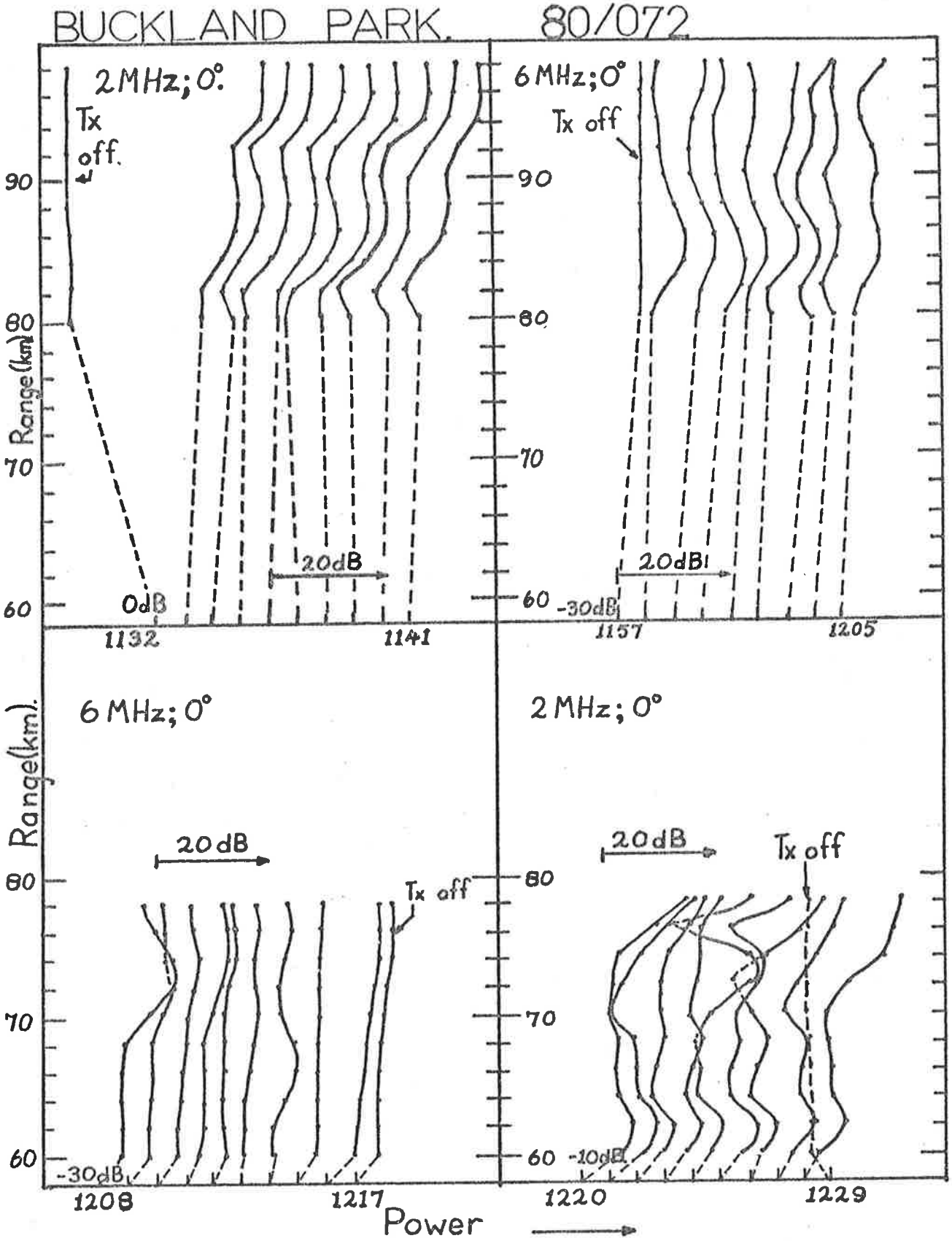

Fig. 10.1 One minute mean power profiles at Buckland Park for day 80/072, using narrow beams. Noise has not been removed. Noise levels can be seen by examining the "Tx off" curves. The reference levels for each set of graphs are shown in the bottom left-hand corners, and each graph is shifted 5dB to the right from the previous one. The times indicated are the start times of each minute. The peak at 62km for 2MHz is a ground echo effect. The 2MHz powers are dBs of $(\mu Pr_{2M})^2$, (sometimes denoted $(\mu Pr_M)^2$) and 6MHz powers are in dBs of $(\mu Pr_{6M})^2$. The large powers at ranges of greater than 94km at 2MHz are due to E-region total reflection. The weak peaks at >94km at 6MHz may be due to a weak scattering layer, or obliques (see text).

10.2 Experimental results

10.2.1 Power profiles and temporal variations

The received signal was digitized as in-phase and quadrature components, at a frequency of 10Hz per range step, and 10 ranges were recorded simultaneously at steps of 2km. Coherent integration over sets of 8 points was then used, to give an effective data rate of 1 point every 0.8 seconds at each range.

The general procedure adopted was to take 10 minute sets of data, at (i) 2MHz,0°; (ii) 2MHz,11.6° and (iii) 6MHz,0°. It was not possible to do all these simultaneously, but in the future this should be possible. During each 10 minute run, the transmitter was turned off for 1 minute, to give a measure of the noise level. At some stage during the day the system was set up to record partial reflection drifts as well, and thus winds were recorded for at least half an hour, close to the periods of observation.

These data were then analyzed on a computer, generally in one minute blocks. Mean noise powers for each 10 minute period were calculated by using the minute of data when the transmitter was turned off, and also by utilizing the spikes at zero lag of the autocorrelation function, as described in Chapter VI. All estimates showed reasonable agreement, although at times a significant non-random noise component occurred. The mean powers for each minute were then calculated, and plotted as a function of height. Fig.10.1 shows some examples. It will be noticed that the heights of enhanced scatter at 2MHz and 6MHz are in good agreement, and the usual temporal variation of scattered power will be noted, particularly below 80km, where bursts of scatter can be seen surrounded by periods of little scatter.

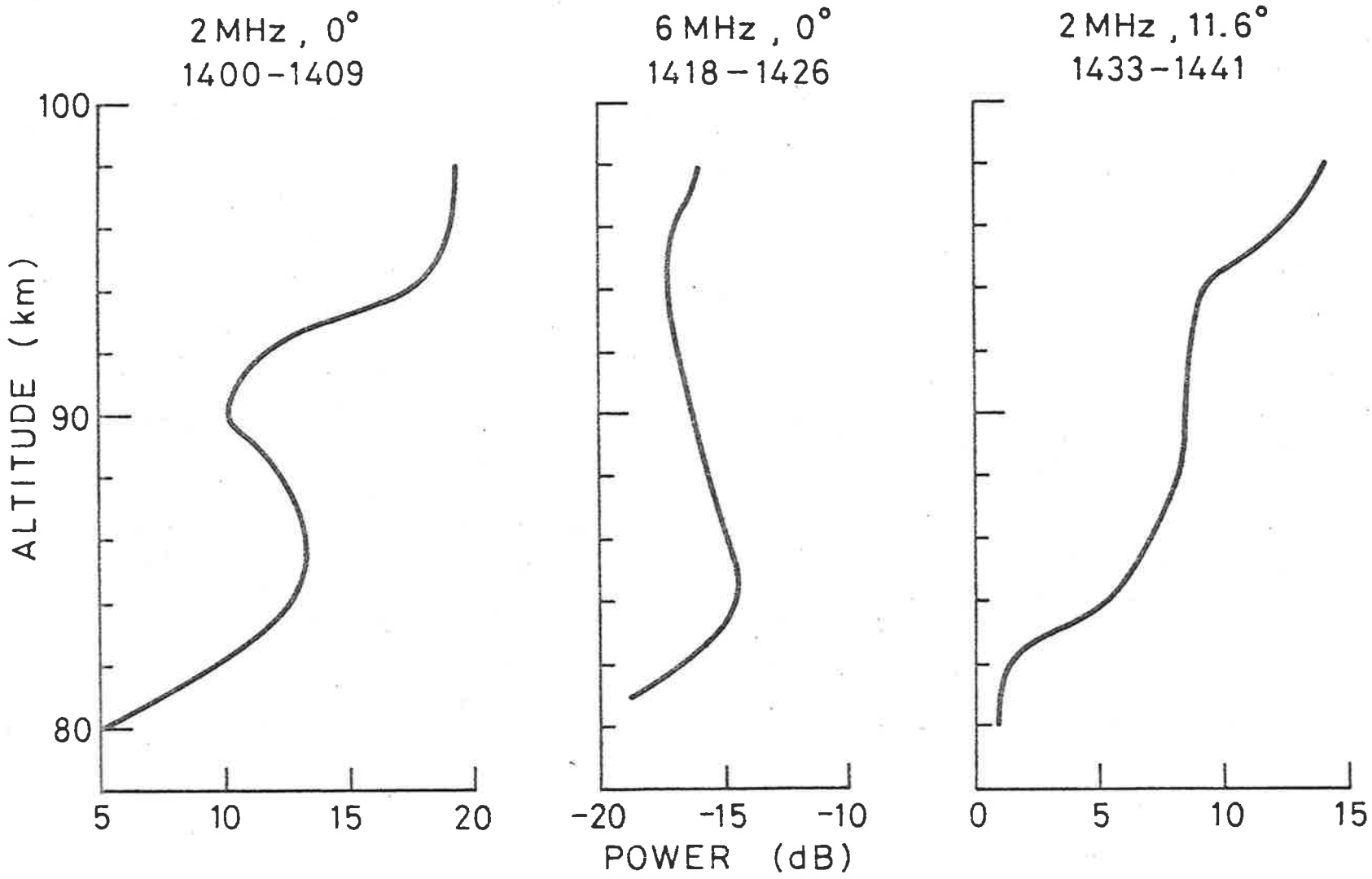

Fig. 10.2 Typical power profiles for day 79/290 at Buckland Park using the narrow beam and 0 mode polarization, for 80-98km. The noise has been subtracted. The powers are in $(\mu Pr_M)^2$ for 2MHz, and $(\mu Pr_{6M})^2$ for 6MHz.

To convert to effective reflection coefficients, see text. Noise levels were typically ≃ - 18dB at 2MHz, and ≃ - 26 dB at 6MHz. [These noise levels are also in units of $(\mu Pr_M)^2$ and $(\mu Pr_{6M})^2$]

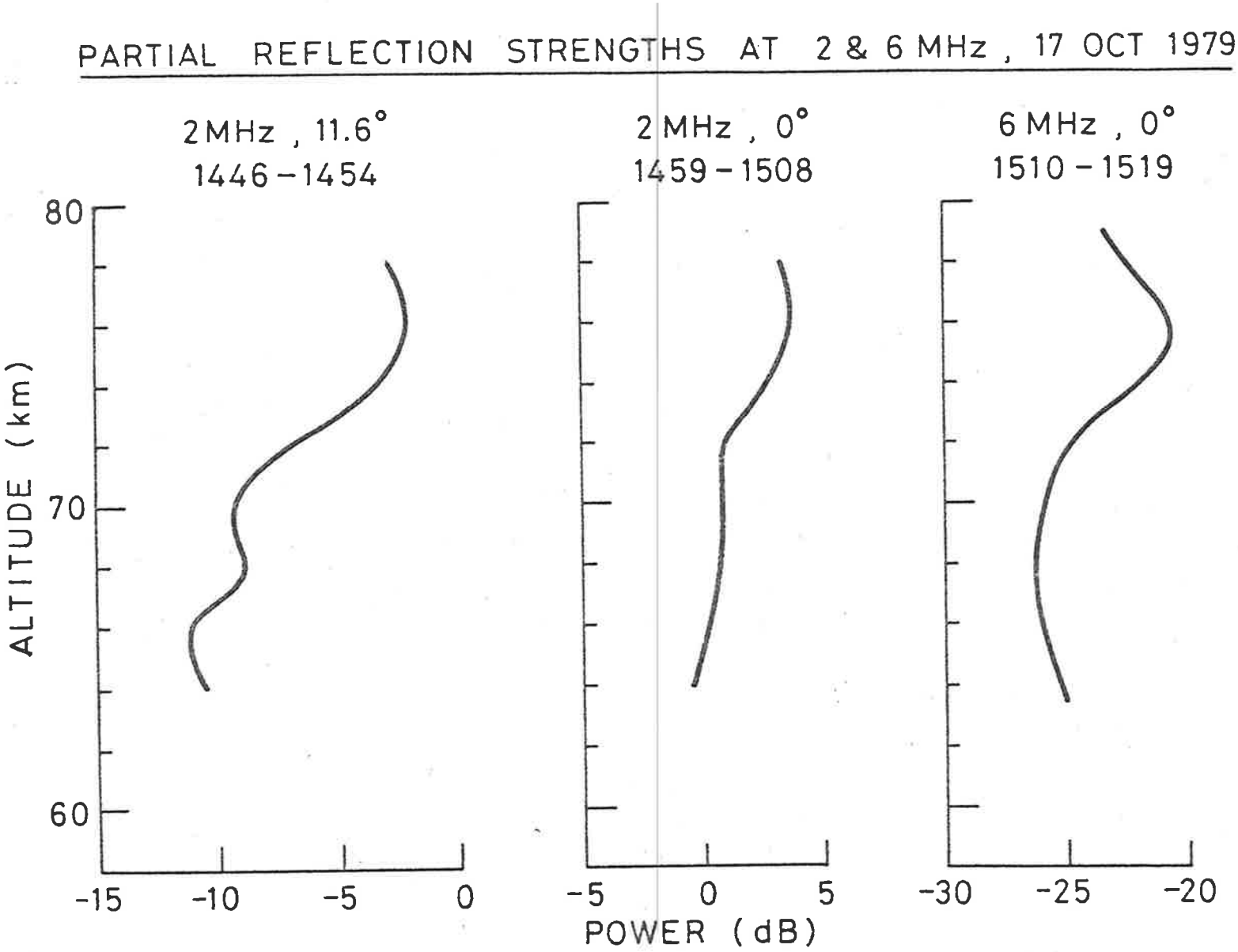

Fig. 10.3 Typical power profiles for day 79/290 at Buckland Park using the narrow beam and 0 mode polarization, for 60-78 km range. Noise has been subtracted. Noise levels were the same as those indicated in Fig. 10.2.

It should be remembered that the powers at 2 and 6MHz cannot be compared directly. However, if effective root mean square reflection coefficients are found [i.e.

(10.2.1.1) $(\overline{R^2})^{\frac{1}{2}} = K_* H \sqrt{\text{Power}}$ (Ch III, equn. 3.3.2.14)],

then these may be compared. Here, H is the range of scatter, and K_* is equal to K_{*2M} for 2MHz and K_{*6M} for 6MHz. According to table 3.1, Chapter III, $K_{*2M} = .8 \pm .4$, and $K_{*6M} = 3.8 \pm 1.6$.

For more accurate comparisons of power, these one minute profiles were averaged and then the noise was subtracted, to leave a profile of signal only. By averaging the full 10 min. set of profiles (except the noise profile), temporal variations in power were reduced.

Figs. 10.2 and 10.3 show typical power-height profiles. In each case, the noise has been subtracted. Noise levels are indicated in the captions, and refer to the levels after coherent integration. It is immediately evident that the ranges of enhanced scatter are similar at 2 and 6MHz. The 2MHz echoes (0°) peak at about 85km, 76.5km and 68km, and those for 6MHz peak at about 84km and 75.5km. It is not clear whether the slight 1 km difference in 2 and 6MHz heights of preferred scatter was due to the fact that the records were taken at different times, whether it was due to an error in setting the range markers, or whether it was due to an error in setting the range markers, or whether it was a real effect. However, the consistent 1 km difference suggests that the reason was instrumental. [The transmitter pulses at 2 and 6MHz were adjusted as nearly as possible to have zero delay with respect to the 0 km range marker, but this could only be done with certainty to about a 1 km accuracy. Further, the 2 and 6MHz

receivers could have had slightly different delay times, and this could also account for the 1 km range difference.] The strong echo at 98 km at 2MHz was due to the leading edge of the E region totally reflected echo. The echo evident above 98km at 6MHz is quite interesting. It could be due to a low sporadic E at around 100km (6MHz is not totally reflected from the regular E region). However, recall from Fig. 3.12b that the array has 4 grating lobes at about 33.5° from the zenith when used at 6MHz. If the scatter from the ~ 85km echo were quasi-isotropic, radiation scattered by this layer at angles of around 33° would be received strongly through these grating lobes and would appear as a peak in power at around 102km range (This effect is illustrated in Fig. 10.10). Thus the rise in power around 100km at 6MHz could indicate that scatter from the 84km layer at 6MHz could contain a significant quasi-isotropic component. More work needs to be done to ascertain if this is so. At 2MHz, the scatter from the ~ 85km certainly contains a quasi-isotropic component. This can be seen by the powers received at 2MHz, 11.6°, which are only about 5dB down on those received at 0°. Further, the range of the echo "peak" is closer to 88-90km at 11.6°, also indicating off-vertical scatter. This contrasts with the ~ 68km echo, where it can be seen that the 11.6° signal at 2MHz is down in strength by ≃ 10dB compared to the 0° signal. For the 76km echo, the 11.6° signal is down by ≃ 6dB compared to the 0° signal at 2MHz. However, notice that the 0° and 11.6° ranges in the latter case are similar, and this suggests that the off-vertical scatter is not very large. The fact that the powers are only ≃ 6dB different may be a result of temporal variations - stronger scatter may have occurred during the 11.6° period. Strong temporal variations are a more serious problem below 80km than above.

Fig. 10.4

Typical power profile (≃ 10 min means) for day 80/072 (12th March, 1980) at Buckland Park using the narrow beam and 0 mode polarization. Noise powers have been subtracted, but the noise levels are also indicated. Powers are in dBs of $(\mu Pr_{2M})^2$ for 2MHz and dBs of $(\mu Pr_{6M})^2$ for 6MHz. The numbers associated with each graph are the frequency used, the angle of tilt of the beam from the vertical, and the start time of each ≃ 10 min block.

The 2 and 6MHz profiles look similar, although the profiles at 1208 and 1220 are a little different. This discrepancy occurs because the 1208 to 1218 profile was dominated by a very strong burst at 1208 to 1209 (see Fig. 10.1) which biased the profile.

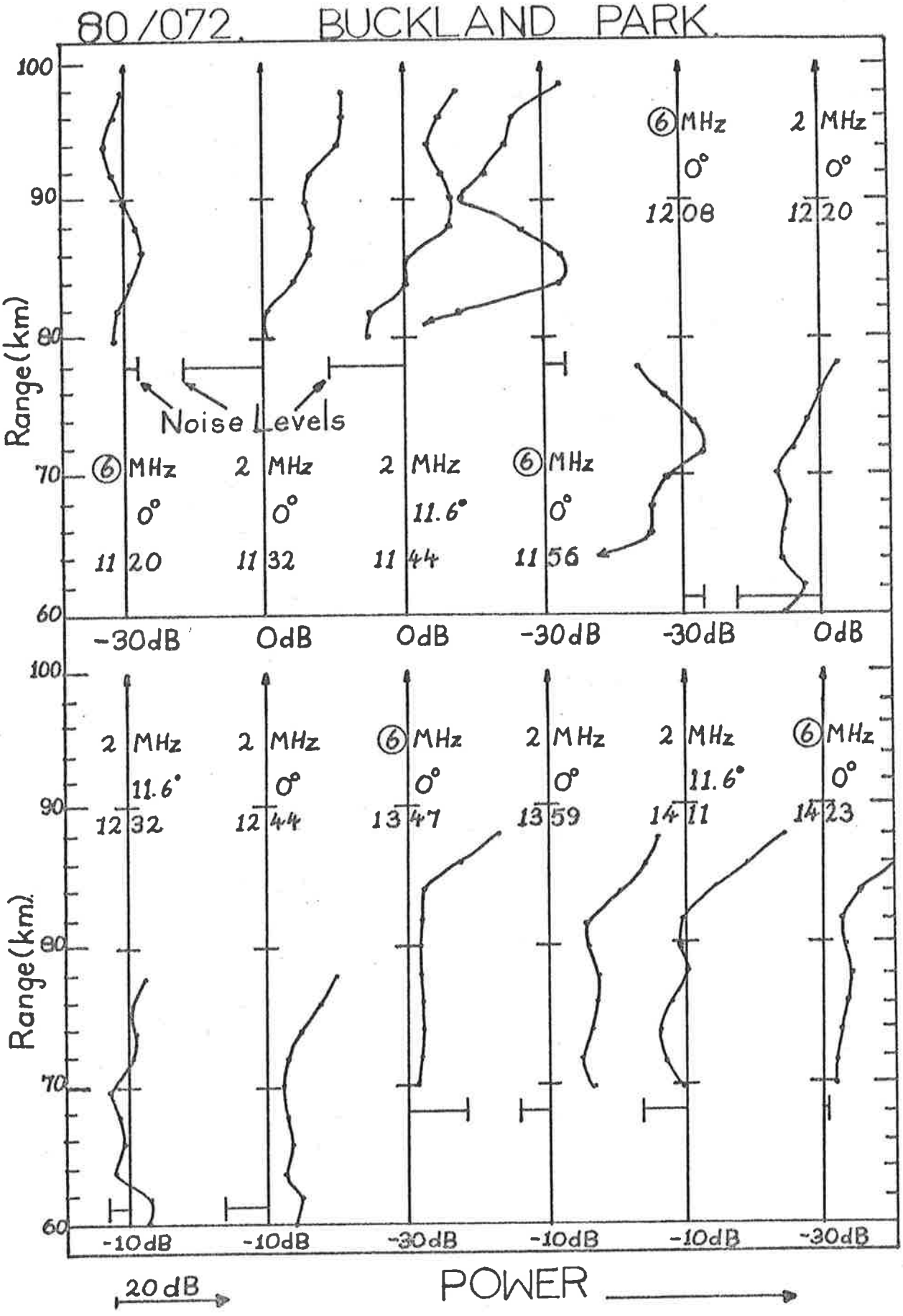
80/072. BUCKLAND PARK.
Range (km)
100
90
80
70
60
Noise Levels
⑥ MHz 0° 11 20
2 MHz 0° 11 32
2 MHz 11.6° 11 44
⑥ MHz 0° 11 56
⑥ MHz 0° 12 08
2 MHz 0° 12 20
-30dB
0dB
0dB
-30dB
-30dB
0dB
2 MHz 11.6° 12 32
2 MHz 0° 12 44
⑥ MHz 0° 13 47
2 MHz 0° 13 59
2 MHz 11.6° 14 11
⑥ MHz 0° 14 23
-10dB
-10dB
-30dB
-10dB
-10dB
-30dB
20dB
POWER

These qualitative results are all quite consistent with conclusions reached in Chapter IV. Of more quantitative importance are the ratios of 2 and 6MHz effective reflection coefficients. According to Table 3.1, Chapter III, K_{*2M}/K_{*6M} is equivalent to -13.5dB ± 9 dB. Then the ratios of effective RMS reflection coefficients $(\overline{R^2_{2MHz}}/\overline{R^2_{6MHz}})^{\frac{1}{2}}$ for day 79/290 were:

(10.2.1.2a)
$$\begin{cases} 14\text{dB} \pm 9\text{dB at 85km, and} \\ 11\text{dB} \pm 9\text{dB at 76km.} \end{cases}$$

However, notice from Table 3.1 that the nearest K_{*6M} value to day 79/290 was taken on day 79/248, when $K_{*6M} = 2.4$. If this value were used, the effective reflection coefficients would have had ratios, for day 79/290, of

(10.2.1.2b)
$$\begin{cases} 18\text{dB at 85km, and} \\ 15\text{dB at 76km.} \end{cases}$$

Similar profiles are shown in Fig. 10.4 for day 80/072. Echo peaks occurred at about 86km, 70-74km and 66km before 1300 hours. Later in the day, an echo from around 78km became noticeable. The profiles shown in Fig. 10.4 have had the noise removed, and the noise levels are also indicated. The noise levels at both 2 and 6MHz are similar to those for day 79/290, but notice that the signal levels are weaker. The signal to noise ratios at 6MHz reach maximum values of only 3 to 4dB. Using K_{*2M}/K_{*6M} equal to - 13.5dB ± 9dB, gives $(\overline{R^2_{2MHz}}/\overline{R^2_{6MHz}})^{\frac{1}{2}}$ values of

(10.2.1.3a)
$$\begin{cases} 18.5\text{dB at 86km} \\ 10\text{dB at 78km} \\ 18.5\text{dB at 66-68km} \end{cases}$$

The value for the 70-74km echo is not given, as a very strong burst of scatter occurred during the 6MHz run, and this would badly bias the results. The value at 66-68km is also considered unreliable, (the period 1208-1230 was used for this estimate), as the signal to noise ratio was no better than -8dB at 6MHz, so small errors in subtraction of the noise powers could severely bias the results.

Notice that from Table 3.1, $K_{*6M} \simeq 2.7$ on day 80/072, and if this value is used for comparing the data, K_{*2M}/K_{*6M} is -10.6dB. Thus $(\overline{R^2}_{2MHz}/\overline{R^2}_{6MHz})$ is equivalent to

(10.2.1.3b) { 21.5dB at 86km, and
13.5dB at 78km

One last point regarding the similarity of the heights of scatter at both frequencies is worthy of comment. It has been assumed all through this thesis that the scattering is due to a structure containing a wide range of Bragg scales (e.g. turbulence, or steps in refractive index). However, a structure which consisted of horizontally stratified sinusoidal oscillations in refractive index in the vertical direction with a Bragg scale of 75.75m could equally cause the specular scatter observed at 1.98MHz. Such a structure would only cause scatter at 1.98MHz, however, and the fact that scatter does occur simultaneously at these two frequencies from the same height helps to dismiss such models.

10.2.2 Fading times and power spectra

As seen in Chapter VII, beam broadening is the dominant contributor to the spectral widths at 2MHz (and hence the width of the autocorrelation function and the fading period). The half-width due to beam broadening is:

(10.2.2.1) $$f_{\frac{1}{2}} \simeq (2/\lambda) \cdot v_H \, \theta_{\frac{1}{2}}$$

(e.g. see Chapter VII, equation 7.3.1.2), $\theta_{\frac{1}{2}}$ being the half-power half-width of the polar diagram produced by the combined effects of the array and the scatterers, λ the probing wavelength, and v_H the horizontal wind velocity. For isotropic scatter, $\theta_{\frac{1}{2}} \simeq 4.5°$ at 1.98MHz and $\theta_{\frac{1}{2}} \simeq 1.4°$ at 6MHz when the whole array at Buckland Park is used for reception (see Chapter III, Figs. 3.12). Thus if the scatterers are reasonably isotropic out to zenith angles of about 10°, and turbulence is not important, then the spectral widths should be similar at 2 and 6MHz, since $\theta_{\frac{1}{2}}/\lambda$ is approximately the same at each frequency.

However, other factors could affect this result. If the scatterers in a layer ℓ_1 are totally isotropic, scatter will be received through the 6MHz grating lobes. This will not affect the fading rates due to the near-vertical scatter from layer ℓ_1, since it will be from a much greater range, but it could affect apparent fading rates and powers in a higher layer. There is thus a possibility of mixing the effects of two layers. A second, more important factor concerns the effective polar diagram. If the scatterers are not isotropic, this will alter the effective polar diagram; the values of $\theta_{\frac{1}{2}}$ may no longer be proportional to λ. A third point concerns the motions of the scatterers themselves. It was seen in Chapter VII that for turbulence at about 86km, the

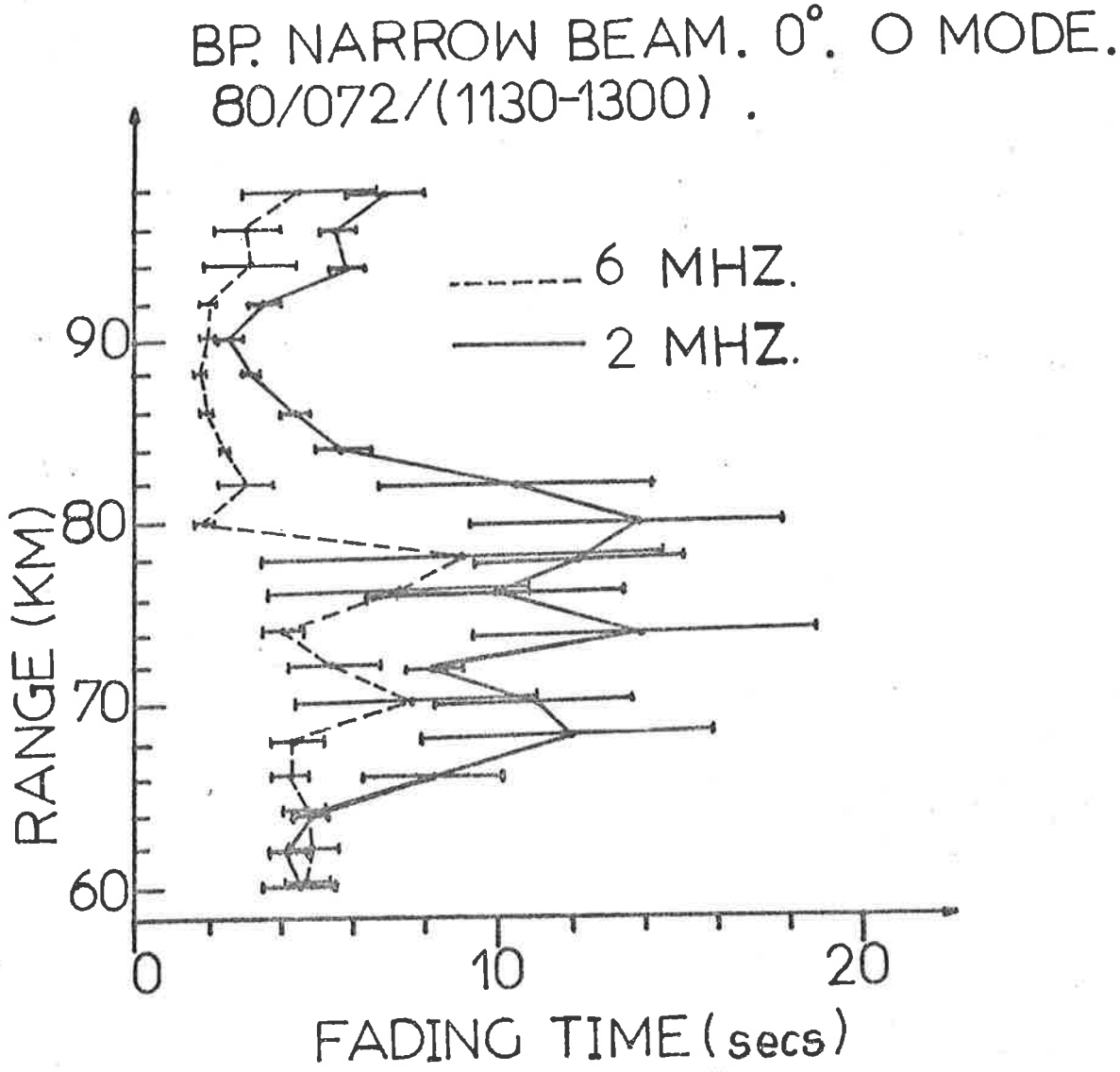

Fig. 10.5

Typical fading times for day 80/072. The fading times were obtained from one-minute complex autocorrelation functions. The 2MHz (1.98MHz) results were also presented in Fig. 7.4, Chapter VII. All points are averages of sets of about 8 to 10 one-minute fading times. Error bars are standard deviations for the mean. The data for 2MHz, 80-98km, was for the period 1132-1142 hrs, and for 2MHz, 60-78km, was for the period 1245-1254hrs. At 6MHz, the 80-98km data was for the period 1156-1206, and the 60-78km data was for the period 1208-1217. The 6MHz data below 80km could be affected by contaminant signals.

RMS velocities associated with Bragg scales for 1.98MHz backscatter were not a major contributor for v_H values of $\simeq 70 ms^{-1}$. Upper limits ($\simeq 3 ms^{-1}$) could be placed on the values, but no more. (The possibility of obtaining v_{RMS} would be improved for smaller v_H values). Turbulence alone would produce a half-power half-width of the spectrum of

(10.2.2.2a) $$f_{\frac{1}{2}} \simeq 2/\lambda \sqrt{2 \ell n 2}\ v_{RMS}$$

(Chapter VII, equation 7.4.2.2). Since $v_{RMS} \simeq (\varepsilon_d \ell)^{1/3}$, $\ell = \frac{\lambda}{2}$ being the Bragg scale (see Chapter II, equation 2.2.3.3a), then

(10.2.2.2b) $$f_{\frac{1}{2}} \propto \lambda^{-2/3}.$$

The beam-broadening effect for isotropic scatter is fairly independent of frequency if the same array is used (equation 10.2.2.1), so turbulence clearly should make a slightly larger contribution at higher probing frequencies. Whether it is a significant contribution or not will be seen shortly.

Fig. 10.5 shows a profile of mean 1 minute fading times, using the complex autocorrelation with the spike at zero lag removed. Clearly the 6MHz values are generally less than the 2MHz values. Some care must be taken before interpreting this data, however, particularly for 6MHz below 80km. Recall that the signal to noise ratio was quite low (often less than 0dB) and some of the noise was at times non-random. Parts of this noise may have been leakage from other parts of the receiving system (e.g. the clock), and some was external. The frequency 5.995MHz is close to a short wave broadcast band, and there was sporadic interference from other short wave sources. The existence of this noise could affect the fading times. The reasons why the fading times are as they are

Fig. 10.6

Raw Power spectrum of 9 minutes of data recorded at Buckland Park using the narrow beam at 6MHz, for the period indicated. This figure may be compared to Figs. 7.6a, 7.7a. Notice also the four very large values close to 0Hz (arrowed). These could indicate specular scatter, but may also be purely statistical effects (see Chapter VII, section 7.3.1).

Fig. 10.7

Fig. 10.6, averaged in frequency blocks of about 20 points. The four very large points in Fig. 10.6 have been ignored, in accordance with the procedure outlined in Chapter VII, Section 7.3.1, since such points unfairly bias the means of their frequency block. The shaded area represents the noise level, and the smooth solid line is an eye-fit to the data. The half-power half-width appears to be about 0.06Hz. Notice this half-width is similar to that for 2MHz ($\simeq$.075Hz; see Fig. 7.13, Chapter VII), as suggested by equation 10.2.2.1 (i.e. λ decreases by 3 times, as does $\theta_{\frac{1}{2}}$, so the two effects cancel).

10.6

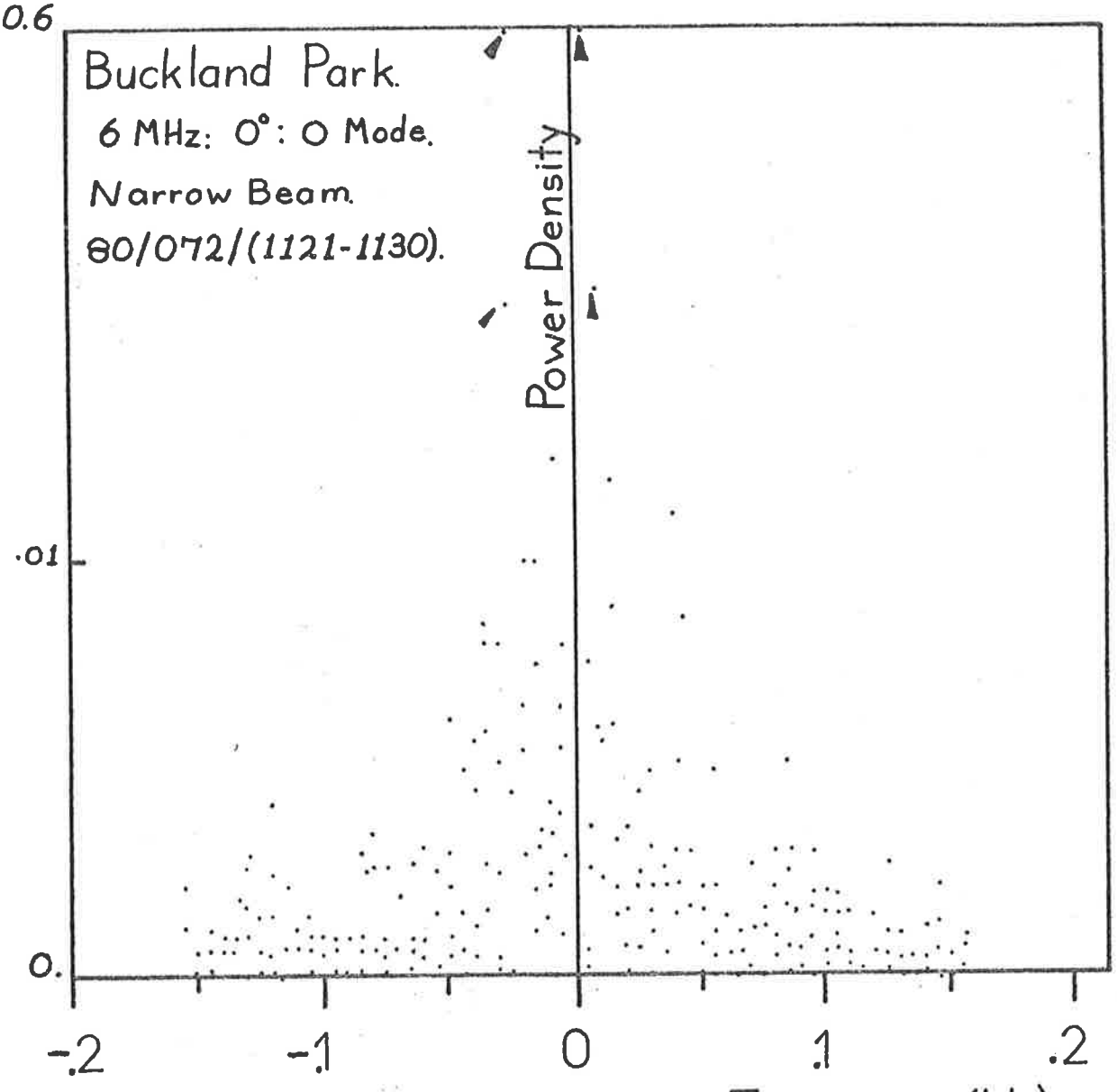
Buckland Park.
6 MHz: 0°: O Mode.
Narrow Beam.
80/072/(1121-1130).
Power Density
.01
0.
-.2
-.1
0
.1
.2
Frequency (Hz)

10.7

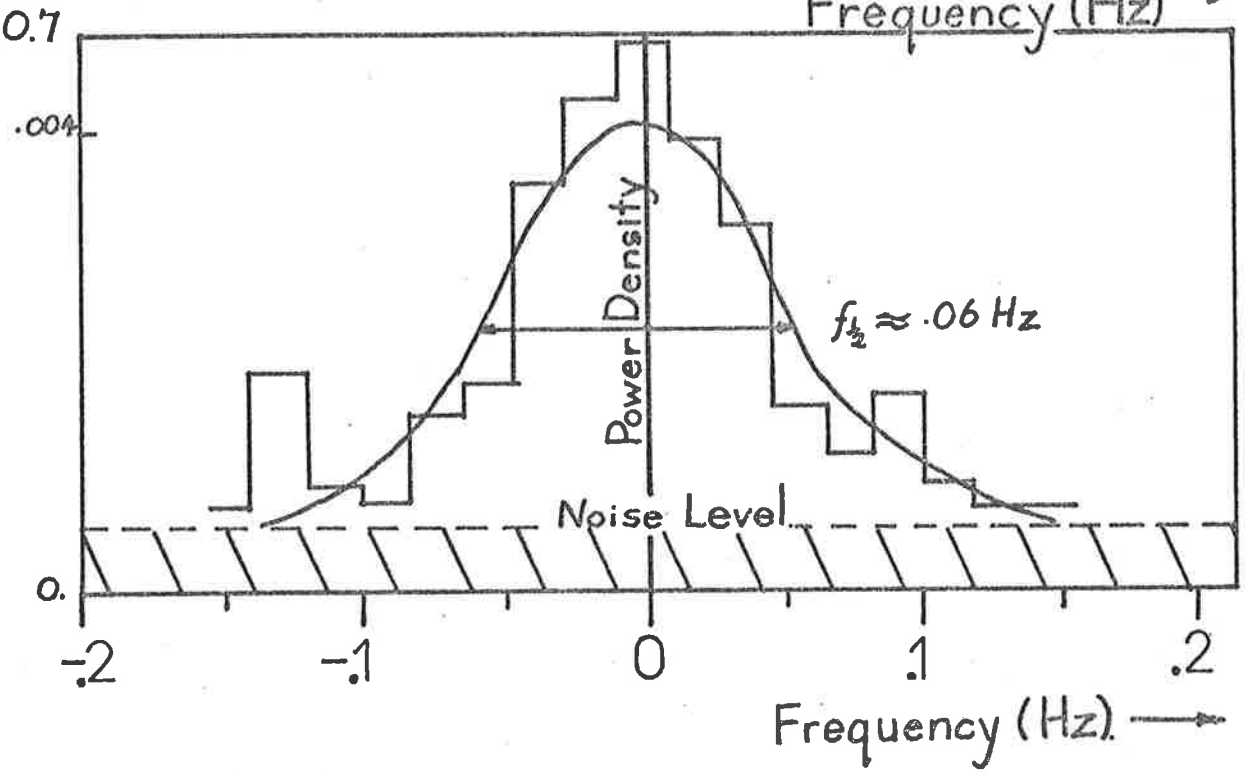
.004
0.
Power Density
$f_{\frac{1}{2}} \approx .06$ Hz
Noise Level
-.2
-.1
0
.1
.2
Frequency (Hz)

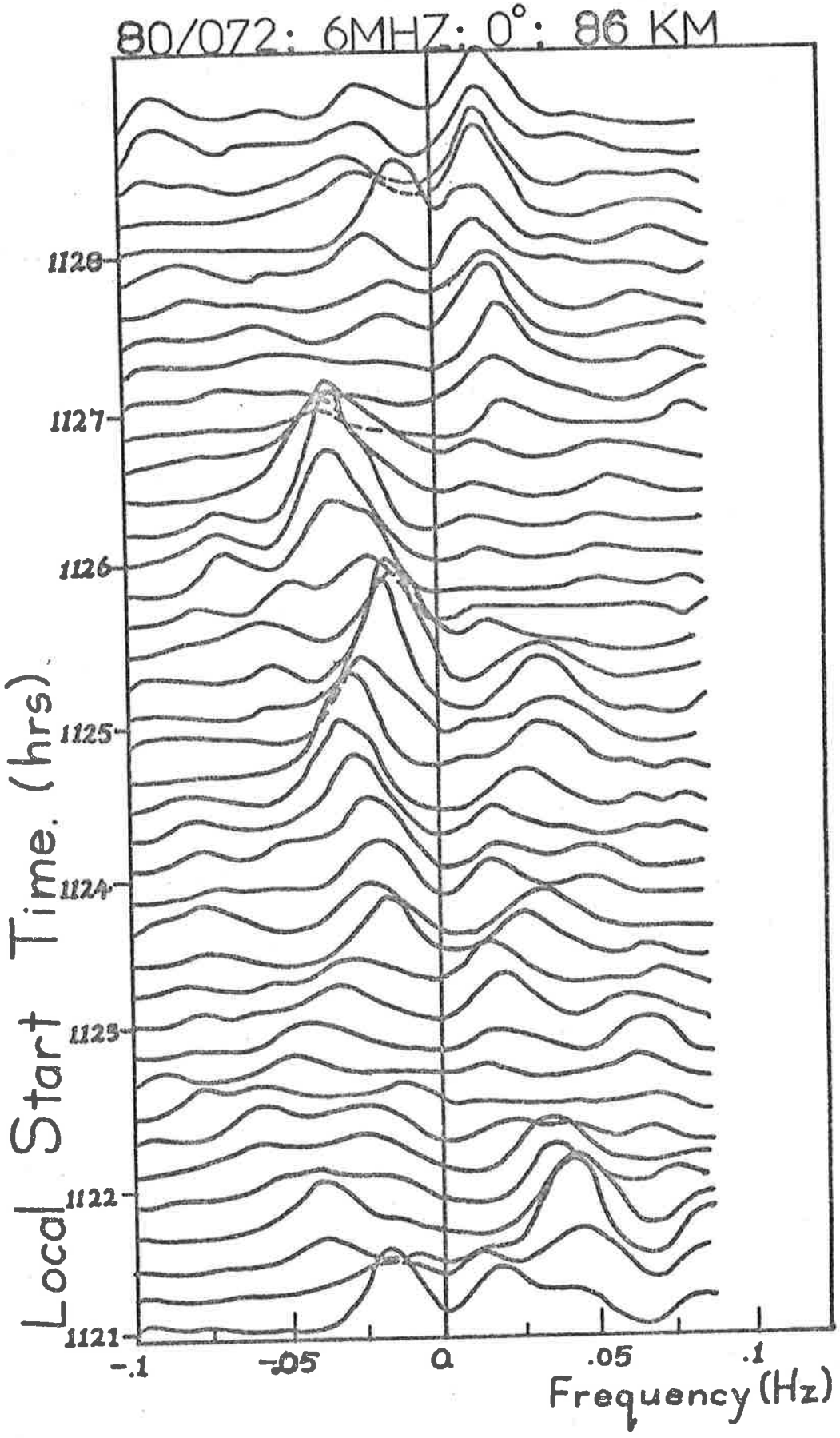

Fig. 10.8

Running power spectra with a 3 point running mean (¼,½,¼) on each spectrum. Each spectrum corresponds to a one minute data block shifted 12 sec along from the previous data block. The spectra are for day 80/072 at 86km range using the narrow beam pointing vertically, for a frequency of 5.995MHz and O mode polarization. Positive frequencies mean a Doppler component towards the receiver. Similar spectra were presented in Chapter VII, Fig. 7.12, for 2MHz. Recall that the appearance of ~5 peaks in succession is not necessarily physically significant.

will not be discussed in much more detail using Fig. 10.5; we saw in Chapter VII that although one minute sets of data can give a rough guide to fading characteristics, they are not reliable for detailed analyses. Meaningless peaks occur in the power spectra, and so forth. Admittedly the values in Fig. 10.5 are means, but it was felt that it would be more useful to examine the power spectra of 5-10 min sets of data.

Fig. 10.6 shows the raw power spectrum, and Fig. 10.7 shows the smoothed power spectrum (compare these to Figs. 7.6c, d, and 7.13, for example), for 80/072, 1121-1130 hrs. The observed half width is about 0.06Hz (error is probably greater than 10%) compared to the expected width due to beam broadening alone (calculated by program Specpol) of about .07Hz. Thus once again, as for 1.98MHz, it is very difficult to detect a significant turbulent scatter contribution. By placing upper limits on the width of the power spectrum, it was possible to say that the RMS velocity of the scatterers at 6MHz was less than $1ms^{-1}$, but little more can be stated with certainty. As a different way of viewing the data, Fig. 10.8 shows the running power spectrum for the 6MHz data at 86km for the period 1121-1130 hrs.

The closeness of the observed and expected spectral widths at 86km suggests that scatter at 6MHz is reasonably constant in strength out to angles of a few degrees. The widths of the observed spectra offers a possibility of determining some information about the nature of the scatterers - if the scatterers were quite specular, the observed spectrum should be narrower than that estimated by equation 10.2.2.1, (or, better, by program Specpol). However, the narrow nature of the 6MHz polar diagram makes this a very difficult experiment, and no useful results were obtained.

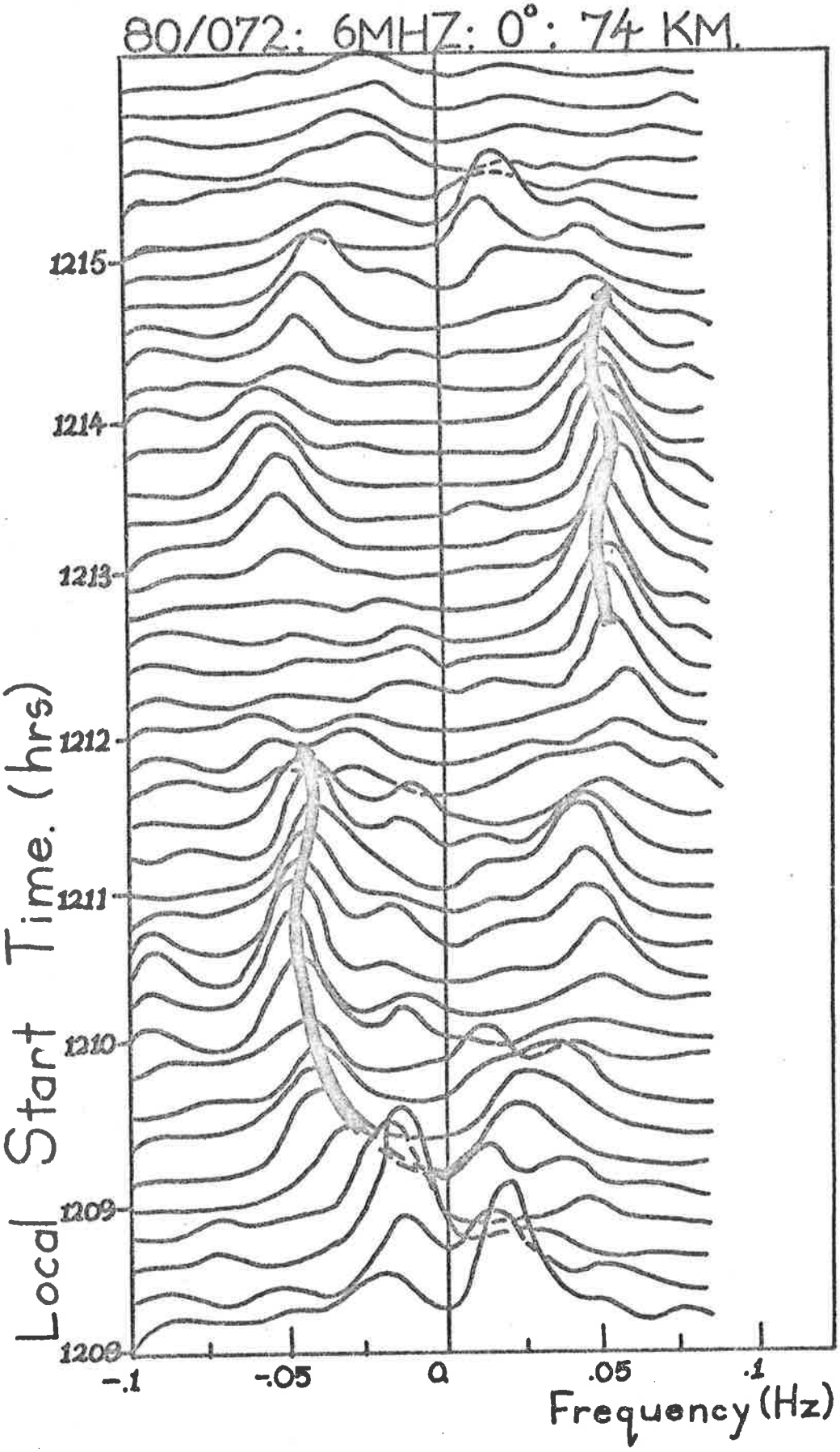

Fig. 10.9

Running power spectra with a 3 point running mean (¼,½,¼) on each spectrum. Each spectrum corresponds to a one minute data block shifted 12 secs along from the previous data block. The spectra are for day 80/072 at 74km range, using the narrow beam pointing vertically and for a frequency of 5.995MHz with O mode polarization. Positive frequencies mean a Doppler component towards the receiver. Similar spectra were presented in Chapter VII, Fig. 7.14, for 2MHz. The black arrows indicate possibly significant strings of spectral peaks.

It would be much easier to do with an array with a wide polar diagram. This is one major experiment at 6MHz which has not yet been performed - direct determination of the height profile of the angular spectrum of the scatterers at 6MHz. Some indirect information will be seen shortly, and in section 10.3. Such determinations would be best done by tilting the array beam, but failing this, calculation of the powers and spectra with both a wide-beamed array and the narrow beam could give information. Isotropic scatter would give a much wider spectrum with the wide beam. For specular scatter, the spectra on the wide and narrow beams would be similar, and the received powers should be the same, after compensation for the different gains of the arrays.

Fig. 10.9 gives some hint as to the angular spectrum of the scatterers at 74km. There appears to be evidence of some frequency peaks maintaining themselves over 2 and 3 minutes, and this could suggest that isolated specular reflectors may cause the signal. For example, a long, flat reflector gradually moving down, and causing mainly vertical reflection, could have caused the string of spectral peaks from 1209 to 1212. The horizontal motion of such a reflector would not be seen in the spectra - the signal would cut in, and disappear, fairly sharply, with a long period of constant signal between appearance and disappearance.

There is clearly more work to be done at 6MHz before a clear appreciation of the nature of the scatterers at that frequency is understood, although the information previously presented for 2 and 50MHz, and the information in Fig. 1.9a, give some idea of the expected results. Turbulent scatter should be weak above about 85km at 6MHz, the scattering scales being in the viscous range (Fig. 1.9a). This is supported by the fact that no strong echoes

above about 86km have yet been detected at 6MHz with the present equipment. Some further support of this statement can be found in Fig. 10.1. The powers at 6MHz fall away much more rapidly with increasing height above 84-86km than those at 2MHz. (The rise in power at 100km at 6MHz has already been discussed).

It is to be expected that below ~70km, scatter should be fairly specular, since it is apparently so at 50MHz (see Fig. 4.24, Chapter IV). The analyses presented in Fig. 9.9 can be repeated at 6MHz to gain a better idea of the 6MHz specular to isotropic scatter transition height. This has been done, and results suggest that this height should be around 74 to 81km for $\gamma=2\pi$ to π.

The following section shows some theoretical attempts to simulate the results presented in "equations" 10.2.1.2 and 10.2.1.3, and the results of this analysis allow better interpretation of the information.

10.3 Theoretical Interpretation

10.3.1 Theory and interpretation

It has been discussed elsewhere (e.g. Appendix B, equation B.25) that for reflection from a stratified step less than a quarter wavelength thick in the ionosphere, the reflection coefficient is

(10.3.1.1) $$R(z) \simeq \tfrac{1}{2}\Delta n,$$

where Δn is the change in refractive index across the step. Thus

(10.3.1.2) $$R(z) \simeq \tfrac{1}{2}\frac{\partial n}{\partial N}\Delta N,$$ ($(\Delta\nu)_m$ is assumed negligible; see Ch. VIII, § 8.2.2)

ΔN being the change in electron density across the step. Thus the ratio of reflection coefficients at 2 and 6MHz is

(10.3.1.3) $$R_2(z)/R_6(z) = \left(\frac{\partial n}{\partial N}\Big|_{2MHz}\right)/\left(\frac{\partial n}{\partial N}\Big|_{6MHz}\right)$$

This parameter has been evaluated at various heights in the atmosphere for a typical D-region electron density profile. It has been found that this ratio is approximately 16dB at about 76km, and 16.5dB at 80 to 90km for a 10% step in electron density. The ratio is relatively independent of the step size so can be taken as a constant. It is useful to compare these values to "equations" 10.2.1.2 and 10.2.1.3. It will be noticed that if the K_{*6M} values measured closest to the days of observation are used, then the ratios of reflection coefficients at 74-78km are indeed about 14 to 15dB. This would thus appear to reinforce previous conclusions that scatter from below 80km is largely by Fresnel reflection from sharp steps in electron density. (The actual measured reflection coefficients also are affected by absorption, but absorption is very

weak up to ≃78km (≃1dB for 0 mode, 2MHz, and ≃.3dB for 0 mode, 6MHz)) Further, under this assumption, it is now possible to place even better estimates on the ratio of (K_{*2M}/K_{*6M}). By equation 10.2.1.1,

$$(K_{*2M/K_{*6M}}) = (\overline{R}_2/\overline{R}_6) \cdot \sqrt{\frac{P_6}{P_2}}, \tag{10.3.1.4}$$

Where P_i are the received powers at i=2 and 6MHz. On day 79/290, $P_2/P_6 \approx 24.7$dB, and on day 80/072, $P_2/P_6 \approx -23.5$dB. The expected $\overline{R}_2/\overline{R}_6$ is about 16dB, as deduced, so

$$K_{*2M}/K_{*6M} \equiv -7.5 \text{ to } \rightarrow 8.7\text{dB}$$

$$\text{i.e. } K_{*2M}/K_{*6M} \simeq .42 \text{ to } .37 \tag{10.3.1.5}$$

Of course, there is some error in the P_2/P_6 ratio, since the P_2 and P_6 measurements were not simultaneous. But this is probably quite a good estimate of the ratio.

What about the scatter from ~85km? We have already seen this could contain an important turbulence component. What would be the expected effective reflection coefficient ratio for turbulent scatter?

Recall from Chapter III, equations 3.3.2.19 and 3.3.2.20, that the measured effective reflection coefficient R' can be related to the scattering cross-section η and the effective volume of scatter by

$$\overline{R'^2} = \eta V_{eff} A \tag{10.3.1.6}$$

where

$$A = \exp\{-4 \int_{s=o}^{L} \frac{\omega}{c} n_I \, ds\},$$

h being the range of scatter, ω the angular frequency, c the speed of light in a vacuum, and n_I the imaginary part of the refractive index. The term A represents absorption.

Henceforth, the " ' " on the R will not be used, and R will be taken as the effective reflection coefficient measured at the ground.

Now 10.3.1.6 implies

$$\overline{R_2^2}/\overline{R_6^2} = (\eta_2/\eta_6)\ (Veff_2/Veff_6)\cdot(A_2/A_6) \qquad (10.3.1.7)$$

where "2" refers to 2MHz (1.98MHz actually), and "6" refers to 6MHz (5.995MHz actually). The received power at a range ξ_o is proportional to

$$V(\xi_o) = \int_{all\ space}\int d\Omega\ G_T(\theta,\phi)G_R(\theta,\phi)\{\gamma \otimes g(r)\}\ (\xi_o), \qquad (10.3.1.8)$$

where $G_T(\theta,\phi)$ is the transmitter polar diagram, $G_R(\theta,\phi)$ is the receiving array's polar diagram, $\gamma(r,\theta,\phi)$ is an aspect sensitivity factor, and g describes the transmitted pulse. This equation is a simplification of equation 7.3.2.9 in Chapter VII. The term σ/r^2 in equation 7.3.2.9 has been approximated by $\gamma\eta/\xi_o^2$ where ξ_o is taken as the height of the layer. The ξ_o^{-2} term has been taken outside the integrals and ignored. The backscatter cross-section η has thus been taken as $\eta = \gamma^{-1}\sigma$. For isotropic turbulence, γ should be $(4\pi)^{-1}$ (see Chapter III equation 3.3.2.15). However, the values $V(\xi_o)$ are used only for comparisons of 6 and 2MHz results, so it is only necessary that a consistent convention be used. Thus γ is taken as 1 for all angles in the case of isotropic scatter. It is for the same reason that the ξ_o^{-2} term discussed above can be ignored - it is the same at 2 and 6 MHz.

Hence $V(\xi_o)$ can be regarded as the effective volume of scatter. Also recall that

(10.3.1.9) $\eta = .38\, C_n^2\, \lambda^{-1/3}$ by equation 2.4.1.5, Chapter II, and $C_n^2 = a^2 L^{4/3} |Me|^2$ by equation 2.3.2.11, where L is the outer scale of turbulence and a is a constant.

Combining these equations with 10.3.1.7 give

(10.3.1.10) $$\overline{R_2^2}(\xi_o)/\overline{R_6^2}(\xi_o) = (\lambda_2/\lambda_6)^{-1/3}(|Me_2|/|Me_6|)^2 \cdot (Veff_2(Ro)/Veff_6(Ro))(A_2/A_6)$$

the Veff value being given by equation 10.3.1.8 (the terms like L and a are constants for any particular patch of turbulence so do not depend on the probing frequency.). Finally,

(10.3.1.11) $$M_e = \frac{\partial n}{\partial N}\left(\frac{N}{T}\frac{d\theta}{dz} - \frac{dN}{dz} + \frac{N}{\rho}\frac{d\rho}{dz}\right) + \frac{\partial n}{\partial \nu_m}\frac{\partial \nu_m}{\partial z}$$

(e.g. Chapter II, equation 2.3.2.10a')

The term $\frac{\partial n}{\partial \nu_m}\frac{\partial \nu_m}{\partial z}$ usually is negligible above 80km (see Chapter IX), and the bracketed term is frequency independent. Thus 10.3.1.1 gives

$$\overline{R_2^2}(\xi_o)/\overline{R_6^2}(\xi_o) = (\lambda_2/\lambda_6)^{-1/3}\left\{\left(\frac{\partial n}{\partial N}\right)_2 / \left(\frac{\partial n}{\partial N}\right)_6\right\}^2 (Veff_2(\xi_o)/Veff_6(\xi_o)) \cdot (A_2/A_6)$$

We have already seen that the second term ({ }) is about 16.5dB at 85km, and $(\lambda_2/\lambda_6)^{-1/3} \simeq .7$, or -1.6dB. Calculations with Sen-Wyller formulae for a typical ionosphere show that, for reflection from 85km, A_2 is equivalent to about -2dB, and A_6 is equivalent to about 0.5dB.

Hence

(10.3.1.13) $$R_2^2(\xi_o)/R_6^2(\xi_o) = 10^{\frac{13.4}{10}}\{Veff_2(\xi_o)/Veff_6(\xi_o)\},$$

Veff being calculated by equation 10.3.1.8 . A computer program was written to accurately calculate these effective volumes. A layer about 2km thick was assumed to be based at 85km. Thus γ, the aspect sensitivity term in (10.3.1.8), was taken as 1.0 inside

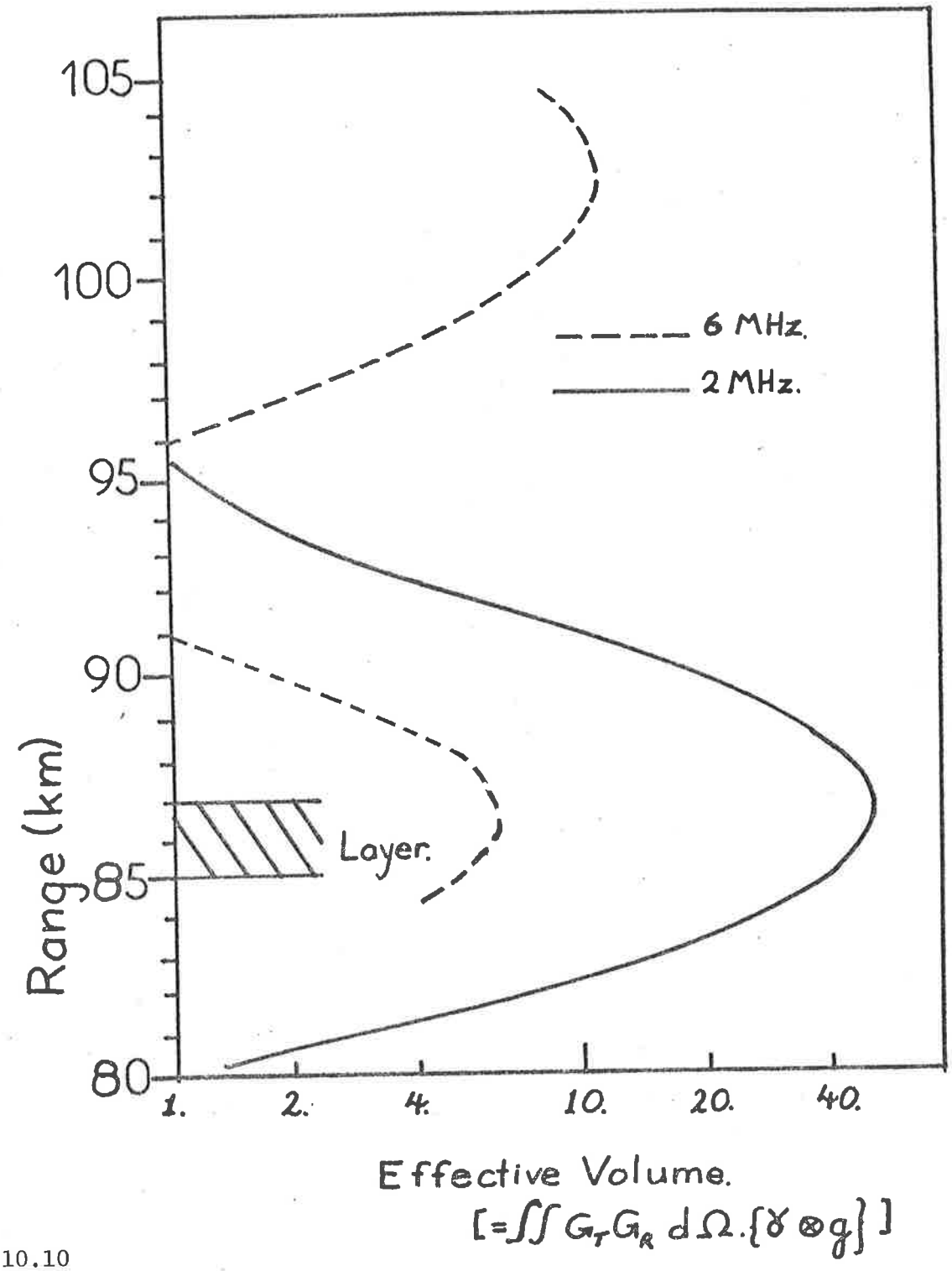

Fig. 10.10

Effective volume as a function of (virtual) range ξ_o, as described by equation 10.3.1.8, for a layer of isotropic scatterers at 85 to 87km. The 2MHz curve peaks about 9.2dB above the 6MHz curve. Notice also the profile peaks at ~102 to 103km for 6MHz. This is due to leakage in through the grating lobes of the array. The assumed pulse had a form $\exp\{-h^2/3^2\}$, which is slightly wider than the pulse normally used at Buckland Park, but adequate for these purposes.

the layer (isotropic scatter), and zero outside, and the effective volume for this layer was calculated as a function of range at 2 and 6MHz using program "Volscat". (see Appendix G). The program is similar to program "Specpol", which was used in Chapter VII, but in this case it has not been necessary to calculate as a function of the Doppler frequencies (alternatively, it would have been possible to integrate the spectrum produced by program "Specpol" over all frequencies). The results of such calculations are shown in Fig. 10.10. At the peaks,

(10.3.1.14) $$Veff_2/Veff_6 = 9.2dB$$

Hence, by equation 10.3.1.14,

(10.3.1.15) $\overline{R_2^2}(\xi_o)/\overline{R_6^2}(\xi_o) = 22.6dB$ for a 2km thick layer at about 80 to 85km.

Thus the expected 2 and 6MHz effective reflection coefficients will be in the ratio of about 23dB for turbulent scatter. This can be compared to the values of 18dB and 21.5dB for days 79/290 and 80/072 respectively at ~85km (see 10.2.1.2b and 10.2.1.3b). These results suggest that there is a turbulence contribution to the signals received from above 80km, since the observed ratios are greater than that expected for purely Fresnel reflection. (A step in refractive index which is not infinitely sharp could also produce an increased $\overline{R_2^2}/\overline{R_6^2}$ value, since reflection would be more efficient at 2MHz. However, such a step is likely to be about a Kolmogoroff microscale (see Chapter IX) in vertical extent, and it was shown in Fig. 9.9 that such a step is quite inefficient as a reflector at 86km and would not be detected. The observed quasi-isotropy of scatter also suggests non-Fresnel reflection. The effect of a

large electron-density ledge at ~86km should be considered, however, and this will be done shortly.)

This observed ratio thus supports previous conclusions regarding turbulent scatter from above 80km. If in fact (K_{*2M}/K_{*6M}) is taken as 0.4, as suggested by equation (10.3.1.5), then the effective reflection coefficient ratios at 2 and 6MHz for the ~85km echoes are about 22dB on day 79/290, and 24dB on day 80/072, (compared with equations 10.2.1.2 and 10.2.1.3) which gives even better agreement with the expected turbulence results.

One more test can be carried out. Recall that specular reflection from the large electron density ledge at ~85km makes a significant contribution to the scatter from this height at 2MHz. Is this also true at 6MHz? Program "Scatprf" was run for the same ledge as that discussed in Chapter VIII, but for a frequency of 6MHz. It was found that the measured 6MHz specular reflection coefficient should be down by 24dB compared to that at 2MHz (this includes the effect of absorption). Thus this is also consistent with the observed experimental values. It is felt that it is coincidental that the ratios of scatter strengths for 2 and 6MHz for specular and turbulent scatter are the same. It does mean, however, that comparisons of 2 and 6MHz strengths from this ledge cannot be used to distinguish between specular and turbulent scatter, but other methods available have already suggested that both processes are important (see Chapter VIII.).

10.4 Conclusions

Calibration and comparison of 1.98 (~2)MHz and 5.995 (~6)MHz ionospherically scattered radiation suggests that at heights below 80km, 6MHz scattering strengths are down by ~16dB when compared to 2MHz, and above this height the ratio is closer to 22-24dB. This evidence supports previous claims that scatter from below about 76-80km is Fresnel-like at both frequencies, and that scatter from above 80km contains a significant (possibly major) contribution from turbulent scatter. As pointed out in Section 10.2.2, the transition height of dominantly specular to dominantly turbulent scatter is probably slightly lower for 6MHz than for 2MHz. It was also found that a large electron density ledge at ~85km, similar to that discussed in Chapter VIII, is also capable of causing a component of specular scatter at 6MHz of similar magnitude to the turbulent scatter. No 6MHz scatter from above ~85-90km has been observed, except for possible weak sporadic-E effects, and this supports information presented in Table 1.9a, Chapter I, which shows that the Kolmogoroff microscale reaches 25m at about 88 to 90km. This is also consistent with Fig. 4.23, Chapter IV. Hence little turbulent scatter would be expected from above these heights at 6MHz.

CHAPTER XI

DISCUSSION AND CONCLUSIONS

11.1 Introduction

It is believed that during the course of this thesis, a clearer picture of D-region scatterers has emerged. Some conclusions have been reached which the author feels confident about, and the next section provides a summary of these points.

However, there are also some points which are still as yet unresolved. These include the reasons for preferred heights of scatter, the reasons for the presence of specularly scattering irregularities, and the causes of the seasonal dependence of the properties of the echoes. Some space is devoted to a discussion of these points in section 11.3, and some speculation is presented.

Finally, possible experiments for the future are discussed.

11.2 Summary of Facts

Most of the earlier conclusions reached by other authors regarding HF scattering in the D-region remain unchanged. These have been discussed in Chapter I, Section 1.4.1. In particular, the echoes occur between 60 and 100km, with reflection coefficients increasing roughly exponentially from 10^{-5} to 10^{-4} at 60 to 70km to about 10^{-3} (and often greater at night) at 90km. Preferred heights of scatter exist, especially at ~65km, 70-74km, ~85km, and ~90-95km. Fading is slowest at the heights below 80km, and faster above this height. Scatter is also quasi-isotropic above 80km, but Fresnel-like below 75-80km. The echoes are strongest in winter, and almost non-existent in summer, particularly those from below 80km. Scattering layers can last from minutes to hours, and even days.

However, the work presented in this thesis has clarified many points concerning these scatterers. The following results have been established.

1. A detailed formula for estimation of turbulent scatter strengths has been developed in Chapter II, (e.g. equations 2.3.2.10a).

2. The first direct investigations at HF of D-region angular scattering characteristics have been presented. Results support previous indirect measurements indicating specular scatter below ~80km and quasi-isotropic scatter above.

3. Detailed plots of power as a function of height and time have shown quite conclusively that preferred heights of scatter do exist on any one day. These plots have also shown that strong temporal variations in power can occur, particularly at heights below 80km. Bursts of power ~10dB stronger than "normal" levels often occur at these lower heights, and typically last for periods of about 1-5 minutes. Above 80 km, bursts are typically ~ 3 dB above "normal" levels.

At all heights, bursts often have a quasi-periodicity, typically of ~ 5 - 15 minutes.

4. Height variations of echoes often show regular, possibly gravity wave induced, fluctuations. The spread in height of scattered pulses also gives an idea of the width of a scattering layer. Above 90km, layers can be quite thick - up to 10km. At about 85km, thicknesses are typically a few kilometres. For heights of ≈70-74km, scatter still often comes from spread of heights of a few kilometres thickness, but on occasions when only 1 reflector appears to be present (very slow fading) the reflector appears to be very well defined in height. It appears that scatter from these lower heights comes from discrete reflectors, sometimes alone and sometimes in groups.

5. The Rice parameter has been investigated in detail, and it has been shown that results using this parameter support the description of scatterers given above. The importance of a specular contribution from the ≈85km echo was noted. The misleading conclusions reached by other authors who have investigated the properties of D-region scatterers by using the Rice parameter have been explained.

6. Some discussion regarding the data lengths necessary for reliable interpretations of fading times and power spectra has been presented. It has also been pointed out that the polar diagram of the scatterers, and the related beam broadening effect, are the main causes of observed fading times , when using the Buckland Park array. Three-dimensional turbulent velocities associated with scales of $\lambda/2$ are a second order effect. If such 3D turbulent velocities can be measured, turbulent energy dissipation rates can be derived ($\varepsilon_d = k_* v^3/\ell$), but k_* is not yet well known. This point has been emphasized in Chapter II.

7. The importance of 2-dimensional turbulence in the mesosphere, particularly for scales corresponding to periods in the winds of less than 5 minutes, has been elucidated. A method for determining turbulent energy dissipation rates utilizing these scales has been described. It has also been pointed out (Chapter VII) that fading times measured using full correlation analysis for the determination of wind velocities are not related to RMS velocities associated with scales of $\lambda/2$ metres, and so estimations of energy dissipation rates by these procedures (such estimates have been presented in the literature) are almost certainly erroneous.

8. The results of what are believed to be the first partial reflection profiles obtained coincidentally in time and space with rocket measurements of electron density have been presented. The ~85km echo appears to be associated with the upper portion of a large electron density ledge at this height, and this ledge has been shown to be capable of producing specular scatter comparable to the observed strengths. The existence of the ledge has been explained in terms of photo-chemical effects by other authors (see Chapter I, Section 1.2.1.). A weaker echo at about ≃80-82km, below the stronger ≃85km echo, may be associated with a small dip in electron density at that height.

9. Investigations did not suggest a strong correlation between wind shears and layers of HF scatter. This is not conclusive however, because the resolution used was about 4km. No temperature measurements were made, so calculation of Richardson's numbers were not possible. Some (weak) evidence did suggest that the echoes at ≃70-74km may be associated with a wind jet at that height.

10. There seems to be evidence that gravity waves are associated with the observed scattering layers. Such waves appear to partly

explain the quasi-periodicity of power bursts.

11. The role of turbulence was discussed quantitatively. It was shown that for typical atmospheric conditions, measurable scatter due to turbulence should occur at HF from above 90km. If a strong electron density ledge occurs at ≃85km, turbulent scatter from this height should also be measurable, with a strength comparable to that produced by specular scatter from the ledge. Below ≃80km, turbulent scatter is unlikely to be observed.

12. It has been shown that if both turbulence, and steps of refractive index with a vertical extent of about one Kolmogoroff microscale, occur in the mesosphere, then the observed variation of the isotropy of scatter of the scatterers with height can be easily explained, and would in fact be expected. Specular scatter should dominate below ≃76 to 80km at 2MHz, and turbulent scatter above.

13. The first quantitative comparisons of simultaneous measurements made at ≃2 and 6MHz have been presented. The previous conclusions have been supported in full. The expected transition height of specular to quasi-isotropic scatter at 6MHz should occur at most a few kilometres below the 2MHz transition height.

VHF experiments and observations by other authors have also helped in understanding these D-region scatterers. A detailed summary has been presented in Chapter IV, Section 4.5. Such experiments have shown evidence of quasi-specular reflection (sometimes called "diffuse reflection" since the scatter does not appear to be completely "mirror-like"; see Chapter IV, Section 4.5) from heights of around 70 to 74km at wavelengths of 6m. This

suggests that horizontally stratified reflecting irregularities with edges less than 1 to 2 metres thick exist in the mesosphere. These are very likely the same irregularities as those causing HF scatter. Experiments at VHF have shown that these reflecting structures are often less than 100m thick.

As well as the above points concerning D-region HF scatter, this thesis has also devoted Chapter VI to the study of the effect of uncorrelated noise on a signal. It has been shown that if amplitude-only data is used, then noise can distort the autocorrelation and autocovariance functions. A formula has also been derived by means of which the root mean square noise level can be estimated from the autocorrelation function.

11.3 Discussion

11.3.1 Discussion of doubtful points

11.3.1a Production of turbulence

Although it was shown in Chapter IX that turbulence does cause scatter from above 80km at HF, considerable doubt still exists concerning the cause of this turbulence. If gravity waves are important, how do they generate the turbulence? This section will discuss some simple ideas.

In Chapter IX, it was seen that mean wind shears of ~4km resolution do not appear to be important. Miller et al. (1978) have shown a case in which gravity waves appear to be breaking, and thus generating turbulent phenomena (e.g. Kelvin-Helmholtz instabilities). Such a process produces turbulence twice per gravity wave cycle. Hodges (1967) has shown that temperature gradients are modified by gravity waves and this can be particularly important if the background temperature gradient is already close to unstable. Once per cycle, the gravity wave could induce unstable temperature gradients, and hence turbulence, as illustrated below.

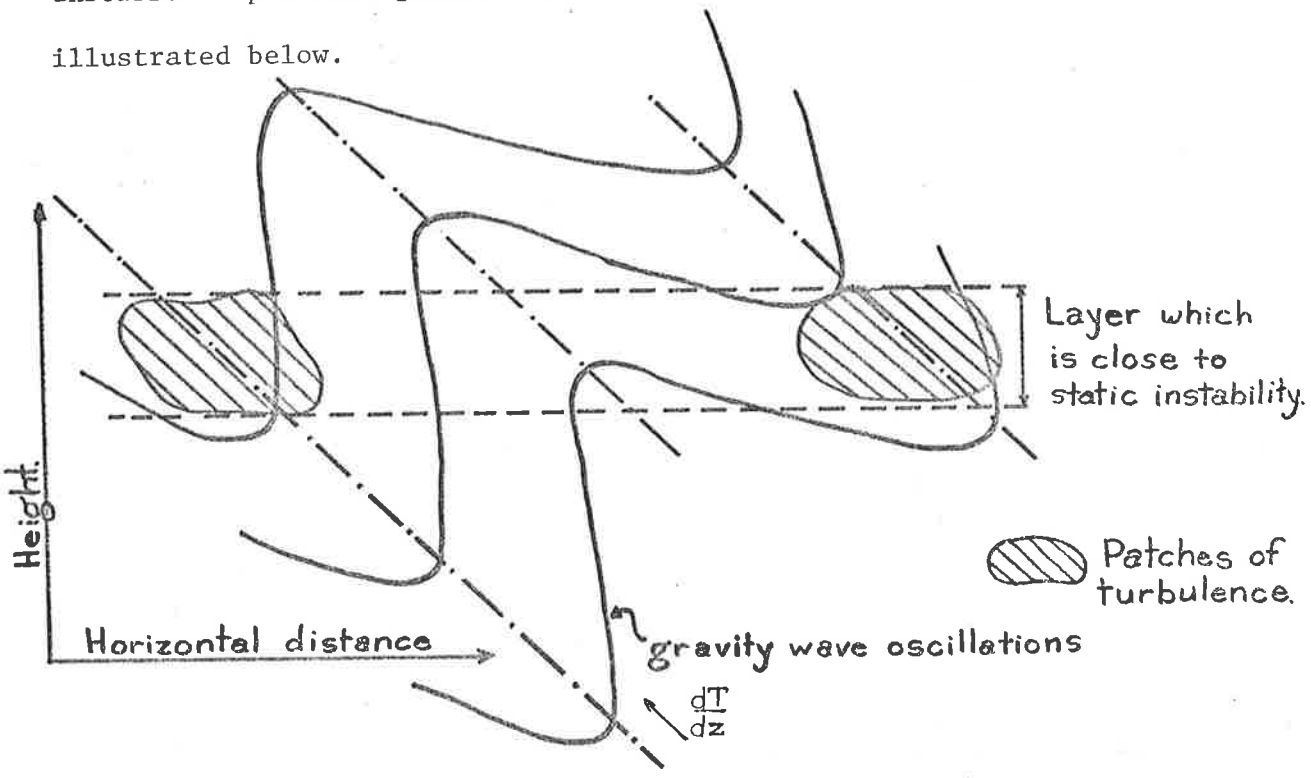

Possible examples of cases with power bursts twice per gravity wave cycle, and once per cycle, have been presented in Chapter IX, and the latter case seemed to be more common.

The suggestion of Hodges is interesting, as it offers the possibility of horizontally stratified layers of turbulence. For example, turbulence would occur more strongly in a region of near-unstable temperature gradient, and temperature profiles are generally horizontally stratified.

Teitelbaum and Sidi (1976) and Sidi and Teitelbaum (1978) have proposed that strong wind shears of short vertical extent (1-2km) can be generated by the non-linear interaction of gravity waves and tides. It is interesting that processes involving non-linear interaction of gravity waves do not involve any requirements upon the background atmospheric state, so stratified turbulence may not necessarily result. However, Sidi and Teitelbaum (1978) do suggest that the processes which they describe may be most important in the region 100 to 110km, although they could operate to some extent down to 90km.

Another process which may be important is critical level interactions between gravity waves and wind jets. These can increase wind speeds at the point of critical level absorption, but not immediately below, thus resulting in quite strong wind shears. For example, Fritts (1978, 1979) has mentioned this process, and Jones and Houghton (1971) have also shown that strong wind shears can result from critical level processes. Fritts (1979) has shown that these wind shears could generate Kelvin-Helmholtz instabilities, and can also radiate gravity waves. The critical level is also expected to move towards the gravity wave source. This might

explain some of the downward motions of scattering layers which have been noted (e.g. see Fig. 4.9, Chapter IV). Fritts (1979) has also suggested that such critical-level interactions could exhibit a quasi-oscillatory nature which could be related to the observed quasi-periodicity of power bursts. (A possibly similar process described by Merrill and Grant (1979) for the Planetary Boundary Layer has been discussed in Chapter IX, Section 9.2.2) Re-radiated gravity waves could also cause critical-level interactions elsewhere.

11.3.1b Reasons for specular scatter

One of the major problems not solved in the work for this thesis concerns the nature of the specular reflectors. Are they steps in electron density - or do they take some other form - for example, narrow strata? e.g.

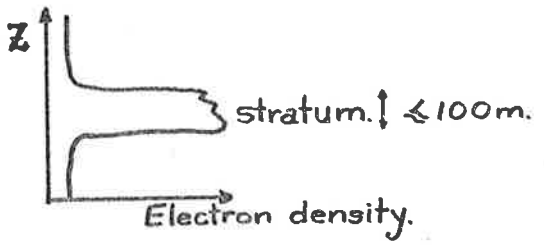

Further, are the sharp electron density changes a tracer of similar changes in the neutral atmospheric density, or are they a separate process - do the steps occur only in the electron density, due perhaps to some chemical process?

Haug et al. (1977) have made some simple calculations, and felt that chemical processes could not account for the rapid changes in electron density which have been observed. Specular reflection has been observed in the troposphere and stratosphere at VHF (see Chapter IV), and in this case the neutral atmosphere does cause the scatter. Steps in refractive index have been observed in the troposphere (e.g. see Crain, 1955) and the oceans (e.g. Simpson and Woods, 1970), and it appears that such steps are not uncommon.

It seems reasonable to assume, then, that the specular reflections observed in the ionosphere are due to horizontally stratified steps in the neutral atmospheric density, and that the electrons are tracers for the neutral density.

This still, however, does not explain why the steps occur. Several possibilities have been offered. The proposal due to Bolgiano (1968) has been mentioned in Chapter IX, Section 9.2.2, in which intense turbulence generates a layer of turbulence with very sharp edges. Röttger (1980b) has also given a review of some other possibilities. One of these which may be important is "lateral convection". In this process, quasi-horizontal displacement of individual layers or "lenses" of air packets are envisaged to occur when two differently stratified masses of air are in contact.

Merrill (1977) has discussed an interesting critical level encounter, and quite sharp steps in density were produced (see his Fig. 6) of less than 10m vertical extent. The effect of the ground may be important for these structures, and the wavelength involved was ≃300-500m. Waves of this wavelength cannot exist strongly above ≃60km, being strongly damped due to viscosity (e.g. see Hines, 1960, Fig. 11). Thus whether such a description is valid for the D-region is debatable, but it may be worth bearing in mind.

Recently, some extremely interesting results due to McEwan (1980) have appeared. McEwan produced two gravity waves in a salt-stratified solution of water, and observed their interaction. Turbulence was produced, but the interesting point was what happened after the turbulence subsided.

Fig. 11.1a

A breaking event in a forced standing internal gravity wave in a linearly salt-stratified water tank 500 mm wide and 250 mm deep. Shown are contours of constant net vertical density gradient derived from quantitative Schlieren photography. The circle of view is 300 mm in diameter and the free upper surface of the water is marked by a triangle. Contours are as : Black: statically unstable ($\rho'>0$); Heavy dots: $0.7\ \rho_o' < \rho' < 0$; Clear: $1.3\ \rho_o' < \rho' < 0.7\rho_o'$; Light dots: $2.0\ \rho_o' < \rho' < 1.3\ \rho_o'$; Dashed boundary: $\rho' < 2\ \rho_o'$. The dark stippled region delineates the fine, three dimensional convoluted structures associated with mixing. Also marked are representative streak paths of neutrally buoyant particles for an interval of $0.5\ N^{-1}$, where $N \simeq 1.26\ s^{-1}$. The dominant elliptical component of the motion is due to the forced primary internal wave mode. Shears are everywhere small, even in the mixing regions. (i) first appearance of well-defined static instability. (ii) $2N^{-1}$ later. (iii) $9N^{-1}$ later.
(from McEwan, 1980)

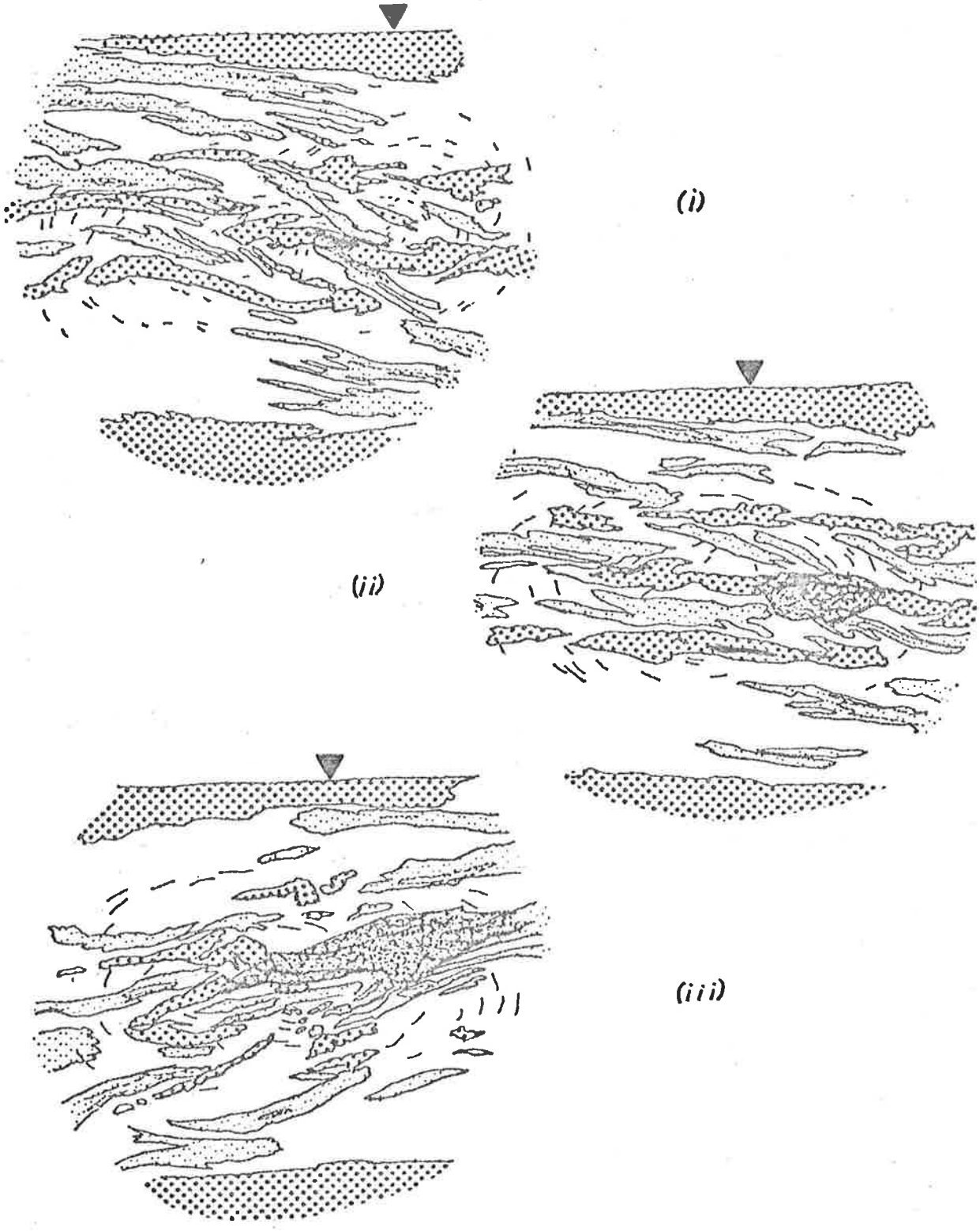
(i)
(ii)
(iii)

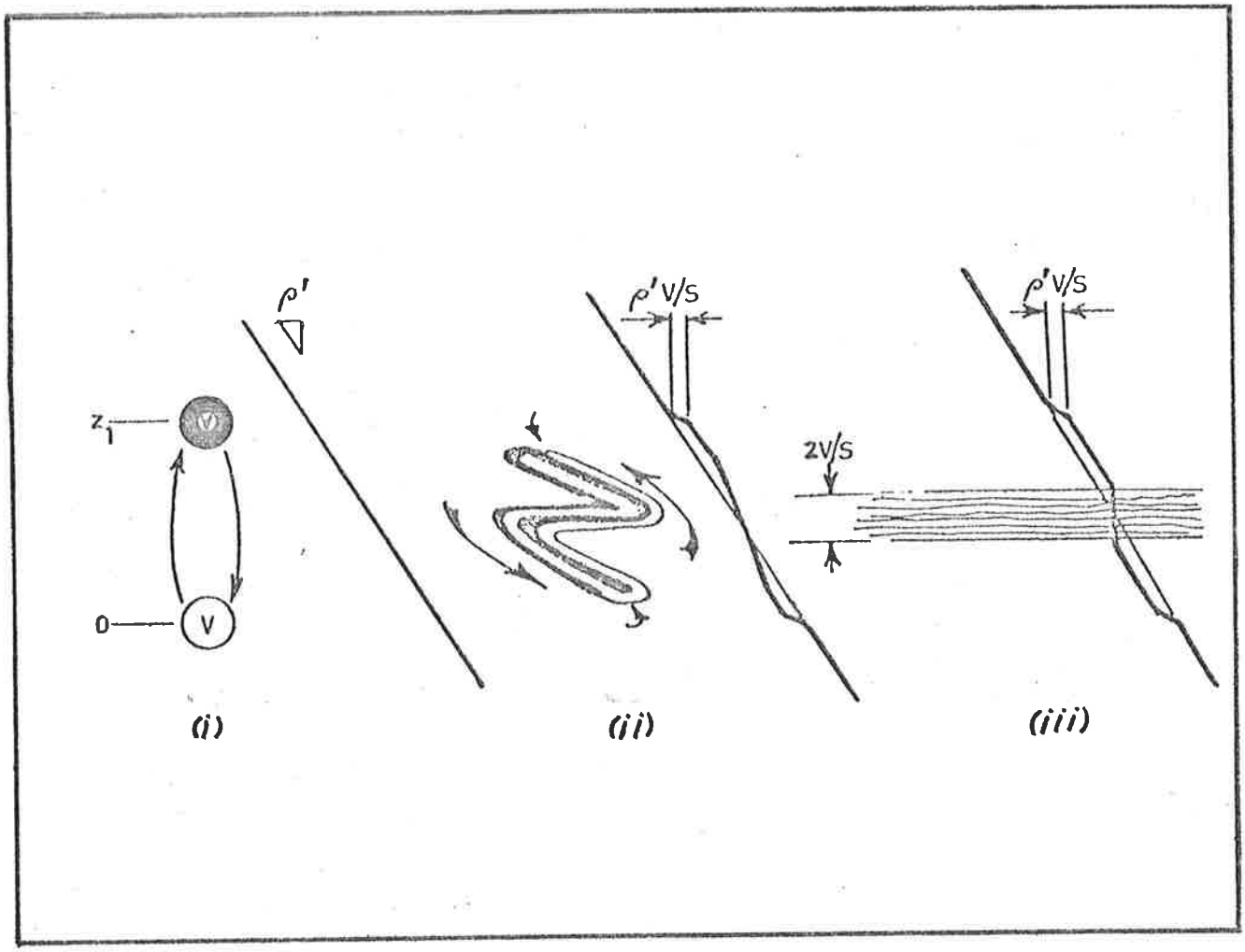

Fig. 11.1b

Kinematical model of mixing by convective overturn.
(i) Particles of volume V are exchanged. The surrounding (linear) static density profile is unaltered.
(ii) The particles extend as adjacent filaments and collapse towards a combined equilibrium layer. The (exaggerated) effect on the surrounding profile is shown.
(iii) After equilibrium, fluid has been permanently removed from levels 0 and z_1 and deposited at $z_1/2$. There is a net gain in static potential energy.
S = horizontal area per unit parcel-exchange event, and
ρ' = density gradient.
(from McEwan, (1980))

During the mixing process, considerable interleaving of regions of similar density occurred, as illustrated in Fig. 11.1a. Then, after the turbulence began to subside, layers of approximately constant density appeared in the water, with very narrow interface regions; e.g.

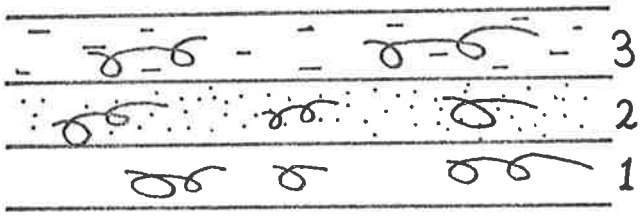

[An approximate physical description for this is also illustrated in Fig. 11.1b (due to McEwan, 1980). The essential feature of the description is that displaced particles stretch and change form, rather than simply mix with the environment. For a more detailed description, see McEwan, (1980).]

Eventually the weak residual turbulence died, leaving these strata. Since the water was hydrostatically stable the layers remained, molecular diffusion being the only process available to mix the layers. It thus appears that turbulence mixed the water, but that when the turbulence ceased, layers of separate fluid resulted. Once the turbulence had died, vertical mixing became quite weak, although horizontal mixing could still occur to a sufficient extent to mix the layers horizontally.

The important point is that turbulence does appear to produce these strata. (Recall also from Chapter IV, Section 4.6, that other experimenters (e.g. Baker, 1971; Calman, 1977) have produced steps in the density of salt-stratified solutions, although in those cases the process was related to differential rotation, so

the process may have been different.) Then assuming such strata do often result from turbulence, it could be envisaged that if turbulence occurred in a very stable region of the atmosphere, perhaps due to gravity wave effects, and then died, stable strata could occur, with interface regions of perhaps a Kolmogoroff microscale in vertical extent. If the region were stable, these laminae could remain for some time. They would be detected by radio waves of wavelength λ for as long as it took for the interface regions to become $\sim\lambda/8$ in vertical extent, at which stage "diffuse reflection" might occur (e.g. see Röttger, 1980a; an interface with corrugation $\simeq\lambda/8$ high would not produce mirror-like reflection). This should be a duration of $t\simeq((\lambda/8)-\eta)^2/\nu$, η being the initial thickness ($\simeq$1 Kolmogoroff microscale), and ν the kinematic viscosity - at 75km, $\eta\simeq$2-3m (table 1.9a), and $\nu\simeq.3m^2s^{-1}$, so for λ = 150m, $t \gtrsim$ 10 mins. Hence in stable regions, these laminae would persist for some time. In regions with background turbulence, these laminae would quickly diffuse so that the interface was $\gtrsim \lambda/4$ in vertical extent, when little specular scatter would occur. This could explain the observations in the lower atmosphere of Gage and Green (1978) and Vincent and Röttger (1980) that specular scatterers are associated with regions of large R_i (high stability). (The Bolgiano model discussed in Chapter IX would suggest specular scatter comes from regions of low R_i.) Intermittent turbulence could be generated, and when the turbulence dies, stable strata result which remain stable if the atmosphere contains no background turbulence. The strong bursts of scatter observed would be related to this intermittency of turbulence generation. It should perhaps be mentioned that other

explanations for the "burstiness" exist, such as focussing and de-focussing of the radiation (e.g. compared to Chapter III, Figs. 3.5a and c), but the author feels such processes are not the major cause of the intermittent bursts. Such focussing possibly does occur (due to spatial oscillations of the reflecting edge height) but since the powers are either very strong or almost non-existent, it suggests that the scatterers are either present or not present, respectively. It would also not be surprising if at times there is some tilt of the reflectors from the horizontal, but these tilts have not been searched for in any detail as yet. Investigations of such tilts, and also examinations of gentle oscillations in the surfaces of the reflectors, might be a useful future project. (For example, it might also be recalled from Chapter V, Fig. 5.17c that a weak hint of specularity at 11.6° occurred for the 86km layer. This could perhaps have been due to gentle spatial oscillations of the height of the strong electron density which was probably associated with the layer, giving some off-vertical specular scatter).

11.3.1c Reasons for preferred heights

Some progress in explaining the reasons why echoes come from preferred heights has been achieved in this thesis, in that the ≈85km echo has been explained.

The suggestion has been made that the ≈70-74km echo may be related to the wind "jet" at that height (see Chapter I, Fig. 1.7. A peak in mean wind velocities occurs at 70-74km, and this has been called a jet here). For upward propagating gravity waves, this jet would be the first time that wind speeds greater than

50m s^{-1} were encountered, so the region is a candidate for critical-level effects. It is also interesting that Schmidlin (1976) claims to have found that temperature inversions can often occur at around 70 to 75km. Such a temperature inversion would produce a hydrostatically stable region, and so could produce the stable conditions required for the stratified layers discussed in the previous section to maintain themselves. If indeed such temperature inversions do exist, they could be the reason for scatter from ≃70 to 74km.

One other major scattering region is that at about 90km. We saw in Chapter IX, Fig. 9.8c, that if turbulence exists, observable scatter (effective reflection coefficient $\gtrsim 10^{-4}$) will be observed at 90-95km. This is independent of the existence of steep electron density gradients - if such gradients exist, however, the scatter will be even more enhanced. To produce effective reflection coefficients of $\simeq 10^{-3}$ probably requires a layer of stronger than usual turbulence combined with a fairly strong electron density gradient. Why such layers of turbulence should occur is unclear, but they do appear to have been observed with rocket observations (e.g. see Blamont and Barat, 1967; Anandarao et al., 1978). Teitelbaum and Sidi (1976), and Sidi and Teitelbaum (1978), have proposed that large wind-shears can be produced by non-linear interactions of gravity waves and tides, and these can produce turbulence. These authors feel that such wind shears occur preferrentially in the region between 100 and 110km (maybe down to 90km), and since D-region echoes cannot be observed above 95kms, (due to the leading edge of the E-region totally reflected pulse) some height preference for echoes to occur between 90 and 95km may

perhaps not be surprising. At night, echoes do indeed occur from 90 to about 110km. The large phase changes which sometimes occur in the tides around 85 to 90km (e.g. Elford and Craig, 1980) would also be associated with large wind shears, and these could possibly induce some turbulence. However, the author feels that these points do not fully explain the echoes. One particularly interesting facet of these "90 km" echoes is the tendency for them to have, on occasion, strengths comparable to E-region total reflection, particularly at Townsville (e.g. See Chapter III, Section 3.4). In such cases they appear to be close to critically reflecting, and perhaps a "wind-shear" mechanism may be acting (e.g. Whitehead 1961; 1976). The wind shear mechanism is usually considered to be ineffective at ≈90km, since the ions are supposedly controlled by neutral motions, but the author has not seen a convincing discussion of this assumption, and the ions could possibly still have weakly independent motions. However, if wind shears are important, they would be of short duration (≃ mins) and would not be maintained over more than one or two km in height, since the work in Chapter IX has shown that wind shears taken with a height resolution of ≈4km are not related to these echoes in general. Sequential E_s layers (see Chapter III) have been noted to descend down to 90km, so this may also support a "wind shear mechanism" for the 90km layer.

11.3.1d Seasonal variations

The author has little new to offer to explain the observed seasonal variations of echo strengths. The suggestion by Vincent (1967) that gravity waves may be more common in winter is very likely a valid comment.

11.3.2 The author's view

Although the information available is inadequate it is difficult to resist the temptation to present a speculative description of D-region scatter. The author's present view of the D-region would be basically described by Fig. 11.3. (Perhaps the most doubtful point is how the Fresnel steps occur. In the following scenario, they are assumed to result after turbulence, but this is by no means certain.)

Intermittent turbulence occurs at all heights in the mesosphere, produced primarily by gravity wave effects. This may occur in both stable and unstable regions. After the turbulence subsides, laminae result, with interfacial layers of about a Kolmogoroff microscale thickness. If the region is normally stable, these laminae can be quite stable, and produce specular HF reflection for heights below about 80km. Above 80km, these interfacial layers are too thick to produce significant specular reflection. If the region is unstable, then these laminae are quickly dispersed. Turbulent scatter is too weak to be observed below 80km (See Fig. 9.8), but above 80km, turbulence is readily observed. Thus below 80km, reflection from stable layers occurs. Above 90km, any process which can produce turbulence, including Hodges (1967) mechanism, wind shears, and so forth, will produce some observable scatter. Turbulent scatter will also be seen at ≈85km if a large electron density ledge exists here. This ledge will also produce a significant component of specular scatter. Gravity wave effects are very large at ≈90-110km, (e.g. Sidi and Teitelbaum effects, 1978), and tide and waves can also break as their amplitudes become large, so considerable turbulence could occur above 90km.

A full description of the quasi-periodicity of power bursts is not yet available. Hodges (1967) proposal may be relevant, since the wind oscillations and power bursts often have equal periods. Another interesting scheme is that discussed in Chapter IX, Section 9.2.2, due to Merrill and Grant (1979), in which an incident gravity wave steepens the wind shear and produces turbulence. This turbulence then decreases the wind shear, and so the turbulence dies. At this stage, laminae may appear, producing specular scatter. The incident gravity wave then begins to steepen the wind shear (and also increase the wind speed at the top of the shear region?), upon which turbulence again is generated, and so the process repeats. This shear region might also be expected to move down in time (e.g. see Fritts, 1978, 1979).

However, other processes such as breaking waves and gravity-wave induced wind shears may also be important, particularly above 90km.

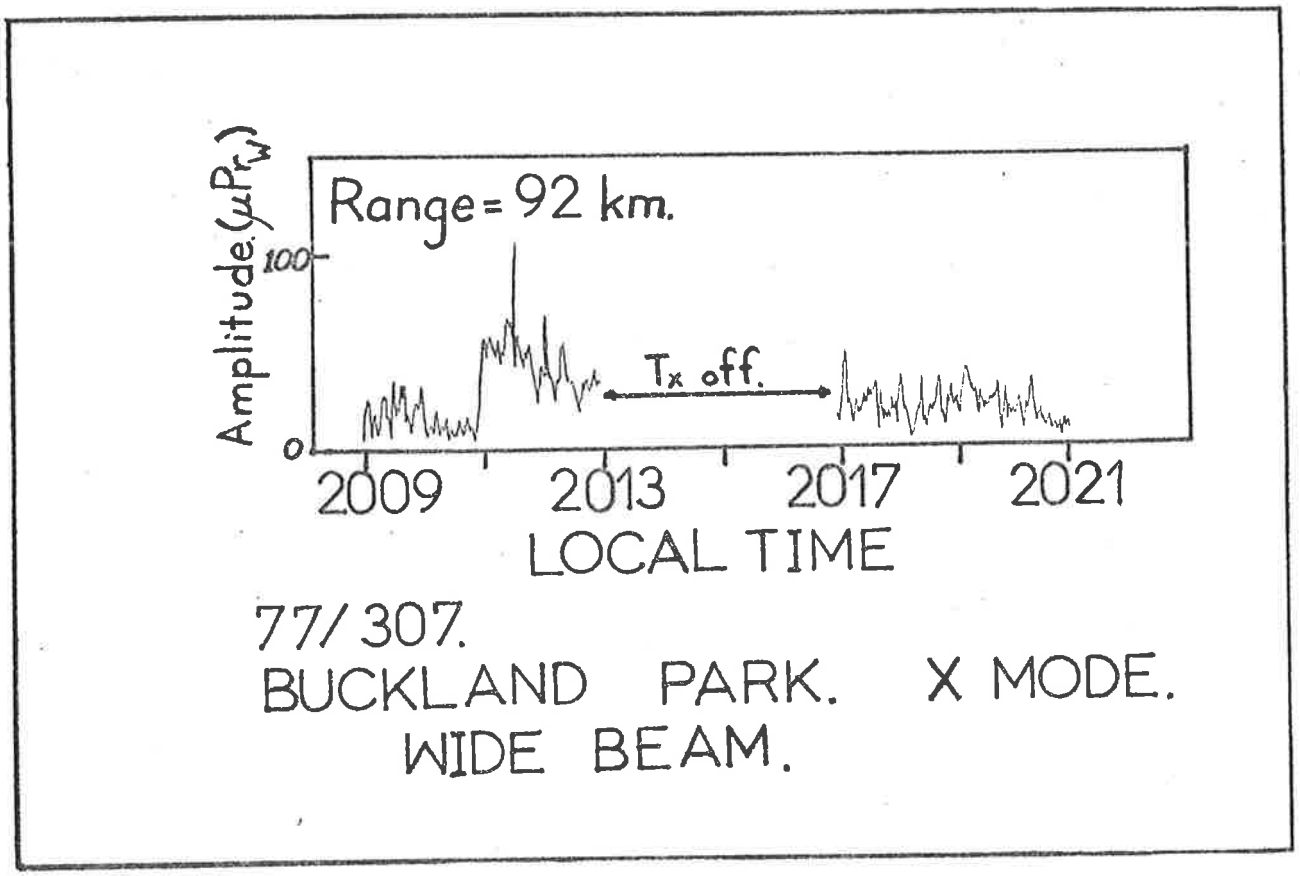

Fig. 11.2

Example of a meteor observed with a wide beam at Buckland Park during November, 1977. This can be recognized by the rapid rise and exponential decay. The transmitter was only on for 2 mins in every 4. The rise time is approximately the time for the meteor to move through 1 Fresnel zone, d; i.e. $t \simeq d/v$, v = meteor velocity, $\simeq$20-60km s^{-1}, and $d = (\frac{R\lambda}{2})^{\frac{1}{2}}$, R = distance to meteor, λ = 151.5 m in this case. Thus $t \sim .3s$. The decay time is

$$\tau \simeq \frac{\lambda^2}{16\pi^2 D},$$

where D is the diffusion coefficient. Initially the trail expands by molecular diffusion so $D \simeq 1\ m^2 s^{-1}$, (e.g. see USSA, 1962) but eventually turbulent diffusion becomes important ($D \simeq 10^2 m^2 s^{-1}$ at 90km altitude for turbulent diffusion e.g. see Chapter I, Fig. 1.9a). As an example, see Rees et al., 1972, Fig. 6; turbulence becomes important after about 30 seconds in that case (rocket cloud release).

For $D \simeq 1 m^2 s^{-1}$, $\tau \simeq 2.5$ mins i.e. a large decay time.

The peak amplitude ($50\mu Pr_w$) corresponds to an effective reflection coefficient of about

$$(1.5)\ (90)\ (50 \times 10^{-6})$$ (see Chapter III, Table 3.1, $k_{*2W} = 1.5$)

or $$R_{peak} \simeq 7 \times 10^{-3}.$$

The meteor probably occurred at an off-zenith angle. Otherwise it would not generally register, since the meteor trail must be aligned perpendicularly to the line of sight, and meteor paths are seldom horizontal in the atmosphere. For this reason, meteors show more frequently with the wide beam than the narrow beam. The possibility exists, however, that meteor trails could form, and be twisted by a wind shear to produce specular scatter. Such scatter would be hard to recognize, however.

11.4 Inconclusive results, future projects and schematic summary

There is still a considerable amount of work to be done before D-region HF scatterers can be fully understood.

One phenomenum which was investigated very briefly was the role of meteors. No doubt these contribute to some (if not most) of the metallic ions observed at ≈90km, and this could be important at night. However, this was briefly discussed in Chapter I, Section 1.2.1, and other processes such as resonant scattering of L_α and L_β radiation by the hydrogen geocorona, and electron precipitation, seemed to be major contributors to night-time electron densities. A search for direct-observations of meteor trails was undertaken, and Fig. 11.2 shows an example of a meteor trail observed at 1.98MHz using a wide beam. Meteors show much more clearly at 6MHz, however. Brown (1976) has also investigated meteors at 2MHz. The author does not feel that meteors make a major contribution to 2MHz scatter, even at night. It is possible that meteor trails could have formed, however, and been twisted by the wind to an angle at which specular reflection could occur. Such a process could not be easily recognized - it would not have the exponential decay used to recognize the meteor in Fig. 11.2.

Other projects which deserve consideration include the following (not in any special order).

1. Experiments using widely spaced antennae with separation of several kilometres to determine more accurately the horizontal dimensions of scattering regions.
2. Better investigations of seasonal variations of various parameters (e.g. the height of transition from specular to quasi-isotropic scatter (Lindner,(1972; 1975a,b) has done preliminary work on this))

3. Curves similar to those shown in Figs. 5.12 (Chapter V) could be prepared for cases other than Rayleigh-distributed data, so that investigations of specular to random scatter component ratios can be made more thoroughly.

4. Simultaneous partial reflection experiments and rocket-measurements of temperature could be performed to test the assumption that the scatterers below ≈80km are associated with stable regions. Simultaneous partial reflection and rocket experiments are desirable in many other contexts as well (e.g. turbulence/partial reflection correlations; more observations of the ≈85km ledge).

5. The work in Chapter VII could be utilized to study the seasonal variations of ε_d.

6. Useful results could be obtained by narrowing the polar diagram of the Buckland Park array, perhaps by interferometer techniques, so that the motions associated with turbulence scales of $\lambda/2$ can be actually observed. Then accurate determinations of k_* ($\varepsilon_d \equiv k_* v^3/\ell$; see Chapter II) will be necessary.

7. Searches for azimuthal assymmetry of scatter could prove interesting (e.g. c.f. Fig. 5, Harper and Gordon, 1980).

8. The programs Specpol and Volscat (see appendices) can be utilized much more to investigate more closely the thicknesses of scattering layers, and also the isotropy of scatter.

9. The angular spectrum of scatter at 6MHz should be investigated more thoroughly (see Chapter X).

10. "Image forming" could prove a useful technique. That is, record amplitude and phase at all aerials of the Buckland Park array separately, and then re-add these later, with appropriate

phase shifts, to simulate looking in all directions of the sky. Thus a 2-dimensional picture of scatter could be built up.

11. DAE experiments could be performed with the view to testing the assumption that the ≃85km echo is always associated with a large electron density ledge. In the past, the DAE has been unreliable above ≃80km, but the use of coherent integration may possibly allow reliable X-mode measurements to be made for heights of up to 85-90km. Such measurements may also be easier using 6MHz.

12. Simultaneous HF partial reflection and VHF experiments at the same location are most desirable. Failing this, typical VHF effective reflection coefficients should be calculated, so that comparisons with HF experiments can be made. Many assumptions have been made about the link between HF and VHF scatterers in this thesis, (e.g. it has been assumed the same scatterers cause both types of scatter), and these assumptions must be tested.

Although there is undoubtedly a lot to be learned about these scatterers, an approximate picture has emerged during the course of this thesis, and Fig. 11.3 is a schematic summary of this picture. With a better understanding of these scatterers, interpretation of many other current D-region experiments should become much more reliable.

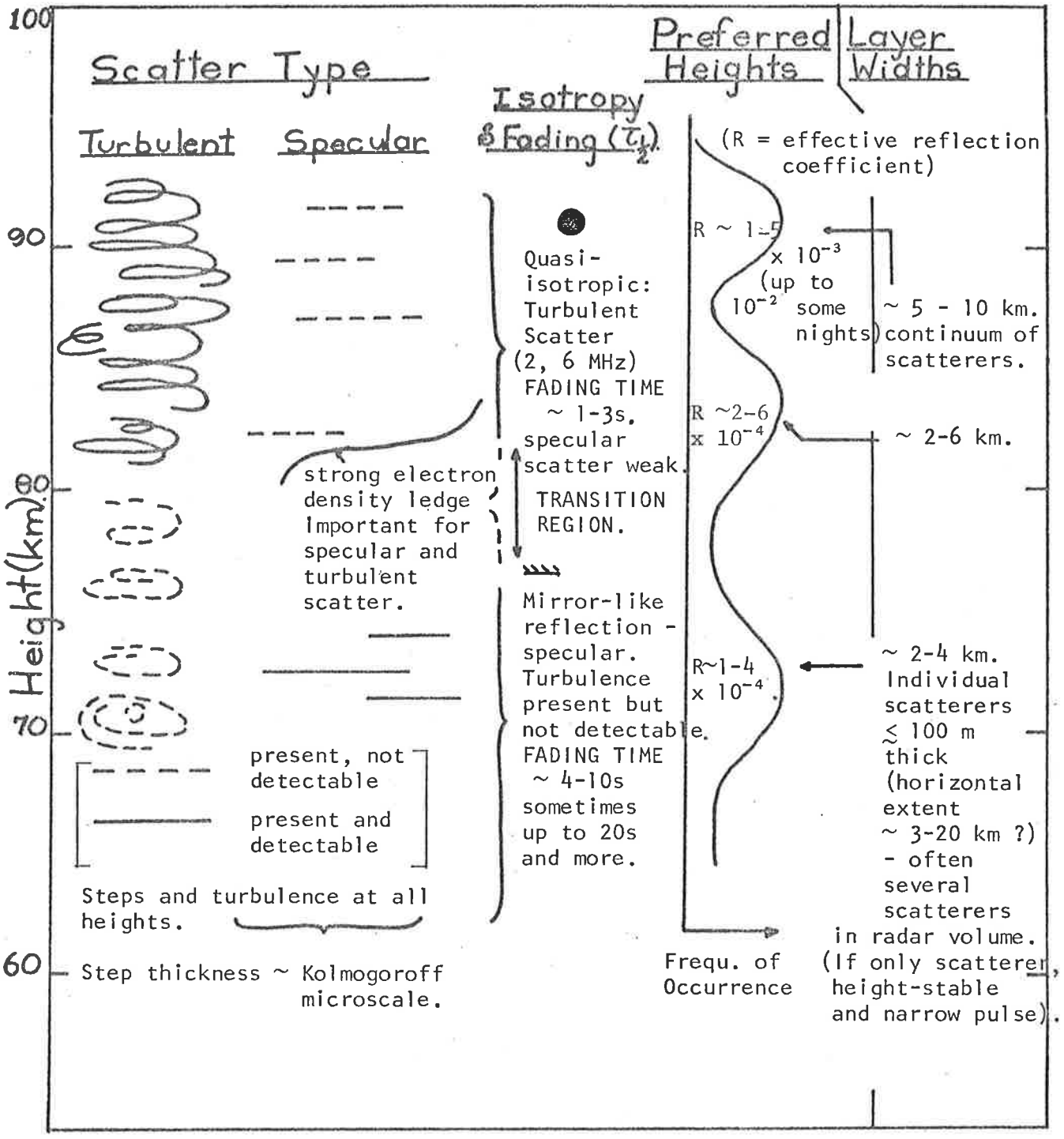

Fig 11.3 Schematic summary of the important points regarding HF D-region scatterers.

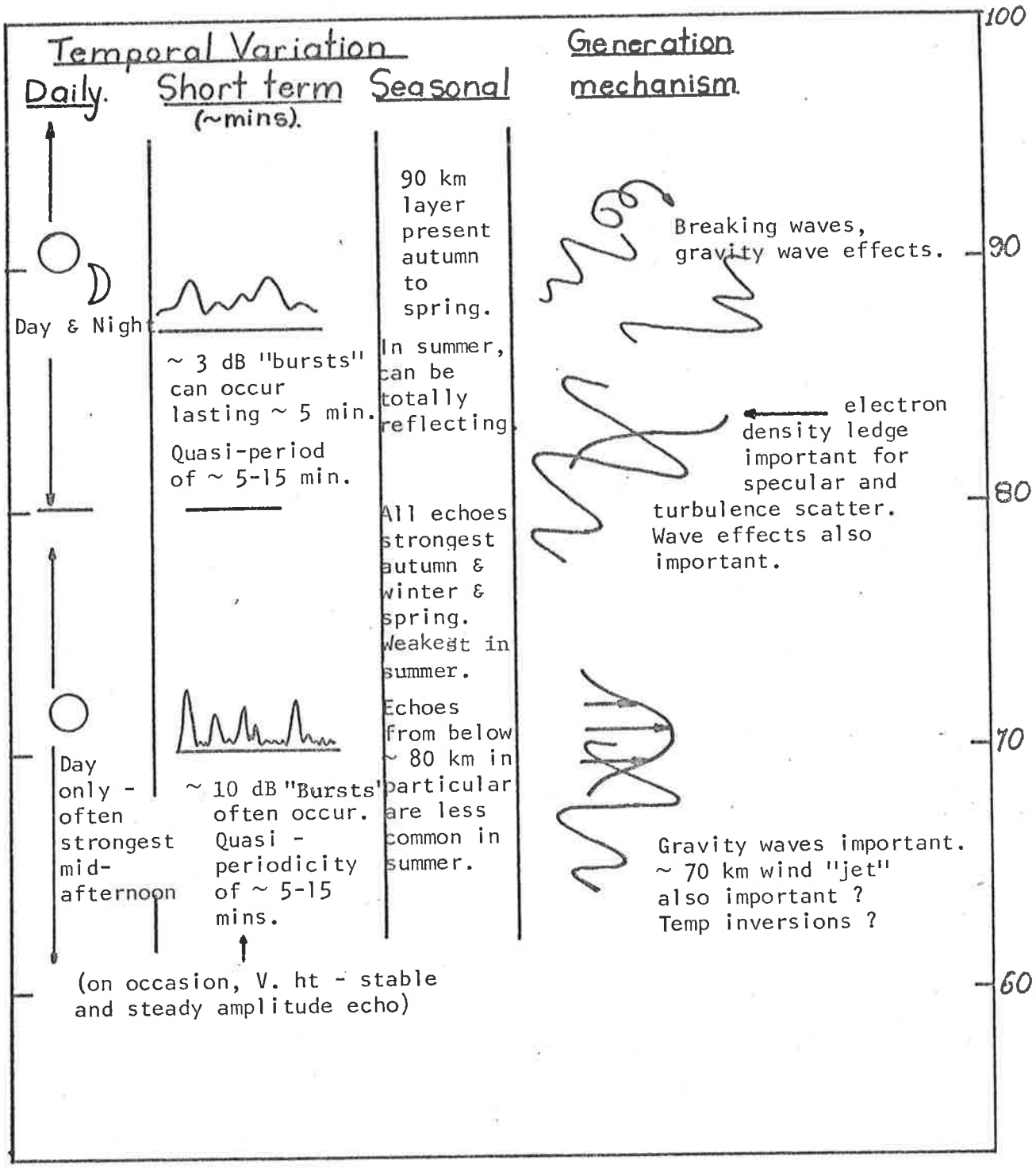
Temporal Variation
Daily.
Short term (~mins).
Seasonal
Generation mechanism.
100
90
80
70
60
Day & Night
~ 3 dB "bursts" can occur lasting ~ 5 min.
Quasi-period of ~ 5-15 min.
90 km layer present autumn to spring.
In summer, can be totally reflecting.
Breaking waves, gravity wave effects.
electron density ledge important for specular and turbulence scatter.
Wave effects also important.
All echoes strongest autumn & winter & spring. Weakest in summer.
Echoes from below ~ 80 km in particular are less common in summer.
Day only - often strongest mid-afternoon
~ 10 dB "Bursts" often occur. Quasi - periodicity of ~ 5-15 mins.
Gravity waves important.
~ 70 km wind "jet" also important ?
Temp inversions ?
(on occasion, V. ht - stable and steady amplitude echo)

APPENDIX A

THE NEUTRAL ATMOSPHERE, AND THE IONOSPHERE ABOVE 100KM

A. (i) The outer regions

A. (ii) Classification of the atmosphere

A. (iii)a Particle densities and structures above 100km

A. (iii)b The Electron density profile above 100km

Appendix A: The Neutral Atmosphere, and the Ionosphere Above 100km

A. (i) The outer regions

The atmosphere is a large system, and the interactions involved are complex and intricate. From the dense boundary layer, to the tennuous remnants thousands of miles into space, there are a wealth of physical processes both fascinating and important to all inhabitants of the Earth.

At large distances free electrons and ions spiral freely along magnetic lines of force and interact strongly with a wind of similar particles flowing from the sun. This "plasma sphere" extends far into space - up to around 25 to 30 Earth radii in places - and is a type of "outer region" for the atmosphere. A review of this region can be found in J. Atmos. Terr. Phys., volume 40, number 3 (March) 1978. Fig. A.1 shows a schematic diagram of the region.

However, it is regions much closer to the Earth's surface which are the subject of this thesis. This appendix will give a very brief account of the main regions of the atmosphere between 100 to 500km, along the lines found in many text books on the atmosphere.

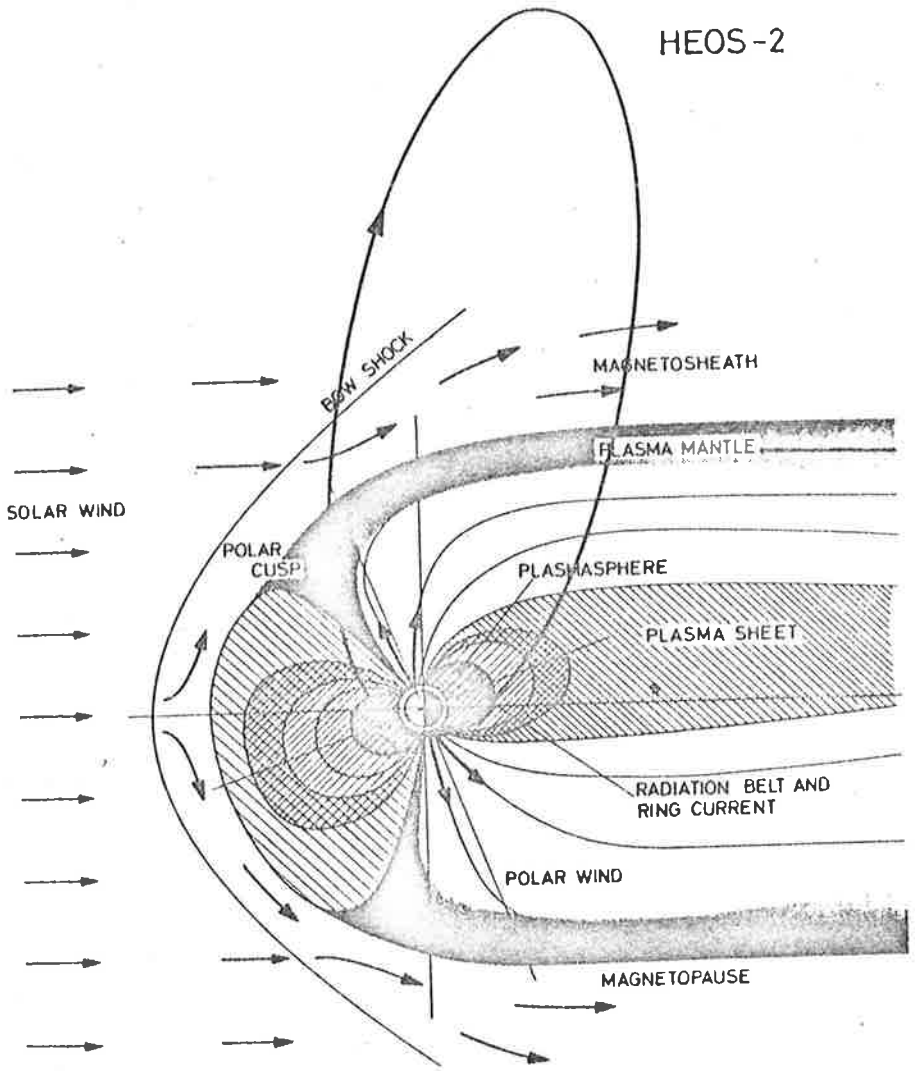

Fig A.1 The Earth's magnetopause and magnetosphere regions. (From Bahnsen (1978)).
Also shown is the orbit of the staellite HEOS-2, which was used for studies of this region. The Bow shock occurs at about 15 Earth radii on the sunward side.

A. (ii) Classification of the atmosphere

Two of the most common classification schemes used in the atmosphere are based upon temperature structure, and electron density. Fig. A.2 shows these classifications.

It is important to note that these sample profiles can only be approximate, since the temperatures and electron densities can vary substantially with time and location.

One important region not presented on this diagram is the turbopause region. Up to about 100-115km turbulence can play a major role in the dynamics of the atmosphere; but above this region, turbulence is a relatively rare phenomenon. The reason is that the mean free path of particles, and the increase in temperature, result in large molecular diffusion rates, and most small scale transfers of heat and particles occur by such molecular transport. The transition region between the turbulent dominated and non-turbulent regimes is quite narrow, and is called the turbopause. This is discussed in more detail elsewhere.

It is useful to consider just why the temperature profile follows the shape given.

Below the tropopause, heating is principally by re-radiation from the ground. The temperature falls off with increasing height, as less radiation penetrates to greater heights. Convection and so forth also act, resulting in a temperature profile approximating the adiabatic lapse rate. Of course many local processes also act to produce local deviation from this picture. This region will not be discussed greatly here.

Above the tropopause, Ozone becomes important. At heights greater than about 50km, there is insufficient O_2 density to produce significant O_3, but at around 20-40km, the O_2 density and incoming UV radiation (less than about 246nm) are in sufficient quantities to produce sig-

Fig. A.2 Typical daytime temperature profile for low sunspot activity. T_n is the neutral kinetic temperature, T_i the ion temperature, and T_e the electron temperature. T_n' shows a typical daytime neutral temperature profile during sunspot maximum. At night, T_n falls to about 600K at sunspot minimum and about 900K at sunspot maximum (King-Hele 1978). Temperature maximum occurs at about 1600 hours local time, and minimum about 0400 hours, in the themosphere (King-Hele 1978). The classifications of the various regions are also shown. The temperatures below 100km are taken from the U.S. Standard Atmosphere 1962, and above from Roble and Schmidtke (1979) (χ = 55.4°), for data taken during 1973 (Sunspot minimum). For sunspot maximum, Garrett and Forbes (1978) Fig. 1 was used. The numbers can only be approximate, as they vary latitudinally and with season. Even the heights of the various regimes can change - for instance, the tropopause height varies both latitudinally and with time of day. In the exosphere (about 500-1000km), kinetic temperature is not a meaningful term since neutral atoms rarely collide (King-Hele 1978).

Approximate atmospheric pressures (from Houghton 1977, Appendix 5) are denoted on the right hand vertical axis. Pressure follows an approximately exponential decrease with height, as a result of the balance of gravity and hydrostatic pressure ($dp = -gpdz$, $p = \frac{mp}{kT}$, m being the mean mass of the atmospheric molecules).

Also shown are "typical" daytime electron densities as a function of height, with the associated nomenclature. However, these densities can vary widely with latitude, sunspot condition, and a variety of other parameters. (For example Ratcliffe 1972, fig. 3.3 shows variations of F region electron densities at different heights and lattitudes). The hatching gives some idea of the variations in electron density which can occur. Data is taken from Craig (1965), figs. 9.11 and 9.15, and Ratcliffe (1972) fig. 3.3. Also shown are some typical E region night time electron densities. The symbols D, E, F1 and F2 denote the ionospheric nomenclature. The E and F2 regions are local peaks in electron density, and F1 is a local peak at times (particularly during Sumspot maximum summers).

This thesis concentrates on the D region (60-100km), which also covers the mesosphere and lower themosphere.

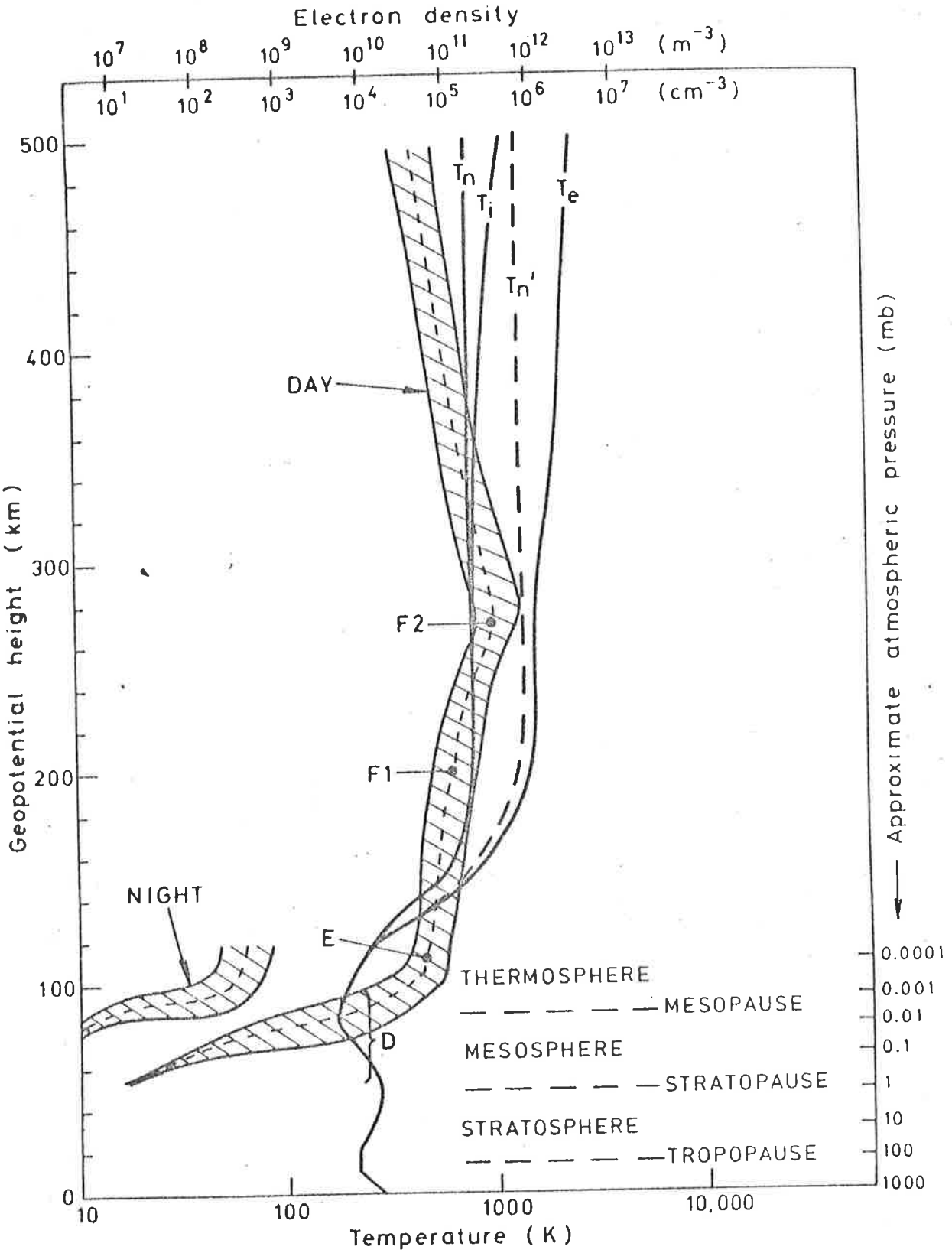
Electron density
10^7 10^8 10^9 10^{10} 10^{11} 10^{12} 10^{13} (m^{-3})
10^1 10^2 10^3 10^4 10^5 10^6 10^7 (cm^{-3})
500
400
300
200
100
0
Geopotential height (km)
T_n
T_i
T_e
T_n'
DAY
F2
F1
NIGHT
E
D
THERMOSPHERE
MESOPAUSE
MESOSPHERE
STRATOPAUSE
STRATOSPHERE
TROPOPAUSE
10
100
1000
10,000
Temperature (K)
Approximate atmospheric pressure (mb)
0.0001
0.001
0.01
0.1
1
10
100
1000

nificant O_3. (The principal reactions can be found in Houghton (1977) §5.5). Minor constituents such as NO, NO_2, OH also play important roles, however. UV radiation of wavelengths less tha 1140nm, but particularly less than 310nm, is also involved, being absorbed in the photo dissociation of Ozone . This production of O_3 absorbs out the UV, and thus at heights below 15-20km, little of the radiation penetrates. The result is a maximum in the O_3 profile at around 25-30km (Houghton 1977, §5.5). These O_3 reactions produce molecular kinetic energy and hence atmospheric heating. Some of the heat is re-radiated by CO_2 at infrared wavelengths, and the balance between O_3 heating and CO_2 losses produces a temperature peak at the stratopause (Houghton, §4.7).

At greater heights, there is little absorption of radiation and the temperature falls away to a minimum at about 90km. Cooling by radiation of wavelengths around 15 microns by CO_2 also contribute significantly to this temperature decrease, e.g. see Allen et al. (1979). Above this height, solar radiation capable of ionizing particles is of sufficient intensity to produce appreciable ionization - particularly of NO, O_2, N_2 and O. Associated with these reactions is an increase in kinetic energy, thus heating the atmosphere, resulting in a rise in temperature. Above about 100km, neutral particles, ions, and electrons no longer collide sufficiently often to have the same temperature, and each therefore has a different temperature.

The reason for the shape of the electron density profile will be discussed shortly.

A. (iii)a. Particle densities and structures above 100km

Fig. A.3 shows the particle densities of the major neutral atmospheric constituents. N_2 dominates below about 100km, but above this height atomic Oxygen (O) is the main constituent in terms of number density. At even greater heights He dominates, since it has a much larger scale height than the heavier O and consequently falls off in density more slowly. Hydrogen dominates at even greater heights, but this species does not follow a simple exponential fall off in density. This arises because the rate of supply of H_2 in the lower atmosphere, and the rate of loss at the top of the atmosphere, are quite rapid. (Houghton 1977, §5.3).

Also shown is the electron density distribution with height. Notice even at the peak of electron density (F2), electrons (and hence positive ions) are only about 1/300 to 1/1000 of the total neutral number density. This is a point worth bearing in mind when considering the ionosphere.

Again, the state of composition can vary considerably with variations in the state of the sun (through a temperature dependence) (e.g. Ratcliffe 1970, p. 131).

The total atmospheric density also varies significantly (King-Hele 1978). During one day the density varies by about 1.5 times at 200km, and by about 6 times at 600km. Variation is maximum at around 600km. Variations over a sunspot cycle are even greater. There are also other types of density variations - semi-annual and irregular being two of the others. King-Hele (1978) gives a comprehensive review of atmospheric densities.

Ionization of these various species is the reason for free electrons appearing in the atmosphere. The F region is produced principally by radiation at 20nm-80nm ionizing N_2, O_2 and, particularly, O. The maximum of ion production is at heights of about 150 to 170km (F1 height).

Below this height the intensity of this radiation falls off, and above there are less particles to be ionized. (The electron density however, continues to rise above this height because recombination is less rapid).

The E region is produced by

(i) Xrays (wavelengths $\lesssim$ 10nm) ionizing O_2 and N_2

(ii) UV (wavelengths ~ 100nm) ionizing O_2.

Fig. A.3 Typical densities of neutral atmospheric constituents (from Houghton 1977, fig. 4.2; Ackerman 1979; and Roble and Schmidtke 1979, fig. 6). The NO density above 100km is from Roble and Schmidtke. The NO, CO_2, H_2O, O_3 and $O_2{}^1\Delta$ ($O_2{}^1\Delta_g$) measurements came from Ackerman. All other values came from Houghton. These densities fluctuate somewhat as the temperature varies. Also shown, for comparison, are typical electron densities (these are shown by the broken line and shading. The shading gives some idea of the possible variations. The long line represents daytime densities, and the short section to the left typical night time densities). It is clear that, even at 300km, the electron number densities are small compared to the total neutral density.

Only some of the more important minor gases are shown below 100km. For a more complete picture, see Ackerman (1979). In particular, CH_4, N_2O and CO have densities greater than or equal to the density of NO, and HNO_3, CH_3Cl, NO_2, HCl, SO_2, CCl_4, ClO, and HF have densities comparable to that of NO (about $10^9 m^{-3}$ at 20-40km). NO has been included because it, along with O_2, are the main two constituents in the D region directly ionizable by incoming radiation .

Above the D region, O_2, O and N_2 are the most important ionizable constituents up to 500-600km. At a thermospheric temperature of 700K, He becomes more dominant than O at about 500km, and H atoms take over from He at about 900km. At a temperature of 900K, the O-He transition is about 600km and He-H transition about 1800K (King-Hele 1978, fig. 2). Above about 2000km, ions become the major form of particle, but below about 1000km, the dominant species are neutral. At ground level, the total number density is $2.5 \times 10^{25} m^{-3}$. The distribution (by number density) is 78.03% N_2, 20.95% O_2, .93% CO_2 (Chemical Rubber Co. Handbook of Chemistry and Physics, 51st ed., 1970, p. F147).

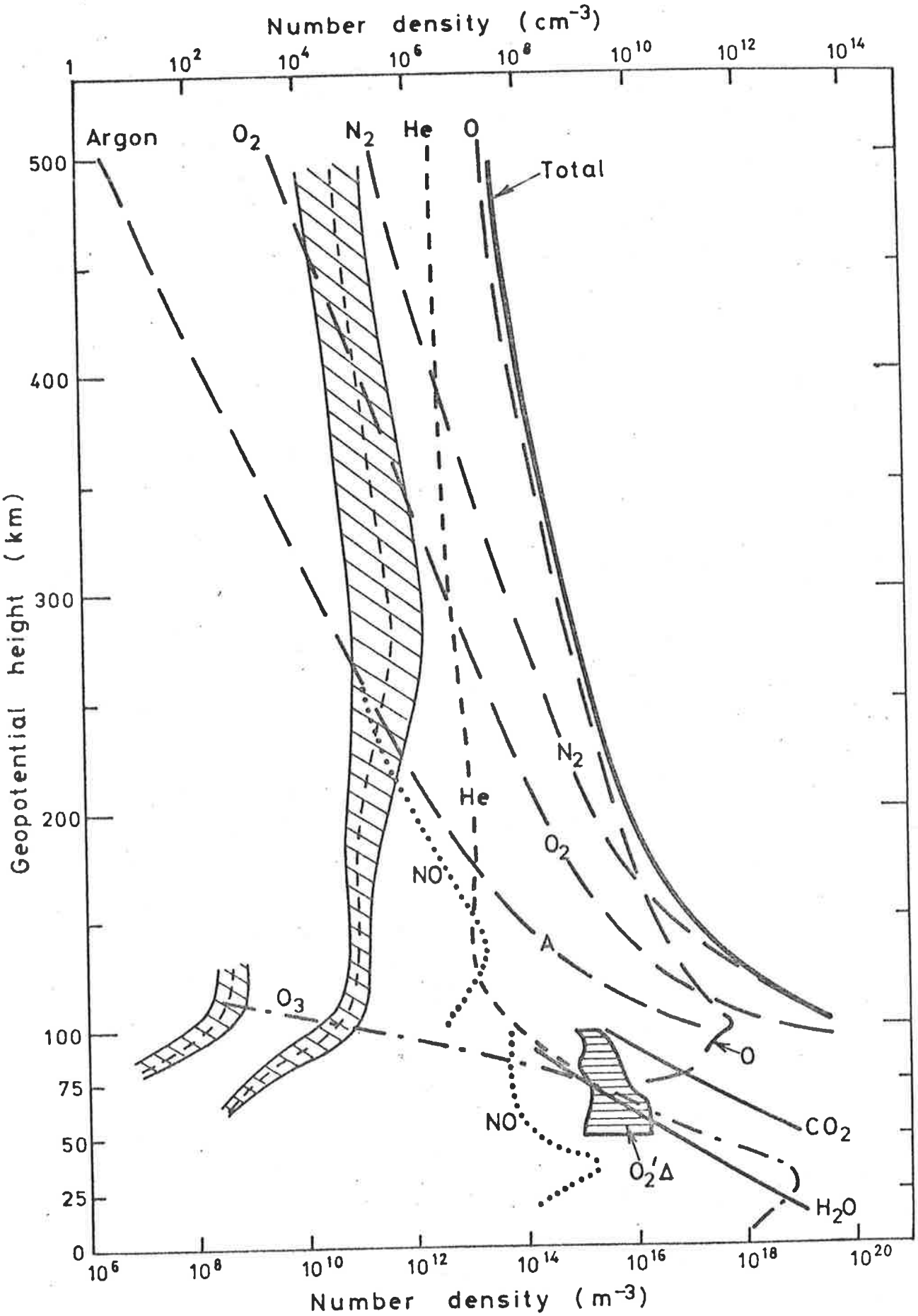
Number density (cm⁻³)
1
10²
10⁴
10⁶
10⁸
10¹⁰
10¹²
10¹⁴
Argon
O₂
N₂
He
O
Total
500
400
300
200
100
75
50
25
0
Geopotential height (km)
N₂
He
O₂
NO
A
O₃
O
CO₂
NO
O₂'Δ
H₂O
10⁶
10⁸
10¹⁰
10¹²
10¹⁴
10¹⁶
10¹⁸
10²⁰
Number density (m⁻³)

A. (iii)b. The Electron density profile above 100km

How is the electron density profile explained?

Consider the constituents N_2, O_2 and O. Each decreases in number density above 100km. The particular solar EM radiation which is capable of ionizing these particles weakens as it penetrates deeper into the atmosphere, as more and more of it is absorbed via these ionization processes.

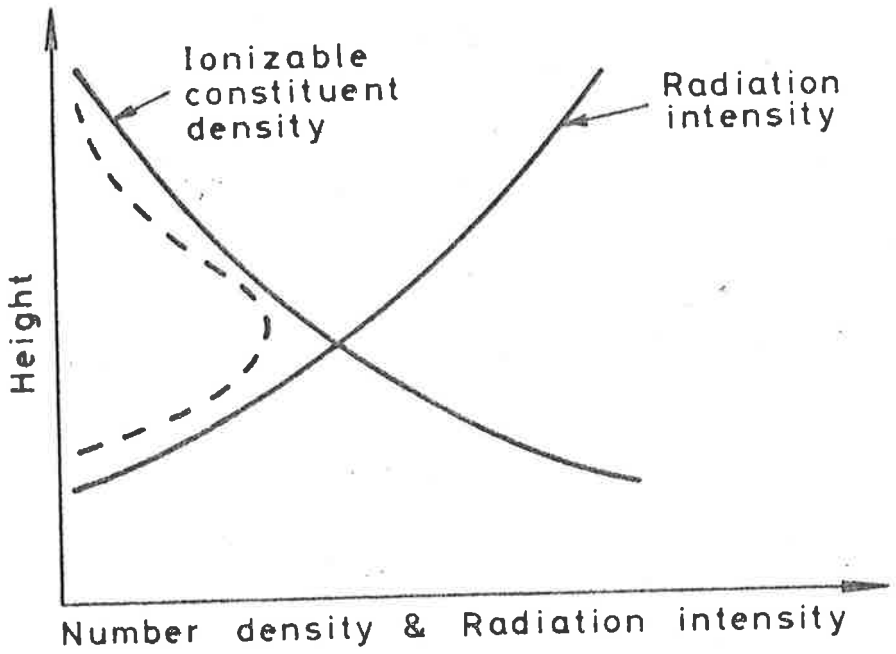

Fig. A.4

The result is a peak in the production rate of electrons, as illustrated in Fig. A.4. (A little similar to the formation of the Ozone layer).

There are 2 major such peaks in production rate in the upper ionosphere - at the E region (110-130km) and the F1 region (about 150-200km).

However, in looking at the overall electron density, one must also consider electron loss rates. It appears recombination is the dominant electron loss process

A.1 $$X^+ + e^- \rightarrow X + h\nu \quad .$$

This is the reverse of the ionizing process.

A.2 Attachment, $N + e^- \rightarrow N^- + h\nu$, appears not to be important. However, A.1 is a reaction with a very small rate coefficient (about $10^{-12} cm^3 s^{-1}$) compared to the expected coefficient of about 10^{-8}, as judged from the decay rate of electron density after sunset. However,

A.3 $$e^- + XY^+ \rightarrow X + Y$$ is a much faster reaction, since conservation of energy and momentum are satisfied more easily. Thus

A.4 $$e^- + N_2^+ \rightarrow N + N$$

A.5 and $$e^- + O_2^+ \rightarrow O + O$$ are 2 major recombination reactions.

For O^+, 2 reactions are involved;

A.6 (i) $$O^+ + N_2 \rightarrow NO^+ + N$$

(ii) $$e^- + NO^+ \rightarrow N + O \quad .$$

In this reaction pair, the rate is determined by the slowest of (i) and (ii). Up to about 200km, (ii) is the slowest. The reaction coefficient of (ii) is height independent, and thus up to around 200km, the electron density profile is roughly given by the production rate. Hence E and F1 are generally Chapman-like Layers. But above this height, (i) is slowest. This arises because the rate of (i) depends on the concentration of N_2, which has fallen to quite low values. Thus above F1, both the production and loss rates fall off, as the concentration of N_2 falls off. It so happens the loss rate falls off faster, resulting in an increase in electron density above F1. Sometimes the F1 layer shows as a peak, before this rise, and sometimes it is hidden by this

increase of electron density. F1 is particularly prominent in the summer of solar maximum years.

Then why does the electron density finally fall off at about 300km (F2)? (Ratcliffe 1979, p. 112). Quite simply, diffusion takes place very rapidly (due to the long mean free paths) and the electrons form into a density distribution governed by the hydrostatic equation $dp = -\rho g dv$. Thus the electron density simply decreases exponentially with height, with a scale height H (in principle) much larger than that for the ions (H is about $30{,}000H_I$ if the electrons were free to diffuse alone). However, electrostatic forces draw the ions and electrons together, and as a result the two species combine to produce an almost common scale height $H \simeq 2H_I$.

APPENDIX B

PROPAGATION OF RADIO WAVES THROUGH THE IONOSPHERE

B. (i) General discussion

B. (ii) Ray Theory, Differential Absorption, and Groups

Appendix B: Propagation of Radio Waves Through the Ionosphere

B. (i) General discussion

The detailed examination of the propagation of radio waves through the ionosphere is an extremely complex problem. The two classic references on the subject are Ratcliffe (1959) and Budden (1966). However, some of the formulae - particularly the Appleton-Hartree formula - have been updated since these earlier books (Sen and Wyller 1960, with corrections by Manchester 1965; Budden 1965).

Fortunately, however, many simplifications can be made at frequencies above about 2MHz in the D region, and many of the more difficult aspects of a full treatment are not important. The frequencies used for investigations in this thesis all lie in the region close to and above 2MHz. This short review will broadly consider the equations governing the full solution, and simply mention the D region simplifications. A brief mention will be made of critical levels, and cases where the ray theory breaks down - partly to give a feel for the conditions for which ray theory is relevant, and partly because later, when gravity waves are considered, similar complications arise which in that case are important. In fact the passage of radio waves through the ionosphere, and of gravity waves moving through an atmosphere, have many common features.

Budden (1954) gives a good overall summary of the derivation of the relevant formulae, and the main points are repeated here.

One begins by considering the effects of an electromagnetic (EM) wave on free electrons. In the Appleton approach (Appleton 1932; Hartree's approach was somewhat different (Hartree 1930; Budden 1954)), an effective polarization $\underline{P}$ of the medium was assumed to occur due to the passage of an EM (Electromagnetic) wave.

B.1 $$\underline{P} = Ne\underline{r},$$

where N = electron density, e = charge of an electron,

$\underline{r}$ = electron displacement.

Maxwell's equations were used to relate $\underline{P}$ to the electric and magnetic fields $\underline{E}$ and $\underline{H}$ of the wave.

The electron's equation of motion was assumed to be

$$\text{B.2} \quad m_e\left(\frac{d^2\underline{r}}{dt^2}\right) + m_e\nu_m \frac{d\underline{r}}{dt} = e\left(\frac{d\underline{r}}{dt} \times \underline{B}\right] + e\underline{E},$$

where m_e = electron rest mass, t = time, ν_m is the collision frequency of an electron with neutral molecules, and $\underline{B} = \frac{\underline{H}}{\mu}$.

B.2 thus gives the so-called "constitutive relations" of the medium. The electron has been assumed to have a damping force proportional to its velocity $\frac{d\underline{r}}{dt}$. Modification of this assumption was the basis of the approach of Sen and Wyller, who made use of more recent experiments which showed that the electron collision frequency itself is not constant, but proportional to the square of the electron velocity. Such modifications will not be considered here, although all work involving refractive indices in this thesis are calculated by the Sen-Wyller formulae. For a discussion of these modifications Budden (1965) is a useful reference.

Maxwell's equations lead to equations 2.30 of Budden(1966)- namely,

$$\text{curl } \underline{E} = -ik\underline{H}, \quad \text{curl } H = \frac{ik}{\varepsilon_0}\underline{D},$$

where $H = Z_0\underline{H}$, $\underline{H}$ being the magnetic field of the electromagnetic radiation, $Z_0 = \sqrt{\mu_0/\varepsilon_0}$, and μ_0 and ε_0 are the permeability and permittivity of free space. The term k is the wave number of the radiation, and $\underline{D}$ is the displacement current = $\varepsilon_0\underline{E} + \underline{P}$.

All equations not involving the constitutive relations (B.2) are valid independent of the modifications of Sen and Wyller.

The polarization is then related to $\underline{E}$ by

$$\text{B.3} \qquad \underline{P} = \varepsilon_0[M]\underline{E},$$

where [M] is called the susceptibility matrix, and is derived from considerations of the constitutive relations.

Suppose one uses a cartesian co-ordinate system with z vertical, and considers the situation of a plane wave with wave normal in the x - z plane at angle θ to the vertical, incident upon the ionosphere. Manipulation of the formulae presented leads to four coupled linear differential equations - equations 18.10 to 18.13 of Budden (1966) viz -

B.4 $$\frac{1}{ik}\frac{dE_x}{dz} = \frac{-SM_{zx}}{(1+M_{zz})} - \frac{SM_{zy}}{(1+M_{zz})}E_y + \left(\frac{C^2+H_{zz}}{1+M_{zz}}\right)H_y,$$

B.5 $$-\frac{1}{ik}\frac{dE_y}{dz} = -H_x,$$

B.6 $$-\frac{1}{ik}\frac{dH_x}{dz} = \left(-M_{yx} + \frac{M_{yx}M_{zx}}{(1+M_{zz})}\right)E_x - \left(C^2 + M_{yy} - \frac{M_{yz}M_{zy}}{(1+M_{zz})}\right)E_y + \frac{SM_{yz}}{(1+M_{zz})}H_y,$$

B.7 $$-\frac{1}{ik}\frac{dH_y}{dz} = \left(1 + M_{xx} - \frac{M_{xz}M_{zx}}{(1+M_{zz})}\right)E_x + \left(M_{xy} - \frac{M_{xz}M_{zy}}{(1+M_{zz})}\right)E_y - \frac{SM_{xz}}{1+M_{zz}}H_y.$$

Here, $M = \begin{bmatrix} M_{xx} & M_{xy} & M_{xz} \\ M_{yz} & M_{yy} & M_{yz} \\ M_{zx} & M_{zy} & M_{zz} \end{bmatrix}$, and $C = \cos\theta$,

$S = \sin\theta$, θ being the angle of incidence (angle to the vertical). $\underline{H} = Z_0\underline{H}$, Z_0 being $\sqrt{\frac{\mu_0}{\epsilon_0}}$ = impedance of free space. The parameter k is the wave number in free space of the radiation.

In these equations, a time dependence $e^{j\omega t}$, $j = \sqrt{-1}$, $\omega = 2\pi f$ = angular frequency, and a term e^{-jkSx}, expressing the wave variation in the x direction, have been removed. To obtain the full solution, the solution of B.4 to B.7 should be multiplied by these terms.

In the case of an homogeneous atmosphere all the coefficients of the H_x, E_y etc. are independent of z, and the solution is of the term e^{-jkqz}. Substitution of this into B.4 to B.7 leads to a characteristic equation for the system of differential equations which can be written

$$\text{B.8} \quad \begin{vmatrix} -\frac{SM_{zx}}{1+M_{zz}} - q & -\frac{SM_{zy}}{1+M_{zx}} & 0 & \frac{C^2+M_{zz}}{1+M_{zz}} \\ 0 & -q & -1 & 0 \\ -M_{yx} + \frac{M_{yz}M_{zx}}{1+M_{zz}} & -C^2 - M_{yy} + \frac{M_{zy}M_{yz}}{1+M_{zz}} & -q & \frac{SM_{yz}}{1+M_{zz}} \\ 1 + M_{xx} - \frac{M_{xz}M_{zx}}{1+M_{zz}} & M_{zy} - \frac{M_{xz}M_{zy}}{1+M_{zz}} & 0 & -\frac{SM_{xz}}{1+M_{zz}} - q \end{vmatrix} = 0$$

where $|\ |$ ≡ determinant. This is the so called Booker quartic for a homogeneous (though possibly anisotropic) ionosphere. Four solutions of q generally result, with corresponding solutions for E_x, E_y, H_x, H_y. A typical solution might be

$$\text{B.9} \quad E_x = E_x^{(1)} e^{-jkq_1 z}, \; E_y = E_y^{(1)} e^{-jkq_1 z}, \; H_x = H_x^{(1)} e^{-jkq_1 z}, \; H_y = H_y^{(1)} e^{-jkq_1 z},$$

q_1 being one root of the Booker quartic. $E_x^{(1)}$ etc. are constants. Of course the ionosphere is not homogeneous, but these equations give some insight into the complexities of a full theory.

Now assume an ionosphere which varies with height, but is horizontally stratified. Let the density and collision frequency for electrons vary slowly with height, (the precise meaning of "slow" will be seen shortly), so the Booker quartic is still roughly valid in any region. In each "region" then, a solution

B.10 $e^{-jkq_1 z}$ is still valid, but q_1 varies with height, z.

It can be shown, at least for an isotropic ionosphere (viz. no magnetic field), that

B.11 $q = \mu\cos\psi,$

ψ being the angle between the wave normal and the vertical, and μ the phase refractive index, at height z (see Budden 1966, section 13.3).

Then the solution to the differential equations B.4 to B.7 becomes of the form

B.12 $q^{-\frac{1}{2}}\exp\{-jk\int_0^z q\,d\xi\}$.

This is one form of the Wentzel, Kramers, Brillouin and Jeffreys approximation (the WKBJ, or sometimes simply called WKB, approximation), and is valid provided terms like $(\frac{dq}{dz})/kq$, $(\frac{d^2q}{dz^2})/k^2q$ are small (that is, the medium is slowly varing, and q is not small). The exponential term is sometimes called the phase memory term.

The full solution then becomes 4 sets of the form

B.13 $E_x(z) = E_x^{(1)}(z)q_i(z)^{-\frac{1}{2}}e^{-jk\int_0^z q_i d\xi}\,e^{-jkx\sin\theta}\,e^{j\omega t}$

$i = 1, 2, 3, 4.$

Similarly E_y, H_x, H_y.

Each one of these sets corresponds to the normal concept of a ray. If the q_i are all unequal, the WKB solution is valid, and the 4 solutions correspond to 2 upgoing waves, and 2 downgoing waves. The waves are denoted O (ordinary) and X or E (extraordinary), there being one upgoing and one downgoing O mode solution, and one upgoing and one downgoing X mode solution. Each is a plane wave solution, elliptically polarized. These solutions are the only waves which will maintain their form while propagating through the particular quasi-homogeneous part of the ionosphere

under consideration. The solutions naturally vary at different points in the non-homogeneous ionosphere. From the values of q, μ may also be found, μ being the (complex) refractive index. However, q is the really important parameter, since it is the term which appears in the solution.

In the case of an isotropic ionosphere, $\mu = \sqrt{K_e}$ (just as in the case of light passing through glass), where $\underline{D} = K_e \varepsilon_0 \underline{E} = \varepsilon \underline{E}$. That is, the susceptibility matrix has all diagonal elements equal, and all other elements = 0, so

$\underline{P} = \varepsilon_0 [M] \underline{E}$ becomes a scalar set of equations,

$\underline{P} = \varepsilon_0 (K_e - 1) \underline{E}$. The susceptibility matrix has diagonal elements $(K_e - 1)$. In this isotropic case, the solution of μ then becomes particularly simple (for example, Ratcliffe 1972, chapter 8). The solution in the undamped case ($\nu_m = 0$) is

$$\mu^2 = 1 - X_e,$$

$X_e = \frac{\omega_0^2}{\omega^2}$, ω = angular frequency of the radiation, and ω_0 = plasma frequency = $(Ne^2/\varepsilon_0 m_e)^{\frac{1}{2}}$, N being the electron density, e the change of an electron, m_e the mass of an electron.

In this case, the role of positive ions has been ignored, since their much larger mass means they respond far more sluggishly to the electric field of the radiation than the electrons. Ratcliffe (1972) discusses the effects of positive ions in his section 8.5.3, but the case will not be discussed here.

In the case of radiation propagating vertically,

$$\mu^2 - 1 = \frac{P_x}{\varepsilon_0} E_x = \frac{P_y}{\varepsilon_0} E_y \qquad \text{(Raticliffe 1972, equation 8.10),}$$

and this is valid even in an anisotropic ionosphere. Ratcliffe uses this formula to discuss the simple cases of isotropic ionosphere ($\mu = \sqrt{K_e}$ can

be seen to come out of this, as $\underline{D} = \varepsilon_0\underline{E} + \underline{P} = K_e\varepsilon_0\underline{E}$, so that $\underline{P} = \varepsilon_0(K_e-1)\underline{E}$ and $\frac{P_x}{\varepsilon_0 E_x} = K_e - 1)$. Some simple anisotropic cases are also considered, but all with zero damping. In the most general case of non vertical propagation, recourse to the Booker quartic is generally the best approach.

A refractive index is really only relevant if a WKB (ray) solution is valid. Ratcliffe (1972, ch. 8) assumes a WKB (plane wave) solution, and really simply substitutes this form into Maxwell's equations to derive μ. Similarly Budden (1965), adopts this assumption of a WKB solution in his derivation of the Sen-Wyller refractive indices (section 8). Hence he derives the refractive indices given by his equation (82) (there are two solutions - one for the O mode and one for the X mode), with axial ratios of the ellipses given by equations 76, 77. There is little point in giving the actual forms here. A computer program has been written to calculate the Sen-Wyller O and X mode refractive indices, and appears in the appendices. The O and X modes correspond to identical elliptical polarizations, at right angles to each other, with opposite senses of rotation.

The WKB solution, however, is not always valid. For most purposes in this dissertation it is adequate, but a brief consideration of some of its limits may be useful, again based on Budden's (1954) paper.

When q gets small, the WKB solution breaks down, as we have seen; $q = 0$ corresponds to the case of critical reflection - an upgoing WKB wave "turns around" and heads back to the ground. Such cases of small q can still be treated in a relatively simple manner, until q gets very close to zero, however, for an isotropic atmosphere (Budden 1954, equation (12)). Because we are dealing with equations of the form

$$\frac{d^2E}{dz^2} + k^2q^2(z)E = 0,$$

and because q^2 is a linear function of electron density, in cases of small q this differential equation can be reduced to

$$\frac{d^2E}{dz^2} = \beta z E, \quad \beta = \text{constant},$$

and this can be solved (Budden 1954), via Airy solutions (or, alternatively, numerically on a computer). In fact, for an isotropic ($\underline{B} = 0$) ionosphere, the ray-type WKB solution is a reasonable approximation even near $q = 0$.

For an anisotropic ionosphere, the WKB solution is still usually valid provided no two roots of the Booker quartic become nearly equal (Booker 1936). Airy functions can still be used close to these points, but there are limits. These points where two q values are equal are called branch points.

Another case where the WKB solution breaks down is the case where the refractive index μ becomes infinite, or where one of the roots of the Booker quartic tends to infinity. It has been suggested that radio waves are reflected at this level, (Budden 1954) but WKB solutions are not valid, and a full numerical solution of the differential equations is necessary. Ratcliffe (1972, section 8.3) discusses in a little more detail the effects of zero and infinite refractive index.

Thus far, we have regarded all solutions of the equations B.4 to B.7 as propagating independently. This is valid in the cases where the WKB approximation is valid. Since terms like $\frac{dq}{dz}/kq$ etc. can be ignored, the four equations can be reduced to four independent equations giving rise to the four WKB solutions, and the waves propagate independently. But this is not always possible in cases where the WKB solution is invalid - the differential equations have coupling terms. A more complete analysis is then necessary. (For vertical incidence, the Booker quartic reduces to a bi-quadratic, $(q^2 - k_1)(q^2 - k_2) = 0$, with solutions $\pm\sqrt{k_1}$, $\pm\sqrt{k_2}$, corresponding to up and downgoing O mode, and up and downgoing X mode.

The q solutions are + and - the appropriate O and X mode refractive indices, since $\theta = 0$. For the isotropic case, the system B.4 to B.7 reduces to two differential equations, and there is only one refractive index for all plane waves. We thus see, once again, that this is a much simpler situation. Its simplified treatment in Ratcliffe 1972, has already been mentioned).

Budden (1954) discusses coupling in a little more detail, and of course Budden (1966), has a more extensive account. Physically, the O and X modes can be regarded as "interacting" to some degree when such coupling is important between O and X modes. Reflections, too, are a form of coupling - in this case, interaction between the upgoing and downgoing modes occurs.

B. (ii) Ray Theory, Differential Absorption and Groups

As has been seen, the WKB theory is appropriate for many cases. In the D-region below about 95 to 100km and for frequencies greater than 2MHz, it is generally applicable, since the phase refractive index does not approach 0.

The solution for these cases is a ray, as we have seen (equation B.13)

$$\text{B.14}\quad E_x(z,t) = E_x^{(1)}(z)q^{-\frac{1}{2}}e^{-jk\int_0^z q\,dz}\,e^{-jkx\sin\theta}\,e^{j\omega t}\quad .$$

In this thesis, vertical propagation will be considered in most cases. Thus $\theta = 0$, so $q = \mu$.

The following approximation will therefore be used. Generally point-like transmitters are used, so spherical wave fronts result

$$\text{B.15a}\quad E(z,t) = \frac{1}{S}E^{(1)}(z)e^{-jk\int_0^z \underline{\mu}\cdot\underline{ds}}\,e^{j\omega t}$$

where $\underline{ds}$ is an element of the ray path, and $\underline{\mu}$ is the complex phase refractive index. The $q^{\frac{1}{2}}$ term has been dropped, as $|\mu|$ is close to 1. S is the path distance travelled. The $\frac{1}{S}$ term arises because we have spherical radiation.

$$\mu \text{ is complex, } = \mu_R + j\mu_I$$

$$j = \sqrt{-1}$$

B.15a can also be written

$$\text{B.15b}\quad E(z) = \frac{1}{S}E^{(1)}(z)e^{-j\frac{\omega}{c}[\int_0^z \mu_R\,ds]}\,e^{j\omega t}\,e^{\frac{\omega}{c}\int_0^z \mu_I ds}\quad .$$

When the μ_I term is -ve, the $e^{\frac{\omega}{c}\int_0^z \mu_I ds}$ term represents absorption. In the real ionosphere, μ_I is always negative. In some simple approximations involving low absorption, $\mu_I \alpha (-N\nu_m)$, N = electron density, ν_m = collision frequency of an electron with neutral particles. However, in the more general case, this is not valid. This subject is discussed to some degree

in Dyson and Bennett (1979), although that reference does not use the general Sen-Wyller formulae, but rather a modification of the Appleton-Hortree formula which approximates the Sen-Wyller formula (e.g. see Budden 1965).

However, the constant of proportionality between μ_I and $N\nu$ is different for X and O modes

B.16 $$\mu_I\left(\begin{matrix}X\\O\end{matrix}\right) = -k_{\left(\begin{matrix}X\\O\end{matrix}\right)} N\nu_m \quad .$$

This relation forms the basis of the so called Differential Absorption Experiment. In the D-region of the ionosphere, weak partial reflections occur from small changes in refractive index with height. The reflections are not critical reflections, as the electron densities are too low. Reflection coefficients are in the range 10^{-6} to 10^{-3}. These reflections are discussed in detail in this thesis. If, then, the strengths of O and X modes partial reflections are compared, and the expected reflection coefficient ratio of O and X modes is known, and k_x, k_0, and ν are known, then the electron density N as a function of height in the D-region can be deduced. The method was first introduced by Gardner and Pawsey (1953), and has since been improved to some degree, (Flood 1968; Von Biel 1970; Belrose 1970; Coyne and Belrose 1973; Von Biel 1977), although the essentials remain the same as the original procedures. Perhaps the major modifications are the use of the Sen-Wyller refractive indices to get k_x, k_0 and the use of large arrays to cut down scatter from the off-vertical. The more careful treatment of O and X modes is the subject of Von Biel's 1977 paper. Von Biel et al. (1970) and Jones and Kopka (1978), discussed the use of phase measurements to improve the experiment. There has also been some debate as to the role of rapid changes in collision frequency in causing reflections, as distinct from the usual assumption that changes in electron density are the principal

cause of the refractive index changes (Piggott and Thrane 1966; Jones and Kopka 1978). Generalization of B.16 is also desirable, as the assumption of linearity between $N\nu$ and μ_I is not really valid (e.g. Dyson and Bennett 1979). The relation (B.16) can be generalized ($\mu_I = f_{(X)}^{(O)}(N,\nu_m)$), and the DAE theory generalized around this. The objective, however, remains the same - determination of the electron density profile as a function of height, given the collision frequency profile ν_m. Lindner (1972) gives a review of the DAE experiment, as does Belrose (1970).

It is important to note that although the DAE experiment has been fairly successful, there is room for improvement. For example, its vertical resolution is only of the order of kilometres. Further, various assumptions have been made about the nature of the reflecting irregularities (some of which have already been mentioned) which have not been fully validated. A fuller understanding of these scatterers is necessary before the DAE results can be interpreted unambiguously. The reflections are generally assumed to be Fresnel reflections from steps in electron density, and this has not yet been confirmed fully. The angular spectrum of scatter is important, too - is there scatter only from the vertical, or is there significant off-vertical scatter? If there is significant scatter from the off-vertical, some DAE results which use aerials with wide beams will be invalid.

In most ionospheric studies in this dissertation, and indeed in many D-region studies, radio wave pulses are used. This is to gain an idea of the height of scatter of the radio waves, since the delay in time between transmission and receival of the pulses gives an estimate of this quantity. DAE also uses pulses to get its estimates of heights. Hence a brief discussion of wave groups in the ionosphere will be given here.

Wave groups may, of course, be regarded as a sum of many infinite sinusoidal plane waves, each of whose time and space history is given by an equation like (B.15b). The wave normal directions of these component waves vary, and their speeds also vary. The resultant has an envelope moving at speed v_g. Inside the envelope is a continuous wave moving at speed v, this being approximately the mean phase speed of the component frequencies. The field strength thus follows the form

B.17 $E(z,t) = g(t-\int_0^z \frac{Re(\mu_g')ds}{c}) \frac{1}{S} E^{(1)}(z) e^{-j\frac{\omega}{c}\int_0^z \underline{\mu}.\underline{ds}} e^{j\omega t}$, where Re="Real part of",

where $g(t-\int_0^z \frac{Re(\mu_g')ds}{c})$ describes the envelope, and $\mu_g' = \frac{c}{v_g}$. The formulae for μ_g', v_g will be discussed shortly (B.18, B.22).

A description of the form B.17 requires that the phase refractive index vary linearly as a function of frequency across the range of frequencies composing the group, and that this range of frequencies is "small". If this is not valid, a group representation is not possible. In such cases, the propagation of a pulse is best considered by treating each of its Fourier components individually, and re-summing these components upon their arrival at the receiver.

But in the case of a pulse which does propagate with an unchanging envelope, the group (envelope) velocity (that is, the velocity along the ray direction) is

B.18 $$\underset{\sim}{v}_g = \underset{\sim}{\nabla}_k w, = \frac{\partial\omega}{\partial|k|} \cdot \frac{1}{\cos\alpha}$$

where $\underset{\sim}{\nabla}_k = \underset{\sim}{i}\frac{\partial}{\partial k_x} + \underset{\sim}{j}\frac{\partial}{\partial k_y} + \underset{\sim}{k}\frac{\partial}{\partial k_z}$, and the wave number vector of frequency f is (k_x, k_y, k_z). Here, α is the angle between the ray path and the wave normal of the Fourier component of angular frequency ω, and

B.19 $$\tan\alpha = -\frac{1}{\mu}\frac{\partial\mu}{\partial\theta},$$

θ being the angle of the wave normal to the vertical.

There can be some confusion regarding group velocities. Some ionospheric workers call

B.20 $$v_n = \frac{\partial \omega}{\partial |k|} = v_g \cos \alpha$$

the "group velocity", and call v_g the ray-group velocity, or wave packet velocity. The v_n is the velocity component of the group along the wave normal of the Fourier component of frequency f (see Ratcliffe 1972 §8.8). Theorists, on the other hand, often call v_g the group velocity. Workers do, generally, agree on the definition of group refractive index, however; namely,

B.21 $$\mu_g = \frac{c\omega}{v_n} = \frac{\partial}{\partial \omega}(\omega\mu) = \mu + \omega\frac{\partial \mu}{\partial \omega} \quad .$$

The quantity denoted μ_g' in 1.2.2.16 is

B.22 $$\mu_g' = \frac{c}{v_g} = \mu_g \cos \alpha \quad .$$

Ratcliffe 1972, §8.8, is a good reference for derivation of some of the equations B.18 to B.22.

One can also define group and phase paths. These are given by

B.23 $$\text{Phase path} = \int \mu \cos\alpha \, ds,$$

and

B.24 $$\text{Group path} = \int \mu_g' \, ds$$

where the integrations are performed along the path of the ray (Dyson and Bennett 1979).

As mentioned, group representations are not always valid, particularly in cases where μ is not sufficiently linear in ω over the range of frequencies considered. For example, for frequencies close to the electron gyro frequency $\Omega_e = \frac{\omega B}{m_e}$ in the ionosphere, the X mode refractive index varies rapidly and non linearly with frequency (see Fig. B.1). In such

Fig. B.1 Real and imaginary components of the Sen-Wyller refractive index μ (note $\mu < 1$) for the electron densities and heights shown. (Multiply the vertical scale by the Power of 10 shown). The imaginary part has been converted to an absorption term, so amplitude up to height z is

$$\alpha \exp\{-\int_0^z A\,ds\},$$

where $A = -(\omega/c)*\mathrm{Im}(\mu)$, ω is the angular frequency and c the speed of light in a vacuum.

The refractive indices were calculated using the Sen-Wyller subroutines presented in the appendices.

The following assumptions were made

(i) Magnetic field $\underline{B}$ is given by

$$|\underline{B}| = 6 \times 10^{-5}/(1 + \frac{\text{height(km)}}{6370\text{km}})^3 \quad \text{Tesla},$$

(ii) Collision frequency of an electron is

$$\nu_m \begin{cases} 5.217 \times 10^{10}.\exp\{-\text{height(km)}/7.297\} & \text{for height} \leq 71\text{km} \\ 2.989 \times 10^{11}.\exp\{-\text{height(km)}/6.187\} & \text{for height} \geq 71\text{km} \end{cases}$$

(iii) The angle of incidence to the $\underline{B}$ field is assumed to be 22.5°.

Note in particular how the X mode refractive index changes very rapidly near the gyrofrequency (~1.6MHz).

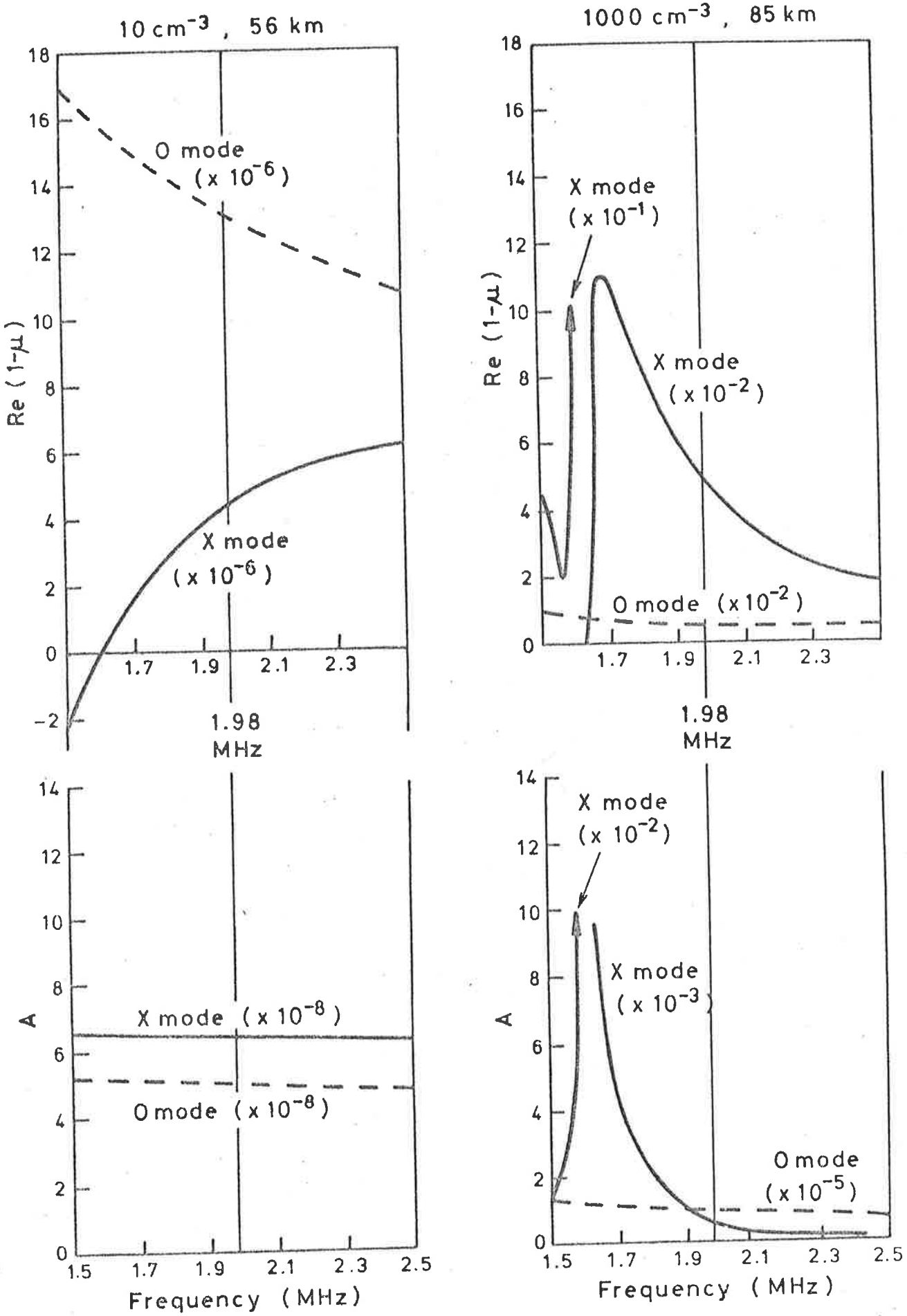
10 cm^{-3} , 56 km
1000 cm^{-3} , 85 km
Re (1-μ)
O mode (x 10^{-6})
X mode (x 10^{-6})
X mode (x 10^{-1})
X mode (x 10^{-2})
O mode (x10^{-2})
1.98 MHz
A
X mode (x 10^{-8})
O mode (x 10^{-8})
X mode (x 10^{-2})
X mode (x 10^{-3})
O mode (x 10^{-5})
Frequency (MHz)

cases equation B.21 can produce $\mu_g \lesssim 1.0$ at 2MHz. This would appear to imply that the "group" actually moves at faster than the speed of light in a vacuum! But what it actually says is that the "envelope" of the "group" changes form as it propagates. (Also see Jackson 1975, pp. 302-326). Then the "Fourier decomposition" technique discussed previously is necessary to fully investigate the propagation of such a pulse.

Given a horizontally stratified refractive index profile the reflection coefficient for an incident radio wave arriving vertically is

$$\text{B.25} \qquad R_0(z)dz = \frac{\mu_0(z+dz) - \mu_0(z)}{\mu_0(z+dz) + \mu_0(z)} \left(\simeq \frac{d\mu_0(z)}{2\mu_0(x)} \right) .$$

This relation comes simply from the reflection coefficient for light incident on the plane boundary of two slabs of optically transparent material with refractive indices μ_1 and μ_2. In such a case $R = \frac{\mu_1 - \mu_2}{\mu_1 + \mu_2}$ for perpendicular incidence (e.g. Jackson 1975, p. 281). The relation for non-perpendicular incidence is a little more complex, but can be found in most optics books. R is usually given for two orthogonal plane polarizations, however, so in the ionosphere the incident radiation would have to be broken up into two such plane waves to calculate the reflected radiation.

Then the returned echo structure, given a transmitted pulse envelope g(t) at the transmitter (z = 0) is, crudely, a convolution of the pulse and reflection coefficient structure, - viz.

$$\text{B.26a} \qquad E(\tau) = R_0(\tfrac{ct}{2}) \otimes g(t), \text{ where } \otimes \text{ represents convolution,}$$

$$(= \int_{-\infty}^{\infty} R_0(\tfrac{ct}{2}) . g(\tau - t)dt \quad \text{(Champeney 1973, p. 66))}$$

is the returned echo as a function of time τ. The pulse has been

assumed to propagate at speed c, so height z corresponds to time $\frac{ct}{2}$, t being the time for the pulse to go to the height z and return if the pulse travelled at speed c. In most cases the delay time τ is converted to an effective (or "virtual") range

$$z_1 = \frac{c\tau}{2} \quad .$$

In fact, most recording systems use such virtual ranges, rather than delay time τ, as indicators of the pulse delay. Thus in this thesis, reference may be made to, say, "the amplitude at a height of 68km was ..."; this will really mean the "amplitude at a virtual height of 68km"; but for the D-region, virtual and real heights are very nearly equal and there is rarely a need to discriminate between the two. Then B.26a becomes

$$\text{B.26b} \qquad E_1(z_1) = \underset{(X)}{R_0(z)} \otimes g_1(z)_X \quad (= \int_{-\infty}^{\infty} \underset{X}{R_0}(z)\, g(z_1 - z)\, dz)$$

where $E_1(z_1) = E(\tau)$, $z_1 = \frac{c\tau}{2}$,

and $g_1(z) = g(t)$, $z = \frac{ct}{2}$.

A crude approximation like this has been used by Austin et al. (1969). However, a more accurate formula for the resultant echo structure will be derived later, which takes account of the spherical wavefronts of the probing radiation, and does not assume a wave speed equal to the speed of light in a vacuum. It also considers the effects of absorption. In some cases in this thesis the even more accurate Fourier decomposition method already discussed will be used.

Of course all these formulae assume a one-dimensional atmosphere. This amounts to assuming the ionosphere is horizontally stratified, with no off-vertical scatter. In fact this is not always the case. In cases where horizontal stratification is not valid, one must integrate the

returned echo strengths over all directions, and consider such effects as the polar diagram of the transmitting and receiving arrays. But such considerations can no longer be regarded as "introductory", and are considered in more detail elsewhere in the thesis.

APPENDIX C

THE DYNAMICAL EQUATIONS GOVERNING THE ATMOSPHERE

Appendix C: The Dynamical Equations Governing the Atmosphere

To put the atmospheric motions on a basis from which understanding and prediction can be best achieved, it is necessary to represent them mathematically. Theoretical solution of the resulting differential equations can then be undertaken. Usually some simplifications are necessary before this can be done. Different simplifications allow investigations of different members of a whole family of solutions. Examples of these will be seen later. Only the basic equations are given below. The derivations can be found in most books on Fluid Dynamics.

The basic equations for a general fluid can be written, in cartesian coordinates (x_1, x_2, x_3)

C.1 $$\frac{\partial \rho}{\partial t} + \frac{\partial}{\partial x_i}\rho v_i = 0$$ Continuity equation

C.2 $$\rho\left(\frac{\partial v_i}{\partial t} + v_j\frac{\partial v_i}{\partial x_j}\right) = \sigma_{ij,j} + F_i$$ Equations of motion (i = 1, 2, 3)

C.3 $$\rho\frac{D\varepsilon}{Dt} + \rho\frac{D\phi}{Dt} = -\frac{\partial h_i}{\partial x_i} + \sigma_{ij}\dot{e}_{ij}$$ Energy equation

(A form of the first law of thermodynamics, E = Q + W, E = energy, Q = heat input, W = work done by the system)

These equations are quite general. Repeated common subscripts imply a sum (for example

$$v_j\frac{\partial v_i}{\partial x_j} = v_1\frac{\partial v_i}{\partial x_1} + v_2\frac{\partial v_i}{\partial x_2} + v_3\frac{\partial v_i}{\partial x_3}) \cdot$$

Here, ρ is the fluid density

t is time

x_i, i = 1, 2, 3 refer to 3 cartesian coordinate axes

σ_{ij} are stress tensors, and will be described below,

F_i are the coordinates of the force applied externally per unit volume

$\frac{D}{Dt} = \frac{\partial}{\partial t} + v_i \frac{\partial}{\partial x_i}$ (the time derivative following the motion of a fluid element)

v_i, i = 1, 2, 3 are fluid velocities in the x_1, x_2, x_3 directions, and are a function of ($\underline{x}$, t)

ε is the internal energy per unit volume

$\underline{h_i}$ is a heat flux vector

- if ds is a surface element, with unit outward normal vector $\underset{\sim}{n}$, then the rate at which heat is transmitted across the surface ds is

$h_i n_i ds$ in the direction n_i, and the repeated i implies a sum as usual. The total heat input rate is

$$\frac{\partial Q}{\partial t} = -\oint h_i n_i ds = -\iiint \frac{\partial h_i}{\partial x_i} dv$$

e_{ij} is the deformation tensor expressing particle displacement

,j represents differentiation with respect to x_j ($\sigma_{ij,j} = \frac{\partial}{\partial x_j} \sigma_{ij}$)

$\dot{e}_{ij}$ is the time derivative of the deformation tensor, = $\frac{1}{2}(v_{i,j} + v_{j,i})$

ϕ is the gravitational potential energy per unit volume (= gx_3 for a system with g, the acceleration due to gravity, = constant, and x_3 = vertical displacement from a reference point x_3 = 0)

Equations C.1 to C.3 are 5 equations in 12 unknowns:- ρ, ε, v_i, T, σ_{ij}. (The h_i are functions of temperature T). There are only 12 unknowns here, as σ_{ij} is a symmetric matrix. This follows from considerations of angular momentum. Notice also that these equations are not strictly tensor equations, as $\sigma_{ij,j}$ is not a tensor. Seven more equations are necessary to close the system. Six come from so called constitutive relations, which relate σ_{ij} to e_{ij} and $\dot{e}_{ij}$, and the seventh is the equation of state, which connects the mechanical and thermal properties of the media.

The equation of state can take several forms, generally based upon

the second law of thermodynamics,

C.4 $dQ = \frac{ds}{T}$,

where s is the entropy ("degree of disorder") of the system, and Q the heat input. Appropriate manipulation, possibly with the first law of thermodynamics and a statistical mechanical approach, can lead this to other forms, such as

$p = \rho k_m T$ (for an ideal gas)

or $p = (C_p - C_v)\rho T$ (ideal gas)

where p = pressure, k_m is the gas constant when ρ is in mass per unit volume, and C_p and C_v are the specific heats at constant pressure and volume respectively - viz.

$$C_p = \left(\frac{dQ}{dT}\right)_{\text{const } p}, \quad C_v = \left(\frac{dQ}{dT}\right)_{\text{const } v}$$

In these formulae p is strictly $= -\left(\frac{\partial E}{\partial V}\right)_{\text{const } s}$, E being the internal energy, V the volume. In a compressible fluid at rest, p may be identified with the usual mechanical pressure of a fluid.

The constitutive equations, just as in the case of radio wave propagation, depend on the medium. Their derivation can be quite complicated. In general, though, the σ_{ij} are function of ρ, T, the deformation tensor e, and the rate of deformation $\dot{e}$. For solids, σ_{ij} is a function of ρ, T and e. For fluids, σ_{ij} is a function of ρ, T and $\dot{e}$ - forces σ_{ij} produce a movement $\dot{e}$, rather than a distinct measurable displacement e. Only fluids will be considered here. (For a linear solid, the constitutive equations are a generalization of Hooke's law:-

$$\nu_{ij} = L_{ijk\ell} e_{k\ell})$$

Before considering the constitutive equations, some definitions are necessary. Consider firstly Fig. C.1 .

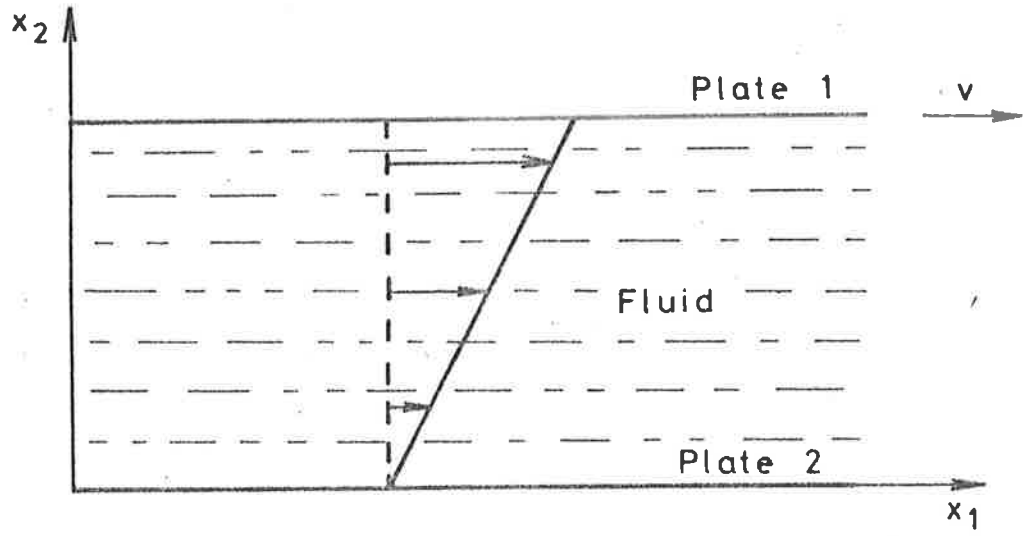

Fig. C.1

A fluid exists between two plates, 1 and 2. Plate 1 moves at velocity v, plate 2 is fixed. Then for so called "Newtonian fluids", the velocity as a function of x_2 is linear, increasing to velocity v at plate 1. In such a case,

$$\sigma_{12} = 2\mu\dot{e}_{12} = \mu(v_{1,2} + v_{2,1})$$

where μ is the Dynamic (or shear, or first) Coefficient of Viscosity [alternatively as $v_2 = 0$, $\sigma_{12} = \mu\frac{dv_1}{dx_2}$, σ_{12} being the "drag" force per unit area on the plate].

However, not all fluids are Newtonian. There are generally 3 classes - Ideal ($\mu = 0$), Newtonian (μ = const.), and finally non-Newtonian. [The parameter $\nu = \frac{\mu}{\rho}$, ρ = density, is called the kinematic viscosity]. Gases are Newtonian fluids.

Most studies of fluids revolve around Stokesian fluids - that is, those in which σ_{ij} are a continuous function of $e_{k\ell}$ only, ($\sigma_{ij} = f(\dot{e}_{k\ell})$), σ_{ij} is independent of position in the fluid (homogeneous), the function f is independent of axis orientation (isotropic), and where $\sigma_{ij} = -p\delta_{ij}$, $\dot{e}_{ij} = 0$ when there is no deformation (viz. the stress is hydrostatic).

As a first order approximation for Stokesian fluids,

C.5 $$\sigma_{ij} = (-p + \lambda \dot{e}_{kk})\delta_{ij} + 2\mu \dot{e}_{ij},$$

where λ is called the coefficient of compressibility viscosity, or the volume viscosity, or the second viscosity (as distinct from the shear viscosity μ, which is sometimes called the first viscosity).

In cases where $3\lambda + 2\mu = 0$, or $\dot{e}_{kk} = 0$, the mechanical pressure $p_m (\stackrel{\text{defn}}{=} -\frac{1}{3}\sigma_{ii})$ is equal to the thermodynamic pressure $p = -(\frac{\partial E}{\partial V})_s$. Fluids which obey this relation are said to obey Stoke's condition. The quantity $(\lambda + \frac{2}{3}\mu) = K$ is sometimes called the bulk viscosity.

Then equations C.1 to C.5 define the behaviour of a linear Stokesian (Newtonian) fluid. For cases where the fluid is non-Newtonian, μ, λ and K do not really have meanings. Hines (1977) in a tutorial paper, discusses these concepts of viscosity. Volume viscosity turns out to be a very poorly defined term, and Hines feels it would have been better if it had never been defined. He develops a new formalism which bypasses this definition, and, rather, invokes a complex thermal capacitance which expresses the equations far more generally. However, the concept of volume viscosity has been retained above, as the discussion here is purely descriptive, and the lack of generality of volume viscosity will not upset the results.

Equations C.2 and C.5 can be combined to give the Navier-Stoke equations,

C.6a $$\rho \frac{Dv_i}{Dt} = F_i - \frac{\partial p}{\partial x_i} + \lambda v_{k,ki} + \mu(v_{i,jj} + v_{j,ij})$$

where [,ki] means differentiation wrto x_k, and then again wrto x_i.

For incompressible fluids, $\frac{\partial v_i}{\partial x_i} = 0$, by C.1, leading to

C.6b $$\rho \frac{D\underset{\sim}{v}}{Dt} = \underset{\sim}{F} - \underset{\sim}{\nabla} p + \mu \nabla^2 \underset{\sim}{v} \quad .$$

Often C.6a (or b) is used as a replacement for C.2.

Then the solution of these equations, subject to applied boundary conditions, and with appropriate forces, leads to the space-time evolution of the Eulerian description of the atmosphere. Generally, to simplify the solution, one assumes a background state, and assumes that the result of modifications to the system produce only small perturbations. This is a particularly useful technique for investigations of the propagation of waves (that is, regular oscillations of pressure, temperature, velocity and so forth moving through the atmosphere - for example sound consists of such waves).

Thus pressure is written as $p = p_0 + p'$, density as $\rho = \rho_0 + \rho'$, and so on. Insertion of these forms into the equations above, and elimination of terms involving multiplication of more than one "dashed" term (e.g. $\rho' \frac{dp'}{dt}$), leads to the linear approximation of the fluid equations. Many wave propagation studies can be done by such methods. Hines (1960) is perhaps the classic reference for studies of the propagation of these waves. His equations 6 to 9 are basically simplifications of C.1, C.3, C.4, C.5 and C.6. Viscosity is assumed to be zero. The term C in $C^2 = \frac{\gamma p_0}{\rho_0}$ is the speed of sound, assuming adiabatic transport. This is in effect another form of the equation of state. Only gravity is considered as an external force, and it is assumed $\sigma_{ij} = -p\delta_{ij}$. For ease of reference, Hine's equations are reproduced here, but with $\frac{D}{Dt} = \frac{\partial}{\partial t} + \underset{\sim}{v}.\underset{\sim}{\nabla}$ used in place of $\frac{\partial}{\partial t}$, as discussed in Hines 1970, p. 1474. (Also see Pitteway and Hines 1965, equations 1 to 4)

C.7 $\rho \frac{D\underset{\sim}{v}}{Dt} = \rho g - \underset{\sim}{\nabla} p$ — Force equation

C.8 $\frac{Dp}{Dt} + \underset{\sim}{v}.\underset{\sim}{\nabla} p_0 = C^2 [\frac{D\rho}{Dt} + \underset{\sim}{v}.\underset{\sim}{\nabla}\rho_0]$ — Adiabatic equation of state

C.9 $\frac{D\rho}{Dt} + \underset{\sim}{v}.\underset{\sim}{\nabla}\rho_0 + \rho_0 \underset{\sim}{\nabla}.\underset{\sim}{v} = 0$ — Continuity

C.10 $C^2 = \frac{\gamma p_0}{\rho_0}$, $H = \frac{C^2}{\gamma g}$ $\gamma = \frac{C_p}{C_v}$

$\rho = \rho_0 + \rho'$ etc.

$\underset{\sim}{v}$ is the total velocity, $= \underline{U}_0 + \underline{u}_j$; $\underline{U}_0$ is the background wind, $\underline{u}$ the perturbation velocity.

These equations do not look exactly like C.1 to C.6 but could be derived from those by suitable manipulation.

Having discussed these basic equations and their use, some results will briefly be discussed. However, there are numerous books discussing properties of gravity waves and other related features, and hence detail will be kept to a minimum.

Hines (1960) begins by discussing an isothermal atmosphere with zero background wind, in which case the solutions are of a complex Fourier form - namely,

C.11 $$\frac{p'}{pp_0} = \frac{\rho'}{R\rho_0} = \frac{U_x}{X} = \frac{U_z}{Z} = A \exp\{j(\omega t - K_x x - K_z z\}$$

The wave is assumed to have wave normal in the xz plane, z being the vertical coordinate.

Substitution in C.7 to C.10 relates the Complex constants P, R, X, Z and A. These are given by equations 15 to 18 of Hines (1960). A relation between ω, K_x and K_z also results - the dispersion relation

C.12 $$\omega^4 - \omega^2 C^2(K_x^2 + K_z^2) + (\gamma - 1)g^2 K_x^2 + j\gamma g \omega^2 K_z = 0$$

where $\gamma = \frac{C_p}{C_v}$.

Various solution-types result. Generally K_x is taken as real, $= k_x$ (that is, the wave propagates horizontally). K_z may be purely imaginary, or of the type $K_z = k_z + j\frac{\gamma g}{2C^2} = k_z + \frac{j}{2H}$.

If K_z is purely imaginary ($k_z = 0$) the wave propagates horizontally, but just falls off (generally) in amplitude with increasing height. It is called an evanescent, or surface, or external wave. If K_z is of the second form ($k_z + \frac{j}{2H}$), the wave can propagate vertically as well as horizontally. It increases in amplitude with increasing height as $\exp\{\frac{z}{2H}\}$. This is to conserve energy, as the atmospheric density decreases exponentially with increasing height.

There are two branches, as far as frequency is concerned. Frequencies with $\omega > \omega_a = \frac{\gamma g}{2C}$ are members of the so called "acoustic branch". They behave much as sound behaves - in fact sound as heard by the ear is a part of this acoustic branch. The waves have ellipsoidal wave fronts, and near spherical fronts at high frequencies. The angular frequency ω_a corresponds roughly to a period $\tau_a = \frac{2\pi}{\omega_a} = 4.4$ minutes for $\gamma = 1.4$, $g = 9.5 ms^{-2}$, $H = 6km$ (typical conditions in the lower atmosphere).

Frequencies between ω_a, and $\omega_g = \frac{(\gamma-1)^{\frac{1}{2}}g}{C}$, cannot exist in the atmosphere. Frequencies with $\omega < \omega_g$ are members of the so called "gravity wave" branch. They are largely affected by gravity, due to their long periods, and behave quite differently to the acoustic branch. Particles oscillate nearly transverse to the phase velocity vector, in contrast to the longitudinal motion of the acoustic branch. For the γ, g and H parameters given above, ω_g corresponds to a period $\tau_g = \frac{2\pi}{\omega_g} = 4.9$ minutes (Hines, 1960). In fact ω_g is also the Brunt-Vaisala frequency ω_B for an isothermal atmosphere - that is, the angular frequency at which a parcel of air would oscillate adiabatically in the atmosphere. For a non-isothermal atmosphere, ω_B has additional terms. For a more detailed discussion of these isothermal solutions, see Hines (1960). One important point concerning gravity waves relates to wave groups. The group velocity and phase velocities in a group are generally in very different directions. Downward phase propagation generally implies upward group (and hence energy) propagation.

A more complicated situation arises when the temperature and background wind vary as a function of height. The coefficients in the resultant differential equations can at times become undefined (infinite). For this reason, the equations C.7 to C.10 are usually modified, with new variables. Two commonly used variables are

C.13
$$\begin{cases} f_1 = \dfrac{U_z}{(p_0^{\frac{1}{2}}\Omega)} \\ f_2 = \dfrac{\chi}{(p_0^{\frac{1}{2}}\Omega)} \end{cases},$$

where $\chi = \nabla.\underline{u}$, p_0 is the background pressure, and $\Omega = \omega - k_x U_x$ is the Doppler shifted frequency of the gravity wave when viewed from the background wind. (The background wind has velocity U_x in the x direction). (Recall the gravity wave is propogating in the xz plane. In a more general case, $\Omega = \omega - \underline{k}.\underline{U}$). Then the differential equations to be solved become (Vincent 1969; a different set of equations, though similar technique, can be found in Pitteway and Hines 1965):-

C.14
$$\frac{df_1}{dz} = a_{11}f_1 + a_{12}f_2$$
$$\frac{df_2}{dz} = a_{21}f_1 + a_{22}f_2$$

where
$$a_{11} = -\left(\frac{\gamma g}{2C^2}\right) + \left(\frac{gk_x^2}{\Omega^2}\right)$$
$$a_{12} = 1 - \frac{C^2k_x^2}{\Omega^2}$$
$$a_{21} = (g^2k_x^2)/(C^2\Omega^2) - \frac{\Omega^2}{C^2}$$
$$a_{22} = -a_{11} \quad .$$

These refined equations do not suffer from singularities in the coefficients a_{ij}. The various perturbation parameters ρ', p' etc. can be then related to f_1, f_2 (e.g. Pitteway and Hines 1965).

It turns out that when $\Omega = \omega_B$, reflection occurs, much as in the case q = 0 for radio wave propagation (Appendix B). The gravity wave turns around and heads back away from the $\Omega = \omega_B$ level. If $\Omega \leq 0$, a critical level occurs. The wave energy may in fact be absorbed into the layer (e.g. Vidal-Madjar 1978). Jones and Houghton (1971) have done a more thorough investigation of gravity wave-critical layer coupling, looking at non linear effects. In fact many investigations of gravity waves lately have been looking at non linear effects, and this is necessary to examine some of the more intricate aspects of gravity wave effects (e.g. also see Teitelbaum and Sidi 1976; Fritts 1978, 1979).

One method to solve the case of a height dependent temperature is discussed in Hines (1960) - namely the WKB approximation. This can give some useful insight into the characteristics of gravity waves in a real atmosphere. Einaudi and Hines (1970) also show applications of such an approximation, as does Smith (1977). More exact numerical techniques can be found in Hines and Reddy (1967); Klostermeyer (1972); and Bowman and Thomas (1976).

When reducing the equations of the atmosphere to workable form, two linear differential equations result, as seen above. These can be reduced to one second order differential equation in one variable. For example, if the variable

$$\phi = \underset{\sim}{v}.\underset{\sim}{v}\exp\{-\int\frac{dz}{2H}\} \text{ is used, an equation of the form}$$

$$\frac{\partial^2\phi}{\partial z} + \frac{1}{H}\frac{\partial H}{\partial z}.(\frac{\partial\phi}{\partial z}) + q^2\phi = 0$$

results. Here,

$$q^2 = k_x^2(\frac{\omega_B^2}{\omega^2} - 1) + \frac{(\omega^2-\omega_a^2)}{C^2}$$

and $\omega_B^2 = ((\gamma-1) + \frac{\gamma dH}{dz})\frac{g^2}{C^2}$ is the Brunt-Vaisala frequency.

The WKB solution is then of the form (e.g. Hines 1960; Einaudi and Hines 1970)

$$\phi = |qH|^{-\frac{1}{2}} \exp\{-j\int q\,dz\} \cdot$$

(This is only valid if $\frac{\partial q}{\partial z}/k_q$ terms etc. are small - much as in Appendix B).

Then the case q = 0 can occur. Analogously to radio wave propagation, this is assumed to result in reflection of the wave. Interestingly, the height of critical reflection by this WKB approximation varies depending on the variable used (ϕ, or u, or whatever). However, the critical reflection heights all lie within the region where the WKB approximation is no longer valid, so the use of the WKB approximation is misleading (Pitteway and Hines 1965, Einaudi and Hines 1970) near the reflection level. If $q^2 < 0$, the wave becomes evanescent, and no longer propagates vertically.

Gravity waves can be generated by a variety of processes; these are discussed in Chapter 1.

In the foregoing discussion, the Coriolis force due to the Earth's rotation, was ignored. If one takes a coordinate system on the Earth's surface, bodies moving in this frame do not move as they would in an inertial frame since the frame is really rotating. The Coriolis force is a "pseudo-force" to some degree, in that a frame on the Earth's surface is assumed to be inertial, but all bodies moving in this frame are taken to have this Coriolis force acting on them. In this way, the motions can be described correctly from the point of view of the revolving frame. (Houghton 1977, section 7.2). For periods greater than about 1 hour, this force becomes important (Klostermeyer 1972). Klostermeyer also gives a summary of the main forces acting in the ionosphere, although below 100km ion drag forces and so forth are not important. These forces are inserted

in equation C.1 to C.6 wherever "$\underset{\sim}{F}$" occurs. The Coriolis force on a body moving over the Earth's surface at speed $\underline{v}$ is given by

$$\underline{F}_C = 2\underset{\sim}{v} \times \underset{\sim}{\Omega}$$

$\underset{\sim}{\Omega}$ being the angular velocity of the Earth (aligned along the spin axis). Consideration of this force in the atmospheric equations leads to studies of very long wavelength (1, ½, 1/3 etc. of the Earth's circumference) waves propagating in the Earth's atmosphere. Such waves driven by the Coriolis force are called Rossby Waves. In general, such large scale waves are called Planetary waves (Houghton 1977, Ch. 8). Proper investigations of these waves, both theoretically and experimentally, are still in their early stages.

While planetary waves and gravity waves are discussed separately above, note that they are all solutions of the same set of equations. It just so happens that the Coriolis force is unimportant for gravity waves of period less than about 1 hour, but strictly the force should be considered. Another member of this family of waves is the set of tides. In the atmosphere, strong regular heating of water vapour in the troposphere and stratosphere, and Ozone (about 30-50km), provides another type of force in the atmospheric equations. (Solar and Lunar gravitational effects have been considered for forcing atmospheric tides, but are generally of second order (e.g. Lindzen and Hong 1974). This contrasts to the oceans where tides are almost entirely gravitational). Because the heating is not purely sinusoidal, but rather "on" for 12 hours and "off" for 12 hours, etc., oscillations with periods of 24, 12, 8, ... 24/n hours (n an integer) result. These oscillations are known as atmospheric tides. Perhaps one of the better earlier references on tides is Chapman and Lindzen (1970), and another is Lindzen (1974). Groves (1976), gives a good review of experimental and theoretical progress concerning tides. Various

modes of the tides exist for each period, each having different latitudinal and longitudinal distributions, and differing vertical wavelengths.

The 12 hour tide seems to be basically forced by Ozone heating, and the 24 hour tide below 100km forced mainly by water vapour heating in the lower atmosphere (though Ozone heating is still significant) (Lindzen 1974; Groves 1976). Some of the 24 hour tides are in fact evanescent (i.e. do not propagate vertically). These are particularly important poleward of 45°, where propagating modes have difficulty existing (Groves 1976, p. 443). The most important modes in the atmosphere are denoted S^1_1, S^1_{-1}, S^1_{-2}, S^2_2, S^2_4 and S^2_6. (See Lindzen 1974 for a description). The superscript denotes n, where the wave period is 24/n hours, and the subscripts denote the various modes. Larger n values generally correspond to a more complex latitudinal structure. Negative subscripts denote evanescent modes. Other modes apart from these generally do not occur significantly in the mesosphere, because they are hard to force (although Groves 1976, considers some quite high order 12 hour tides). High order modes often have very short vertical wavelengths, which is part of the reason they are hard to force (Lindzen 1974).

Tides occur in both the NS and EW wind components. In many cases these components have roughly equal amplitudes above 30° latitude (see Groves 1976, p. 450). (Forbes and Lindzen 1976a, shows graphs of the amplitude of EW and NS components of the various modes). The NW and EW components also have phase differences of about 90° often, too, and this results in a rotating wind vector (of constant amplitude if the NS and EW components have equal amplitude). For upward propagating energy (downward phase propagation), clockwise rotation of the vector with increasing time generally results in the Northern hemisphere, and anticlockwise rotation

in the Southern hemisphere, when viewed from above (e.g. see Craig (1965), p. 351; Elford and Craig (1980)). It should also be borne in mind that if no energy is lost while propagating, the tidal amplitude will grow with height as $\exp\{\frac{z}{(2H)}\}$, H being the scale height.

Tides also follow the Sun westward (in theory), so the phases (two phases are defined; the hour of maximum northward wind, and hour of maximum eastward wind) are in principle the same at all locations at any one latitude if expressed in local time.

Atmospheric tides are presently the subject of some quite vigorous research. Experimental observations are starting to give a picture of the Earth's tides, and theoretical investigations are having some success in simulating these results. Much remains to be done, however. Some papers on theoretical investigations include Lindzen and Hong (1974) (in which the importance of the background wind is considered); Hong and Lindzen (1976); Forbes and Lindzen (1976a, b); Garrett and Forbes (1978) and Forbes and Garrett (1978). One particularly interesting feature which may have to be considered is the asymmetry of the Ozone distribution in the northern and southern hemispheres (Tietelbaum and Cot 1979). This may result in a larger contribution to tide by asymmetric modes than had been previously realised (most emphasis to date has been on examination of modes which are symmetric about the equator). Some recent results, particularly some obtained by satellite observations, have illustrated that the northern and southern hemispheres may not be as similar as would perhaps be intuitively expected.

APPENDIX D

Angular and Temporal Characteristics of Partial Reflection from the D-Region of the Ionosphere

by

W. K. Hocking

A paper presented in Journal of Geophysical Research, 84, 845, (1979).

VOL. 84, NO. A3 JOURNAL OF GEOPHYSICAL RESEARCH MARCH 1, 1979

ANGULAR AND TEMPORAL CHARACTERISTICS OF PARTIAL REFLECTIONS FROM THE D - REGION OF THE IONOSPHERE

W. K. Hocking

Department of Physics, University of Adelaide, Adelaide, Australia 5000

Abstract. Radio pulses have been used as a probe to investigate scattering characteristics of ionospheric irregularities in the D - region at a frequency of 1.98 MHz, at Adelaide, South Australia (35° S). The angular distribution of the returned energy was investigated as a function of time and height. Distinct layers of strong scatter have frequently been detected, the heights of which differ on different days. The layers appear to be of two distinct types - those occurring above 80 km and those below - the two groups having different temporal and angular characteristics. The higher layers exhibit scatter from a much larger range of off-vertical angles, and the power returned from them varies less in time than for the lower layers, which tend to show short 'bursts' of scatter.

Introduction

Observations of partial reflections of radio frequency pulses as a function of time, height and angle from the zenith are useful for investigating the dynamic processes and electron density structure of the D - region of the ionosphere. Stratification of echo structure was observed as early as 1953 [Gardner and Pawsey, 1953; Gregory, 1956] and some temporal and seasonal variations have been studied [Gregory, 1961]. Investigations of angular reflection characteristics of D - region irregularities have also been carried out [Lindner, 1975a,b; Vincent and Belrose, 1978], and these can be useful in interpreting the differential absorption experiment [e.g. Belrose, 1970]. They are also of great interest for examining the structure of D - region irregularities. However, most determinations of the angular distribution of returned energy have been made by indirect means, and many earlier investigations of temporal variations sampling over several heights simultaneously have been made using photographic film, which can only show amplitude fluctuations qualitatively.

This paper discusses direct observations made by swinging the beam of the 900 m diameter Buckland Park Aerial Array, near Adelaide, South Australia (35° S, 138° E) [Briggs et al., 1969] to an off-zenith angle, and compares the results with echoes received with a vertical beam. Comparisons are also made with observations taken with a smaller array having a wider beam. For all observations, amplitudes were recorded over a range of heights several times per second and stored on digital magnetic tape. The system was calibrated before recording so that observations on different days could be compared and effective voltage reflection coefficients obtained.

Recently, D - region studies have been undertaken using high power VHF scatter techniques at Jicamarca, [Woodman and Guillen, 1974; Rastogi and Bowhill, 1976b] and some comparisons with these observations are also discussed.

Techniques

Pulses with an approximately Gaussian envelope and half power width ~ 25 μs were transmitted at a repetition rate of 50 Hz from a square array of 4 half-wave folded dipoles situated close to the receiving array. Either O(ordinary) or X (extraordinary) circularly polarized modes could be transmitted. The receiving array comprised a square grid of 89 pairs of crossed orthogonal half-wave dipoles with a circular perimeter, the dipoles being separated by 0.6 wavelength and the array diameter being 900 m. The dipoles were resonant at the transmitted frequency of 1.98 MHz. Each dipole was connected independently to the central receiving hut [Briggs et al., 1969]. In the experiment described here the east-west aligned dipoles were phased to produce a receiving array with a polar diagram beam width of ± 4.5° to half power, and first minima of ± 11.6°. This beam could be swung in approximately 1° steps away from the zenith in either the north-south or east-west vertical planes by phasing rows of dipoles with suitable lengths of cable. However, most measurements were made with either a vertical beam or with the beam at 11.6° off-zenith in the east-west vertical plane. The angle of 11.6° was chosen because this places the first minimum of the polar diagram in a vertical direction thus reducing leakage into the system from the stronger vertical reflections.

The phasing system used to swing the beam was tested initially by measuring E - region reflected powers at a variety of angles, on those occasions when the E - region appeared to be behaving as a smooth mirror. The received signal strength varied as a function of angle in the manner expected from the theoretically predicted polar diagram.

Twelve of the north-south aligned dipoles of the array were used to measure winds by the partial reflection drift technique. These 12 dipoles were used to form a triangle of three sets, each set comprising four adjacent dipoles in a square coupled together. The half power width of the reception beam of such a square was approximately ± 20°. Such a beam will be called a wide beam, in contrast to the narrow beam of the full array. For more information concerning measurements of winds see Stubbs [1973].

Echo amplitudes as a function of range using the narrow beam array and the three wide beam arrays were recorded with an incremental magnetic tape recorder using 64 levels of digitization. Records were taken either in steps of 2 km over a 20-km range interval, on all four receivers, with 0.2s between successive records at any one height, or, alternatively, in 2-km steps over 40 km with

Paper number 8A0903.

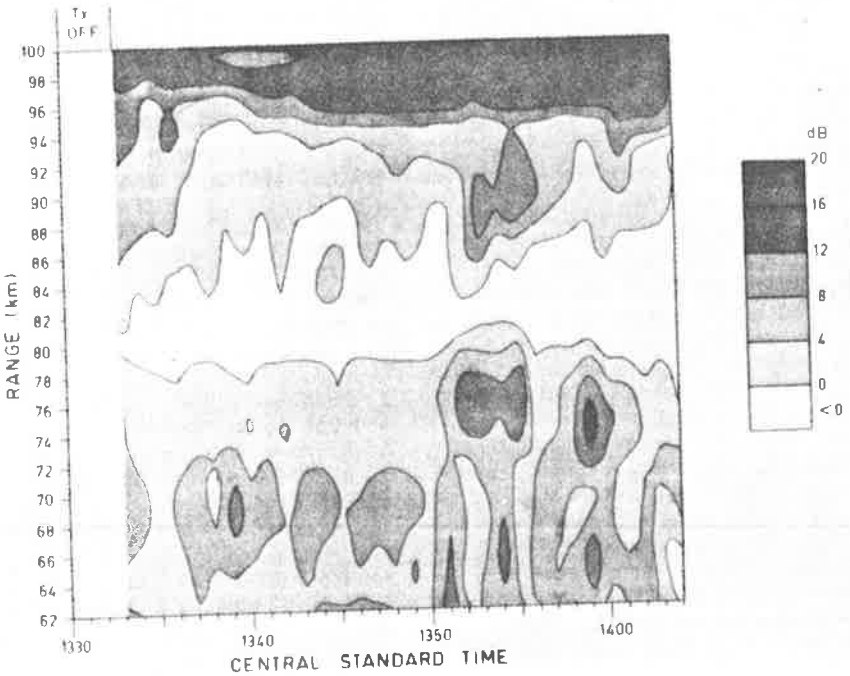

Fig. 1. Contour plot of 1-min means of power versus range and time taken using a narrow beam on day 77/151. The means are smoothed by interpolation. X mode polarization was used for transmission. The presence of a distinct minimum at 80-82 km is the most obvious feature. Strong bursts of power at 66-70, 74-76 and 90 km can be seen.

0.4s between successive records. Fading was removed by computing mean powers over successive intervals of 1 min.

The narrow beam receiver and one wide beam receiver were calibrated before each set of measurements. All graphs presented here are in dB of such calibrated power, and can be compared directly. The powers on the wide beam have been adjusted in such a way that both beams would record the same value for reflection from a mirror reflector. However, it should be noted that the shading densities in Figure 2 correspond to different levels to those in Figures 1 and 3. Effective voltage reflection coefficients were also obtained, although no allowance has been made for absorption. Thus these reflection coefficients are underestimates of the true reflection coefficients of the scattering irregularities, particularly above 80 km. No compensation for varying angular characteristics has been included either.

Results

Observations were made on several days during 1976-1977. Data from May 31, 1977 (this being the 151st day of the year, in early winter in the southern hemisphere), will be used to illustrate the main features. Most observations were confined to daylight hours and on day 77/151 covered the period 0800-1700 hours local time (universal time + 9½ hours).

Figure 1 is a contour diagram of power as a function of range and time using the narrow beam pointing vertically and using X mode polarization for transmission. The values are computed from the 1-min means of echo power, taken in 2-km steps of range, and then smoothed by computer interpolation [Akima, 1974].

Increases of signal power will be noted at ranges of approximately 66 to 70 km, 74 km and 90 km. The X mode is strongly absorbed above 80 km, and so the 90 km reflection coefficients are actually much larger than they appear from these results. A very definite 'valley' can be noted at 80-82 km. The strong signal above 96 km is due to total reflection from the E - region which saturates the receivers. The time interval shown in Figure 1 coincides with the period of most frequent bursts of powers at 66 km on this particular day, and as this layer was short-lived, the following discussion relates mainly to the two upper layers at 74 km and 90 km.

A layer in the region 85 to 95 km is a common feature at Adelaide, and this layer often persists throughout day and night. The 90-km layer on day 151 had a minimum O mode reflection coefficient of $\sim 6 \times 10^{-4}$ rising to 1.3×10^{-3} on some occasions. The 74-km layer X mode reflection coefficients varied from $2\text{-}4 \times 10^{-5}$ to $\gtrsim 2 \times 10^{-4}$ and the 66-km layer reached an X mode reflection coefficient of 5×10^{-5}.

Fig. 2 shows contour diagrams of power returned from 82 to 100 km during the period 0915 to 1034 on both narrow and wide beams, and Fig. 3 is a similar pair of diagrams for the ranges 62 to 80 km from 1445 to 1604.

One feature of both graphs is the occurrence of strong bursts of power, those at 90 km rising by ~ 3 dB over the normal level- and those at 74 km by ~ 10 dB. The bursts at each height have a quasi-periodicity of ~5 to 15 min. For the 74-km layer, bursts often last less than 2 min. Wind speeds were a maximum at 74 km

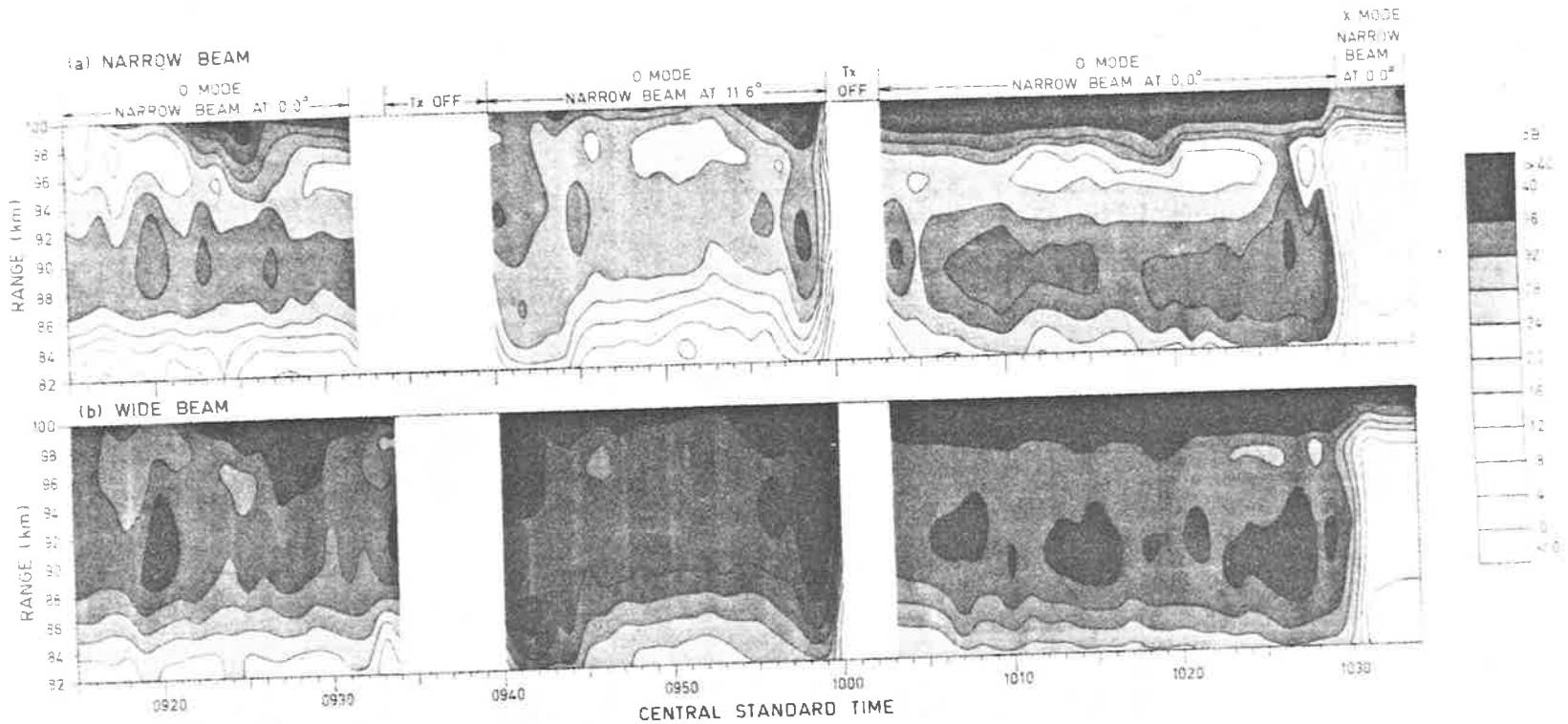

Fig. 2 Contour diagram of smoothed 1-min power means versus range and time, taken with (a) a narrow and (b) a wide beam on day 77/151. The plots have been corrected to allow for differing gains of the two antennae. Powers are strongest in a layer centred on 88-90 km with the narrow beam, and strongest at 88-92 km with the wide beam. The larger powers on the wide beam, the increase in range when the narrow beam is pointed at 11.6° off-zenith, and the strong powers at 11.6° all indicate significant off-vertical scatter for this layer. O mode polarization was used, since this suffers less absorption than X mode. Maximum powers correspond to reflection coefficients of $\sim 1.3 \times 10^{-3}$.

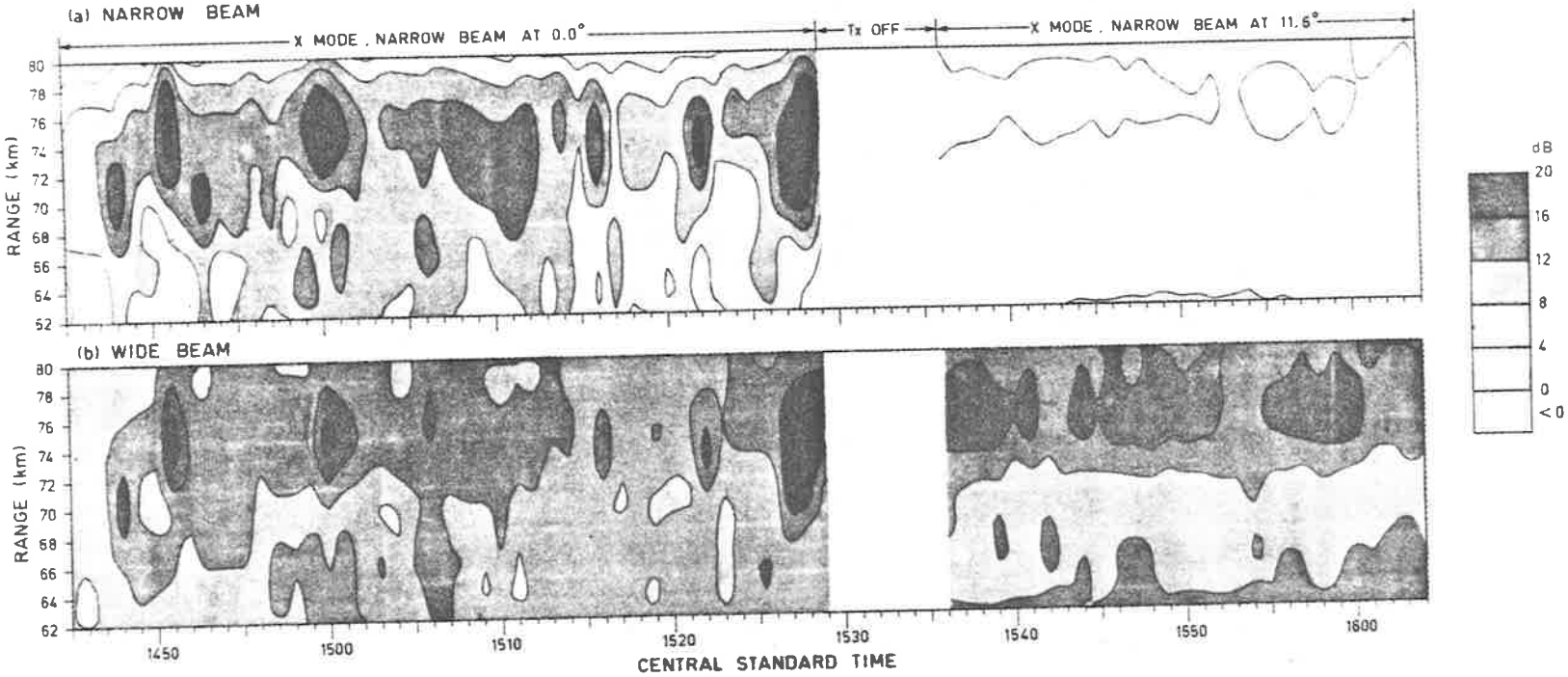

Fig. 3 Contour plot of smoothed 1-min power means versus range and time, taken with (a) a narrow beam and (b) a wide beam on day 77/151. Again, the plots are corrected to allow for differing antenna gains. Strong bursts of scatter will be noted in a layer centred on 74 km. The lack of significant power recorded whilst the narrow beam was at 11.6° and the very close similarity between corrected echo powers on the two beams suggest that most scatter comes from the vertical. X mode polarization was transmitted, since it is reflected more effectively than O mode, and there is little absorption up to such heights. Maximum powers correspond to reflection coefficients of ~ 2 to 4×10^{-4}.

(principally eastward), attaining speeds of 70 m s^{-1} for much of the day. It is interesting that this peak coincides with the layer of strong reflection at 74 km.

Fig. 3 shows that the 74-km layer backscatters very little power at 11.6° relative to that at 0.0°. There is a slight increase in range of this layer at 11.6° at this time of measurement. This would be expected if there were some reflection from 11.6°, since reflections from that angle would have their range increased by a factor sec(11.6°). However, the wide beam shows a similar change in range on this occasion, suggesting that this increase is due to an actual increase of the layer height with time, rather than being a result of tilting the beam. Observations at other times show little or no increase in range at 11.6°. Hence it seems reasonable to assume that the majority of the power recorded at 11.6° is really leaking in from the near vertical, through the edge of the main lobe, and through the first side-lobe, of the polar diagram.

If the power reflected is assumed to obey a function proportional to $\exp\{-(\sin\theta/\sin\theta_0)^2\}$, θ being the angle from the vertical, then it can be concluded that $\theta_0 \lesssim 2°-3°$ for this layer [c.f. Lindner, 1975b]. Only an upper limit can be placed on θ_0, since much of the power apparently received from 11.6° is probably from the vertical. These small values of θ_0 indicate that the 74-km layer is almost a specular reflector.

In contrast to the 74-km layer, the higher 90-km layer clearly shows strong scatter at 11.6° off-zenith (Figure 2). Further, the received power on the wide beam is ~ 6 dB larger than on the main beam, when allowance is made for the different gains, and this also suggests the existence of strong scatter from off-vertical angles. An increase in the range of the layer of ~ 2 km at 11.6° compared to 0.0° can also be seen, further suggesting significant off-vertical scatter. Similarly, the mean range of the layer observed with the wide beam is greater than the range measured using the narrow beam.

Occasionally it is possible to determine the location of individual bursts. One might expect all bursts received on the narrow beam to be received on the wide beam, but the wide beam might on occasion pick up a burst at some angle from the zenith which the narrow beam might not receive. For example, at 1007, the wide beam receives a strong burst whilst the narrow beam does not show a similar structure, suggesting the bulk of reflections came from the off-vertical on this occasion. On the other hand at 1010, a strong burst shows on the narrow beam, but only weakly on the wide beam. This was probably a small region of scatter directly overhead. Its relative strength on the wide beam would probably be small compared to the normal wide beam strengths because that beam receives much of its signal from the off-vertical. The range of this echo is 88 km on both beams, compared with the normal 90 km mean height on the wide beam, again suggesting an overhead reflection.

In general, for the 88-90 km layer, the average power at 11.6° is reduced by a factor of 3 compared with the vertical beam, suggesting $\theta_0 \sim 12°$ in an $\exp\{-(\sin\theta/\sin\theta_0)^2\}$ model. This is again consistent with Lindner [1975b].

Preliminary analysis of the fading statistics has shown that layers above 80 km exhibit more rapid fading than those below this height. Also amplitude probability distributions show that well-defined layers of strong scatter usually produce fading with a significant specular component, especially at the lower height. [Chandra and Vincent, 1977].

It is useful to examine the heights of the peak powers of the 1 min means as a function of time. Although such plots exhibit some degree of random fluctuation, at times it is possible to see quasi-periodic oscillations with periods 10 to 120 mins and amplitude ~ ½ km. It is possible that these are evidence of internal gravity waves. Of course the actual height resolution of the system is much greater than ½ km and any 1 min average 'pulse' of scattered power may have contributions from a range of heights. The presence of height oscillations may indicate either that one thin oscillating layer produces most of the reflection or that the relative contributions within the region follow a regular pattern of height variation.

Discussion

Briggs and Vincent [1973] have discussed the relation between electron density distribution and angular reflection characteristics and have concluded that clouds of electrons with a horizontal extent significantly greater than their depth produce scatter with small values of θ_0, whilst more isotropic irregularities produce scatter from a wide range of angles and hence have larger values of θ_0. This suggests that the 90-km layer on 77/151 may have consisted of approximately isotropic irregularities, whilst irregularities at 74 km were anisotropic, with horizontal dimensions much larger than their vertical dimension.

Another point of interest is the large variation in power within a short space of time, particularly at 74 km. This is somewhat similar to results obtained at Jicamarca, where ~ 20 dB bursts in power have been observed in D - region echoes. However, it must be pointed out that Jicamarca works at wavelength of 6 m and hence examines irregularities of much smaller scale than those involved in the present observations. It should also be noted that although only 3 dB increases in power were observed at 90 km, this may partly be due to the fact that echoes are received from a wide range of angles, and a burst in power at one angle may not have the same relative effect on the total power as a similar burst overhead at 74 km.

Rastogi and Bowhill [1976a] have discussed the possible role of turbulence in the formation of ionospheric irregularities, although principally with respect to scale sizes of a few meters. As suggested by Cunnold [1975] and others, it seems likely that both the partial reflections reported here, and the coherent echoes observed with VHF radars are due to scattering from turbulent irregularities, which are confined to narrow layers. The turbulence may be intermittent both in time and in space [Rastogi and Bowhill, 1976b]. The bursts

reported here at 74 km show similar durations to those observed at 50 MHz. Wind measurements show speeds ~ 70 m s^{-1} at 74 km, so possibly the most reasonable suggestion to explain the duration of the echoes would be that it is the time for a region of high scatter to move through the array beam, rather than the life time of the scattering region. The region would only be detected near the zenith at this height, since θ_0 is small, which explains why the echo lasts a similar time on the wide and narrow beams at Buckland Park. Assuming the echo is first detected at 2° from the zenith, taking a typical duration time as 2-4 min and assuming a velocity of 70 m s^{-1} gives a scatter region length of 3-10 km at 74 km [c.f. Rastogi and Bowhill, 1976b].

A major difference between low-frequency results and VHF radar results for vertical incidence concerns the echoes from 90 km. There appear to be no reports of vertical incidence coherent echoes from heights as great as this at VHF, whereas at 1.98 MHz they have the strongest partial reflection strengths. [Booker 1959] has discussed echoes from 90 km at VHF, but these were for very oblique incidence (4-6° to the horizontal) with widely spaced transmitter and receiver and correspond to vertical turbulence wavelengths much greater than those examined by vertical incidence). This difference between VHF and lower frequencies could be quite consistent with a turbulence mechanism. Figure 5 of Rastogi and Bowhill [1976b] shows that at 1.98 MHz the irregularities at 90 km would be in or close to the inertial range, whereas the scales required for vertical incidence 50 MHz scatter at this height would be in the viscuous range and consequently heavily damped.

Conclusions

The characteristics of D - region scatter echoes have been described for 1 day. A more thorough statistical analysis will be carried out when sufficient data has been accumulated. However, from a study of this and several other days, the following conclusions are believed to be typical:

1. Scatter appears to come from discrete layers in the D - region.

2. There appears to be considerable difference in the angular structure of the D - region echoes above and below 80 km at a radio wavelength of 150 m . The 90-km layer scatters quite strongly at off-zenith angles (θ_0 ~ 10° to 15°), while the 74-km layer behaves more like a specular reflector ($\theta_0 \lesssim 2°-3°$).

3. Temporal variations of power occur with frequent strong bursts, these bursts having a quasi-periodicity of 5 to 15 min. The power may increase by ~ 10 dB over the 'quiet' powers at 74 km, but only by ~ 3 dB at 90 km.

4. The occurrence of height oscillations of these layers has been noted, with quasi-periods similar to those expected for internal gravity waves.

Acknowledgements. The author would like to thank B. H. Briggs and R. A. Vincent for helpful discussion and comments during the course of these observations and during the writing of the paper. The work was supported by the Australian Research Grants Committee.

The Editor thanks P. K. Rastogi for his assistance in evaluating this brief report.

References

Akima, H., Algorithm 474, Bivariate interpolation and smooth surface fitting based on local procedures, Commun. Ass. Comput. Mach. 17, 26, 1974.

Belrose, J.S., Radio wave probing of the ionosphere by partial reflection of radio waves (from heights below 100 km), J. Atmos, Terr. Phys. 32, 567, 1970.

Booker, H. G., Radio wave scattering in the lower ionosphere, J. Geophys. Res., 64, 2164, 1959.

Briggs, B. H., W. G. Elford, D. G. Felgate, M. G. Golley, D. E. Rossiter and J. W. Smith, Buckland Park Aerial Array, Nature, 223, 1321, 1969.

Briggs, B. H. and R. A. Vincent, Some theoretical considerations on remote probing of weakly scattering irregularities. Aust, J. Phys., 26,805, 1973.

Chandra, H., and R. A. Vincent. Radio wave scattering from the southern hemisphere D - region, J. Atmos. Terr. Phys., 39, 1011, 1977.

Cunnold, D. M. Vertical transport coefficients in the mesosphere obtained from radar observations, J. Atmos. Sci., 32, 2191, 1975.

Gardner, F. F. and J. L. Pawsey, Study of the ionospheric D - region using partial reflections, J. Atmos. Terr. Phys., 3, 321, 1953.

Gregory, J. B., Ionospheric reflections from heights below the E - region., Aust. J. Phys. 9, 324, 1956.

Gregory, J. B., Radio wave reflections from the mesosphere, 1, Heights of occurrence, J. Geophys. Res., 66, 429, 1961.

Lindner, B. C., The nature of D - region scattering of vertical incidence radio waves, I, Generalized statistical theory and diversity effects between spaced receiving antennae, Aust. J. Phys., 28, 163, 1975a.

Lindner, B. C., The nature of D - region scattering of vertical incidence radio waves, II, Expérimental observations using spaced antenna reception, Aust. J. Phys. 28, 171, 1975b.

Rastogi, P. K., and S. A. Bowhill, Scattering of radio waves from the mesosphere, I, Theory and observations, J. Atmos. Terr. Phys., 38, 399, 1976a.

Rastogi, P. K., and S. A. Bowhill, Scattering of radio waves from the mesosphere, II evidence of intermittent mesospheric turbulences, J. Atmos. Terr. Phys., 38, 449, 1976b.

Stubbs, T. J., The measurement ot winds in the

D - region of the ionosphere by the use of partial reflected radio waves, J. Atmos. Terr. Phys., 35, 909, 1973.

Vincent, R. A., and J. S. Belrose, The angular distribution of radio waves partially reflected from the lower ionosphere, J. Atmos. Terr. Phys., 40, 35, 1978.

Woodman, R. F., and A. Guillen, Radar observations of winds and turbulence in the stratosphere and mesosphere, J. Atmos. Sci. 31, 493, 1974.

Received May 23, 1978
Revised August 16, 1978
Accepted August 17, 1978.

APPENDIX E

Computer Program Specpol

See Chapter VII for explanation of use

The polar diagram is described by function BPRES. The coordinates of the aerials are entered as data cards (not shown).

```
      PROGRAM SPECPOL(INPUT,OUTPUT)                                                    SPECPOL     2
      EXTERNAL  PHINT                                                                  SPECPOL     3
      COMMON/T/THETA                                                                   SPECPOL     4
      COMMON/P/PHI                                                                     SPECPOL     5
      COMMON/W/ WAVELT,HTREC,HTTX,DIPLEN,ATTEN,RADX(2),PHIX(2)                         SPECPOL     6
      COMMON/PH/ PHO(99),NAER,RAD(99)                                                  SPECPOL     7
      COMMON/H/ HT,DEP,WIDH          ,EPS,RO,PI                                        SPECPOL     8
      COMMON/DEL/DEL                                                                   SPECPOL     9
      COMMON/I/IPULSTP                                                                 SPECPOL    10
      COMMON/J/PHIWIND,V,PHASE,PHREF                                                   SPECPOL    11
      DIMENSION VR(100),FUNCT(100)                                                     SPECPOL    12
C   PROGRAM TO FIND POWER SPECTRUM  AS A FUNCTION OF VIRTUAL RANGE                     SPECPOL    13
C    FOR AN IONOSPHERIC SCATTERING LAYER,AND A SPECIFIED POLAR DIAG                   SPECPOL    14
      XX=1.0                                                                           SPECPOL    15
      PI=ASIN(1.0)*2.0                                                                 SPECPOL    16
      EPS=1.0E-02                                                                      SPECPOL    17
C * * * * * * * * * * * * * * * * * * * * *                                          SPECPOL    18
C   DATA                                                                             SPECPOL    19
C* * * * * * * * * * * * * * * * * * * * * * * * * * * * * * * * * * * * * * * *    SPECPOL    20
C   WIND ANGLE IS PHIWIND (RADIANS)                                                  SPECPOL    21
      PHIWIND=0.                                                                       SPEC        1
C   PHASE SPECIFIES TILT OF RX ARRAY POLAR DIAG,PHREF IS DIRECTION OF TIL            SPECPOL    23
      PHASE=-0.2*2.0*PI $ PHREF=0.                                                     SPEC        2
C   TX COORDS                                                                        SPECPOL    25
C   SEE NOTES IN U/D FOLDER,PROG POLAR.-SHOULD USE ALL 4 AERIALS IN SPECI            SPECPOL    26
C   WAY --BUT I ONLY USE THE 2 DIPOLES PARALLEL TO RXER DIPOLES                      SPECPOL    27
      RADX(1)=151.5/4.  $  RADX(2)=151.5/4.                                            SPEC        3
      PHIX(1)=PI/2.  $  PHIX(2)=-PI/2.                                                 SPEC        4
C    RX AERIALS,AND COORDS                                                           SPECPOL    30
      NAER=89 $ CALL READE(PHO,RAD,99)                                                 SPECPOL    31
C    WAVELENGTH,DIPOLE LENGTH IN HALF WAVELENGTHS FOR RX                             SPECPOL    32
      WAVELT=151.5  $  DIPLEN=1.0                                                      SPEC        5
C    HT OF TX AERIALS ABOVE IMAGE $ HT OF RX AERIALS ABOVE IMAGES                    SPECPOL    34
      HTTX=60.0  $  HTREC=23.0                                                         SPEC        6
C   REFLECTION COEFF OF GRD                                                          SPECPOL    36
      ATTEN=1.0                                                                        SPEC        7
C   SET HT,DEPTH OF LAYER IN KM                                                      SPECPOL    38
      HT=80.0 $ DEP=0.5                                                                SPEC        8
C   IPULSTP IS PULSE TYPE -EXP OR COS                                                SPECPOL    40
C    WIDH-- IF PULSE TYPE IS EXP,WIDH IS 1/E HALF WIDTH OF PULSE                     SPECPOL    41
C   IN KM.   ---   IF PULSE TYPE IS COS,WIDH=BASE FULL WIDTH /8. IN KM               SPECPOL    42
C    MUST USE BASE  WIDTH /8. SO DOES NOT STUFF UP THETA LIMITS IN                   SPECPOL    43
C    PHINT  -- IE WANT ANGLES OF INTEGRATION SI THERE IS NON ZERO SCATTER             SPECPOL    44
CC    AT START OF INTEGRAL LIMITS AND END OF LIMITS                                   SPECPOL    45
      IPULSTP=3HCOS  $  WIDH=8.5/8.                                                    SPEC        9
C   DEL= SMALL NO LT PULSE HALF WIDTH AND LAYER DEPTH BUT GT ROUNDOFF ERR            SPECPOL    47
      DEL=1.0E-15                                                                      SPECPOL    48
      PI2=PI/2.                                                                        SPECPOL    49
C    NORMALIZATION FACTOR FOR LATER                                                  SPECPOL    50
      THETA=0.0 $ PHI=0.0                                                              SPECPOL    51
C   XX IS DUMMY PARAMETER - NOT USED                                                 SPECPOL    52
      PRINT 46                                                                         SPECPOL    53
      RESMAX=POLAR(THETA,PHI)                                                          SPECPOL    54
      PRINT 46                                                                         SPECPOL    55
46    FORMAT(1X,1H*)                                                                   SPECPOL    56
      PRINT 80                                                                         SPECPOL    57
80    FORMAT(1H1)                                                                      SPECPOL    58
```

```
      PRINT 81,EPS                                                          SPECPOL    59
81    FORMAT(1X,27HINTEGRATION ACCURACY IS =    ,E9.3)                      SPECPOL    60
      PRINT 82,RADX(1),RADX(2)                                              SPECPOL    61
82    FORMAT(1X,11HTX RADII =    ,2F11.4)                                   SPECPOL    62
      PRINT 83,PHIX(1),PHIX(2)                                              SPECPOL    63
83    FORMAT(1X,19HTX DIPOLE ANGLES = ,2F11.4)                              SPECPOL    64
      PRINT 84,NAER,WAVELT,DIPLEN                                           SPECPOL    65
84    FORMAT(1X,68HNO OF AERIALS,WAVELENGTH,AND RX DIPOLE LENGTH IN HALF    SPECPOL    66
     $ WAVELENGTHS =   ,I5,2F11.4)                                          SPECPOL    67
      PRINT 85,HTTX,HTREC,ATTEN                                             SPECPOL    68
85    FORMAT(1X,69HHT OF TX ABOVE IMAGE,HT OF RX ABOVE IMAGE,AND GRD REF    SPECPOL    69
     $LECTION COEFF =   ,3F11.4)                                            SPECPOL    70
      PRINT 86,HT,DEP                                                       SPECPOL    71
86    FORMAT(1X,41HHT OF BASE OF LAYER,AND DEPTH OF LAYER = ,2F11.4,1X,3    SPECPOL    72
     $HKMS  )                                                               SPECPOL    73
      PRINT 87,IPULSTP,WIDH                                                 SPECPOL    74
87    FORMAT(1X,29HPULSE TYPE,AND PULSE WIDTH =  ,A10,F11.4)                SPECPOL    75
      PRINT 88                                                              SPECPOL    76
88    FORMAT(1X,117HFOR EXP PULSE,WIDTH IS WIDTH BETWEEN 1/E PTS OF POWE    SPECPOL    77
     $R PROFILE OF PULSE-- FOR COS PULSE,WIDTH IS 1/8*WIDTH OF BASE    )    SPECPOL    78
      PRINT 89                                                              SPECPOL    79
89    FORMAT(1X,52H- - COS ACTUALLY MEANS COS**4 POWER PROFILE OF PULSE)    SPECPOL    80
      PRINT 91,RESMAX                                                       SPECPOL    81
91    FORMAT(1X,62HCURRENT TOTAL WRTO 1 DIPOLE SUMMED FOR VERTICAL PROPO    SPECPOL    82
     $GATION =    ,E11.4)                                                  SPECPOL    83
      DO 11 I=1,20                                                          SPEC       10
      RO=85.0+FLOAT(I-1)                                                    SPEC       11
C  VARY THE NORMALISED RADIAL VELOCITIES                                    SPECPOL    86
C  NO OF LOOPS                                                            SPECPOL    87
      NL=11                                                                 SPEC       12
      DO 21 J=1,NL                                                          SPECPOL    89
      V=-0.5+FLOAT(J-1)/FLOAT(NL-1)+.02                                     SPEC       13
      V=V*0.3                                                               SPEC       14
      VR(J)=V                                                               SPECPOL    92
C  PHI LIMITS                                                             SPECPOL    93
C  STHO IS THE SINE OF THE MAX THETACONSIDERED---- THIS MAX  THETA        SPECPOL    94
C  IS FOUND AS THE THETA WHICH RESULTS FOR RO+4.0 *WIDH TO INTERSECT      SPECPOL    95
C  WITH THE BOTTOM OF THE LAYER                                           SPECPOL    96
C  NO NEED TO GO OUT TO 90 DEGS--TOO MUCH COMPUTER TIME,FOR ONLY SMALL    SPECPOL    97
C  NUMBERS                                                                SPECPOL    98
      CTHO=HT/(RO+4.0*WIDH)                                                 SPECPOL    99
      STHO=SQRT(1.-CTHO*CTHO)                                               SPECPOL   100
C  FOR LARGE V,THO,SIN THETA AS DEFINED BY THIS DEFN MAY BE TOO SMALL     SPECPOL   101
C  SO PHMIN AND PHMAX WONT WORK                                           SPECPOL   102
C   BUT THEN NOT MUCH PT IN DOING THE ANALYSIS,AS NOS WILL BE CLOSE TO 0  SPECPOL   103
C  SO SET FUNCT TO 0                                                      SPECPOL   104
      XST=    (2.*V*V/STHO/STHO-1.)                                       SPECPOL   105
      IF(XST.GE.1.)FUNCT(J)=0.                                            SPECPOL   106
      IF(XST.GE.1.)GO TO 21                                               SPECPOL   107
      PHIRG=0.5*ACOS(XST)                                                 SPECPOL   108
                                                                          SPECPOL   109
      PH MIN=PHIWIND-PHIRG                                                SPECPOL   110
      PH MAX=PHIWIND+PHIRG                                                SPECPOL   111
C  IF V +VE,USE OTHER HALF OF PLANE                                       SPECPOL   112
      IF(V.GT.0.)PHMIN=PHMIN+PI                                           SPECPOL   113
      IF(V.GT.0.)PHMAX=PHMAX+PI                                           SPECPOL   114
      CALL SIMPSB(PHINT,PHI,PHMIN,PHMAX,EPS,N,FI)                         SPECPOL   115


C  DESIRED FUNCTION                                                       SPECPOL   116
      FUNCT(J)=FI                                                         SPECPOL   117
      PRINT 78,VR(J),FUNCT(J)                                             SPECPOL   118
78    FORMAT(1X,2E9.3)                                                    SPECPOL   119
21    CONTINUE                                                            SPECPOL   120
      CALL QIKPLT(VR,FUNCT,-NL,1,9H*RAD VEL*,7H*POWER*)                   SPECPOL   121
      PRINT 456,RO,PHIWIND,PHREF,PHASE                                    SPECPOL   122
456   FORMAT(1X,11HVIRTUAL HT=,F9.3,16HWIND DIRECTION = ,F9.3,20HDIRECTI  SPECPOL   123
     $ON OF TILT =   ,F9.3,8HPHASE =   ,F9.3,13R(ALL RADIANS)    )        SPECPOL   124
      ANGMAX=ASIN(PHASE/(2.0*PI))*(-1.0)*180.0/PI                         SPECPOL   125
      VMAXM=PHASE/(2.0*PI)                                                SPECPOL   126
      PRINT 457,ANGMAX,VMAXM                                              SPECPOL   127
457   FORMAT(1X,46HANGLE OF MAX RESPONSE ALONG TILT DIRECTION =    ,      SPECPOL   128
     $F9.4,9H DEGREES   ,41H ,AND NORMALISED VELOCITY OF MAX POWER =    , SPECPOL   129
     $F9.4,21H (+VE TOWARD ARRAY )        )                              SPECPOL   130
11    CONTINUE                                                            SPECPOL   131
      END                                                                 SPECPOL   132
```

```
      FUNCTION PHINT(PHI)                                                    SPECPOL   133
      COMMON/J/PHIWIND,V,PHASE,PHREF                                         SPECPOL   134
      EXTERNAL CONV                                                          SPECPOL   135
                                                                             SPECPOL   136
      COMMON/W/ WAVELT,HTREC,HTTX,DIPLEN,ATTEN,RADX(2),PHIX(2)               SPECPOL   137
      COMMON/PH/ PHO(99),NAER,RAD(99)                                        SPECPOL   138
      COMMON/H/ HT,DEP,WIDH          ,EPS,RO,PI                              SPECPOL   139
      COMMON/DEL/DEL                                                         SPECPOL   140
      PI2=PI/2.                                                              SPECPOL   141
C  INTEGRAND OF PHI INTEGRATION                                              SPECPOL   142
                                                                             SPECPOL   143
C  FIND THETA APPROPRIATE TO V,PHI                                           SPECPOL   144
      STHA= (2.0*V*V)/(1.0+COS(2.0*(PHIWIND-PHI)))                           SPECPOL   145
      THETA=ASIN(SQRT(STHA))                                                 SPECPOL   146
C  FIND CONVOLUTION                                                          SPECPOL   147
C  BOUNDS OF CONVOLUTION                                                     SPECPOL   148
      RMIN=HT/COS(THETA)   $  RMAX=(HT+DEP)/COS(THETA)                       SPECPOL   149
      CALL SIMPSN(CONV,R,RMIN,RMAX,EPS,N,FI,PHI)                             SPECPOL   150
C  THUS FI HOLDS CONVOLUTION VALUE FOR LAG RO                                SPECPOL   151
C  FULL INTEGRAND                                                            SPECPOL   152
      Y=POLAR(THETA,PHI)                                                     SPECPOL   153
CC  RECALL POLAR FINDS AMPLITUDE                                             SPECPOL   154
      PHINT=FI*Y*Y*ABS(V)                                                    SPECPOL   155
      PHINT=PHINT/SQRT(1.0-STHA)                                             SPECPOL   156
      XX=0.5*(1.0+COS(2.0*(PHIWIND-PHI)))                                    SPECPOL   157
      PHINT=PHINT/XX                                                         SPECPOL   158
      RETURN                                                                 SPECPOL   159
      END                                                                    SPECPOL   160
```

```
      FUNCTION CONV(R,PHI)                                                   SPECPOL   161
C  CONVOLUTION FUNCTION                                                      SPECPOL   162
      COMMON/J/PHIWIND,V,PHASE,PHREF                                         SPECPOL   163
                                                                             SPECPOL   164
      COMMON/W/ WAVELT,HTREC,HTTX,DIPLEN,ATTEN,RADX(2),PHIX(2)               SPECPOL   165
      COMMON/PH/ PHO(99),NAER,RAD(99)                                        SPECPOL   166
      COMMON/H/ HT,DEP,WIDH          ,EPS,RO,PI                              SPECPOL   167
      COMMON/I/IPULSTP                                                       SPECPOL   168
      SIGMA=1.0                                                              SPECPOL   169
C  SIGMA DESCRIBES ANISOTROPY OF SCATTER                                     SPECPOL   170
C   I USE TX PULSE HERE,BUT SHOULD REALLY USE                                SPECPOL   171
C  FOURIER TRANSFORM OF RX FN*(FT OF TX PULSE)                               SPECPOL   172
      IF(IPULSTP.NE.3HEXP)GO TO 77                                           SPECPOL   173
C  HERE PULSE TYPE IS EXP                                                    SPECPOL   174
      ARG=(RO-R)*(RO-R)/(WIDH*WIDH)                                          SPECPOL   175
      XINT=SIGMA/(R*R)*EXP(-ARG)                                             SPECPOL   176
      GO TO 78                                                               SPECPOL   177
77    CONTINUE                                                               SPECPOL   178
C  HERE,USE COS FN                                                           SPECPOL   179
C  IE POWER PULSE IS COS**4 FN                                               SPECPOL   180
      COSS=COS((RO-R)/(WIDH*8.)*PI)                                          SPECPOL   181
      IF(ABS(RO-R).GT.WIDH*4.)COSS=0.0                                       SPECPOL   182
      XINT=COSS*COSS*COSS*COSS                                               SPECPOL   183
      XINT=XINT*(SIGMA/(R*R))                                                SPECPOL   184
78     CONTINUE                                                              SPECPOL   185
      CONV=XINT                                                              SPECPOL   186
      RETURN                                                                 SPECPOL   187
      END                                                                    SPECPOL   188
```

```
      FUNCTION POLAR(THETA,PHI)                                              SPECPOL   189
      COMMON/J/PHIWIND,V,PHASE,PHREF                                         SPECPOL   190
                                                                             SPECPOL   191
      COMMON/W/ WAVELT,HTREC,HTTX,DIPLEN,ATTEN,RADX(2),PHIX(2)               SPECPOL   192
      COMMON/PH/ PHO(99),NAER,RAD(99)                                        SPECPOL   193
      COMMON/H/ HT,DEP,WIDH          ,EPS,RO,PI                              SPECPOL   194
      RES=BPRES(THETA,PHI,WAVELT,RAD,PHO,PHASE,NAER,PHREF,HTREC,DIPLEN,      SPECPOL   195
     $ATTEN)                                                                 SPECPOL   196
      RES=RES*BPRES(THETA,PHI,WAVELT,RADX,PHIX,0.0,2,0.0,HTTX,1.0,ATTEN)     SPECPOL   197
      POLAR=RES                                                              SPECPOL   198
      RETURN                                                                 SPECPOL   199
      END                                                                    SPECPOL   200
```

```
      SUBROUTINE SIMPSN (F,Z,A,B,EPS,N,FI,PHI)                          SPECPOL  201
C     INTEGRATES F(X)FROM A TOB WITH AN ERROR LESS THAN EPS,            SPECPOL  202
C     USING N SUBINTERVALS                                              SPECPOL  203
C     WITH AN UPPER LIMIT OF 2500 INTERVALS                             SPECPOL  204
C     THE INTEGRAL IS FI                                                SPECPOL  205
C     NOBLE,VOL.2,P239                                                  SPECPOL  206
      H=0.5*(B-A)                                                       SPECPOL  207
      AJ=H*(F(A,THETA,PHI)+F(B,THETA,PHI))                              SPECPOL  208
      AI1=3.0*AJ                                                        SPECPOL  209
      N=1                                                               SPECPOL  210
    3 BB=0.0                                                            SPECPOL  211
      DO 5 K=1,N                                                        SPECPOL  212
    5 BB=BB+F(A+(2.0*K-1.0)*H,THETA,PHI)                                SPECPOL  213
      AIO=AJ+4.0*H*BB                                                   SPECPOL  214
      IF(ABS(AIO).LT.1.0E-50)GO TO 10                                   SPECPOL  215
    7 IF(ABS((AIO-AI1)/AIO).LT.EPS)GO TO 10                             SPECPOL  216
      AJ=0.25*(AJ+AIO)                                                  SPECPOL  217
      AI1=AIO                                                           SPECPOL  218
      N=2*N                                                             SPECPOL  219
      IF(N.GT.2500) GO TO 10                                            SPECPOL  220
      H=0.5*H                                                           SPECPOL  221
      GO TO 3                                                           SPECPOL  222
   10 FI=AIO/3.0                                                        SPECPOL  223
      RETURN                                                            SPECPOL  224
      END                                                               SPECPOL  225
```

```
      SUBROUTINE SIMPSB (F,Z,A,B,EPS,N,FI)                              SPECPOL  226
C     INTEGRATES F(X)FROM A TOB WITH AN ERROR LESS THAN EPS,            SPECPOL  227
C     USING N SUBINTERVALS                                              SPECPOL  228
C     WITH AN UPPER LIMIT OF 2500 INTERVALS                             SPECPOL  229
C     THE INTEGRAL IS FI                                                SPECPOL  230
C     NOBLE,VOL.2,P239                                                  SPECPOL  231
      H=0.5*(B-A)                                                       SPECPOL  232
      AJ=H*(F(A)+F(B))                                                  SPECPOL  233
      AI1=3.0*AJ                                                        SPECPOL  234
      N=1                                                               SPECPOL  235
    3 BB=0.0                                                            SPECPOL  236
      DO 5 K=1,N                                                        SPECPOL  237
    5 BB=BB+F(A+(2.0*K-1.0)*H)                                          SPECPOL  238
      AIO=AJ+4.0*H*BB                                                   SPECPOL  239
      IF(ABS(AIO).LT.1.0E-50)GO TO 10                                   SPECPOL  240
    7 IF(ABS((AIO-AI1)/AIO).LT.EPS)GO TO 10                             SPECPOL  241
      AJ=0.25*(AJ+AIO)                                                  SPECPOL  242
      AI1=AIO                                                           SPECPOL  243
      N=2*N                                                             SPECPOL  244
      IF(N.GT.2500) GO TO 10                                            SPECPOL  245
      H=0.5*H                                                           SPECPOL  246
      GO TO 3                                                           SPECPOL  247
   10 FI=AIO/3.0                                                        SPECPOL  248
      RETURN                                                            SPECPOL  249
      END                                                               SPECPOL  250
```

```
      SUBROUTINE READE(PHI,RAD,NNO)                                     SPECPOL  251
      DIMENSION PHI(NNO),RAD(NNO)                                       SPECPOL  252
      PI=3.14159                                                        SPECPOL  253
C  READS IN TELESCOPE DIMENSIONS                                        SPECPOL  254
      DO 11 I=1,15                                                      SPECPOL  255
      J1=(I-1)*6+1                                                      SPECPOL  256
      J2=J1+5                                                           SPECPOL  257
      IF(I.EQ.15)J2=J2-1                                                SPECPOL  258
      READ 100,(RAD(JK),PHI(JK),JK=J1,J2)                               SPECPOL  259
100   FORMAT(12F6.2)                                                    SPECPOL  260
11    CONTINUE                                                          SPECPOL  261
C  CONVERT TO RADIANS                                                   SPECPOL  262
      DO 12 IJ=1,89                                                     SPECPOL  263
      PHI(IJ)=PHI(IJ)*PI/180.0                                          SPECPOL  264
12    CONTINUE                                                          SPECPOL  265
      RETURN                                                            SPECPOL  266
      END                                                               SPECPOL  267
```

```
      FUNCTION BPRES(ANGLE,PHIO,WAVELT,RAD,PHI,PHASE,NNO,PHREF,HTDIF,     SPECPOL   268
     $ DIPLEN,ATTEN)                                                      SPECPOL   269
      DIMENSION RAD(NNO),PHI(NNO)                                         SPECPOL   270
C   THIS SUBROUTINE CALCULATES RESPONSE OF BUCKLAND PARK ARRAY IN DIRECTI SPECPOL   271
C   AND AT ANGLE OF VIEW=ANGLE                                           SPECPOL   272
C   DIPLEN= DIPOLE LENGTH IN HALF WAVELENGTHS                            SPECPOL   273
C   ATTEN=ATTENUATION FACTOR DUE TO GRD ON REFLECTION -CAN ONLY BE REAL I SPECPOL   274
C   PROGRAM -- GENERALLY 1                                               SPECPOL   275
C   NEEDS READE ALSO TO GET DATA                                         SPECPOL   276
C   CALCULATE DISTANCE TO REFERENCE LINE                                 SPECPOL   277
      PI=3.14159                                                          SPECPOL   278
      SUM=0.0                                                             SPECPOL   279
      SUM1=0.0                                                            SPECPOL   280
      SUM2=0.0                                                            SPECPOL   281
C   INCLUDE DIPOLE RESPONSE                                              SPECPOL   282
C   BEWARE IF BETA= ZERO                                                 SPECPOL   283
      SINB=SQRT(1.0-(COS(PHIO)**2.0)*(SIN(ANGLE)**2.0))                   SPECPOL   284
      IF(SINB.LT.0.001)GO TO 9                                            SPECPOL   285
      COSB=SIN(ANGLE)*COS(PHIO)                                           SPECPOL   286
      RESP=COS(DIPLEN*PI/2.0*COSB)/SINB                                   SPECPOL   287
      GO TO 10                                                            SPECPOL   288
9     RESP=0.0                                                            SPECPOL   289
10    CONTINUE                                                            SPECPOL   290
      DO 11 I=1,NNO                                                       SPECPOL   291
      DIST=RAD(I)*SIN(PI/2.0+PHIO-PHI(I))                                 SPECPOL   292
C   NOTICE DIST IS -VE WHERE NECESSARY                                   SPECPOL   293
C   ALSO FIND PHASE OF AERIAL DUE TO INTRODUCED PHASE                    SPECPOL   294
      DIS1=RAD(I)*SIN(PI/2.0+PHREF-PHI(I))                                SPECPOL   295
C   CALCULATE PHASE OF AERIAL W.R.TO REFERENCE LINE                      SPECPOL   296
      PSE=(DIST*SIN(ANGLE))/WAVELT*2.0*PI+PHASE*(DIS1/WAVELT)             SPECPOL   297
C   CALCULATE CONTRIBUTION TO SUM                                        SPECPOL   298
      SUM1=SUM1+COS(PSE)                                                  SPECPOL   299
      SUM2=SUM2+SIN(PSE)                                                  SPECPOL   300
C   NOTE RESPONSE OF DIPOLE,RESP,AFFECTS ALL CPTS EQUALLY-WE COULD MULTIP SPECPOL   301
C   RESP AT THE END(OR WE CAN INCORPORATE AS WE GO                       SPECPOL   302
C   DURING ANY CALL TO BPRES,RESP IS A CONSTANT FOR THAT CALL            SPECPOL   303
11    CONTINUE                                                            SPECPOL   304
      SUM=SQRT(SUM1**2.0+SUM2**2.0)                                       SPECPOL   305
      SUM=SUM*RESP                                                        SPECPOL   306
C   NOW INCORPORATE GROUND EFFECTS                                       SPECPOL   307
C   TAKE PHASE OF DIPOLE SUM ABOVE AS ZERO-MEANS SIN CPT IS ZERO         SPECPOL   308
      PHGRD=(HTDIF*COS(ANGLE)*2.0*PI/WAVELT+PI)                           SPECPOL   309
      SUM=SQRT((SUM+SUM*ATTEN*COS(PHGRD))**2.0+(SUM*ATTEN*SIN(PHGRD))     SPECPOL   310
     $ **2.0)                                                             SPECPOL   311
      BPRES=SUM                                                           SPECPOL   312
      RETURN                                                              SPECPOL   313
      END                                                                 SPECPOL   314
```

APPENDIX F

Program Scatprf

Program to Simulate Partial Reflection Profiles

For a Full Description of the Program, See Chapter VIII, Section 8.2.1b

```
      PROGRAM SCATPRF (INPUT,OUTPUT,TAPE1=140,TAPE2=140)                    SCATPRF    2
      COMPLEX L2                                                            SCATPRF    3
C   PROGRAM TO CALCULATE RETURN ECHO STRUCTURE AS A FN OF VIRTUAL HEIGHT     SCATPRF    4
C   FOR AN ELECTRON DENSITY PROFILE AS GIVEN ON TAPE1(FORNAT IS              SCATPRF    5
C   1X,10E13.6--HT,ELECT DENSITY(E/CM**3) PAIRS--5 PER CARD)                SCATPRF    6
C   METHOD INVOLVES SUMMING ALL RETURN CW CPTS AFTER THEY RETURN            SCATPRF    7
C   --AND AS SUCH IS A  IS A MORE EXACT METHOD THAN A GROUP ANALYSIS         SCATPRF    8
C   FINAL DATA IS WRITTEN ON TAPE2 AS REAL AND IMAGINARY PARTS              SCATPRF    9
C    ASSUME TX PEAK AMPLITUDE                                               SCATPRF   10
C   = 1 UNIT AT 1 KM--THEN AMPLITUDES OF RETURN ARE REFLECTION COEFFS       SCATPRF   11
C   AS I WOULD CALCULATE AT BP,PROVIDED WE MULTIPLY BY 2*HT                 SCATPRF   12
C   IE EFFECTIVE TX AMPLITUDE AT GRD ON RETURN AFTER REFLECTION COEEF       SCATPRF   13
C   OF 1 IS VALUE AT 1KM DIVIDED BY DISTANCE OF TRAVEL                      SCATPRF   14
      COMPLEX PHASPTH,XNTGRAL,DNDZ,TERM,REC,XN2                             SCATPRF   15
      COMPLEX MO3,MX3                                                       SCATPRF   16
      COMPLEX MX1,MX2,MO1,MO2                                               SCATPRF   17
      DIMENSION PULSE(100),PULSI(100),PULSI2(100),FREQU(100)                SCATPRF   18
      DIMENSION REC(100),PHASPTH(100)                                       SCATPRF   19
      DIMENSION XNTGRAL(100),H(5),E(5),XN2(100)                             SCATPRF   20
      COMPLEX NREFS                                                         SCATPRF   21
      DIMENSION NREFS(100)                                                  SCATPRF   22
C   SEN WHYLLER ARRAYS AND VARIABLES                                        SCATPRF   23
      COMPLEX NO,NX,RHO,RHX                                                 SCATPRF   24
      COMPLEX RO,RX,NO1,NO2,NX1,NX2                                         SCATPRF   25
      COMMON NO,NX,FREG,THETA,BM,VM,ENCH,WL                                 SCATPRF   26
      COMMON RHO,RHX                                                        SCATPRF   27
      COMPLEX NREF1,NREF2                                                   SCATPRF   28
C   INPUT DATA ---EVENTUALLY PUT THESE ON DATA CARDS                        SCATPRF   29
C   SEN WHYLLER PARAMS                                                      SCATPRF   30
C   FCENT=CENTRAL FREQU OF TX PULSE                                         SCATPRF   31
C   FCENT IS IN MHZ                                                         SCATPRF   32
C   MODE TYPE                                                               SCATPRF   33
      READ 1441,THETA,FCENT,MODE                                            SCATPRF   34
1441    FORMAT(F6.2,1X,F6.3,1X,A6)                                          SCATPRF   35
      PRINT 14441,THETA,FCENT,MODE                                          SCATPRF   36
14441 FORMAT(1X,F6.2,1X,F6.3,1X,A6)                                         SCATPRF   37
C   NT=NO OF PTS TAKEN IN TX ENVELOPE (=NO OF FREQU BANDS USED)             SCATPRF   38
C   DELT=SPACING BETWEEN PTS IN MICROSECS                                   SCATPRF   39
C   TZSHIF ONLY ACCURATE TO DELT--PROG ASSUMES 0 VIRTUAL HT TO BE 1ST       SCATPRF   40
C   PT OF PULSE AT OR AFTER TZSHIF FROM 1ST PT                              SCATPRF   41
C   MAKE TZSHIF A MULTIPLE OF DELT                                          SCATPRF   42
C   TZSHIF=SHIFT IN MICROSECS BETWEEN FIRSTPT AND PT USED FOR 0 VIRTUAL     SCATPRF   43
C    HEIGHT                                                                 SCATPRF   44
C   (USUALLY USE MAX OF PULSE FOR ZERO HT)                                  SCATPRF   45
C - - - - - - - - - - - - - - - - - - - - - - - - - - - - - - - - - -       SCATPRF   46
C   - NOTE TOTAL DATA LENGTH MUST BE GE TIME FOR PULSE TO                   SCATPRF   47
C   - GO UP TO MAX HT AND RETURN (=2*100/(3*10**5) SECS =667                SCATPRF   48
C   - MICRO SECS FOR 100 KM.--OTHERWISE PULSE IS REPEATED                   SCATPRF   49
C   - OVER INTERVALS OF LENGTH XLEN,AS WE GET DISCRETE                      SCATPRF   50
C   - FREQUENCY SPECTRUM--IE IN EFFECT THE PRF IS TOO HIGH                  SCATPRF   51
C   - NOTE THE SPACING BETWEEN PTS,DELT,DEFINES FREQUENCY                   SCATPRF   52
C   - WIDTH-THUS IF REFLECTED PROFILE    HAS V HIGH FREQUS                  SCATPRF   53
C   - ALIASING WILL RESULT --DELT MUST BE CHOSEN TO ENSURE                  SCATPRF   54
C   - THIS DOES NOT OCCUR                                                   SCATPRF   55
C   - - - - - - - - - - - - - - - - - - - - - - - - - - - - - - - - -       SCATPRF   56
      READ 1442,NT,DELT,TZSHIF                                              SCATPRF   57
1442  FORMAT(I5,2F14.3)                                                     SCATPRF   58
      PRINT 14442,NT,DELT,TZSHIF                                            SCATPRF   59
14442 FORMAT(1X,I5,2F14.3)                                                  SCATPRF   60
C   TOTAL DATA LENGTH                                                       SCATPRF   61
      XLEN=FLOAT(NT)*DELT                                                   SCATPRF   62
C    STEP SIZE TO BE USED IN INTEGRATION IS XNTSTP KM                       SCATPRF   63
C   XNTRES=STEP SIZE IN KM TO BE USED TO PRINT RESULTANTS                   SCATPRF   64
      READ 1443,XNTSTP,XNTRES                                               SCATPRF   65
1443  FORMAT(2F14.6)                                                        SCATPRF   66
      PRINT 14443,XNTSTP,XNTRES                                             SCATPRF   67
14443 FORMAT(1X,2F14.6)                                                     SCATPRF   68
C   HT1 AND HT2 ARE FIRST AND LAST HTS TO BE USED FOR FINAL OUTPUT PROFIL   SCATPRF   69
C    STARTHT=START HEIGHT FOR INTEGRATIONS                                  SCATPRF   70
C   STARTHT MUST BE LT 1ST TIME ON TAPE                                     SCATPRF   71
C   FINHT=FINAL HT FOR INTEGRATIONS--SET V LARGE IF WISH TO GO TO END       SCATPRF   72
C   OF TAPE.                                                                SCATPRF   73
      READ 1444,STARTHT,FINHT,HT1,HT2                                       SCATPRF   74
1444  FORMAT(4F7.3)                                                         SCATPRF   75
      PRINT 14444,STARTHT,FINHT,HT1,HT2                                     SCATPRF   76
14444 FORMAT(1X,4F7.3)                                                      SCATPRF   77
      PI=3.14159 & C=3.*10.**5.0                                            SCATPRF   78
C   C= SPEED OF LIGHT IN KM/SEC                                             SCATPRF   79
      DO 452 IR=1,NT                                                        SCATPRF   80
452   NREFS(IR)=(1.0,0.0)                                                   SCATPRF   81
C   DEFINE THE PULSE ENVELOPE SHAPE AT 0 HT(AN CEXP(JWT) TIME DEPENDENCE    SCATPRF   82
C    IS ASSUMED)                                                            SCATPRF   83
      DO 11 I=1,NT                                                          SCATPRF   84
      T=FLOAT(I-1)*DELT-TZSHIF                                              SCATPRF   85
C   PULSE--IN THIS CASE,FASTER RISE THAN FALL                               SCATPRF   86
      SG=-1.0                                                               SCATPRF   87
      IF(I.LE.NT/2)PULSE(I)=EXP((T/15.0)**2.0*SG)                           SCATPRF   88
      IF(I.GT.NT/2)PULSE(I)=EXP((T/20.0)**2.0*SG)                           SCATPRF   89
C   TEMPORARILY STORE TIME                                                  SCATPRF   90
      FREQU(I)=T                                                            SCATPRF   91
11    CONTINUE                                                              SCATPRF   92
      CALL GIKPLT(FREQU,PULSE,-NT,1,17H*TIME(MICROSECS)*,11H*AMPLITUDE*)    SCATPRF   93
C   RECEIVER FN                                                             SCATPRF   94
      DO 456 IU=1,NT                                                        SCATPRF   95
C   STORE FREQ RESPONSE FN ST START AT CENTRAL FREQ AS 1ST PT,              SCATPRF   96
C    WORK THRO TO  NT/2          PT,THEN START FROM MOST -VE FREQ           SCATPRF   97
C   AND WORK TOWARD  MAIN FREQ AGAIN                                        SCATPRF   98
C   IE TO MATCH FFT OUTPUT                                                  SCATPRF   99
      REC(IU)=(1.0,0.0)                                                     SCATPRF  100
456   CONTINUE                                                              SCATPRF  101
C   OBTAIN FOURIER TRANSFORM-1ST GET IMAG CPTS=0,AND STORE PTS IN PULS2     SCATPRF  102
C   LEAVE PULSE IN PULSE AND PULSI                                          SCATPRF  103
C    FIND PT TO BE USED FOR 0TH TIME                                        SCATPRF  104
      DO 43 I=1,NT                                                          SCATPRF  105
C   ADD DELT/10. SO NO PROBLEM WITH T=0                                     SCATPRF  106
      T=DELT*FLOAT(I-1)-TZSHIF+DELT/10.                                     SCATPRF  107
      IF(T.GE.0.0)GO TO 44                                                  SCATPRF  108
43    CONTINUE                                                              SCATPRF  109
C   THUS ITH PT IS CLOSEST TO 0--PROG ASSUMES THIS IS 0 PT                  SCATPRF  110
44    NZR=I                                                                 SCATPRF  111
      DO 12 I=1,NT                                                          SCATPRF  112
      PULSI(I)=0. & PULSI2(I)=0                                             SCATPRF  113
                                                                            SCATPRF  114
                                                                            SCATPRF  115
```

```
      IF(I.LT.NZR)PULS2(NT-NZR+I+1)=PULSE(I)                                    SCATPRF  116
      IF(I.GE.NZR)PULS2(I-NZR+1)=PULSE(I)                                       SCATPRF  117
12    CONTINUE                                                                  SCATPRF  118
C  RESET TIMES FOR PLOTTING                                                    SCATPRF  119
      DO 441 I=1,NT                                                             SCATPRF  120
441   FREQU(I)=FLOAT(I-1)*DELT                                                  SCATPRF  121
      CALL QIKPLT(FREQU,PULS2,-NT,1,17H*TIME(MICROSECS)*,11H*AMPLITUDE*)        SCATPRF  122
      CALL FFT(PULS2,PULSI2,NT,NT,NT,-1)                                        SCATPRF  123
C  GET FREQUENCIES                                                            SCATPRF  124
      DO 13 I=1,NT                                                              SCATPRF  125
      IF(I.LE.NT/2+1)FREQU(I)=1.0/XLEN*FLOAT(I-1)                               SCATPRF  126
      IF(I.GT.NT/2+1)FREQU(I)=1.0/XLEN*FLOAT(I-NT-1)                            SCATPRF  127
C   FREQU IN MHZ                                                              SCATPRF  128
      FREQU(I)=FCENT+FREQU(I)                                                   SCATPRF  129
C  ALSO FFT GETS SUM OF PULSE*EXP(JWT)                                        SCATPRF  130
C  SO TO GET INTEGRAL OF PULSE*EXP( )*DELT,X DELT                             SCATPRF  131
      PULS2(I)=PULS2(I)*DELT                                                    SCATPRF  132
      PULSI2(I)=PULSI2(I)*DELT                                                  SCATPRF  133
13    CONTINUE                                                                  SCATPRF  134
      PRINT 478,(FREQU(JR),PULS2(JR),JR=1,NT)                                   SCATPRF  135
478   FORMAT(1X,10E9.3)                                                         SCATPRF  136
      CALL QIKPLT(FREQU,PULS2,-NT,1,11H*FREQ(MHZ)*,5H*AMP*)                     SCATPRF  137
                                                                                SCATPRF  138
C D D D D D D D D D D D D D D DD D D D D D DD DD DD DD D                         SCATPRF  139
C  CALCULATE INTEGRAL TERM FOR EACH FREQ AND STORE IN XNTGRAL                   SCATPRF  140
      DO 41 I=1,NT                                                              SCATPRF  141
41    XNTGRAL (I)=(0.,0.)                                                       SCATPRF  142
      IZ=0 $ H(5)=-0.1 $ E(5)=0.0 $ H0=0. $ E0=0.                               SCATPRF  143
      DO 407 KLK=1,NT                                                           SCATPRF  144
C  ASSUME 0 ELEC DENS FROM 0 TO STARTHT                                       SCATPRF  145
407   PHASPTH(KLK)=CMPLX (STARTHT,0.0)                                          SCATPRF  146
C   PHASPTH FINDS INTEGRAL OF N*DZ                                            SCATPRF  147
                                                                                SCATPRF  148
C  STORE FIRST PREVIOUS HT                                                    SCATPRF  149
      HPRES=STARTHT-XNTSTP                                                      SCATPRF  150
7     CONTINUE                                                                  SCATPRF  151
      IZ=IZ+1                                                                   SCATPRF  152
C  STORE HT FROM LAST LOOP                                                    SCATPRF  153
      HST=HPRES                                                                 SCATPRF  154
C   PRESENT HT                                                                SCATPRF  155
      HPRES=FLOAT(IZ-1)*XNTSTP+STARTHT                                          SCATPRF  156
C  READ TAPE IF PRESENT HT NOT LT H(5)-BUT STORE H(5) FIRST                   SCATPRF  157
      IF(HPRES.GT.H(5))H0=H(5)                                                  SCATPRF  158
      IF(HPRES.GT.H(5))E0=E(5)                                                  SCATPRF  159
      IF(HPRES.GT.H(5))READ(1,200)(H(I),E(I),I=1,5)                             SCATPRF  160
200   FORMAT(1X,10E13.6)                                                        SCATPRF  161
      IF(EOF(1))76,77                                                           SCATPRF  162
77    CONTINUE                                                                  SCATPRF  163
      IF(HPRES.GE.FINHT)GO TO 76                                                SCATPRF  164
C  FIND ELECTRON DENSITY FOR THIS HT BY LINEAR INTERPOLATION OF DATA          SCATPRF  165
      DO 31 I=1,5                                                               SCATPRF  166
      IF(HPRES.LE.H(I))GO TO 32                                                 SCATPRF  167
31     CONTINUE                                                                 SCATPRF  168
32    CONTINUE                                                                  SCATPRF  169
       IF(I.EQ.1)GO TO 33                                                       SCATPRF  170
       ENCM=(E(I)-E(I-1))/(H(I)-H(I-1))*(HPRES-H(I-1))+E(I-1)                   SCATPRF  171
C  STORE E(I-1) H(I-1)                                                        SCATPRF  172
      E2=E(I-1) $ H2=H(I-1)                                                     SCATPRF  173
      GO TO 34                                                                  SCATPRF  174
33    CONTINUE                                                                  SCATPRF  175
      ENCM=(E(1)-E0)/(H(1)-H0)*(HPRES-H0)+E0                                    SCATPRF  176
      E2=E0 $ H2=H0                                                             SCATPRF  177
34    CONTINUE                                                                  SCATPRF  178
                                                                                SCATPRF  179
C  GET LAST HT                                                                SCATPRF  180
C  OVERWRITE PREVIOUS H2 VALUES WHICH I CALCULATED BEFORE PROG                SCATPRF  181
C  WAS FINALISED BUT NO LONGER NEED                                           SCATPRF  182
      H2=HST                                                                    SCATPRF  183
C *  * * * * * * * * * * * ** * * * * * * * *                                  SCATPRF  184
C  CALCULATE SEN WHYLLER REFRACTIVE INDICES                                   SCATPRF  185
      VM=COLL(HPRES,2) $ BM=BFIELD(HPRES)                                       SCATPRF  186
C  *  TO PUT IN A MODEL*                                    *                  SCATPRF  187
C  *  1.CHANGE ENCM (IE  OVERRIDE TAPE1                     *                  SCATPRF  188
C  * IE USE IF STATEMENTS TO INSERT SHARP LEDGES                              SCATPRF  189
C  TO DO FULL ANALYSIS CORRECTLY,DO   CARDS BETWEEN *** BELOW                 SCATPRF  190
C  IE CALCULATE N AT EACH FREQ                                                SCATPRF  191
C  * * * * * * * * *                                                          SCATPRF  192
C  DO 51 I=1,NT                                                               SCATPRF  193
C      FMEG=FREQU(I)                                                          SCATPRF  194
C  CALL SEWY                                                                  SCATPRF  195
C      NX1=NX $ NO1=NO                                                        SCATPRF  196
C* * * * * * * * * * *                                                        SCATPRF  197
                                                                                SCATPRF  198
C  * * * * * * * * * * * * * * * * * * * * * * * * * * * * *                  SCATPRF  199
C  BUT FOR A SHORT CUT,ASSUME N VS F IS QUADRATIC OVER RGE                    SCATPRF  200
C  OF FREQUS WE HAVE                                                          SCATPRF  201
C  AND FIT L2(F)                                                              SCATPRF  202
C  THIS GIVES MAX ERROR IN N-1 OF .7 PC FOR 90 KM,ENCM=10000,X MODE           SCATPRF  203
C  AND LT .01 PC ON O MODE -- IE V GD FIT                                     SCATPRF  204
C* * * * * * * * * * * * *                                                    SCATPRF  205
      FMEG=FREQU(NT/2+2)                                                        SCATPRF  206
      X1=FMEG                                                                   SCATPRF  207
      CALL SEWY                                                                 SCATPRF  208
      MX1=NX $ MO1=NO                                                           SCATPRF  209
      FMEG=FREQU(1)                                                             SCATPRF  210
      X2=FMEG                                                                   SCATPRF  211
      CALL SEWY                                                                 SCATPRF  212
      MX2=NX $ MO2=NO                                                           SCATPRF  213
      FMEG=FREQU(NT/2+1)                                                        SCATPRF  214
      X3=FMEG                                                                   SCATPRF  215
      CALL SEWY                                                                 SCATPRF  216
      MX3=NX $ MO3=NO                                                           SCATPRF  217
      DO 51 I=1,NT                                                              SCATPRF  218
      FMEG=FREQU(I)                                                             SCATPRF  219
      NX1=L2(X1,X2,X3,MX1,MX2,MX3,FMEG)                                         SCATPRF  220
      NO1=L2(X1,X2,X3,MO1,MO2,MO3,FMEG)                                         SCATPRF  221
C  GET RIGHT MODE                                                             SCATPRF  222
       IF(MODE.EQ.6HO MODE)NREF1=NO1                                            SCATPRF  223
       IF(MODE.EQ.6HX MODE)NREF1=NX1                                            SCATPRF  224
C  ALSO RECALL PREVIOUS PTS                                                   SCATPRF  225
       NREF2=NREFS(I)                                                           SCATPRF  226
C  NOW STORE PRESENT NREF1 IN NREFS FOR NEXT TIME                             SCATPRF  227
       NREFS(I)=NREF1                                                           SCATPRF  228
C  ADD PHASE INTEGRAL                                                         SCATPRF  229
```

```
      PHASPTH(I)=PHASPTH(I)+NREF1*XNTSTP                                SCATPRF  230
C  GET DN/DZ                                                           SCATPRF  231
      DNDZ=(NREF1-NREF2)/(NREF1+NREF2)/CMPLX(HPRES-H2,0.)               SCATPRF  232
C GET TERM IN INTEGRAL NOT RELATED TO FREQU                           SCATPRF  233
      TERM=(1.0,0.0)*DNDZ*CMPLX(0.5/HPRES*XNTSTP,0.)                    SCATPRF  234
C  GET XNTGRAL                                                        SCATPRF  235
      XNTGRAL(I)=XNTGRAL(I)+TERM*CEXP((0.0,-2.0)*CMPLX(2.0*PI/C*FREQU(I SCATPRF  236
     $)*10.0**6.0,0.)*PHASPTH(I))                                       SCATPRF  237
   51 CONTINUE                                                          SCATPRF  238
      GO TO 7                                                           SCATPRF  239
   76 CONTINUE                                                          SCATPRF  240
C  HERE                                                                SCATPRF  241
C  HERE,HAVE DESIRED INTEGRAL TERMS                                    SCATPRF  242
C  IE FREQ DISN OF RETURN ECHOES FOR EACH FREQ WITH UNIT AMPL,         SCATPRF  243
C  WITHOUT EXP(JW(2Z0)/C ) TERM                                        SCATPRF  244
C  NOW TO WORK UP THE Z0 VALUES AND SUM THE TERMS,WITH WEIGHTINF ACCORDI SCATPRF  245
C  TO PULSE                                                            SCATPRF  246
C  NO OF Z0 VALUES                                                     SCATPRF  247
      NZ0=INT((HT2-HT1)/XNTRES+1.0)                                     SCATPRF  248
      NZ5=NZ0/5+1                                                       SCATPRF  249
      DO 61 IZ0=1,NZ5                                                   SCATPRF  250
      DO 62 J=1,5                                                       SCATPRF  251
      XN2(J)=0.                                                         SCATPRF  252
       H(J)=HT1+FLOAT((IZ0-1)*5+J-1)*XNTRES                             SCATPRF  253
      KPT=(IZ0-1)*5+J                                                   SCATPRF  254
      DO 63 JI=1,NT                                                     SCATPRF  255
      L=JI                                                              SCATPRF  256
      XN2(J)=CEXP((.0,1.0)*CMPLX(2.0*PI*FREQU(L)*10.**6.0*2.0*H(J)/C,0.) SCATPRF  257
     $)*XNTGRAL(  L)*REC(  L)*CMPLX(PULS2(  L),PULSI2(  L))*CMPLX(1./XLE SCATPRF  258
     $N,0.)+XN2(J)                                                      SCATPRF  259
   63 CONTINUE                                                          SCATPRF  260
   62 CONTINUE                                                          SCATPRF  261
      WRITE(2,201)(H(IL),XN2(IL),IL=1,5)                                SCATPRF  262
  201 FORMAT(1X,5(F9.5,2E9.3))                                          SCATPRF  263
   61 CONTINUE                                                          SCATPRF  264
C  THUS DATA NOW STORED ON TAPE SHOULD                                 SCATPRF  265
C  BE PROFILE OF RTN ECHO                                              SCATPRF  266
      END                                                               SCATPRF  267
```

```
      SUBROUTINE SEWY                                                   SCATPRF  268
C     COMPUTATION OF SEN AND WYLLER MAGNETOIONIC FORMULAS               SCATPRF  269
C     SEN AND WYLLER,J.G.R.,VOL 65,P.3931, DEC 1960                     SCATPRF  270
C     SUBPROGRAM FOR CALCULATION OF C-INTERGRALS USING APPROXIMATIONS   SCATPRF  271
C     BY HARA(J.G.R.,VOL 68,P4388, JULY 1963)                           SCATPRF  272
      COMPLEX NO,NX,I,EPS1,EPS2,EPS3,O,P,Q,R,S,                         SCATPRF  273
     1T,U,V,ARG,R1,R2                                                   SCATPRF  274
      DOUBLE PRECISION C3,C5                                            SCATPRF  275
      COMPLEX RHO,RHX                                                   SCATPRF  276
      REAL    A,B,C,D,E,F,G1,G2,G3,G4,WO,X,ZM,Y,WL                      SCATPRF  277
      COMMON NO,NX,FMEG,THETA,BM,VM,ENCM,WL                             SCATPRF  278
      COMMON RHO,RHX                                                    SCATPRF  279
      DATA EO/8.85415E-12/,EQ/1.60199E-19/,EM/9.1055E-31/,              SCATPRF  280
     1PI/3.14159265/                                                    SCATPRF  281
C     UNITS OF FMEG ARE MEGAHERTZ                                       SCATPRF  282
C     UNITS OF ENCM ARE ELECTRONS/CM**3                                 SCATPRF  283
C     UNITS OF VM   ARE COLLISIONS/SEC                                  SCATPRF  284
C     UNITS OF THETA    DEGREES                                         SCATPRF  285
C     UNITS OF BM   ARE WEBERS/M**2                                     SCATPRF  286
      RADS=2.0*PI/360.0                                                 SCATPRF  287
      I=(0.0,1.0)                                                       SCATPRF  288
      PHI=THETA*RADS                                                    SCATPRF  289
      CO=COS(PHI)                                                       SCATPRF  290
      SQ=SIN(PHI)*SIN(PHI)                                              SCATPRF  291
      W=PI*FMEG*2.0E06                                                  SCATPRF  292
    3 WL=EQ*BM/EM                                                       SCATPRF  293
      WO=ENCM   *1.0E+06*EQ*EQ/EO/EM                                    SCATPRF  294
      X=WO/(W*W)                                                        SCATPRF  295
      ZM=VM/W                                                           SCATPRF  296
      Y=WL/W                                                            SCATPRF  297
C     DEFINE COEFFICIENTS                                               SCATPRF  298
      G1=X/ZM                                                           SCATPRF  299
      G2=1.0/ZM                                                         SCATPRF  300
      G3=(1.0-Y)/ZM                                                     SCATPRF  301
      G4=(1.0+Y)/ZM                                                     SCATPRF  302
      A=G1*G2*C3(G2)                                                    SCATPRF  303
      B=2.5*G1*C5(G2)                                                   SCATPRF  304
      C=G1*G3*C3(G3)                                                    SCATPRF  305
      D=2.5*G1*C5(G3)                                                   SCATPRF  306
      E=G1*G4*C3(G4)                                                    SCATPRF  307
      F=2.5*G1*C5(G4)                                                   SCATPRF  308
C                                                                       SCATPRF  309
C     TENSOR COEFFICIENTS                                               SCATPRF  310
      EPS1=(1.0-A)-I*B                                                  SCATPRF  311
      EPS2=0.5*(F-D)+0.5*I*(C-E)                                        SCATPRF  312
      EPS3=(A-0.5*(C+E))+I*(B-0.5*(F+D))                                SCATPRF  313
C     MORE COEFFICIENTS                                                 SCATPRF  314
C                                                                       SCATPRF  315
      O=2.0*EPS1*(EPS1+EPS3)                                            SCATPRF  316
      P=EPS3*(EPS1+EPS3)+EPS2*EPS2                                      SCATPRF  317
      Q=2.0*EPS1*EPS2                                                   SCATPRF  318
      R=2.0*EPS1                                                        SCATPRF  319
      S=2.0*EPS3                                                        SCATPRF  320
C     CALCULATE THE SQUARE OF THE REFRACTIVE INDEX N                    SCATPRF  321
C                                                                       SCATPRF  322
      T=O+P*SQ                                                          SCATPRF  323
      ARG=P*P*SQ*SQ-Q*Q*CO*CO                                           SCATPRF  324
      U= CSQRT(ARG)                                                     SCATPRF  325
      IF(AIMAG(ARG).LT.0.0)U=-U                                         SCATPRF  326
      V=R+S*SQ                                                          SCATPRF  327
C     ORDINARY REFRACTIVE INDEX IS NO                                   SCATPRF  328
C     EXTRAORDINARY REFRACTIVE INDEX IS NX                              SCATPRF  329
      NO= CSQRT((T+U)/V)                                                SCATPRF  330
      NX= CSQRT((T-U)/V)                                                SCATPRF  331
C     RHO AND RHX ARE RESPECTIVE POLARIZATIONS                          SCATPRF  332
      RHO=-(P*SQ-U)/(Q*CO)                                              SCATPRF  333
      RHX=-(P*SQ+U)/(Q*CO)                                              SCATPRF  334
      RETURN                                                            SCATPRF  335
      END                                                               SCATPRF  336
```

```
      DOUBLE PRECISION FUNCTION C5(X)                                   SCATPRF   337
      REAL    A0,A1,A2,B0,B1,B2,B3,B4,X                                 SCATPRF   338
      DATA K/0/                                                         SCATPRF   339
      IF(K.GT.0 )GO TO 1                                                SCATPRF   340
      K=K+1                                                             SCATPRF   341
      A0=1.1630641                                                      SCATPRF   342
      A1=16.9901002                                                     SCATPRF   343
      A2=6.6945939                                                      SCATPRF   344
      B0=4.3605732                                                      SCATPRF   345
      B1=64.093464                                                      SCATPRF   346
      B2=68.920505                                                      SCATPRF   347
      B3=35.355257                                                      SCATPRF   348
      B4=6.6314497                                                      SCATPRF   349
    1 C5=(X**3+A2*X*X+A1*X+A0)/(X**5+B4*X**4+B3*X**3+B2*X*X+           SCATPRF   350
     1B1*X+B0)                                                          SCATPRF   351
      RETURN                                                            SCATPRF   352
      END                                                               SCATPRF   353
```

```
      DOUBLE PRECISION FUNCTION C3(X)                                   SCATPRF   354
      REAL    A0,A1,A2,A3,B0,B1,B2,B3,B4,B5,X                           SCATPRF   355
      DATA K/0/                                                         SCATPRF   356
      IF(K.GT.0 )GO TO 1                                                SCATPRF   357
      K=K+1                                                             SCATPRF   358
      A0=2.3983474E-2                                                   SCATPRF   359
      A1=1.1287513E+1                                                   SCATPRF   360
      A2=1.1394160E+2                                                   SCATPRF   361
      A3=2.4653115E+1                                                   SCATPRF   362
      B0=1.8064128E-2                                                   SCATPRF   363
      B1=9.3877372                                                      SCATPRF   364
      B2=1.4921254E+2                                                   SCATPRF   365
      B3=2.8958085E+2                                                   SCATPRF   366
      B4=1.2049512E+2                                                   SCATPRF   367
      B5=2.4656819E+1                                                   SCATPRF   368
    1 C3=(X**4+A3*X**3+A2*X*X+A1*X+A0)/                                 SCATPRF   369
     1  (X**6+B5*X**5+B4*X**4+B3*X**3+B2*X*X+B1*X+B0)                   SCATPRF   370
      RETURN                                                            SCATPRF   371
      END                                                               SCATPRF   372
```

```
      SUBROUTINE SIMPSN (F,Z,A,B,EPS,N,FI)                              SCATPRF   373
C     INTEGRATES F(X)FROM A TOB WITH AN ERROR LESS THAN EPS,            SCATPRF   374
C     USING N SUBINTERVALS                                              SCATPRF   375
C     WITH AN UPPER LIMIT OF 2500 INTERVALS                             SCATPRF   376
C     THE INTEGRAL IS FI                                                SCATPRF   377
C     NOBLE,VOL.2,P239                                                  SCATPRF   378
      H=0.5*(B-A)                                                       SCATPRF   379
      AJ=H*(F(A)+F(B))                                                  SCATPRF   380
      AI1=3.0*AJ                                                        SCATPRF   381
      N=1                                                               SCATPRF   382
    3 BB=0.0                                                            SCATPRF   383
      DO 5 K=1,N                                                        SCATPRF   384
    5 BB=BB+F(A+(2.0*K-1.0)*H)                                          SCATPRF   385
      AIO=AJ+4.0*H*BB                                                   SCATPRF   386
      IF(ABS(AIO).LT.1.0E-50)GO TO 10                                   SCATPRF   387
    7 IF(ABS((AIO-AI1)/AIO).LT.EPS)GO TO 10                             SCATPRF   388
      AJ=0.25*(AJ+AIO)                                                  SCAT      1
      AI1=AIO                                                           SCATPRF   389
      N=2*N                                                             SCATPRF   390
      IF(N.GT.2500) GO TO 10                                            SCATPRF   391
      H=0.5*H                                                           SCATPRF   392
      GO TO 3                                                           SCATPRF   393
   10 FI=AIO/3.0                                                        SCATPRF   394
      RETURN                                                            SCATPRF   395
      END                                                               SCATPRF   396
```

```
      FUNCTION COLL(Z,I)                                                SCATPRF   397
C     SUBPROGRAM TO CALCULATE COLLISION FREQUENCIES FOR 43S             SCATPRF   398
C     I =1 - WINTER                                                     SCATPRF   399
C     I = 2 - EQUINOX                                                   SCATPRF   400
C     I = 3 - SUMMER                                                    SCATPRF   401
      IF(Z.GT.71.0)GO TO 1                                              SCATPRF   402
      IF(I -2)2,3,4                                                     SCATPRF   403
    2 COLL =3.579E+10*EXP(-Z/7.47)                                      SCATPRF   404
      RETURN                                                            SCATPRF   405
    3 COLL=5.217E+10*EXP(-Z/7.297)                                      SCATPRF   406
      RETURN                                                            SCATPRF   407
    4 COLL=4.351E+10*EXP(-Z/7.55)                                       SCATPRF   408
      RETURN                                                            SCATPRF   409
    1 IF(I-2)5,6,7                                                      SCATPRF   410
    5 COLL =1.434E+11*EXP(-Z/6.35)                                      SCATPRF   411
      RETURN                                                            SCATPRF   412
    6 COLL =2.989E+11*EXP(-Z/6.187)                                     SCATPRF   413
      RETURN                                                            SCATPRF   414
    7 COLL =1.592E+12*EXP(-Z/5.45)                                      SCATPRF   415
      RETURN                                                            SCATPRF   416
      END                                                               SCATPRF   417
```

```
      FUNCTION BFIELD(Z)                                                SCATPRF   418
C     FIELD AT 31S (WOOMERA) IN W/M**2                                  SCATPRF   419
      A=1.0/(1.0+Z/6370.0)**3                                           SCATPRF   420
      BFIELD=6.0000E-05*A                                               SCATPRF   421
      RETURN                                                            SCATPRF   422
      END                                                               SCATPRF   423
```

```
      COMPLEX FUNCTION L2(X1,X2,X3,M1,M2,M3,X)                          SCATPRF   424
      COMPLEX M1,M2,M3,SUM                                              SCATPRF   425
      SUM=CMPLX((X-X2)*(X-X3)/((X1-X2)*(X1-X3)),0.)*M1                  SCATPRF   426
      SUM=SUM+CMPLX((X-X1)*(X-X3)/((X2-X1)*(X2-X3)),0.)*M2              SCATPRF   427
      SUM=SUM+CMPLX((X-X1)*(X-X2)/((X3-X1)*(X3-X2)),0.)*M3              SCATPRF   428
      L2=SUM                                                            SCATPRF   429
      RETURN                                                            SCATPRF   430
      END                                                               SCATPRF   431
```

APPENDIX G

Program Volscat

See Chapter X for Description
(equation 10.3.1.8)

```
      PROGRAM VOLSCAT(INPUT,OUTPUT)                                          VOLSCAT     2
      EXTERNAL PHINT                                                         VOLSCAT     3
      COMMON/T/THETA                                                         VOLSCAT     4
      COMMON/P/PHI                                                           VOLSCAT     5
      COMMON/W/ WAVELT,HTREC,HTTX,DIPLEN,ATTEN,RADX(2),PHIX(2)               VOLSCAT     6
      COMMON/PH/ PHO(99),NAER,RAD(99)                                        VOLSCAT     7
      COMMON/H/ HT,DEP,WIDH          ,EPS,RO,PI                              VOLSCAT     8
      COMMON/DEL/DEL                                                         VOLSCAT     9
      COMMON/I/IPULSTP                                                       VOLSCAT    10
C  PROGRAM TO CALCULATE EFFECTIVE VOLUME OF BACKSCATTER FROM A LAYER OF      VOLSCAT    11
C  DEPTH DEP,LOWER EDGE AT HEIGHT HT,FOR POLAR SPECIFIED BY POLAR            VOLSCAT    12
      XX=1.0                                                                 VOLSCAT    13
      PI=3.14159    $  EPS=1.0E-02                                           VOLSCAT    14
C * * * * * * * * * * * * * * * * * * * * * * * * *                         VOLSCAT    15
C  DATA                                                                      VOLSCAT    16
C* * * * * * * * * * * * * * * * * * * * * * * * * * * * * * * * * * * *     VOLSCAT    17
C  TX COORDS                                                                 VOLSCAT    18
      RADX(1)=12.5 $ RADX(2)=12.5                                            VOL        1
      PHIX(1)=PI/2. $ PHIX(2)=-PI/2.                                         VOLSCAT    20
C   RX AERIALS,AND COORDS                                                    VOLSCAT    21
      NAER=89 $ CALL READE(PHO,RAD,99)                                       VOLSCAT    22
C   WAVELENGTH,DIPOLE LENGTH IN HALF WAVELENGTHS FOR RX                      VOLSCAT    23
      WAVELT=50.0 $ DIPLEN=3.0                                               VOL        2
C   HT OF TX AERIALS ABOVE IMAGE $ HT OF RX AERIALS ABOVE IMAGES             VOLSCAT    25
      HTTX=23.0 $ HTREC=23.0                                                 VOL        3
C  REFLECTION COEFF OF GRD                                                   VOLSCAT    27
      ATTEN=1.0                                                              VOL        4
C  SET HT,DEPTH OF LAYER IN KM                                               VOLSCAT    29
      HT=80.0 $ DEP=2.0                                                      VOL        5
C  IPULSTP IS PULSE TYPE -EXP OR COS                                         VOLSCAT    31
C   WIDH-- IF PULSE TYPE IS EXP,WIDH IS 1/E HALF WIDTH OF PULSE              VOLSCAT    32
C  IN KM.  .---    IF PULSE TYPE IS COS,WIDH=BASE FULL WIDTH /8. IN KM      VOLSCAT    33
C   MUST USE BASE  WIDTH /8. SO DOES NOT STUFF UP THETAL AND THETAIN IN      VOLSCAT    34
C   PHINT   -- IE WANT ANGLES OF INTEGRATION ST THERE IS NON ZERO SCATTER    VOLSCAT    35
CC   AT START OF INTEGRAL LIMITS AND END OF LIMITS                           VOLSCAT    36
      IPULSTP=3HEXP $ WIDH=3.0                                               VOL        6
C  DEL= SMALL NO LT PULSE HALF WIDTH AND LAYER DEPTH BUT GT ROUNDOFF ERR     VOLSCAT    38
      DEL=1.0E-15                                                            VOLSCAT    39
C  FIND EFFECTIVE VOLUME FOR RANGE RO                                        VOLSCAT    40
      PI2=PI/2.                                                              VOLSCAT    41
C   NORMALIZATION FACTOR FOR LATER                                           VOLSCAT    42
      THETA=0.0 $ PHI=0.0                                                    VOLSCAT    43
C  XX IS DUMMY PARAMETER - NOT USED                                          VOLSCAT    44
      PRINT 46                                                               VOLSCAT    45
      RESMAX=POLAR(THETA,PHI)                                                VOLSCAT    46
      PRINT 46                                                               VOLSCAT    47
46    FORMAT(1X,1H*)                                                         VOLSCAT    48
      PRINT 80                                                               VOLSCAT    49
80    FORMAT(1H1)                                                            VOLSCAT    50
      PRINT 81,EPS                                                           VOLSCAT    51
81    FORMAT(1X,27HINTEGRATION ACCURACY IS =    ,E9.3)                       VOLSCAT    52
      PRINT 82,RADX(1),RADX(2)                                               VOLSCAT    53
82    FORMAT(1X,11HTX RADII =   ,2F11.4)                                     VOLSCAT    54
      PRINT 83,PHIX(1),PHIX(2)                                               VOLSCAT    55
83    FORMAT(1X,19HTX DIPOLE ANGLES = ,2F11.4)                               VOLSCAT    56
      PRINT 84,NAER,WAVELT,DIPLEN                                            VOLSCAT    57
84    FORMAT(1X,68HNO OF AERIALS,WAVELENGTH,AND RX DIPOLE LENGTH IN HALF     VOLSCAT    58
     $ WAVELENGTHS =  ,I5,2F11.4)                                            VOLSCAT    59
      PRINT 85,HTTX,HTREC,ATTEN                                              VOLSCAT    60
85    FORMAT(1X,69HHT OF TX ABOVE IMAGE,HT OF RX ABOVE IMAGE,AND GRD REF     VOLSCAT    61
     $LECTION COEFF =  ,3F11.4)                                              VOLSCAT    62
      PRINT 86,HT,DEP                                                        VOLSCAT    63
86    FORMAT(1X,41HHT OF BASE OF LAYER,AND DEPTH OF LAYER = ,2F11.4,1X,3     VOLSCAT    64
     $HKMS )                                                                 VOLSCAT    65
      PRINT 87,IPULSTP,WIDH                                                  VOLSCAT    66
87    FORMAT(1X,29HPULSE TYPE,AND PULSE WIDTH =  ,A10,F11.4)                 VOLSCAT    67
      PRINT 88                                                               VOLSCAT    68
88    FORMAT(1X,117HFOR EXP PULSE,WIDTH IS WIDTH BETWEEN 1/E PTS OF POWE     VOLSCAT    69
     $R PROFILE OF PULSE-- FOR COS PULSE,WIDTH IS 1/8*WIDTH OF BASE    )     VOLSCAT    70
      PRINT 89                                                               VOLSCAT    71
89    FORMAT(1X,52H- - COS ACTUALLY MEANS COS**4 POWER PROFILE OF PULSE)     VOLSCAT    72
      PRINT 91,RESMAX                                                        VOLSCAT    73
91    FORMAT(1X,62HCURRENT TOTAL WRTO 1 DIPOLE SUMMED FOR VERTICAL PROPO     VOLSCAT    74
     $GATION =    ,E11.4)                                                   VOLSCAT    75
      DO 11 I=1,100                                                          VOLSCAT    76
      RO=99.5+FLOAT(I-1)/2.                                                  VOL        7
C  INTEFRAL FOR RANGE RO                                                     VOLSCAT    78
      CALL SIMPSB(PHINT,PHI,0.,PI2,EPS,N,FI)                                 VOLSCAT    79
C  INTEGRATED FROM 0 TO PI/2,SO X4                                           VOLSCAT    80
      VOLEFF=4.0*FI                                                          VOLSCAT    81
      VOLEFF=VOLEFF/(RESMAX*RESMAX)                                          VOLSCAT    82
      PRINT 411,RO,VOLEFF                                                    VOLSCAT    83
411   FORMAT(1X,9HAT RANGE ,2X,F7.2,2X,24H, EFFECTIVE VOLUME IS = ,2X,       VOLSCAT    84
     $E11.5)                                                                 VOLSCAT    85
11    CONTINUE                                                               VOLSCAT    86
      END                                                                    VOLSCAT    87
```

```
      FUNCTION PHINT(PHI)                                                    VOLSCAT    88
      EXTERNAL THETINT                                                       VOLSCAT    89
                                                                             VOLSCAT    90
      COMMON/W/ WAVELT,HTREC,HTTX,DIPLEN,ATTEN,RADX(2),PHIX(2)               VOLSCAT    91
      COMMON/PH/ PHO(99),NAER,RAD(99)                                        VOLSCAT    92
      COMMON/H/ HT,DEP,WIDH          ,EPS,RO,PI                              VOLSCAT    93
      COMMON/DEL/DEL                                                         VOLSCAT    94
      PI2=PI/2.                                                              VOLSCAT    95
C  INTEGRATION OF THETA FROM 0 TO PI/2                                       VOLSCAT    96
C  ONLY INTEGRATE BETWEEN REASONABLE LIMITS OF THETA                         VOLSCAT    97
      ARG1=HT/(RO+4.*WIDH-DEL)   $ ARG2=(HT+DEP)/(RO-4.*WIDH+DEL)            VOLSCAT    98
      IF(ARG1.GE.1.0)ARG1=1.0                                                VOLSCAT    99
      IF(ARG2.GE.1.0)ARG2=1.0                                                VOLSCAT   100
      THETAL=ACOS(ARG1) $ THETAIN=ACOS(ARG2)                                 VOLSCAT   101
      CALL SIMPSA(THETINT,THETA,THETAIN,THETAL,EPS,N,FI,PHI)                 VOLSCAT   102
      PHINT=FI                                                               VOLSCAT   103
      RETURN                                                                 VOLSCAT   104
      END                                                                    VOLSCAT   105
```

```
      FUNCTION THETINT(THETA,PHI)                                          VOLSCAT  106
      EXTERNAL CONV                                                        VOLSCAT  107
                                                                           VOLSCAT  108
      COMMON/W/ WAVELT,HTREC,HTTX,DIPLEN,ATTEN,RADX(2),PHIX(2)             VOLSCAT  109
      COMMON/PH/ PHO(99),NAER,RAD(99)                                      VOLSCAT  110
      COMMON/H/ HT,DEP,WIDH          ,EPS,RO,PI                            VOLSCAT  111
      XX=1.0                                                               VOLSCAT  112
      PI2=PI/2.0                                                           VOLSCAT  113
C  INTEGRATION OF CONVOLUTION TIMES POLAR DIAGS                            VOLSCAT  114
C  BDS OF R INTEGRAL-ONLY INTEGRATE OVER R VALUES WITHIN LAYER             VOLSCAT  115
      RMIN=HT/COS(THETA) $ RMAX=(HT+DEP)/COS(THETA)                        VOLSCAT  116
      CALL SIMPSN(CONV,R,RMIN,RMAX,EPS     ,N,FI,THETA,PHI)                VOLSCAT  117
C  NOW MULTIPLY BY POLAR DIAG FUNCTION                                     VOLSCAT  118
      Y=POLAR(THETA,PHI)                                                   VOLSCAT  119
      THETINT=FI*Y*Y       *SIN(THETA)                                     VOLSCAT  120
      RETURN                                                               VOLSCAT  121
      END                                                                  VOLSCAT  122
```

```
      FUNCTION CONV(R,THETA,PHI)                                           VOLSCAT  123
C  CONVOLUTION FUNCTION                                                    VOLSCAT  124
                                                                           VOLSCAT  125
      COMMON/W/ WAVELT,HTREC,HTTX,DIPLEN,ATTEN,RADX(2),PHIX(2)             VOLSCAT  126
      COMMON/PH/ PHO(99),NAER,RAD(99)                                      VOLSCAT  127
      COMMON/H/ HT,DEP,WIDH          ,EPS,RO,PI                            VOLSCAT  128
      COMMON/I/IPULSTP                                                     VOLSCAT  129
      SIGMA=1.0                                                            VOLSCAT  130
C  SIGMA DESCRIBES ANISOTROPY OF SCATTER                                   VOLSCAT  131
C   I USE TX PULSE HERE,BUT SHOULD REALLY USE                              VOLSCAT  132
C  FOURIER TRANSFORM OF RX FN*(FT OF TX PULSE)                             VOLSCAT  133
      IF(IPULSTP.NE.3HEXP)GO TO 77                                         VOLSCAT  134
C  HERE PULSE TYPE IS EXP                                                  VOLSCAT  135
      ARG=(RO-R)*(RO-R)/(WIDH*WIDH)                                        VOLSCAT  136
      XINT=SIGMA       *EXP(-ARG)                                          VOLSCAT  137
      GO TO 78                                                             VOLSCAT  138
77    CONTINUE                                                             VOLSCAT  139
C  HERE,USE COS FN                                                         VOLSCAT  140
C  IE POWER PULSE IS COS**4 FN                                             VOLSCAT  141
      COSS=COS((RO-R)/(WIDH*8.)*PI)                                        VOLSCAT  142
      IF(ABS(RO-R).GT.WIDH*4.)COSS=0.0                                     VOLSCAT  143
      XINT=COSS*COSS*COSS*COSS                                             VOLSCAT  144
      XINT=XINT*SIGMA                                                      VOLSCAT  145
78     CONTINUE                                                            VOLSCAT  146
      CONV=XINT                                                            VOLSCAT  147
      RETURN                                                               VOLSCAT  148
      END                                                                  VOLSCAT  149
```

```
      FUNCTION POLAR(THETA,PHI)                                            VOLSCAT  150
                                                                           VOLSCAT  151
      COMMON/W/ WAVELT,HTREC,HTTX,DIPLEN,ATTEN,RADX(2),PHIX(2)             VOLSCAT  152
      COMMON/PH/ PHO(99),NAER,RAD(99)                                      VOLSCAT  153
      COMMON/H/ HT,DEP,WIDH          ,EPS,RO,PI                            VOLSCAT  154
      RES=BPRES(THETA,PHI,WAVELT,RAD,PHO,0.0,NAER,0.0,HTREC,DIPLEN,ATTEN   VOLSCAT  155
     $)                                                                    VOLSCAT  156
      RES=RES*BPRES(THETA,PHI,WAVELT,RADX,PHIX,0.0,2,0.0,HTTX,1.0,ATTEN)   VOLSCAT  157
      POLAR=RES                                                            VOLSCAT  158
      RETURN                                                               VOLSCAT  159
      END                                                                  VOLSCAT  160
```

```
      SUBROUTINE SIMPSN (F,Z,A,B,EPS,N,FI,THETA,PHI)                       VOLSCAT  161
C     INTEGRATES F(X)FROM A TOB WITH AN ERROR LESS THAN EPS,               VOLSCAT  162
C     USING N SUBINTERVALS                                                 VOLSCAT  163
C     WITH AN UPPER LIMIT OF 2500 INTERVALS                                VOLSCAT  164
C     THE INTEGRAL IS FI                                                   VOLSCAT  165
C     NOBLE,VOL.2,P239                                                     VOLSCAT  166
      H=0.5*(B-A)                                                          VOLSCAT  167
      AJ=H*(F(A,THETA,PHI)+F(B,THETA,PHI))                                 VOLSCAT  168
      AI1=3.0*AJ                                                           VOLSCAT  169
      N=1                                                                  VOLSCAT  170
    3 BB=0.0                                                               VOLSCAT  171
      DO 5 K=1,N                                                           VOLSCAT  172
5     BB=BB+F(A+(2.0*K-1.0)*H,THETA,PHI)                                   VOLSCAT  173
      AIO=AJ+4.0*H*BB                                                      VOLSCAT  174
      IF(ABS(AIO).LT.1.0E-50)GO TO 10                                      VOLSCAT  175
    7 IF(ABS((AIO-AI1)/AIO).LT.EPS)GO TO 10                                VOLSCAT  176
      AJ=0.25*(AJ+AIO)                                                     VOLSCAT  177
      AI1=AIO                                                              VOLSCAT  178
      N=2*N                                                                VOLSCAT  179
      IF(N.GT.2500) GO TO 10                                               VOLSCAT  180
      H=0.5*H                                                              VOLSCAT  181
      GO TO 3                                                              VOLSCAT  182
   10 FI=AIO/3.0                                                           VOLSCAT  183
      RETURN                                                               VOLSCAT  184
      END                                                                  VOLSCAT  185
```

```
      SUBROUTINE SIMPSA (F,Z,A,B,EPS,N,FI,PHI)                          VOLSCAT  186
      INTEGRATES F(X)FROM A TOB WITH AN ERROR LESS THAN EPS,            VOLSCAT  187
C     USING N SUBINTERVALS                                              VOLSCAT  188
C     WITH AN UPPER LIMIT OF 2500 INTERVALS                             VOLSCAT  189
C     THE INTEGRAL IS FI                                                VOLSCAT  190
C     NOBLE,VOL.2,P239                                                  VOLSCAT  191
      H=0.5*(B-A)                                                       VOLSCAT  192
      AJ=H*(F(A,PHI)+F(B,PHI))                                          VOLSCAT  193
      AI1=3.0*AJ                                                        VOLSCAT  194
      N=1                                                               VOLSCAT  195
    3 BB=0.0                                                            VOLSCAT  196
      DO 5 K=1,N                                                        VOLSCAT  197
    5 BB=BB+F(A+(2.0*K-1.0)*H,PHI)                                      VOLSCAT  198
      AIO=AJ+4.0*H*BB                                                   VOLSCAT  199
      IF(ABS(AIO).LT.1.0E-50)GO TO 10                                   VOLSCAT  200
    7 IF(ABS((AIO-AI1)/AIO).LT.EPS)GO TO 10                             VOLSCAT  201
      AJ=0.25*(AJ+AIO)                                                  VOLSCAT  202
      AI1=AIO                                                           VOLSCAT  203
      N=2*N                                                             VOLSCAT  204
      IF(N.GT.2500) GO TO 10                                            VOLSCAT  205
      H=0.5*H                                                           VOLSCAT  206
      GO TO 3                                                           VOLSCAT  207
   10 FI=AIO/3.0                                                        VOLSCAT  208
      RETURN                                                            VOLSCAT  209
      END                                                               VOLSCAT  210
```

```
      SUBROUTINE SIMPSB (F,Z,A,B,EPS,N,FI)                              VOLSCAT  211
      INTEGRATES F(X)FROM A TOB WITH AN ERROR LESS THAN EPS,            VOLSCAT  212
C     USING N SUBINTERVALS                                              VOLSCAT  213
C     WITH AN UPPER LIMIT OF 2500 INTERVALS                             VOLSCAT  214
C     THE INTEGRAL IS FI                                                VOLSCAT  215
C     NOBLE,VOL.2,P239                                                  VOLSCAT  216
      H=0.5*(B-A)                                                       VOLSCAT  217
      AJ=H*(F(A)+F(B))                                                  VOLSCAT  218
      AI1=3.0*AJ                                                        VOLSCAT  219
      N=1                                                               VOLSCAT  220
    3 BB=0.0                                                            VOLSCAT  221
      DO 5 K=1,N                                                        VOLSCAT  222
    5 BB=BB+F(A+(2.0*K-1.0)*H)                                          VOLSCAT  223
      AIO=AJ+4.0*H*BB                                                   VOLSCAT  224
      IF(ABS(AIO).LT.1.0E-50)GO TO 10                                   VOLSCAT  225
    7 IF(ABS((AIO-AI1)/AIO).LT.EPS)GO TO 10                             VOLSCAT  226
      AJ=0.25*(AJ+AIO)                                                  VOLSCAT  227
      AI1=AIO                                                           VOLSCAT  228
      N=2*N                                                             VOLSCAT  229
      IF(N.GT.2500) GO TO 10                                            VOLSCAT  230
      H=0.5*H                                                           VOLSCAT  231
      GO TO 3                                                           VOLSCAT  232
   10 FI=AIO/3.0                                                        VOLSCAT  233
      RETURN                                                            VOLSCAT  234
      END                                                               VOLSCAT  235
```

```
      SUBROUTINE READE(PHI,RAD,NNO)                                     VOLSCAT  236
      DIMENSION PHI(NNO),RAD(NNO)                                       VOLSCAT  237
      PI=3.14159                                                        VOLSCAT  238
C  READS IN TELESCOPE DIMENSIONS                                        VOLSCAT  239
      DO 11 I=1,15                                                      VOLSCAT  240
      J1=(I-1)*6+1                                                      VOLSCAT  241
      J2=J1+5                                                           VOLSCAT  242
      IF(I.EQ.15)J2=J2-1                                                VOLSCAT  243
      READ 100,(RAD(JK),PHI(JK),JK=J1,J2)                               VOLSCAT  244
100   FORMAT(12F6.2)                                                    VOLSCAT  245
11    CONTINUE                                                          VOLSCAT  246
C  CONVERT TO RADIANS                                                   VOLSCAT  247
      DO 12 IJ=1,89                                                     VOLSCAT  248
      PHI(IJ)=PHI(IJ)*PI/180.0                                          VOLSCAT  249
12    CONTINUE                                                          VOLSCAT  250
      RETURN                                                            VOLSCAT  251
      END                                                               VOLSCAT  252
```

```
      FUNCTION BPRES(ANGLE,PHIO,WAVELT,RAD,PHI,PHASE,NNO,PHREF,HTDIF,     VOLSCAT   253
     $ DIPLEN,ATTEN)                                                      VOLSCAT   254
      DIMENSION RAD(NNO),PHI(NNO)                                         VOLSCAT   255
C   THIS SUBROUTINE CALCULATES RESPONSE OF BUCKLAND PARK ARRAY IN DIRECTI VOLSCAT   256
C   AND AT ANGLE OF VIEW=ANGLE                                           VOLSCAT   257
C   DIPLEN= DIPOLE LENGTH IN HALF WAVELENGTHS                            VOLSCAT   258
C   ATTEN=ATTENUATION FACTOR DUE TO GRD ON REFLECTION -CAN ONLY BE REAL I VOLSCAT   259
C   PROGRAM -- GENERALLY 1                                               VOLSCAT   260
C   NEEDS READE ALSO TO GET DATA                                         VOLSCAT   261
C   CALCULATE DISTANCE TO REFERENCE LINE                                 VOLSCAT   262
      PI=3.14159                                                          VOLSCAT   263
      SUM=0.0                                                             VOLSCAT   264
      SUM1=0.0                                                            VOLSCAT   265
      SUM2=0.0                                                            VOLSCAT   266
C   INCLUDE DIPOLE RESPONSE                                              VOLSCAT   267
C   BEWARE IF BETA= ZERO                                                 VOLSCAT   268
      SINB=SQRT(1.0-(COS(PHIO)**2.0)*(SIN(ANGLE)**2.0))                   VOLSCAT   269
      IF(SINB.LT.0.001)GO TO 9                                            VOLSCAT   270
      COSB=SIN(ANGLE)*COS(PHIO)                                           VOLSCAT   271
      RESP=COS(DIPLEN*PI/2.0*COSB)/SINB                                   VOLSCAT   272
      GO TO 10                                                            VOLSCAT   273
9     RESP=0.0                                                            VOLSCAT   274
10    CONTINUE                                                            VOLSCAT   275
      DO 11 I=1,NNO                                                       VOLSCAT   276
      DIST=RAD(I)*SIN(PI/2.0+PHIO-PHI(I))                                 VOLSCAT   277
C   NOTICE DIST IS -VE WHERE NECESSARY                                   VOLSCAT   278
C   ALSO FIND PHASE OF AERIAL DUE TO INTRODUCED PHASE                    VOLSCAT   279
      DIS1=RAD(I)*SIN(PI/2.0+PHREF-PHI(I))                                VOLSCAT   280
C   CALCULATE PHASE OF AERIAL W.R.TO REFERENCE LINE                      VOLSCAT   281
      PSE=(DIST*SIN(ANGLE))/WAVELT*2.0*PI+PHASE*(DIS1/WAVELT)             VOLSCAT   282
C   CALCULATE CONTRIBUTION TO SUM                                        VOLSCAT   283
      SUM1=SUM1+COS(PSE)*RESP                                             VOLSCAT   284
      SUM2=SUM2+SIN(PSE)*RESP                                             VOLSCAT   285
C   NOTE RESPONSE OF DIPOLE,RESP,AFFECTS ALL CPTS EQUALLY-WE COULD MULTIP VOLSCAT   286
C   RESP AT THE END(OR WE CAN INCORPORATE AS WE GO                       VOLSCAT   287
C   DURING ANY CALL TO BPRES,RESP IS A CONSTANT FOR THAT CALL            VOLSCAT   288
11    CONTINUE                                                            VOLSCAT   289
      SUM=SQRT(SUM1**2.0+SUM2**2.0)                                       VOLSCAT   290
C   NOW INCORPORATE GROUND EFFECTS                                       VOLSCAT   291
C   TAKE PHASE OF DIPOLE SUM ABOVE AS ZERO-MEANS SIN CPT IS ZERO         VOLSCAT   292
      PHGRD=(HTDIF*COS(ANGLE)*2.0*PI/WAVELT+PI)                           VOLSCAT   293
      SUM=SQRT((SUM+SUM*ATTEN*COS(PHGRD))**2.0+(SUM*ATTEN*SIN(PHGRD))     VOLSCAT   294
     $ **2.0)                                                             VOLSCAT   295
      BPRES=SUM                                                           VOLSCAT   296
      RETURN                                                              VOLSCAT   297
      END                                                                 VOLSCAT   298
```

Data Cards.

```
466.25191.31457.20180.00466.25168.69457.20216.87408.93206.56377.02194.04
365.76180.00377.02165.96408.93153.44457.20143.13457.20233.13387.95225.00
329.70213.69289.16198.44274.32180.00289.16161.56329.69146.31387.95135.00
457.20126.87408.93243.44329.70236.31258.63225.00204.47206.57182.88180.00
204.47153.44258.63135.00329.69123.69408.93116.56129.32 45.00457.20 36.87
377.02 75.96408.93296.56457.20360.00204.47333.44204.47 26.56466.25258.69
377.02255.96289.16251.56204.47243.44129.32225.00 91.44180.00129.32135.00
204.47116.56289.16108.44377.02104.04466.25101.31457.20270.00365.76270.00
274.32270.00182.88270.00 91.44270.00  0.00  4.00 91.44 90.00182.88 90.00
274.32 90.00365.76 90.00457.20 90.00466.25281.31377.02284.04289.16288.44
204.47296.56129.32315.00 91.44360.00204.47 63.44289.16 71.56466.25 78.69
329.69303.69258.63315.00182.88360.00258.63 45.00329.69 56.31457.20306.87
329.69326.31274.82360.00329.69 33.69457.20 53.13408.93333.43365.76360.00
408.93 26.56466.25348.69466.25 11.31408.93 63.43387.95315.00289.16341.56
289.16 18.44387.95 45.00457.20323.13377.02345.96377.02 14.04
```

APPENDIX H

Coordinates of Some Important Middle-Atmosphere Observatories (Past and Present)

COORDINATES OF SOME IMPORTANT MIDDLE-ATMOSPHERE OBSERVATORIES
(PAST AND PRESENT)

Station	Geographic Coordinates		Geomagnetic Coordinates		L Shell [=1/cos² (geomag. lat.)]	Geomagnetic dip.
	Lat.	Long.	Lat. (N)	Long. (E)		
Woomera (Aust.)	30°45'S	136°18'E	-41°	209°	1.75	-62°
Adelaide (Aust.)	34°56'S	138°30'E	-45°	213°	2.0	-67°
Buckland Park (Aust.)	34°38'S	138°29'E	-45°	213°	2.0	-67°
Woodstock near Townsville (Aust.)	19°40'S	146°54'E	-29°	219°	1.3	-48°
Tantanoola (Aust.) near Mt. Gambier	37°50'S	140°47'E	-48°	216°	2.2	-67°
Christchurch Meteor facility (N.Z.)	43°27'S	172°24'E	-48°	253°	2.2	-71°
Birdlings Flat near Christchurch (N.Z.)	44°S	173°E	-48°	253°	2.2	-71°
Broken Hill (Aust.)	31°54'S	141°30'E	-42°	214°	1.8	-64°
Saskatoon (Canada)	52°N	107°W	61°	309°	4.35	78°
Ottowa (Canada)	45°N	76°W	56°	350°	3.2	75°
Kyoto (Japan)	34°51'N	136°06'E	27°	203°	1.3	50°
Jicamarca (Peru)	11°57'S	76°52'W	-1°	352°	1.0	0°
Boulder (Col, U.S.A.)	40°2'N	105°16'W	49°	317°	2.3	68°
Sunset (16 km West of Boulder)	40°2'N	105°29'W	49°	317°	2.3	68°
Platterville (Col, U.S.A.)	40°13'N	104°50'W	49°	317°	2.3	68°
Poker Flat (Alaska)	65°08'N	147°27½'W	60°	302°	4.0	78°
Sydney (Aust.)	33°52'S	151°00'E	-43°	226°	1.9	-64°
SOUSY (Harz Mts. Germany)	51°42'N	10°30'E	53°	94°	2.8	68°
Tromso (Norway)	69°58'N	19°22'E	67°	117°	6.7	77.5°
Urbana (Illinois U.S.A.)	40°07'N	88°12'W	51°	336°	2.5	71°
Atlanta (Georgia U.S.A.)	34°N	84°W	45°	342°	2.0	62°
Sheffield (U.K.)	53°N	2°W	57°	83°	3.45	68°
Ionospheric Research Lab., State College Pennsylvania U.S.A.	40°N	77°W	51°	351°	2.5	72°
Mawson base for Australian Research	67°37'S	62°52'E	71°	103°	9.4	-70°
Garchy (France)	47°N	3°E	49°	84°	2.3	64°
Arecibo (Puerto Rico)	18°20'N	66°45'W	29°	2°	1.3	52°

References

In the following list of references, the following abbreviations will be adhered to as much as possible. Other journals and conference proceedings will be written in full.

Ann. Geophys.	= Annals de Geophysique.
Aust. J. Phys.	= Australian Journal of Physics.
Bell Sys. Tech. Jour.	= Bell System Technical Journal.
Bull. Amer. Meteor. Soc.	= Bulletin of the American Meteorological Society.
Can. J. Phys.	= Canadian Journal of Physics.
Comm. of the A.C.M.	= Communications of the Association for Computing Machinery.
Dyn. Atmos. and Oceans	= Dynamics of Atmospheres and Oceans.
Geophys. Fluid Dyn.	= Geophysical Fluid Dynamics.
Geophys. Res. Letts.	= Geophysical Research Letters.
IEEE Trans. Geosci. Electr.	= Institute of Electrical and Electronics Engineers; Transactions on Geoscience electronics.
J. Atmos. Terr. Phys.	= Journal of Atmospheric and Terrestrial Physics.
J. Atmos. Sci.	= Journal of the Atmospheric Sciences.
J. Appl. Meteor.	= Journal of Applied Meteorology.
J. Br. Interplan. Soc.	= Journal of the British Interplanetary Society.
J. Fluid Mech.	= Journal of Fluid Mechanics.
J. Geophys. Res.	= Journal of Geophysical Research.
J. Inst. Elec. Engineers	= Journal of the Institution of Electrical Engineers.
J. Res. Nat. Bur. Standards	= Journal of Research of the National Bureau of Standards (USA).
Nature	= Nature.
Phil. Trans.Roy.Soc.(Lond.)	= Philosophical Transactions of the Royal Society (London).
Planet. Space. Sci.	= Planetary and Space Science.
Proc. Camb. Phil. Soc.	= Proceedings of the Cambridge Philosophical Society.
Proc. I.E.E.	= Proceedings of the Institution of Electrical Engineers.
Proc. I.E.E.E.	= Proceedings of the Institute of Electrical and Electronics Engineers.
Proc. Indian Acad. Sci.	= Proceedings of the Indian Academy of Sciences.
Proc. I.R.E.	= Proceedings of the Institute of Radio Engineers.
Proc. Phys. Soc.	= Proceedings of the Physical Society (London).
Proc. Roy. Soc.	= Proceedings of the Royal Society (London).
Quart. J. Roy. Met. Soc.	= Quarterly Journal of the Royal Meteorological Society (London).
Rad. Sci.	= Radio Science.
Reps. Prog. Phys.	= Reports on Progress in Physics.
Revs. Geophys. Space Phys.	= Reviews of Geophysics and Space Physics.
Science	= Science.
Scientific American	= Scientific American.
Space Research	= Space Research.
Tellus	= Tellus.
Weather	= Weather.

Abramowitz, M., and Stegun, I.A. "Handbook of mathematical functions" Dover publ. Inc., New York, (1970).

Ackerman, M. "In situ measurements of middle atmospheric composition" J. Atmos. Terr. Phys., 41, 723, (1979)

Aikin, A.C., Goldberg, R.A., Jones, W., and Kane, J.A. "Observations of the mid-latitude Lower Ionosphere in Winter" J. Geophys. Res., 82, 1869, (1977).

Akima, H. "Algorithm 474; Bivariate interpolation and smooth surface fitting based on local procedures." Comm. of the A.C.M., 17, 26, (1974).

Allen, D.C., Haigh, J.D., Houghton, J.T., and Simpson, C.J.S.M. "Radiative cooling near the mesopause." Nature, 281, 660, (1979).

Anandarao, B.G., Raghavarao, R., Desai, J.N., and Haerendel, G. "Vertical Winds and turbulence over Thumba ". J. Atmos. Terr. Phys., 40, 157, (1978).

Appleton, E.V. "On some measurements of the equivalent height of the atmospheric ionized layer". Proc. Roy. Soc., A126, 542, (1930).

Appleton, E.V. "Wireless Studies of the Ionosphere". J. Inst. Elec. Engineers, 71, 642, (1932).

Atlas, D. "Advances in Meteorology", Vol. 10, p.317 (Academic; New York) (1964).

Austin, G.L. and Manson, A.H. "On the nature of the irregularities that produce partial reflections of radio waves from the lower ionosphere (70-100 km)". Rad. Sci., 4, 35, (1969).

Austin, G.L., Bennett, R.G.T., and Thorpe, M.R. "The phase of waves partially reflected from the lower ionosphere (70-120km)" J. Atmos. Terr. Phys., 31, 1099, (1969).

Awe, O. "Errors in correlation between time series". J. Atmos. Terr. Phys., 26, 1239, (1964).

Bahnsen, A. "Recent techniques of observations and results from the magnetopause regions". J. Atmos. Terr. Phys., 40, 235, (1978).

Baker, D.J.(Jr.). "Density gradients in a rotating stratified fluid: experimental evidence for a new instability". Science, 172, 1029, (1971).

Ball, S.M., Stubbs, T.J., and Vincent, R.A. "Upper Atmosphere wind observations over Southern Australia during the Total Solar Eclipse of 23 October 1976). J. Atmos. Terr. Phys., 42, 21, (1980).

Ball, S.M. (unpublished) "Upper atmosphere tides and internal gravity waves at mid-and low-latitudes." Thesis, University of Adelaide, Adelaide, Australia. To be submitted in 1981.

Balsley, B.B. "Electric fields in the equatorial ionosphere; a review of techniques and measurements". J. Atmos. Terr. Phys., 35, 1035, (1973).

Balsley, B.B., Ecklund, W.L., Carter, D.A., and Johnston, P.E. "The MST radar at Poker Flat, Alaska". Rad. Sci., 15, 213, (1980).

Batchelor, G.K. "The theory of homogeneous turbulence". Cambridge Univ. Press, (1953).

Beckmann, P. "Statistical distribution of the amplitude and phase of a multiply scattered field". J. Res. Nat. Bur. Standards, 66D, 231, (1962).

Belrose, J.S., and Hewitt, L.W. "Variation of collision frequency in the lowest ionosphere with solar activity". Nature, 202, 267, (1964).

Belrose, J.S., and Burke, M.J. "Study of the lower ionosphere using partial reflection. 1. Experimental technique and method of analysis". J. Geophys. Res., 69, 2799, (1964).

Belrose, J.S., Bourne, I.A., and Hewitt, L.W. "A critical review of the partial reflection experiment". Proceedings of Conference on Ground-Based Radio Wave propagation studies of the lower ionosphere (11-15 April, 1966), pp. 125-151. Defence Research Board (Ottawa) (1967).

Belrose, J.S., Bourne, I.A., and Hewitt, L.W. "A preliminary investigation of diurnal and seasonal changes in electron distribution over Ottawa, Churchill and Resolute Bay". Proceedings of Conference on Ground-Based Radio Wave propagation studies of the Lower Ionosphere (11-15 April, 1966), pp. 167-188, Defence Research Telecommunications Establishment, Ottawa, Canada. (1967).

Belrose, J.S. "Radio Wave probing of the ionosphere by the partial reflection of radiowaves (from heights below 100 km). J. Atmos. Terr. Phys., 32, 567, (1970).

Belrose, J.S., Burke, M.J., Coyne, T.N.R., and Reed, J.E. "D-region measurements with the Differential-absorption, Differential-phase partial-reflection experiments". J. Geophys. Res., 77, 4829, (1972).

Bennett, F.D.G., Hall, J.E., and Dickinson, P.H.G. "D-region electron densities and collision frequencies from Faraday rotation and differential absorption measurements." J. Atmos. Terr. Phys., 34, 1321, (1972).

Bertin, F., Hughes, K.A., and Kersley, L. "Atmospheric waves induced by the solar eclipse of 30 June 1973". J. Atmos. Terr. Phys., 39, 457, (1977).

Bertin, F., Testud, J., Kersley, L., and Rees, P.R. "The meteorological jet stream as a source of medium scale gravity waves in the themosphere : an experimental study". J. Atmos. Terr. Phys., 40, 1161, (1978).

Bevington, P.R. "Data reduction and error analysis for the physical sicences". McGraw-Hill Book Co., New York, San Francisco, St. Louis, Toronto, London, Sydney, (1969).

Beynon, W.J.G., Williams, E.R., Arnold, F., Krankowsky, P., Bain, W.C., Dickinson, P.H.G. "D-region rocket measurements in winter anomaly absorption conditions". Nature, 261, 118, (1976).

Beynon, W.J.G., and Williams, E.R. "The long term variation in the ionospheric winter absorption anomaly". J. Atmos. Terr. Phys., 38, 423, (1976a).

Beynon, W.J.G., and Williams, E.R. "Rocket measurements of D-region electron density profiles". J. Atmos. Terr. Phys., 38, 1319, (1976b).

Bjelland, B., Holt, O., Landmark, B., and Lied, F. "The D region of the ionosphere". Nature, 184, 973, (1959).

Blair, J.C., Davis, R.M.Jr., and Kirby, R.C. "Frequency dependence of D-region scattering at VHF". J. Res. Nat. Bur. Standards, 65D, 417, (1961).

Blamont, J.E., and Barat, J. "Dynamical structure of the atmosphere between 80 and 120 km." in "Aurora and Airglow", Ed. B.M. McCormac, p.159. Reinhold Publ. Co., (1967).

Blum, P.W., Schuchardt, K.G.H., and von Zahn, U. "Semi-empirical models of the neutral atmosphere based on turbopause height and exospheric temperature variations". J. Atmos. Terr. Phys., 40, 1131, (1978).

Blum, P.W., and Schuchardt, K.G.H. "Semi-theoretical global models of the eddy diffusion coefficient based on satellite data". J. Atmos. Terr. Phys., 40, 1137, (1978).

Bolgiano, R.,Jr. "The General Theory of turbulence - turbulence in the atmosphere". from p.371, "Winds and Turbulence in the Stratosphere, Mesosphere and Ionosphere". Ed. K. Rawer. Publ. North-Holland, (1968).

Booker, H.G. "Oblique Propagation of Electromagnetic Waves in a Slowly-Varying Non-Isotropic Medium." Proc. Roy. Soc., A155, 235, (1936).

Booker, H.G. "A theory of scattering by nonisotropic irregularities with application to radar reflections from the aurora". J. Atmos. Terr. Phys., 8, 204, (1956).

Booker, H.G., and Cohen, R. "A theory of long-duration meteor-echoes based on atmospheric turbulence with experimental confirmation." J. Geophys. Res., 61, 707, (1956).

Booker, H.G. "Radio scattering in the lower ionosphere". J. Geophys. Res., 64, 2164, (1959).

Bowman, M.R., and Thomas, L. "The Numerical Calculation of wave fields for gravity waves propagating in an inhomogeneous atmosphere". Planet. Space. Sci., 24, 1199, (1976).

Bremer, J., and Singer, W. "Diurnal, seasonal, and solar-cycle variations of electron densities in the ionospheric D- and E-regions". J. Atmos. Terr. Phys., 39, 25, (1977).

Briggs, B.H., Phillips, G.J., and Shinn, D.H. "The Analysis of observations on spaced receivers of the fading of radio signals". Proc. Phys. Soc., 63B, 106, (1950).

Briggs, B.H., and Spencer, M. "The variability of time shifts in measurements of ionospheric movements". Report of the Physical Society Conference on Physics of the Ionosphere, Cambridge, p. 123, (Sept., 1954).

Briggs, B.H., Elford, W.G., Felgate, D.G., Golley, M.G., Rossiter, D.E., and Smith, J.W. "Buckland Park Aerial Array". Nature, 223, 1321, (1969).

Briggs, B.H., and Vincent, R.A. "Some theoretical considerations on remote probing of weakly scattering irregularities". Aust. J. Phys., 26, 805, (1973).

Briggs, B.H. "Ionospheric drifts". J. Atmos. Terr. Phys., 39, 1023, (1977a).

Briggs, B.H. "The analysis of moving patterns by correlation methods". Commemorative Volume on Ionospheric and Space Physics, University of Waltair. Ed. by B.R. Rao, (1977b).

Briggs, B.H. "Radar observations of atmospheric winds and turbulence : a comparison of techniques". Univ. of Adelaide, Dept. of Physics, report ADP no. 161, March 1980. Also submitted to J. Atmos. Terr. Phys., due late 1980-early 1981.

Brown, G.M., and John, J.I. "Vertical penetration of planetary waves into the lower ionosphere". J. Atmos. Terr. Phys., 41, 379, (1979).

Brown, N. "Radio echoes from meteor trains at a radio frequency of 1.98 MHz". J. Atmos. Terr. Phys., 38, 83, (1976).

Budden, K.G. "The Mathematics of Wave Propogation through the ionosphere". Report of the Physical Society Conference on The Physics of the Ionosphere held at Cavendish Laboratory, Cambridge, (Sept., 1954).

Budden, K.G. "Effect of Electron collisions on the Formulas of magneto-ionic theory". Rad. Sci., 69D, 191, (1965).

Budden, K.G. "Radio Waves in the ionosphere". Cambridge University Press, (1966).

Butcher, E.C., Downing, A.M., and Cole, K.D. "Wavelike variations in the F-region in the path of totality of the eclipse of 23 October 1976". J. Atmos. Terr. Phys., 41, 439, (1979).

Calman, J. "Experiments on high Richardson number instability of a rotating stratified shear flow". Dyn. Atmos. and Ocean, 1, 277, (1977).

Caughey, S.J., Crease, B.A., Asimakapoulos, D.N., and Cole, R.S. "Quantitative bistatic acoustic sounding of the atmospheric boundary layer". Quart. J. Roy. Met. Soc., 104, 147, (1978).

Chakrabarty, D.K., Chakrabarty, P., and Witt, G. "An attempt to identify the obscured paths of water cluster ions build-up in the D-region". J. Atmos. Terr. Phys., 40, 437, (1978a).

Chakrabarty, D.K., Chakrabarty, P., and Witt, G. "The effect of variations in temperature and nitric oxide density on ion-clustering in the mesopause region during winter anomaly". J. Atmos. Terr. Phys., 40, 1147, (1978b).

Chakrabarty, D.K., Chakrabarty, P., and Witt, G. "A theoretical attempt to explain some observed features of the D region". J. Geophys. Res., 83, 5763, (1978c).

Chamberlain, M.T., and Jacka, F. "Optical evidence for mid-latitude charged particle precipitation". J. Atmos. Terr. Phys., 41, 111, (1979).

Champeney, D.C. "Fourier Transforms and their physical applications" publ. Academic press, Lond and NY.,(1973).

Chandra, H., and Vincent, R.A. "Radio wave scattering from the southern hemisphere D-region". J. Atmos. Terr. Phys., 39, 1011, (1977).

Chandra, H., and Vincent, R.A. "Remote probing of D-region irregularities". Proc. Indian Acad. Sci., A88, 57, (1979).

Chapman, S., and Lindzen, R.S. "Atmospheric Tides". D. Reidel Publ. Co., Dordrecht, Holland. (1970).

Chemical Rubber Co. Handbook of Chemistry and Physics, 51st Ed., (1970).

Chiu, Y.T., and Straus, J.M. "Rayleigh-Taylor and wind-driven instabilities in the night-time equatorial Ionosphere". J. Geophys. Res., 84, 3283, (1979).

C.I.R.A. 1972 COSPAR International Reference Atmosphere. produced by Committee on Space Research (established by The International Council of Scientific Unions). Akademie-Verlag. Berlin, (1972).

Clark, D.H., and Raitt, W.J. "Wave-like structure in the ionosphere at low and middle latitude". J. Atmos. Terr. Phys., 38, 1245, (1976).

Cooper, J.W., and Stommel, H. "Regularly spaced steps in the main thermocline near Bermuda". J. Geophys. Res., 73, 5849, (1968).

Cornelius, D.W., and Essex, E.A. "HF doppler observations of 23 Oct., 1976 total solar eclipse over South Eastern Australia" J. Atmos. Terr. Phys., 40, 497, (1978).

Coyne, T.N.R., and Belrose, J.S. "An investigation into the effects of limited height resolution in the differential-absorption partial-reflection experiment". J. Geophys. Res., 78, 8276, (1973).

Craig, R.A. "The upper atmosphere - meteorology and physics". International Geophysics Series Vol 8. Ed. J.V. Miegham. Academic Press, NY and London, (1965).

Crain, C.M. "Survey of airborne Microwave refractometer measurements". Proc. I.R.E., 43, 1405, (1955).

Crane, R.K. "A review of radar observations of turbulence in the lower stratosphere". Rad. Sci., 15, 177, (1980).

Crochet, M., Tabbagh, J., and Makiese, N. "Simultaneous ionospheric drift observations by different techniques at low and mid-latitudes". J. Atmos. Terr. Phys., 39, 463, (1977).

Croxton, F.E. "Elementary statistics with applications in medicine and the biological sciences". Dover Publ. Inc., New York, (1959).

Cunnold, D.M. "Vertical transport coefficients in the mesosphere obtained from radar observations". J. Atmos. Sci., 32, 2191, (1975).

Curnow, R.J. (unpublished) "Upper Atmosphere Turbulence - a review". Dept. of Supply, Australian Defence Service, Weapons Research Establishment, Salisbury, South Australia, Technical note pad 118, (1966).

Czechowsky, P., Ruster, R., and Schmidt, G. "Variations of mesospheric structures in different seasons". Geophys. Res. Letts., 6, 459, (1979).

Dieminger, W. "On the causes of excessive absorption in the ionosphere on winter days". J. Atmos. Terr. Phys., 2, 340, (1952).

Dieminger, W. "D-region phenomena associated with meteorological influences". p.143, "Winds and Turbulence in the Stratosphere, Mesosphere and Ionosphere". North Holland press. Ed. K. Rawer, (1968).

Doviak, R.J., and Berger, M. "Turbulence and waves in the optically clear planetary boundary layer resolved by dual-Doppler radars". Rad. Sci., 15, 297, (1980).

Dutton, J.A., and Panofsky, H.A. "Clear Air Turbulence : a mystery may be unfolding". Science, 167, 937, (1970).

Dwight, H.B. "Tables of integrals and other mathematical data". Macmillan & Co., New York, Toronto, (1961).

Dyson, P.L., and Bennett, J.A. "General Formulae for absorption of radio waves in the ionosphere". J. Atmos. Terr. Phys., 41, 367, (1979).

Ebel, A. "Travelling (wave) disturbances of ionospheric absorption near 100 km height". J. Atmos. Terr. Phys., 40, 1323, (1978).

Einaudi, F., and Hines, C.O. "WKB approximation in application to acoustic-gravity waves". Can. J. Phys., 48, 1458, (1970).

Elford, W.G., and Roper, R.G. "Turbulence in the lower thermosphere" Space Research VII, p.42. Ed. R.L. Smith-Rose. North Holland; Amsterdam (1967).

Elford, W.G. "Momentum Transport due to Atmospheric tides". J. Geophys. Res., 84, 4432, (1979).

Elford, W.G., and Craig, R.L. "Upper atmospheric wind observations at Adelaide 35°S, August 1974". J. Atmos. Terr. Phys., 42, 61, (1980).

Ellyett, C., and Watts, J.M. "Stratification in the Lower Ionosphere". J. Res. Nat. Bur. Standards, 63D, 117, (1959).

Fejer, J.A. "The interaction of pulsed radio waves in the ionosphere". J. Atmos. Terr. Phys., 7, 322, (1955).

Fejer, J.A., and Vice, R.W. "An investigation of the ionospheric D-region". J. Atmos. Terr. Phys., 16, 291, (1959).

Ferguson, E.E. "Review of laboratory measurements of aeronomic ion-neutral reactions". Ann. Geophys., 28, 389, (1972).

Flock, W.L., and Balsley, B.B. "VHF radar returns from the D-region of the Equatorial Ionosphere". J. Geophys. Res., 72, 5537, (1967).

Flood, W.A. "Revised Theory for partial reflection D-region measurements". J. Geophys. Res., 73, 5585, (1968).

Flood, W.A. "Reply to a paper by O. Holt, entitled ('Discussion of Paper by W.A. Flood "Revised theory for partial reflection D-Region Measurements"')". J. Geophys. Res., 74, 5183, (1969).

Foldés, G. "The Lognormal distribution and its applications to atmospheric studies". p.227 of "Statistical Methods in radio wave propagation", Ed. by W.C. Hoffman, California University, Los Angeles, (1960).

Fooks, G.F. "Ionospheric drift measurements using correlation analysis; methods of computation and interpretation of results". J. Atmos. Terr. Phys., 27, 979, (1965).

Forbes, J.M., and Lindzen, R.S. "Atmospheric solar tides and their electrodynamic effects : I. The global Sq current system". J. Atmos. Terr. Phys., 38, 897, (1976a).

Forbes, J.M., and Lindzen, R.S. "Atmospheric solar tides and their electrodynamic effects : II. The equatorial electrojet". J. Atmos. Terr. Phys., 38, 911, (1976b).

Forbes, J.M., and Garrett, H.B. "Seasonal-latitudinal structure of the diurnal thermospheric tide". J. Atmos. Sci., 35, 148, (1978).

Fraser, G.J. "The Measurement of atmospheric winds at altitudes of 64-120 km using ground based radio equipment". J. Atmos. Sci., 22, 217, (1965).

Fraser, G.J. "Seasonal Variation of southern hemisphere mid-latitude winds at altitudes of 70-100 km". J. Atmos. Terr. Phys., 30, 707, (1968).

Fraser, G.J., and Vincent, R.A. "A study of D-region irregularities". J. Atmos. Terr. Phys., 32, 1591, (1970).

Fraser, G.J. "The 5-day wave and ionospheric absorption". J. Atmos. Terr. Phys., 39, 121, (1977).

Friend, A.W. "Theory and practice of tropospheric soundings by radar". Proc. IEEE, 37, 116, (1949).

Fritts, D.C. "The Nonlinear Gravity wave - critical level Interaction ". J. Atmos. Sci., 35, 397, (1978).

Fritts, D.C. "The Excitation of Radiating Waves and Kelvin-Helmholtz Instabilities by the Gravity Wave-critical level Interaction". J. Atmos. Sci., 36, 12, (1979).

Fukao, S., Sato, T., Kato, S., Harper, R.M., Woodman, R.F., and Gordon, W.E. "Mesospheric winds and waves over Jicamarca on May 23-24, 1974". J. Geophys. Res., 84, 4379, (1979).

Fukao, S., Wakasugi, K., and Kato, S. "Radar measurement of short-period atmospheric waves and related scattering properties at the altitude of 13-25 km over Jicamarca". Rad. Sci., 15, 431, (1980a).

Fukao, S., Sato, T., Harper, R.M., and Kato, S. "Radio wave scattering from the tropical mesosphere observed with the Jicamarca radar". Rad. Sci., 15, 447, (1980b).

Gadsden, M. "The sizes of particles in Noctilucent clouds : Implications for mesospheric water vapour". J. Geophys. Res., 83, 1155, (1978).

Gage, K.S., and Balsley, B.B. "Doppler Radar probing of the clear atmosphere". Bull. Amer. Meteor. Soc., 59, 1074, (1978).

Gage, K.S., and Green, J.L. "Evidence for specular reflection from monostatic VHF radar observations of the stratosphere". Rad. Sci., 13, 991, (1978).

Gage, K.S. "Evidence for a $k^{-5/3}$ Law inertial range in mesoscale two dimensional Turbulence ". J. Atmos. Sci., 36, 1950, (1979).

Gage, K.S., and Balsley, B.B. "On the scattering and reflection mechanisms contributing to clear air radar echoes from the troposphere, stratosphere and mesosphere". Rad. Sci., 15, 243, (1980).

Gage, K.S., Green, J.L., and Van Zandt, T.E. "Use of Doppler radar for the measurement of atmospheric turbulence parameters from the intensity of clear-air echoes". Rad. Sci., 15, 407, (1980).

Gallet, R.M. "Aerodynamical Mechanisms producing electronic density fluctuations in turbulent ionized layers". Proc. I.R.E., 43, 1210, (1955).

Gardner, F.F., and Pawsey, J.L. "Study of the ionospheric D-region using partial reflections". J. Atmos. Terr. Phys., 3, 321, (1953).

Garrett, H.B., and Forbes, J.M. "Tidal structure of the thermosphere at equinox". J. Atmos. Terr. Phys., 40, 657, (1978).

Geller, M.A., Hess, G.C., and Wratt, D. "Simultaneous partial reflection and meteor wind observations at Urbana, Illinois, during the Winter of 1974-75". J. Atmos. Terr. Phys., 38, 287, (1976).

Geller, M.A. "Dynamics of the middle atmosphere". J. Atmos. Terr. Phys., 41, 683, (1979).

Gnanalingam, S., and Weekes, K. "Weak echoes from the ionosphere with radio waves of frequency 1.42mc." Nature, 170, 113, (1952).

Gnanalingam, S., and Kane, J.A. "Shortcomings in our understanding of the lower atmosphere as revealed by an analysis of radio wave absorption measurements". J. Atmos. Terr. Phys., 40, 629, (1978).

Goldstein, H. "Propagation of short radio waves". Ed. D. Kerr, McGraw-Hill, New York. 580 pp. (1951).

Gossard, E.D., and Hooke, W.H. "Waves in the atmosphere", 456 pp., Elsevier, New York, (1975).

Gossard, E.E., Chadwick, R.B., Moran, K.P., Strauch, R.G., Morrison, G.E., and Campbell, W.L. "Observations of winds in the clear air using an FM-CW doppler radar". Rad. Sci., 13, 285, (1978).

Green, J.L., and Gage, K.S. "Observations of stable layers in the troposphere and stratosphere using VHF radar". Rad. Sci., 15, 395, (1980).

Gregory, J.B. "Ionospheric reflections from heights below the E region". Aust. J. Phys., 9, 324, (1956).

Gregory, J.B. "Radio wave reflections from the mesosphere 1. Heights of occurrence". J. Geophys. Res., 66, 429, (1961).

Gregory, J.B. "The influence of atmospheric circulation on mesospheric electron densities in winter". J. Atmos. Sci., 22, 18, (1965).

Gregory, J.B., and Manson, A.H. "Mesospheric electron number densities at 35°S Latitude". J. Geophys. Res., 72, 1073, (1967).

Gregory, J.B., and Vincent, R.A. "Structure of partially reflecting regions in the lower ionosphere". J. Geophys. Res., 75, 6387, (1970).

Groves, G.V. "Wind models from 60-130 km altitude for different months and latitudes". J. Br. Interplan. Soc., 22, 285, (1969).

Groves, G.V. "Rocket studies of atmospheric tides". Proc. Roy. Soc., A351, 437, (1976).

Haltiner, G.J., and Martin, F.L. "Dynamical and Physical Meteorology". Publ. McGraw-Hill, NY, Toronto, Lond., (1957).

Harper, R.M., and Woodman, R.F. "Preliminary multiheight radar observations of waves and winds in the mesosphere over Jicamarca". J. Atmos. Terr. Phys., 39, 959, (1977).

Harper, R.M., and Gordon, W.E. "A review of radar studies of the middle atmosphere". Rad. Sci., 15, 195, (1980).

Hartree, D.R. "The propagation of Electromagnetic waves in a refracting medium in a magnetic field". Proc. Camb. Phil. Soc., 27, 143, (1930).

Haug, A., Thrane, E.V., Bjorna, K., Brekke, A., and Holt, O. "Observations of unusually strong partial reflections in the auroral D-region during an absorption event". J. Atmos. Terr. Phys., 39, 1333, (1977).

Hill, R.J., and Bowhill, S.A. "Relaxation to photochemical equilibrium of charged species within displaced air parcels in the D-region". J. Atmos. Terr. Phys., 41, 607, (1979).

Hines, C.O. "Internal atmospheric gravity waves at Ionospheric heights". Can. J. Phys., 38, 1441, (1960).

Hines, C.O., and Reddy, C.A. "On the propagation of atmospheric gravity waves through regions of wind shear". J. Geophys. Res., 72, 1015, (1967).

Hines, C.O. "Generalizations of the Richardson Criterion for the onset of atmospheric turbulence". Quart. J. Roy. Met. Soc., 97, 429, (1971).

Hines, C.O. "Motions in the ionospheric D and E regions". Phil. Trans. Roy. Soc. Lond., A271, 457, (1972).

Hines, C.O. "The Upper Atmosphere in Motion". A selection of papers with annotation. American Geophysical Union, Washington, DC, (1974).

Hines, C.O. "Relaxational Dissipation in Atmospheric Waves - I. Basic Formulation". Planet. Space, Sci., 25, 1045, (1977a).

Hines, C.O. "Relaxational Dissipation in Atmospheric Waves. - II. Application to the Earth's upper Atmosphere". Planet. Space. Sci., 25, 1061, (1977b).

Ho, K.L., Mavrokoukoulakis, N.D., and Cole, R.S. "Determination of the atmospheric refractive index structure parameter from refractivity measurements and amplitude scintillation measurements at 36GHz". J. Atmos. Terr. Phys., 40, 745, (1978).

Hocking, W.K. (Unpublished) "Scattering properties of D-region irregularities". Report for the degree of Hons. B. Sc., Adelaide University, (1978).

Hocking, W.K. "Angular and temporal characteristics of partial reflection from the D-region of the ionosphere". J. Geophys. Res., 84, 845, (1979).

Hodges, R.R.(Jr.) "Generation of Turbulence in the Upper Atmosphere by Internal Gravity waves". J. Geophys. Res., 72, 3455, (1967).

Hogg, R.V., and Tanis, E.A. "Probability and Statistical Inference". MacMillan publ. Co., New York; Collier MacMillan publ., Lond., (1977).

Holt, A. "Discussion of Paper by W.A. Flood, 'Revised Theory for Partial Reflection D-region Measurements'". J. Geophys. Res., 74, 5179, (1969).

Hong, S.S., and Lindzen, R.S. "Solar Semi-diurnal Tide in the Thermosphere". J. Atmos. Sci., 33, 135, (1976).

Houghton, J.T. "The physics of atmospheres". Cambridge University Press., Cambridge, London, (1977).

Houghton, J.T. "The Stratosphere and Mesosphere". Quart. J. Roy. Met. Soc., 104, 1, (1978).

Howard, L.N. "Note on a paper of John W. Miles". J. Fluid Mech., 10, 509, (1961).

Hung, R.J., Phan, T., and Smith, R.E. "Observation of gravity waves during the extreme tornado outbreak of 3 April 1974". J. Atmos. Terr. Phys., 40, 831, (1978).

Huntsberger, D.V., and Billingsley, P. "Elements of Statistical Inference". Allyn and Bacon Inc., Boston, (1973).

Jackson, J.D. "Classical Electrodynamics". 2nd Ed. J. Wiley and Sons, Inc., NY, Lond., Sydney, Toronto, (1975).

James, P.K. "A review of radar observations of the troposphere in clear air conditions". Rad. Sci., 15, 151, (1980).

Johnson, F., and Wilkins, E. "Thermal upper limit on eddy diffusion in the mesosphere and lower thermosphere". J. Geophys. Res., 70, 1281, (1965). (+ Correction p.4063).

Jones, R.M., and Kopka, H. "The sensitivity of D-region partial reflections to irregularity composition". J. Atmos. Terr. Phys., 40, 723, (1978).

Jones, W.L., and Houghton, D.D. "The coupling of momentum between internal gravity waves and mean flow : a numerical study". J. Atmos. Sci., 28, 604, (1971).

Justus, C.G. "The Eddy diffusivities, energy balance parameters, and heating rate of upper atmosphere turbulence". J. Geophys. Res., 72, 1035, (1967).

Justus, C.G. "A theory for the energy spectrum of shear-dependent turbulence". J. Atmos. Sci., 26, 1238, (1969).

Justus, C. "Upper atmosphere mixing by gravity waves". Paper 73-495 presented at AISS/AMS Intern. Conf. Environmental impact of Aerospace operations in the high atmosphere, Denver, Colorado, 11-13 June, (1973). (Graph used in this thesis taken from Cunnold, (1975)).

Kaimal, J.C., Wyngaard, J.C., Izumi, Y., and Coté, O.R. "Spectral characteristics of surface layer turbulence". Quart. J. Roy. Met. Soc., 98, 563, (1972).

Kent, G.S., and Wright, R.W.H. "Movements of ionospheric irregularities and atmospheric winds". J. Atmos. Terr. Phys., 30, 657, (1968).

King-Hele, D.G. "The Earth's Neutral Upper Atmosphere". Revs. Geophys. Space. Phys., 16, 733, (1978).

Klostermeyer, J. "Numerical calculation of gravity wave propagation in a realistic thermosphere". J. Atmos. Terr. Phys., 34, 765, (1972).

Koshelev, V.V. "Variations of transport conditions and winter anomaly in the D-ionospheric region". J. Atmos. Terr. Phys., 41, 431, (1979).

Kotadia, K.M., and Gupta, A. "On the use of f-min as an index of ionospheric absorption". J. Atmos. Terr. Phys., 38, 295, (1976).

Lilly, D.K., Waco, D.E., and Adelfang, S.I. "Stratospheric mixing estimated from high altitude turbulence measurements". J. Appl. Meteor., 13, 488, (1974).

Lincoln, J.V. "Geomagnetic and solar data". J. Geophys. Res., 81, 4806, (1976).

Lindner, B.C. (Unpublished) "Radio studies of the lower ionosphere". Thesis, University of Adelaide, Adelaide, Australia, (1972).

Lindner, B.C. "The nature of D-region scattering of vertical incidence radio waves I. Generalized statistical theory of diversity effects between spaced receiving antennas". Aust. J. Phys., 28, 163, (1975a).

Lindner, B.C. "The nature of D-region scattering of vertical incidence radio waves II. Experimental observations using spaced antenna reception". Aust. J. Phys., 28, 171, (1975b).

Lindzen, R.S. "Tides and internal gravity waves in the atmosphere". From "Developments in atmospheric science, I. - Structure and Dynamics of the upper Atmosphere". Ed. F. Vernieni, Elsevier Scientific publ. Co., Amsterdam-Oxford-NY, (1974).

Lindzen, R.S., and Hong, S.S. "Effects of mean winds and horizontal temperature gradients on solar and lunar semidiurnal tides in the atmosphere". J. Atmos. Sci., 31, 1421, (1974).

Lindzen, R.S., and Tung, K.K. "Wave over-reflection and shear instability". J. Atmos. Sci., 35, 1626, (1978).

Liu, C.H., and Yeh, K.C. "Scattering of VHF and UHF radar signals from the turbulent air". Rad. Sci., 15, 277, (1980).

Lloyd, K.H., Low, C.H., McAvaney, B.J., Rees, D., and Roper, R.G. "Thermospheric observations combining chemical seeding and ground based techniques - I. Winds, Turbulence and the parameters of the neutral atmosphere". Planet. Space Sci., 20, 761, (1972).

Lloyd, K.H., Low, C.H., and Vincent, R.A. (Unpublished) "Turbulence billows and gravity waves in a high shear region of the upper atmosphere". Weapons Research Establishment technical note 670 (WR&D), June, (1972). (See Lloyd et al. 1973 for published version).

Lloyd, K.H., Low, C.H., and Vincent, R.A. "Turbulence, billows and gravity waves in a high shear region of the upper atmosphere". Planet. Space Sci., 21, 653, (1973).

Lumley, J.L., and Panofsky, H.A. "The structure of atmospheric turbulence". N.Y., Interscience publishers (1964). 239 pp.

MacDougall, J.W. "110 km neutral zonal wind patterns". Planet. Space Sci., 22, 545, (1974).

MacDougall, J.W. "Seasonal variation of semidiurnal winds in the dynamo region". Planet. Space Sci., 26, 705, (1978).

McEwan, A.D. "Mass and momentum diffusion in internal breaking events". To appear in Volume II of the Proceedings of the 2nd IAHR (International Association for Hydraulic Research) symposium on stratified flows, (Trondheim, Norway, (1980)).

McIntyre, M.E. "The axis symmetric convective regime for a rigidly bound rotating annulus". J. Fluid Mech., 32, 625, (1968).

McIntyre, M.E. "Diffusive destabilization of the baroclinic circular vortex". Geophys. Fluid Dyn., 1, 19,(1970a).

McIntyre, M.E. "Role of diffusive overturning in non-linear axisymmetric convection in a differentially heated rotating annulus". Geophys. Fluid Dyn., 1, 59, (1970b).

McNamara, L.F. "Statistical model of the D-region". Rad. Sci., 14, 1165, (1979).

McPetrie, J.S. "The reflection coefficient of the Earth's surface for radio waves". J. Inst. Elec. Engineers, 82, 214, (1938).

Manchester, R.N. "Correction to paper by H.K. Sen and A.A. Wyller "On the generalization of the Appleton-Hartree Magnetionic Formulas" ". J. Geophys. Res., 70, 4995, (1965).

Manson, A.H. "Comments on the theory of the differential absorption experiment". J. Geophys. Res., 71, 3783, (1966).

Manson, A.H., Merry, M.W.J., and Vincent, R.A. "Relationship between the partial reflection of radio waves from the lower ionosphere and irregularities as measured by rocket probes". Rad. Sci., 4, 955, (1969).

Manson, A.H., Meek, C.E., and Stening, R.J. "The role of atmospheric waves (1.5h to 10 days) in the dynamics of the mesosphere and lower thermosphere at Saskatoon (52°N, 107°W) during the seasons of 1976". J. Atmos. Terr. Phys., 41, 325, (1979).

Manson, A.H., and Meek, C.E. "Gravity waves of short period (5-90 min) in the lower thermosphere at 52°N (Saskatoon, Canada)." J. Atmos. Terr. Phys., 42, 103, (1980).

Marcum, J.I. "A statistical theory of target detection by pulsed radar". I.R.E. transactions on Information Theory, IT6, 59-267, (1960).

Mathews, J.D., Shapiro, J.H., and Tanenbaum, B.S. "Evidence for distributed scattering in D-region partial reflection processes". J. Geophys. Res., 78, 8266, (1973).

Mechtly, E.A., and Smith, L.G. "Growth of the D-region at Sunrise" J. Atmos. Terr. Phys., 30, 363, (1968).

Mechtly, E.A., Bowhill, S.A., and Smith, L.G. "Changes of lower ionosphere electron concentrations with solar activity". J. Atmos. Terr. Phys., 34, 1899, (1972).

Meek, C.E., and Manson, A.H. "Comparisons between time variations in D-region winds and electron densities at Saskatoon, Canada (52°N, 106°W). J. Atmos. Terr. Phys., 40, 1267, (1978).

Merrill, J.T. "Observational and theoretical study of shear instability in the airflow near the ground". J. Atmos. Sci., 34, 911, (1977).

Merrill, J.T., and Grant, J.R. "A gravity-wave-critical-level encounter observed in the atmosphere". J. Geophys. Res., 84, 6315, (1979).

Miles, J.W. "On the stability of heterogeneous shear flows". J. Fluid Mech., 10, 496, (1961).

Miller, K.L., Bowhill, S.A., Gibbs, K.P., and Countryman, I.D. "First measurements of mesospheric vertical velocities by VHF radar at temperate latitudes". Geophys. Res. Letts., 5, 939, (1978).

Miller, K.L., and Smith, L.G. "Incoherent scatter radar observations of irregular structure in mid-latitude sporadic-E layers". J. Geophys. Res., 83, 3761, (1978).

Mitra, S.N. "A radio method of measuring winds in the ionosphere" Proc. I.E.E., 96, 441, (1949).

Montbriand, L.E., and Belrose, J.S. "Changes in electron precipitation inferred from spectra deduced from D-region electron densities during a post-magnetic storm effect". J. Geophys. Res., 81, 2213, (1976).

Muller, H.G. "Simultaneous observations of meteor winds and ionospheric drifts". J. Atmos. Terr. Phys., 30, 701, (1968).

Muller, H.G., and Nelson, L. "A travelling quasi 2-day wave in the meteor region". J. Atmos. Terr. Phys., 40, 761, (1978).

Murgatroyd, R.J. "The global circulation of the atmosphere" (Ed. G.A. Corby), Roy. Met. Soc., Lond., p.159, (1969).

Newman, D.B., and Ferraro, A.J. "Amplitude distributions of partially reflected signals from the mid-latitude D region". J. Geophys. Res., 81, 2442, (1976).

Nicol, J.L. (Unpublished) "An investigation into the effects of the earth upon the properties of horizontal antennas at high frequencies". Ph.D. Thesis, James Cook University, Queensland, (1974).

Nicol, J.L. "The input impedance of horizontal antennas above an imperfect plane earth". Rad. Sci., 15, 471, (1980).

Norton, K.A., Vogler, L.E., Mansfield, W.V., and Short, P.J. "The probability distribution of the amplitude of a constant vector plus a Rayleigh distributed vector". Proc. I.R.E., 43, 1354, (1955).

Offermann, D. "Recent advances in the study of the D-region winter anomaly". J. Atmos. Terr. Phys., 41, 735, (1979).

Ottersten, H. "Mean vertical gradient of potential refractive index in turbulent mixing and radar detection of CAT". Rad. Sci., 4, 1247, (1969a).

Ottersten, H. "Radar backscattering from the turbulent clear atmosphere". Rad. Sci., 4, 1251, (1969b).

Parameswaran, K., and Krishnamurthy, B.V. "Ionospheric absorption at the magnetic equator using the A1 technique". J. Atmos. Terr. Phys., 40, 1211, (1978).

Parthasarathy, R. "Mesopause dust as a sink for ionization". J. Geophys. Res., 81, 2392, (1976).

Phillips, G.J., and Spencer, M. "The effects of anisometric amplitude patterns in the measurement of ionospheric drifts". Proc. Phys. Soc., 68B, 481, (1955).

Piggott, W.R., Beynon, W.J.G., Brown, G.M., and Little, C.G. "The measurement of ionospheric absorption". Annals International Geophysical Year, 3, 175, (1957). Pergamon Press, Lond., N.Y., Paris.

Piggott, W.R., and Thrane, E.V. "The effect of irregularities in collision frequency on the amplitude of weak partial reflections". J. Atmos. Terr. Phys., 28, 311, (1966).

Pitteway, M.L.V., and Hines, C.O. "The reflection and ducting of atmospheric acoustic-gravity waves". Can. J. Phys., 43, 2222, (1965).

Proctor, R.F. "Input impedance of horizontal dipole aerials at low heights above the ground". J. Inst. Elec. Engineers, 97, 188, (1950).

Ranta, H., and Ranta, A. "Daily variation of absorption in the D-region using riometer data at high latitudes". J. Atmos. Terr. Phys., 39, 309, (1977).

Rastogi, P.K., and Woodman, R.F. "Mesospheric studies using the Jicamarca incoherent-scatter radar". J. Atmos. Terr. Phys., 36, 1217, (1974).

Rastogi, P.K., and Bowhill, S.A. "Scattering of radio waves from the mesosphere - 1. Theory and observations". J. Atmos. Terr. Phys., 38, 399, (1976a).

Rastogi, P.K., and Bowhill, S.A. "Scattering of radio waves from the mesosphere - 2. Evidence for intermittent mesospheric turbulence". J. Atmos. Terr. Phys., 38, 449, (1976b).

Ratcliffe, J.A. "Some aspects of diffraction theory and their application to the ionosphere". Reps. Prog. Phys., 19, 188, (1956).

Ratcliffe, J.A. "The magneto-ionic theory and its applications to the ionosphere". Cambridge University Press, (1959).

Ratcliffe, J.A. "Sun, Earth and Radio", World University Library, Weidenfeld and Nicolson, London, (1970).

Ratcliffe, J.A. "An introduction to the ionosphere and magnetosphere". Cambridge University Press, London, (1972).

Rayleigh, Lord. "Theory of Sound" Vol.I, pp.35-42. Pr. by McMillan and Co., (1894).

Rees, D., Roper, R.G., Lloyd, K.H., Low, C.H. "Determination of the structure of the atmosphere between 90 and 250 km by means of contaminant releases at Woomera, May 1968". Phil. Trans. Roy. Soc., A271, 631, (1972).

Reid, G.C. "The production of water-cluster positive ions in the quiet day-time D region". Planet. Space Sci., 25, 275, (1977).

Rice, S.O. "Mathematical Analysis of Random Noise". Bell Sys. Tech. Jour., 23, 282-332, (1944).

The above is an incomplete article, and was continued in the following reference:-

Rice, S.O. "Mathematical Analysis of Random Noise". Bell Sys. Tech. Jour., 24, 46-156, (1945).

[Rice's works were also published as "Bell Telephone Monograph B-1589", and have been included in "Selected Papers on Noise and Stochastic Processes", N. Wax, Ed., Dover Publ., New York, 1954].

Rind, D. "Heating of the lower thermosphere by the dissipation of acoustic waves". J. Atmos. Terr. Phys., 39, 445, (1977).

Roble, R.G., and Schmidtke, G. "Calculated ionospheric variations due to changes in solar EUV flux measured by the AEROS spacecraft". J. Atmos. Terr. Phys., 41, 153, (1979).

Röper, R.G. "Atmospheric turbulence and eddy diffusion in the lower thermosphere". XVth Assembly of the IUGG, Moscow. IAMAP/IAGA Symposium on dynamics of the mesosphere and lower thermosphere. Aug. 6, (1971).

Rose, G., and Widdel, H.U. "An experimental contribution to the question of transient couplings of tropospheric planetary pressure waves and changes in the short wave radio wave absorption in the D region of the ionosphere". J. Atmos. Terr. Phys., 39, 51, (1977).

Röttger, J., and Vincent, R.A. "VHF radar studies of tropospheric velocities and irregularities using spaced antenna techniques". Geophys. Res. Letts., 5, 917, (1978).

Röttger, J., Rastogi, P.K., and Woodman, R.F. "High resolution VHF radar observations of turbulence structures in the mesosphere". Geophys. Res. Letts., 6, 617, (1979).

Röttger, J., and Schmidt, G. "High resolution VHF radar sounding of the troposphere and stratosphere". IEEE Trans. on Geoscience Electronics, GE-17, 182, (1979).

Röttger, J. "Reflection and scattering of VHF radar signals from atmospheric refractivity structures". Rad. Sci., 15, 259, (1980a).

Röttger, J. "Structure and dynamics of the stratosphere and mesosphere revealed by VHF radar investigations". Pure and Applied Geophysics, 118, 494, (1980b).

Rowe, J.F.(Jr.). "Downward transport of night-time E_s-layers into the lower E-region at Arecibo". J. Atmos. Terr. Phys., 30, 225, (1974).

Saxton, J.A., Lane, J.A., Meadows, R.W., and Mathews, P.A. "Layer structure of the troposphere". Proc. IEE, London, 111, 275, (1964).

Schlegel, K., Rose, G., and Widdel, H.U. "Interplanetary magnetic field polarity changes and D-region radio wave absorption". J. Atmos. Terr. Phys., 39, 101, (1977).

Schlegel, K., Brekke, A., and Haug, A. "Some characteristics of the quiet polar D region and mesosphere obtained with the partial reflection method". J. Atmos. Terr. Phys., 40, 205, (1978).

Schmidlin, F.J. "Temperature inversions near 75 km". Geophys. Res. Letts., 3, 173, (1976).

Schmidt, G., Ruster, G.R., and Czechowsky, P. "Complementary code and digital filtering for detection of weak VHF radar signals from the middle atmosphere". IEEE. Trans. Geosci. Electr., GE-17, 154, (1979).

Schminder, R., and Kurschner, D. "On the behaviour of wind systems in the upper mesopause region during the transition from summer to winter conditions". J. Atmos. Terr. Phys., 40, 165, (1978).

Schwentek, H. "The variation of ionospheric absorption from 1956 till 1963". J. Atmos. Terr. Phys., 25, 733, (1963).

Schwentek, H. "Some results obtained from the European Co-operation concerning studies of the winter anomaly in ionospheric absorption". Proc. Symp. on Lower Ionosphere Structure, ed. by K. Rawer, Akademie, Berlin, p.293 (1974).

Schwentek, H. "Ionospheric absorption between 53°N and 53°S observed on board ship". J. Atmos. Terr. Phys., 38, 89, (1976).

Scorer, R.S. "Environmental aerodynamics". publ. by John Wiley and Sons; NY, Lond., Sydney, Toronto, (1978).

Sen, H.K., and Wyller, A.A. "On the generalization of the Appleton-Hartree Magnetionic Formulas". J. Geophys. Res., 65, 3931, (1960).

Sidi, C., and Teitelbaum, H. "Thin shear turbulent layers within the lower thermosphere induced by non-linear interaction between tides and gravity waves". J. Atmos. Terr. Phys., 40, 529, (1978).

Simpson, J.H., and Woods, J.D. "Temperature microstructure in a fresh-water thermocline". Nature, 226, 832, (1970).

Sinno, K. "On the time delay of the appearance of sporadic E following meteor activity". J. Atmos. Terr. Phys., 42, 35, (1980).

Slater, J.C., and Frank, N.H. "Electromagnetism". McGraw-Hill Book Co., NY and Lond. (1947).

Smith, L.G., Walton, E.K., and Mechtly, E.A. "Vertical incidence absorption calculated using electron density profiles from rocket experiments and comparison with observations during the winter anomaly". J. Atmos. Terr. Phys., 40, 1185, (1978).

Smith, L.G., and Miller, K.L. "Sporadic-E layers and unstable wind shears". J. Atmos. Terr. Phys., 42, 45, (1980).

Smith, M.S. "Theoretical properties of atmospheric acoustic-gravity waves". J. Atmos. Terr. Phys., 39, 69, (1977).

Sprenger, K., and Schminder, R. "On the significance of ionospheric drift measurements in the LF range". J. Atmos. Terr. Phys., 30, 693, (1968).

Starling, S.G., and Woodall, A.J. "Physics". Longmans, Green & Co; Lond., New York, Toronto, (1950).

Stewart, R.W. "Turbulence and waves in a stratified atmosphere". Rad. Sci., 4, 1269, (1969).

Stubbs, T.J. "The measurement of winds in the D region of the ionosphere by the use of partially reflected radiowaves". J. Atmos. Terr. Phys., 35, 909, (1973).

Stubbs, T.J., and Vincent, R.A. "Studies of D-region drifts during the winters of 1970-1972". Aust. J. Phys., 26, 645, (1973).

Stubbs, T.J. "Mean and periodic components of ionospheric drifts in the D region at 35°S during 1972". J. Atmos. Terr. Phys., 38, 979, (1976).

Stubbs, T.J. "A study of ground diffraction parameters associated with D-region partial reflections". J. Atmos. Terr. Phys., 39, 589, (1977).

Sudan, R.N., Akinrimisi, J., and Farley, D.T. "Generation of small-scale irregularities in the equatorial electrojet". J. Geophys. Res., 78, 240, (1973).

Tabor, D. "Gases, liquids and solids". Penguin Library of Physical Sciences; Physics/Chemistry. Printed in Gr. Britain by Bell and Bain Ltd., Glasgow, (1970).

Tatarski, V. "Wave propagation in a turbulent medium" Translated from Russian by Silverman. McGraw-Hill, (1961). 285 pp.

Taubenheim, J. "Information on the ionizing radiation of solar flares from the ionospheric absorption effect". J. Atmos. Terr. Phys., 24, 191, (1962).

Teitelbaum, H., and Sidi, C. "Formation of discontinuities in atmospheric gravity waves". J. Atmos. Terr. Phys., 38, 413 , (1976).

Teitelbaum, H., and Blamont, J.E. "Variations of the turbopause altitude during the night". Planet. Space Sci., 25, 723, (1977).

Teitelbaum, H., and Cot, C. "Antisymmetric tidal modes under equinoctial conditions induced by ozone heating". J. Atmos. Terr. Phys., 41, 33, (1979).

Tennekes, H., and Lumley, J.L. "A first course in turbulence". Cambridge, Mass., MIT Press (1973). 300 pp.

Thomas, L. "The lower ionosphere". J. Atmos. Terr. Phys., 33, 157, (1971).

Thomas, L. "Mesospheric temperatures and the formation of water cluster ions in the D-region". J. Atmos. Terr. Phys., 38, 1345, (1976).

Thorpe, S.A. "Instability and waves". Weather, 34, 102, (1979).

Thrane, E.V., Haug, A., Bjelland, B., Anastassiades, M., and Tsagakis, E. "Measurements of D-region electron densities during the International Quiet Sun Years". J. Atmos. Terr. Phys., 30, 135, (1968).

Titheridge, J.E. "The electron density in the lower ionosphere". J. Atmos. Terr. Phys., 24, 269, (1962a).

Titheridge, J.E. "The stratification of the lower ionosphere". J. Atmos. Terr. Phys., 24, 283, (1962b).

Tohmatsu , T., and Wakai, N. "An investigation of night-time ionizing sources in low- and mid-latitudes". Ann. Geophys., 26, 209, (1970).

Torr, D.G., and Torr, M.R. "Chemistry of the thermosphere and ionosphere". J. Atmos. Terr. Phys., 41, 797, (1979).

Trost, T.F. "Electron concentrations in the E and upper D region at Arecibo". J. Geophys. Res., 84, 2736, (1979).

Trott, G.W. (Unpublished). "Buckland Park Aerial problems". Report for the degree of Hons. B.Sc., University of Adelaide, (1967).

USSA. U.S. Standard Atmosphere, (1962).

Van Allen, J.A. "Propagation of a Forbush decrease in Cosmic Ray Intensity to 15.9AU". Geophys. Res. Letts., 6, 566, (1979).

Van der Ziel, A. "Noise". Prentice Hall Inc., NJ, (1954).

Van Zandt, T.E., Green, J.L., Gage, K.S., and Clark, W.L. "Vertical profiles of refractivity turbulence structure constant: Comparison of observations by the Sunset radar with a new theoretical model". Rad. Sci., 13, 819, (1978).

Van Zandt, T.E., Green, J.L., Clark, W.L., and Grant, J.R. "Buoyancy waves in the troposphere; Doppler radar observations and a theoretical model". Geophys. Res. Letts., 6, 429, (1979).

Verlarde, M.G., and Normand, C. "Convection". Scientific American, 243, No.1., p.78, (1980).

Vidal-Madjar, D. "Gravity wave detection in the lower thermosphere with the French Incoherent scatter facility". J. Atmos. Terr. Phys., 40, 685, (1978).

Villars, F., and Weiskopf, V.F. "On the scattering of radio waves by turbulent fluctuations in the atmosphere". Proc. I.R.E., 43, 1232, (1955).

Vincent, R.A. (Unpublished). "Lower ionospheric irregularities". Thesis, University of Canterbury, Christchurch, New Zealand, (1967).

Vincent, R.A. "A Criterion for the Use of the Multi-layer approximation in the study of Acoustic-Gravity Wave propagation". J. Geophys. Res., 74, 2996, (1969).

Vincent, R.A. "The interpretation of some observations of radio waves scattered from the lower ionosphere". Aust. J. Phys., 26, 815, (1973).

Vincent, R.A., Stubbs, T.J., Pearson, P.H.O., Lloyd, K.H., and Low, C.H. "A comparison of partial reflection drifts with winds determined by rocket techniques". J. Atmos. Terr. Phys., 39, 813, (1977).

Vincent, R.A., and Ball, S.M. "Tides and gravity waves in the mesosphere at mid and low latitudes". J. Atmos. Terr. Phys., 39, 965, (1977).

Vincent, R.A., and Stubbs, T.J. "A study of motions in the Winter Mesosphere using the partial reflection drift technique". Planet. Space Sci., 25, 441, (1977).

Vincent, R.A., and Belrose, J.S. "The angular distribution of radio waves partially reflected from the lower ionosphere". J. Atmos. Terr. Phys., 40, 35, (1978).

Vincent, R.A., and Röttger, J. "Spaced antenna VHF radar observations of tropospheric velocities and irregularities". Rad. Sci., 15, 319, (1980).

Von Biel, H.A., Flood, W.A., and Camnitz, H.G. "Differential-phase partial-reflection technique for the determination of D region ionization". J. Geophys. Res., 75, 4863, (1970).

Von Biel, H.A. "Amplitude Distributions of D-Region Partial Reflections". J. Geophys. Res., 76, 8365, (1971).

Von Biel, H.A. "The phase-switched correlation polarimeter - a new approach to the partial reflection experiment". J. Atmos. Terr. Phys., 39, 769, (1977).

Von Biel, H.A. "The use of amplitude distributions in practical data assessment problems". J. Atmos. Terr. Phys., 41, 1201, (1979).

Wakasugi, K., Kato, S., and Fukao, S. "Depolarization of a 50-HHz radio wave back scattered from the middle atmosphere". Rad. Sci., 15, 439, (1980).

Weinstock, J. "On the theory of turbulence in the buoyancy subrange of stably stratified flows". J. Atmos. Sci., 35, 634, (1978).

Whalen, A.D. "Detection of signals in noise". Academic Press, New York and Lond., (1971).

Whitehead, J.D. "The formation of the sporadic-E layer in the temperate zones". J. Atmos. Terr. Phys., 20, 49, (1961).

Whitehead, J.D. "The partially aligned gradient instability in the ionosphere". J. Geophys. Res., 81, 1361, (1976).

Wofsy, S., and McElroy, M. "On vertical mixing in the Upper Stratosphere and Mesosphere". J. Geophys. Res., 78, 2619, (1973).

Woodman, R.F., and Guillen, A. "Radar observations of winds and turbulence in the stratosphere and mesosphere". J. Atmos. Sci., 31, 493, (1974).

Woodman, R.F. "High-altitude-resolution stratospheric measurements with the Arecibo 430 MHz radar". Rad. Sci., 15, 417, (1980a).

Woodman, R.F. "High-altitude-resolution stratospheric measurements with the Arecibo 2380-MHz radar". Rad. Sci., 15,423, (1980b).

Woods, J.D. "On Richardson's number as a criterion for laminar-turbulent-laminar transition in the ocean and atmosphere". Rad. Sci., 4, 1289, (1969).

Wratt, D.S. "Variations in electron density in the middle latitude D-region above Urbana, Illinois". J. Atmos. Terr. Phys., 39, 607, (1977).

Wright, J.W. "The interpretation of ionospheric radio drift measurements. I. Some results of experimental comparisons with neutral wind profiles". J. Atmos. Terr. Phys., 30, 919, (1968).

Wright, J.W., and Pitteway, M.L.V. "Computer simulation of ionospheric radio drift measurements and their analysis by correlation methods". Rad. Sci., 13, 189, (1978).

Wunsch, C. "Temperature microstructure on the Bermuda slope with application to the mean flow". Tellus, 24, 350, (1972).

Zimmerman, S.P., and Narcisi, R.S. "The winter anomaly and related transport phenomena". J. Atmos. Terr. Phys., 32, 1305, (1970).

THESIS ERRATA

1. P.356 7 lines and 9 lines down. "Fig 7.18" should read "Fig 7.19"

2. Appendix H : Platteville NOT Plattarville

3. P. 389 delete one ")" after "equation B.21"; and add a ")" at end of paragraph

4. P. 239 : 10 lines down : delete "Rastogi" - replace with "Röttger"

5. P. 97 : 4th to last line : "wirte" becomes "write"

6. P. 98 : 2nd line : "$\ell = 1/k_{turb} = \lambda/4\pi$", NOT "$4\lambda/4\pi$"

7. P. 359 : equation 7.4.4.12 : v_{radt}, NOT V_{radt}

8. P. 395 : 6 lines up from bottom : "measurements"

9. P. 398 : 2.8R on upleg ; 1.6R on downleg

10. P. 400 : 2nd to bottom line " "control" becomes "central"

11. P. 401 : 8 lines down "warranged" becomes "warranted"

12. P. 72 : ½ way down page : "Weisokopf" becomes "Weisskopf"

13. P. 407 : (i) " echoes appear" → " echoes appear"

14. 3rd page of table at end of Chapter 2 (after p. 147)
" $\ell = 4\pi/\lambda_i$ " is wrong - should read " $\ell = \lambda_i/4\pi$ "

15. Fig 8.6 (i) "95.1 km" should be "95.9 km"
(ii) The "800m" arrow should be stretched to 62mm long.

16. P. 365 equation 7.4.5.5 $\varepsilon_d \approx A^{-\frac{2}{3}} v_H^3/\ell$ becomes $\varepsilon_d \approx A_i^{-3/2} v_H^3/\ell$.

17. Equation prior to 7.4.5.6b should read $\overline{v_H^2} = \alpha_i \varepsilon_d^{\frac{2}{3}} \cdot \frac{3}{2} \cdot (2\pi/\ell_1)^{-\frac{2}{3}}$.

[In connection with 16 and 17, also see "SPECIAL ERROR" pages.]

18. P. 366 : 9 lines from bottom : ")" after "Tatarski"

19. Page E.4 : Program error : use F(A, Phi), F(B, Phi)
and F(A + (2*K-1)**H, Phi)
i.e. delete reference to "θ" - the convolution is a function of R and ϕ only.

20. P. 174 : middle equation (un-numbered)
"steradian is $\underline{\sigma}\ (Pt/h^2)\ e^{-\frac{2\omega}{c}\int_o^h \mu_I ds}\ V_{eff}$, "

21. Equation 10.3.1.6 $A = \exp\{-4\int_{s=o}^{h} \ldots$, NOT $\exp\{-4\int_{s=o}^{L} \ldots$

22. Equation 3.3.2.19 $R^2 = (\frac{4\sigma}{h^2})\ V_{eff}$, NOT $(\frac{4\sigma}{h})\ V_{eff}$

23. P. xii : para 4, line 4; Chapter IV, not II

24. P. xiv : line 10, after "determination of turbulence parameters" add "if beam broadening is significant"

25. P. 13 : line 8, Dieminger (1968)

26. P. 30 : para 2, line 9 : NOT "sodium-based vapour trails" but "tri methyl aluminium vapour trails"

27. P. 91 : last line $< [\ \underline{v}\ (\underline{x}) - \underline{v}(\underline{x}+\underline{\ell})\ ]^2 >^{\frac{1}{2}}$

28. P. 93 : line 7, "(ignoring small fluctuations)" [i.e. insert ")" after "fluctuations"]

29. P. 110 : line 16; "viscous dissipation rate" should strictly be prefaced by "turbulent"

30. P. 116 : line 12, add "(provided P_r is known)" after "into it"

31. P. 120 : bottom : $g = f + \frac{1}{2}r\frac{df}{dr}$, NOT $f + \frac{1}{2}r\frac{dp}{dr}$.

32. P. 121 : Insert "inertial" in front of "isotropic" on line 13.

33. P. 141 : 5 lines from bottom : delete "by" which occurs in front of "(or"

34. P. 152 : line 11, Replace "beaten down" with "heterodyned".

35. P. 320 : para 3, line 1 : "cpapble" → "capable"

36. P. 345 : para 3, line 3, Delete reference to Elford and Roper, 1961.

37. P. 372 : 5 lines from bottom : "sidebbe" → "sidelobe"

38. P. 359 : equation 7.4.4.11 becomes

$$\theta = \sin^{-1} V/ \{\tfrac{1}{2} (1 + \cos 2(\phi_0 - \phi)) \}^{\frac{1}{2}}$$

39. P. 413 : para 1, line 8 : "at least" → "at best"

40. P. 434 : delete 7th line from bottom.

41. P. 444 : One examiner found that equation (10.3.1.5) read as " ≈ .42 to - .37" However, the original, and my copy, has ≈ .42 to .37". The "-" may have been some dust which got in during photocopying.

42. P. 468 : line 4, "phenomenum" → "phenomenon"

43. P. C1 : bottom of page : F_i are the "components", not "co-ordinates"

44. P. C3 : line 6, "can lead this to other...." delete "this"

45. References

Curnow, Technical note PAD 118 (1966)
Lindzen, ed. F. Verniani, (1974)
Sen....Magnetoionic (1960)

46. P. 91 : 11 lines up from bottom - insert after "v_ℓ and ℓ" -

" But it now becomes important to decide on the units of v_ℓ and ℓ "

SPECIAL ERRORS

This item discusses the only serious errors found to date. (Ch VII, II)

On P365 - 366, there are several errors.

Firstly, at the bottom of P.365, I have given the wrong normalizations. The bottom 5 lines of P. 365, and p. 366, should be replaced with the following. (There was also a numerical error on P.366 which has now been corrected)

Then

$$\overline{v_H^2} = \int_{-\infty}^{-k_1} E_i(k_i)\,dk_i + \int_{k_1}^{\infty} E_i(k_i)\,dk_i = 2\int_{k_1}^{\infty} \alpha_i\, \varepsilon_d^{2/3}\, k_i^{-5/3}\, dk_i$$

where $k_1 = 2\pi/\ell_1$

[Recall that two normalizations can be used;

(i) $$\int_{-\infty}^{-k_1} E_i(k_i)\,dk_i + \int_{k_1}^{\infty} E_i(k_i)\,dk_i = \overline{u'^2}\,, \quad \text{and}$$

(ii) $$\int_{-\infty}^{k_1} E_i(k_i)\,dk_i + \int_{k_1}^{\infty} E_i(k_i)\,dk_i = \overline{u'^2}/2.$$

where u' is the fluctuating component. I shall use case (i), as the formulae derived willl involve longitudinal and transverse spectra, and the α_ℓ, α_t values given in Table 2.1, Chapter II, assumed this normalization].

Thus $$\overline{v_H^2} \approx 2\alpha_i\, \varepsilon_d^{2/3} \cdot \frac{3}{2} \cdot (2\pi/\ell_1)^{-2/3}\,,$$ (note typographical errors in this formula in original text),

or

(7.4.5.6b) $$\varepsilon_d \approx T_{2D}^{-1}\, \frac{v_H^3}{\ell_1} \quad \text{(assuming } (\overline{v_H^2})^{3/2} \approx v_H^3\text{)},$$

where $T_{2D} = 0.827\,(\alpha_i)^{3/2}$

(It can be seen that this differs from the equation

$T_{2D} \approx 11.5\,\alpha_i^{3/2}$ on P. 366: this is partly due to the re-normalization and partly due to a numerical error on P. 366).

Then by Tatarski (1961, Equation 2.22),

(7.4.5.6c) $\alpha_i \approx 2.488\ A_i$ (after appropriate change of notation, and compensation for the fact that the normalization

$\int E_i(k_i)dk_i = \overline{u'^2}/2$ is used in Tatarski).

Hence $T_{2D} \approx 0.1026\ A_i^{3/2}$

Thus, for the longitudinal component, if $A_\ell = 2.0$ then $T_{2D} \approx 0.29$, and for the transverse component in 2-D turbulence, using

$$A_t = 3.3, \quad T_{2D} \approx 0.62.$$

It is instructive to compare 7.4.5.4 (i.e. $\varepsilon_d \approx A_i^{-3/2}\ \sigma^3/\ell$)

with $\varepsilon_d \approx (.1026\ A_i^{3/2})^{-1}\ v_H^3/\ell$

We then see

$$* \quad \sigma \approx 2.13\ v_H \quad *$$

In equation 7.4.5.5 I assumed $\sigma \approx v_H$ and we now see this is not valid. Yet both σ and v_H "look like" RMS velocities. Whey are they different ?

Consider the diagram below of the energy spectrum:

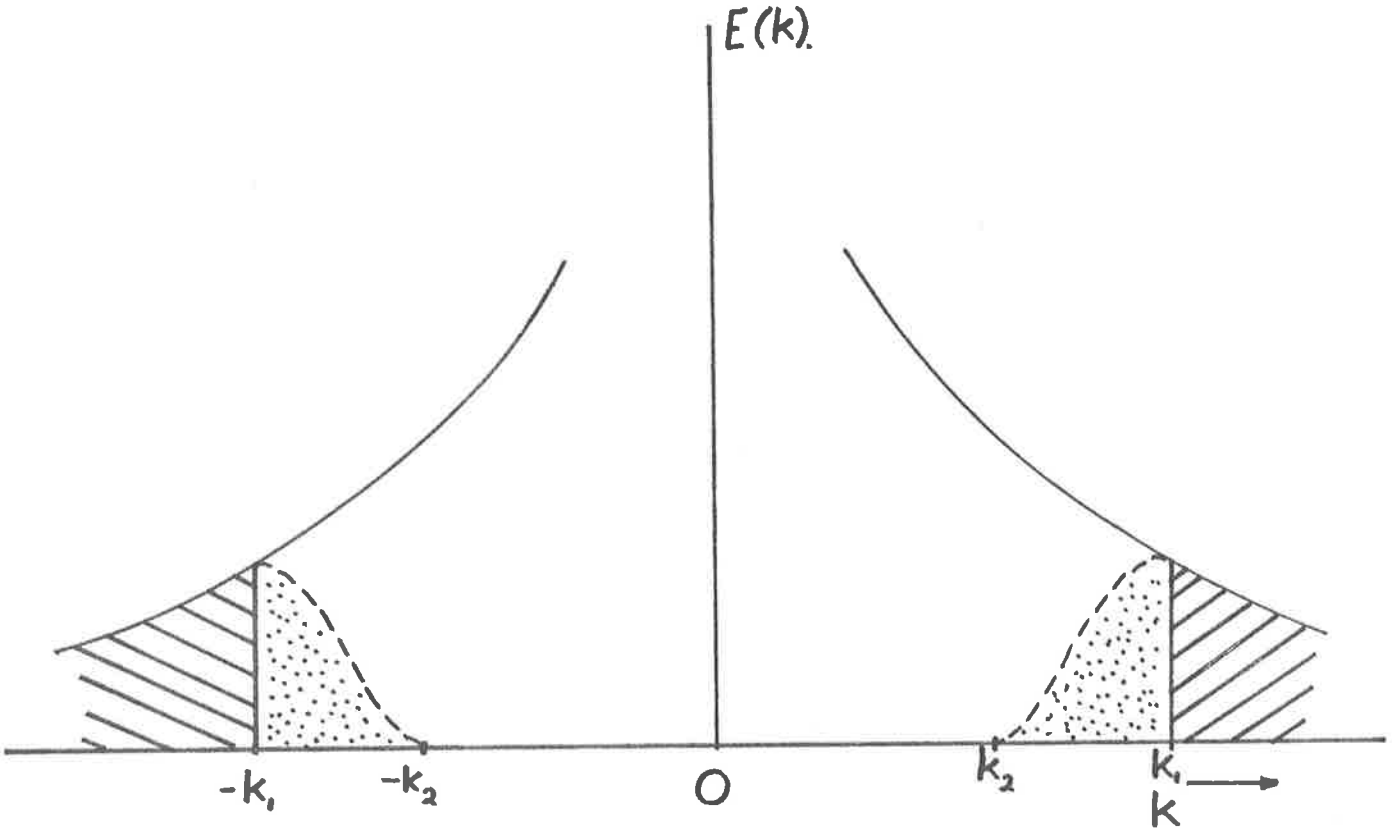

In the derivation of

$$\varepsilon_d \approx (.1026\ A_i^{3/2})^{-1}\ v_H^{\ 3}/\ell_1,$$

I assumed (defined) that the hatched area was equal to $\overline{v_H^{\ 2}}$. Only scales less than ℓ_1 contribute. But when the structure function between two separated points with separation ℓ_1 is formed, this in fact contains contribution from scales $> \ell_1$ (e.g. a scale of length $2\ell_1$ can fit half an oscillation in this distance). The larger the scale, however, the less its contribution to the structure function. Thus σ^2 can be regarded as the shaded area plus the dotted area.

Hence it can be seen that there is a subtle difference between σ and v_H.

(Note that the equation $\sigma = 2.13\ v_H$ is only valid if the form of $E(k)$ is $k^{-5/3}$ over the region $(-\infty$ to $-k_2)$ and $(k_2$ to $\infty)$ - otherwise the result is different. If the spectral form changes, so will the constant. For example, if the spectrum fell abruptly to 0 at scales between $-k_1$ and k_1, then $\sigma = v_H$).

I shall not carry these corrections through the rest of the thesis. These results mean that my ε estimates following P.366 are too small (although the calculations using Fig 7.22 will be accurate)

If the correct T_{2D} values are used, it will be seen that the true ε estimates are much too large to be due to turbulence. Values $\gtrsim 1$ Wkg^{-1} usually result, and turbulence produces ε values of $\lesssim 0.1$ Wkg^{-1}.

[In connection with ε, I should point out a conceptual consideration. In 3-D turbulence, ε refers to the energy dissipation rate. For 2-D turbulence, there is no energy dissipation. In two-dimensional atmospheric turbulence, the process of smaller eddies acting coherently to produce larger ones is important (e.g. theory due to Kraichnan: e.g. see Phys. Fluids 10, 1417, (1967); J. Atmos. Sci., 33, 1521, 1976). It is not correct to regard the energy as being dissipated as heat; - the smallest scales involved are much larger than the Kolmogoroff microscale. So in this sense, it may be erroneous to interpret "ε" as determined from a spectrum of two-dimensional motions as an "energy dissipation rate"]

As a further point, notice that for transverse motion we now have

$$(1a) \quad \varepsilon_d \approx 6.4\ v^3/\ell$$

This is more compatible with, say, Weinstock, J. Atmos. Sci. 35, 1022 (1978) Equation 26, where he suggests

$$(1b) \quad v^2 \approx 1.5\ \varepsilon^{2/3}\ k^{-2/3}, \quad \text{or} \quad \varepsilon \approx 3.4\ v^3/\ell$$

Other authors at times assume $\varepsilon \approx v^3\ k^{-1}$, or

$$1(c) \quad \varepsilon \approx 6.3\ v^3/\ell$$

e.g. Zimmerman and Murphy, "Dynamical and Chemical Coupling between the neutral and ionized atmospheres" Proc. NATO Advanced Study Institute held at Spatind, Norway, 1977. P35-47. It will also be noted in that reference that the formula $\varepsilon_d = 1/3\ \overline{v_{RMS}}^2\ f_b$ is derived (this formula is discussed on P. 371 of the thesis), and v_{RMS} refers to the velocity associated with the transition wavenumber between the bouyant and inertial subranges of turbulence (not the Kolmogoroff microscale, as I speculate on P. 371).
In connection with the formula

$$\varepsilon \sim \frac{v^3}{\ell}$$

I should mention another point. At times, various authors (e.g. Cunnold, 1975) have assumed $\ell \sim \lambda/4\pi$, λ being the radar wavelength. I made a similar assumption in Chapter II; e.g. pages 91-99.

I have since realized that this is not valid. True, only eddies of scale $\sim \lambda/4\pi$ will be seen by the radar. However, these will be carried by the motions of larger eddies; and if the radar volume is much larger than the largest eddies, the appropriate scale for ℓ is the transition scale between the inertial and bouyancy ranges, since horizontal motions are suppressed at larger scales. If this is assumed, and we take the transition scale as $L_B \sim \varepsilon^{\frac{1}{3}}\ \omega_B^{-3/2}$ (e.g. equation 2.2.4.2a, p. 108), we arrive at the formula $\varepsilon \sim v^2 \omega_B$.

This is similar to the formula on P. 371 of the thesis. Perhaps one of the best derivations of the formula to date is that due to Wanstock, J. Atmos. Sci., 38, 880-883, (1981), who obtains

$$\varepsilon = 0.4\, v_{RMS}^{2}\, \omega_{B}$$